Year : 2019

ICE-EXTENT VARIATIONS AND POST-GLACIAL EROSION IN THE MONT BLANC MASSIF

Lehmann Benjamin

Lehmann Benjamin, 2019, ICE-EXTENT VARIATIONS AND POST-GLACIAL EROSION IN THE MONT BLANC MASSIF

Originally published at : Thesis, University of Lausanne

Posted at the University of Lausanne Open Archive http://serval.unil.ch
Document URN : urn:nbn:ch:serval-BIB_2077596C0B8A1

UNIL | Université de Lausanne
Institut des dynamiques
de la surface terrestre

Faculté des géosciences et de l'environnement

Institut des dynamiques de la surface terrestre

Ice-extent variations and post-glacial erosion in the Mont Blanc massif

Thèse de doctorat

présentée à la Faculté des géosciences et de l'environnement de l'Université de Lausanne

pour l'obtention du grade de Docteur en sciences de la Terre par

Benjamin Lehmann

Master en Sciences de la Terre et de l'Environnement, spécialité Terre Solide

de l'Université Grenoble Alpes

Jury

Prof. Dr. Christian Kull	Université de Lausanne	Président du jury
Prof. Dr. Frédéric Herman	Université de Lausanne	Directeur de thèse
Prof. Dr. Georgina E. King	Université de Lausanne	Expert interne
Prof. Dr. Andreas Lang	Université de Salzburg, Autriche	Expert externe
Prof. Dr. Derek Fabel	Université de Glasgow, Scotland, UK	Expert externe
Dr. Pierre G. Valla	Université de Grenoble Alpes, France	Expert externe

Lausanne, 2019

UNIL | Université de Lausanne
Faculté des géosciences et de l'environnement
bâtiment Géopolis bureau 4631

IMPRIMATUR

Vu le rapport présenté par le jury d'examen, composé de

Président de la séance publique :	M. le Professeur Christian Kull
Président du colloque :	M. le Professeur Christian Kull
Directeur de thèse :	M. le Professeur Frédéric Herman
Experte interne :	Mme la Professeure Georgina King
Expert externe :	M. le Professeur Andreas Lang
Expert externe :	M. le Professeur Derek Fabel
Expert externe :	M. le Docteur Pierre Valla

Le Doyen de la Faculté des géosciences et de l'environnement autorise l'impression de la thèse de

Monsieur Benjamin LEHMANN

Titulaire d'un
Master en sciences de la Terre et de l'Environnement, spécialité Terre solide de l'Université Grenoble Alpes

intitulée

Ice-extent variations and post-glacial erosion in the Mont Blanc massif

Lausanne, le 1er mai 2019

Pour le Doyen de la Faculté des géosciences et de l'environnement

Professeur Christian Kull

In dedication to my parents, Cécile and Michel,

to my brothers, David and Jérémie,

and to Gwladys, still shining wherever the sun is smiling.

“Ah! Young people, travel if you can,
and if you cannot - travel all the same!”
Jules Verne

Acknowledgements

I am going start to this acknowledgements section by addressing some words to my SUPERvisors. Frédéric thanks a lot for giving me the opportunity to work in your team. You teach me so much during this four years, always focussing positively on the science, supporting me during the up and down, even when I went off track :D! I consider you as my mentor but also as a great friend. Georgina thank you so much for all your help, your support and your positivity during these years and for teaching me luminescence! I owe you some whiskey bottles after my passage in Cologne... Pierre, thanks a lot for you constant support, your enthusiasm for science, for all the priceless discussions late at night, at skype or while drinking free EGU beers.

I had the chance to evolve in a cheerful team, where everyone brought its best part to share! Thanks Vjeran for being a true gentleman, and if our academic futur does not work, remember that we could start a moving company. Thanks Nadja for being so honest, the trip in Chile remain a highlight of my PhD. Thanks Joanne for being so cheerful and for feeding me! Thanks also Renske, Aleksandar and Chloé. I had also the chance to interact with skilful and high-spirited post-doct. Rabiul, Günther, Luca and Antoine, it was a great pleasure to evolve on your side! I had a great pleasure to work with outstanding student. Dilan, Aurélie, Arnaud, Ugo, Alexis, Fien, Arthur and Alexandre, it was a great fun to work with you!

I thank Andreas Lang and Derek Fabel for the time invested in reading my dissertation and giving their comments as well as judging my work, as well as the Swiss National Fund for the funding of my PhD, and the Societ Academique Vaudoise for integrating the funding at the end of my contract.

The fieldwork was one a the most challenging part of this PhD. I won't have as successful without the expert help of Dr. Sylvain Coutterand, thank you so much for that! Thanks also to Sebastian, Julia, Ugo, Gil and Nadja for the epic field excursions we made together.

I get the chance to spend few months in the ETH at Zürich to perform preparations and analysis. This has being made possible by Susan Ivy-Ochs and the help of Olivia Kronig, Ewelin Opyrchal and Stefano Casale. Thanks a lot! We had the chance in the institute to have skilful and cheerful support for lab, field and administrative sides. I would to thank Micaela Faria, Leatitia Montbaron, Aurelien Ballu, Sabrina Diamini and Carole Schrocker for their support!

Well, a PhD is a big piece of work but can also be a great piece of joke and laugh if you find the good friends and I was quite lucky here. Thanks to the Donkeys, you made my life as stupid as exciting. Mike, Seb, Femi, Gab, Maga, Nath, Giu, Sté, Martinou, Nico, Krikri, Alexis, Manu, Leanne, Erica, Zozo, Elfie, Elisa, Monica, Inigo, Aline, Pascal, Gilles, Francois, Lionel, Fina, JB, Nic ... tough to put the names on all these joyfull faces, but remember I LOVE YOU!

Je dedis ma thése à Gwladys Govin, ma petite soeur, grand sourrire lumineux qui nous laiss beaucoup trop tot. Je t'embrasse ma belle! Merci aux copains de toujours pour leur soutients: Dodo, Vincent, Romain Léo, Sonzo, Marion, Chouchou (Max), Sophie, Féfé, Sylvestre, Romain Prost, Alex, Matou, Paloma, Audrey.

Je finis par remercier ma famille. Mes parents Cécile et Michel pour être toujours là pour moi, pour nous avoir élever, mes frères et moi, dans l'amour, l'intégrité et la curiosité. Merci à mes frêres Jérémie et David pour m'avoir montrer la voie et pour avoir toujours cru en moi!

Lausanne, 8 juillet 2019

Synopsis

Afin d'appréhender l'effet des variations climatiques sur les environnements alpins, il est nécessaire d'étudier le passé des systèmes montagneux. Depuis le dernier maximum glaciaire (LGM), il y a environ 20 000 ans, les glaciers alpins se sont retirés des régions de plaine et de leurs zones d'accumulation en altitude. Cette transition modifia considérablement la géographie alpine en allimentant de grands lac d'eau douce, en libérant de considérable quantitée de sédiments et en exposant d'importantes étendues de surfaces rocheuses. Pourtant, les reconstitutions des conditions environnementales depuis le LGM restent peu documentées. Une des principales limitations est le manque de contraintes temporelles précises dans la reconstruction des extensions glaciaires passées.

Différentes méthodes géochronologiques ont été développées et appliquées pour dater les marqueurs géomorphologiques ou sédimentaires spécifiques de la dynamique des glaciers. Récemment, la datation de l'exposition de surface par luminescence stimulée optiquement (OSL) a été développée, offrant l'occasion d'améliorer les reconstructions des extensions glaciaires passées. Cette méthode est basée sur la sensibilité du signal OSL des minéraux à la lumiére. Lors d'une exposition le signal OSL est remis à zéro dans les premiers millimètres supérieurs de la surface rocheuse exposée.

Dans cette thèse, j'étudie le potentiel de la datation d'exposition de surface OSL à partir de polis glaciaires sur les flancs de la Mer de Glace, glacier emblématique du massif du Mont-Blanc. Je montre tout d'abord que cette méthode permet de reconstruire les épaisseurs passées du glacier depuis le Petit Âge Glaciaire, c'est à dire depuis la deuxime moitié du XIX^e siècle. Je montre ensuite que sur de plus longues périodes, la méthode est sensible à l'érosion de surface. En la combinant avec une autre méthode de datation: la datation par cosmogénie nucléide, je montre qu'il est possible de contraindre l'évolution de l'érosion de surface et des variations d'épaisseur du glacier depuis 20 000 ans.

En appliquant cette nouvelle approche sur des profiles verticaux de surfaces de roches moutonées sur les bords de la Mer de Glace, je démontre que l'intensité de l'érosion varie avec l'altitude. Plus les surfaces sont haute, plus l'érosion est faible. De plus, les résultats montrent des intensités d'érosion très fortes par rapport à ce qui est généralement admis dans ces environnements de montagnes. La distribution vertical et l'intentisté des taux d'érosion pourraient la conséquence des facteurs morphomètrique et climatiques propres aux environnement de haute montagne, comme la pente des surfaces rocheuses ou la distribution du manteau neigeux. Enfin, les reconstitutions glaciaires suggèrent des secnarios d'amincissement glaciaire potentiellement rapide à la fin du dernier maximum glaciaire.

Contents

Abstract

Assessing the impact of Quaternary glaciation at the Earth's surface implies understanding of the long-term evolution of alpine landscapes. In particular, it requires simultaneous quantification of the impact of climate variability on past glacier fluctuations and on bedrock erosion. Since the Last Glacial Maximum (LGM), about 20 kyr ago, Alpine glaciers retreated rapidly from lowland regions and thinned in their high-elevation source areas. This transition created widespread bare-bedrock surfaces that could then erode by a combination of large-scale debuttressing or local frost cracking and weathering. During this period, paleo-glacier reconstructions are limited because they often lack precise temporal constraint.

Different geochronological methods have been developed and applied to date specific geomorphological or sedimentological markers for paleo-glacier dynamics. Recently, optically stimulated luminescence (OSL) surface exposure dating has been introduced and provides us with an opportunity to improve paleo-environmental conditions. This method is based on the sensitivity of the OSL signal from rock minerals to light, resulting in bleaching of the OSL signal within the upper first millimeters of the exposed rock surface, a process that depends on the exposure age, the rock type, the surface erosion and the local setting (e.g., topographic shielding, bedrock orientation).

In this thesis, I first investigate the potential of OSL surface exposure along a vertical cross-section of polished bedrock surfaces with known post-LIA (Little Ice Age) exposure ages (from 3 to 137 years) along the Mer de Glace glacier (Mont Blanc massif, France). The luminescence signals from rock slices exhibit increasingly deep bleaching profiles with elevation and thus exposure age, which is consistent with progressive glacier thinning since the LIA.

Then, I present a new approach for evaluating post-glacial erosion of "roche moutonnées" over timescales from 10^1 to 10^4 years by combining in terrestrial cosmogenic nuclide (TCN) dating with ^{10}Be and OSL surface exposure dating. Using a numerical approach, I show how it is possible to simultaneously invert OSL signals and ^{10}Be concentrations into quantitative estimates of post-glacial exposure duration and bedrock surface erosion.

Finally, I apply this new approach on nine bedrock surfaces sampled over two elevation profiles located on the flanks of the Mer de Glace. My results reveal bedrock surface erosion rates from 3.5×10^{-3} to 4.3 mm a^{-1} over $\sim$500-m elevation gradient, with a clear anti-correlation between erosion rate and elevation. The observed spatial variability in erosion rates and surprisingly high rates might reflect morphometric (elevation and surface slope) and climate (temperature and snow cover) controls. Furthermore, and more importantly, the derived erosion rates can be used to correct the timing of deglaciation based on TCN dating, potentially suggesting very rapid ice thinning post-LGM.

Résumé

L'évaluation de l'impact des glaciations quaternaires à la surface de la Terre requiert de comprendre l'évolution à long terme des paysages alpins. En particulier, cela nécessite la quantification simultanée de l'impact de la variabilité climatique sur les fluctuations passées des glaciers et sur l'érosion du substratum rocheux. Depuis le dernier maximum glaciaire (LGM), il y a environ 20 000 ans, les glaciers alpins se sont retirés des régions de plaine et de leurs zones d'accumulation en altitude. Cette transition denuda de grandes étendues de surfaces rocheuses qui subirent ensuite l'action combinée de processus de désagrégation à grande échelle, de cryoclastie et d'altération. Durant cette période, les reconstructions paléo-glaciaires sont délicates car elles manquent souvent de contraintes temporelles précises.

Différentes méthodes géochronologiques ont été développées et appliquées pour dater les marqueurs géomorphologiques ou sédimentaires spécifiques de la dynamique des glaciers. Récemment, la datation de l'exposition de surface par luminescence stimulée optiquement (OSL) a été développée et offre l'occasion d'améliorer les reconstructions des étendues glaciaires du passées. Cette méthode est basée sur la sensibilité du signal OSL des minéraux à la lumiére. Lors d'une exposition le signal OSL est remis à zéro dans les premiers millimètres supérieurs de la surface rocheuse exposée.

Dans cette thèse, j'étudie le potentiel de la datation d'exposition de surface OSL à partir de polis glaciaires sur les flancs de la Mer de Glace, glacier emblématique du massif du Mont-Blanc. Je montre tout d'abord que cette méthode permet de reconstruire les épaisseurs passées du glacier depuis le Petit Âge Glaciaire, c'est à dire depuis la deuxime moitié du XIX^e siècle. Je montre ensuite que sur de plus longues périodes, la méthode est sensible à l'érosion de surface. En la combinant avec une autre méthode de datation: la datation par cosmogénie nucléide, je montre qu'il est possible de contraindre l'évolution de l'érosion de surface et des variations d'épaisseur du glacier depuis 20 000 ans.

Enfin, j'applique cette nouvelle approche sur neuf surfaces du substrat rocheux provenant de deux profils d'altitude situés sur les flancs de la Mer de Glace. Mes résultats révèlent des taux d'érosion de la surface du substrat rocheux allant de 3,5 à 4,3 mm a^{-1} sur un gradient d'altitude de 500 mètres, avec une nette corrélation entre le taux d'érosion et l'altitude. La variabilité spatiale observée ainsi que l'intensité étonnement élevée des taux d'érosion reflétent potentiellement le contrôle des conditions morphométriques (élévation et pente de surface) et climatiques (température et couverture de neige) locales. De plus, les taux d'érosion calculés permettent de corriger la chronologie de déglaciation obtenus grâce aux datation cosmogéniques, suggèrent un amincissement glaciaire post-LGM potentiellement trés rapide.

CHAPTER 1

Introduction

1.1 Scientific context and introduction

The evolution of the Earth's surface and everything that develops there, lakes, mountains, biodiversity and so on is governed by a sensitive balance between tectonic activity, surface processes and climate. During the Quaternary, the last 2.6 million years of Earth history, this equilibrium was mainly dominated by surface processes and climate since tectonics acts at longer timescales. The Earth's global climate, for instance, has shown important variability. Reconstructions extracted from polar ice cores and deep-water sediments (e.g., Emiliani, 1955; Shackleton and Opdyke, 1973; Dansgaard et al., 1993; Augustin et al., 2004) provided us with key insights into climate alternations, at a global scale, between glacial and interglacial cycles of about 100 000 years for at least the last million years (Hays et al., 1976; Augustin et al., 2004). Records from Antarctica covering the paleo-climatic records onshore, about 800 000 years (EPICA members, 2004; Jouzel et al, 2007), have highlighted the forcing, essentially orbital, at the origin of these cycles.

In the European Alps and other mountain ranges at mid-latitude, reconstructions of climate and the effects of its fluctuations on the Earth's surface are more challenging. Given that the necessary altitude to maintain cold-based glaciers is higher than 3500 or 4000 m.a.s.l. in the Alps, conditions of alpine mountain glaciers for paleo-climatic reconstructions are limited (Haeberli and Alean, 1985; Haeberli and Funk, 1991; Lüthi and Funk, 2001; Suter et al., 2001; Suter, 2002; Vincent et al., 2007). To overcome the difficulties of reconstructing the paleo-climate in mid-latitude regions, scientists have developed techniques based on the study of lacustrine or marsh sediments (e.g., Schmidt et al., 2008; Giguet-Covex et al., 2012; Heiri et al., 2003; Millet et al., 2009; Ilyashuk et al., 2011), treelines (e.g., Haas et al., 1998; Tinner and Theurillat, 2003; Nicolussi et al., 2005; Blarquez et al., 2010; Berthel et al., 2012), tree rings (e.g., Baillie and Pilcher,1973; Schweingruber, 2007; LeRoy et al., 2015) and speleothems (e.g., Vollweiler et al., 2006; Boch and Spötl, 2011). Nevertheless, the study of glacial landforms and chronologies represents the reference series against which other paleo-environmental reconstructions are evaluated. Because mountain glaciers respond quickly to slight changes in climatic forcing and because they are widely distributed in the Alps, they represent the climatic proxy with the greatest potential (e.g., Denton and Karléen, 1973; Hoelzle et al., 2003; Beedle et al., 2009; Six and Vincent, 2014).

In the European Alps, most of the glacial landforms that remain in the foreland are related to the last important Alpine glaciation, the Last Glacial Maximum (LGM; Ivy-Ochs, 2015) and except in few areas most of the evidence of previous glacial cycles has been superimposed by the LGM glacial processes and other later geomorphological processes. Although the glacial history of the European Alps has been studied for nearly 300 years (e.g., Windham and Martel, 1744, p. 21; de Saussure, 1779; Venetz, 1821; de Charpentier, 1841; Agassiz,1840; Forbes, 1846; Penck and Bruckner, 1901/1909), the spatial variations and the timing of

the LGM remain uncertain (e.g., Ivy-Ochs et al., 2006; Ivy-Ochs, 2015 and Monegato et al., 2018). Past ice-extent in foreland regions have been widely investigated, bringing a considerable knowledge about horizontal fluctuation of alpine glaciers. Yet, in order to fully extract climatic signals from glacier fluctuations, the variation of ice thickness should also be constrained. Indeed, more studies in the high part of the Alps (i.e., High Alps; Wirsig et al., 2016) should be conducted. New methodological approaches should also be developed to better link the Lateglacial, Holocene and Little Ice Age timescales relative to the ice thickness variation since the LGM. The studies presented in this manuscript address these challenges.

Associated with glacier fluctuations, surface processes are a major component of the development of the alpine morphology. The retreat of glaciers commonly exposes a landscape that is susceptible to rapid change (e.g., Łoziński, 1909; Anderson and Anderson, 2010; Hall et al., 2012; Moses et al., 2014). In this context, glacially-polished bedrock, or so-called "roches moutonnées", are extensively present in the High Alps. Their wide distribution both vertically and horizontally, offers the possibility to reconstruct past ice-extents and paleo-environmental conditions through the quantification of postglacial bedrock erosion (e.g., Gianotti et al., 2008, 2015; Wirsig et al., 2016b). In this thesis, efforts are made to characterize the development of deglaciated bedrock surfaces, surfaces where new methodological techniques (optically-stimulated luminescence) can be developed to extract paleo-environmental conditions from the evolution of such surfaces.

The primary objectives of this PhD thesis are:

1. **To constrain the ice extent history of a high alpine environment since the LGM at both Little Ice Age and Lateglacial timescales.**

2. **To explore the geomorphological processes experienced by deglaciated bedrock surfaces.**

3. **To develop a new approach based on both terrestrial cosmogenic nuclide and luminescence dating to achieve 1) and 2).**

In this introduction, I first present the glacial history of the European Alps and the different uncertainties relative to the spatial variation, the timing of the LGM and post-LGM history. Later, I discuss the morphological evolution induced by ice-extent fluctuations with a focus on the evolution of deglaciated bedrock surface. Then I introduce the different methodological approaches that will be tackled to work on both ice-extent reconstruction and bedrock surface erosion. I finally introduce the study site (Mer de Glace, Mont-Blanc massif), justifying my choice by a short state-of-the-art of the evolution of the alpine environment in this specific region since the LGM.

1.2 Glacial history of the European Alps

In the Alps, the observations of naturalists, travelers and the alpine population watching their fields being destroyed by glacier advances brought understanding about how ice extents change in time. The scientific interest for alpine glaciers was first stimulated by fear rather than curiosity. In May 1595, the rupture of an ice pocket of the glacier Giétroz located in the Swiss Alps, destroyed more than 500 buildings and killed 140 people. In the same area, another historic disaster occurred after a landslide in spring 1818, blocks of ice obstructed the local river and created a natural dam (Fig. 1.1). When the dam broke, the flood and ice blocks caused the death of 44 people as well as a lot of damage. The preoccupation caused by these repetitive glacial disasters led to the first scientific studies on glaciers. They had to be understood to better protect the population.

Figure 1.1: Illustration of the lake formed by the Gietroz glacier disaster, 1818 (gietroz1818.ch).

The discovery of distant rock blocks and therefore erratic provenances has also stimulated the study of glaciers. The size of the blocks, their contradictory nature with their environment and their inexplicable positions by known geomorphological processes had intrigued geologists. The existence of these blocks was initially interpreted as a biblical proof of the Flood. Louis Agassiz was the first to defend the "glacial theory" (Agassiz 1837). He claimed during the famous "Neuchtel speech" and in front of the Swiss Academy of Natural Sciences that the enormous accumulations of erratic blocks were formed by an old glacial extension. His theory gained general acceptance once the two actual ice sheets on Earth were discovered and explored: Greenland and Antarctica (e.g., Emiliani, 1955; Shackleton and Opdyke, 1973). In

the European Alps, the systematic classification of fluvio-glacial deposits on the alpine margin led to the designation of the existence of four large glaciations (Penck and Bruckner, 1909). Later on, studies of glaciofluvial stratigraphy in the foreland indicate at least 15 Pleistocene glaciations (Schluchter, 1988; Ivy-Ochs et al., 2008; Preusser et al., 2011).

From the mid-20th century, paleo-climatic records extracted from polar ice cores and deep-water sediments provided a much better understanding of Earth's environmental history (e.g., Dansgaard et al., 1993; Augustin et al., 2004). describing several dozen glacial and interglacial periods. During the last 800 kyr, these ice cycles followed each other with a frequency of about 100 ka (Hays et al., 1976; Augustin et al., 2004).

However, this global signal is governed in a large part by the ice caps of North America and Eurasia. The climatic signal of the Alps remains difficult to characterize where the ice sheets did not leave a continuous trace in the landscape, and much of this evidence has been superimposed by glacial processes and other later geomorphological processes (e.g., Kleman, 1994; Kleman et al., 2006, 2010).

In the European Alps, the last glacial cycle (Würm) was marked by two or three periods of glacier advance during which piedmont lobes were formed (Preusser, 2004; Ivy-Ochs et al., 2008). Most of the glacial formations that remain in the foreland present a record of the last important glaciation of the Alps, the Last Glacial Maximum (LGM; Ivy-Ochs, 2015). The spatial extent and thickness of the LGM glaciers in the Alps have been reconstructed through mapping and dating moraine deposits, erratic boulders and trimlines across the mountain range (e.g., Penck and Brückner, 1909; Castiglioni, 1940; van Husen, 1987; Bini et al., 2009; Coutterand, 2010). Nevertheless, after being studied for three centuries, the spatial variations and the timing of the LGM remain uncertain.

The trimline for instance, representing in the topography the boundary between an ice-moulded downslope area and a frost-shattered upslope zone (Florineth and Schlüchter, 1998; Kelly et al., 2004), is generally assumed in the Alps to be the maximum elevation of the active LGM ice surface (subaerial/subglacial boundary) (Florineth and Schlüchter, 1998; Kelly et al., 2004; Cossart et al., 2012). This assumption has been repeatedly questioned in other glaciated regions of the globe (e.g., Kleman, 1994; Kleman et al., 2010; Fabel et al., 2012; Ballantyne and Stone, 2015) and recent studies involving ice dynamic modelling of the Alps showed that the maximum ice thickness is about several hundred meters higher than the mapped trimlines (Cohen et al., 2017; Seguinot et al., 2018). These results have been obtained with a model set-up correcting the basal topography with an estimation of present-day ice thickness but without removing post-glacial sediment fills and lake surface topography. The true maximum elevation of the active LGM ice surface might be somewhere in between the lowest and the highest endmembers, corresponding to the mapped trimlines and the maximum ice thickness

inferred by ice dynamic modelling respectively. These differences in ice thickness might have important consequences for our understanding of ice-climate interactions.

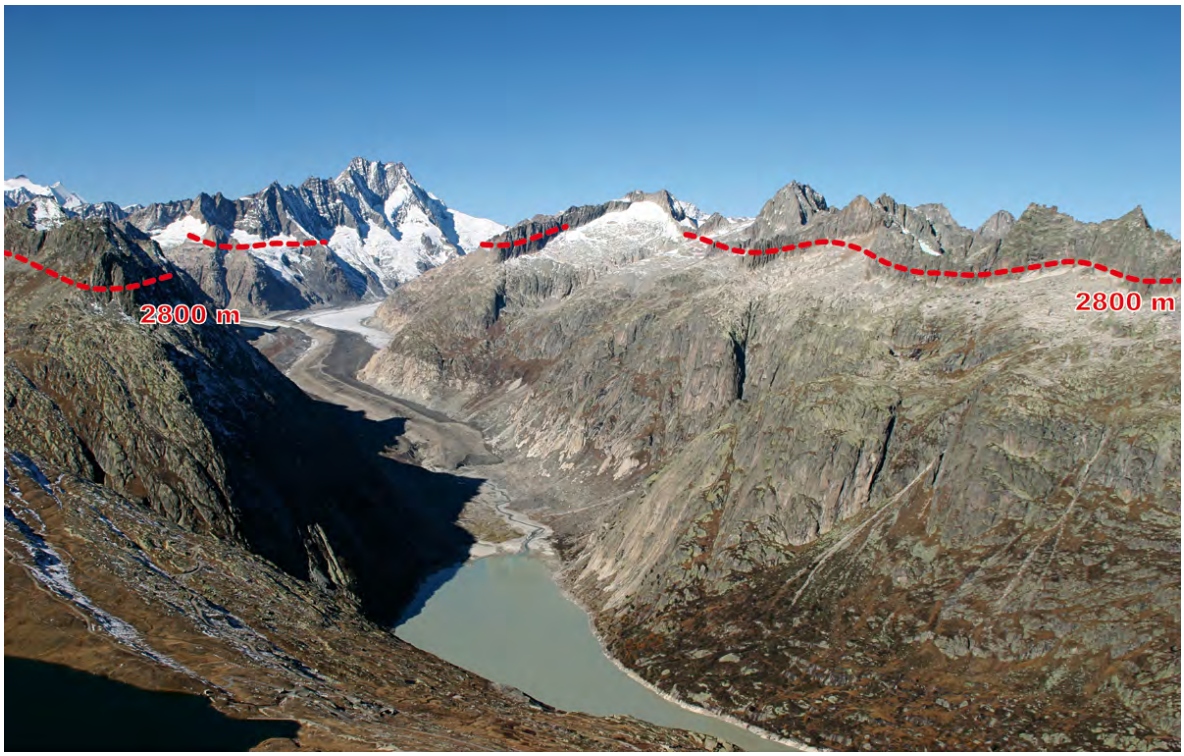

Figure 1.2: Example of trimline mapping the Grimsel Aar region (Switzerland) performed by S. Coutterand (www.glaciers-climat.com).

The timing of the transition from the LGM to its present state in the Alps has been intensely studied (Schlüchter and Röthlisberger, 1995; Ivy-Ochs et al., 2004; Ivy-Ochs, 2015, and references therein; Fig. 1.3). Most available data are from the forelands, where fluctuations of the ice margin are better recorded than elevation changes of the ice surface in the high part of the Alps. The last LGM advance phase is recognized on both sides of the Alps ending around 21-19 ka, followed by retreat of the glacier lobes from the forelands (Lister, 1988; Monegato et al., 2007; Starnberger et al., 2011; Ravazzi et al., 2012; Fontana et al., 2014; Reber et al., 2014). Even if this timing is in good agreement with the maximum expansion of continental ice sheets recorded by marine oxygen isotope stage (MIS) 2 (29-14 ka; Lisiecki and Raymo, 2005), the regional variation between different piedmont lobes exists (Wirsig et al., 2016). It is unclear whether these differences relate to climate or glacier dynamics, uncertainties in the dating methods, or both (Seguinot et al., 2018).

Comparably little chronological information is available from the High Alps. In the Central Alps, the highest ice surface appears to have been maintained until 23 $\pm$ 1 ka (Wirsig et al., 2016a) and severe ice surface lowering initiated at $\sim$ 18 *ka* (Dielforder and Hetzel, 2014; Wirsig et al., 2016). A recent study has shown synchronicity between the ice surface lowering on

the southern side of the Mont Blanc massif (Western Alps) and in the Zillertal Alps (Eastern Alps) at approximately 19-18 *ka* (Wirsig et al., 2016b).

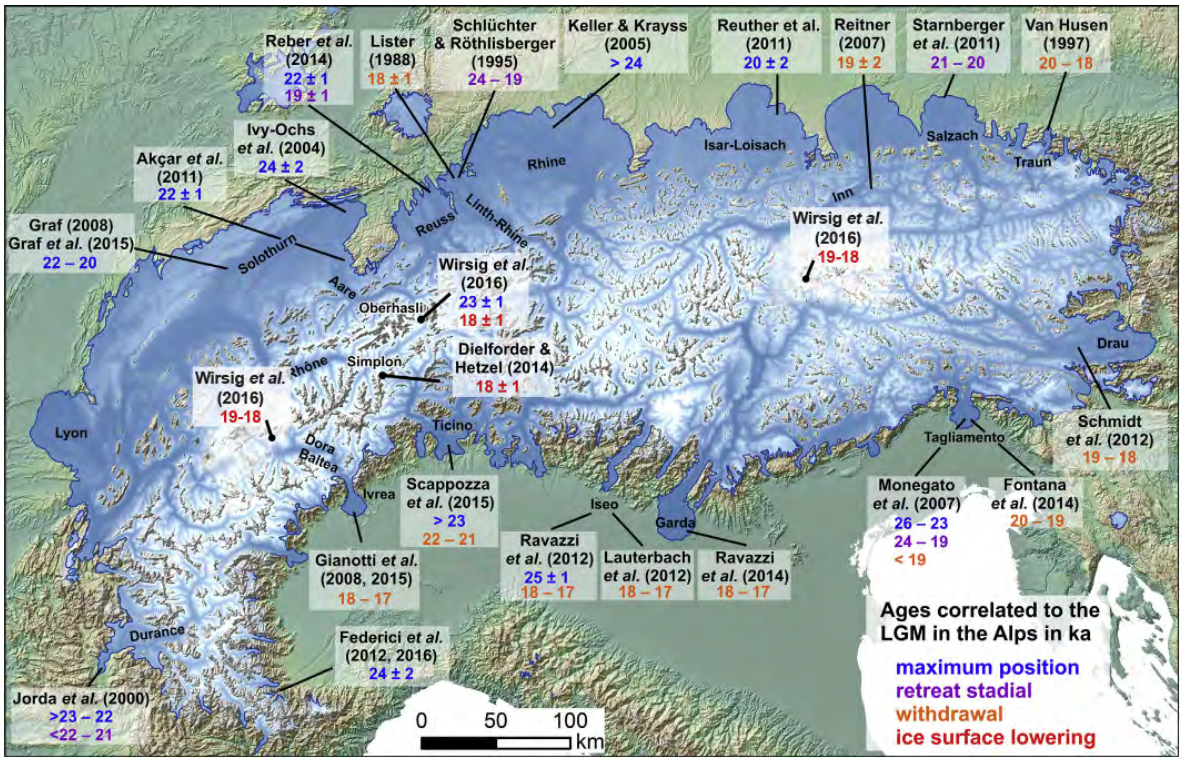

Figure 1.3: Ages correlated to the LGM in the Alps. The map shows a compilation of published ages by Ivy-Ochs (2015) and Wirsig et al (2016b) that were correlated to the end of the LGM in the Alps. The color type indicates in which context an age has been interpreted by the authors. The LGM ice extent is from Ehlers and Gibbard (2004, http://www.qpg.geog.cam.ac.uk/lgmextent.html). Figure modified from Wirsig et al. (2016b).

1.3 Lateglacial and Holocene chronology in the Alps

The first part of the transition from the LGM to its present state is called the Lateglacial and refers to the time between the retreat of the LGM glaciers from the forelands and the beginning of the Holocene (starting at 11.7 *ka*). Vegetation re-colonized some ice-free inner-Alpine valleys prior to 18 *ka* (Reitner, 2007; Klasen et al., 2007; Gianotti et al., 2015). The ice retreat was disrupted by at least two major and several minor glacier re-advances into ice-free valleys (e.g., Penck and Bruckner, 1901/1909; Ivy-Ochs, 2015). The Gschnitz stadial re-advance (Hantke, 2011) is caused by consistent atmospheric cooling at 17 - 16 *ka* (Ivy-Ochs et al., 2006a). Later on, glaciers diminished due to temperature increases of 4-6°C at the beginning of the Bølling-Allerød interstadial at around 14.5 *ka* (Vescovi et al., 2007). Therefore, the ice disappeared from main and tributary valleys across the Alps (Maisch, 1987; van Husen, 1997; Ivy-Ochs et al., 2006b; Heiri et al., 2014). Finally, climatic deterioration

during the Younger Dryas at 12.9-11.5 *ka* (Bond et al., 1992; Clark et al., 2012) caused the last major Alpine-wide re-advance: the Egesen stadial that is dated to 13.0-11.5 *ka* (e.g., Ivy-Ochs et al., 1996, 1999, 2008; Schindelwig et al., 2012). This event marks the end of the Lateglacial and the beginning of the Holocene.

During the initiation of the Holocene (11.5-10.5 *ka*), conditions remained cold but increasingly dry leading to slow reduction of the ice-extent. Warm and possibly dry conditions in the early and mid-Holocene caused glaciers to be mostly smaller than today (e.g., Maisch et al., 1999; Nicolussi and Schluchter, 2012). During the late Holocene at around 3.3 *ka*, the shift towards generally glacier-friendly climate is marked by a depression in treelines (Holzhauser et al., 2005; Nicolussi et al., 2005; Joerin et al., 2006).

The last period favorable to the glaciers is the Little Ice Age (LIA) extending from 1350 to 1850 AD. It is characterized by the most important glacial recurrence of the Holocene, with four maxima: around 1350, 1600, 1820 and 1850 AD. This cold climatic period has affected the entire globe and is characterized by successive advances of glaciers, which correspond to several minima of average temperatures (1 to 1.5°C lower than today) and noticeable increase in precipitation (e.g., Vincent et al., 2015). This situation has generated positive glacier mass balances and, consequently, a significant development of glacial tongues. In the Alps, the traces of the LIA are generally well underlined by the immense lateral moraines (several hundred meters; e.g., Bosson glacier, Mont Blanc massif) built or simply reloaded at this time, as well as by some frontal moraines located downstream.

1.4 Evolution of the alpine landscape in Lateglacial/Holocene context

Associated with the climatic variability of the Lateglacial and Holocene and the recurrent glacier lowering, the Earth's surface has suffered important morphological modifications. Such changes are even more expressed in alpine environments, where the main erosion agents vary from ice (i.e., glacial processes) to water (i.e., fluvial processes) and landslides (i.e., gravitational processes). Debuttressing of glacially steepened rockwalls may result in slope failure or enhanced rockfall activity; glacier forelands are exposed to wind erosion, frost action and chemical weathering and rivers entrain and redistribute large amounts unconsolidated glaciogenic sediment that is subsequently redeposited in a variety of terrestrial, lacustrine and marine sediment sinks (Ballantyne, 2002). However, quantifying their respective contributions in sediment production and their respective control on morphological evolution of high mountain environments remains challenging because both ice-extent fluctuations and associated bedrock surface erosion must be reconstructed simultaneously.

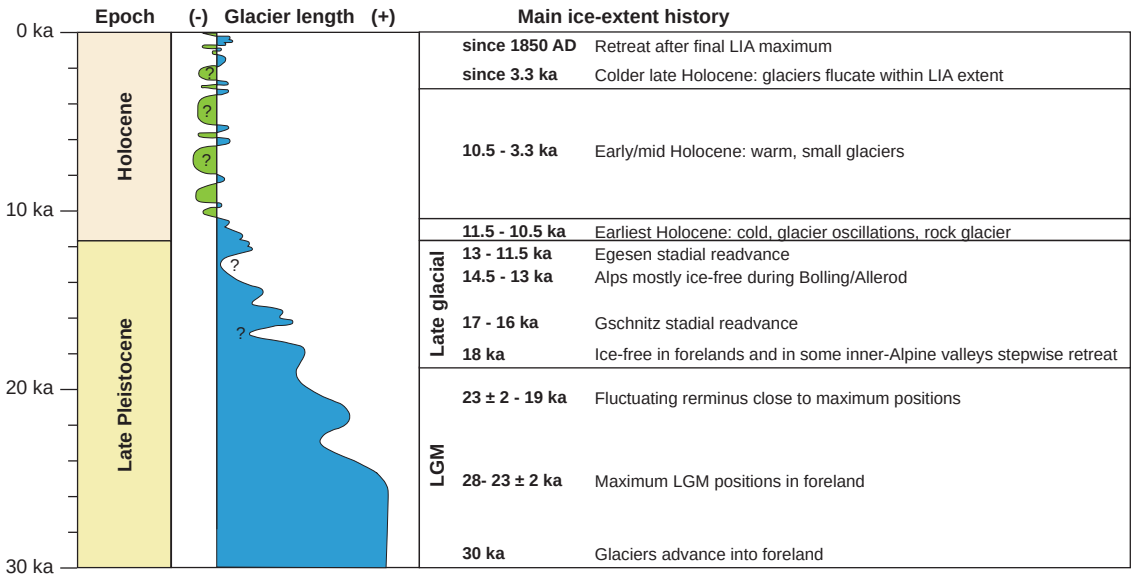

Figure 1.4: Simplified scheme of general patterns and chronology of glacial fluctuations since the LGM in the Alps modified from Wirsig (2016) and from www.glaciers-climat.com/cg/le-tardiglaciaire. The given ages are approximate. Please refer to the text for details and references. Ivy-Ochs et al. (2008, 2009) and Ivy-Ochs (2015) provide in depth discussions of the chronology of the Alpine LGM, Lateglacial and Holocene.

Because glacially-polished bedrock, or so-called "roche moutonnées", are widely distributed in the High Alps both vertically and horizontally, they offer the possibility to reconstruct past ice-extents and paleo-environmental conditions through the quantification of bedrock surface erosion. These landforms are smooth and glossy, resulting from glacial abrasion, quarrying and melt-water erosion during glacial periods (e.g., Sudgen et al., 1992; Bennett and Glasser, 2009; Siman-Tov, 2017). Indeed, striations are the products of individual rocks that were embedded in the sole of the glacial ice as it slid across the bedrock. The erosion resulting from the sum of all these scratches is the process called subglacial abrasion. It is abrasion that smoothed the bed. It is the short wavelength bumps in the bed that are gone, making it look smoother (Anderson and Anderson, 2010). Following ice retreat, these striated bedrock surfaces are exposed to post-glacial erosion, which results in the transition from a well-preserved glacially-polished surface to a coarse-grained rough surface.

Post-glacial bedrock surface erosion is due to the alteration of rock surfaces exposed to atmospheric conditions. Their evolution is the result of a combination between physical (e.g., frost-cracking), chemical and biological processes that weaken which modify the rock surface (e.g., deterioration, decay, crumbling, decomposition, rotting, disintegration, disaggregation or breakdown) and ultimately results in its progressive erosion (e.g., Łoziński, 1909; Anderson and Anderson, 2010; Hall et al., 2012; Moses et al., 2014).

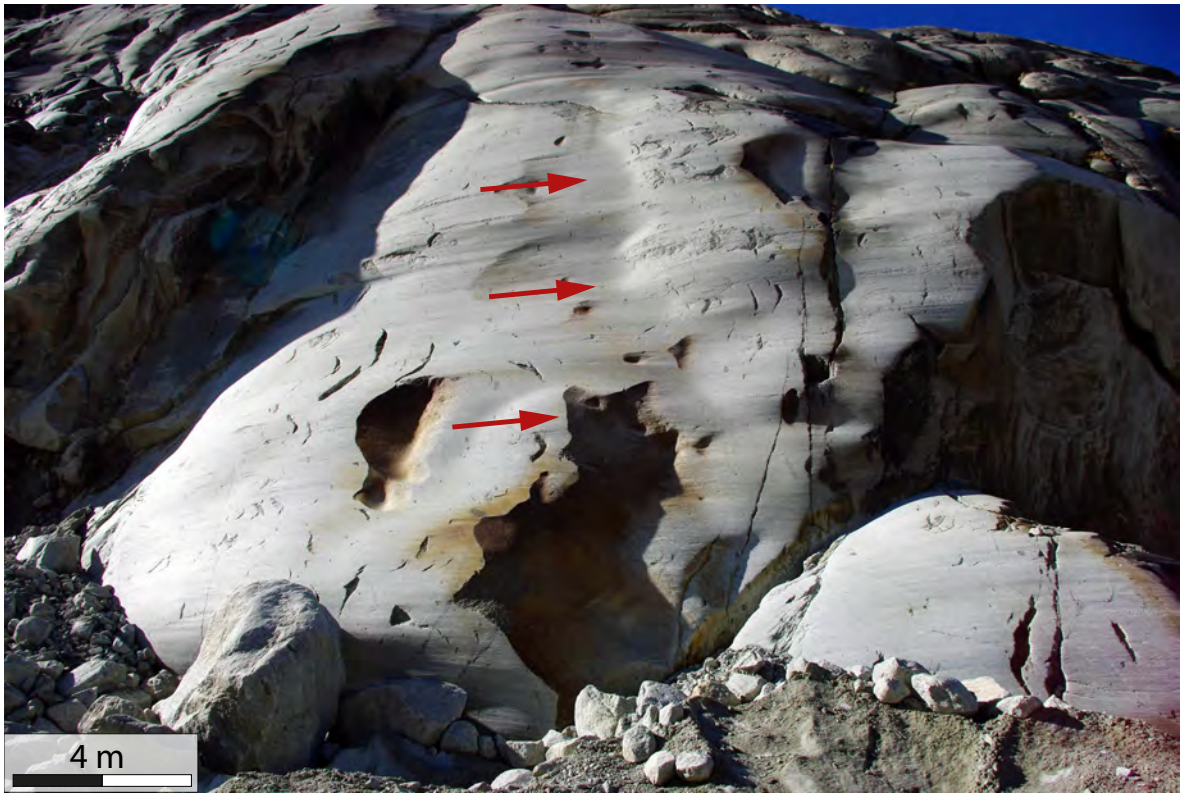

Figure 1.5: Picture of a post-LIA glaciated polished bedrock surface on the side of the Mer de Glace, Mont Blanc massif (France). Red arrows show the direction of ice flux.

Over contemporary timescales, the effect of atmospheric temperature variations on bedrock surfaces in alpine regions has been discussed (see Matsuoka, 2008 for a review). These variations are strongly influenced by slope inclination, slope aspect, local climatic conditions (including the seasonal snow cover), and the thermal properties of the rock (Coutard and Francou, 1989; Matsuoka, 1990, 2008; Gruber et al., 2004a; Grab, 2007; Noetzli et al., 2007). Combination of laboratory experiment, theoretical approaches, numerical modelling and field monitoring have highlighted the different controls of rock weathering and especially frost weathering. It results from freezing and thawing of water within rock or mineral particles. The generation of new microcracks within the bedrock provides additional avenues for surface water to penetrate the rock, carrying with it the ability both to attack the rock chemically, and to remove the solutes produced (Anderson, 1998). The efficacy of frost weathering depends mainly on the duration passed by the bedrock surface into the frost cracking window (approximatively -3° C and -6°C; Hallet et al.,1991; Anderson, 1998) but also on the number of freeze-thaw cycles it experienced (Kellerer-Pirklbauer, 2017). Finally, the intensity duration of the seasonal snow cover has a major role by shielding the bedrock surface from atmospheric temperature fluctuations.

Over Holocene timescale, the very efficient frost-driven processes that control the geomorphic activity has been questioned among the international scientific community. Instead, the role of non-cold-related processes, such as chemical, biogenic and rainfall-induced processes, is being emphasized (e.g., André, 2003; Dixon and Thorn, 2005). To assess the impact of postglacial rock weathering over those timescales (centuries to millennial), ice-polished quartz veins preserved on roches moutonnées were used as reference surfaces (André, 1996). This approach is commonly used to perform surface erosion correction for surface exposure dating using terrestrial cosmogenic nuclides (e.g., Lal et al., 1991; Balco et al., 2008; Wirsig et al., 2016b). Results range from 0.1 to 10 mm ka^{-1} depending of the lithology and the location (Colman, 1981; Zimmerman et al., 1994; André, 2002; Nicholson, 2008; Kirkbride and Bell, 2010).

Despite their potential to reconstruct paleo-climatic conditions, post-glacial bedrock surface have been poorly studied. This is a consequence of a methodological gap to estimate the erosion rate these surfaces are experiencing between contemporary and Lateglacial timescales.

1.5 Methodological approaches

1.5.1 Terrestrial cosmogenic nuclide dating

The ice-extent reconstruction of the Lateglacial and Holocene epochs presented in the previous sections were mainly achieved using terrestrial cosmogenic nuclide (TCN) surface exposure dating of polished bedrock or erratic boulders (see Ivy-Ochs et al., 2006, 2009, 2015 for reviews). This method has been developed over the last decades to determine both surface exposure duration and erosion rate over timescales of 10^3 - 10^6 years (Lal, 1991; Goss and Philips, 2000; Balco, 2011; Ivy-Ochs and Briner, 2014). TCN surface exposure dating relies on the production of cosmogenic isotopes in material at or near the Earth's surface (Gosse and Philips, 2001). By exposure to cosmic rays, cosmogenic nuclides are produced in minerals located in the top few meters of soil or bedrock (Lal and Peters, 1967). The quantification of the TCN concentration into targeted crystal gives information about either the exposure duration or the surface erosion rate since deglaciation for glacial bedrock surfaces.

Because, beryllium-10 (^{10}Be) is produced mainly by cosmogenic rays from the parent isotope oxygen-16 (^{16}0), which is abundant in the most common mineral at the Earth's surface, quartz, ^{10}Be is the appropriate isotope in surface dating (Nishiizumi et al., 1989). Production rates are strongly influenced by geomagnetic latitude (Lal, 1991), altitude (Stone, 2000), through shielding by surrounding topography (Dunne et al., 1999; Choi et al., 2012; Regard et al., 2012), and through seasonal shielding of snow, sediment, or peat (Gosse and Phillips, 2001). The cosmogenic nuclide concentrations must also be corrected for surface erosion since the first exposure in the context of glacial polish, which can potentially lead to an underestimation of

the exposure age (Gosse and Phillips, 2001). Erosion is often estimated from field observations (Gosse and Phillips, 2001). The combination of different cosmogenic nuclide pairs (e.g., ^{10}Be and ^{14}C; e.g., Goehring et al., 2012; Hippe et al., 2017) provides us with important information on Alpine glacier paleo-geography since the LGM (Ivy-Ochs et al., 2006; Wirsig et al., 2016). However, the cosmogenic nuclide production rate and the integration of production over the first 1-2 m below a rock surface may limit the resolution of such methods for recent and/or complex exposure histories.

To sum up, in glacial and paraglacial landscapes, TCN surface exposure dating provides a unique method to directly date the formation of glacial landforms and to quantify rock surface weathering over timescales of 10^3 to 10^6 years (Ivy-Ochs and Briner, 2014; Hippe, 2017).

1.5.2 Reconstruction of ice-extent and post glacial erosion over contemporary timescale

From centennial to annual timescales and especially since the Little Ice Age (LIA: 15^{th} to 19^{th} centuries), past glacier extents in the European Alps are well constrained using historical maps, survey reports and aerial photogrammetry, glacier fluctuations have been precisely reconstructed over the last two centuries (e.g., Nussbaumer et al., 2007; Vincent et al., 2014). Nevertheless, it appears not possible to use these approaches in remote areas where there are no historical documents on glaciers. In an effort to improve the continuity of glacier reconstructions, it is important to bridge the time gap between the short and long timescales. Different geochronological methods have been developed in this sense, such as lichenometry (Winkler, 2004), varve chronologies (Stewart et al., 2011), dendrochronology (Baillie, 1995) and radiocarbon dating (Hajdas, 2008). However, organic matter can be scarce for glacial/periglacial deposits because of the extremely active geomorphic processes associated with glacial environments.

Analytical methods to quantify erosion differ depending on the timescale of interest (see Moses et al., 2014 for a complete review). Over short timescales (from a few seconds to decades) erosion can be quantified through remote sensing (e.g., photogrammetric methods; Terrestrial Laser Scanner; c.f., Armesto-Gonzlez et al., 2010; Duffy et al., 2013) or measured relatively to anthropogenic reference features (historic or experimental; e.g., Nicholson, 2008; Häuselmann, 2008; Stephenson and Finlayson, 2009).

Consequently, complementary approaches are still needed to quantify both ice-extent variation and bedrock erosion over multiple timescales, and more specifically methods that can bridge short and long timescales. The important contributions of this thesis are made through new applications of optically stimulated luminescence (OSL) dating.

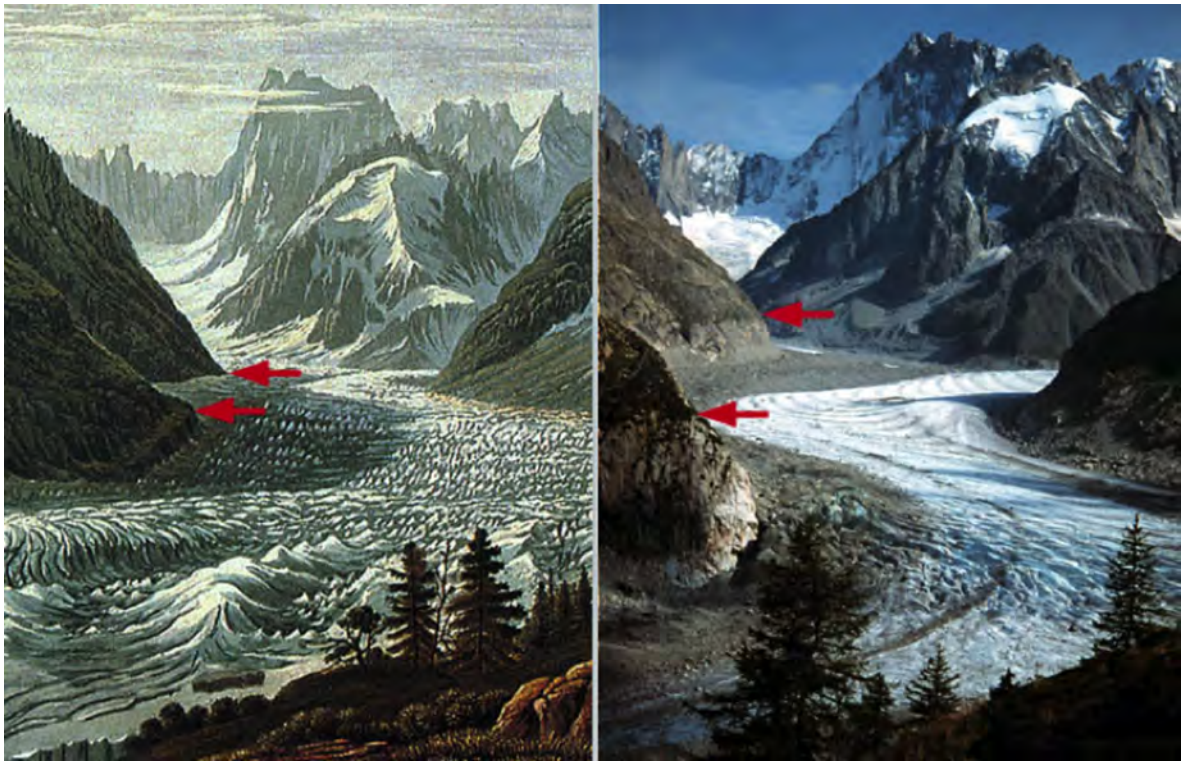

Figure 1.6: Example of a reconstruction made possible using painting with two different views of the Mer de Glace from the Montenvers (Mont Blanc massif, France). On the left, a painting from Burmese just after the maximum of the Little Ice Age (around 1850). The photograph on the right was taken at the same position in 2000. The arrows indicate the same positions on the glacier margin, and indicate the level of lowering of the glacier surface. Painting from the Gugelmann Collection, Swiss National Library, Bern. Photo of M. J. Hambrey, 2000 (swisseduc.ch).

1.5.3 Optically stimulated luminescence dating

Luminescence dating is based on the accumulation of electrons through time in the crystalline lattice of certain minerals that are sensitive to sunlight exposure (Aitken, 1985; Huntley et al., 1985). Minerals such as Quartz or Feldspar have defects or impurities in their crystal lattice. Due to the energy released by radioactive decay of the surrounding material, electrons escape from their equilibrium state (valence band) and are trapped into the crystal defects after passing by the conduction band (Fig. 1.7A). Because of the finite number of traps, electron filling occurs until saturation is reached.

By giving energy to the system as light or heat (bleaching processes), electrons are released and return to their equilibrium state, producing photons. The energy signal released is called luminescence (Fig. 1.7B). The intensity of the luminescence signal is thus proportional to the number of trapped electrons. If the luminescence is reset by photon stimulation in the laboratory, the signal emitted from the mineral is called optically stimulated luminescence

(OSL) (Aitken, 1985; Huntley et al., 1985). In OSL dating, the system records the last bleaching event through exposure to light. In a rock surface continuously exposed to daylight, this bleaching will propagate deeper into the surface with time (Sohbati et al. 2012).

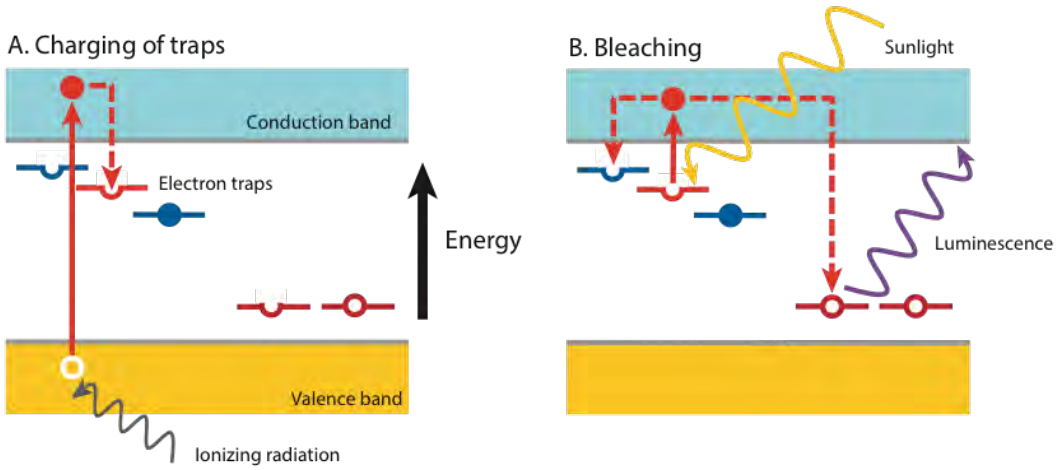

Figure 1.7: Schematics of trap charging and charge bleaching processes (modified from Rhodes, 2011). (A) Excited by ionizing radiation, electrons from the valence band move to the conduction band of the crystal and become trapped in crystal defects or impurities. (B) Through stimulation by sunlight, electrons may receive sufficient energy to escape their trap and recombine with a hole, thereby releasing energy in the form of light: the luminescence.

Luminescence dating is commonly used to date sediment burial in a range of geomorphological environments (e.g., Duller, 2008; Rhodes, 2011; Fuchs and Owen, 2008) but can also be used to determine rates of bedrock cooling (Guralnik et al., 2015; King et al., 2016; Brown et al., 2017), and the exposure age of rock surfaces (Polikreti et al., 2003; Sohbati et al., 2011). This latter application is based on the principle that when a rock surface is exposed to light, the luminescence signal, which is initially homogenous within the rock sample, will progressively decrease at depth until being completely zeroed, a phenomenon called “bleaching” (Aitken, 1998).

In surface exposure dating, the assumption is made that the longer a surface has been exposed to daylight, the deeper the bleaching signal will be (Polikreti et al., 2002). In granitic and gneissic rocks, bleaching through time has been shown to occur over the first few centimetres of the rock surface depth (Vafiadou et al., 2007; Sohbati et al., 2011; Freiesleben et al., 2015). The luminescence signal of a rock surface is reflecting an equilibrium between electron trapping, due to ambient radiation (cosmic rays, high energy solar particle flux and radioactive decay in the rock matrix), electron detrapping due to anomalous fading and/or thermal signal losses, electron detrapping due to bleaching processes and surface erosion.

Rock surface exposure dating using OSL has recently shown promising potential (e.g., Sohbati et al., 2012a). Sohbati et al. (2012c) were able to quantify the exposure age of historical rock art from the Great Gallery rock art panel in Canyonlands National Park (south-eastern Utah, USA). Some of the paintings were damaged by a rockfall, burying them under sediment. Using a road cut of known age to constrain the bleaching rate for this specific site and lithology, Sohbati et al. (2012c) were able to quantify the exposure age of both the modern analogue ($\sim 130\ yr$) and the rock art ($\sim 700\ yr$). This method is attractive because of the short time required for sample preparation (Sohbati et al., 2011), although one current disadvantage is the requirement for calibration of this chronometer on rock surfaces with independently-known exposure ages (Sohbati et al., 2012a).

Besides the promising potential of OSL surface exposure dating, it has never been applied in alpine environments. The primary objective of this thesis is to use OSL surface exposure dating to constrain both ice-extent history and surface erosion rate from deglaciated bedrock of the Mer de Glace in the Mont Blanc massif (France) over late Pleistocene to Holocene timescales.

1.6 Study area

In order to develop, validate and apply new methodology to quantify both ice-extent variation and bedrock erosion over multiple timescales, the Mer de Glace, in the Mont Blanc massif, is an appropriate laboratory. This iconic massif of the Alps was the site of the development of glaciology. It has received high interest since the beginning of the study of Quaternary glaciations (de Saussure, 1779-1796). In 1842, physicist James David Forbes settled in the Mer de Glace and began a long series of measurements of the movement and temperature of the ice. From 1891 to 1899, Joseph Vallot measured the speed of the ice on the terminal tongue of the Mer de Glace with a line of painted stones. This survey method was then adopted by Waters and Forests management services from 1907 to 1960, providing a unique half-century database for changes in glacier shape and flow. Due to easy access to glaciers from the Chamonix valley, the Mont Blanc massif has been followed by glaciologists of all nationalities.

The Mont Blanc massif is one of the Alpine external crystalline massifs that form a discontinuous belt along the periphery of the Alps. The Mont Blanc massif is mostly composed of calcalkaline granite, locally called “Protogine” that constitutes the “needles” of the Aiguilles de Chamonix (Leloup et al., 2005). To the NW, the Mont Blanc massif is separated from the Aiguilles Rouges massif by a strip of Mesozoic sedimentary rocks, commonly called “the Chamonix syncline”, outcropping in the Chamonix glacial valley. The Aiguilles Rouges are mostly composed of Variscan metamorphic rocks and granites.

In the Mont-Blanc massif, glaciers cover an area of 145 km^2 approximately 30% of the massif including Europe's highest summit, the Mont Blanc at 4810 m (Deline et al., 2012). There are more than 101 glaciers involving 15 glaciers of more than 5 km^2 and among them the Mer de Glace (Fig. 1.8). The Mer de Glace glacier is about 11.5 km long and is located in the Mont Blanc massif. The modern glacier covers an area of 30.4 km^2 (excluding former tributary Talèfre Glacier) and spans an elevation range from 4205 m to 1531 m.a.s.l. (data from 2008; Gardent et al., 2014). The mean equilibrium line altitude (ELA), reconstructed using remote sensing methods, was about 2880 m.a.s.l. between 1961 and 1990 for five of the main north-facing Mont Blanc massif glaciers, including the Leschaux Glacier for the period 1984-2010 (Rabatel et al., 2013).

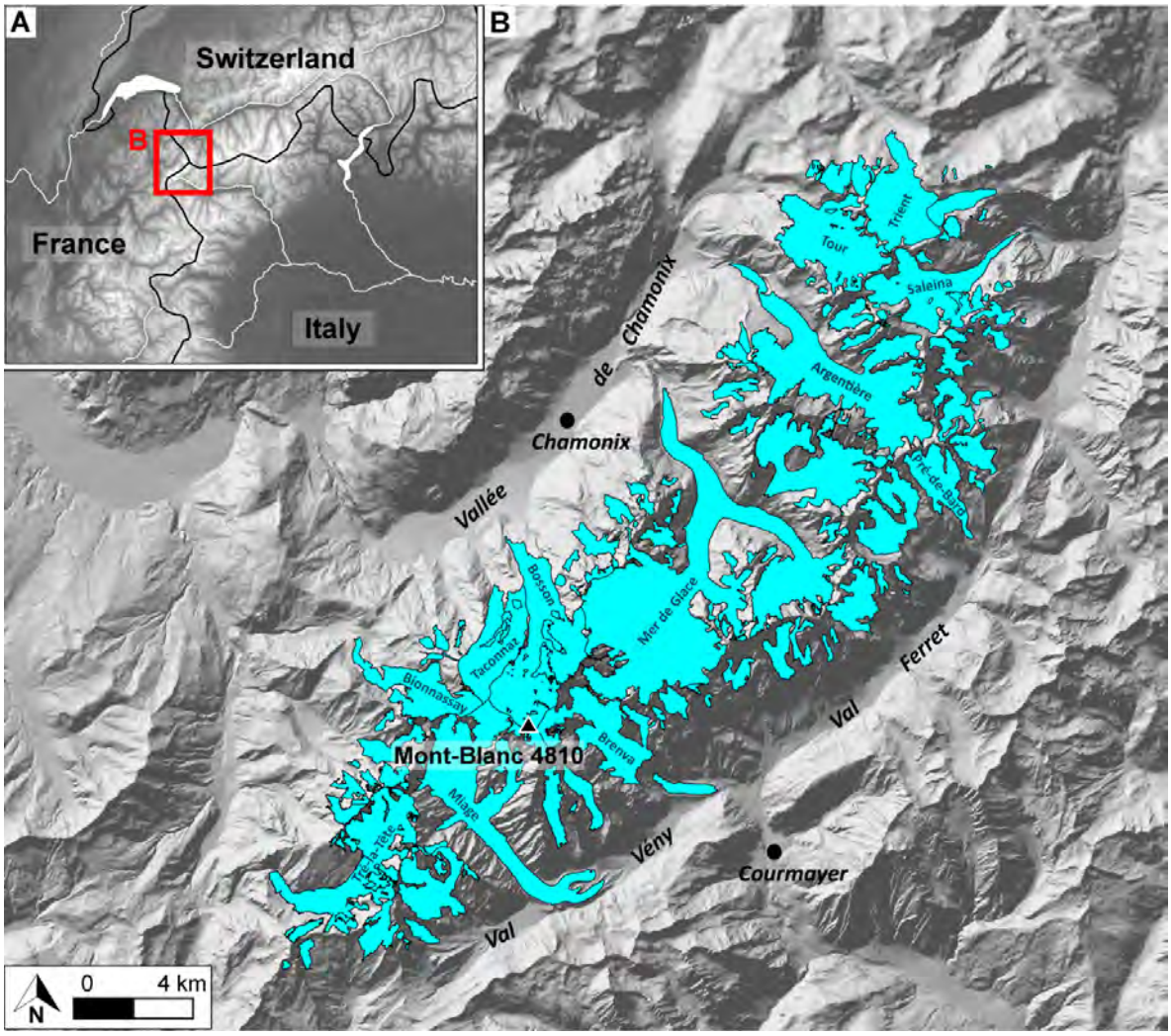

Figure 1.8: Extent of glaciers in the Mont-Blanc massif. The ice extent was downloaded from the GLIMS database (Global Land Ice Measurements from Space, Raup et al., 2007). The ice extent in Switzerland were produced from images of 2011 by Smiraglia et al. (2015). The ice extent in Italy was produced from 2009 images by Fischer et al. (2015). The ice extent in France was produced from of 2004 images by Rabatel et al. (2016).

The ice cover of the Mont Blanc massif was completely different during the cold stages of the Quaternary period, when the Mont Blanc glaciers were anastomosed and flowed into the valleys down to the Alpine lowlands. Through mapping and dating glaciological deposits (moraines, erratic boulders or glacio-lacustrine deposits, Bini et al., 2009) of the LGM extent, it was possible to reconstruct its paleo-geography (Fig. 1.9). Coutterand (2010) summarized existing work on the ice-extent reconstitution of the LGM in the north-western Alps.

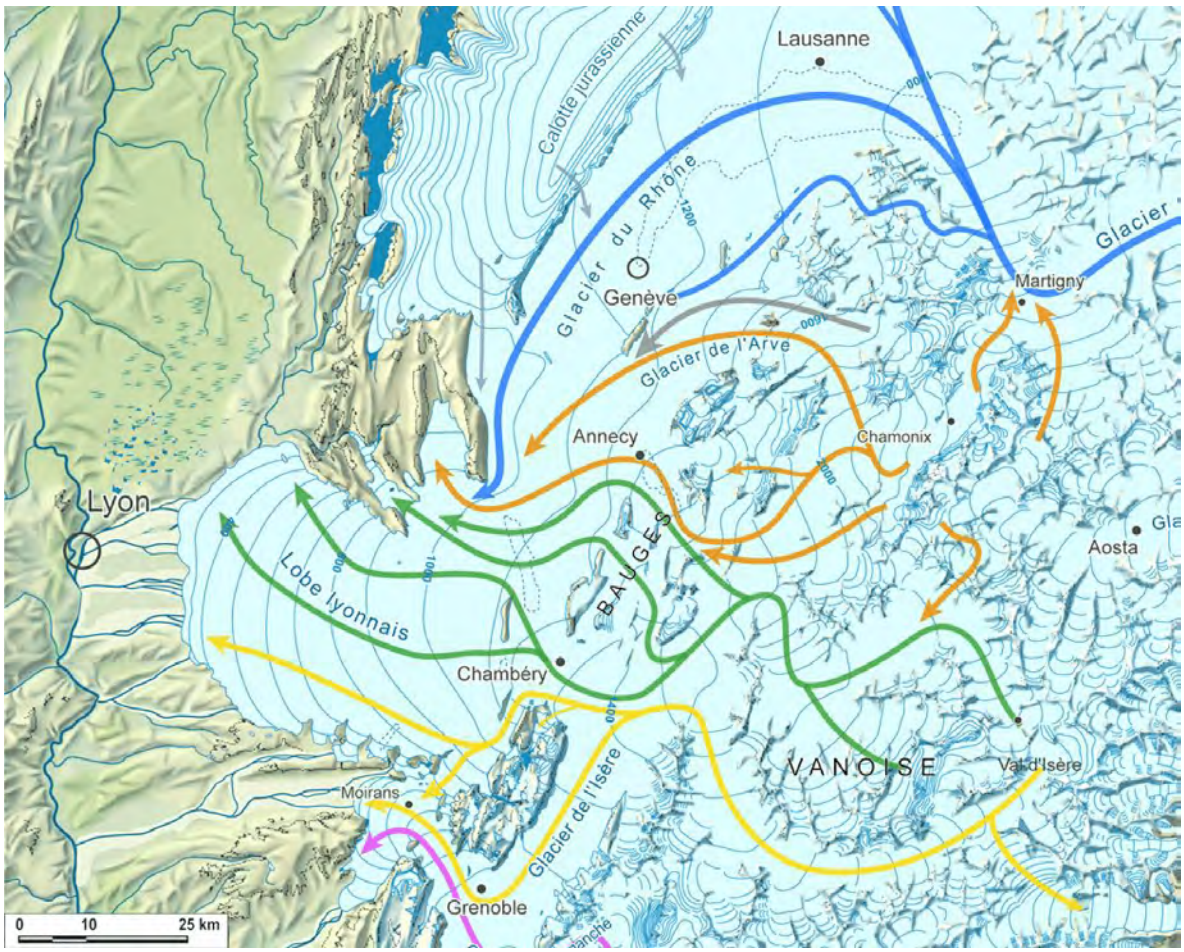

Figure 1.9: Paleo-geographic map of the western Alps during the LGM (Bini et al., 2009; Coutterand, 2010). Glacial flux interpreted by S. Coutterand (www.glaciers-climat.com/cg/le-quaternaire-dans-les-alpes/).

LGM ice thickness in accumulation areas was assessed by performing trimline mapping (e.g., Coutterand and Buoncristiani, 2006). This method is useful for identifying the maximum ice elevation, 2300 m.a.s.l. at the actual glacier tongue of the Mer de Glace for instance, but needs to be coupled with absolute dating methods (Fig. 1.10). Using TCN dating, Wirsig et al. (2016b) shows that identical ages from both Mont Blanc (Italy) and Zillertal Alps (Austria) suggest synchronous decay of the LGM glaciers in the accumulation zones of the Western and Eastern Alps. Thus, the High Alpine ice surface started to lower roughly synchronously to

the downwasting of the glacier tongues in the forelands that was completed 19-18 *ka* (Wirsig et al., 2016b).

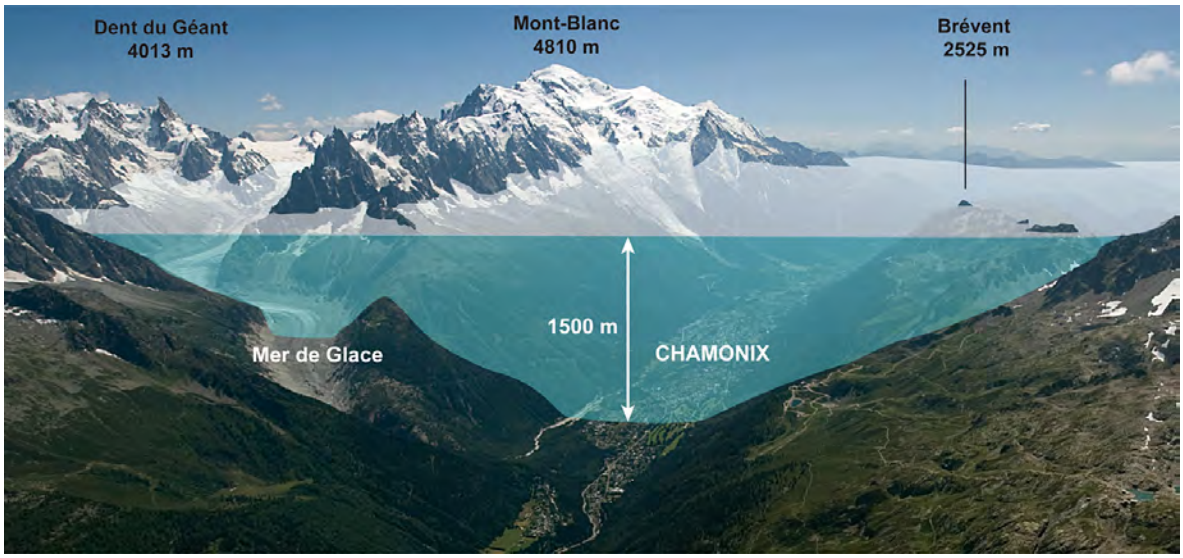

Figure 1.10: Cross-section of the glacier which occupied the valley of Chamonix during the LGM. Illustration realized by S. Coutterand (www.glaciers-climat.com/cg/le-quaternaire-dans-les-alpes/).

Le Roy et al. (2015) studied the pre- and early Little Ice Age of the Mer de Glace glacier. Their study is based on both radiocarbon and dendrochronological analysis of over 240 glacially buried Pinus cembra subfossil logs and wood remains found either embedded-in-till or as detrital material collected on the right lateral moraine in front of the Montenvers train station. Past glacier margin behavior was reconstructed in space and time since 4000 cal. year BP. The results showed a synchronicity of late Holocene glacier variability and forcing at a regional scale, although occasional differences could be detected between "Western" and "Eastern" records. The Mer de Glace record also confirms the link between the timing of sediment erosion in a high-elevation glaciated Alpine catchment and subsequent deposition in the sub-alpine Lake Bourget.

Nussbaumer (2007) reconstructed the history of the Mer de Glace from 1570 to 2003 according to pictorial and written documents. The comparison of the new Mer de Glace curve length with the curve length from the Unterer Grindelwaldgletscher (Swiss Central Alps, Aar massif) yielded an astonishing simultaneity between the two glaciers, despite the different settings of the glaciers in the western, and central Alps, respectively. Similarities between the different glaciers suggest that the western and central European Alps were affected on the whole in a similar way by the climate during the LIA.

Vincent et al. (2014) constrained the changes in ice thickness observed along the tongue of the Mer de Glace. They used historical maps surveyed between 1900 and 1905, cou-

pled with photogrammetric measurements performed using aerial photographs (French National Geographic Institute in 1958 and by Laboratoire de Glaciologie et Géophysique de l'Environnement, Grenoble in 2003 and 2008) and results from satellite-derived digital elevation models (DEMs). According to these results, Vincent et al. (2014) showed that the Mer de Glace lost about 180 meters of thickness since 1890, with 100 meters lost over the last 25 years on the Montenvers cross section and about 120 meters since 1923 on the Trélaporte cross section.

Although studied for several centuries, the evolution of the glaciers of Mont Blanc since the LGM is still not entirely constrained. The rate of Lateglacial deglaciation as well as the evolution of morphology should be better characterized. The Mont Blanc area being dominated by prevailing westerlies, this could, for example, make it possible to evaluate the influence of the different climatic regimes of the Alps and contributing to the development of a more detailed understanding of the deglaciation chronology in the High Alps.

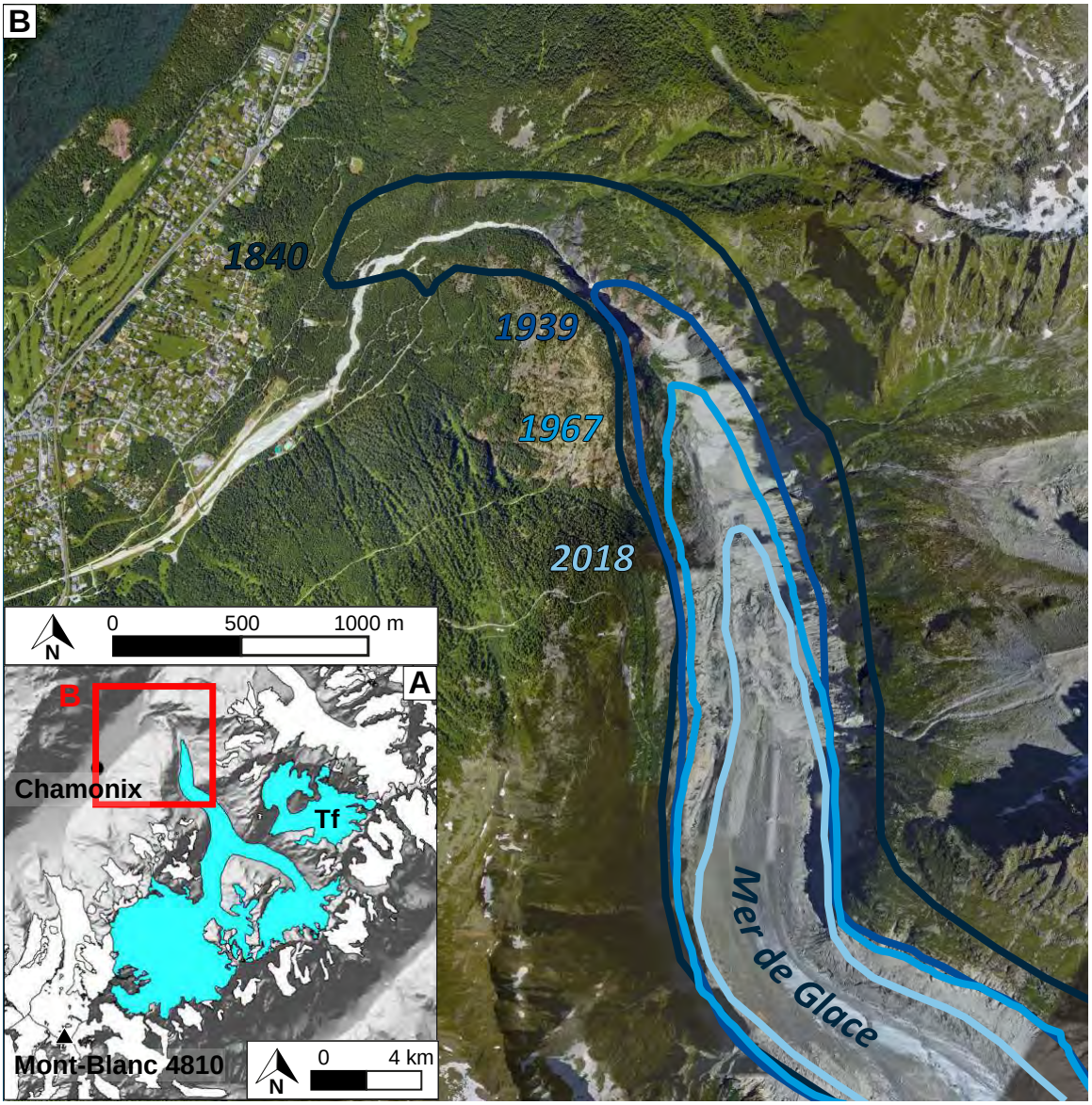

Figure 1.11: (A) Ice-extent of the Mer de Glace with the formerly connected Talèfre (Tf) at the East, the survey was produced from 2004 images by Rabatel et al. (2016). (B) Diachronic map of glacier extension of the Mer de Glace. 1840 extent is from the General Staff surveyed by Captain Jean-Joseph Mieulet. 1939 was extracted from the map of the French National Institute of Geography (IGN). 1967 extent was extracted by Gardent et al.,(2014). 2018 extent was interpreted from the orthorectified aerial photograph of the Mer de Glace acquired in 2018 (source: www.geoportail.gouv.fr).

1.7 Organisation of the dissertation

This dissertation is composed of three publications supported by a framework of detailed information on the systematics, methodology and interpretation of the relevant luminescence and cosmogenic nuclides dating. The thesis is structured in 4 main parts.

The first part investigates the potential of OSL surface exposure dating along a vertical cross-section of polished bedrock surfaces with known post-LIA (Little Ice Age) exposure ages (from 3 to 137 years) along the Mer de Glace glacier. The luminescence signals from rock slices exhibit increasingly deep bleaching profiles with elevation and thus exposure age, which is consistent with progressive glacier thinning since the LIA. In this part, I show that OSL surface exposure dating can be applied to periglacial environments, and is a promising tool for high-resolution reconstruction of ice extent fluctuations, both in space and time over timescales from 10^1 to 10^2 years.

The second part is introducing a new approach for evaluating post-glacial bedrock surface erosion in mountainous environments by combining TCN and OSL surface exposure dating. Using a numerical approach, I show how it is possible to simultaneously invert bedrock OSL signals and ^{10}Be concentrations into quantitative estimates of both post-glacial exposure duration and bedrock surface erosion.

In the third part, this new approach is applied on nine bedrock surfaces sampled over two elevation profiles located on the flanks of the Mer de Glace. The results show a clear anti-correlation between erosion rate and elevation which bring new insight on spatial variability of erosion rates reflecting geometric and climate controls. The derived erosion rates can be used to correct the timing of deglaciation age based on TCN data, suggesting very rapid ice thinning after 18 *ka*.

The final part provides a synthesis of the results and conclusions presented in this dissertation. It further discusses potential directions for future studies addressing the open questions of the deglaciation chronology, bedrock erosion and potential of OSL surface exposure dating.

References are listed in a single bibliography at the end of the dissertation to avoid duplication. The appendix of the Chapter 2, 3 and 4 are regrouped in one main Appendix chapter in order to facilitate the reading of the manuscript. Later on the publications that I contributed to during my PhD are provided, including a brief statement of my own contribution, as well as datasets not shown in the previous sections.

CHAPTER 2

Investigation of OSL surface exposure dating to reconstruct post-LIA glacier fluctuation in the French Alps (Mer de Glace, Mont Blanc massif)

Benjamin Lehmann[1], Pierre G. Valla[1,2], Georgina E. King[1,2]and Frédéric Herman[1]

[1]Institute of Earth Surface Dynamics, University of Lausanne, Lausanne, 1012, Switzerland.
[2]Institute of Geological Sciences and Oeschger Centre for Climate Change Research, University of Bern, Bern, 3012, Switzerland.

Abstract

Providing quantitative constraints on late Pleistocene glacier fluctuations remains an important challenge for understanding glacier response to past and future climate changes. In most mountainous settings, paleo-glacier reconstructions are limited because they often lack precise temporal constraint. Different geochronological methods have been developed and applied to date specific geomorphological or sedimentological markers for paleo-glacier dynamics. Recently, OSL (optically stimulated luminescence) surface exposure dating has been introduced and provides us with an opportunity to improve paleo-glacier reconstructions. This method is based on the sensitivity of the OSL signal from rock minerals to light, resulting in bleaching of the OSL signal within the upper first millimeters of the exposed rock surface, a process that depends on the exposure age, the rock type and the local setting (e.g., topographic shielding, bedrock orientation). Here, we investigate the potential of OSL surface exposure along a vertical cross-section of polished bedrock surfaces with known post-LIA (Little Ice Age) exposure ages (from 3 to 137 years) along the Mer de Glace glacier (Mont Blanc massif, France). The infra-red stimulated luminescence (IRSL) signals from rock slices exhibit increasingly deep bleaching profiles with elevation and thus exposure age, which is consistent with progressive glacier thinning since the LIA. Our results show that OSL surface exposure dating can be applied to periglacial environments, and is a promising tool for high-resolution reconstruction of ice-extent fluctuations, both in space and time.

2.1 Introduction

During the last ca. 5 Ma of the Earth's history, global climate cooled and evolved towards oscillating climatic conditions that intensified towards the present (e.g., Zachos et al., 2001; Herbert et al., 2016). This climate shift left a strong imprint on mountain topography (e.g., Penck, 1905; Broecker and Denton, 1990; Molnar and Engand, 1990; Peizhen et al., 2001; Egholm et al., 2009). However, understanding paleo-climatic conditions in mountainous areas over the Plio-Pleistocene epochs remains difficult. Local records of successive glacial/interglacial cycles are scarce or poorly preserved over such long timescales (Ehlers and Gibbard, 2007). Polar ice-sheets and marine cores are useful for providing long-term global climatic records but are unable to describe regional continental climate. In contrast, glaciers and their fluctuations through time provide invaluable information on past mountain climatic conditions. Through mapping and dating moraine deposits and erratic boulders, it is possible to reconstruct the history of ice-extent (e.g., for the European Alps: Ivy-Ochs et al., 2006; Bini et al., 2009; Preusser et al., 2011; Schimmelpfennig et al. 2014; Ivy-Ochs et al., 2015; Wirsig et al., 2016).

Past glacier extents in the European Alps are well constrained since the Little Ice Age (LIA: 15^{th} to 19^{th} centuries). Using historical maps, survey reports and aerial photogrammetry, glacier fluctuations have been precisely reconstructed over the last two centuries (e.g., Vincent et al., 2014). To go further back in time into the Pleistocene, different geochronological methods can be used such as lichenometry (Winkler et al., 2004), varve chronologies (Stewart et al., 2011), dendrochronology (Baillie, 1995) and radiocarbon dating (Hajdas, 2008). However, organic matter can be scarce for glacial/periglacial deposits because of extremely active geomorphic systems associated with glacial environments. In addition to these methods, surface exposure dating of polished bedrock or erratic boulders using terrestrial in situ cosmogenic nuclides has been developed over the last decades (Lal et al., 1991; Gosse and Philips, 2001; Balco, 2011; Ivy-Ochs and Briner, 2014), and has been widely used in the European Alps (see Ivy-Ochs et al., 2006; 2009 for reviews). The combination of different cosmogenic nuclide pairs (e.g., ^{10}Be and ^{14}C: e.g., Goehring et al., 2012; Hippe et al., 2014) provides us with important information on Alpine glacier paleo-geography since the Last Glacial Maximum (LGM; Ivy-Ochs et al., 2006; Wirsig et al., 2016). However, the cosmogenic nuclide production rate and the integration of production over the first 1-2 meters below a rock surface may limit the resolution of such methods for recent and/or complex exposure histories.

Here we investigate whether optically stimulated luminescence (OSL) surface exposure dating can be used to reconstruct recent glacier fluctuation. Luminescence dating is based on the accumulation of trapped electrons through time in the crystalline lattice of certain minerals (e.g., quartz or feldspar). Some of these trapped electrons are sensitive to daylight exposure (Aitken, 1985; Huntley et al., 1985). Luminescence dating is commonly used to date sediment

burial in a range of geomorphological environments (e.g., Duller, 2008; Rhodes, 2011; Fuchs and Owen, 2008) but can also be used to determine rates of bedrock cooling (Guralnik et al., 2015; King et al., 2016; Brown et al., 2017), and the exposure age of archaeological rock surfaces (Polikreti et al., 2003; Sohbati et al., 2011). This latter application is based on the principle that when a rock surface is exposed to light, the luminescence signal, which is initially homogenous within the rock sample (at a given level or in field steady-state; e.g., Valla et al., 2016), will progressively decrease at depth until being completely zeroed, a phenomenon called "bleaching" (Aitken, 1998). The assumption used in this study is that the longer a surface has been exposed to daylight, the deeper the signal bleaching will be (Polikreti et al., 2002). In granitic and gneissic rocks, bleaching through time has been shown to occur over the first few centimetres depth of the rock surface (Vafiadou et al., 2007; Sohbati et al., 2011; Freiesleben et al., 2015). In alpine environments, glacier advances during the late Pleistocene to Holocene have been associated with subglacial erosion of bedrock at the centimetre-scale (e.g., Goehring et al., 2011). This means that only the most recent exposure history of the bedrock will be recorded, as earlier exposure histories and OSL bleaching evidence will have been eroded by subsequent glacier advances. OSL surface exposure dating would thus in theory, enable past glacier extents to be reconstructed with a high temporal resolution for both recent and complex exposure histories. Furthermore, this method is attractive because of the short time required for sample preparation (Sohbati et al., 2011), although one current disadvantage is the requirement for calibration of this chronometer on rock surfaces with independently known exposure ages (Sohbati et al., 2012a).

In the following, we first introduce the study site, i.e., the Mer de Glace, and our sampling strategy. We have targeted several independently dated glacially eroded bedrock surfaces, which represent past elevations of the glacier surface since the LIA. We then review the basic principles of the method and present the luminescence signals for six different surfaces along a vertical cross section above the present-day Mer de Glace. Our results show a strong correlation between sample elevation, exposure age and bleaching depth. Finally, we use this dataset to show that model calibration requires multiple samples of known age to take full advantage of OSL surface exposure dating in both glaciated and formerly glaciated environments.

2.2 Setting and sampling strategy

2.2.1 Geomorphological setting

The Mer de Glace glacier (Fig. 2.1) is about 11.5 km long and is located in the Mont Blanc massif. The modern glacier covers an area of 30.4 km^2 (excluding former tributary Talèfre Glacier) and spans an elevation range from 4205 m to 1531 m.a.s.l. (data from 2008; Gardent et al., 2014). The mean equilibrium line altitude (ELA), reconstructed using remote sensing

methods, was about 2880 m.a.s.l. between 1961 and 1990 for five of the main north-facing Mont Blanc massif glaciers, including the Leschaux Glacier for the period 1984-2010 (Rabatel et al., 2013).

The Mer de Glace is an appropriate laboratory for validating the application of OSL surface exposure dating for paleo-glacier reconstruction. Numerous studies have provided detailed reconstructions of Mer de Glace fluctuations from the LGM towards the Holocene and present day (Coutterand and Buoncristiani, 2006; Nussbaumer et al, 2007; Vincent et al., 2014; LeRoy et al., 2015). The Montenvers site (Fig. 2.1) was chosen as an optimal study site as the evolution of the glacier thickness since the LIA has been reconstructed by Vincent et al. (2014) using historical maps, aerial photogrammetry and satellite-derived digital elevation models (see Section 2.3 for details). Furthermore, the rock type is generally homogenous along the valley flank (i.e., orthogneiss; Dobmeier et al., 1998), avoiding any lithological dependency of the OSL surface exposure dating approach although occasional granitic lenses are exposed in the lower part of the profile (see Section 2.2 for details).

Our sampling strategy was to collect glacially polished bedrock surfaces with the best-preserved erosion patterns (glacial striations, roches moutonnées; Fig. 2.2) to ensure that sample bleaching profiles reflect the period of time since post-LIA deglaciation. The samples were also selected to have low topographic shielding and vegetation cover (e.g., lichen). Steep slopes were selected (i.e., above 30°) to limit any potential snow cover effects. In particular, we focused on rock surfaces exhibiting striations parallel to the Mer de Glace flow line in order to avoid the potential influence of tributary glaciers.

2.2.2 Sample description

We collected six samples along the Montenvers profile during several field campaigns (2015-2016), ranging in elevation from 1841 to 1696 m.a.s.l. (Fig. 2.1 and Table 2.1). Samples MBMV1, MBMV7, MBMV8, MBMV10 and MBMV11 consist of coarse-grained orthogneiss, typical for the Aiguilles Rouges massif (Dobmeier et al., 1998). These rocks mainly comprise coarse K-feldspar crystals, quartz, biotite and muscovite. Only MBMV6 was collected from a granitic lens, which consists of bigger quartz and feldspar crystals than the orthogneiss (Fig. 2.3). Because differences in crystal properties may influence light penetration, i.e., due to both crystal size and distribution, sample MBMV6 is used to explore any potential lithological effect on the OSL surface exposure dating approach.

2.2.3 Independent age calibration from glacier thickness reconstruction

We use the historical post-LIA reconstruction of the Mer de Glace thickness (Vincent et al., 2014) available for two cross-sections: Montenvers and Echelets (Fig. 2.1). Samples

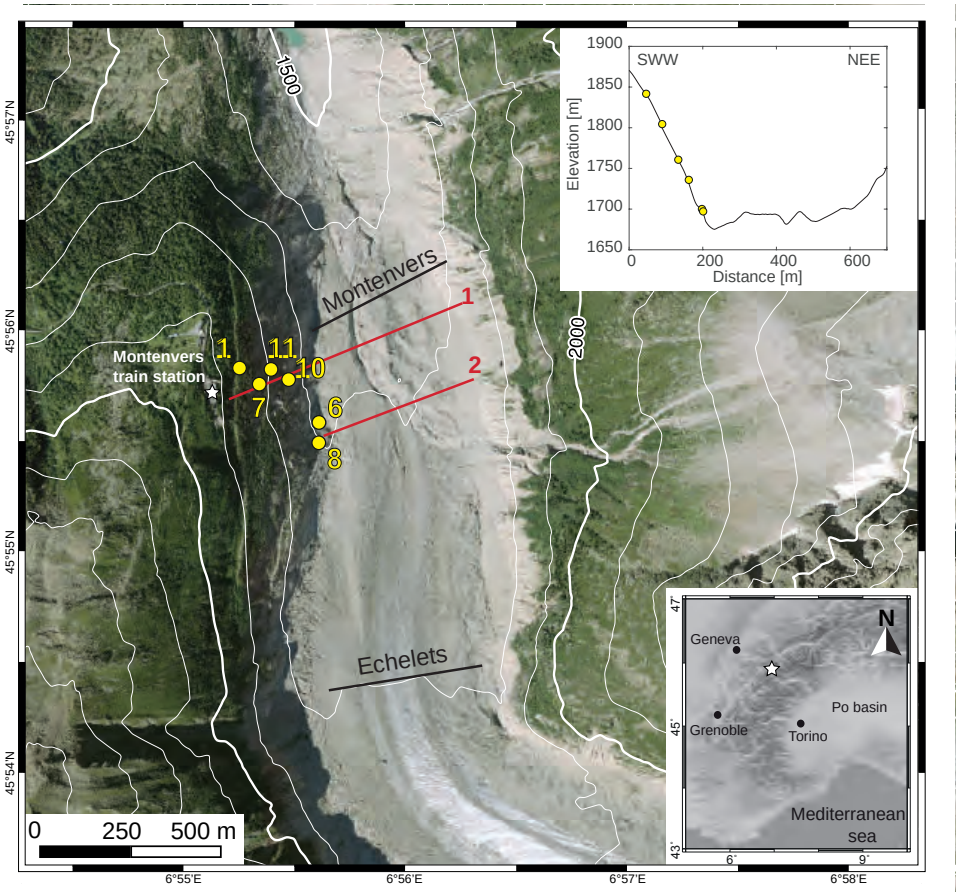

Figure 2.1: Sampling map of the Montenvers site, Mer de Glace. The orthorectified aerial photograph of the Mer de Glace was acquired in 2016 (source: www.geoportail.gouv.fr). The black lines show the two cross-sections produced by Vincent et al. (2014) which we interpolated to reconstruct glacier surface elevations at two different locations (red lines 1 and 2, see Section 2.3 and Appendix Fig. A2.1) where samples were collected (yellow dots with numbers). Upper right inset represents the collected samples projected along cross-section 1. Bottom right inset shows location of the study area within the western Alps.

MBMV1, MBMV7, MBMV10 and MBMV11 were collected from the same profile located 290 m upstream of the Montenvers cross-section and 690 m downstream of the Echelets cross-section (cross-section 1, Figs. 2.1 and 2.4). Samples MBMV6 and MBMV8 were taken along a profile (cross-section 2, Fig. 2.1) located 200 m upstream of the cross-section 1. Because glacial thinning would progressively expose bedrock surfaces at lower elevations, we can use the relationship between exposure age and sample elevation to constrain the temporal evolution of glacial thickness (Figs. 2.1 and 2.4).

Post-LIA thickness reconstructions of the Mer de Glace for cross-sections 1 and 2 have been interpolated from the Montenvers and Echelets cross-sections. Exposure ages from 2 to 137 years were obtained for the different samples, using either cross-section 1 (MBMV1, MBV7,

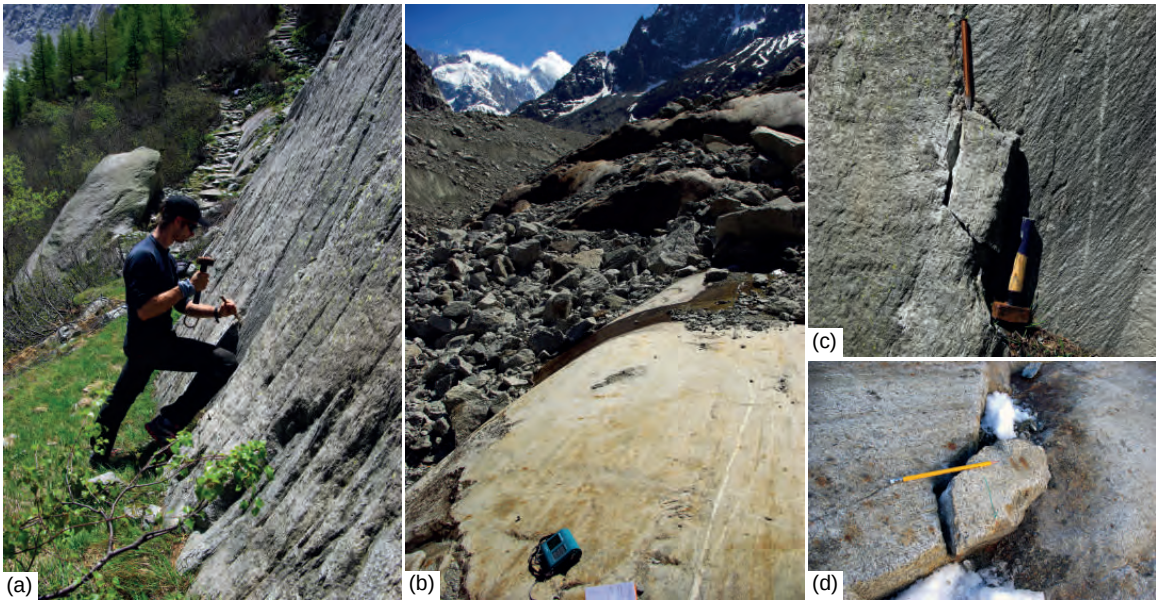

Figure 2.2: Sampling sites and sample details at the Montenvers site. (a-b) Sampling sites for MBMV7 and MBMV6. (c-d) Outcrops and samples MBMV7 and MBMV6.

Table 2.1: Sample characteristics from the Montenvers cross-section. Estimated exposure ages were reconstructed using differential GPS and ice-thickness reconstruction as shown in section 2.3. Shielding factors were calculated with the geometric shielding calculator (CRONUS-Earth project). Note that all estimated exposure ages are referenced from 2015 (date of the first field campaign).

Sample ID	Latitude	Longitude	Elevation	Lithology	Reconstructed	Topographic	Surface
	WGS 84		[m a.s.l.]		Exposure Age [yr BP]	shielding factor	orientation
MBMV1	45°55'54.0"	06°55'07.7"	1841	Gneiss	137 (1)	0.81	N8 55°E
MBMV6	45°55'48.9"	06°55'17.7"	1696	Granite	2 (2)	0.92	N0 30°E
MBMV7	45°55'52.7"	06°55'09.9"	1804	Gneiss	69 (2)	0.79	N374 60°E
MBMV8	45°55'47.7"	06°55'18.5"	1699	Gneiss	3 (2)	0.81	N13 54°E
MBMV10	45°55'54.0"	06°55'14.1"	1735	Gneiss	18 (2)	0.79	N0 60°E
MBMV11	45°55'54.3"	06°55'11.5"	1760	Gneiss	30 (2)	0.88	N355 75°E

MBMV10 and MBMV11) or cross-section 2 (MBMV6 and MBMV8) (see Appendix Chapter A2.1). All exposure ages are relative to the first sampling campaign in summer 2015.

2.3 Methodology: OSL surface exposure dating

2.3.1 Theoretical approach

Minerals such as quartz and feldspar naturally contain defects or impurities in their crystal lattice. Energy released by ambient radiation (i.e., cosmic rays and the flux of high-energy

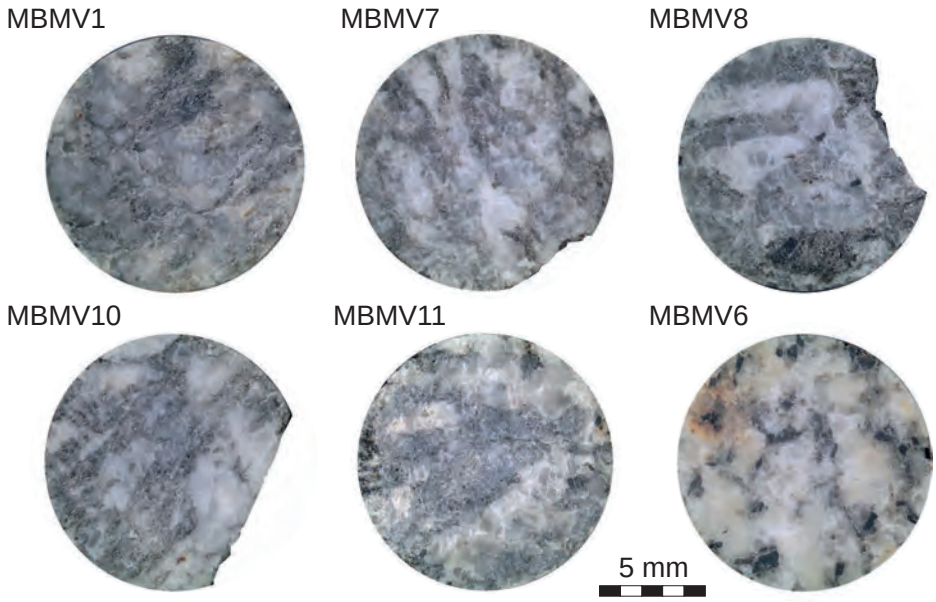

Figure 2.3: Pictures of selected rock slices (see section 3.1 for details), showing the difference in composition and texture between orthogneiss (MBMV1, MBMV7, MBMV8, MBMV10, and MBMV11) and granite (MBMV6).

solar particles or/and radioactive decay in the rock-matrix) excites electrons from their equilibrium state (valence band), and these can become trapped at higher energy levels within the crystal. Because of the finite number of traps, electron filling occurs until saturation is reached. By giving energy to the system in the form of light or heat (natural bleaching processes), electrons are released and return to their equilibrium state, producing photons. This phenomenon is called luminescence and the intensity of a given luminescence signal is thus proportional to the number of trapped electrons (Aitken, 1985; 1998). In a rock surface continuously exposed to daylight, the progressive bleaching of the luminescence signal is expected to propagate deeper into the surface with time (Habermann et al., 2000; Polikreti et al., 2002; Laskaris and Liritzis, 2011).

Rock surface dating was first used in archaeology, and was based on thermally-stimulated measurements, i.e., thermoluminescence (TL; Liritzis et al., 1994; Richards et al., 1994; Theocaris et al., 1997; Polikreti et al., 2002; 2003). More recently, optically stimulated luminescence dating (OSL; e.g., Habermann et al. 2000; Vafiadou et al., 2007) has been introduced to date surface exposure, which benefits from improved measurement reproducibility and more rapid signal bleaching following exposure to daylight than typically-used TL signals (e.g., the 325°C TL peak in quartz). The potential of OSL for dating exposure events in geomorphological (Freiesleben et al., 2015; Sohbati et al., 2015) and archaeological (Liritzis, 2011) contexts has recently been investigated, and a range of applications including relative sea-level changes and coastal geomorphology (Simms et al., 2011; Simkims et al., 2013) have been published.

However, OSL surface exposure dating has not yet been applied to glacially polished bedrock surfaces.

In mountainous environments, OSL dating can be used to evaluate the exposure age of a polished bedrock surface as described in Fig. 2.4. At the initial condition (t_1 in Fig. 2.4), the glacier has reached its maximum thickness. Ice and periglacial sediments cover the bedrock surface, and the luminescence signals of bedrock minerals are in field steady-state and uniform in the rock column. When the glacier retreats, freshly-eroded surfaces are exposed to daylight (point a at time t_2, Fig. 2.4). The initial luminescence signals start to bleach for these exposed surfaces, while the sample at lower elevation is still covered by the glacier and its luminescence signals remain uniform in the rock (point b at time t_2, Fig. 2.4). As the glacier continues to thin, the lower part of the bedrock flanks are uncovered (t_3, Fig. 2.4) and the luminescence signals start to bleach for the lower-elevation surfaces. Therefore, in a setting affected by progressive glacier retreat and thinning, there is a direct correlation between the elevation of the studied site and the exposure age, with the assumption that the longer a surface is exposed to daylight, the deeper into the rock the luminescence signal is bleached (Freiesleben et al., 2015; Sohbati et al., 2011).

2.3.2 Modelling approach

To assess rock surface exposure durations to daylight from a luminescence depth profile, we use the model proposed by Sohbati et al. (2011; 2012a,b) who provide an in-depth review of each parameter. When a rock surface is exposed to daylight, both detrapping (due to the release of energy by daylight) and trapping (due to absorption of energy from ambient radiation) occur simultaneously. The trapped-charge concentration during light exposure is given by the following differential equation:

$$\frac{\partial n(x,t)}{\partial t} = -E(x)n(x,t) + F(x)[N(x) - n(x,t)] \tag{2.1}$$

Where $n(x,t)$ is the trapped charge concentration $[m^{-3}]$ at time t $[s]$ and depth x $[m]$, $N(x)$ is the concentration of sites $[m^{-3}]$ available for trapping at depth x, $E(x)$ is the charge detrapping rate $[s^{-1}]$, and $F(x)$ is the trap filling rate $[s^{-1}]$. The charge detrapping rate, $E(x)$, is itself given by:

$$E(x) = \overline{\sigma\varphi_0}e^{-\mu x} \tag{2.2}$$

where $\varphi(\lambda, x)$ is the photon flux $[cm^{-2}\ s^{-1}]$ describing the rate of incoming photons that can bleach the trap of interest. $\sigma(\lambda)$ is the photoionization cross section $[cm^2]$ describing the probability of this specific trap to be excited by light stimulation. It is averaged over the

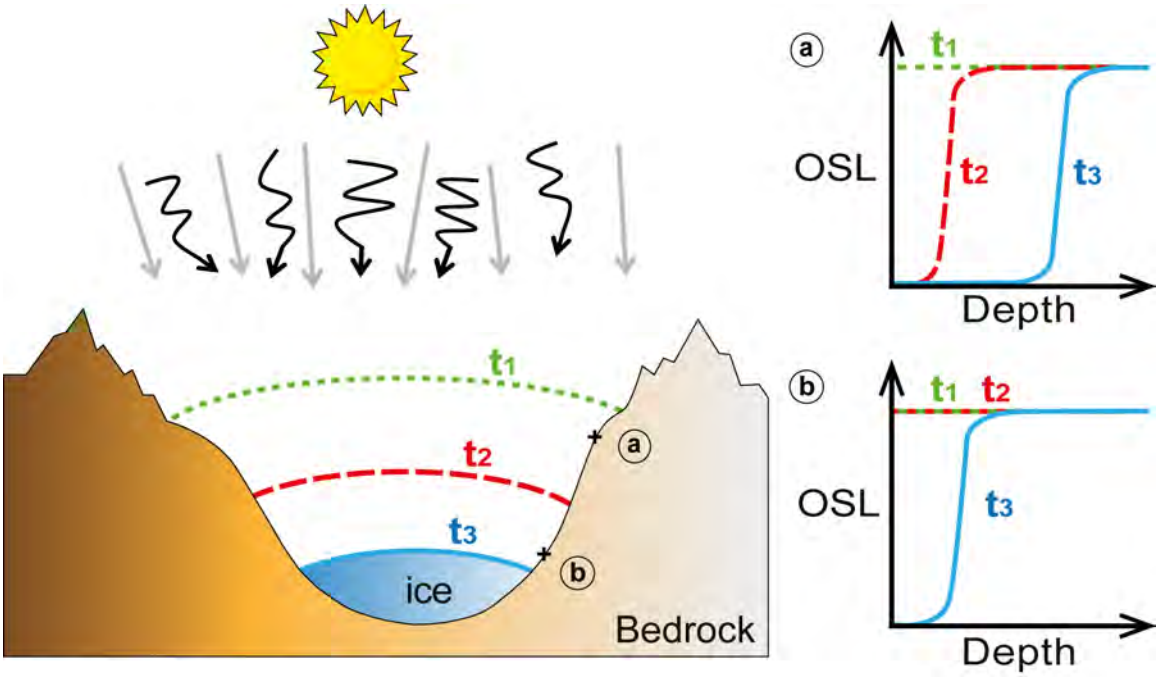

Figure 2.4: Sketch linking glacier thinning and OSL signal evolution for two bedrock surfaces located at different elevations along the valley flank. Straight arrows (grey) represent cosmic rays and high-energy solar particle flux; this radiation, together with radioactive decay in the rock matrix build up the latent luminescence signal. Other arrows (black) represent low energy electromagnetic radiation from the sun; this radiation bleaches the latent luminescence signal. At the initial time t_1, the glacier is at its maximum extent and the OSL signals for both surfaces are in field steady-state and uniform within the rocks, L_0. At time t_2, the glacier has retreated and exposed the surface (a), the OSL signal begins to bleach whilst surface (b) remains covered with its luminescence signal unchanged. In the final step t_3, the glacier size has shrunk, surface (a) remains exposed and its OSL signal is bleached at greater depth while surface (b) has just been exposed to daylight and its OSL signal has been bleached just below the exposed surface.

wavelengths present in the solar spectrum at the surface ($x = 0$). Here, we assume that the photon flux does not fluctuate through time, and we are only concerned with the product of the two parameters, which is given by $\overline{\sigma\varphi_0}$ $[s^{-1}]$ (i.e., the effective decay rate of luminescence; Sohbati et al., 2011). Equation (2.2) also includes a decay term for light attenuation with depth. The light attenuation coefficient μ $[m^{-1}]$ describes how deep into the rock a photon will penetrate and affect the luminescence signal. μ is assumed to be independent of wavelength in the spectral range of interest (Sohbati et al., 2011).

For surface exposure dating of terrestrial surfaces, the effect of trap filling during daylight exposure over short timescales (i.e., centuries) is often negligible (i.e., $F(x) \approx 0$) (see Appendix Chapter 7.1.2). The trapped charge population at a given depth (x) can then be approximated by:

$$n(x) = n_0 e^{-E(x)t} \tag{2.3}$$

where n_0 is the initial charge population $[m^{-3}]$ assumed to be constant with depth within the rock column prior to bleaching. Assuming that the luminescence signal (L) is proportional to n, Eq. (2.3) becomes:

$$L = \frac{Lx}{Tx} = L_0 e^{-\overline{\sigma\varphi_0} t e^{-\mu x}} \tag{2.4}$$

where Ln/Tn is the normalized natural luminescence signal measured at depth x $[m]$ after exposure age t $[s]$. L_0 is the normalized natural luminescence signal before bleaching (Fig. 2.4), which is sample dependent and can be constrained in the laboratory.

Equation 2.4 can predict the rock luminescence profiles for different exposure ages, however the mean photon flux φ_0, the photoionization cross-section σ, and the attenuation coefficient μ must first be quantified. φ_0 is mainly controlled by the latitude and the cloudiness; and it is broadly correlated to elevation (Blumthaler et al., 1997). The solar irradiance is fluctuating over decadal timescales (Lean, 1987) making the independent determination of the photon flux impossible without knowing the time of exposure. The photoionization cross-section σ, depends on both the mineral and the trap targeted (Bailey, 2004). For samples coming from the same region and from a similar lithology, $\overline{\sigma\varphi_0}$ is assumed to be uniform and μ is expected to be of the same order of magnitude between samples, but not necessarily equal.

The OSL-depth profile of exposed rock surfaces with independently constrained exposure durations can be used to calibrate the $\overline{\sigma\varphi_0}$ and μ parameters by fitting the luminescence signal bleaching with depth (Singarayer, 2002; Sohbati et al., 2012a). These constrained parameters can then be used to determine the exposure histories of unknown-age surfaces from the same region.

Here, our objective is to demonstrate the validity of the proposed model (Eq. 2.4) on polished bedrock surfaces and to calibrate the model parameters on surfaces with known exposure age. To do so, the unknown $\overline{\sigma\varphi_0}$ and μ parameters are inverted for each sample using a probability density function of the model parameters, given the observed OSL-depth profile data. This includes a least absolute deviation regression $\mathcal{L}_{sample}$ (Eq. 2.5), in which we randomly prescribed a range of different $\overline{\sigma\varphi_0}$ and μ values. From the residual likelihood $\mathcal{L}_{sample}$ obtained, we select the maximum likelihood values of $\overline{\sigma\varphi_0}$ and μ. The modelled luminescence signals $(\frac{Ln}{Tn})_m$ are calculated for each rock slice of a given sample using the known exposure age of each sampling site, giving:

$$\mathcal{L}_{sample} = exp(-\frac{1}{2a}\sum_{i=1}^{n}\left|\frac{Lx^{(i)}}{Tx}_{obs} - \frac{Lx^{(i)}}{Tx}_{m}\right|) \tag{2.5}$$

where n is the number of rock slices per sample, $\frac{Lx}{Tx}{}_m^{(i)}$ is the luminescence signal calculated using Eq. (2.4), $\frac{Lx}{Tx}{}_{obs}^{(i)}$ is experimentally measured for each rock slice i and a is the uncertainty. Given that the scatter of the plateau signal (L_0) for every independent sample is larger than the analytical error, we use the standard deviation around the plateau value L_0 to estimate a. Then, we compute the combined likelihood for a number of samples p using:

$$\mathcal{L}_{combined} = \prod_{j=1}^{p} \mathcal{L}_{sample(j)} \tag{2.6}$$

This approach provides the most likely common values of $\overline{\sigma\varphi_0}$ and μ. Once the parameters of the model are determined as shown above, it is possible to invert the exposure age for other rock surfaces using the constrained $\overline{\sigma\varphi_0}$ and μ values (cf. Eq. (2.5)).

Table 2.2: Summary of symbols.

Symbol	Unit	Definition
n	m^{-3}	Concentration of trapped charge
x	m	Depth
t	s	Time
N	m^{-3}	Concentration of sites available to trap charge
E	s^{-1}	Charge detrapping rate due to solar radiation
F	s^{-1}	Charge trapping due to ionising radiation
σ	cm^2	Photionization cross-section
φ	$cm^{-2}\ s^{-1}$	Photon flux
$\overline{\sigma\varphi}_0$	s^{-1}	Charge detrapping rate
μ	m^{-1}	Attenuation coefficient
Lx	Counts	Regenerated luminescence signal
Tx	Counts	Test dose signal
L	Counts	Luminescence

In order to verify our modelling approach, we show a synthetic inversion. We produce a synthetic luminescence signal (Lx/Tx for depths between 0 and 14 mm) using Eq. (2.4) and sample-specific $\overline{\sigma\varphi_0}$ and μ parameters (obtained from initially fitting every sample using their independent age control, see Section 5.2 for details) and assuming a constant μ value (i.e., homogenous lithology with rock depth). The first step of the synthetic test is to invert parameters $\overline{\sigma\varphi_0}$ and μ knowing the exposure age t for each individual sample as presented above. Then, using these $\overline{\sigma\varphi_0}$ and μ parameters, we subsequently invert for the exposure age t using Eq. (2.4). In order to study the effect of potential uncertainties from the experimental data on the exposure age determination, we reproduce this synthetic test with white noise on the luminescence signal, with four different amplitudes between 0 and 100 %

on the luminescence signal, with four different amplitudes between 0 and 100 % (Fig. 2.5). Our synthetic results show that our inversion approach can recover the exposure age with 0 to 50% noise. The synthetic test with 100% noise on the luminescence signal provided age outcomes with larger uncertainties (>20%). The best results are obtained using the best-fit of $\overline{\sigma\varphi_0}$ and μ and the median value of the predicted exposure ages. The resulting uncertainties are correlated with the magnitude of the noise, however any potential variability in the luminescence signal does not appear to produce a significant bias on the inverted exposure age.

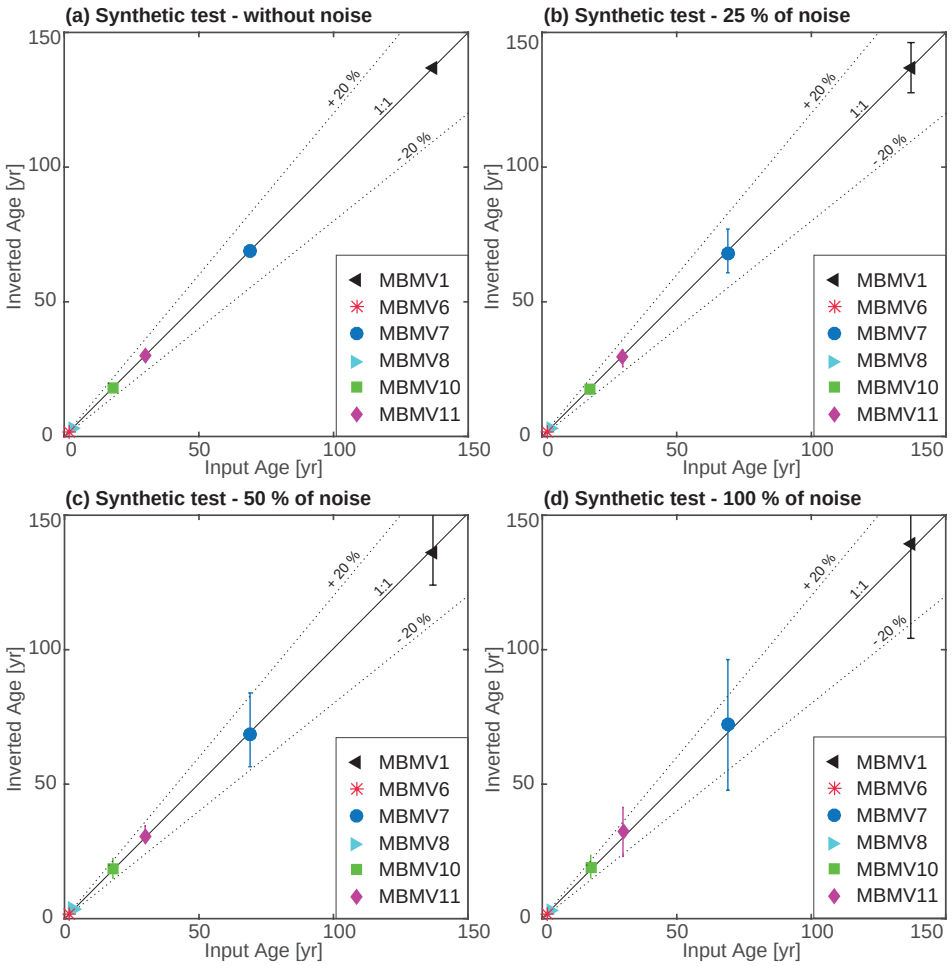

Figure 2.5: Results (median value) of inverted exposure age from the synthetic test, (a) without noise on the luminescence signal, (b) with 25%, (c) 50%, and (d) 100% noise. Error bars represent $\pm 2\sigma$ on the inverted age.

2.4 Sample preparation and analysis

The bedrock samples were cored to 30 mm depth using a Husqvarna DM220 drill, with 10-mm diameter. Cores were then sliced into 0.7-mm thick rock slices with a BUEHLER IsoMet low speed saw equipped with a 0.3-mm thick diamond blade. The samples were drilled and sliced under wet conditions (water and lubricant, respectively) to avoid any heating that could potentially reset the OSL signal. Sample preparation was done under subdued red light conditions. The thickness of each rock slice was measured to determine the precise depth of each luminescence measurement. All luminescence measurements were performed using RisøTL-DA 20 TL/OSL luminescence readers (Bøtter-Jensen et al., 2010) equipped with ^{90}Sr beta sources at the University of Lausanne (Switzerland). The readers have dose rates of ∼0.1 and ∼0.2 Gy s^{-1} and measurement reproducibility of 1.14 % and 1.26 % respectively. We first perform a preheat at 250 °C before giving infrared (IR) stimulation (870 nm, Full Width Half Max (FWHM) 40 nm) at 50 °C. Luminescence signals are detected through a filter combination of a Schott BG-3 and Schott BG-39. A uniform test dose was used (27.2 Gy) to measure the subsequent luminescence response (Tx) and to normalize the natural infrared stimulated luminescence (IRSL) signal (L_x) for every rock slice. Infrared stimulated luminescence was measured for 200 s and signals were integrated over the first 6 seconds whereas the background signal was integrated between 70-100 seconds. Measurements were analysed using Analyst v.3.22b (Duller, 2005). All thermal treatments and stimulations at temperatures greater than 200°C (i.e., preheat step) were carried out in nitrogen atmosphere. The experimental approach was validated using a dose recovery and preheat plateau test (see Appendix Chapter 7.1.3; Murray and Wintle, 2000; Wintle and Murray, 2006).

2.5 Results

2.5.1 Experimental results

Figure 2.6 shows the luminescence measurements for representative samples MBMV1 and MBMV10 (results of the others samples are presented in Fig. 2.8). Three replicates (i.e., individual cores) per sample were sliced in a way that a depth and an IRSL signal can be attributed to each rock slice (unique colour/symbol for each individual rock slice in Fig. 2.6). The results show similar behaviour between the different cores for a given sample (Fig. 2.6). The IRSL signal is bleached near the surface and reaches a plateau at depth. Furthermore, and more importantly, the transition from a bleached signal to the plateau varies with the exposure age. The three core measurements reproduce well for both samples illustrated in Fig. 2.6, with the mean standard deviation between the three cores ranging from 7 to 27%

for all the studied samples. These results confirm experimentally that cores extracted from one individual sample record the same exposure history, supporting the proposed approach.

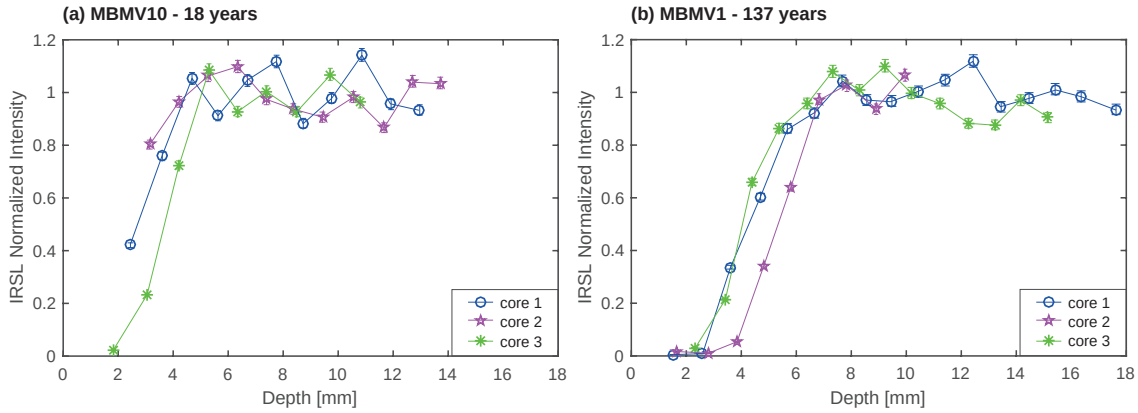

Figure 2.6: Infrared stimulated luminescence (IRSL) signal with depth for samples (a) MBMV10 and (b) MBMV1. Each coloured data point represents an individual rock slice. IRSL signals were normalized by L_0, which was determined by taking the average of the luminescence measurements along the plateau. The plateau was defined when the luminescence signal is fluctuating by less than 20%.

2.5.2 Independent parameter determination

In this section, we determine the $\overline{\sigma\varphi_0}$ and μ parameters individually for each sample in order to study their potential variability from one rock surface to another (Table 2.3). As explained in Section 3.2, bedrock surfaces from the same location should share a common $\overline{\sigma\varphi_0}$ parameter (i.e., same order of magnitude; Blumthaler et al., 1997). Similarly, we expect that the μ parameter should be similar for samples from a uniform lithology. The determined parameters are then used in the inversion of the exposure ages for each sample individually (see Section 2.5.5). All inversion outcomes are summarized in Table 2.3. Samples MBMV1, MBMV8, MBMV10 and MBMV11 share similar effective decay rates ($\overline{\sigma\varphi_0}$) with the same order of magnitude (from $1.4{\times}10^{-8}$ to $2.2{\times}10^{-7}$ s^{-1}) and show attenuation coefficients (μ) between 1.07 and 1.89 mm^{-1}. Samples MBMV6 and MBMV7 behave differently with much lower effective decay rates ($\overline{\sigma\varphi_0}$ of $2.0{\times}10^{-6}$ and $4.2{\times}10^{-6}$ s^{-1}, respectively), and different attenuation coefficients (μ of 0.92 and 2.50 mm^{-1}, respectively).

2.5.3 Parameter determination from joint probability estimates

We evaluate now the parameter determination from joint probability estimates in order to illustrate the benefit of having several known-age calibration samples. Figure 2.7a presents modelled results for sample MBMV10, which is representative of the other samples (except MBMV6 and MBMV7, see Section 5.2). The results show that log ($\overline{\sigma\varphi_0}$) and μ co-vary,

which we attribute to measurement uncertainties and variability between the different cores. Figure 2.7b shows the area of acceptable fits when all the gneissic samples are included (i.e., excluding the granitic sample MBMV6).

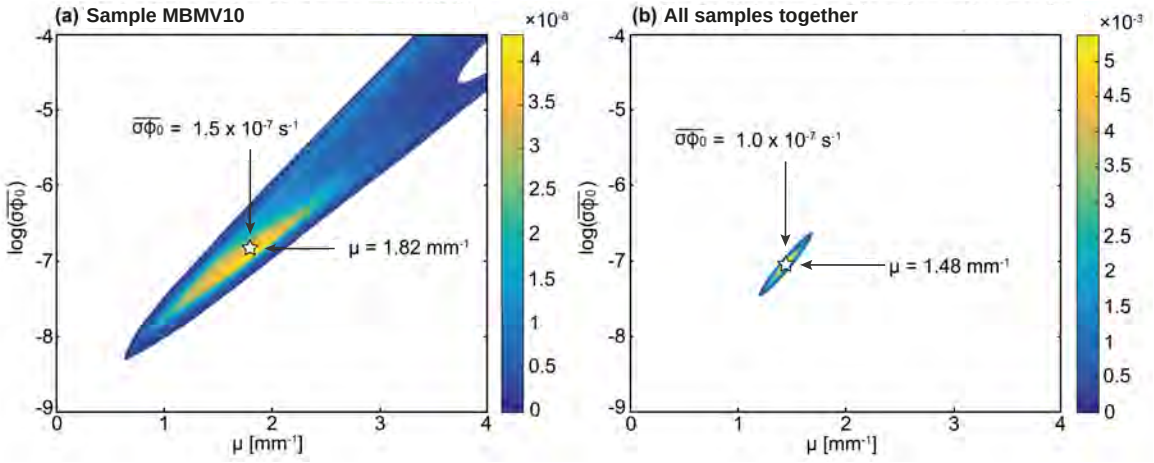

Figure 2.7: Relationship between the $\overline{\sigma\varphi_0}$ and μ parameters (a) for sample MBMV10, and (b) for all of the gneiss samples (i.e., excluding MBMV6) enabling determination of the shared $\overline{\sigma\varphi_0}$ and μ parameters (1.0×10^{-7} s^{-1} and 1.48 mm^{-1} respectively). For both Figures, the colour scale shows the likelihood between modelled and experimental data (Eq. 2.6, note the differences in scaling between the two panels), and the star is the best-fit parameter values. Zero probability is not shown for clarity.

We then contrasted individual estimates of $\overline{\sigma\varphi_0}$ and μ for each sample, using different combinations of samples to estimate these parameters. The results are summarized in Tables 2.3 and A2.3. When inverting the model parameters with any combinations of three samples, all estimates of the effective decay rates are between 6.6×10^{-8} and 1.4×10^{-7} s^{-1}, and all estimates of the attenuation coefficients are between 1.33 and 1.57 mm^{-1}. Combinations of four samples provide $\overline{\sigma\varphi_0}$ values ranging from 7.2×10^{-8} to 1.2×10^{-7} s^{-1} and μ values between 1.38 and 1.53 mm^{-1}. According to Table 2.3 and Fig. 2.7b, a common likelihood exists for all the gneissic samples calibrated together, giving an effective decay rate of 1.0×10^{-7} s^{-1} and an attenuation coefficient of 1.48 mm^{-1}.

Figure 2.8 depicts the normalized IRSL signals measured for all samples and their individually-constrained best-fit models (red lines) as described previously and illustrated in Fig. 2.7a. The obtained outcomes show that the proposed model accurately describes the luminescence bleaching process through depth and time. The best-fit model calibrated with all of the gneissic samples together (black dashed lines, parameters in Table 2.3) fits close to the best-fit model determined for each sample individually (except MBMV6). These results confirm a key objective of the study, which is the possibility to calibrate the model parameters using different surfaces along a vertical profile, with the same lithology and different (independently-determined) exposure ages.

Table 2.3: Best-fit values of $\overline{\sigma\varphi_0}$ and μ determined for every sample individually and for all samples excluding MBMV6. Combinations of three or four samples are presented in Table A2.3 (Appendix Chapter 7).

Parameter	$\overline{\sigma\varphi_0}$ [s^{-1}]			μ [mm^{-1}]		
Samples	Best-fit	+1 σ	-1 σ	Best-fit	+1 σ	-1 σ
Individually						
MBMV1	1.4×10^{-8}	1.5×10^{-8}	1.3×10^{-8}	1.07	1.08	1.05
MBMV6	2.0×10^{-6}	2.2×10^{-6}	1.8×10^{-6}	0.92	0.95	0.92
MBMV7	4.0×10^{-6}	5.0×10^{-6}	3.6×10^{-6}	2.52	2.56	2.46
MBMV8	2.2×10^{-7}	2.4×10^{-7}	1.5×10^{-7}	1.89	1.98	1.70
MBMV10	1.5×10^{-7}	1.5×10^{-7}	1.1×10^{-7}	1.82	1.87	1.75
MBMV11	4.2×10^{-8}	5.3×10^{-8}	3.9×10^{-8}	1.21	1.22	1.13
All samples together excluding MBMV6	1.0×10^{-7}	1.1×10^{-7}	9.5×10^{-8}	1.48	1.50	1.44

2.5.4 Evolution of the luminescence signal through time

Compiling the best-fit models determined for each sample individually, a positive correlation between the exposure age and the depth at which the natural IRSL signal is zeroed can be clearly observed for samples within the same lithology (Fig. 2.9a). If we consider the inflection point of each individual model (Lx/Tx= 0.5 on Fig. 2.9a) as a proxy for the bleaching depth, this value ranges between 1.7 and 4.2 mm for 3 and 137 years of daylight exposure, respectively (Fig. 2.9b). The granitic sample MBMV6 does not follow this correlation, its bleaching depth being at 7 mm after 2-yr exposure to daylight.

2.5.5 Inversion for exposure age

Once the model parameters have been determined by different sample combinations, it is possible to subsequently invert the exposure age as explained above. Figure 2.10 compares the exposure ages inverted from the different sample combinations, with the observed exposure age (all results are compiled in the Appendix Chapter Table A2.4 and Fig. A2.3). Figure 2.10a shows that our modelling approach is able to recover the observed exposure ages using parameters determined for each individual sample (<10% difference). When the exposure ages are inverted using the parameters determined for all of the gneissic samples together (as shown in Fig. 2.7b), there are slight differences between the inverted exposure age and independent age control (Fig. 2.10b, Table A2.4 and Fig. A2.3). The inverted ages are almost all within 20% of the observed ages except for sample MBMV11, which is overestimated by 90%.

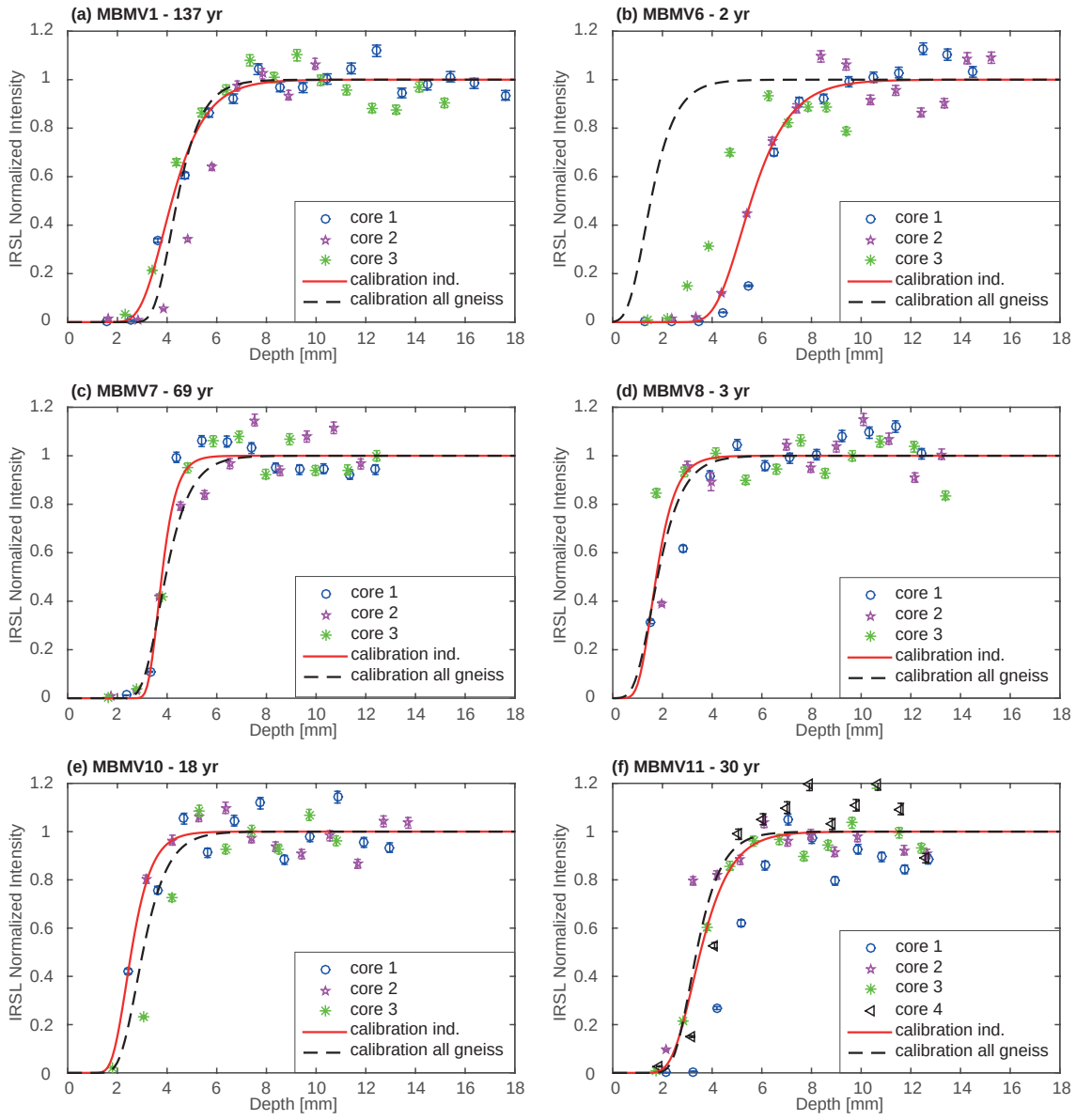

Figure 2.8: Normalized infrared stimulated luminescence (IRSL) profiles with depth and best-fit models. Coloured data point represents individual rock slice (each symbol/colour represents one core). The red lines show the best-fit model for each sample taken individually. The dashed black lines represent the best-fit model from a common calibration of the parameters using all gneiss samples together $\overline{\sigma\varphi_0} = 1.0{\times}10^{-7}\ s^{-1}$ and μ =1.48 mm^{-1}, cf. Fig. 2.7b and Table 2.3). Raw IRSL data are presented in Table A2.2 (Appendix Chapter 7)

Taking different calibration combinations with four (Fig. 2.10c) or three (Fig. 2.10d) samples also results in different performance regarding age predictions. For all gneissic samples, except MBMV11, the inverted exposure ages at 2σ are still within 20% of the observed ages. Note that in our approach the inverted exposure ages with four and three samples calibrations

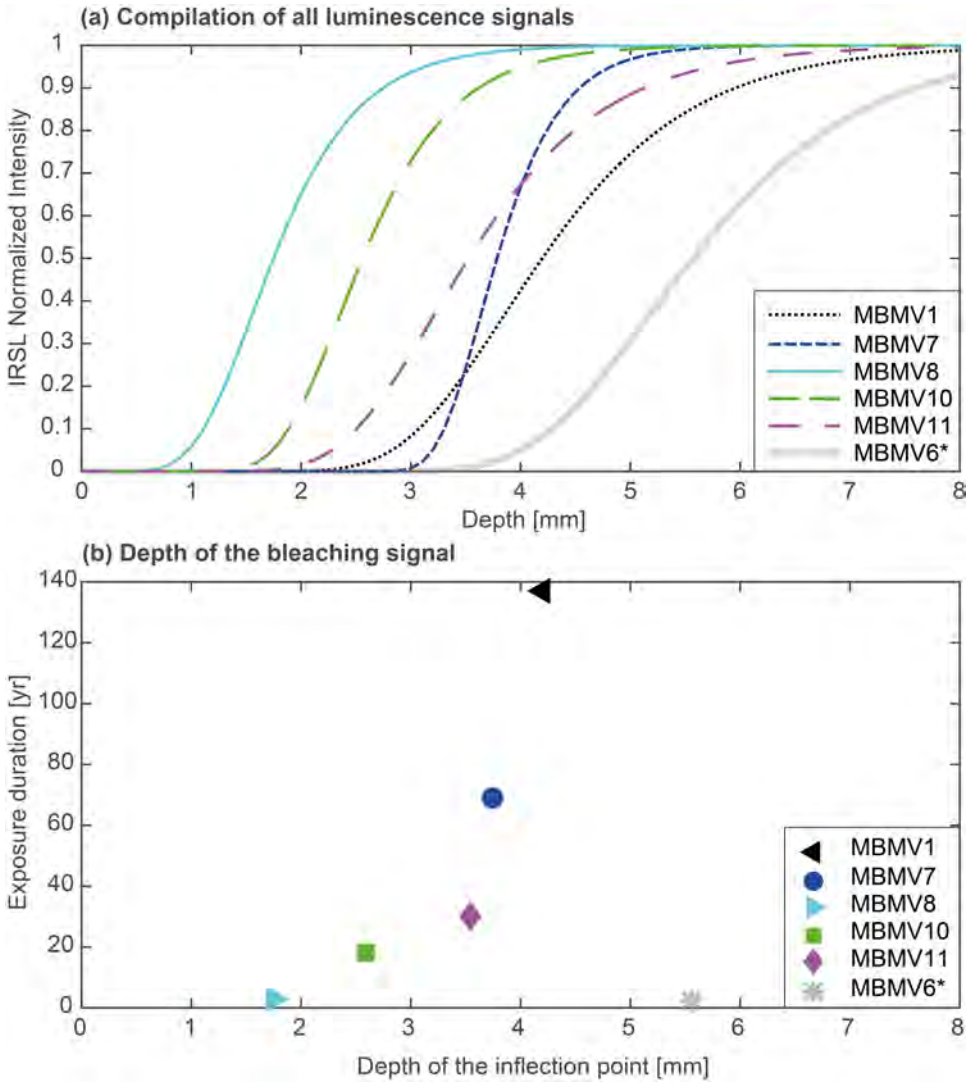

Figure 2.9: (a) Compilation of the best-fit models for each individual sample (cf. red lines in Fig. 2. 8). (b) Correlation between the IRSL bleaching depth (i.e., the inflection point of the models presented in (a)) and the exposure age of each individual sample. The star symbol indicates the granitic sample (MBMV6); all the other samples are gneiss.

are only shown when the specific sample is not part of the calibration combination (grey shadow in the Appendix Chapter Table A2.4). Although the match between the inverted and observed ages, as well as the trend between samples, is preserved independent of the calibration approach, our results show that the higher the number of calibration sites is, the better the inversion of exposure ages would be.

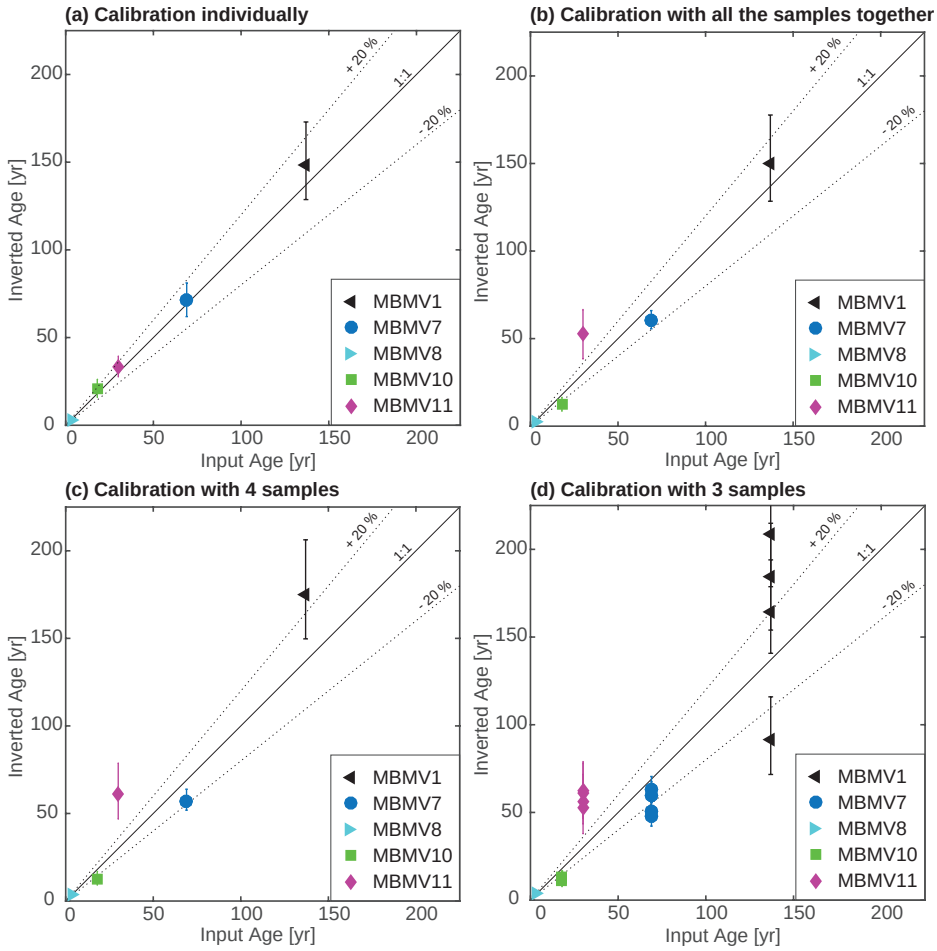

Figure 2.10: (a) Correlation between inverted (median values) and observed exposure ages resulting from different calibration combinations to constrain the model parameters. The error bars on the inverted exposure ages are $\pm 2\sigma$ as presented in Table 2.3 (all results presented in the Appendix Chapter Table A2.4).

2.6 Discussion

Our results from the Mer de Glace glacier have allowed validation, over post-LIA timescales (i.e., over 2-137 years), of the assumption that the longer a rock surface has been exposed to daylight, the deeper the luminescence signal has been bleached (Polikreti et al., 2002; 2003; Sohbati et al., 2011; 2012). Using the mathematical model proposed by Sohbati et al. (2011), we accurately describe the time evolution of luminescence within a rock column. The different combinations of samples used to calibrate the model give parameter values ($\overline{\sigma\varphi_0}$ and μ) that are on the same order of magnitude for samples within similar regions and lithology, and which agree with published values (Sohbati et al., 2011; 2012a,b).

We also observe that the evolution of luminescence signals with both time and depth within bedrock is mainly controlled by rock characteristics (lithology, texture, weathering and min-

eral composition). These rock properties will govern the light attenuation and penetration into rocks (parameter μ in Eq. 2.4), and thus the net bleaching effect on the luminescence signal. At the regional scale, the lithology should preferably be uniform to enable model calibration on some known-age surfaces (through independent dating) before application to reconstruct the exposure history of other bedrock surfaces with unknown exposure age. We see that in a granitic rock, comprising coarse quartz and feldspar grains (translucent minerals), the luminescence-bleaching front will propagate much faster than in gneiss bedrock.

Our inversion approach to constrain rock surface exposure ages from OSL data, reveals that the number of calibration samples is critical for constraining the model parameters and thus obtaining accurate exposure ages. Fortunately, calibration rock surfaces in periglacial environments can often be found from historical or remote-sensing paleo-glacier reconstructions. Other types of bedrock surfaces can be used for independent constraint, e.g., anthropogenic structures such as road-cut outcrops (e.g., Sohbati et al., 2012a) or landslide scars. The combined investigation of OSL systems with other surface exposure dating methods such as terrestrial in situ cosmogenic nuclides will also enable us to quantitatively assess the method's accuracy over longer timescales such as the late Pleistocene.

Experimental luminescence data presented in Fig. 2.8 confirms that each individual sample's exposure history has been recorded in its luminescence depth profile. For the six bedrock surfaces studied here, each luminescence profile exhibits a fully-bleached signal at shallow depth (i.e., from 1 to 7 mm depending on both the exposure age and lithology, Fig. 2.9), followed by a sharp transition to a plateau of intensity deeper into the rock. These simple and homogeneous luminescence profiles can be compared with complex profiles previously observed following multi-stage exposure histories obtained from buried cobbles (Freiesleben et al., 2015; Sohbati et al., 2015). This confirms that the glacially-polished surfaces we sampled along the Montenvers cross-sections have experienced a simple exposure history. Furthermore, field evidence for surface preservation with glacial features (striations, flutes) indicate that the bedrock surfaces have been eroded and polished by subglacial processes before deglaciation. Weathering or mechanical erosion may lead to an underestimation of the true exposure age. Thereby, the inferred exposure history from these well-preserved rock surfaces can be used to reconstruct the paleo-glacier thickness and extent since the LIA.

Bleaching of the OSL signal has occurred at less than 1 cm depth below the exposed surface after more than 137 years of daylight exposure, highlighting the high temporal resolution of this novel method for paleo-glacier reconstruction. In mountainous locations such as the Mont Blanc massif, where the glacial history has been complex with several glacier fluctuations during the late Pleistocene to Holocene (recurrent retreat/advance cycles; e.g., LeRoy et al., 2015), the application of absolute dating methods such as terrestrial in situ cosmogenic nuclides are difficult due to potential inheritance from previous exposure events (e.g., Goehring et al., 2011). One of the main advantages of OSL surface exposure dating is that

daylight bleaching of the OSL signal occurs within the first few millimetres below the exposed rock surface. Short glacier re-advances over the late Holocene (e.g., LeRoy et al., 2015) would have easily eroded the first centimetres of bedrock, consequently resetting the OSL system before the post-LIA glacier retreat. We have thus shown in this study that well-preserved polished bedrock surfaces can be used for the application of OSL surface exposure dating in order to constrain the timing of the last glacial retreat from the LIA to present day, improving our temporal resolution for glacier reconstruction. Over such timescales, the contribution of the trap filling rate ($F(x)$ in Section 2.3) from radioactive decay in gneissic or granitic rock can be assumed to be negligible (see Appendix Chapter Fig. A2.2). However, this contribution may have to be taken into account when extending paleo-glacier reconstruction using OSL surface exposure dating to longer timescales, e.g., since the Last Glacial Maximum or further back into the Quaternary. Over the same timescales, weathering and erosion of the surface are likely to play a significant role.

2.7 Conclusion

In this study, we have investigated the potential of OSL surface exposure dating for quantitatively reconstructing post-LIA glacier retreat. We worked along an altitudinal cross-section of the Mer de Glace glacier (Mont Blanc massif, France), and collected glacially-polished bedrock surfaces with known exposure ages (from 3 to 137 years) along the Montenvers profile from around 1841 m.a.s.l. elevation to the present-day glacier position (1696 m.a.s.l.). We have developed a statistical approach to calibrate the bleaching model parameters from known-age samples. Experimental IRSL depth-profile data for five different polished bedrock surfaces show an increase of the luminescence signal bleaching depth with exposure age. We conclude that OSL surface exposure dating can be applied to glacial and periglacial environments, and is a promising tool for high-resolution reconstruction of recent ice-extent and thickness fluctuations, both in space and time. However, we find that several calibration samples must be used to calibrate the model parameters before inferring exposure ages on bedrock surfaces within a specific area, taking into account the potential variation in bedrock lithology. We also find that measurement uncertainties, intrinsic data noise or both can result in large uncertainties on inverted ages, especially when applying this method over 10^3-10^4 years timescales.

Acknowledgments
We thank N. Brown and an anonymous reviewer for constructive and helpful comments. This work was supported by the Swiss National Science Foundation (SNFS) funded SwissAlpArray SINERGIA project ($CRSII2{-}154434/1$). PGV acknowledges support from SNFS grants PZ00P2−148191 and PP00P2−170559, and GEK from SNFS grant PZ00P2−167960.

The authors would like to thank the French glacier observatory GLACIOCLIM ($www - lgge.ujf - grenoble.fr/ServiceObs/index.htm$) for providing their data. We are grateful to S. Coutterand, M. Delasoie, A. Lićul, N. Stalder and V. Višnjević for fieldwork support; M. Faria and K. Haring for laboratory support.

CHAPTER 3

Evaluating post-glacial bedrock erosion and surface exposure duration by coupling in-situ OSL and $^{10}\mathrm{Be}$ dating

Benjamin Lehmann[1], Frédéric Herman[1], Pierre G. Valla[2,3], Georgina E. King[1], Rabiul H. Biswas[1]

[1]Institute of Earth Surface Dynamics, University of Lausanne, Lausanne, 1012, Switzerland.
[2]Univ. Grenoble Alpes, Univ. Savoie Mont Blanc, CNRS, IRD, IFSTTAR, ISTerre, 38000 Grenoble, France
[3]Institute of Geological Sciences and Oeschger Centre for Climate Change Research, University of Bern, Bern, 3012, Switzerland.

Abstract

Assessing the impact of Quaternary glaciation at the Earth's surface implies understanding of the long-term evolution of alpine landscapes. In particular, it requires simultaneous quantification of the impact of climate variability on past glacier fluctuations and on bedrock erosion. Here we present a new approach for evaluating post-glacial bedrock surface erosion in mountainous environments by combining terrestrial cosmogenic nuclide ^{10}Be (TCN) and optically stimulated luminescence (OSL) surface exposure dating. Using a numerical approach, we show how it is possible to simultaneously invert bedrock OSL signals and ^{10}Be concentrations into quantitative estimates of post-glacial exposure duration and bedrock surface erosion. By exploiting the fact that OSL and TCN data are integrated over different timescales, this approach can be used to estimate how bedrock erosion rates vary spatially and temporally since glacier retreat in an alpine environment.

3.1 Introduction

During the last few million years of the Earth's history, global climate cooled and evolved towards cyclic glaciations in high-latitude and high-altitude regions (e.g., Miller et al., 1987; Zachos et al., 2001; Lisiecki and Raymo, 2005, 2007). It has been suggested that rates of erosion varied during these multiple cycles, and that such variations could in turn feedback into climate (e.g., Molnar and England, 1990; Raymo and Ruddiman, 1992; Champagnac et al., 2007; Herman and Champagnac, 2016). Such erosion rate variations are most expressed in alpine environments, where the main erosion agents vary from ice to water and landslides, during glacial and interglacial periods respectively. However, quantifying how their respective contributions in sediment production have varied remains challenging because both ice-extent fluctuations and associated bedrock surface erosion must be reconstructed simultaneously.

Glacially-polished bedrock offers the possibility to reconstruct past ice-extents and quantify concomitant bedrock surface erosion. These landforms are smooth and glossy, resulting from glacial abrasion, quarrying and melt-water erosion during glacial periods (e.g., Bennett and Glasser, 2009; Siman-Tov, 2017). Following ice retreat, they are exposed to post-glacial erosion, which results in the transition from a well-preserved glacially-polished surface (Figs. 3.1a and 3.1b) to a coarse-grained rough surface (Figs. 3.1c and 3.1d). Post-glacial bedrock surface erosion is due to the alteration of rock surfaces exposed to atmospheric conditions. Rock alteration can occur through different ways, involving physical (e.g., frost-cracking), chemical and biological processes that weaken and modify the rock surface and ultimately results in its progressive erosion (e.g., Łoziński, 1909; Anderson and Anderson, 2010; Hall et al., 2012; Moses et al., 2014). Because we are concerned with the removal of bedrock surface material since exposure to the atmosphere following glacial retreat, rather than the modification of its physical and chemical characteristics caused by weathering, we hereafter use the term "erosion". Our objective is to develop an approach that may be used to address the following questions: How fast is the transition from a polished bedrock to a coarse-grained surface (Fig. 3.1)? How much information about postglacial exposure is preserved on weathered rock surfaces? What analytical tools or approach can we use to quantify this morphological transition?

Analytical methods to quantify erosion of rock surfaces differ depending on the timescale of interest (see Moses et al., 2014 for a complete review). Over short timescales (from a few seconds to decades) erosion can be quantified through remote sensing (e.g., photogrammetric methods; Terrestrial Laser Scanner; c.f., Armesto-Gonzàlez et al., 2010; Duffy et al., 2013) or measured relatively to anthropogenic reference features (historic or experimental; e.g., Nicholson, 2008; Häuselmann, 2008; Stephenson and Finlayson, 2009). Over longer timescales (10^3-10^7 years), erosion can be measured relative to a natural reference feature (e.g., resistant mineral veins such as quartz or a surface of known age), or quantified using surface exposure

dating with terrestrial cosmogenic nuclides (TCN; Lal, 1991; Balco et al., 2008; Bierman and Nichols, 2004; Brandmeier et al. 2011; Liu and Broecker, 2007). TCN methods rely on the production of specific isotopes in terrestrial material by cosmic rays at or near the Earth's surface (Gosse and Philips, 2001), such as minerals located in the top few meters of soil or bedrock (Lal and Peters, 1967). In glacial and paraglacial environments, the formation of glacial landforms can be directly dated over timescales of 10^3 to 10^6 years with TCN surface exposure dating (Ivy-Ochs and Briner, 2014). However, TCN concentrations must also be corrected for surface erosion, which would otherwise lead to an underestimation of the exposure age (Gosse and Phillips, 2001). The combination of short-lived radionuclides such as ^{14}C with long-lived radionuclides (i.e., ^{10}Be, ^{26}Al, ^{36}Cl) can be used to resolve and quantify complex exposure histories with burial episodes, but this approach does not allow the quantification of erosion during exposure (Hippe, 2017).

Consequently, complementary approaches are still needed to quantify bedrock erosion over multiple timescales, and more specifically methods that can bridge short and long timescales. In this study, we couple TCN with optically stimulated luminescence (OSL) dating. Rock surface exposure dating using optically stimulated luminescence (named hereafter as OSL surface exposure dating) has recently shown promising potential (e.g., Sohbati et al., 2012a; 2018; King et al., 2019). Luminescence dating is based on the accumulation of trapped electrons through time in the crystalline lattice of specific minerals (e.g., quartz or feldspar), which are sensitive to daylight (Aitken, 1985; Huntley et al., 1985). In addition to its common application to date sediment burial in a range of geomorphological environments (e.g., Duller, 2008; Rhodes, 2011; Fuchs and Owen, 2008), luminescence dating can also be used to determine the exposure of both naturally formed and anthropogenically formed rock surfaces (e.g., Polikreti et al., 2003; Sohbati et al., 2011; Gliganic et al., 2018; Lehmann et al., 2018). This latter application is based on the principle that when a rock surface is exposed to daylight, the luminescence signal, which is initially homogenous within the rock, will progressively decrease at depth until completely zeroed, a phenomenon called "bleaching" (Aitken, 1998). The assumption is that the longer a surface has been exposed to daylight, the deeper the OSL signal bleaching will be (Polikreti et al., 2002). In granitic and gneissic rocks, bleaching through time has been shown to occur over the first few millimeters to centimeters below the rock surface (Vafiadou et al., 2007; Sohbati et al., 2011; Freiesleben et al., 2015). Due to attenuation of daylight, the bleaching rate decreases exponentially with depth. It becomes negligible at depth where the luminescence signal is effectively unbleached and remains in field saturation. For long timescales, trapping due to ionizing radiation will compete with detrapping due to daylight exposure at all depths (after $\sim 10^4$ a in Fig. A3.1), ultimately resulting in an equilibrium bleaching profile (after $\sim 10^6$ a in Fig. A3.1, cf. Sohbati et al., 2012a).

For a bedrock OSL profile which is not in equilibrium, measuring and calibrating the depth-dependent luminescence signal beneath the exposed surface by generating multiple luminescence depth profiles enables estimation of an apparent exposure age. OSL surface exposure dating is thus presented as a relatively new surface exposure dating method and has already been applied on both geological and archaeological rock surfaces (Polikreti, 2007; Sohbati et al., 2012a; Freiesleben et al., 2015; Lehmann et al., 2018; Meyer et al., 2018; Gliganic et al., 2018). Sohbati et al. (2012c) were able to quantify the exposure age of historic rock art from the Great Gallery rock art panel in Canyonlands National Park (southeastern Utah, USA). Some of the paintings were damaged by a rockfall event, and conventional luminescence was applied on a rockfall boulder and buried sediments (Chapot et al., 2012). This provided a minimum age for the event. Using a road cut of known age to constrain the bleaching rate for this specific site and lithology, Sohbati et al. (2012c) were able to quantify the exposure age of both the modern analogue ($\sim$130 a) and the rock art ($\sim$ 700 a). In a periglacial environment, Lehmann et al. (2018) showed that the infrared stimulated luminescence at 50°C (IRSL50) signals from crystalline bedrock slices exhibit increasingly deep bleaching profiles with elevation and thus exposure age, which is consistent with progressive glacier thinning since the Little Ice Age (LIA, 10^1-10^2 a). Note that several signals can be targeted in the same rock slice depending on the mineral (e.g., Sohbati et al., 2015; Jenkins et al., 2018). OSL is usually used to analysed the luminescence of quartz (Murray and Wintle, 2000) and IRSL for potassium-rich feldspar signal (both at 50C and 225C, Buylart et al., 2009).

Recently, Sohbati et al. (2018) showed that surface erosion has to be taken into consideration when OSL surface exposure dating is applied to natural bedrock surfaces. Indeed, removal of material would bring the bleaching front towards the surface, which may lead to a considerable underestimation of the OSL surface exposure age if not accounted for. When bedrock surface erosion is high ($> 10^{-2}$ mm a^{-1}), the competition between bleaching and surface removal will potentially prevent the use of OSL surface exposure dating as a chronometer for bedrock surface exposure (Sohbati et al., 2018). In practice, when erosion is maintained long enough, an equilibrium between trapping, bleaching (i.e., detrapping) and erosion is reached, consequently the bleaching profile reaches steady state. Sohbati et al. (2018) explained that the sensitivity difference to erosion between TCN and OSL surface exposure dating can be exploited to calculate erosion rate experienced by rock surfaces. Indeed, TCN dating is mainly sensitive to cosmic rays over the top $\sim$50-60 cm below the exposed bedrock surface (depending on rock density; Lal et al., 1991) while OSL surface exposure dating is sensitive to light penetration of only millimeters to centimeters (Sohbati et al., 2011, 2012a, 2012b). Thus, using both OSL surface exposure dating and TCN methods, it is possible in theory to quantify surface erosion over different timescales (i.e., 10^2 -10^4 a).

Here we couple TCN and OSL surface exposure dating to quantify post-glacial erosion in paraglacial environments. To achieve this, we developed a new model which depends on

the exposure age, the surface erosion, the trapping and detrapping (bleaching) rates and the athermal loss (c.f. Eq. 3.1, Section 3.2.1). Using this model, we then investigate different synthetic scenarios in which erosion rates follow a series of step functions in time. After this synthetic experiment, the model is used to invert OSL surface exposure data from two glacially polished bedrock surfaces sampled along the Mer de Glace glacier (Mont Blanc massif, European Alps). We find that the relationships between the depth of luminescence bleaching, the exposure age and the surface erosion allow discrimination between transient and steady state regimes. Finally, we discuss our findings regarding post-glacial surface erosion in paraglacial environments, and the benefits of OSL surface exposure dating combined with TCN surface exposure dating.

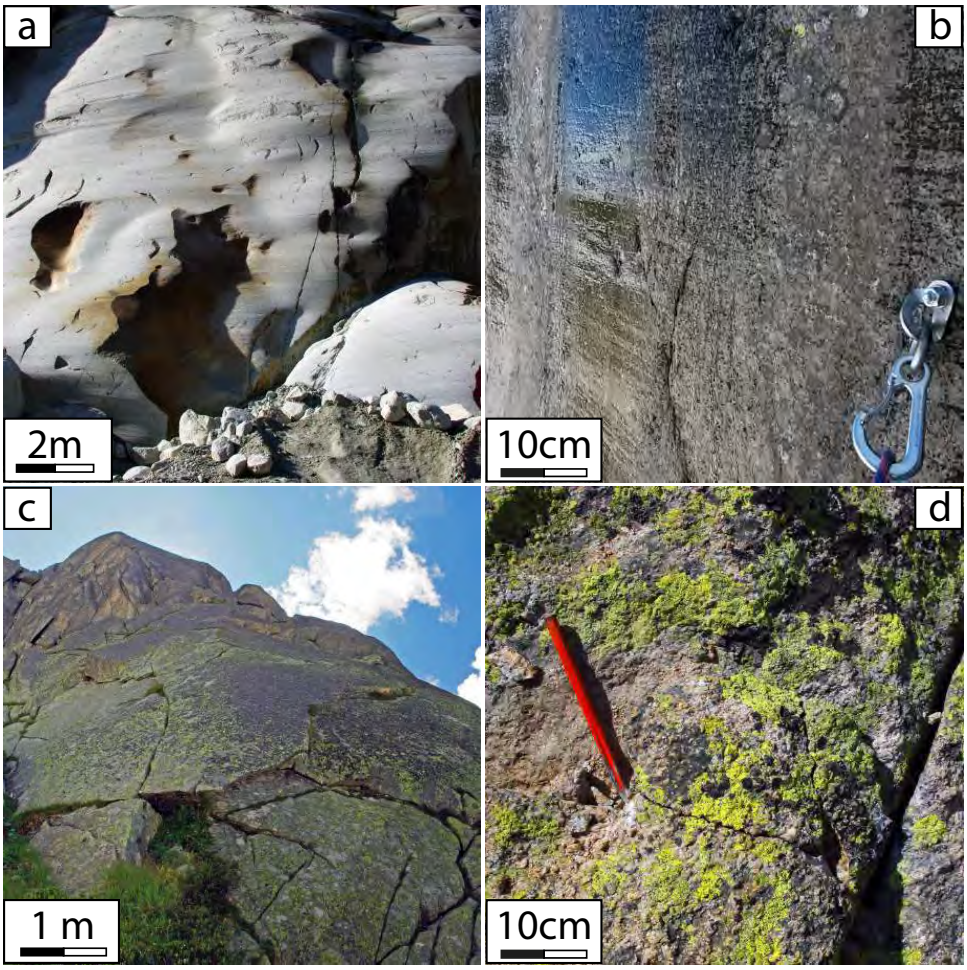

Figure 3.1: Granitic bedrock surfaces along the Mer de Glace glacier (Mont-Blanc massif, European Alps). Surfaces (a) and (b) present well-preserved glacial morphologies exposed for only a few years (striations). Surfaces with longer aerial exposure (Late Glacial to Holocene timescales) show glacially abraded surfaces at the macro-scale (c), but at the cm-scale they reveal a coarse-grain rough surface (d).

3.2 Methodology: combining TCN ^{10}Be and OSL surface exposure dating

In the following, we focus on the theoretical aspects of both OSL and TCN ^{10}Be surface exposure dating methods. We show how different time-dependent exposure and erosion histories are recorded by each technique. Finally, we combine OSL surface exposure and TCN ^{10}Be dating to constrain erosion rate and exposure duration simultaneously. Note that all the symbols used below are defined in Table 3.1.

3.2.1 OSL surface exposure dating

The bleaching model

The intensity of a luminescence signal reflects the number of trapped electrons (Aitken, 1985). For a rock surface exposed to daylight, the luminescence signal intensity, i.e., the trapped electron concentration, is controlled by the competing processes of electron trapping in response to ambient radiation and electron detrapping due to daylight exposure combined with anomalous fading for feldspar IRSL (Habermann et al., 2000; Polikreti et al., 2003; Sohbati et al., 2011). Sohbati et al. (2011, 2012a, b) introduced a mathematical model that describes the process of luminescence bleaching with depth in a homogeneous lithology, enabling the quantification of rock surface exposure duration. Here we propose a new model describing the evolution of luminescence in rock surface as a function of different parameters characterizing the probability of charge trapping, the wavelength-specific photon flux (φ), the mineral- and wavelength-specific photo-ionization cross-section (σ) and the lithology-specific light attenuation factor (μ) (Eq. 3.1). Thus, the measured luminescence signal $L(x,t,r')$ [dimensionless] at given depth x [mm], time t [a] and recombination center distance r' [dimensionless], can be described by the following differential equation:

$$\frac{dL(x,t,r')}{dt} = \frac{\dot{D}}{D_0}[1 - L(x,t,r')] - L(x,t,r')\overline{\sigma\varphi_0}e^{-\mu x} - L(x,t,r')se^{-\rho'^{-\frac{1}{3}}r'} + \dot{\varepsilon}(t)\frac{dL(x,t,r')}{dx} \tag{3.1}$$

The first term on the right-hand side of Eq. (3.1) describes the electron-trapping rate in response to ambient radiation with $\dot{D}$ (x) the environmental dose rate [Gy a^{-1}] at depth x [m] and D_0 the characteristic dose [Gy]. In the context of bedrock surface exposure dating, the dose rate can be approximated as a depth-independent constant in the case of homogeneous lithology i.e., $\dot{D}(x)$= *const* (e.g., Sohbati et al., 2018).

The second term describes the electron-detrapping or bleaching rate due to daylight exposure where $\sigma(\lambda)$ is the luminescence photoionization cross section [mm^2] defining the probability

of a specific trap being excited by light stimulation. $\varphi_0\ (\lambda, x)$ is the photon flux $[mm^{-2}\ a^{-1}]$ as a function of wavelength at the rock surface ($x = 0$) and describes the rate of incoming photons that can bleach the trap of interest. Here we assume that the photon flux does not fluctuate through time (Sohbati et al., 2011). We are only concerned with $\overline{\sigma\varphi_0}$ $[a^{-1}]$, which is the effective decay rate of luminescence at the rock surface following exposure to a particular light spectrum (Sohbati et al., 2011). The light attenuation coefficient μ $[mm^{-1}]$ describes how deep into the rock a photon will penetrate and affect the luminescence signal. μ is assumed to be independent of wavelength in the spectral range of interest (Sohbati et al., 2011).

The third term on the right-hand side of Eq. (3.1) represents the athermal loss of the IRSL signal of feldspar thought to be due to quantum mechanical tunneling of trapped electrons (Wintle, 1973; Visocekas et al., 1998) to the nearest available recombination centers (Huntley, 2006). s is the frequency factor equal to $3{\times}10^{15}\ s^{-1}$, and ρ' is the dimensionless recombination center density (Tachiya and Mozumder, 1974; Huntley, 2006).

The fourth term describes the advection of the luminescence signal in response to erosion $\dot{\varepsilon}\ (t) = dx/dt\ [mm\ a^{-1}]$ on the propagation of the luminescence bleaching front into the rock, using a Eulerian system of reference. Equation (3.1) is solved using the finite difference method including a second-order upwind scheme for the advection term. This approach is different to the one recently proposed by Sohbati et al. (2018), who used an analytical solution that is based on a confluent hypergeometric function and that requires steady erosion rates. We benchmarked our approach against that of Sohbati et al. (2018) and obtain exactly the same results using our numerical solution (Fig. A3.3).

Ou et al. (2018) experimentally derived μ for different rock types (greywacke, sandstone, granite and quartzite) using both direct measurements with a spectrometer and bleaching experiments. They showed that the attenuation coefficients are different according the energy of stimulation (e.g., IRSL measured at 50°C and the post-IR IRSL signal measured at 225°C). Meyer et al. (2018) and Gliganic et al. (2018) have shown that the distribution of opaque minerals between rock slices can significantly affect the reproducibility of luminescence-depth profiles. They conclude the need for close petrographic analysis of luminescence-depth profile samples to ensure that the rock cores from calibration and application sites have a similar mineralogical composition and therefore share similar μ parameter. In this study, we refer to Sohbati et al. (2011, 2012a) for a complete description of $\overline{\sigma\varphi_0}$ and μ parameters and their control on the penetration of the bleaching front into a rock surface.

Alternatively, $\overline{\sigma\varphi_0}$ and μ can be determined from a known-age rock surface with no erosion ($\dot{\varepsilon}\ (t) = 0$) with a uniform lithology (Sohbati et al., 2012a, Lehmann et al., 2018, Meyer et al., 2018) and a negligible contribution of athermal loss (as presented in Fig. A3.2). Under these

conditions, Sohbati et al. (2012a) proposed the following analytical solution for Eq. (3.1), neglecting the athermal loss:

$$L(x,t) = \frac{\overline{\sigma\varphi_0}e^{-\mu x}e^{-t(\overline{\sigma\varphi_0}e^{-\mu x}+\frac{\dot{D}}{D_0})} + \frac{\dot{D}}{D_0}}{\overline{\sigma\varphi_0}e^{-\mu x} + \frac{\dot{D}}{D_0}} \tag{3.2}$$

For non-eroding surfaces, OSL surface exposure dating can theoretically be used for a broad range of timescales from 0.01 to 10^5 years (Fig. A3.1, and Sohbati et al., 2012a, 2012b, 2018). Under these geomorphic conditions for natural rock surfaces (e.g., glacially-polished bedrock), OSL surface exposure dating has been successfully applied by solving Eq. (3.2) over 10^1-10^2 a timescales (Lehmann et al., 2018; Gliganic et al., 2018). At longer timescales and/or for rock surfaces affected by erosion, the measured OSL signals do not only reflect the exposure age.

Sensitivity analysis to model parameters

In this section, we investigate the respective contribution of the different terms in Eq. (3.1) for the interpretation of a measured OSL bleaching profile. We investigate the sensitivity of the model to athermal loss, trapping rate and erosion. We use $\overline{\sigma\varphi_0} = 129\ a^{-1}$ and $\mu = 0.596\ mm^{-1}$ that were determined from two calibration rock surfaces of similar granitic lithology from the Mont Blanc massif, with no erosion and known exposure age (Fig. A3.2). The values $\dot{D} = 8$ Gy ka^{-1} (Table 3.2) and $D_0 = 500$ Gy were selected as they are comparable to the average values for samples used in this study.

Athermal loss In this section, we investigate the role of athermal loss when constant erosion rates are low (i.e., $10^{-5}\ mm\ a^{-1}$) and high (i.e., $10^{1}\ mm\ a^{-1}$). In Eq. (3.1), ρ' is varied between 10^{-10} and 10^{-5} (natural values vary between $10^{-6.5}$ and $10^{-4.5}$; Valla et al., 2016; King et al., 2018), and is integrated over dimensionless distances, r', ranging from 0 to 2.5 (Kars et al., 2008) in all cases. Four model runs were done to test whether the shape of the bleaching profile (i.e., luminescence signal vs. depth) changes with different athermal loss rates, rather than the absolute luminescence signal intensity level which reduces as ρ' increases. To remove this effect, the luminescence signals were normalized using the steady state luminescence plateau as unity (NLS for Normalized Luminescence Signal; Figs. 3.2 and A3.2a). Figure 3.2 shows that the shape of the IRSL profiles would be indistinguishable within uncertainties for the two end-member athermal fading rates. We thus find that athermal loss is negligible, and it is not included in the following calculations or considered further.

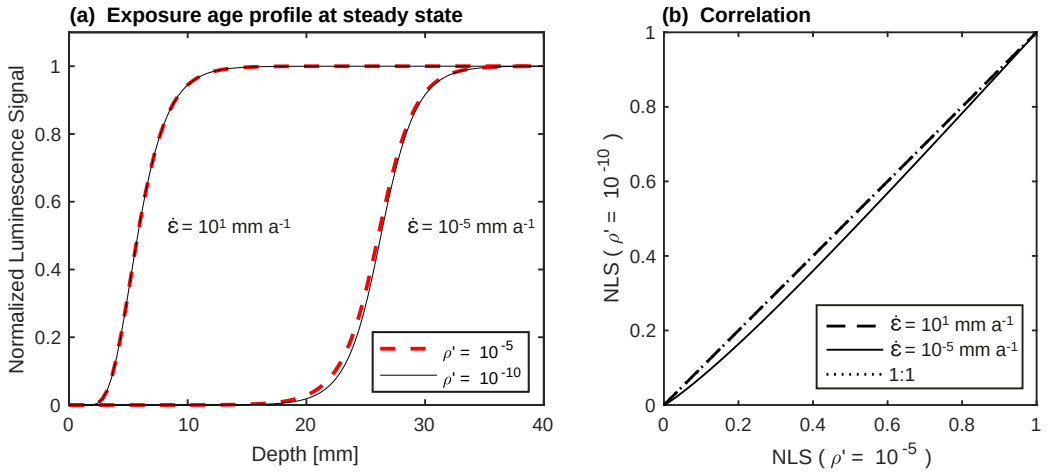

Figure 3.2: (a) Synthetic luminescence profiles predicted by Eq. (3.1) for two dimensionless recombination center densities ρ' (10^{-10} and 10^{-5}) and two erosion rates $\dot{\varepsilon}$ (10^{-10} and 10^{-5} $mm\ a^{-1}$). (b) Comparison of the normalized luminescence signal (NLS) for the different values of ρ' and $\dot{\varepsilon}$. Values for the different parameters $\overline{\sigma\varphi_0}$, μ, $\dot{D}$ and D_0 are described in Sect. 2.1.2.

Trapping Here we illustrate the importance of the trapping term and the effect of the different trapping parameters, i.e., the environmental dose rate ($\dot{D}$) and the characteristic dose of saturation (D_0), on OSL surface exposure dating. Assuming a non-eroding rock surface, the bleaching front will keep propagating with time if trapping is not accounted for (Fig. A3.1; of Sohbati et al., 2012). In contrast, a secular equilibrium (Sohbati et al., 2018) defined by the steady state between trapping and light-stimulated detrapping at depth, can be reached when trapping is considered. In this case, the depth and the time at which the secular equilibrium occurs depends only on $\dot{D}$, D_0, $\overline{\sigma\varphi_0}$ and μ parameters. Using the parameters mentioned in Sect. 3.1.2., and solving Eq. (3.1) without considering athermal loss, our simulations show that for typical granitic rocks (i.e., $\dot{D}$ between 2 and 8 Gy ka^{-1}) the bleaching front stabilizes at around 20-25 mm depth after an exposure duration of 10^5-10^6 a (Fig. 3.3).

In Figure 3.4 we investigate the effects of $\dot{D}/D_0$ on setting the depth of the bleaching front. We use extreme values of D_0 of 100 and 2000 Gy and $\dot{D}$ of 2×10^{-3} and 10^{-2} Gy a^{-1} (King et al., 2016; Jenkins et al., 2018; Biswas et al., 2018), resulting in $\dot{D}/D_0$ from 10^{-6} a^{-1} to 10^{-4} a^{-1}. Our simulations show that the higher the $\dot{D}/D_0$, the closer to the surface the steady-state bleaching profile is which is a consequence of more rapid saturation of the sample luminescence signal. The steady state bleaching depth varies between around 22 and 31 mm (measured at the inflection point) for our end-member simulations (Fig. 3.4). The influence of $\dot{D}/D_0$ on the bleaching profile is minor relative to the other parameters (μ, $\dot{\varepsilon}$), however, dose rate can vary by an order of magnitude between rock slices and may possibly explain part of the noise observed in reported experimental data (Meyer et al., 2018).

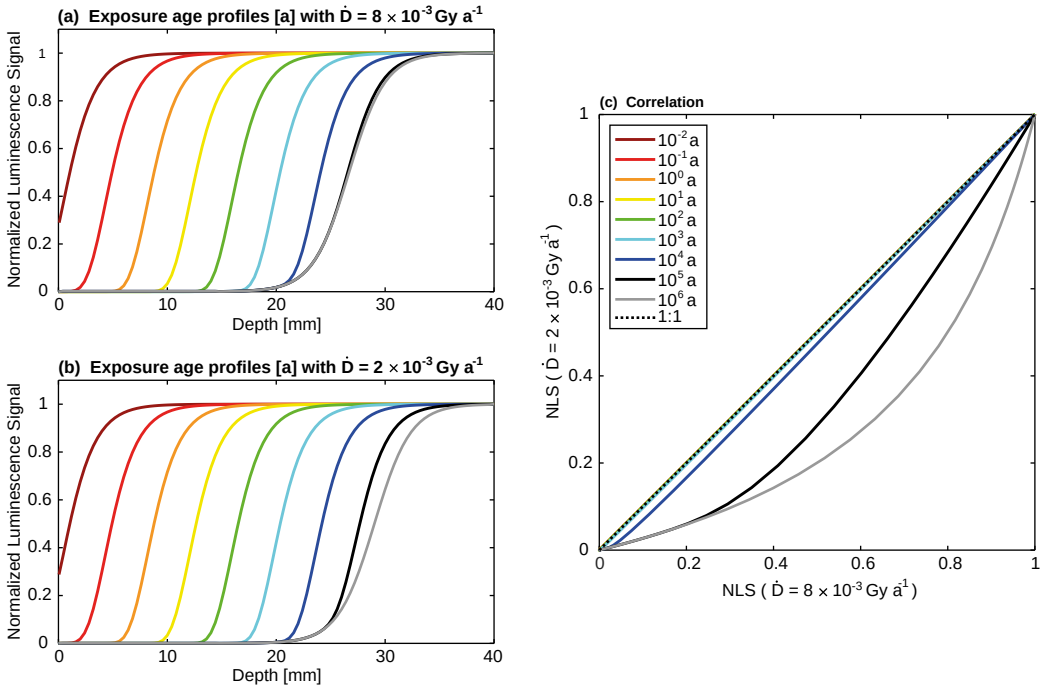

Figure 3.3: Synthetic luminescence profiles for bleaching models with exposure ages from 10^{-2} to 10^{-6} a and considering trapping rates of (a) $8{\times}10^{-3}$ and (b) $2{\times}10^{-3}$ Gy a^{-1}. Panel (c) shows the comparison of the normalized luminescence signal (NLS) for both models after the different exposure ages. As there is no difference between the modeled profiles for both scenarios between 10^{-2} and 10^{-3} a, the curves are overlying. The choice of parameters $\overline{\sigma\varphi_0}$, μ, $\dot{D}$ and D_0 is described in Sect. 3.1.2.

Erosion The effect of surface erosion on the luminescence signal has recently been highlighted by Sohbati et al. (2018) who proposed an analytical solution to account for this process. In this section, we numerically solve Eq. (3.1), neglecting athermal loss, and test the effect of different erosion rates on luminescence profiles. Figure 3.5a shows the resulting synthetic luminescence profiles at steady state with erosion rates from 0 to 10^2 mm a^{-1}. Under these synthetic conditions, the effect of surface erosion starts to be noticeable from around 10^{-4} mm a^{-1}; and for an erosion rate of 10^2 mm a^{-1}, the steady state bleaching front is brought forward to 2 mm below the exposed surface. Indeed, surface erosion advects the luminescence signal closer to the surface (Fig. 3.5). As a result, rock luminescence profiles reflect a competition through time between erosion, trapping and detrapping. When the effects of the three processes are in disequilibrium, such as following initial bedrock surface exposure or onset of surface erosion, a transient state occurs during which the luminescence signal continues to evolve. After prolonged exposure, and assuming constant erosion, the competing effects equilibrate, leading to a steady state where the bleaching profile is no longer propagating into the rock. In Figure 3.5b, we evaluate the evolution of the luminescence profiles from transient to steady state using a dimensionless parameter calculated from the product

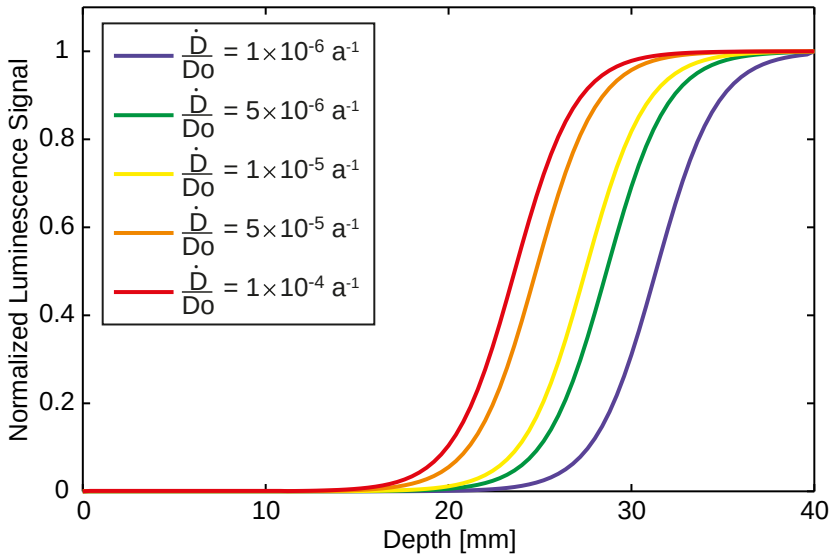

Figure 3.4: Synthetic luminescence profiles predicted by Eq. (3.1) for different values of the ratio $\dot{D}/D_0$ (10^{-6}, $5{\times}10^{-6}$, 10^{-5}, $5{\times}10^{-5}$ and 10^{-4} a^{-1}) and assuming no erosion. The choice of parameters $\overline{\sigma\varphi_0}$, μ, $\dot{D}$ and D_0 is described in Sect. 3.1.2.

of the profile depth at which luminescence reaches 50% of its saturation value ($x_{50\%}$), defined as the inflection point NLS($x_{50\%} = 0.5$) and the light attenuation coefficient μ (Sohbati et al., 2018). We see that the higher the erosion rate is, the faster the system reaches steady state. Consequently, to characterize how a surface is affected by erosion through time, an independent temporal framework is needed to determine the duration of rock surface exposure. This can be achieved through combining OSL surface exposure with TCN dating, which is briefly introduced in the following section.

3.2.2 Terrestrial cosmogenic nuclide (TCN) dating

TCN dating is based on the observation that when cosmic rays reach Earth's surface, they produce cosmogenic isotopes in specific targets, such as the production of ^{10}Be in quartz (e.g., Gosse and Philips, 2001, Dunai, 2010). The in situ production of quartz ^{10}Be occurs predominantly within a few meters of Earth's surface and decreases exponentially with depth (Fig. A3.4a; Portenga and Bierman, 2011 and references therein). The evolution of cosmogenic nuclide C [atoms g^{-1}] in time t [a] and rock depth x [mm] is a function of the disintegration constant λ [a^{-1}], the production rate of a radionuclide P [atoms $g^{-1}a^{-1}$] and the erosion $\dot{\varepsilon}$ and can be described by the following equation (Gosse and Phillips, 2001):

$$\frac{dC(x,t)}{dt} = -C(x,t)\lambda + P(0,t)e^{-\nu x} + \dot{\varepsilon}(t)\frac{dC(x,t)}{dx} \tag{3.3}$$

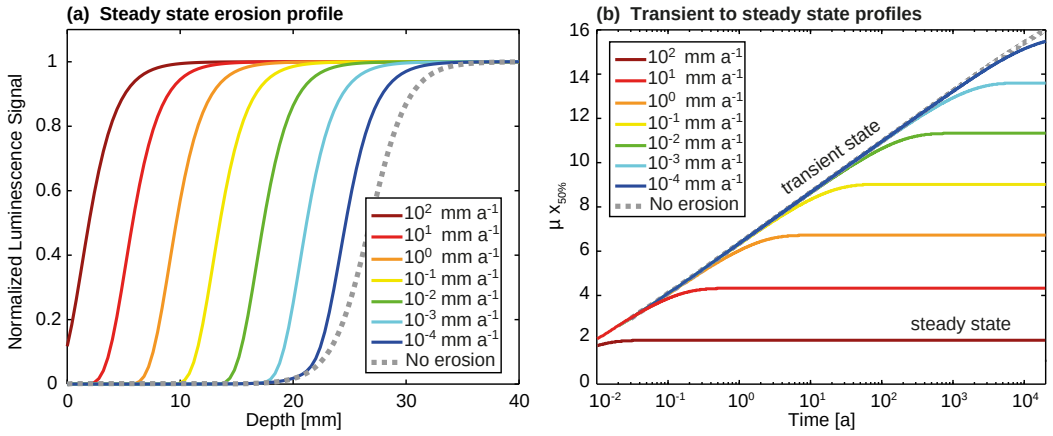

Figure 3.5: Sensitivity of luminescence-depth profiles with erosion. (a) Synthetic luminescence profiles at steady state with erosion rates from 0 to 10^2 $mm\ a^{-1}$. (b) Transient to steady state profile for erosion rates from 0 to 10^2 $mm\ a^{-1}$, as a function of time $[a]$ and as the product of the attenuation factor μ $[mm^{-1}]$ and the depth $x_{50\%}$ defined as NLS($x_{50\%}$ = 0.5). The choice of parameters $\overline{\sigma\varphi_0}$, μ, $\dot{D}$ and D_0 is described in Sect. 3.1.2.

$P(0)$ is the production rate of the radionuclide at the target surface. The symbol ν defines the absorption coefficient $[mm^{-1}]$ of the target: $\nu = \frac{\rho}{\Lambda}$. Λ is the mean attenuation length for nuclear particles interacting within the target $[g\ mm^{-2}]$. If the radionuclide concentration at the surface represents the last exposure event, assuming there is no inheritance from a potential previous exposure and that the erosion rate is constant, Eq. (3.3) can be solved analytically (Lal, 1991), which gives:

$$C(x,t) = \frac{P(0)}{\lambda + \nu\dot{\varepsilon}} e^{-\nu x}[1 - e^{-(\lambda+\nu\dot{\varepsilon})t}] \tag{3.4}$$

When $t >> 1/(\lambda + \nu\ \dot{\varepsilon})$ the radionuclide concentration reaches a steady state, i.e., a secular equilibrium is reached (Lal, 1991). Under these circumstances, a measured cosmogenic nuclide concentration can be interpreted in terms of a maximum steady-state erosion rate. Here we solve Eq. (3.3) numerically using the finite difference method, and use the analytical solution to estimate the maximum possible erosion rate. The general behavior of the quartz ^{10}Be concentration with erosion and exposure age is well documented in the literature (e.g., Lal, 1991), and we illustrate it in Figure A3.4 for comparison with OSL surface exposure dating (Fig. 3.5). Note that for solving Eq. (3.3), the experimental measurement of ^{10}Be concentration C_{exp} must first be corrected by the depth normalization factor f_E and by the topographic shielding factor SF of the surface following the equation (Martin et al., 2017):

$$C_{corr} = \frac{C_{exp}}{f_E \times SF} \tag{3.5}$$

with f_E computed by integrating average production over the sample thickness using a single exponential spallation attenuation equation (Balco et al., 2008):

$$f_E = \frac{\Lambda}{\rho \times E}\left[1 - \frac{-\rho \times E}{\Lambda}\right] \tag{3.6}$$

where ρ is the mean density of the targeted rock $[g\ mm^{-3}]$ and E the sample thickness $[mm]$. As we discussed previously, OSL surface exposure and TCN dating both depend on the timing of surface exposure and erosion. These two processes are recorded at different depths into the rock surface: centimeter-scale for OSL surface exposure dating and meter-scale for TCN, therefore OSL surface exposure dating is potentially sensitive to surface erosion over shorter timescales than TCN dating. To combine the two methods, one needs to solve Eqs. (1) and (3) simultaneously, where the two unknowns are the exposure age t and the erosion rate $\dot{\varepsilon}$.

Table 3.1: Symbol table

Symbol	Unit	Description
Both methods		
x	mm	Rock depth
t	a	Exposure age
$\dot{\varepsilon}$	mm a^{-1}	Erosion rate
t_S	a	Erosion onset time
OSL surface exposure dating		
n	mm^{-3}	Concentration of trapped charge
L	a^{-1}	Maximum possible number of trapped electrons
σ	mm^2	Luminescence photoionization cross section
φ_0	$mm^{-2}\,a^{-1}$	Photon flux
μ	mm^{-1}	Attenuation coefficient
λ	mm	Wave of light stimulation
$\dot{D}$	Gy a^{-1}	Environmental dose rate
D_0	Gy	Characteristic dose of saturation
s	s^{-1}	Frequency factor
ρ'		Dimensionless recombination center density
r'		Dimensionless recombination center distance
TCN dating		
t_0	a	TCN exposure age without erosion correction
t_C	a	TCN exposure age with erosion correction
C	atoms g^{-1}	Number of atoms of the radionuclide within the rock
P	atoms $g^{-1}\,a^{-1}$	Radionuclide production rate
υ	mm^{-1}	Absorption coefficient of the specific target
ρ	g mm^{-3}	Mean density of the targeted rock
Λ	g mm^{-2}	Absorption mean free path for nuclear interacting particles in the target
λ	a^{-1}	Disintegration constant
E	mm	Sample thickness
SF		Topographic shielding factor

3.3 Inversion approach for synthetic erosion rates

In this section, we generate a series of forward and inverse models. The forward model calculates a luminescence signal and a ^{10}Be concentration from synthetic erosion and exposure histories. The inverse model starts with the results (i.e., IRSL signal and ^{10}Be concentration) and then recover the parameters (i.e., erosion and exposure histories). To validate the inversion procedure, we use the forward model to create synthetic data which we then retrieve using the inverse model. For these tests, we use the same OSL surface exposure dating parameters explored in the previous sections. $\overline{\sigma\varphi_0}$ = 129 a^{-1} and μ = 0.596 mm^{-1}. The value $\dot{D}$ = 8×10^{-3} Gy a^{-1} was selected as average value obtained for samples used in this study ($\dot{D}$ = 7.4 and 8.4 ×10^{-3} Gy a^{-1} in Table 3.2). D_0 = 500 Gy was selected as representative value for IRSL50 signals from granite. The ^{10}Be exposure age is estimated using the measured quartz ^{10}Be concentration of sample MBTP1 collected on a polished granitic bedrock surface at 2545 m.a.s.l. from the Tête de Trélaporte located on the left bank of the Mer de Glace glacier (Mont-Blanc massif, European Alps). Note that the lithology of this sample is similar to that of the OSL surface exposure dating calibration site from which the model parameters are taken (Fig. A3.2; Lehmann et al., 2018). The sample was located on a surface presenting a shielding factor 0.963 and has a thickness of 8 cm (Table 3.2). Its non-corrected ^{10}Be concentration is equal to 474750 ± 17530 $at\ g_{qtz}^{-1}$ using the sea level high latitude (SLHL) rescaled local production rate of the Chironico landslide: 4.16 ± 0.10 $at\ g_{qtz}^{-1}$ a^{-1} (Claude et al., 2014), corrected for the samples' longitude, latitude and elevation and considering no erosion correction and the ERA40 atmospheric model (Uppala et al. 2005). We use a disintegration constant λ of 4.9×10^{-7} a^{-1}, a mean attenuation length for nuclear interacting particles in the target Λ of 1.6×10^{3} $g\ mm^{-2}$ (Gosse and Phillips, 2001; Nishiizumi et al., 2007). The density of the Mont-Blanc granite is measured at around 2.55×10^{-3} $g\ mm^{-3}$.

3.3.1 Forward modeling experiments

In the first scenario, a series of synthetic luminescence profiles were generated using Eq. (3.1) in a forward model, together with erosion rates of $\dot{\varepsilon}$ = 10^{-2} $mm\ a^{-1}$ and $\dot{\varepsilon}$ = 1 $mm\ a^{-1}$. This range of values is based on the results of the numerical experiment reported in Sect. 3.1.2. For this scenario, erosion rates are assumed to be constant over the TCN exposure age ts = t_0, ts being the onset time of erosion (dashed lines in Figs. 3.7a-d). A reference luminescence profile is also calculated assuming no erosion, using t_0 and Eq. (3.2) (black dot in Fig. 3.6b and black lines in Fig. 3.6c and Figs. 3.7a-d). In the third scenario, another set of synthetic luminescence profiles were again generated using Eq. (3.1) in a forward model, but the erosion rate was allowed to vary with time (Fig. 3.6 and green dots in Figs. 3.7a-d). The assumption made here, is that the evolution of erosion in time can follow a step function (Figs. 3.6a and

3.6b). This kind of erosion function in time was chosen to explore the effect of a non-constant erosion rate in time on both the luminescence signal and ^{10}Be concentration, but without the intention of simulating climatic transitions. Initially null between the corrected exposure age, tc and an onset time of erosion, ts, the erosion rate was fixed at zero (Fig. 3.6a). Between ts and today a non-zero rate of erosion was included. Figure 3.6 illustrates the schematic representation of four different erosion scenarios through time (Figs. 3.6a and 3.6b) and their resulting luminescence signal (Fig. 3.6c). Note that the corrected exposure age tc is part of the calculation and is obtained by solving Eq. (3.3) and using the nuclide concentration and an entire erosion rate history. We report the four model outputs calculated using ts between 1 and 100 a, and erosion rates $\dot{\varepsilon}$ between 10^{-2} and 1 $mm\ a^{-1}$ (green dots respectively in Figs. 3.7a-d). Note that we added 10% of white noise to the predicted OSL surface exposure dating profiles (used for the inversion approach in Sect. 3.2).

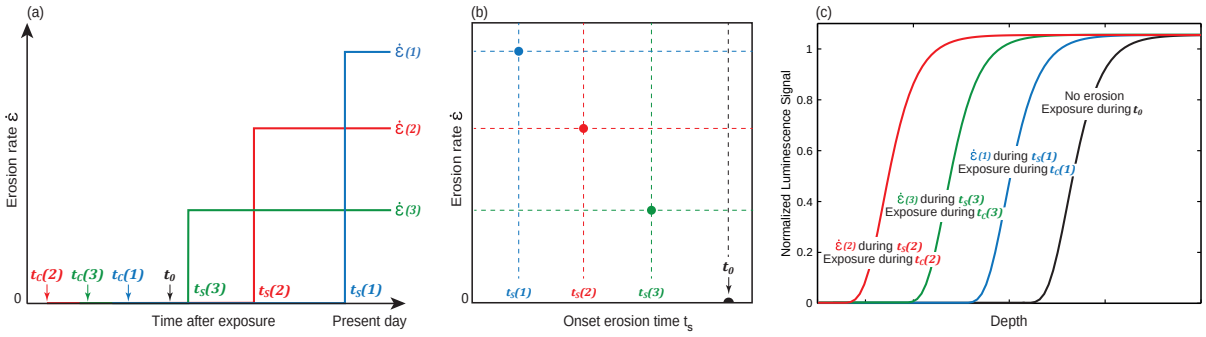

Figure 3.6: Schematic representation of four different erosion scenarios through time (a) and (b) and their resulting luminescence signal (c). t_0 is the uncorrected ^{10}Be exposure age, ts the onset times of erosion, tc the corrected exposure ages, and $\dot{\varepsilon}$ the erosion rate. Note that the luminescence plots in (c) are not model outputs but drawings, with the aim of conceptualizing how the experiments are designed.

By applying a constant erosion rate of 10^{-2} $mm\ a^{-1}$ to a rock surface exposed since t_0 (16428 $\pm$ 589 a), the luminescence signal is brought 7.8 mm closer to the surface (i.e., 17 mm deep from the surface) compared to the reference signal (luminescence signal exposed since t_0 and no affected by erosion; black line in Figs. 3.7a-d at 24.8 mm deep from the surface). For a constant erosion rate of 1 $mm\ a^{-1}$, the luminescence signal is brought 15.4 mm closer to the surface (i.e., 9.4 mm deep from the surface) compared to the reference signal (difference between black lines and dash lines measured at NLS = 0.5 in Figs. 3.7a-d).

If an erosion rate of 10^{-2} $mm\ a^{-1}$ is applied for a duration of 1 a before sampling and integrated over its specific corrected exposure age (since $tc = 16428 \pm 589\ a$), the luminescence signal is brought 0.4 mm closer to the surface compared to the reference signal (green dots in Fig. 3.7a) and 1.2 mm if the same erosion rate is applied for 100 a before sampling and integrated over its specific tc (16455 $\pm$ 588 a; green dots in Fig. 3.7b). In both scenarios,

the predicted luminescence profiles do not overlap the luminescence profile predicted for a constant erosion rate indicating that the system is in a transient state.

For an erosion rate of 1 $mm\ a^{-1}$ applied during 1 a before sampling and for an exposure time corrected with its specific erosion history tc (16455 $\pm$ 593 a), the luminescence profile (green dots in Fig. 3.7c) is brought 1.2 mm closer to the surface compared to the reference signal (black line in Fig. 3.7c). In this case, the luminescence profile is in transient state with erosion because it is not overlapping the luminescence profile produced by applying the same erosion rate for an infinite time (dashed line in Fig. 3.7c). Interestingly, the same effect on the luminescence signal is produced by applying an erosion rate of 1 $mm\ a^{-1}$ during 1 a (green dots in Fig. 3.7c) and an erosion rate 10^{-2} $mm\ a^{-1}$ during 100 a before sampling (green dots in Fig. 3.7b). For an erosion rate of 1 $mm\ a^{-1}$ applied during 100 a before sampling and for an exposure time corrected with its specific erosion history tc (16945 $\pm$ 600 a), the luminescence signal is brought 15.4 mm closer to the surface (green dots in Fig. 3.7d) compared to the reference signal (black lines in Fig. 3.7d). A similar result is obtained when erosion rate is applied for an infinite time (dashed line in Fig. 3.7d): in this scenario, the steady state with erosion is reached.

3.3.2 Inverse modeling experiments

The synthetic data are now inverted to assess the extent to which it is possible to recover the values of $\dot{\varepsilon}$ and ts. Ultimately, our objective is to establish and validate a numerical protocol that enables erosion rate histories to be estimated from paired OSL surface exposure and TCN dating measurements on bedrock surfaces. To find the most likely solutions, we test 10^4 pairs of both $\dot{\varepsilon}$ and ts (combination of 100 values of both parameters) in log space. The range of possible erosion rates $\dot{\varepsilon}$ varies between 10^{-5} and 10^{1} $mm\ a^{-1}$. These end-member values were selected from the erosion sensitivity test performed in Sect. 3.1.2. The erosion onset times ts range between $5{\times}10^{-1}$ a and $3{\times}10^{4}$ a, this range being arbitrarily decided with the upper boundary set to approximately twice the initial TCN age.

As mentioned above, the measured ^{10}Be concentration has be to corrected for erosion. If the applied erosion rate is too high or the duration is too long, or both, the ^{10}Be concentration must remain small (Fig. A3.4). On that basis, there is a range of solutions with high erosion rates and durations which is unable to predict the observed ^{10}Be concentration (Lal, 1991). We call this the "forbidden zone", and exclude it from the parameter search. Expressed differently, for each $\dot{\varepsilon}$ and ts pair, Eq. (3.3) is first solved and a first estimate of the corrected exposure age tc is calculated. However, Eq. (3.3) does not yield a solution for a range of values that produce too much erosion and thus too high ^{10}Be concentration loss to fit the measured sample concentration. In the studied cases, the forbidden zone is defined by the

values between the pairs of $\dot{\varepsilon} = 10\ mm\ a^{-1}$, ts ~110 a and $\dot{\varepsilon} \sim 5{\times}10^{-1}\ mm\ a^{-1}$, $ts = 29210$ a.

For all the other pairs of $\dot{\varepsilon}$ and ts, the corrected exposure age tc is subsequently used to predict luminescence profiles ($NLS_{inverse}$) that are compared to the synthetic luminescence profiles ($NLS_{forward}$) presented in the previous section (green dots in Figs. 3.7a-d). The quality of these fits are evaluated using a misfit function and the inversion results are converted into probability density functions using a likelihood function (Eq. 3.7). The least square deviations regression method minimizes the sum of the square differences between the forward $NLS_{forward}$ and the inverted values $NLS_{inverse}$ giving:

$$\mathcal{L} = exp(-\frac{1}{\sigma^2}\sum_{i=1}^{n}\left[NLS^{(i)}_{forward} - NLS^{(i)}_{inverse}\right]^2) \tag{3.7}$$

Where n is the number of rock slices per sample and σ is the standard deviation of the normalized saturated luminescence signal intensities that form the plateau at depth ($0.053 \leqslant \sigma \leqslant 0.059$ for our samples).

The results of these inversions are shown in Figures 3.7e-h with the parameter space for erosion rate/time and the resulting likelihood. The green circles depict the synthetic forward modelled pair of $\dot{\varepsilon}$ and ts ($NLS_{forward}$) which should be recovered in the inversion (green dots in Fig. 3.7a-d), and the black circles show the $\dot{\varepsilon}$ - t_0 pair used to produce the model assuming erosion is constant (dashed lines in Figs. 3.7a-d). We then select the pairs of $\dot{\varepsilon}$ and ts leading to the maximum 5% likelihood values which are fitting the synthetic data (the threshold of 5% is arbitrarily chosen), and plot their corresponding luminescence profile values (red lines in Figs. 3.7a-d).

The first noticeable observation is that the erosion rate $\dot{\varepsilon} = 10^{-2}\ mm\ a^{-1}$ could be applied over every time period below ~$3\ {\times}10^{-3}\ a$. The numerical solutions for both constant and non-constant erosion rate lay outside of the forbidden zone (black and green circles respectively in Figs 7e-f). As another example, an erosion rate equal to $\dot{\varepsilon} = 1\ mm\ a^{-1}$ could also be applied for any time lower than 1200 a. Indeed, it is not possible to apply an erosion $\dot{\varepsilon} = 1$ $mm\ a^{-1}$ during t_0 as this pair of values would lie in the forbidden zone (Figs 7g, h) since such a high erosion rate would imply too high ^{10}Be concentration loss to fit the measured sample concentration.

For the first scenario, the synthetic luminescence profile produced by applying an erosion rate $\dot{\varepsilon} = 10^{-2}\ mm\ a^{-1}$ during time period $ts = 1\ a$ has a great number of possible pairs of $\dot{\varepsilon}$ and ts that would reproduce this specific luminescence signal (Normalized likelihood ¿ 0.9: yellow area in Fig. 3.7e). The acceptable solutions range between pairs of values below $\dot{\varepsilon}$ ~$2\ {\times}10^{-2}$ $mm\ a^{-1}$ with $ts = 5\ {\times}10^{-1}\ a$ and $\dot{\varepsilon} = 10^{-5}\ mm\ a^{-1}$ with $ts = 10^3\ a$. These low values do not produce enough erosion to significantly alter the TCN exposure age ($tc \sim t_0$).

In the second scenario, the erosion rate is $\dot{\varepsilon} = 10^{-2}\ mm\ a^{-1}$ during a time period $ts = 100\ a$ and the forward model pair values can be successfully recovered from the inversion with a more restrained range of numerical solutions (Fig. 3.7f). The transient state with erosion is well illustrated by trade-offs between erosion rate and time. To fit the forward luminescence profile, low erosion rates should be associated with long time periods following the trend from $\dot{\varepsilon} \sim 2\ mm\ a^{-1}$ with $ts = 5{\times}10^{-1}\ a$ to $\dot{\varepsilon} \sim 1.4{\times}10^{-4}\ mm\ a^{-1}$ with $ts = 1.2{\times}10^{4}\ a$. When the erosion rate of $1.4{\times}10^{-4}\ mm\ a^{-1}$ is applied longer than $1.2{\times}10^{4}\ a$, a steady state with erosion is reached and this specific erosion rate could be applied for an infinite time. The highest correction of the TCN exposure age possible with these solutions is of the order of 0.1% ($t_0 = 16428 \pm 589\ a$ and $tc = 16455 \pm 588\ a$), which is insignificant compared to the 3.6% uncertainties on t_0.

The third scenario, where the erosion rate is $\dot{\varepsilon} = 1\ mm\ a^{-1}$ during time period $ts = 1\ a$, shares the exact same solution as the second case ($\dot{\varepsilon} = 10^{-2}\ mm\ a^{-1}$ with $ts = 100\ a$). This confirms the observation made with the forward modeling where both scenarios predicted similar luminescence profile depths. This can be explained because both pairs of $\dot{\varepsilon}$ - ts lie on the trend from $\dot{\varepsilon} \sim 2\ mm\ a^{-1}$ with $ts = 5{\times}10^{-1}\ a$ and $\dot{\varepsilon} \sim 1.4{\times}10^{-4}\ mm\ a^{-1}$ with $ts = 1.2{\times}10^{4}\ a$.

In the fourth scenario, the erosion rate $\dot{\varepsilon} = 1\ mm\ a^{-1}$ is applied during time $ts = 100\ a$, the range of solutions is much more restrained than for the other scenarios. The synthetic luminescence profile is at steady state with erosion, where the erosion rate $\dot{\varepsilon} = 1\ mm\ a^{-1}$ can be applied from 18 to 1200 a. For longer time of erosion, the pairs of $\dot{\varepsilon}$ - ts lie within the forbidden zone regarding the TCN concentration. In this case, the maximum correction of the TCN exposure age is around 3.1% ($t_0 = 16428 \pm 589\ a$ and $tc_{max} = 16945 \pm 600\ a$), which is comparable to the initial uncertainty on t_0.

3.4 Application to natural samples

In this section, we apply the method presented above on two natural rock surfaces. Samples MBTP1 and MBTP6 were collected from glacially-polished bedrock surfaces at 2545 and 2084 m.a.s.l. respectively from the Tête de Trélaporte located on the left bank of the Mer de Glace glacier (Mont-Blanc massif, European Alps). Rock surfaces were collected for application of both the TCN and OSL surface exposure dating methods (Fig. 3.9 and Tables 3.2 and 3.3). Both samples are from the same phenocristalline granitic lithology of the Mont Blanc massif (Fig. 3.8).

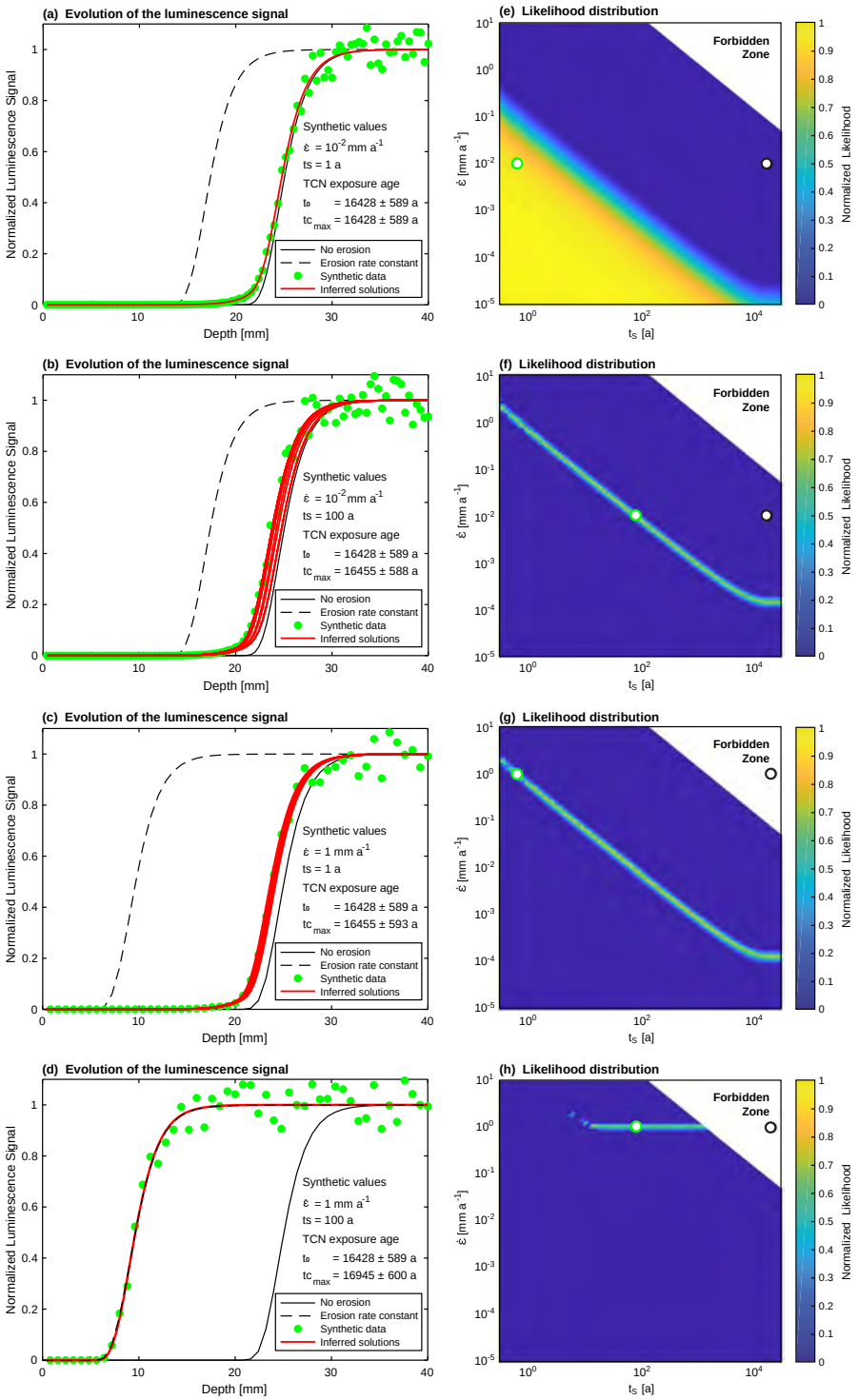

Figure 3.7: Caption on the next page

Figure 3.7 on the previous page: Results of forward and inverse modeling experiments. Green dots represent the simulated luminescence profiles for rock surfaces exposed to (a) an erosion rate of $\dot{\varepsilon} = 10^{-2}$ mm a^{-1} during time $ts = 1$ a, (b) an erosion rate of $\dot{\varepsilon} = 10^{-2}$ mm a^{-1} during time $ts = 100$ a, (c) an erosion rate of $\dot{\varepsilon} = 1$ mm a^{-1} during time $ts = 1$ a and (d) an erosion rate of $\dot{\varepsilon} = 1$ mm a^{-1} during time $ts = 100$ a. Black lines represent the reference luminescence profiles for a surface exposed since $t_0 = 16428 \pm 589$ a with no erosion. Dashed lines show the luminescence profiles produced by applying a constant erosion rates of (a) (b) $\dot{\varepsilon} = 10^{-2}$ mm a^{-1} and (c) (d) $\dot{\varepsilon} = 1$ mm a^{-1} during t_0. Red lines represent the best-fitting profiles inverted for all numerical solutions with likelihood >5%. tc_{max} represents the maximum corrected TCN exposure age using the forward modeled values of $\dot{\varepsilon}$ and ts. (e), (f), (g) and (h) represents the likelihood distributions inverted from the synthetic luminescence profiles respectively in (a), (b), (c) and (d). Green open circles represent the pairs of values of $\dot{\varepsilon}$ and ts used in the forward model to produce the profiles, and the black open circles represent the values $\dot{\varepsilon}$ and t_0 used to predict luminescence profiles with constant erosion (dashed lines insets (a), (b), (d) and (c)). All models were performed by solving Eq. (3.1) using the following parameters: $\overline{\sigma\varphi_0} = 129$ a^{-1}, $\mu = 0.596$ mm^{-1}, $\dot{D}$ = $8{\times}10^{-3}$ Gy a^{-1} and $D_0 = 500$ Gy. TCN ages were calculated by solving Eq. (3.3) for the ^{10}Be concentration of sample MBTP1 presented in the following section.

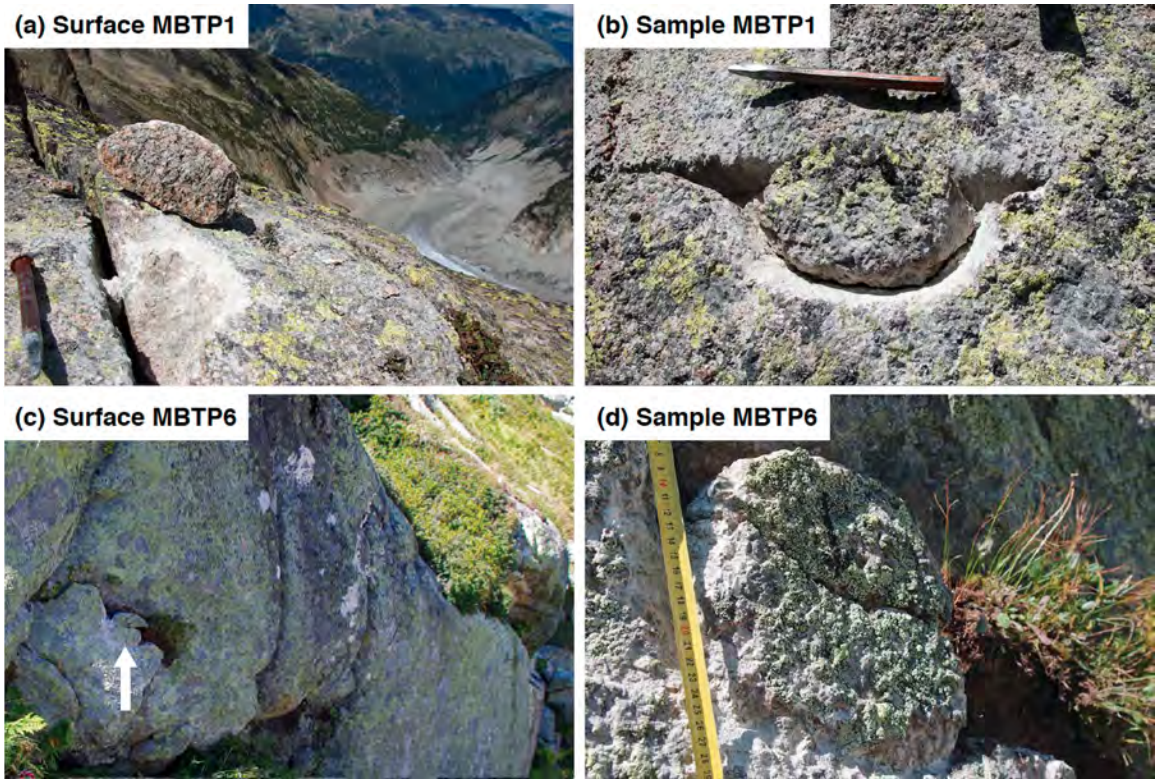

Figure 3.8: Locations and sample pictures of MBTP1 and MBTP6, both located on the Tête de Trélaporte along the Mer de Glace glacier (Mont Blanc massif, European Alps).

3.4.1 Sample preparation, measurement and age calculation

The ^{10}Be sample preparation method is comprehensively described in the literature (e.g., Kohl and Nishiizumi, 1992; Ivy-Ochs, 1996). We used quartz separates from grain sizes between 250 μm and 1 mm. The addition of a commercial ^{9}Be carrier was followed by quartz dissolution in HF and Be purification using ion-exchange columns and selective precipitation. The ^{10}Be/^{9}Be ratio was measured by accelerator mass spectrometry (AMS) on the 600 KV TANDY system at the Laboratory of Ion Beam Physics (LIP) at ETH Zürich (Switzerland) against the standard S2007N (Christl et al., 2013) that is calibrated against the 07KNSTD standard (Nishiizumi et al., 2007). We correct for a long-term average full chemistry procedural blank of ^{10}Be/^{9}Be (3.7 ± 2.2) $\times 10^{-15}$. Ages are calculated using the SLHL rescaled local production rate of the Chironico landslide: 4.16 ± 0.10 at g_{quartz}^{-1} a^{-1}(Claude et al., 2014), corrected for the samples' longitude, latitude and elevation and considering no erosion correction, with the Lifton-Sato-Dunai (LSD) scaling scheme (Lifton et al., 2014), the ERA40 atmospheric model (Uppala et al., 2005) and the Lifton VDM 2016 geomagnetic database (for ages between 0-14 ka, Pavon-Carrasco et al., 2014 and for ages between 14-75 ka, GLOPIS-75, Laj et al., 2004) with a modified version of the CREp online calculator to process non-linear erosion rate correction by solving Eq. (3.3) (Martin et al., 2017). The reported errors propagate uncertainties from AMS standard reproducibility, counting statistics, the standard mean error of the samples, blank correction and the local production rate. These external errors are used to compare absolute ages to independent chronologies. All errors are reported at 1σ.

For luminescence analysis we followed the methodology of Lehmann et al. (2018). The bedrock samples were cored down to 30 mm depth using a Husqvarna DM220 drill, with 10-mm diameter. Cores were then sliced into 0.7-mm thick rock slices with a BUEHLER IsoMet low speed saw equipped with a 0.3-mm thick diamond blade. The samples were drilled and sliced under wet conditions (water and lubricant, respectively) to avoid any heating that could potentially reset the OSL signal. Sample preparation was done under subdued red-light conditions. The thickness of each rock slice was measured to determine the precise depth of each luminescence measurement. Luminescence measurements were performed using Risø TL-DA 20 TL/OSL readers (Bøtter-Jensen et al., 2010) equipped with ^{90}Sr beta sources at the University of Lausanne (Switzerland). We performed a preheat at 250°C before giving infrared (IR) stimulation (870 nm, FWHM 40 nm) at 50°C (the sample preparation and analysis are described in further detail in the Figs. A3.2 and A3.5). The calculation of $\dot{D}$ was achieved through the measurement of the concentrations of U, Th, K and Rb of the bulk rock sample and the use of the DRAC online calculator (Table 3.2 and details in Table A1; Durcan et al., 2015). The determination of D_0 was done by constructing a dose response curve (DRC) of the IRSL signal measured at 50°C using a single aliquot regenerative dose (SAR) protocol (Murray and Wintle, 2000; Wallinga et al., 2000) and fitting the DRC with single saturating

exponential. The validity of the measurement protocol was confirmed using a dose-recovery experiment (Wallinga et al., 2000). Recovered doses were within 10% of unity.

Table 3.2: Sample list and measurements

Sample ID	Latitude	Longitude	Elevation	Thickness	Topographic	^{10}Be conc.[a]	*P(0)* local[b]	$\dot{D}$ spec.[c]
	WGS 84		[m.a.s.l.]	[cm]	Shielding factor	[at g_{qtz}^{-1}]	[at g_{qtz}^{-1}]	Gy a^{-1}
MBTP1	45.9083	6.9311	2545	8	0.963	474750 ± 17530	30.20 ± 0.72	7.4 10^{-3}
MBTP6	45.9129	6.9326	2094	7	0.594	84100 ± 13060	21.74 ± 0.52	8.4 10^{-3}

(a) Measured against standard 07KNSTD (Nishiizumi et al., 2007), corrected for full process blank of (3.7 ± 2.2) × 10^{-15} ^{10}Be/^{9}Be. (b) Local production rate using the sea level high latitude (SLHL) rescaled local production rate of the Chironico landslide: 4.16 ± 0.10 at g_{quartz}^{-1} a^{-1} (Claude et al., 2014), corrected for the samples' longitude, latitude and elevation and considering no erosion correction, with the LSD scaling scheme (Lifton et al., 2014), the ERA40 atmospheric model (Uppala et al., 2005) and the Lifton VDM 2016 geomagnetic database (for ages between 0-14 ka, Pavon-Carrasco et al., 2014 and for ages between 14-75 ka, GLOPIS-75, Laj et al., 2004). (c) Dose rates were calculated using the concentrations of U, Th and K of the bulk rock sample and the DRAC online calculator (details in Table A1; Durcan et al., 2015).

(a) Measured against standard 07KNSTD (Nishiizumi et al., 2007), corrected for full process blank of (3.7 ± 2.2) ×10^{-15} ^{10}Be/^{9}Be.

(b) Local production rate using the sea level high latitude (SLHL) rescaled local production rate of the Chironico landslide: 4.16 ± 0.10 at g_{quartz}^{-1} a^{-1} (Claude et al., 2014), corrected for the samples' longitude, latitude and elevation and considering no erosion correction, with the LSD scaling scheme (Lifton et al., 2014), the ERA40 atmospheric model (Uppala et al., 2005) and the Lifton VDM 2016 geomagnetic database (for ages between 0-14 ka, Pavon-Carrasco et al., 2014 and for ages between 14-75 ka, GLOPIS-75, Laj et al., 2004).

(c) Dose rates were calculated using the concentrations of U, Th and K of the bulk rock sample and the DRAC online calculator (details in Table A1; Durcan et al., 2015).

4.2 Experimental results

Sample MBTP1 provided a ^{10}Be concentration of 474750 ± 17530 at g_{qtz}^{-1}. The solution of Eq. (3) gives an apparent ^{10}Be age for sample MBTP1 of t_0 = 16428 ± 588 a assuming sample thickness of 8 cm and a shielding factor of 0.963 (Tables 2 and 3). In the same way, the measured ^{10}Be concentration of 84100 ± 13060 at g_{qtz}^{-1} for sample MBTP6 gives a ^{10}Be age of t_0 = 6667 ± 1062 a, assuming a sample thickness of 7 cm and a shielding factor of 0.594 (Tables 2 and 3). Apparent ^{10}Be ages were calculated as described in Sect. 4.1, assuming no erosion.

3.4.2 Experimental results

Sample MBTP1 provided a ^{10}Be concentration of 474750 ± 17530 *at* g_{qtz}^{-1}. The solution of Eq. (3) gives an apparent ^{10}Be age for sample MBTP1 of $t_0 = 16428 \pm 588$ a, assuming a sample thickness of 8 cm and a shielding factor of 0.963 (Tables 3.2 and 3.3). In the same way, the measured ^{10}Be concentration of 84100 ± 13060 at g_{qtz}^{-1} for sample MBTP6 gives a ^{10}Be age of $t_0 = 6667 \pm 1062$ a, assuming a sample thickness of 7 cm and a shielding factor of 0.594 (Tables 3.2 and 3.3). Apparent ^{10}Be ages were calculated as described in Section 3.4.1, assuming no erosion.

Figure 3.9 shows the infrared stimulated luminescence at 50°C (IRSL50, Normalized Signal) measurements of samples MBTP1 and MBTP6. Three replicates (i.e., individual cores) per sample were sliced in a way that a depth and an IRSL50 signal can be attributed to each rock slice (Tables A3.2 and A3.3). The IRSL50 signal is bleached near the surface and reaches a plateau at depth (even for sample MBTP1 where the plateau is poorly defined). The scattering of the measurements between rock slices is probably due to the granitic nature of the samples. Indeed, the phenocryst lithology can cause heterogeneity in the resulting IRSL50 signals (Meyer et al., 2018) caused by differential bleaching and possibly variations in the environmental dose rate, mainly beta dose heterogeneity (Morthekai et al. 2006) and thus the rate of electron trapping.

Figure 3.9 shows the infrared stimulated luminescence at 50°C (IRSL50, Normalized Signal) measurements of samples MBTP1 and MBTP6. Three replicates (i.e., individual cores) per sample were sliced in a way that a depth and an IRSL50 signal can be attributed to each rock slice. The IRSL50 signal is bleached in the surface and reaches a plateau at depth (even for sample MBTP1 where the plateau is poorly defined). The scattering of the measurements between rock slices is probably due to the granitic nature of the samples. Indeed, the phenocryst lithology can cause heterogeneity in the resulting IRSL50 signals (Meyer et al., 2018) caused by differential bleaching and possibly variations in the environmental dose rate, mainly beta dose heterogeneity (Morthekai et al. 2006) and thus the rate of electron trapping.

As a reference profile, a model is computed by solving Eq. (2) using t_0 and considering no erosion (black line in Fig. 9a) and lies at 25 mm below the rock surface. The bleaching front measured from the IRSL50 signal of sample MBTP1 (green dots in Fig. 9a) is located 4 mm closer to the surface compared to the reference profile (21 mm from the surface). The IRSL50 profile considering no erosion correction gives an apparent age of about 2 orders of magnitude lower compared to t_0, about 642 ± 160 a (1σ, Table 3 and Fig. A5).

For sample MBTP6, the reference profile is lying at 23.5 mm below the surface (black line in Fig. 9b). The measured IRSL50 profile (green dots in Fig. 9b) is approximately 16.5 mm closer to the surface in comparison to the reference profile

As a reference profile, a model is computed by solving Eq. (3.2) using t_0 and considering no erosion (black line in Fig. 3.9a) and lies at 25 mm below the rock surface. The bleaching front measured from the IRSL50 signal of sample MBTP1 (green dots in Fig. 3.9a) is located 4 mm closer to the surface compared to the reference profile (21 mm from the surface). The IRSL50 profile considering no erosion correction gives an apparent age of about 2 orders of magnitude lower compared to t_0, about 642 ± 160 a (1σ; Table 3.3 and Fig. A3.5).

For sample MBTP6, the reference profile is at 23.5 mm below the surface (black line in Fig. 3.9b). The measured IRSL50 profile (green dots in Fig. 3.9b) is approximately 16.5 mm closer to the surface in comparison to the reference profile (7 mm from the surface). The OSL surface exposure apparent age for sample MBTP6 is about 0.39 ± 0.02 a (1σ; Table 3.3 and Fig. A3.5).

3.4.3 Inversion results

In this section, we report the results from the inversion of $\dot{\varepsilon}$ and ts for the IRSL50 profiles of samples MBTP1 and MBTP6 following the procedure presented in Section 3.2. For both samples, the corrected ^{10}Be age are calculated using Eq. (3.3) with a range of erosion rates from 10^{-5} and 10^{1} $mm\ a^{-1}$ and ts ranging from $5{\times}10^{-1}$ a to $10^{log(t_0)+0.25}$ a (this formula limits the search to ∼30 ka because these surfaces are known to be post-LGM; Coutterand and Buoncristiani, 2006).

The resulting forbidden zone for sample MBTP1 lies between the erosion rate/time pairs of $\dot{\varepsilon} = 10$ $mm\ a^{-1}$, ts ∼110 a and $\dot{\varepsilon} \sim 5{\times}10^{-1}$ $mm\ a^{-1}$, $ts = 29210$ a (already discussed in Sect. 3.2). The inversion results indicate that sample MBTP1 reached a steady state with erosion characterized by an erosion rate of $\dot{\varepsilon} = (3.5 \pm 1.2){\times}10^{-3}$ (1σ) $mm\ a^{-1}$ applied during a minimum duration of 2300 a (Fig. 3.9c). In these conditions, the corrected TCN age is tc_{ss} = 16647 ± 593 a (1.1% of correction). The maximum corrected TCN age tc_{max} = 17396 ± 621 a is obtained by using $\dot{\varepsilon} = (3.5 \pm 1.2){\times}10^{-3}$ (1σ) $mm\ a^{-1}$ and the maximum ts possible (29214 a), this comprises a correction of about 5.8%.

For sample MBTP6, the forbidden zone lies in between the erosion rate/time pairs of $\dot{\varepsilon} = 10$ $mm\ a^{-1}$, ts ∼150 a and $\dot{\varepsilon} \sim 1{\times}10^{-10}$ $mm\ a^{-1}$, $ts = 11860$ a. The inversion results show that the IRSL50 profile of sample MBTP6 reaches steady state with erosion for an erosion rate $\dot{\varepsilon} = 4.3 \pm 0.56$ $mm\ a^{-1}$ (1σ) applied since at least 4 a. In these conditions, the corrected TCN age is $tc_{ss} = 6857 \pm 980$ a (2.8% of correction). This steady state cannot be maintained for longer than 344 a because further values correspond to the forbidden zone (Fig. 3.9d). The maximum corrected TCN age tc_{max} = 68692 ± 10617 a would represent a significant correction of 930%.

At steady state, the surfaces MBTP1 and MBTP6 would have lost 8.05 mm and 17.2 mm respectively. These values seem realistic regarding the natural surface textures observed on

site: no smooth surface or striations are preserved on the roches moutonnes (Fig. 3.8). By taking the end-member hypothetical erosion values, the surfaces MBTP1 and MBTP6 would have lost maximum 102 mm and 1479 mm respectively.

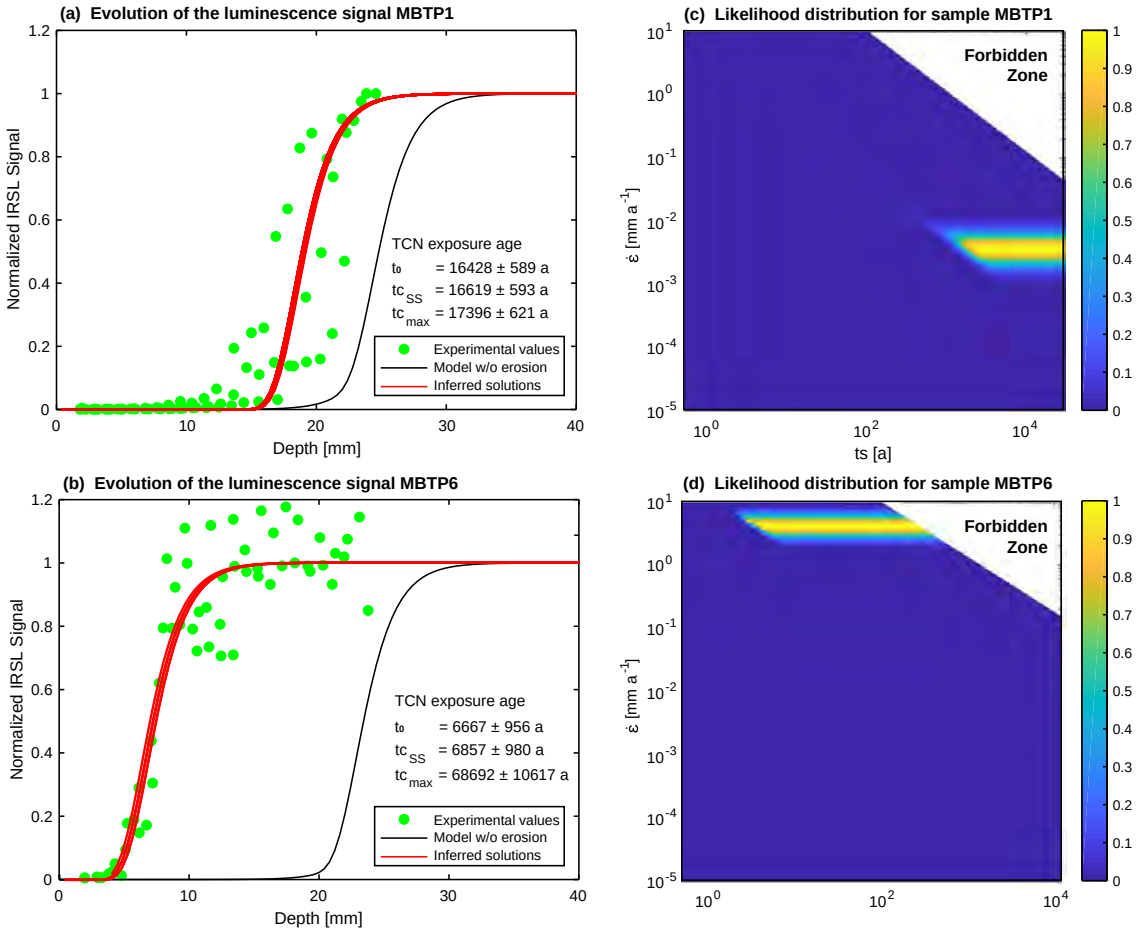

Figure 3.9: IRSL50 profiles and inversion results for samples MBTP1 and MBTP6. (a) and (b) Green dots represent the measured IRSL50 profiles for samples MBTP1 and MBTP6 respectively. Black lines represent the reference profiles calculated using Eq. (3.2) and taking the TCN exposure age with no erosion correction (t_0). Red lines represent inferred fits where the likelihood is greater 0.95. tc_{ss} represents the corrected TCN exposure age calculated at the steady state. tc_{max} represents the maximum corrected TCN exposure age. (c) and (d) represent the likelihood distributions inverted from respective insets (a) and (b). All models were computed by solving Eq. (3.1) and using the following parameters: $\overline{\sigma\varphi_0}$ = 129 a^{-1}, μ = 0.596 mm^{-1}, D_0 = 500 Gy, $\dot{D}$ = 7.4×10^{-3} Gy a^{-1} and $\dot{D}$ = 8.4×10^{-3} Gy a^{-1} for samples MBTP1 and MBTP6. Dose rates were calculated using the concentrations of U, Th, K and Rb of the bulk rock sample and the DRAC online calculator (details in Table A1; Durcan et al., 2015).

Table 3.3: TCN and OSL surface ages and inversion results for samples MBTP1 and MBTP6.

Table 3: TCN and OSL surface ages and inversion results for samples MBTP1 and MBTP6

Sample ID	TCN apparent age t_0 (1)	TCN age corr. t_{Css} (2)	TCN age corr. t_{Cmax} (2)	OSL surface exposure apparent age (3)	t_S at SS*	$\dot{\varepsilon}$ at SS*	total erosion at SS*
	[a]	[a]	[a]	[a]	[a]	[mm a^{-1}]	[mm]
MBTP1	16428 ± 588	16619 ± 593	17396 ± 621	642 ± 160	2300	3.5 ± 1.2 × 10^{-3}	8.05
MBTP6	6667 ± 965	6857 ± 980	68692 ± 10617	0.39 ± 0.02	4	4.3 ± 0.56	17.2

(1) Ages are calculated using the sea level high latitude (SLHL) rescaled local production rate of the Chironico landslide: 4.15 ± 0.10 *at* g^{-1} a^{-1} rescaled for every longitude (Claude et al., 2014), latitude and elevation and considering no erosion correction, with the LSD scaling scheme (Lifton et al., 2014), the ERA40 atmospheric model (Uppala et al., 2005) and the Lifton VDM 2016 geomagnetic database (for ages in between 0-14 ka, Pavon-Carrasco et al., 2014 and for ages in between 14-75 ka, GLOPIS-75, Laj et al., 2004) by solving Eq. (3). (2) TCN age corr. tc_{max} correspond to the maximum corrected TCN exposure ages calculating from the best maximum 5% solution. For (1) and (2) the errors represent the internal errors. (3) Ages were inverted using Eq. (2) and prescribing 10^6 solutions for a range of time from 0 to t_0 (TCN age calculated using the ^{10}Be concentration of each sample and solving Eq. (3) without erosion correction). All models were calculated using the following parameters: $\overline{\sigma\varphi_0}$ = 129 a^{-1}, μ = 596 m^{-1}, D_0 = 500 Gy and $\dot{D}$ = 7.4 × 10^{-3} Gy a^{-1} and $\dot{D}$ = 8.4 × 10^{-3} Gy a^{-1} respectively for sample MBTP1 and sample MBTP6. The uncertainties represent 1σ of the distribution presented in Fig. A5. *SS means steady state.

(1) Ages are calculated using the sea level high latitude (SLHL) rescaled local production rate of the Chironico landslide: 4.15 ± 0.10 *at* g^{-1} a^{-1} rescaled for every longitude (Claude et al., 2014), latitude and elevation and considering no erosion correction, with the LSD scaling scheme (Lifton et al., 2014), the ERA40 atmospheric model (Uppala et al., 2005) and the Lifton VDM 2016 geomagnetic database (for ages in between 0-14 *ka*, Pavon-Carrasco et al., 2014 and for ages in between 14-75 *ka*, GLOPIS-75, Laj et al., 2004) by solving Eq. (3.3). (2) TCN age corr. tc_{max} correspond to the maximum corrected TCN exposure ages calculating from the best maximum 5% solution. For (1) and (2) the errors represent the internal errors. (3) Ages were inverted (Fig. A3.5) using Eq. (3.2) and prescribing 10^6 solutions for a range of time from 0 to t_0 (TCN age calculated using the ^{10}Be concentration of each sample and solving Eq. (3.3) without erosion correction). All models were calculated using the following parameters: $\overline{\sigma\varphi_0}$ = 129 a^{-1}, μ = 0.596 mm^{-1}, D_0 = 500 Gy, $\dot{D}$ = 7.4×10^{-3} Gy a^{-1} and $\dot{D}$ = 8.4×10^{-3} Gy a^{-1} respectively for sample MBTP1 and sample MBTP6. The uncertainties represent 1σ of the distribution presented in Fig. A3.5. *SS means steady state.

3.5 Discussion

The mismatch between OSL surface exposure and TCN ages presented in this study clearly show how significant the impact of erosion for OSL surface exposure dating is. If the luminescence bleaching front is interpreted without considering erosion, the resulting exposure age will be strongly underestimated (Figs. 5, 7 and 9). For samples MBTP1 and MBTP6 the apparent OSL surface exposure ages are 642 ± 160 a and 0.32 ± 0.02 a, respectively while apparent TCN exposure ages are 16428 ± 589 a and 6667 ± 965 a respectively. We demonstrated in Sect. 2.1.2 that OSL surface exposure dating is hardly applicable to natural rock surfaces that experience even a minimal erosion rate about 10^{-4} mm a^{-1}. Our models and results show that the position of the bleaching front is highly sensitive to the erosion rate history. Recent studies (e.g., Freiesleben et al., 2015; Sohbati et al., 2012a, 2015; Rades el al., 2018) have showed very convincingly that OSL-exposure can be used to identify multiple burial and exposure events in the history of a single clast. However, our results imply that erosion cannot be neglected. We show in this study that this high sensitivity to erosion can instead be used to estimate the erosion history of such rock surfaces.

The mismatch between OSL surface exposure and TCN ages presented in this study clearly show how significant the impact of erosion for OSL surface exposure dating is. If the luminescence bleaching front is interpreted without considering erosion, the resulting exposure age will be strongly underestimated (Figs. 3.5, 3.7 and 3.9). For samples MBTP1 and MBTP6 the apparent OSL surface exposure ages are 642 ± 160 a and 0.32 ± 0.02 a, respectively while apparent TCN exposure ages are 16428 ± 589 a and 6667 ± 965 a respectively. We demonstrated in Section 3.2.1 that OSL surface exposure dating is hardly applicable to natural rock surfaces that experience even a minimal erosion rate of about 10^{-4} mm a^{-1}. Our models and results show that the position of the bleaching front is highly sensitive to the erosion rate history. Recent studies (e.g., Freiesleben et al., 2015; Sohbati et al., 2012a, 2015; Rades el al., 2018) showed very convincingly that OSL-exposure can be used to identify multiple burial and exposure events in the history of a single clast. However, our results imply that erosion cannot be neglected. We show in this study that this high sensitivity to erosion can instead be used to estimate the erosion history of such rock surfaces.

To do so, we have numerically solved the equation describing the evolution of luminescence signal of a rock surface exposed to light and erosion (Eqs. (1) and (3.2)). The validation of the model was tested on synthetic data and applied to two different glacially polished bedrock surfaces. We assumed a simple erosion rate history following a step function. However, it is very likely that rock surfaces are subject to stochastic erosion processes (e.g., Ganti et al., 2016). These stochastic processes could potentially explain, convincingly, why we observe fluctuations along the scarp. The numerical approach adopted here

the model was tested on synthetic data and applied to two different glacially-polished bedrock surfaces. We assumed a simple erosion rate history following a step function. However, it is very likely that rock surfaces are subject to stochastic erosion processes (e.g., Ganti et al., 2016). These stochastic processes cover potentially temperature, moisture, snow cover or wind fluctuations along the year. The numerical approach adopted here would potentially enable us to consider any type of erosion history (inverse exponential, stochastic distribution...). We considered the erosion rate to be non-constant in time but instead to follow a step function which changes from zero to a constant erosion rate at certain times of the exposure history. We observed that the resulting erosion histories can follow two states: a transient state or a steady state. Indeed, an experimental luminescence signal can be either at steady or transient state with erosion. To identify at which state the signal is, a model using Eq. (3.1) should try to fit the experimental luminescence signal considering a range of constant erosion rates applied over the TCN exposure age t_0 of the specific surface. If one specific erosion rate enables the model to fit the experimental luminescence signal, the system is at steady state with this specific erosion rate. If there is no unique solution, the system is at transient state with erosion. Note that some erosion rates cannot be applied for long durations. Indeed, the quantity of material removed and the concentration of cosmogenic nuclides in the rock surface would not match with the measured nuclide concentrations. To avoid that, we have defined a forbidden zone which characterized the range of pairs $\dot{\varepsilon}$ and ts for which Eq. (3.3) could not be solved.

When a luminescence profile is derived from multiple erosion rate $\dot{\varepsilon}$ and time ts pairs, the system is experiencing a transient state with erosion. This situation is characterized by a trade-off between erosion rate and the time of erosion. During this state, the luminescence signal does not evolve with depth if an increase of the erosion time is compensated by a decrease of the erosion rate. On the other hand, when a luminescence signal is derived from an erosion rate applied across a range of times ts, the system can be considered at steady state regarding the luminescence profile. In this case, the erosion rate can be considered as constant in time over the entire exposure age given by TCN dating providing that this solution falls outside of the forbidden zone. At steady state, the time during which the erosion rate is applied is always lower or equal to the maximum corrected TCN age (i.e., $ts \leq tc_{max}$).

The luminescence profile from a given rock surface is able to give information about the erosion history of this surface at both transient and steady state with erosion. The coupling with TCN dating allows the determination of a limit in time of the steady state with erosion, which cannot tend to infinity as discussed above (i.e., the forbidden zone). According to the inverse modeling of sample MBTP1, the total erosion experienced by the rock surface is about 8.05 mm when the system reached steady state with erosion ($\dot{\varepsilon} = 3.5{\times}10^{-3}$ $mm\ a^{-1}$ during $ts = 2300$ a) and 17.2 mm for sample MBTP6 ($\dot{\varepsilon} = 4.3$ $mm\ a^{-1}$ during $ts = 4$ a). This quantity of material removal is plausible given field observations, where the micro-structures

of striations (coated layer and glacial polish) are not preserved but where the macro-patterns of glacial erosion can still be observed (moulded forms, whalebacks, grooves). By taking the endmembers authorized by our model, we explore the limit of our method. The maximum total erosion is about 102 mm for MBTP1 (3.5×10^{-3} mm a^{-1} during 29214 a) and about 1479 mm for MBTP6 (4.3 mm a^{-1} during 344 a). Such high difference of erosion between two locations of the same vertical profile is unlikely.

The quantification of the erosion rate distribution brings the opportunity to quantitatively correct TCN ages. These corrections can be minor but significant: for example about 1.1% for MBTP1 by taking the steady state values, about 5.8% using the endmember values. For sample MBTP6, the correction is about 2.8% by taking the steady state values. Using the endmember values, the maximum corrected TCN age for the highest sample is tc_{max}(MBTP1) = 17396 ± 621 a and the lowest sample is tc_{max}(MBTP6) = 68692 ± 10617 a (representing a maximum correction of about 930%). The assumption that a surface at 2094 m.a.s.l. high (surface MBTP6) was exposed almost 50 ka longer than a surface located 451 meters higher (surface MBTP1 at 2545 m.a.s.l.) on the same vertical profile and in context of glacial thinning is hardly acceptable. According to the known glaciological evolution of Western Alps during LGM, exposure ages of > 25 ka are simply not possible. Surfaces at 2600 m.a.s.l. located in accumulation zone of former glaciated area were covered by ice at least until the LGM (e.g., Penck and Brückner, 1909; Bini et al., 2009; Coutterand, 2010; Seguinot et al., 2018) which implies that the age estimates must be treated with caution. However, our results imply that the uncertainty on the exposure age could be large. A correction of exposure age of few thousand years would have significant implications when investigating how post-LGM climate variability regionally impacted past ice extent.

We have presented the results using one luminescence signal only (IRSL50). Jenkins et al., (2018) and Sohbati et al. (2015) showed that multiple luminescence signals can be exploited. Since the bleaching propagates at different rates within the rocks (c.f., Ou et al., 2018), using multiple signals (e.g., pIR225 and OSL125) should enable us to better assess whether the position of the bleaching front is steady or not and thus to further constrain the erosion history (both erosion rate and duration).

Our results confirm the results of Sohbati et al. (2018), who derived an analytical solution assuming steady erosion and using a confluent hypergeometric function. Here we solve the transient solution of Eq. (3.1) using the finite difference method. An important difference to the earlier study of Sohbati et al. (2018) is that here the system is fully coupled between OSL and TCN surface exposure dating. OSL dating brings information about the evolution of the erosion rate in time and TCN dating give a realistic timeframe to this evolution by setting a forbidden zone.

The most striking outcome of this new approach is the ability to quantify surface erosion rates over timescales from 10 to 10^4 a. The quantification of erosion rates using TCN concentration is limited (expressed in Sect. 2) with the minimum time given by $t >> 1/(\lambda + \nu\ \dot{\varepsilon})$. By taking the two endmembers of erosion of this study, $\dot{\varepsilon} = 10^{-5}$ $mm\ a^{-1}$ and $\dot{\varepsilon} = 10$ $mm\ a^{-1}$, the time limits are respectively $2{\times}10^6$ and $6{\times}10^4$ a which means that one cannot use TCN to constrain the erosion history of post-LGM surfaces. Consequently, the coupling of OSL and TCN surface exposure dating makes the quantification of bare bedrock surface erosion possible at the timescale of a single interglacial event and might bring insight into the processes of topographic evolution in alpine environments.

3.6 Conclusion

In this study, we couple OSL and TCN surface exposure dating to constrain post-glacial bedrock erosion and surface exposure duration. We numerically solve the equation describing the evolution of luminescence signals in rock surfaces considering exposure age, bedrock surface erosion and the trapping and detrapping rates due to bleaching and athermal losses. We show that it is critical to account for bedrock surface erosion while interpreting luminescence bleaching profiles. Even at low erosion rates (10^{-4} $mm\ a^{-1}$) for periglacial environments, only few years are needed to affect the luminescence profile of a rock surface.

We were able to discriminate between two regimes characterizing the relationships between the depth of the luminescence bleaching, the exposure age and the bedrock surface erosion. The transient state describes a rock surface with a luminescence profile in disequilibrium. In contrast a rock surface in steady state is produced when the influence of bedrock surface erosion, exposure age and trapping rate compensate one another. If the system is maintained under these conditions, the luminescence signal no longer evolves with time. Indeed, the determination of the time at which the steady state with erosion occurs is critical. For the two natural surfaces we analyzed here, this time can range from 4 years (at an erosion rate of 4.3 $mm\ a^{-1}$) to 2300 years (at an erosion rate of $3.5{\times}10^{-3}$ $mm\ a^{-1}$). The approach developed in this study thus brings a new asset to directly quantify an erosion correction for TCN dating. We see that this correction can range from 1.2% to 930% for natural surfaces, although one must keep in mind that the exposure age may be overestimated if not compared to independent observations.

Finally, this new approach enables the quantification of erosion rates over surfaces exposed for 10-10^4 a, filling a methodological gap in between short timescales (from few seconds to decades) and long-time scales ($> 10^5$ a). The contribution of this approach will allow quantification of the contribution of bare bedrock surface in sediment production and topographic evolution of alpine environments over glacial-interglacial cycles. Measurements in locations

where bedrock surface erosion is very low (e.g., polar areas, high mountain) need to be investigated to check if OSL surface exposure is potentially applicable to timescale $> 10^2$ years without accounting for the effect of erosion rates. Another perspective is to investigate the control of temperature and climate on erosion rate evolution in time, along an elevation transect. Using this approach, the contribution of post-glacial bedrock erosion can be quantified and the feedback between erosion and climate evaluated.

Acknowledgments

This work was supported by the Swiss National Science Foundation (SNFS) funded SwissAlpArray SINERGIA project ($CRSII2{-}154434/1$) and project ($PP00P2{-}170559$) (P.G.V.). GEK acknowledges support from project ($Pz00P2{-}167960$). The authors thank S. Ivy-Ochs, M. Christl, O. Kronig, E. Opyrchal, S. Casale and the Laboratory of Ion Beam Physics (LIP) at ETH Zürich for making the TCN dating preparation and analysis possible. The authors thank P.-H. Blard for sharing the code of the CREp calculator; D. Six and C. Vincent for GLACIOCLIM Alps data availability. We thank J. Braun for constructive input on the modeling. We thank S. Coutterand for his expertise of the Quaternary of the Mont-Blanc massif and his help during the sampling campaign. The authors would like to thank N. Stalder, J. González Holguera, G. Bustarret and U. Nanni for their support during field excursions M. Faria and K. Haring are thanked for laboratory support.

CHAPTER 4

Post-glacial erosion of bedrock surfaces and deglaciation timing: new insights from the Mont Blanc massif (Western Alps)

Benjamin Lehmann[1], Frédéric Herman[1], Pierre G. Valla[2,3], Georgina E. King[1], Rabiul H. Biswas[1], Susan Ivy-Ochs[4], Olivia Kronig[4], Marcus Christl[4]

[1]Institute of Earth Surface Dynamics, University of Lausanne, Lausanne, 1012, Switzerland.
[2]Univ. Grenoble Alpes, Univ. Savoie Mont Blanc, CNRS, IRD, IFSTTAR, ISTerre, 38000 Grenoble, France
[3]Institute of Geological Sciences and Oeschger Centre for Climate Change Research, University of Bern, Bern, 3012, Switzerland.
[4]Laboratory of Ion Beam Physics (LIP), ETH Zürich, Otto-Stern-Weg 5, 8093 Zurich, Switzerland.

Abstract

Since the Last Glacial Maximum, about 20 *kyr* ago, Alpine glaciers retreated rapidly from lowland regions and thinned in their high-elevation source areas. This transition created widespread bare-bedrock surfaces that could then erode by a combination of large-scale debuttressing or local frost cracking and weathering. Quantifying the respective contribution of these processes is necessary to understand the links between long-term climate forcing and erosion dynamics in mountainous environments. Here we quantify the erosion histories of post-glacial exposed bedrock along glacial valley profiles, to investigate potential variability with elevation and time. Using a new approach that relies on optically stimulated luminescence (OSL) and terrestrial cosmogenic nuclides (TCN) surface exposure dating, we estimate the erosion rate of bedrock surfaces over timescales from 10^1 to 10^4 years. Nine bedrock surfaces were sampled over two elevation profiles located on the flanks of the Mer de Glace (Mont Blanc massif - European Alps). Our results reveal bedrock surface erosion rates from 3.5×10^{-3} to 4.3 $mm\ a^{-1}$ over $\sim$500-m elevation gradient, with a clear anti-correlation between erosion rate and elevation. The observed spatial variability in erosion rates and surprisingly high rates cannot be explained by chemical weathering alone and must reflect morphometric (elevation and surface slope) and climate (temperature and snow cover) controls. Furthermore, and more importantly, the derived erosion rates can be used to correct the timing of deglaciation age based on TCN data, potentially suggesting very rapid ice thinning post Gschnitz.

4.1 Introduction

To understand the long-term evolution of alpine landscapes, the respective contributions of various surface processes to sediment production and transport must be quantified. During the Quaternary period, the alternation between glacial and interglacial periods has modulated the efficiency of glacial, fluvial and hillslope processes (Koppes and Montgomery, 2009). In that context, changes in bedrock morphology and corresponding sediment delivery have been directly related to glacier extent, as glaciation is often thought to be the most efficient erosional and sediment transport mechanism in mountain environments (e.g., Brozović et al., 1997; Hallet et al., 1996; Montgomery, 2002; Mitchell and Montgomery, 2006; Egholm et al., 2009; Herman et al., 2013). Recent studies have also revealed the importance of periglacial processes during interglacial periods, operating over hillslope and bedrock valley flanks, such that glaciers and rivers serve to transport material out of the system (Burbank et al, 1996; Ballantyne, 2002; Scherler, 2015). Yet how quickly bare-bedrock surfaces weather and erode during interglacials remains poorly known (e.g., Colman, 1981; Zimmerman et al., 1994; André, 2002; Nicholson, 2008; Kirkbride and Bell, 2010).

The erosion of hillslopes in periglacial environments is governed by a combination of landsliding, rock shattering and weathering (e.g., Anderson and Anderson, 2010). Their relative contribution to sediment production has been estimated over specific bedrock surfaces or integrated over entire fluvial catchments using terrestrial cosmogenic nuclide (TCN) dating (e.g., Portenga and Bierman, 2011 for a review). During the last decades, the development of TCN dating, mainly using in-situ produced ^{10}Be in quartz crystals, has significantly improved our ability to quantify bedrock surface erosion over timescales from 10^4 to 10^6 years, assuming that erosion occurs steadily through time (Balco et al., 2008; von Blanckenburg and Willenbring, 2014; Hippe, 2017). Over modern timescales, geomorphologists working on frost weathering processes have highlighted the feedbacks between temperature variation and snow cover and their effects on the evolution of bedrock surfaces over diurnal to decadal timescales (e.g., Łoziński, 1909; Matsuoka and Murton, 2008). However, how the temporal gap between these erosion estimates can be bridged remains challenging, in part because of the stochastic nature of geomorphic processes (Ganti et al., 2016).

To address these issues, we have adopted a new method that combines optically stimulated luminescence (OSL) and terrestrial cosmogenic nuclide (TCN) surface exposure dating (Sohbati et al., 2018; Lehmann et al., in review) to quantify bedrock surface erosion in periglacial environments from 10^1 to 10^4 years. Our results from the deglaciated bedrock surfaces of the Mer de Glace (Mont Blanc massif, European Alps) reveal erosion rates that vary from $3.5 \pm 1.2 \times 10^{-3}$ to 4.3 ± 0.56 $mm\ a^{-1}$ over an elevation difference of 451 m. These surprisingly high rates of bedrock surface erosion, compared to previous studies in periglacial settings (e.g., Colman, 1981; Zimmerman et al., 1994; André, 2002; Nicholson, 2008; Kirkbride and

Bell, 2010) shed new light on the contribution of deglaciated bedrock surfaces in sediment production and topographic evolution. Furthermore, by using these bedrock surface erosion rates to correct exposure ages based on TCN data, our results suggest very rapid ice thinning post Gschnitz stadial ($\sim$ 17-16 ka).

4.2 Methods

We measured both ^{10}Be concentrations (e.g., Gosse and Phillips, 2001; Ivy-Ochs and Briner, 2014) and OSL profiles (Sohbati et al., 2012) on exposed granitic rock samples to constrain the erosion rate histories of natural bedrock surfaces (see Appendix A4.1). ^{10}Be concentrations provide us with constraints on the time since the rocks were exposed to cosmic rays (t_0 and t_C in Fig. 4.1) and thus set a temporal framework for the possible erosion histories. OSL profiles provide us with constraints on the erosion history since the rock has been exposed to light following glacier retreat and ice thinning (t_S and $\dot{\varepsilon}$ in Fig.4.1; Lehmann et al., in review). Note it is the difference of sensitivity between ^{10}Be and OSL that makes it possible to quantify surface erosion rate histories over short ($< 10^2$ a) and long ($> 10^4$ a) timescales (Sohbati et al., 2018; Lehmann et al., in review).

The evolution in time of the OSL bleaching front into the rock surface depends on the exposure age, the surface erosion, the trapping and detrapping (bleaching) rates and the athermal loss (Eq. (3.1) in Chapter 3). While the trapping and detrapping rates and the athermal loss can be constrained from laboratory measurements, the erosion rate history is unknown. Here we constrain the erosion rate history by performing a joint inversion of the OSL and cosmogenic nuclide data for each sample (Lehmann et al., in review). In the procedure, we assume that erosion rates evolve as a step functions from no erosion to erosion going forward in time (Lehmann et al., in review). The inferred erosion rate history includes a magnitude of erosion rate, and two times; t_S, the time at which erosion increases, and t_C, the corrected exposure age. It is worth to stress the t_C is estimated by combining OSL and cosmogenic nuclide data (Lehmann et al., in review). In turn, a range of solutions for the erosion rate history and t_C are inferred. Note that high erosion rates and durations which do not fit the observed ^{10}Be concentration (Lal, 1991) are excluded from the parameter search, defining a "forbidden zone" (see details in Appendix 4.1).

4.3 Study site

We collected samples along two elevation profiles at the Mer de Glace, European Alps, which was deglaciated since the last glacial maximum (LGM, around 21 ka; Coutterand and Buoncristiani, 2006; Wirsig et al., 2016). The Mer de Glace glacier (Fig. 4.2) is about 11.5 km

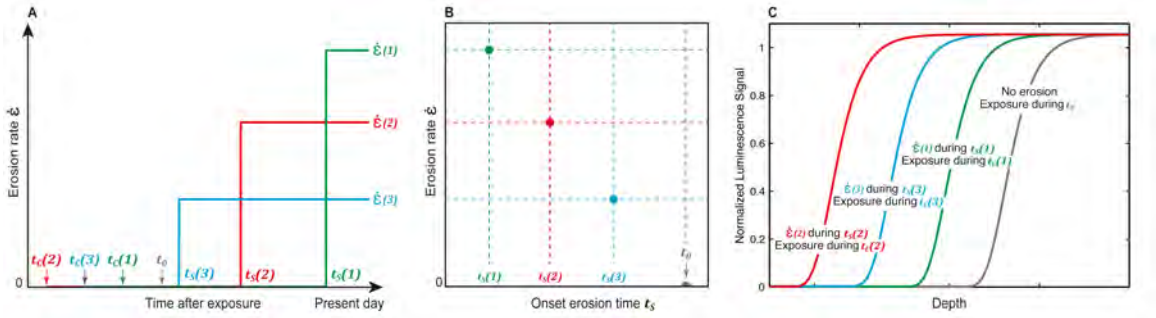

Figure 4.1: Schematic representation of four different erosion scenarios through time (A) and (B) and their resulting luminescence signal (C). t_0 is the uncorrected ^{10}Be exposure age, t_S the onset times of erosion, t_C the corrected exposure ages, and $\dot{\varepsilon}$ the erosion rate. Note that the luminescence plots in (C) are not model outputs but drawings, with the aim of conceptualizing how the experiments are designed.

long and is located in the Mont Blanc massif. The modern glacier covers an area of 30.4 km^2 (excluding former tributary Talèfre Glacier) and spans an elevation range from 4205 to 1531 m.a.s.l. (data from 2008; Gardent et al., 2014). The mean equilibrium line altitude (ELA) was about 2880 m.a.s.l. between 1961 and 1990 for five of the main north-facing Mont Blanc massif glaciers, including the Leschaux Glacier for the period 1984-2010 (Rabatel et al., 2013; LeRoy et al., 2015). During the Little Ice Age (LIA), the ELA was around 2745 m.a.s.l. (Protin, pers. communication). At the onset of the Younger Dryas (∼13 ka) and the Gschnitz stadial (∼17-16 ka), ELAs were 150-400 m and 650-700 m lower than during the LIA respectively (Ivy-Ochs et al., 2006).

The first profile is located below the Tête de Trélaporte on the West side of the glacier (Fig. 4.3). Six bedrock surfaces were sampled (from 2545 to 2094 m.a.s.l). The second profile is located below the Aiguille du Moine on the East side of the glacier (Fig. 4.3), where we collected from three bedrocks surfaces at elevations ranging from 2447 to 2259 m.a.s.l. All the surfaces are from the same phenocristalline granitic lithology of the Mont Blanc massif and selected sampling sites can all be classified as glacially eroded bedrock surfaces (see Appendix A4.1 for details). The surfaces are rough and exhibit a weathered texture without glacial striations. All studied bedrock surfaces are located between the elevation limits of the LIA and the LGM (Coutterand and Buoncristiani, 2006; Vincent et al., 2014) and were most likely deglaciated in between ∼18-20 ka BP (Wirsig et al., 2016) and 1850 AD.

4.4 Results

In Fig. 4.4a, we report the estimated erosion rates and the timescales. The first observation is that inferred erosion rates vary between 3.5 ± 1.2 $\times 10^{-3}$ to 4.3 ± 0.56 $mm\ a^{-1}$ (Fig. 4.4a). The high rates are constrained over timescales from 10^1 to 10^3 years, while the low erosion

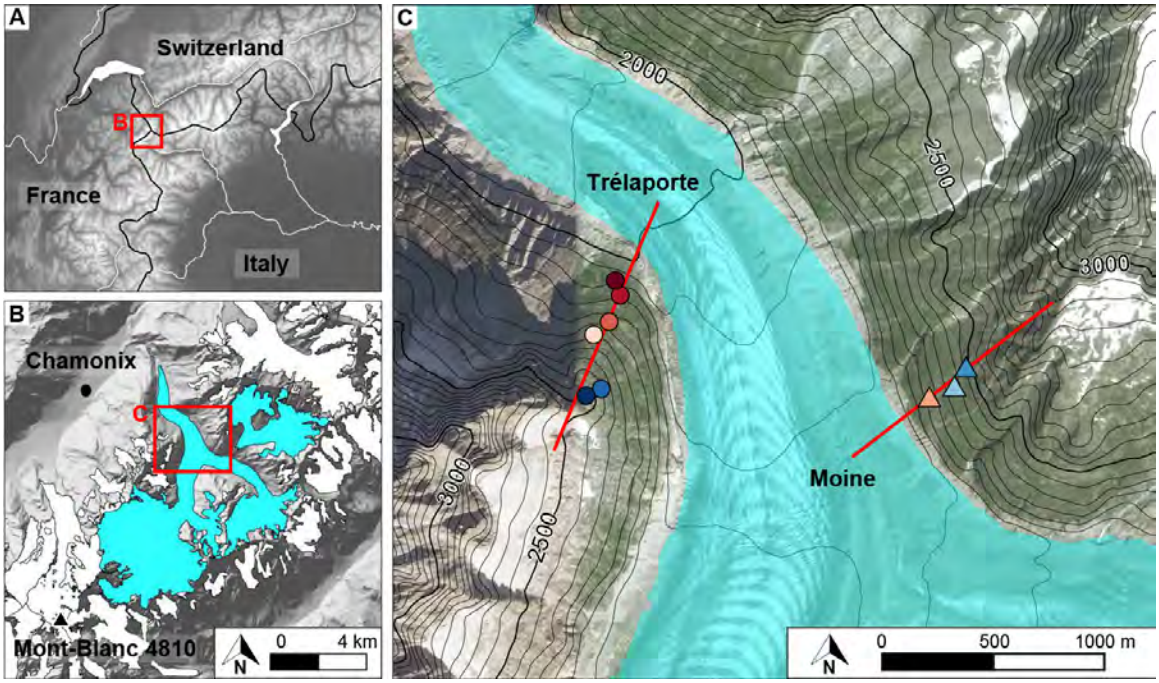

Figure 4.2: Study sites sampled along the Mer de Glace glacier at respectively A: Regional scale, B: massif scale, C: local scale. The blue area shows the extent of the Mer de Glace determined from aerial images in 2004 (Rabatel et al., 2016). The red lines depict the two vertical profiles Trélaporte and Moine along which the bedrock surfaces were sampled (each coloured dot represents a specific sample, round and triangle dots from Trélaporte and Moine profiles respectively, see Fig. 4.3).

rates are constrained over longer timescales, from 10^1 to 10^3 years. Although the observed trend may suggest that fresh surfaces are more prone to erosion, the decrease of erosion rates within increasing time is common to most techniques that are used to constrain erosion rates. Such a relationship has been argued to reflect a bias caused by the stochastic nature of geomorphic processes (e.g., Koppes and Montgomery, 2009; Schumer and Jerolmack, 2009; Ganti et al., 2016). Irrespective of this, as OSL surface exposure dating spans the gap between contemporary observations and TCN estimations of erosion rates, it offers new insights into erosion rate estimations.

The second striking result is the existence of an anti-correlation between erosion rate and elevation ($r^2 = 0.53$; Fig. 4.4b). The high erosion rates are observed at the lowest elevation, and vice-versa. The decay of erosion rate with altitude is opposite to what is expected for frost cracking (Anderson, 1998; Hales and Roering, 2007). Frost cracking predicts high erosion rates at high altitude, where freeze-thaw cycles are most efficient. From present-day temperature records (Argentière weather station located at 2400 m.a.s.l., Glacioclim observatory), elevations at 1800, 2400 and 3200 m.a.s.l. are spending 8, 17 and 21% of the year respectively in the frost cracking windows (-3 to -8°C; Hales and Roering, 2007). Furthermore, the decay of erosion rates with altitude is too pronounced to be explained by

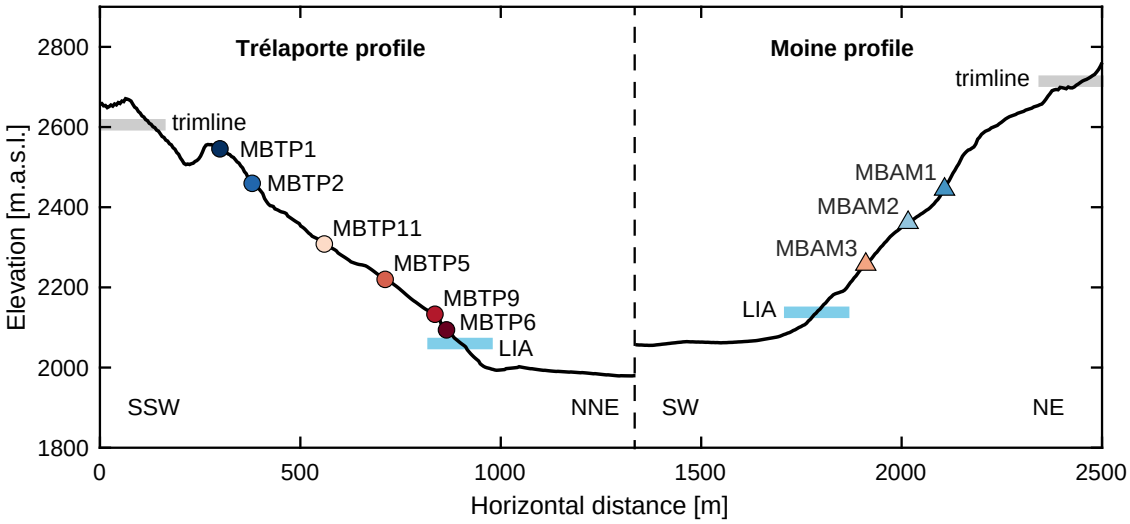

Figure 4.3: Topographic cross sections of the Trélaporte (West side) and Moine (East side) vertical profiles along the Mer de Glace and corresponding sampled surfaces (MB stand for Mont Blanc, TP for Trélaporte and AM for Aiguille du Moine). Grey lines represent the elevation of trimlines (Coutterand et al., 2006) and blue lines represents elevation LIA (Vincent et al., 2014).

chemical weathering alone, which is governed by temperature and therefore altitude (Lasaga et al., 1994; West, 2012). In Fig. 4.4c, we investigate the relationship between the erosion rates and surface slope (measured at the outcrop scale). Interestingly, a positive correlation between erosion rates and surface slopes is observed, though the correlation is less significant ($r^2 = 0.22$) than with altitude. This may imply that water stagnates on the bedrock surface may not have a primary effect on setting the erosion rate. An alternative possibility is snow cover. The surfaces at high elevation with flatter slopes experience higher solid precipitation and periods of snow cover during yearly cycles, which maintains the rock surface at 0°C, and in turn suppresses the efficiency of frost cracking. Surfaces at lower elevations with steeper slopes, are less shielded by snow cover and thus experience more time in the frost cracking window and are exposed to more freeze-thaw cycles. We also speculate that surfaces in the vicinity of the glacier are influenced by cold katabatic winds coming from the glacier, which in turn promotes frost cracking at lower elevation.

Finally, we show in Fig. 4.3d TCN exposure ages with elevation (detailed results are presented in Table A4.2). If erosion is ignored, we observe a correlation between age and elevation that corresponds to what is known as the deglaciation history of the Alps (Ivy-Ochs, 2015; Wirsig et al., 2016). However, the exposure ages are significantly different when the full range of estimated erosion is included. The range of corrected TCN exposure ages older than the corrected age at the highest elevation (16.6 ± 0.6 *kyr* for MBTP1; Fig. 4.3d and Table A4.2) are not physically plausible as a low altitude sample cannot be exposed before a high-altitude

sample (grey area in Fig. 4.3d). In the worst-case scenario, the ages could potentially indicate extremely rapid, synchronous deglaciation of the catchment.

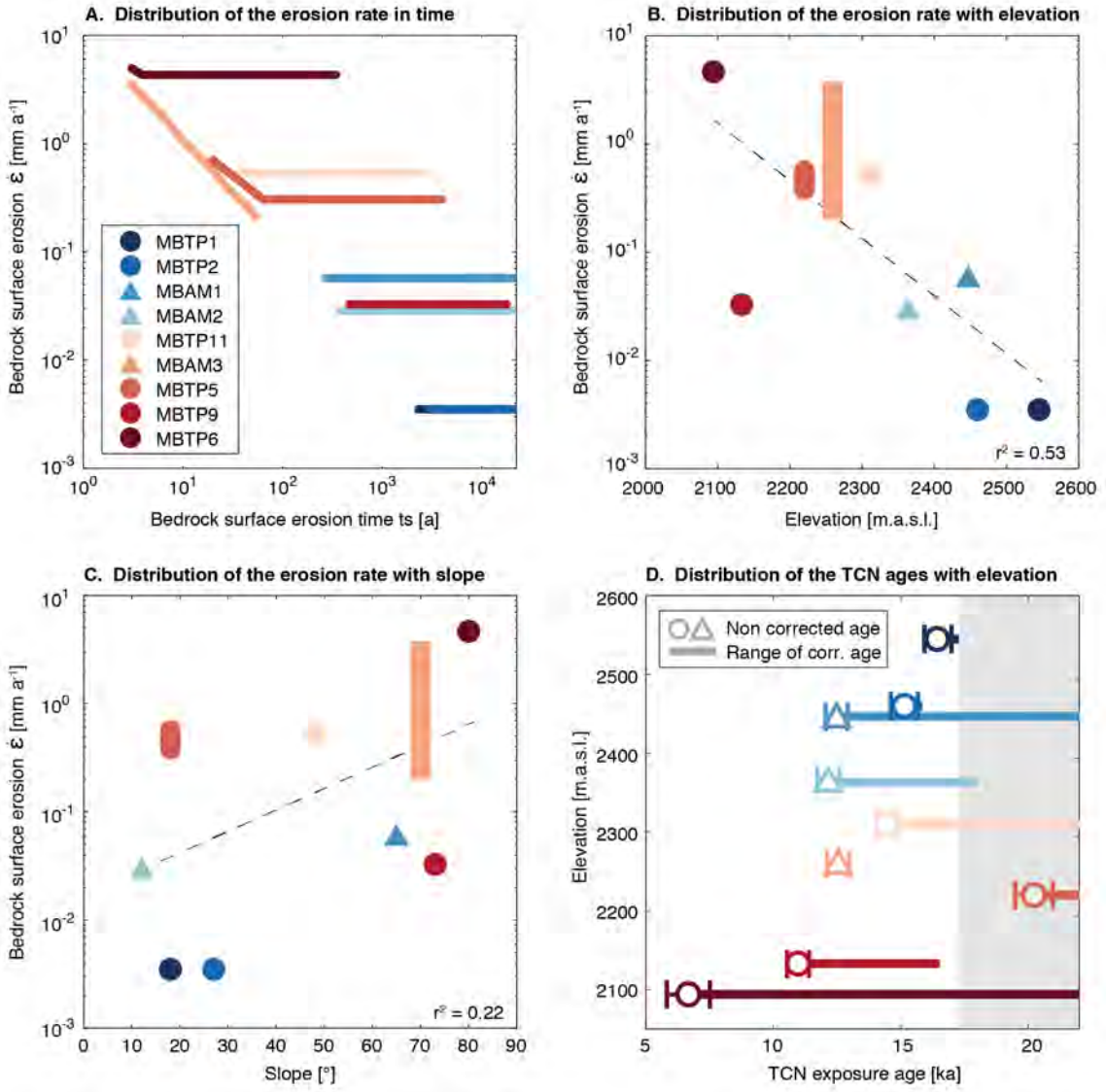

Figure 4.4: Inverted values of bedrock surface erosion rate $\dot{\varepsilon}$ $[mm\ a^{-1}]$ and erosion onset time t_S $[a]$ for the Trélaporte and Moine samples. (b) Distribution of the bedrock surface erosion rate $\dot{\varepsilon}$ with elevation [m.a.s.l.]. (c) Distribution of the bedrock surface erosion rate $\dot{\varepsilon}$ against surface slope [°]. (d) Distribution of the ^{10}Be surface exposure ages with elevation, circles represent the erosion uncorrected ages, lines show all the possible ages corrected with specific inverted values of $\dot{\varepsilon}$ and t_S presented in panel (a). Grey area in panel (d) shows the area with low reliability in the present geomorphological context.

4.5 Discussions and conclusions

Our results reveal bedrock surface erosion rates that range from 3.5×10^{-3} to 4.3 $mm\ a^{-1}$ over a 451 m elevation difference. This dramatic variation is not due to lithological changes since the geology is uniform. The surfaces are within the same tectonic unit, without tectonic fault intersecting the profiles, which in turn excludes a tectonic control on setting the erosion rates. Biological processes and the influence of vegetation are also likely to be minor. Because of the high elevation (between 2094 and 2447 m.a.s.l.), vegetation is not a major component of the environment (i.e., small patches of alpine meadow) and lichen cover does not differ significantly along the profiles. We assumed that these surfaces are mainly affected by grain-by-grain erosion because the character of the glacially polished bedrock surface is preserved i.e. they do not present evidence or rockfall scar. The decrease in erosion rates with altitude is also too pronounced to be explained by chemical alteration alone. This leads us to postulate that erosion is governed by a combination of mechanical and chemical weathering since frost cracking due to freeze-thaw cycle promotes water diffusion at both rock surface and grain boundaries where chemical weathering is effective (e.g., Hoke and Turcotte, 2010). Therefore, we conclude that a combination of climatic (temperature and snow cover) and morphometric (elevation and surface slope) factors are controlling the variation of erosion rates.

Our results highlight an unexpected anti-correlation between erosion rate and elevation, i.e., lowest elevation, highest erosion rates. We also observe a correlation between erosion rate and surface slope. We suggest that surfaces at high elevation with flatter slopes experience more intense and longer snow cover during yearly cycles. Such a shielding preserves the rock surface from frost cracking by keeping it at 0°C. In contrast, surfaces at lower elevation with steeper slope, are less shielded by snow cover and thus experience more time in the frost cracking window and are exposed to more freeze-thaw cycles. The temperature gradient might also be inverted at low elevation where the cold katabatic winds are flowing down the glacier which in turn promotes frost cracking for surfaces at the vicinity of the glacier. The snow covers surely have different effect on TCN and OSL dating. This aspect is not considered in the presented methodological approach but should by address in future studies.

The high erosion rate intensities, between 3.5×10^{-3} to 4.3 $mm\ a^{-1}$, are one to two orders of magnitude greater than previously observed. Portenga and Bierman (2011) compiled ^{10}Be erosion rates of outcropping bedrock surfaces and determined a mean erosion of about 12×10^{-3} $mm\ a^{-1}$ (median = 5.4×10^{-3} $mm\ a^{-1}$). Small et al. (1997) determined erosion rates of alpine bedrock summit surfaces deduced from in-situ ^{10}Be and ^{26}Al. Their results exhibit a maximum mean bare-bedrock erosion rate of about 7.6×10^{-3} $mm\ a^{-1}$. Part of this conflict is likely due to the timescale over which TCN erosion rates are averaged, which is typically 10^{4-6} years. Using reference surfaces such as ice-polished quartz veins preserved on roches moutonnées, erosion rates from (0.1-10)$\times10^{-3}$ $mm\ a^{-1}$ were measured depending of

the lithology and the location (André, 2002; Nicholson, 2008; Kirkbride and Bell, 2010). In contrast the intensities of erosion rates observed in this study are comparable to other erosion processes such as debris flows and rock falls (Norton et al., 2010) or glacial erosion (Herman et al., 2015).

Finally, we would like to stress that the use of terrestrial cosmogenic nuclides concentration to compute erosion rates is only feasible under the assumption that erosion rates are constant over timescales between 10^4 and 10^6 years. However, our new approach that relies combining OSL and TCN surface exposure dating enables us to constrain time-varying erosion rates over short (from a few years to decades) and long ($< 10^5$ years) timescales. Ice surface lowering starting at $\sim$16.6 $\pm$ 0.6 ka at an elevation of 2550 m.a.s.l. shows synchronicity with dating from the southern side of the Mont Blanc massif (Wirsig et al., 2016). The large differences between TCN exposure ages with or without erosion correction show the importance of carefully estimating the erosion rates to estimate deglaciation histories. If true, the corrected ages could mean an extreme deglaciation event that coincides with the end of last glacial maximum. The rapid thinning would have important implication for paleo-climate reconstruction and the potential controls of precipitation and temperature on the regional climate.

Acknowledgments

This work was supported by the Swiss National Science Foundation (SNFS) funded Swiss-AlpArray SINERGIA project ($CRSII2$-154434/1) and project $PP00P2$-170559 (P.G.V.). GEK acknowledges support from project $PZ00P2$-167960. The authors thank P.-H. Blard for sharing the code of the CREp calculator; D. Six and C. Vincent for GLACIOCLIM Alps data availability. We thank R.S. Anderson, A. Cogez, N. Gribenski, F. Mettra for their constructive inputs. We thank S. Coutterand for its expertise of the Quaternary of the Mont-Blanc massif and its help during sampling campaign. The authors would like to thank N. Stalder, J. González Holguera, G. Bustarret, U. Nanni and S. Vivero for their support during field excursions; J. El Kadi, M. Faria and K. Haring are thanked for laboratory support.

CHAPTER 5

General Conclusion

In the first chapter, I have investigated the potential of OSL surface exposure dating for quantitatively reconstructing post-LIA glacier retreat. This work involved setting up the laboratory for that kind of experiments. I have worked along an altitudinal cross-section of the Mer de Glace glacier (Mont Blanc massif, France), and collected glacially-polished bedrock surfaces with known exposure ages (from 3 to 137 years) along the Montenvers profile from around 1841 m.a.s.l. elevation to the present-day glacier position (1696 m.a.s.l.). I have developed a statistical approach to calibrate the bleaching model parameters from known-age samples. Experimental IRSL depth-profile data for five different polished bedrock surfaces show an increase of the luminescence signal bleaching depth with exposure age. This work led me to the conclusion that OSL surface exposure dating can be applied to glacial and periglacial environments, and is a promising tool for high-resolution reconstruction of recent ice-extent and thickness fluctuations, both in space and time. However, I found that several calibration samples must be used to calibrate the model parameters before inferring exposure ages on bedrock surfaces within a specific area, considering the potential variation in bedrock lithology. I also found that measurement uncertainties, intrinsic data noise or both can result in large uncertainties on inverted ages, especially when applying this method over 10^3 - 10^4 years timescales.

In the second chapter, I discovered how critical it is to account for bedrock surface erosion while interpreting luminescence bleaching profiles. Even at low erosion rates (10^{-4} mm a^{-1}) for periglacial environments, only few years are needed to affect the luminescence profile of a rock surface. Indeed, I coupled OSL and TCN surface exposure dating to constrain post-glacial bedrock erosion and surface exposure duration. I numerically solved the equation describing the evolution of luminescence signals in rock surfaces considering exposure age, bedrock surface erosion and the trapping and detrapping rates due to bleaching and athermal losses. Doing so, I was able to discriminate between two regimes characterizing the relationships between the depth of the luminescence bleaching, the exposure age and the bedrock surface erosion. The transient state describes a rock surface with a luminescence profile in disequilibrium. In contrast, a rock surface in steady state is produced when the influence of bedrock surface erosion, exposure age and trapping rate compensate one another. If the system is maintained under these conditions, the luminescence signal no longer evolves with time. Indeed, the determination of the time at which the steady state with erosion occurs is critical. For the two natural surfaces I analyzed, this time can range from 4 years (at an erosion rate of 4.3 mm a^{-1}) to 2300 years (at an erosion rate of 3.5×10^{-3} mm a^{-1}). The approach developed in this study thus brings a new asset to directly quantify the correction TCN dating of erosion. In turn, I found that this correction can range from 1.2% to 930% for natural surfaces, although one must keep in mind that the exposure age may be over-estimated if not compared to independent observations. Finally, I demonstrated that this new approach enables the quantification of erosion rates over surfaces exposed for 10-10^4 a,

filling a methodological gab in between short timescales (from few seconds to decades) and long-time scales ($> 10^5$ a). The contribution of this approach will enable the quantification of the contribution of bare bedrock surface in sediment production and topographic evolution of alpine environments over glacial-interglacial cycles.

In the last and final chapter, I have applied the method described in Chapter 2 on two vertical profile of the side of the Mer de Glace. My results reveal that bedrock surface erosion rates range from $3.5{\times}10^{-3}$ to 4.3 $mm\ a^{-1}$ over a 451 m elevation difference. This dramatic variation is not due to lithological changes since the geology is uniform. The surfaces are within the same tectonic unit, without tectonic fault intersecting the profiles, which in turn excludes a tectonic control on setting the erosion rates. Biological processes and the influence of vegetation are also likely to be minor. Because of the high elevation (between 2094 and 2447 m.a.s.l.), vegetation is not a major component of the environment (i.e., small patches of alpine meadow) and lichen cover does not differ significantly along the profiles. I speculate that these surfaces are mainly affected by grain-by-grain erosion because the character of the "roche moutonnées" is preserved i.e., they do not present evidence or rockfall scar. The decrease in erosion rates with altitude is also too pronounced to be explained by chemical alteration alone. This leads me to propose that erosion is governed by a combination of mechanical and chemical weathering since frost cracking due to freeze-thaw cycle promotes water diffusion at both rock surface and grain boundaries where chemical weathering is effective (e.g., Hoke and Turcotte, 2010). Therefore, I conclude that a combination of climatic (temperature and snow cover) and morphometric (elevation and surface slope) factors are controlling the variation of erosion rates.

My results highlight an unexpected anti-correlation between erosion rate and elevation, i.e., lowest elevation, highest erosion rates. I also observe a correlation between erosion rate and surface slope. I suggest that surfaces at high elevation with flatter slopes experience more intense and longer snow cover during yearly cycles. Such a shielding preserves the rock surface from frost cracking by keeping it at 0°C. In contrast, surfaces at lower elevation with steeper slope, are less shielded by snow cover and thus experience more time in the frost cracking window and are exposed to more freeze-thaw cycles. The temperature gradient might also be inverted at low elevation where the cold katabatic winds are flowing down the glacier which in turn promotes frost cracking for surfaces at the vicinity of the glacier. The snow covers surely have different effect on TCN and OSL dating. This aspect is not considered in the presented methodological approach but should by address in future studies.

The high erosion rate intensities, between $3.5{\times}10^{-3}$ to 4.3 $mm\ a^{-1}$, are one to two orders of magnitude greater than previously observed. Portenga and Bierman (2011) compiled ^{10}Be erosion rates of outcropping bedrock surfaces and determined a mean erosion of about $12{\times}10^{-3}$ $mm\ a^{-1}$ (median = $5.4{\times}10^{-3}$ $mm\ a^{-1}$). Small et al. (1997) determined erosion rates of alpine bedrock summit surfaces deduced from in situ ^{10}Be and ^{26}Al. Their results

exhibit a maximum mean bare-bedrock erosion rate of about 7.6×10^{-3} $mm\ a^{-1}$. Part of this conflict is likely due to the time-scale over which TCN erosion rates are averaged, which is typically 10^{4-6} years. Using reference surfaces such as ice-polished quartz veins preserved on roches moutonnes, erosion rates from $(0.1\text{-}10)\times10^{-3}$ $mm\ a^{-1}$ were measured depending of the lithology and the location (André, 2002; Nicholson, 2008; Kirkbride and Bell, 2010). In contrast the intensities of erosion rates observed in this study are comparable to other erosion processes such as debris flows and rock falls (Norton et al., 2010) or glacial erosion (Herman et al., 2015).

Finally, I would like to stress that the use of terrestrial cosmogenic nuclides concentration to compute erosion rates is only feasible under the assumption that erosion rates are constant over timescales between 10^4 and 10^6 years. However, our new approach that relies combining OSL and TCN surface exposure dating enables us to constrain time-varying erosion rates over short (from a few years to decades) and long ($< 10^5$ years) timescales. Ice surface lowering starting at $\sim$16.6 $\pm$ 0.6 ka at an elevation of 2550 m.a.s.l. shows synchronicity with dating from the southern side of the Mont Blanc massif (Wirsig et al., 2016). The large differences between TCN exposure ages with or without erosion correction show the importance of carefully estimating the erosion rates to estimate deglaciation histories. If true, the corrected ages could mean an extreme deglaciation event that coincides with the end of last glacial maximum. The rapid thinning would have important implication for paleo-climate reconstruction and the potential controls of precipitation and temperature on the regional climate.

CHAPTER 6

Perspectives

The results presented in this manuscript open up perspectives both in methodological development and in the understanding of the processes of the Earth's surface. In this section, I will first discuss the different methodological challenges that will need to be addressed in future studies. Then, I set the perspectives for the understanding of the evolution of paleo-environmental conditions.

6.1 Methodological perspective

The experiments carried out during this project represent only the beginning of the development of the promising OSL surface dating method already well addressed by R. Sohbati, M. Meyer, L. Gliganic and X. Ou and others.

6.1.1 Calibration

The calibration of $\overline{\sigma\varphi_0}$ and μ has been proved to be of major importance to extract information from OSL surface exposure signal. As shown in Chapter 2, the calibration can be made with an independent age control. It can also be made by revisiting the sampling site and collecting the scar remaining after earlier sample collection, which has a precisely known exposure age. This approach has been performed in Gliganic et al., (2018) and is currently being tested during the PhD project of J. Elkadi (University of Lausanne). This calibration and the sensitivity of $\overline{\sigma\varphi_0}$ and most importantly μ could be assessed with laboratory experiments. The latest development of CCD camera which enables the quantification of the luminescence potential of a rock surface could bring improvement to our understanding of the control of heterogeneity, grain size and lithology on the light attenuation coefficient μ. This approach is going to be tested during the PhD project of J. Elkadi

6.1.2 Insolation and orientation control

To better understand how the OSL surface exposure signal evolves according to the insolation, the exposure or the snow cover, a block of specific lithology could be exposed in a well-controlled setting. Indeed, unbleached surfaces of a rock block could be exposed together with insolation measurement placed on replicate of the rock block and recording the potential snow cover during few months or years. Meyer and Gliganic, (pers. com.) performed this experiment during 2017. Their preliminary results show no control of the insolation on the bleaching profiles. To constrain the effect of the photon flux variability, similar experiments could be performed in different locations of the globe with the same specific lithology and the same experimental setting.

Although, such measurements are not representative of the time-scale of interest to study the paleo-environmental conditions over 10^2-10^4 years; time-scales at which surface exposure might have an important effect. The problematic to use calibration site and to apply it on surfaces with different expositions, could be addressed with the topographic shielding correction factor (TSF) on each sampled surface. This factor varies from 1 for not shielding to 0 for a total shielding. The parameter $\overline{\sigma\varphi_0}_{\,cal}$ of the calibration site will be equal to:

$$\overline{\sigma\varphi_0}_{cal} = TSF_{cal} \times \overline{\sigma\varphi_0}_{initial} \tag{6.1}$$

The $\overline{\sigma\varphi_0}_{\ initial}$ parameter represents the charge detrapping rate for a flat surface with no shielding (TSF=1). When OSL surface exposure is applied to a surface with a different topographic shielding than the calibration site (TSF_{cal}), the model should use

$$\overline{\sigma\varphi_0}_{local} = TSF_{local} \times \overline{\sigma\varphi_0}_{initial} \tag{6.2}$$

6.1.3 Snow cover control

The snow covers surely has different effects on TCN and OSL dating. This aspect is not considered in the methodological approach presented in Chapter 2. For TCN dating the snow cover correction is well constrained. The correction factor for TCN dating is already established (e.g., Equation (3.76) in Gosse and Phillips, 2001). By considering a snow cover of 50 cm during 6 months of the year (as mentioned by Wirsig et al., 2016), the correction of TCN ages are significant. The maximum correction is about 5.8% (i.e., sample MBAM2, from 12.2 ± 0.5 ka to 12.9 ± 0.5 ka) and the minimum correction is about 5.1% (i.e., sample MBAM5, from 20.3 ± 0.9 ka to 21.3 ± 0.9 ka).

Table 6.1: Comparison of TCN exposure age with and without snow cover correction, correction made using Equation (3.76) in Gosse and Phillips, 2001.

Sample	TCN age [ka]	TCN age [ka]	Diff.
Correction	no corr.	50 cm 6 months	%
MBAM1	12.4 ± 0.5	13.1 ± 0.5	5.6
MBAM2	12.1 ± 0.5	12.8 ± 0.5	5.8
MBAM3	12.5 ± 0.5	13.2 ± 0.5	5.6
MBTP1	16.4 ± 0.6	17.4 ± 0.6	5.6
MBTP2	15.1 ± 0.6	15.9 ± 0.6	5.7
MBTP5	20.3 ± 0.9	21.3 ± 0.9	5.1
MBTP6	6.6 ± 0.9	7.0 ± 0.9	5.7
MBTP9	10.9 ± 0.5	11.5 ± 0.5	5.3
MBTP11	14.4 ± 0.5	15.2 ± 0.5	5.5

In case of the OSL surface exposure dating, for a snow cover sufficiently thick, the importance bleaching processes is going to be considerably reduced, while the trapping rate is not going to be influenced. Indeed, the dose rate should be integrated over the entire time calculated with TCN dating (t_{Be}). Although, bleaching processes should be applied over t_{OSL}=t_{Be} × $Snow_{corr}$. $Snow_{corr}$ being the snow cover correction defined as $Snow_{corr}$= t_{snow}/12 with t_{snow} being the persistence of the snow cover [$months/year$]. I propose to integrate both

bleaching and trapping (dose rate) processes over the same time t_{Be}, and use the following modified Equation 3.1 of Chapter 3:

$$\frac{dL(x,t,r')}{dt} = \frac{\dot{D}}{D_0}[1 - L(x,t,r')] - Snow_{corr} \times L(x,t,r')\overline{\sigma\varphi_0}e^{-\mu x} + \dot{\varepsilon}(t)\frac{dL}{dx} \tag{6.3}$$

Note that the athermal loss component is not considered. The snow thickness at which the bleaching process stops is still to be determined. This threshold will be dependent of the snow density, the luminescence signals studied and the intensity of the photon flux. Another question is how surface erosion rates are going to evolve in presence of snow cover. Following the reasoning used in the interpretation of the Chapter 4, erosion rate might be considerably reduced by snow cover. Finally, an important limitation comes from the difficulty to extrapolate modern snow cover reports over longer time-scales. To explore the effect of snow cover in the Mont Blanc massif specifically, two end-members could be considered, one with no snow correction and one considering 50 *cm* during 6 months of the years (as mentioned by Wirsig et al., 2016).

6.1.4 Multi-signal approach

In the studies of this manuscript, I presented results using the luminescence stimulation (IRSL50) with the most sensitive signal. Using a specific combination of filters (AH3 and U340), I was able to extract three different natural luminescence signals during the same SAR analysis (e.g., IR50, pIR225 and OSL125; Fig. 6.1). The use of multiple luminescence signals from the same sample (Jenkins et al., 2018 and Sohbati et al., 2015), should enable to better OSL surface exposure dating. For lithologies presenting both K-feldspar (mainly sensitive to IR50 and pIR225 stimulations) and quartz (sensitive to OSL125 stimulation), the inversion of exposure time from the bleaching front position for the different signals can lead to different scenarios. If all stimulations give the same results, the reliability of the exposure age is validated. If not, it gives information about potential complex burial/exposure history.

Another approach is to compare the propagation rate for every stimulation for surfaces experiencing erosion or not. Since the bleaching propagates at different rates within the rocks (c.f., Ou et al., 2018 and Fig. 6.1), using multiple signals should enable us to better assess whether the position of the bleaching front is steady or not and thus to further constrain the erosion history (both erosion rate and duration).

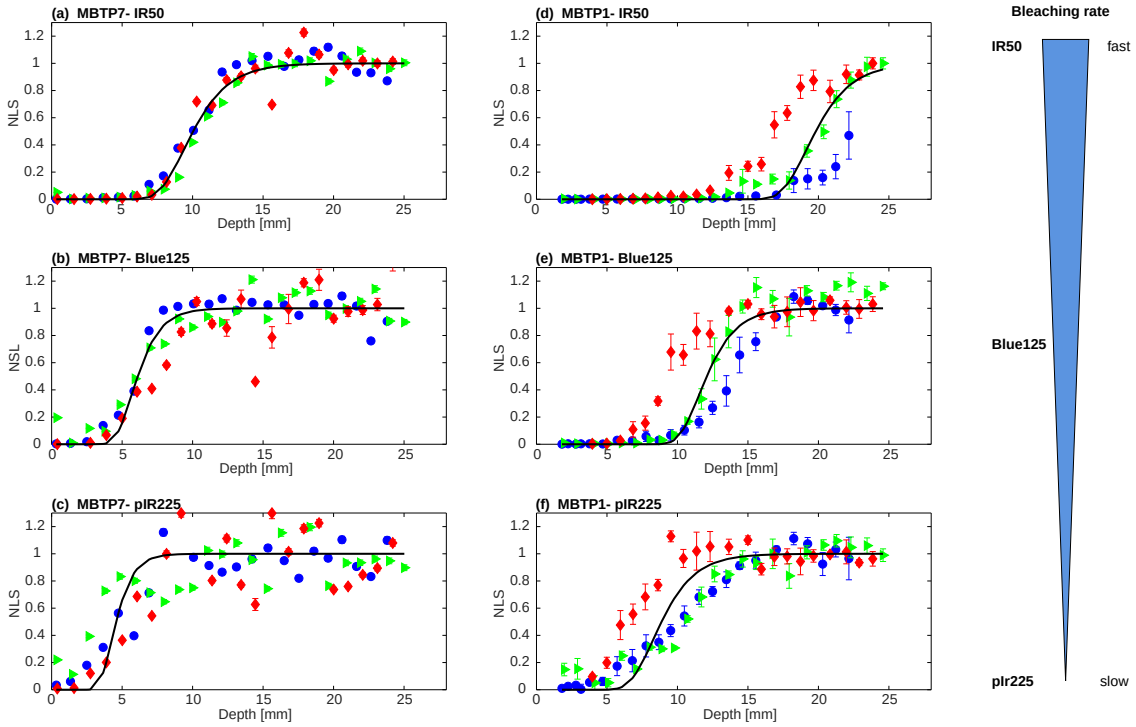

Figure 6.1: Normalized luminescence signal (NLS) profiles for (a)(d) IR50, (b),(e) Blue125 and (c),(f) pIR225 stimulations for sample MBTP7 and MBTP1.Coloured data point represents individual rock slice (each symbol/colour represents one core). The dashed black lines represent the best-fit model using parameters $\overline{\sigma\varphi_0} = 129\ a^{-1}$, $\mu = 0.596\ mm^{-1}$.

6.2 Geomorphological perspective

6.2.1 Distribution of the erosion rate in time

The method developed in Chapter 2 is assuming a simple erosion rate history following a step function. However, it is very likely that rock surfaces are subject to stochastic erosion processes (e.g., Ganti et al., 2016; Fig. 6.2). These stochastic processes (Fig. 6.2) cover potentially temperature, moisture, snow cover or wind fluctuations throughout the year. Future studies should challenge the numerical approach adopted here by considering any type of erosion history (inverse exponential, stochastic distribution...).

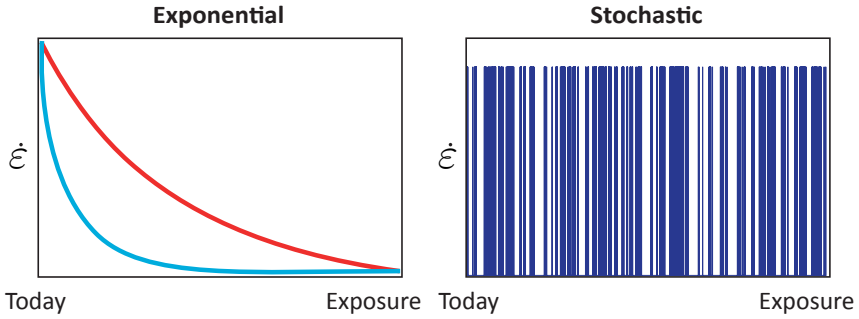

Figure 6.2: Example of exponential and stochastic erosion rate function in time.

6.2.2 Ice-extent modelling

In Chapter 3, the different corrections performed on TCN ages are making different scenarios of deglaciation post-LGM possible. Indeed, the climatic conditions controlling the ice-extent in the Alps following the LGM are still debated (e.g., Florineth and Schlüchter, 2000; Kuhlemann et al., 2008; Clark et al., 2009; Luetscher et al., 2015). A scenario recently proposed implies the waxing of the North American Ice Sheet (NAIS) at 26-23 *ka* pushed the North Atlantic jet stream southwards (e.g., Monegato et al., 2017). This enhanced precipitation rates in southern Europe by advection of moisture from the Mediterranean Sea, triggering expansion of the Alpine glaciers. The decline of the North Atlantic Ice Sheet after 23 *ka* would have led to the gradual re-establishment of westerly circulation and renewal of a moisture supply to northern Europe, feeding the European ice sheet to its maximum volume. The Alpine glaciers previously fed by advection of moisture from the Mediterranean Sea, would have entered a final recessional phase after 22 *ka* and faded out after 17.5 *ka* (Monegato et al., 2017). By challenging the different deglaciation scenarios presented in Chapter 3 and using inverse approach to reconstruct the equilibrium line altitudes (ELA) (Višnjević et al., 2018), paleo-environmental conditions could be inferred. A pilot study has already been made during the Bachelor project of A. Moreau (University of Lausanne). Using reference map of the Magland stadial (∼17.4-17.7 *ka*) of the Arve glacier (Mont Blanc massif) made by Coutterand (www.glaciers-climat.com/cg/le-tardiglaciaire/), he could infer the ELA variability in the Mont Blanc region.

6.2.3 Application to different geomorphological contexts

In Chapter 3, I demonstrated how surface erosion rate controls the evolution of the OSL signal of a rock surface. In order to challenge the potential application of OSL surface exposure dating to time-scales $> 10^2$ years, measurements in locations where bedrock surface erosion is very low (e.g., polar areas, high mountain) need to be investigated without accounting for the effect of erosion rates.

Another exciting perspective is to apply the methodological approach developed in Chapter 2 and applied in Chapter 3 on steep cliff faces in order to investigate the control of temperature and climate on erosion dynamics. Suitable sites would be rockwalls presenting consistent lithology and slope along several hundred meters. Such surfaces could be found in different part of the world (e.g., El Capitan from Yosemite Valley, Sam Ford Fjord in Baffin Island, Trango Towers in Pakistan, Troll Wall in Norway, Cerro Torre in Patagonia). In high mountain and glaciated areas, climate change, through deglaciation and frost cracking processes, controls the spatial and temporal distribution of rockfall, which is a high hazard, sometimes associated with high risks for infrastructure and people.

A pilot study has already been set up for the Master project of D. Rech (Unviersity of Lausanne) focusing on the Aiguille du Midi and the Eperon des Cosmiques in the Mont Blanc massif. These sites have already been dated with TCN and spectrometric reflectance (e.g., Bolhert et al, 2008; Gallach et al., 2017). The combination of the results from these rock surfaces with the results presented in this manuscript, will represent a unique dataset spreading over a ∼3000 meters (from ∼1900 to 3842 m.a.s.l) vertical transect with consistent lithology and will allow the characterization of topographic evolution of the Mont Blanc massif. Indeed, the development and application of new dating techniques allow the calculation surface erosion and the reconstruction of both paleo-glaciers and rockfall dynamics which will bring crucial and novel insights into the importance of climate in the evolution of the Earth's surface.

Figure 6.3: Sampling picture of the Éperon des Cosmiques cliff under the supervision of the Mont Blanc summit and the Dôme du Gouter (Picture from F. Pallandre)

CHAPTER 7

Appendix

7.1 Appendix Chapter 2

7.1.1 Ice surface reconstruction

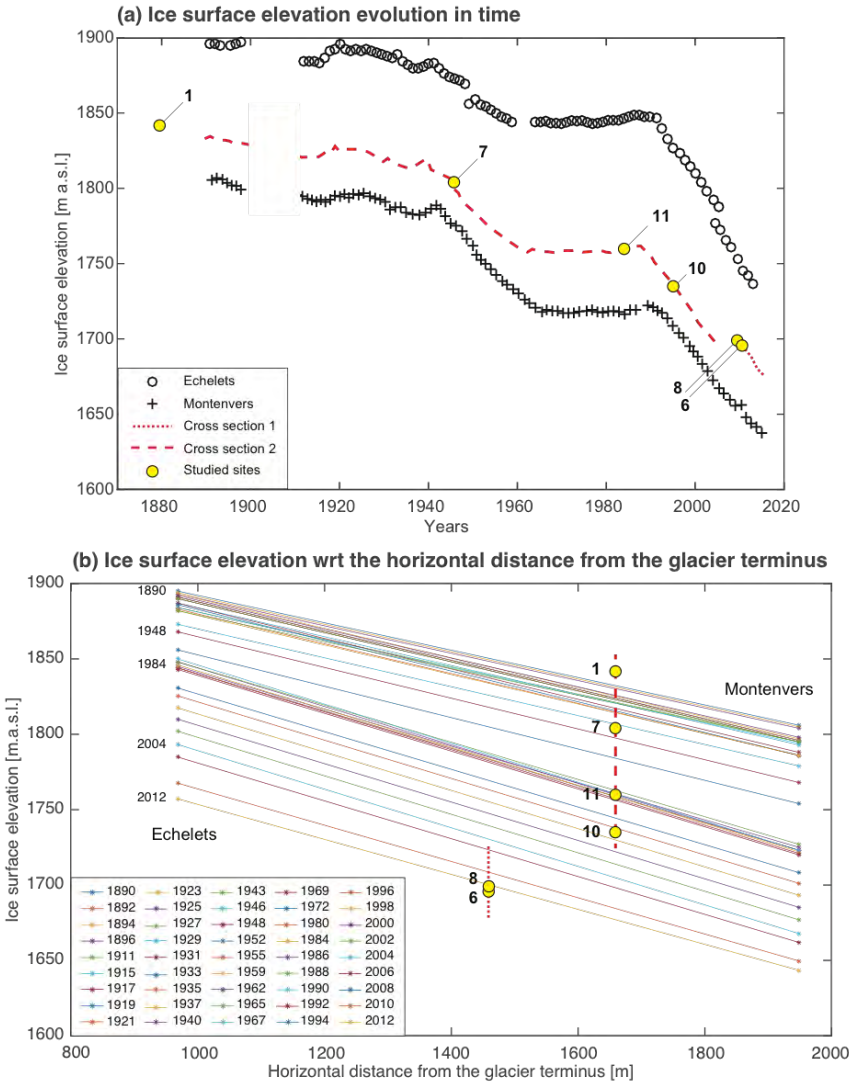

Figure A2.1: (a) Reconstruction of averaged ice-surface elevation [m.a.s.l.] through time along the Mer de Glace glacier (see locations of cross-sections on Figure 2.1). Averaged ice-surface elevations at the Montenvers (crosses) and Echelets (circles) cross-sections. The cross-sections 1 and 2 (red dashed lines) have been interpolated from the Montenvers and Echelets cross-sections, and used to project the studied samples (yellow circles). (b) Ice-surface elevation with respect to the horizontal distance from the glacier terminus used for the interpolation of the Montenvers and Echelets cross-sections. The ice surface elevations have been reconstructed from historical maps, survey reports and aerial photogrammetry (modified from Vincent et al., 2014). The dataset was kindly provided by the French glacier observatory GLACIOCLIM (http://www-lgge.ujf-grenoble.fr/ServiceObs/index.htm).

7.1.2 Dose rate sensitivity

The sensitivity of luminescence signal evolution to the dose rate is tested after four different daylight exposure times (1, 10, 100 and 1000 years of exposure), with a null dose rate and an extremely high dose rate ($\dot{D} \approx 14$ Gy ka^{-1}, King et al., 2016). We used an equation developed by Sohbati et al. (2012) describing the luminescence evolution $L(x)$ as a function of the exposure time t [s], depth x [mm], charge detrapping rate $\overline{\sigma\varphi_0}$ [s^{-1}], attenuation factor μ [mm^{-1}], a sample-dependent constant that characterises filling rate D_0 [Gy] and the natural dose rate $\dot{D}$ [Gy s^{-1}].

$$L(x) = \frac{\overline{\sigma\varphi_0} e^{-\mu x} e^{-t[\overline{\sigma\varphi_0} e^{-\mu x} + \frac{\dot{D}(x)}{D_0}]} + \frac{\dot{D}(x)}{D_0}}{\overline{\sigma\varphi_0} e^{-\mu x} + \frac{\dot{D}(x)}{D_0}} \tag{A2.1}$$

The resulting comparison shows that the luminescence signal is not sensitive to dose rate over millenial timescales. We thus consider the dose rate as negligible for our applications of OSL surface exposure dating, and do not take it into account in the luminescence evolution equation.

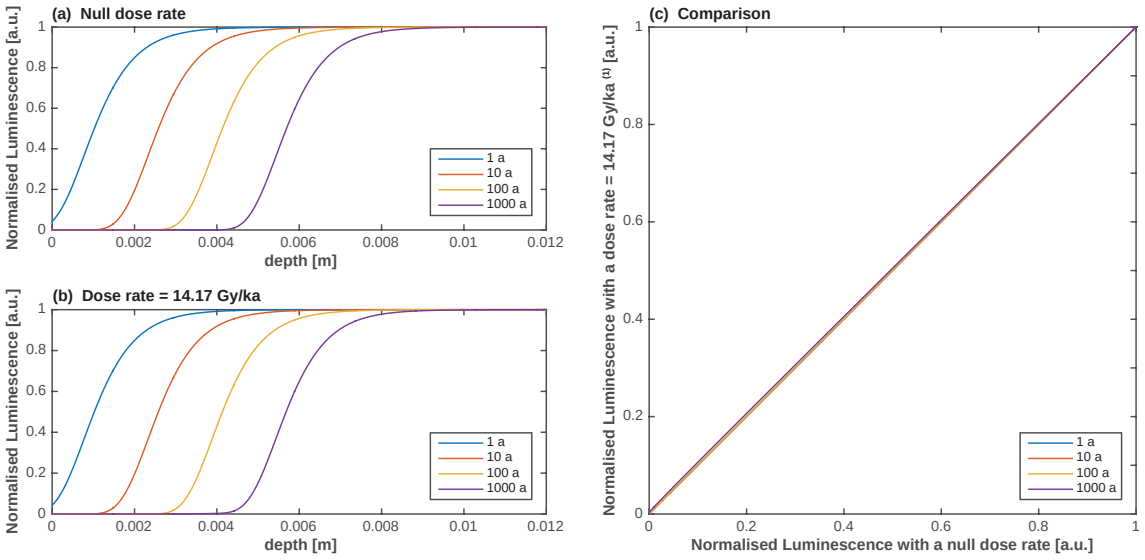

Figure A2.2: Evolution of the nomalised luminescence signal through time and depth for 1, 10, 100 and 1000 years of daylight exposure, taking into account (a) a null dose rate and (b) an extremely high dose rate of ~14 Gy ka^{-1} (King et al., 2016). Inset (c) shows the comparison between the result with two different dose rates.

different dose rates.

A3. Luminescence measurement tests

7.1.3 Luminescence measurement tests

The purpose of the following tests is to find the most appropriate infrared stimulated luminescence (IRSL) measurement conditions for analysis of the collected samples from the Montenvers site. We first performed a residual dose determination. Under natural daylight conditions, luminescence signals of feldspar may not be completely reset, leaving a residual dose. The residual test allows the evaluation of this remaining natural dose (which may also originate from other sources e.g. thermal transfer). We first reset the luminescence signal by exposing rock slices (3 slices for a representative sample of Montenvers site) to daylight for about 3 hours before analysing both slide sides. We then measured the residual dose using infrared stimulation at 50°C ($IRSL_{50}$) following different preheat temperatures (during 60 s). The residual dose after a preheat temperature of 250°C is 0.25 ± 0.45 Gy. With preheat temperature equal to 275°C, the residual dose is 0.85 ± 0.43 Gy. For preheat temperature equal to 300°C and 325°C, the residual doses increase to 2.94 ± 0.41 Gy and 2.10 ± 0.52 Gy respectively.

We then proceeded to a dose recovery test with preheat-plateau to determine the most appropriate preheat temperature. Thereby we quantified the recovered doses with $IRSL_{50}$ for the same range of preheat temperatures explored in the residuals test. We analyzed 3 rock slices with a laboratory beta dose of 27.25 Gy after complete optical bleaching (both disk sides exposed to daylight for about 3 hours). The samples were not heated prior the daylight bleaching. Preheat temperatures 250°C, 275°C, 300°C, 325°C were investigated, and results are corrected for the residual dose values reported in Table A1. For preheat temperatures of 250°C, 275°, 300°C and 325°C, we obtained dose recovery ratios of 0.90 ± 0.10, 0.87 ± 0.17, 0.77 ± 0.23 and 0.85 ± 0.15, respectively (Table A1). The optimal preheat temperature for both the residual dose and dose recovery is thus 250°C, and was used in all subsequent experiments.

Table A1: Table A2 of the residual test and the dose recovery preheat plateau test after a given beta dose of 27.25 Gy.

Preheat Temperature (°C)	250	275	300	325
Residual dose (Gy)	0.25 ± 0.45	0.85 ± 0.43	2.94 ± 0.41	2.1 ± 0.52
Dose recovery ratio	0.9 ± 0.10	0.87 ± 0.17	0.77 ± 0.23	0.85 ± 0.15

Table A2: Sensitivity corrected luminescence signal intensities with depth. The depth x (cm) is measured during core slicing with a high-precision numerical micrometre. IRSL measurements (Lx/Tx) are the results of the luminescence analysis (as explained in Section 4) and the analytical error on the

Table A2.2: Sensitivity corrected luminescence signal intensities with depth. The depth x [cm] is measured during core slicing with a high-precision numerical micrometre. IRSL measurements ($\frac{Lx}{Tx}$) are the results of the luminescence analysis (as explained in Section 2.4) and the analytical error on the measurement ($\frac{Lx}{Tx}err.$) is calculated in Analyst v.4.31.7 including a measurement error of 1.5%. Note: Each line corresponds to the measurement of one single rock slice.

MBMV1			MBMV6			MBMV7			MBMV8			MBMV10			MBMV11		
x [cm]	Lx/Lx	Lx/Tx err.	x [cm]	Lx/Lx	Lx/Tx err.	x [cm]	Lx/Lx	Lx/Tx err.	x [cm]	Lx/Lx	Lx/Tx err.	x [cm]	Lx/Lx	Lx/Tx err.	x [cm]	Lx/Lx	Lx/Tx err.
1.6	0.00	0.000	1.3	0.00	0.000	2.3	0.01	0.000	1.5	0.31	0.007	2.4	0.42	0.009	2.2	0.00	0.000
2.6	0.01	0.000	2.4	0.00	0.000	3.3	0.11	0.002	2.8	0.62	0.013	3.6	0.76	0.016	3.3	0.01	0.000
3.6	0.34	0.007	3.4	0.00	0.000	4.4	0.99	0.021	3.9	0.92	0.020	4.7	1.05	0.022	4.2	0.27	0.006
4.7	0.60	0.013	4.5	0.04	0.001	5.4	1.06	0.023	5.0	1.04	0.022	5.6	0.91	0.019	5.2	0.62	0.013
5.7	0.86	0.018	5.5	0.15	0.003	6.4	1.06	0.022	6.1	0.96	0.020	6.7	1.05	0.022	6.1	0.86	0.019
6.7	0.92	0.020	6.5	0.70	0.015	7.4	1.03	0.022	7.1	0.99	0.021	7.8	1.12	0.024	7.1	1.05	0.022
7.7	1.04	0.022	7.5	0.91	0.019	8.4	0.95	0.020	8.2	1.00	0.021	8.7	0.88	0.019	8.0	0.97	0.021
8.6	0.97	0.021	8.5	0.92	0.020	9.3	0.94	0.020	9.2	1.08	0.023	9.8	0.98	0.021	9.0	0.80	0.017
9.5	0.97	0.021	9.5	0.99	0.021	10.3	0.95	0.020	10.3	1.10	0.023	10.9	1.14	0.024	9.9	0.93	0.020
10.4	1.00	0.021	10.5	1.01	0.021	11.4	0.92	0.020	11.4	1.12	0.024	11.9	0.96	0.020	10.8	0.89	0.019
11.4	1.05	0.022	11.5	1.03	0.022	12.4	0.94	0.020	12.4	1.01	0.021	13.0	0.93	0.020	11.8	0.84	0.018
12.4	1.12	0.024	12.5	1.13	0.024										12.7	0.88	0.019
13.5	0.95	0.020	13.5	1.10	0.023	1.7	0.01	0.000	2.0	0.39	0.008	3.1	0.80	0.017			
14.5	0.98	0.021	14.5	1.03	0.022	2.8	0.03	0.001	3.0	0.96	0.020	4.2	0.96	0.020	2.1	0.10	0.002
15.4	1.01	0.021				3.7	0.42	0.009	4.0	0.89	0.037	5.3	1.06	0.023	3.2	0.80	0.017
16.4	0.98	0.021	2.4	0.01	0.000	4.5	0.79	0.017	7.0	1.05	0.022	6.4	1.10	0.023	4.2	0.82	0.018
17.6	0.94	0.020	3.3	0.02	0.000	5.5	0.84	0.018	8.0	0.95	0.020	7.4	0.97	0.021	5.1	0.88	0.019
			4.4	0.12	0.002	6.5	0.97	0.021	9.0	1.04	0.022	8.4	0.94	0.020	6.1	1.04	0.022
1.7	0.01	0.000	5.4	0.45	0.009	7.5	1.15	0.024	10.1	1.15	0.024	9.4	0.91	0.019	7.0	0.96	0.021
2.8	0.01	0.000	6.4	0.75	0.016	8.6	0.94	0.020	11.1	1.07	0.023	10.6	0.98	0.021	8.0	0.99	0.021
3.8	0.05	0.001	7.4	0.88	0.019	9.6	1.08	0.023	12.2	0.91	0.019	11.7	0.87	0.018	8.9	0.92	0.020
4.8	0.34	0.007	8.4	1.10	0.023	10.7	1.12	0.024	13.2	1.01	0.021	12.7	1.04	0.022	9.8	0.98	0.021
5.8	0.64	0.014	9.4	1.06	0.022	11.8	0.97	0.021				13.7	1.04	0.022	11.7	0.92	0.020
6.8	0.97	0.021	10.4	0.92	0.020				1.8	0.85	0.018				12.7	0.91	0.020
7.8	1.02	0.022	11.4	0.96	0.020	1.6	0.00	0.000	2.9	0.93	0.020	1.8	0.02	0.000			
8.9	0.94	0.020	12.4	0.86	0.018	2.8	0.04	0.001	4.2	1.01	0.022	3.1	0.23	0.005	1.8	0.01	0.000
10.0	1.07	0.023	13.4	0.90	0.019	3.8	0.42	0.009	5.4	0.90	0.019	4.2	0.73	0.015	2.8	0.21	0.005
			14.3	1.09	0.023	4.8	0.95	0.020	6.6	0.94	0.020	5.3	1.09	0.023	3.8	0.60	0.013
2.3	0.03	0.001	15.2	1.09	0.023	5.9	1.06	0.022	7.6	1.06	0.023	6.4	0.93	0.020	4.7	0.86	0.018
3.4	0.21	0.005				6.9	1.08	0.023	8.6	0.93	0.020	7.4	1.00	0.021	5.7	0.96	0.021
4.4	0.66	0.014	1.4	0.01	0.000	8.0	0.92	0.020	9.7	1.00	0.021	8.5	0.93	0.020	6.7	0.97	0.021
5.4	0.86	0.018	2.2	0.01	0.000	8.9	1.07	0.023	10.7	1.06	0.023	9.7	1.07	0.023	7.7	0.90	0.019
6.4	0.96	0.020	3.0	0.15	0.003	10.0	0.94	0.020	12.1	1.04	0.022	10.8	0.96	0.021	8.7	0.94	0.020
7.3	1.08	0.023	3.9	0.31	0.007	11.3	0.94	0.020	13.4	0.84	0.018				9.6	1.04	0.022
8.3	1.01	0.021	4.7	0.70	0.015	12.4	1.00	0.021							10.6	1.21	0.026
9.2	1.10	0.023	6.3	0.93	0.020										11.5	1.00	0.021
10.2	1.00	0.021	7.1	0.82	0.017										12.4	0.93	0.020
11.2	0.96	0.020	7.9	0.89	0.019												
12.3	0.88	0.019	8.6	0.89	0.019										1.9	0.03	0.001
13.2	0.88	0.019	9.4	0.79	0.017										3.2	0.15	0.003
14.2	0.97	0.021													4.1	0.53	0.011
15.2	0.90	0.019													5.1	0.99	0.021
															6.1	1.05	0.022
															7.0	1.1	0.024
															7.9	1.2	0.026
															8.8	1.0	0.022
															9.8	1.1	0.024
															10.7	1.2	0.026
															11.6	1.1	0.024
															12.6	0.9	0.019

3.8	0.05	0.001	7.4	0.88	0.019	9.6	1.08	0.023	12.2	0.91	0.019	11.7	0.87	0.018	8.9	0.92	0.020
4.8	0.34	0.007	8.4	1.10	0.023	10.7	1.12	0.024	13.2	1.01	0.021	12.7	1.04	0.022	9.8	0.98	0.021
5.8	0.64	0.014	9.4	1.06	0.022	11.8	0.97	0.021				13.7	1.04	0.022	11.7	0.92	0.020
6.8	0.97	0.021	10.4	0.92	0.020				1.8	0.85	0.018				12.7	0.91	0.020
7.8	1.02	0.022	11.4	0.96	0.020	1.6	0.00	0.000	2.9	0.93	0.020	1.8	0.02	0.000			
8.9	0.94	0.020	12.4	0.86	0.018	2.8	0.04	0.001	4.2	1.01	0.022	3.1	0.23	0.005	1.8	0.01	0.000
10.0	1.07	0.023	13.4	0.90	0.019	3.8	0.42	0.009	5.4	0.90	0.019	4.2	0.73	0.015	2.8	0.21	0.005
			14.3	1.09	0.023	4.8	0.95	0.020	6.6	0.94	0.020	5.3	1.09	0.023	3.8	0.60	0.013
2.3	0.03	0.001	15.2	1.09	0.023	5.9	1.06	0.022	7.6	1.06	0.023	6.4	0.93	0.020	4.7	0.86	0.018
3.4	0.21	0.005				6.9	1.08	0.023	8.6	0.93	0.020	7.4	1.00	0.021	5.7	0.96	0.021
4.4	0.66	0.014	1.4	0.01	0.000	8.0	0.92	0.020	9.7	1.00	0.021	8.5	0.93	0.020	6.7	0.97	0.021
5.4	0.86	0.018	2.2	0.01	0.000	8.9	1.07	0.023	10.7	1.06	0.023	9.6	0.97	0.023	7.7	0.90	0.019
6.4	0.96	0.020	3.0	0.15	0.003	10.0	0.94	0.020	12.1	1.04	0.022	10.8	0.96	0.021	8.7	0.94	0.020
7.3	1.08	0.023	3.9	0.31	0.007	11.3	0.94	0.020	13.4	0.84	0.018				9.6	1.04	0.022
8.3	1.01	0.021	4.7	0.70	0.015	12.4	1.00	0.021							10.6	1.21	0.026
9.2	1.10	0.023	6.3	0.93	0.020										11.5	1.00	0.021
10.2	1.00	0.021	7.1	0.82	0.017										12.4	0.93	0.020
11.2	0.96	0.020	7.9	0.89	0.019												
12.3	0.88	0.019	8.6	0.89	0.019										1.9	0.03	0.001
13.2	0.88	0.019	9.4	0.79	0.017										3.2	0.15	0.003
14.2	0.97	0.021													4.1	0.53	0.011
15.2	0.90	0.019													5.1	0.99	0.021
															6.1	1.05	0.022
															7.0	1.1	0.024
															7.9	1.2	0.026
															8.8	1.0	0.022
															9.8	1.1	0.024
															10.7	1.2	0.026
															11.6	1.1	0.024
															12.6	0.9	0.019

Table A3: Best-fit values of $\overline{\sigma\varphi}_0$ and μ determined for each sample, calculated from combinations of three and four samples.

Table A2.3: Best-fit values of $\overline{\sigma\varphi}_0$ and μ determined for each sample, calculated from combinations of three and four samples.

Calibration combination				$\overline{\sigma\varphi}_0$ [s^{-1}]			μ [mm^{-1}]		
				Best-fit	+1σ	-1σ	Best-fit	+1σ	-1σ
with 3 samples, MBMV...									
1	7	8		1.2×10^{-7}	1.2×10^{-7}	1.1×10^{-7}	1.51	1.52	1.50
1	7	10		6.6×10^{-8}	7.6×10^{-8}	6.4×10^{-8}	1.42	1.43	1.38
1	7	11		9.4×10^{-8}	9.6×10^{-8}	7.8×10^{-8}	1.42	1.45	1.39
1	8	11		7.4×10^{-8}	7.5×10^{-8}	6.1×10^{-8}	1.39	1.39	1.34
1	8	10		1.0×10^{-7}	1.0×10^{-7}	1.0×10^{-7}	1.42	1.43	1.41
1	10	11		6.6×10^{-8}	8.3×10^{-8}	6.0×10^{-8}	1.39	1.39	1.33
7	8	10		1.3×10^{-7}	1.3×10^{-7}	1.3×10^{-7}	1.58	1.58	1.56
7	8	11		1.2×10^{-7}	1.2×10^{-7}	1.2×10^{-7}	1.51	1.52	1.50
7	10	11		1.4×10^{-7}	1.5×10^{-7}	1.3×10^{-7}	1.58	1.60	1.55
8	10	11		8.1×10^{-8}	9.1×10^{-8}	7.3×10^{-8}	1.34	1.37	1.31
with 4 samples, MBMV…									
1	7	8	10	9.5×10^{-8}	9.9×10^{-8}	8.5×10^{-8}	1.48	1.48	1.45
1	7	8	11	1.1×10^{-7}	1.1×10^{-7}	1.1×10^{-7}	1.48	1.49	1.47
1	7	10	11	7.4×10^{-8}	8.1×10^{-8}	6.5×10^{-8}	1.38	1.41	1.36
1	8	11	10	9.0×10^{-8}	9.4×10^{-8}	8.7×10^{-8}	1.42	1.42	1.40
7	10	11	8	1.2×10^{-7}	1.2×10^{-7}	1.2×10^{-7}	1.53	1.53	1.52

Table A4: Inversion results for exposure age using the different calibration combinations of bedrock samples. Grey shading shows the inverted results for a specific sample when not included in the calibration combination (i.e. the exposure age of the specific sample has not used for the calibration of the model). These results are used to produce Figures 10c-d.

Table A2.4: Inversion results for exposure age using the different calibration combinations of bedrock samples. Grey shading shows the inverted results for a specific sample when not included in the calibration combination (i.e. the exposure age of the specific sample has not used for the calibration of the model). These results are used to produce Figures 10c-d.

Calibration combination				MBMV1 - 137 yrs				MBMV7 - 69 yrs				MBMV8 - 3 yrs				MBMV10 - 18 yrs				MBMV11 - 30 yrs			
				Best fit	Median	+2 σ	-2 σ	Best fit	Median	+2 σ	-2 σ	Best fit	Median	+2 σ	-2 σ	Best fit	Median	+2 σ	-2 σ	Best fit	Median	+2 σ	-2 σ
Individually				146	152	172	126	89	79	88	67	2	3	3	2	19	19	23	14	50	42	50	34
with all the sample excluding MBMV6				164	161	185	132	61	63	68	57	3	3	4	3	17	14	18	9	62	57	70	41
with 3 samples, MBMV...																							
1	7	8		184	166	190	136	56	62	67	56	3	3	3	2	9	13	17	9	53	54	69	40
1	7	10		194	183	213	146	77	80	88	71	5	5	5	4	21	18	23	13	90	69	88	50
1	7	11		118	126	149	103	56	56	61	50	3	3	4	3	15	12	16	9	57	50	61	35
1	8	11		122	135	159	104	61	63	70	56	3	4	4	3	13	15	18	10	55	53	68	39
1	8	10		106	113	134	92	50	50	55	45	3	3	3	2	14	12	15	8	50	43	55	31
1	10	11		174	150	181	119	67	71	80	63	4	4	5	4	17	17	21	12	44	61	77	44
7	8	10		181	211	242	173	78	74	82	64	3	3	3	2	16	13	17	9	78	65	78	48
7	8	11		165	162	189	136	66	62	67	56	3	3	3	2	14	13	17	9	40	54	68	40
7	10	11		206	189	216	155	65	65	73	57	3	3	3	2	15	12	15	8	65	58	70	43
8	10	11		116	93	116	71	46	50	55	43	3	3	4	3	11	12	15	9	52	42	52	29
with 4 samples, MBMV…																							
1	7	8	10	176	170	194	139	63	67	73	61	4	4	4	3	10	15	19	10	68	61	75	43
1	7	8	11	177	152	174	125	63	59	64	54	3	3	3	3	15	13	17	9	63	52	66	38
1	7	10	11	129	129	154	98	58	62	69	54	4	4	4	3	13	14	18	10	38	52	66	38
1	8	11	10	117	134	155	106	58	58	64	52	4	3	4	3	16	13	17	9	42	52	64	36
7	10	11	8	159	168	196	141	63	63	69	56	2	3	3	2	16	13	16	9	52	55	69	41

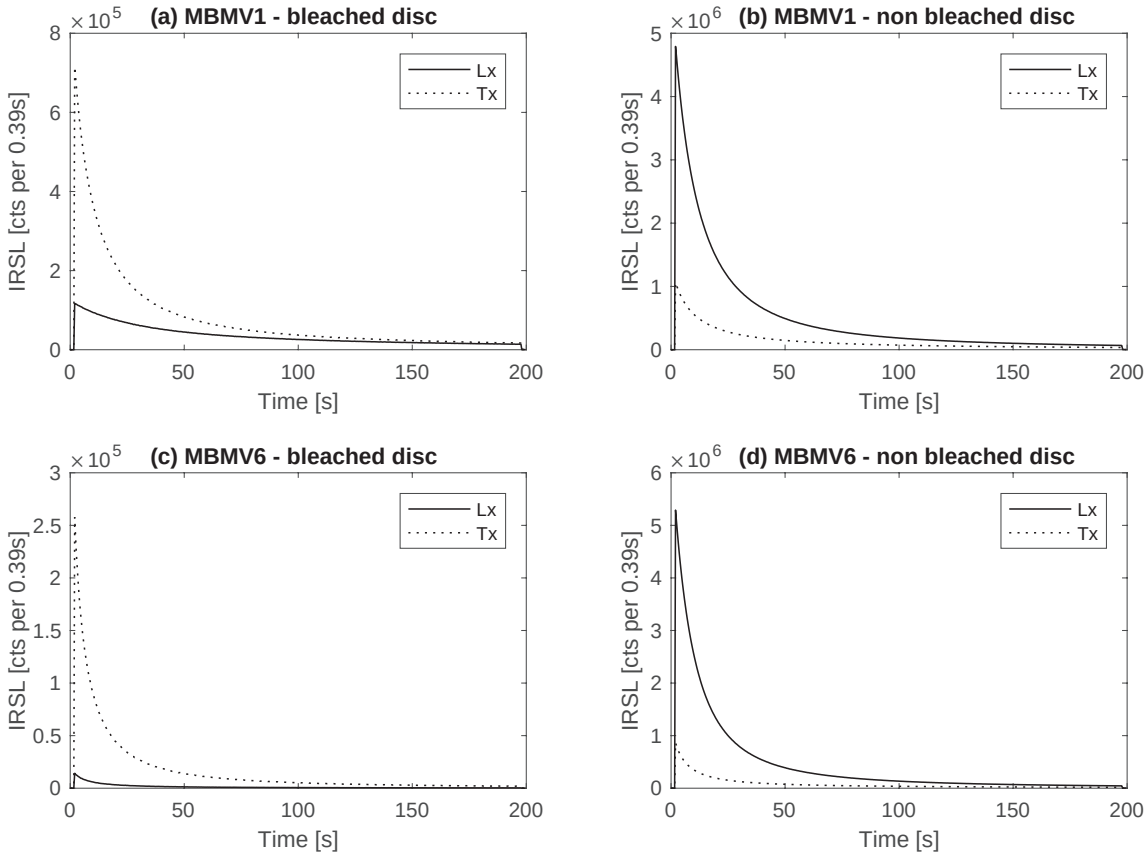

Figure A2.3: Natural infrared stimulated signal (solid line, Lx) and test dose (27.25 Gy) subsequent luminescence response (dashed line, Tx) for a bleached signal (surface disc) (a) and (b) and for non-bleached signal (inside core disc) (b) and (c). (a) and (b) are IRSL signal representative for gneissic lithology (sample MBMV1). (c) and (d) for granitic lithology (sample MBMV6).

7.2 Appendix Chapter 3

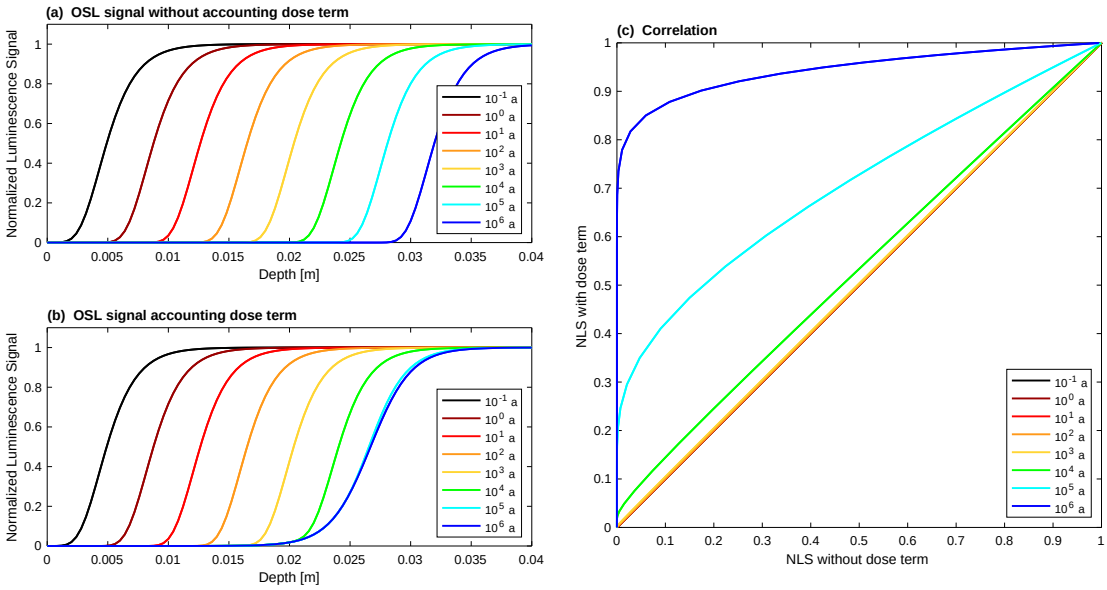

Figure A3.1: Modeled luminescence-depth profiles as predicted by Eq. (3.1) neither accounting for fading nor erosion and (a) without the trapping term and (b) with the trapping term, respectively. The selected parameter values are $\dot{D}$= 8 $\times 10^{-3}$ Gy a^{-1}, D_0= 500 Gy, $\overline{\sigma\varphi_0}$= 129 a^{-1} and μ = 0.596 mm^{-1}. (c) is the comparison between the normalized luminescence (NLS) signal for both scenarios shown in (a) and (b).

Table A3.1: Dosimetry calculations for the feldspar samples analyzed. Conversion factors has been chosen after Adamiec and Aitken (1998). Alpha-particle attenuation and Beta-particle attenuation factors have been chosen after Bell (1980) and Mejdahl (1979) respectively. Cosmic dose rates have been calculated using the method of Prescott and Hutton (1994), assuming an overburden density of 2.7±0.1 g cm^{-3}. Internal K concentration is assumed to be 12±0.5% for both samples. Environmental dose rates were calculated using DRAC online calculator (Durcan et al., 2015), assuming a grain size between 750 and 1000 μm and water content of 2%.

Sample ID	U [ppm]	Th [ppm]	K [ppm]	Thickness [m]
MBTP1	5.69 ± 0.12	36.8 ± 0.6	2.56 ± 0.03	0.08 ± 0.02
MBTP6	8.75 ± 0.19	26.0 ± 0.4	3.88 ± 0.05	0.07 ± 0.02

Table A2: Infrared stimulated luminescence at 50°C (IRSL50) experimental values of s

MBTP1								
C1			C2			C3		
x [mm]	Lx/Tx	Lx/Tx Err.	x [mm]	Lx/Tx	Lx/Tx Err.	x [mm]	Lx/Tx	Lx/Tx Err.
1.81	0.00	0.000	2.24	0.00	0.000	1.97	0.00	0.005
2.80	0.00	0.000	3.16	0.00	0.001	2.91	0.00	0.001
3.76	0.00	0.001	4.14	0.00	0.001	3.96	0.00	0.000
4.70	0.00	0.001	5.09	0.00	0.001	4.99	0.00	0.001

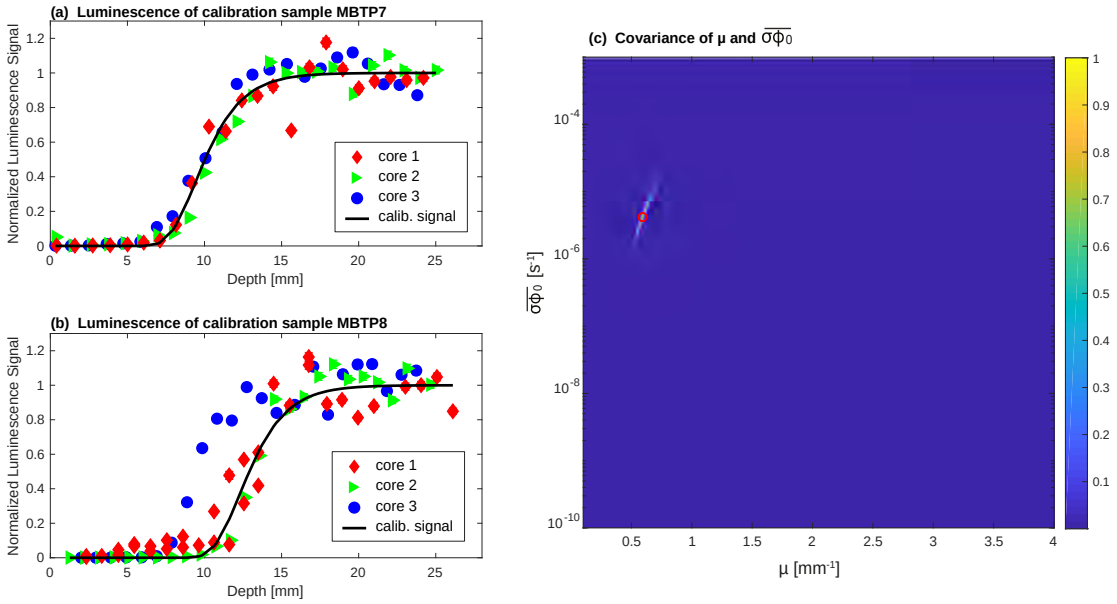

Figure A3.2: Calibration of the parameter μ and $\overline{\sigma\varphi_0}$ using two calibration samples MBTP7 (1936 m.a.s.l.) and MBPT8 (1995 m.a.s.l.) with exposure age of 2±2 a and 11±2 a respectively. These samples were collected at the bottom of the Trélaporte vertical profile in 2016. The surfaces are located between the present-day position of the glacier and the Little Ice Age maximal elevation. These ages were determined using the reconstruction from Vincent et al., 2014. The calibration is made through an inversion protocol by prediction 10^8 luminescence signals corresponding to the combinations of 10^4 values of $\overline{\sigma\varphi_0}$ in the logarithmic space and 10^4 values of μ. The inversed solutions are inferred using a least absolute deviation regression as described in Lehmann et al., 2018.

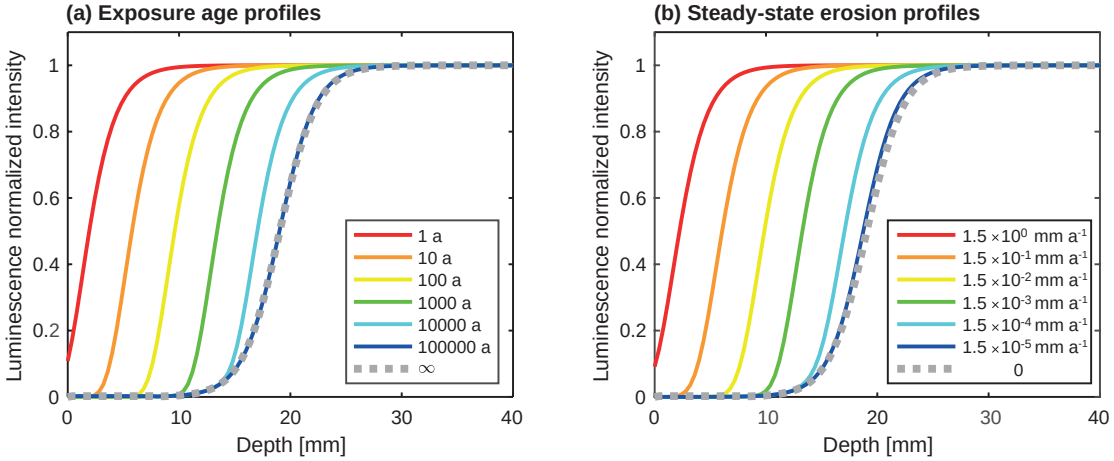

Figure A3.3: Modeled luminescence-depth profiles as predicted by Eq. (3.1) for a (a) non-eroding and (b) eroding rock surface, respectively. The selected parameter values are $\dot{D}$=6×10^{-3} Gy a^{-1}, D_0= 250 Gy, $\overline{\sigma\varphi_0}$ = 2200 ka^{-1} and μ = 0.6 mm^{-1} similar to Sohbati et al. (2018).

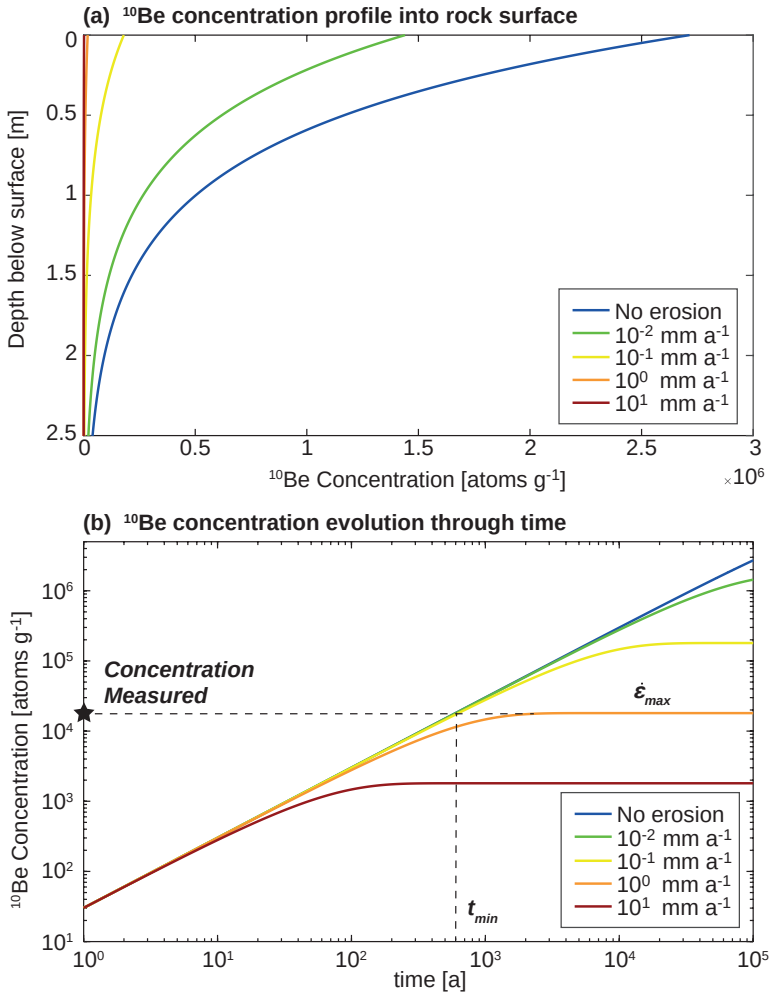

Figure A3.4: Evolution of the ^{10}Be production of a rock surface affected by different rates of erosion as a function of (a) the rock depth (b) the exposure age calculated using a modified version of the CREp online calculator to process non-linear erosion rate correction by solving Eq. (3.3) (Martin et al., 2017) as a modeling exercise and for comparison with OSL surface exposure curves of Fig. 3.5.

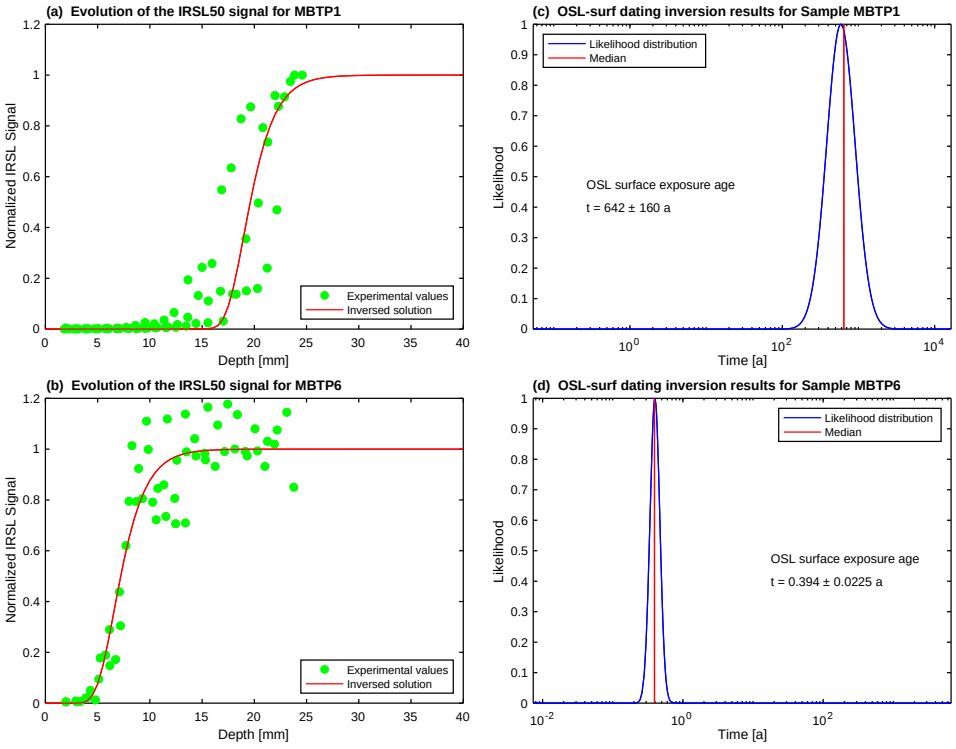

Figure A3.5: Determination of the apparent OSL surface exposure ages for samples MBTP1 and MBTP6. Experimental values in (a) and (b) correspond to the value measured for 3 cores per sample. The likelihood was determined using a probability density function following a least square deviations regression method minimizing the sum of the square differences between the experimental and the inverted values. Redlines in (c) and (d) represent the median value of the distribution. Apparent ages were inverted using Eq. (3.2) and prescribing 10^6 solutions for a range of time from 0 to t_0 (TCN age calculated using the nuclide concentration of each sample and solving Eq. (3.3) without erosion correction). All models were calculated using the following parameters: $\overline{\sigma\varphi_0} = 129\ a^{-1}$, $\mu = 0.596\ mm^{-1}$, D_0= 500 Gy and $\dot{D}$ =7.4×10^{-3} Gy a^{-1} and $\dot{D}$ =8.4×10^{-3} Gy a^{-1} respectively for sample MBTP1 and sample MBTP6 (see main text for details).

Table A3.2: Infrared stimulated luminescence at 50°C (IRSL50) experimental values of sample MBTP1

MBTP1								
C1			C2			C3		
x [mm]	Lx/Tx	Lx/Tx Err.	x [mm]	Lx/Tx	Lx/Tx Err.	x [mm]	Lx/Tx	Lx/Tx Err.
1.81	0.00	0.000	2.24	0.00	0.000	1.97	0.00	0.005
2.80	0.00	0.000	3.16	0.00	0.001	2.91	0.00	0.001
3.76	0.00	0.001	4.14	0.00	0.001	3.96	0.00	0.000
4.70	0.00	0.001	5.09	0.00	0.001	4.99	0.00	0.001
5.72	0.00	0.001	6.07	0.00	0.001	5.95	0.00	0.001
6.80	0.00	0.001	7.10	0.00	0.000	6.85	0.00	0.002
7.77	0.00	0.002	8.04	0.00	0.001	7.72	0.01	0.003
8.68	0.00	0.002	8.89	0.00	0.001	8.62	0.01	0.007
9.52	0.00	0.001	9.77	0.00	0.002	9.54	0.03	0.013
10.49	0.01	0.003	10.72	0.01	0.002	10.42	0.02	0.004
11.53	0.01	0.002	11.70	0.01	0.003	11.36	0.04	0.022
12.49	0.01	0.002	12.64	0.02	0.008	12.32	0.07	0.011
13.47	0.01	0.006	13.63	0.05	0.010	13.65	0.19	0.109
14.41	0.02	0.018	14.63	0.13	0.175	15.00	0.24	0.073
15.56	0.02	0.014	15.60	0.11	0.032	15.95	0.26	0.100
17.02	0.03	0.005	16.76	0.15	0.072	16.88	0.55	0.193
18.25	0.14	0.176	17.93	0.14	0.127	17.79	0.63	0.109
19.24	0.15	0.149	19.19	0.36	0.091	18.73	0.83	0.171
20.30	0.16	0.108	20.38	0.50	0.101	19.65	0.87	0.150
21.23	0.24	0.179	21.29	0.74	0.125	20.82	0.79	0.165
22.16	0.47	0.348	22.30	0.88	0.118	21.98	0.92	0.136
			23.45	0.97	0.139	22.89	0.91	0.073
			24.59	1.00	0.082	23.86	1.00	0.082

Table A3.3: Infrared stimulated luminescence at 50°C (IRSL50) experimental values of sample MBTP6

MBTP6								
C1			C2			C3		
x [mm]	Lx/Tx	Lx/Tx Err.	x [mm]	Lx/Tx	Lx/Tx Err.	x [mm]	Lx/Tx	Lx/Tx Err.
1.96	0.00	0.000	1.96	0.01	0.000	3.32	0.01	0.000
3.00	0.01	0.000	2.90	0.01	0.000	4.30	0.05	0.001
4.05	0.02	0.001	3.84	0.02	0.000	5.25	0.18	0.004
5.11	0.09	0.002	4.80	0.01	0.000	6.17	0.15	0.003
6.13	0.29	0.007	5.76	0.19	0.004	7.09	0.44	0.010
7.19	0.30	0.008	6.72	0.17	0.004	8.00	0.79	0.017
8.29	1.01	0.022	7.71	0.62	0.013	8.93	0.92	0.020
9.29	0.81	0.017	8.69	0.79	0.017	9.85	1.00	0.021
10.27	0.79	0.019	9.68	1.11	0.024	10.76	0.85	0.018
11.34	0.86	0.019	10.61	0.72	0.016	11.67	1.12	0.024
12.39	0.81	0.020	11.53	0.73	0.018	12.58	0.96	0.021
13.40	1.14	0.025	12.46	0.71	0.016	13.50	0.99	0.021
14.29	1.04	0.023	13.40	0.71	0.017	14.41	0.97	0.021
15.26	0.98	0.023	14.49	1.23	0.026	15.33	0.96	0.021
17.48	1.28	0.028	15.56	1.16	0.025	16.25	0.93	0.021
			16.49	1.09	0.024	17.16	0.99	0.021
			17.45	1.18	0.025	18.14	1.00	0.021
			18.38	1.14	0.024	19.14	0.99	0.022
			19.32	0.97	0.021	20.07	1.08	0.023
			20.31	0.99	0.021	21.02	0.93	0.020
			21.26	1.03	0.022	21.93	1.02	0.022
			22.19	1.08	0.023	22.85	1.65	0.037
			23.11	1.14	0.025	23.78	0.85	0.024

7.3 Appendix Chapter 4

7.3.1 Sample preparation, measurement and erosion

For every sample, both OSL-surf and ^{10}Be surface exposure dating analysis were performed.

The method of ^{10}Be sample preparation is comprehensively described in the literature (e.g., Kohl and Nishiizumi, 1992; Ivy-Ochs, 1996). We use grain sizes in between 250 m and 1 mm of quartz separates. The addition of 0.25 mg of a commercial ^{9}Be carrier to the dried quartz mineral seperate is followed by quartz dissolution in supra pure HF (40%). Be purification is made using ion-exchange columns and selective precipitation. The ^{10}Be/^{9}Be ratio is measured by accelerator mass spectrometry (AMS) on the 600 KV Tandy at the Laboratory of Ion Beam Physics (LIP) at ETH Zürich against the standard S2007N (Christl et al., 2013). We used the in house standard S2007N, which is calibrated against the 07KNSTD standard (Nishiizumi et al., 2007). We correct for a long-term average full chemistry procedural blank of ^{10}Be/^{9}Be = (3.7 ± 2.2)×10^{-15}. Ages are calculated using the local production rate of the Chironico landslide: 4.16 ± 0.10 *at* g_{qtz}^{-1} a^{-1}, with the Lifton-Sato-Dunai (LSD) scaling scheme (Lifton et al., 2014), the ERA40 atmospheric model (Uppala et al., 2005) and the Lifton VDM 2016 geomagnetic database (for ages in between 0-14 *ka*, Pavon-Carrasco et al., 2014 and for ages in between 14-75 *ka*, GLOPIS-75, Laj et al., 2004) with a modified version of the CREp online calculator (Martin et al., 2016) to process non-linear erosion rate correction by solving Equation 3 in Lehmann et al., in review. The reported errors propagate uncertainties from AMS standard reproducibility, counting statistics, standard mean error of samples, blank correction and the local production rate value. These external errors are used to compare absolute ages to independent chronologies. Internal errors exclude the uncertainty of the local production rate. All errors are reported on the 1σ level.

For luminescence analysis, the bedrock samples were cored down to 30 mm depth using a Husqvarna DM220 drill, with 10-*mm* diameter. Cores were then sliced into 0.7-*mm* thick rock slices with a BUEHLER IsoMet low speed saw equipped with a 0.3-*mm* thick diamond blade. The samples were drilled and sliced under wet conditions (water and lubricant, respectively) to avoid any heating that could potentially reset the OSL signal. Sample preparation was done under subdued red-light conditions. The thickness of each rock slice was measured to determine the precise depth of each luminescence measurement. Luminescence measurements were performed using Risø TL-DA 20 TL/OSL readers (Bøtter-Jensen et al., 2010) equipped with ^{90}Sr beta sources at the University of Lausanne (Switzerland). We performed a preheat at 250°C before giving infrared (IR) stimulation (870 *nm*, FWHM 40 *nm*) at 50°C. The calculation of $\dot{D}$ was achieved through the measurement of the concentrations of U, Th, K and Rb of the bulk rock sample and the use of the DRAC online calculator (Table 2; Durcan et al., 2015) assuming a grain size between 750 and 1000 μm and water content of 2%. We

use $\overline{\sigma\varphi_0} = 129\ a^{-1}$ and $\mu = 0.596\ mm^{-1}$ that were determined from two calibration rock surfaces of similar granitic lithology from the Mont Blanc massif, exhibit no erosion and have known exposure age, following the protocol presented in Lehmann et al. (2018). The calibration is presented in Fig. A4.2. The determination of D_0 was done by constructing dose response curves (DRC) of the IRSL signal measured at 50°C using a single aliquot regenerative dose (SAR) protocol (Murray and Wintle, 2000; Wallinga et al., 2000) and fitting the DRC with single saturating exponential. The validity of the measurement protocol was confirmed using a dose-recovery experiment (Wallinga et al., 2000). Recovered doses were within 10% of unity.

Table A4.1: Sample list with their characteristics and measured ^{10}Be concentrations

Sample ID	Latitude	Longitude	Elevation	Thickness	Topographic	Surface	Lichen	^{10}Be conc.[a]	P(0) local[b]	Ḋ spec.[c]
	WGS 84		[m.a.s.l.]	cm	Shielding factor	orientation	% of cov.	[at g_{qtz}^{-1}]	[at g_{qtz}^{-1}]	[Gy a^{-1}]
Moine transect										
MBAM1	45.9094	6.9527	2447	7	0.758	135 W 65	0.8	264530 ± 11640	28.17 ± 0.68	7.7×10^{-3}
MBAM2	45.9087	6.9521	2363	2	0.79	152 W 12	0.2	262870 ± 11190	26.51 ± 0.64	7.9×10^{-3}
MBAM3	45.9082	6.9507	2259	4	0.698	170 W 70	0.8	218400 ± 9720	24.58 ± 0.59	7.3×10^{-3}
Trélaporte transect										
MBTP1	45.9083	6.9311	2545	8	0.963	140 E 18	0.7	474750 ± 17530	30.20 ± 0.73	7.4×10^{-3}
MBTP2	45.9086	6.9319	2460	8.5	0.949	14 E 27	0.6	403210 ± 17020	28.43 ± 0.69	7.3×10^{-3}
MBTP5	45.9112	6.9324	2220	8	0.926	108 SE 18	0.9	446710 ± 19740	23.88 ± 0.58	7.7×10^{-3}
MBTP6	45.9130	6.9327	2094	7	0.594	334 E 80	0.7	84100 ± 13160	21.75 ± 0.52	8.4×10^{-3}
MBTP9	45.9124	6.9330	2133	6	0.656	148 E 73	0.6	160300 ± 8180	22.39 ± 0.54	7.0×10^{-3}
MBTP11	45.9108	6.9315	2310	7	0.898	130 E 48	0.8	330490 ± 13010	25.51 ± 0.61	8.1×10^{-3}

[a] Measured against standard 07KNSTD (Nishiizumi et al., 2007), corrected for full process blank of $(3.7 \pm 2.2) \times 10^{-15}$ ^{10}Be/^{9}Be. [b] Local production rate of the Chironico landslide: 4.15 ± 0.10 *at* $g^{-1}\ a^{-1}$ rescaled for every longitude (Claude et al., 2014), latitude and elevation and considering no erosion correction, with the LSD scaling scheme (Lifton et al., 2014), the ERA40 atmospheric model (Uppala et al., 2005) and the Lifton VDM 2016 geomagnetic database (for ages in between 0-14 *ka*, Pavon-Carrasco et al., 2014 and for ages in between 14-75 *ka*, GLOPIS-75, Laj et al., 2004). [c] Dose rates were calculated using the concentrations of U, Th, K and Rb of the bulk rock sample and the DRAC online calculator (details in Table A4.5; Durcan et al., 2015).

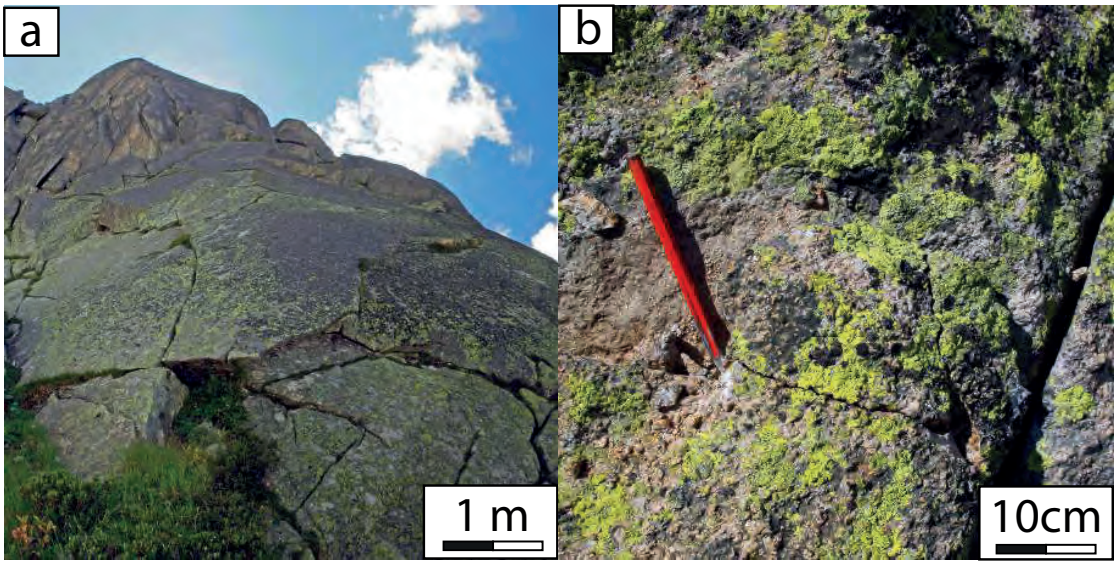

Figure A4.1: Example of the roches moutonnées sampled at two different scales (in this case surface MBTP5 from the Trélaporte profile)

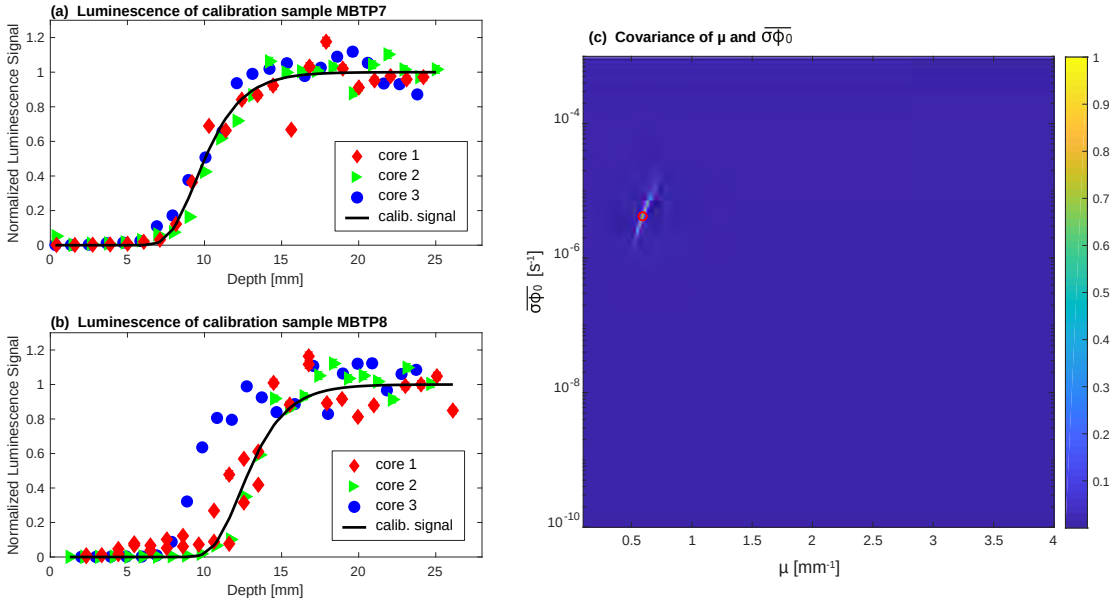

Figure A4.2: Modeled luminescence-depth profiles as predicted by Eq. (3.1) neither accounting for fading nor erosion and (a) without the trapping term and (b) with the trapping term, respectively. The selected parameter values are $\dot{D} = 8{\times}10^{-3}$ Gy a^{-1}, $D_0 = 500$ Gy, $\overline{\sigma\varphi_0} = 129\ a^{-1}$ and $\mu = 0.596\ mm^{-1}$. (c) is the comparison between the normalized luminescence (NLS) signal for both scenarios shown in (a) and (b).

Table A4.2: TCN and OSL surface ages and inversion results for all surfaces

Sample ID	TCN age t_0 [1] [a]	TCN age corr. $tc_{ss}^{(2)}$ [a]	TCN age corr. $tc_{max}^{(2)}$ [a]	OSL-surf. age [3] [a]	t_s at SS [a]	$\dot{\varepsilon}$ at SS [mm a^{-1}]	t_s max [a]	$\dot{\varepsilon}$ max [mm a^{-1}]	t_s min [a]	$\dot{\varepsilon}$ min [mm a^{-1}]
MBTP1	16428 ± 588	16647 ± 593	16657 ± 592	618 ± 147	2610	3.5×10^{-3}	20920	3.5×10^{-3}	-	-
MBTP2	15144 ± 609	15406 ± 625	15847 ± 649	606 ± 144	3146	3.5×10^{-3}	20920	3.5×10^{-3}	-	-
MBTP5	20227 ± 844	20838 ± 862	134090 ± 5852	4.6 ± 0.8	64	3.0×10^{-1}	3998	3.0×10^{-1}	20	7.0×10^{-1}
MBTP6	6667 ± 965	6830 ± 980	68692 ± 10617	0.4 ± 0.04	4	4.3	344	4.3	3	4.9
MBTP9	10970 ± 535	11212 ± 539	16523 ± 817	54 ± 14	486	3.2×10^{-2}	19510	3.2×10^{-2}	-	-
MBTP11	14482 ± 546	14987 ± 564	132250 ± 5101	3.4 ± 0.6	42	5.3×10^{-1}	2673	5.3×10^{-1}	-	-
MBAM1	12485 ± 546	12817 ± 593	45742 ± 2149	34 ± 8	285	5.7×10^{-2}	22200	5.7×10^{-2}	-	-
MBAM2	12157 ± 520	12411 ± 530	17993 ± 734	67 ± 16	461	2.8×10^{-2}	2162	2.8×10^{-2}	-	-
MBAM3	12543 ± 548	-	12780 ± 555	12 ± 2	-	-	56.92	2.0×10^{-1}	3	3.7

[1] Ages are calculated using the sea level high latitude (SLHL) rescaled local production rate of the Chironico landslide: 4.15 ± 0.10 *at* g^{-1} a^{-1} rescaled for every longitude (Claude et al., 2014), latitude and elevation and considering no erosion correction, with the LSD scaling scheme (Lifton et al., 2014), the ERA40 atmospheric model (Uppala et al., 2005) and the Lifton VDM 2016 geomagnetic database (for ages in between 0-14 *ka*, Pavon-Carrasco et al., 2014 and for ages in between 14-75 *ka*, GLOPIS-75, Laj et al., 2004) by solving Eq. (3.3). [2] TCN age corr. tc_{max} correspond to the maximum corrected TCN exposure ages calculating from the best maximum 5% solution. For [1] and [2] the errors represent the internal errors. [3] Ages were inverted using Eq. (3.2) and prescribing 10^6 solutions for a range of time from 0 to t_0 (TCN age calculated using the ^{10}Be concentration of each sample and solving Eq. (3) in Lehmann et al., in review without erosion correction). All models were calculated using the following parameters: $\overline{\sigma\varphi_0} = 129\ a^{-1}$, $\mu = 0.596\ mm^{-1}$ and $D_0 = 500$ Gy. Specific $\dot{D}$ are show in Table A4.5. ⋆SS means steady state.

Table A4.3: Infrared stimulated luminescence at 50°C (IRSL50) experimental values of Trélaporte profile

MBTP1

C1			C2			C3		
x [mm]	Lx/Tx	Lx/Tx Err.	x [mm]	Lx/Tx	Lx/Tx Err.	x [mm]	Lx/Tx	Lx/Tx Err.
1.81	0.00	0.000	2.24	0.00	0.000	1.97	0.00	0.005
2.80	0.00	0.000	3.16	0.00	0.001	2.91	0.00	0.001
3.76	0.00	0.001	4.14	0.00	0.001	3.96	0.00	0.000
4.70	0.00	0.001	5.09	0.00	0.001	4.99	0.00	0.001
5.72	0.00	0.001	6.07	0.00	0.001	5.95	0.00	0.001
6.80	0.00	0.001	7.10	0.00	0.000	6.85	0.00	0.002
7.77	0.00	0.002	8.04	0.00	0.001	7.72	0.01	0.003
8.68	0.00	0.002	8.89	0.00	0.001	8.62	0.01	0.007
9.52	0.00	0.001	9.77	0.00	0.002	9.54	0.03	0.013
10.49	0.01	0.003	10.72	0.01	0.002	10.42	0.02	0.004
11.53	0.01	0.002	11.70	0.01	0.003	11.36	0.04	0.022
12.49	0.01	0.002	12.64	0.02	0.008	12.32	0.07	0.011
13.47	0.01	0.006	13.63	0.05	0.010	13.65	0.19	0.109
14.41	0.02	0.018	14.63	0.13	0.175	15.00	0.24	0.073
15.56	0.02	0.014	15.60	0.11	0.032	15.95	0.26	0.100
17.02	0.03	0.005	16.76	0.15	0.072	16.88	0.55	0.193
18.25	0.14	0.176	17.93	0.14	0.127	17.79	0.63	0.109
19.24	0.15	0.149	19.19	0.36	0.091	18.73	0.83	0.171
20.30	0.16	0.108	20.38	0.50	0.101	19.65	0.87	0.150
21.23	0.24	0.179	21.29	0.74	0.125	20.82	0.79	0.165
22.16	0.47	0.348	22.30	0.88	0.118	21.98	0.92	0.136
			23.45	0.97	0.139	22.89	0.91	0.073
			24.59	1.00	0.082	23.86	1.00	0.082

MBTP2

C1			C2			C3		
x [mm]	Lx/Tx	Lx/Tx Err.	x [mm]	Lx/Tx	Lx/Tx Err.	x [mm]	Lx/Tx	Lx/Tx Err.
2.20	0.00	0.000	3.25	0.00	0.000	3.06	0.00	0.001
3.17	0.00	0.001	4.04	0.00	0.000	4.52	0.00	0.001
4.20	0.00	0.001	4.97	0.01	0.009	5.53	0.01	0.015
5.18	0.04	0.045	5.93	0.01	0.010	6.39	0.00	0.001
6.22	0.01	0.004	6.96	0.01	0.008	7.32	0.01	0.005
7.41	0.02	0.020	7.93	0.01	0.009	8.39	0.02	0.002
8.50	0.02	0.021	8.83	0.04	0.030	9.33	0.02	0.004
9.47	0.01	0.005	9.74	0.02	0.006	10.40	0.05	0.017
10.47	0.06	0.006	10.64	0.04	0.009	11.46	0.13	0.003
11.51	0.01	0.003	11.48	0.09	0.001	12.70	0.06	0.015
12.60	0.05	0.019	12.43	0.06	0.003	13.87	0.40	0.338
13.71	0.06	0.022	13.50	0.07	0.021	14.85	0.17	0.196
14.66	0.09	0.039	14.46	0.06	0.040	15.88	0.46	0.270
15.86	0.15	0.069	15.38	0.25	0.207	16.94	0.47	0.341
17.86	0.07	0.046	16.60	0.35	0.290	18.00	0.24	0.139
19.62	0.34	0.310	18.06	0.47	0.102	18.96	0.41	0.237
20.60	0.51	0.107	19.17	0.60	0.113	19.95	0.67	0.527
21.58	0.35	0.259	20.06	0.61	0.375	21.32	0.90	0.055
22.53	0.43	0.22	21.00	0.78	0.057	22.64	0.83	0.058
23.53	0.58	0.044	22.08	0.94	0.016	23.59	0.97	0.060
24.58	0.96	0.260	23.12	0.96	0.037	24.59	1.00	0.111
25.63	1.00	0.164	23.98	1.00	0.041			
26.63	0.96	0.023						

MBTP5

C1			C2			C3		
x [mm]	Lx/Tx	Lx/Tx Err.	x [mm]	Lx/Tx	Lx/Tx Err.	x [mm]	Lx/Tx	Lx/Tx Err.
3.86	0.01	0.000	3.86	0.01	0.000	2.15	0.01	0.000
6.45	0.06	0.001	4.99	0.04	0.001	3.09	0.01	0.000
7.94	0.25	0.005	6.45	0.04	0.003	4.03	0.01	0.000
9.46	0.31	0.007	7.94	0.06	0.002	4.97	0.05	0.001
10.67	0.70	0.015	9.46	0.38	0.010	5.91	0.06	0.001
11.70	0.87	0.019	10.67	0.21	0.005	6.87	0.19	0.004
12.90	1.00	0.021	11.70	0.23	0.005	7.87	0.17	0.004
13.95	1.00	0.021	12.90	0.46	0.012	8.89	0.27	0.006
15.03	0.99	0.021	13.95	0.39	0.011	9.89	0.20	0.004
16.08	0.94	0.020	15.03	0.82	0.020	10.84	0.21	0.005
17.08	0.98	0.021	16.08	0.88	0.021	11.74	0.50	0.011
18.34	1.00	0.022	17.08	1.02	0.024	12.66	0.46	0.011
19.55	1.03	0.022	18.34	0.72	0.019	13.63	1.05	0.023
20.56	1.05	0.023	19.55	1.01	0.028	14.69	1.06	0.023
21.50	0.89	0.019	20.56	0.91	0.021	15.72	0.80	0.019
22.46	0.91	0.020	21.50	0.95	0.021	16.68	0.98	0.022
23.43	1.16	0.025	22.46	1.10	0.025	17.57	0.93	0.020
24.42	1.04	0.022	23.43	1.13	0.025	18.42	1.02	0.022
			24.42	0.96	0.022	19.32	1.16	0.025
			25.51	0.95	0.021			
			26.61	0.92	0.020			
			27.78	1.17	0.026			

MBTP6

C1			C2			C3		
x [mm]	Lx/Tx	Lx/Tx Err.	x [mm]	Lx/Tx	Lx/Tx Err.	x [mm]	Lx/Tx	Lx/Tx Err.
1.96	0.00	0.000	1.96	0.01	0.000	3.32	0.01	0.000
3.00	0.01	0.000	2.90	0.01	0.000	4.30	0.05	0.001
4.05	0.02	0.001	3.84	0.02	0.000	5.25	0.18	0.004
5.11	0.09	0.002	4.80	0.01	0.000	6.17	0.15	0.003
6.13	0.29	0.007	5.76	0.19	0.004	7.09	0.44	0.010
7.19	0.30	0.008	6.72	0.17	0.004	8.00	0.79	0.017
8.29	1.01	0.022	7.71	0.62	0.013	8.93	0.92	0.020
9.29	0.81	0.017	8.69	0.79	0.017	9.85	1.00	0.021
10.27	0.79	0.019	9.68	1.11	0.024	10.76	0.85	0.018
11.34	0.86	0.019	10.61	0.72	0.016	11.67	1.12	0.024
12.39	0.81	0.020	11.53	0.73	0.018	12.58	0.96	0.021
13.40	1.14	0.025	12.46	0.71	0.016	13.50	0.99	0.021
14.29	1.04	0.023	13.40	0.71	0.017	14.41	0.97	0.021
15.26	0.98	0.023	14.49	1.23	0.026	15.33	0.96	0.021
17.48	1.28	0.028	15.56	1.16	0.025	16.25	0.93	0.021
			16.49	1.09	0.024	17.16	0.99	0.021
			17.45	1.18	0.025	18.14	1.00	0.021
			18.38	1.14	0.024	19.14	0.99	0.022
			19.32	0.97	0.021	20.07	1.08	0.023
			20.31	0.99	0.021	21.02	0.93	0.020
			21.26	1.03	0.022	21.93	1.02	0.022
			22.19	1.08	0.023	22.85	1.65	0.037
			23.11	1.14	0.025	23.78	0.85	0.024

MBTP9

C1			C2			C3		
x [mm]	Lx/Tx	Lx/Tx Err.	x [mm]	Lx/Tx	Lx/Tx Err.	x [mm]	Lx/Tx	Lx/Tx Err.
1.79	0.00	0.000	9.21	0.00	0.000	2.09	0.00	0.000
2.98	0.00	0.000	10.28	0.02	0.000	3.11	0.00	0.000
4.09	0.00	0.000	11.31	0.01	0.000	4.08	0.00	0.000
5.13	0.00	0.000	12.37	0.02	0.000	5.02	0.00	0.000
6.16	0.00	0.000	12.37	0.05	0.000	5.95	0.00	0.000
7.15	0.00	0.000	13.48	0.15	0.000	6.89	0.01	0.000
8.13	0.00	0.000	18.12	0.64	0.010	7.84	0.03	0.001
9.21	0.00	0.000	24.27	1.00	0.020	8.80	0.01	0.000
10.28	0.01	0.000				9.78	0.04	0.001
11.31	0.05	0.000				10.76	0.05	0.001
12.37	0.09	0.000				11.72	0.05	0.001
13.48	0.60	0.012				12.70	0.06	0.001
14.77	0.15	0.000				13.66	0.13	0.003
15.99	0.77	0.012				14.60	0.40	0.009
17.05	0.77	0.012				15.59	0.63	0.013
18.12	0.94	0.023				16.57	0.34	0.007
19.13	0.88	0.023				17.44	0.76	0.016
20.17	0.93	0.023				18.30	0.97	0.021
21.23	0.93	0.02				19.24	0.93	0.020
22.26	1.06	0.023				20.22	1.10	0.023
23.27	1.09	0.023						
24.27	1.11	0.023						
25.28	1.07	0.023						

MBTP11

C1			C2			C3		
x [mm]	Lx/Tx	Lx/Tx Err.	x [mm]	Lx/Tx	Lx/Tx Err.	x [mm]	Lx/Tx	Lx/Tx Err.
1.17	0.00	0.000	2.42	0.00	0.000	2.62	0.05	0.000
2.05	0.00	0.000	3.37	0.00	0.000	3.57	0.01	0.000
2.98	0.00	0.000	4.32	0.00	0.000	4.67	0.01	0.000
3.90	0.02	0.000	5.23	0.00	0.000	5.67	0.08	0.002
4.83	0.00	0.000	6.16	0.00	0.000	6.75	0.04	0.001
5.77	0.03	0.001	7.14	0.02	0.000	7.85	0.06	0.001
6.71	0.02	0.000	8.02	0.08	0.002	8.89	0.08	0.002
7.66	0.04	0.001	8.93	0.32	0.007	9.97	0.34	0.007
8.60	0.19	0.004	9.99	0.47	0.010	12.61	0.54	0.012
9.50	0.49	0.012	11.03	0.29	0.006	15.20	0.72	0.016
10.39	0.38	0.009	11.96	0.67	0.014	16.37	0.90	0.020
11.33	0.56	0.012	12.89	0.71	0.015	17.50	1.07	0.023
12.29	0.77	0.018	15.17	0.80	0.017	18.49	0.92	0.020
13.15	1.02	0.023	17.45	1.02	0.022	19.65	1.00	0.021
14.09	0.94	0.022	18.58	0.96	0.020	20.77	1.03	0.022
15.11	0.89	0.021	19.73	0.97	0.021	21.83	1.03	0.022
16.09	0.97	0.025	20.68	1.14	0.024	22.93	1.05	0.022
17.03	0.88	0.036	21.72	1.03	0.022			
17.96	1.01	0.03	22.73	1.12	0.024			
18.91	1.00	0.022	23.71	0.87	0.019			
19.82	1.13	0.025	24.69	0.79	0.017			
20.70	1.00	0.026	25.69	1.12	0.024			
21.71	1.04	0.024	26.67	0.99	0.021			
22.82	1.10	0.025						

Table A4.4: Infrared stimulated luminescence at 50°C (IRSL50) experimental values of Moine profile

MBAM1								
	C1			C2			C3	
x [mm]	Lx/Tx	Lx/Tx Err.	x [mm]	Lx/Tx	Lx/Tx Err.	x [mm]	Lx/Tx	Lx/Tx Err.
1.44	0.00	1.445	2.13	0.00	0.00	2.19	0.93	0.02
2.86	0.00	2.865	3.18	0.00	0.00	3.12	1.00	0.02
4.15	0.00	4.155	4.02	0.00	0.00	4.03	1.04	0.02
5.25	0.00	5.259	4.85	0.00	0.00	4.88	1.21	0.03
6.23	0.00	6.243	5.69	0.00	0.00	5.76	0.86	0.02
7.14	0.00	7.152	6.99	0.01	0.00	6.72	1.13	0.02
8.04	0.00	8.049	8.95	0.02	0.00	7.65	0.85	0.02
8.99	0.00	9.000	10.71	0.03	0.00	8.51	0.64	0.01
9.86	0.00	9.877	11.66	0.39	0.02	9.37	0.66	0.01
10.67	0.00	10.686	12.71	0.20	0.01	10.22	0.76	0.02
11.65	0.00	11.667	13.83	0.20	0.00	11.18	0.62	0.01
12.67	0.00	12.689	14.72	0.63	0.02	12.17	0.65	0.01
13.62	0.00	13.643	15.74	0.51	0.01	13.06	0.83	0.02
14.57	0.00	14.597	17.24	0.87	0.02	13.99	0.72	0.02
15.51	0.00	15.532	18.74	0.73	0.02	14.90	0.79	0.02
16.40	0.00	16.423	19.64	0.94	0.02	15.79	0.69	0.02
17.28	0.00	17.307	20.58	1.22	0.04	17.10	0.76	0.02
18.29	0.00	18.324	21.50	1.00	0.02	18.38	0.81	0.02
19.61	0.00	19.641	22.40	0.94	0.04	19.26	0.54	0.01
20.78	0.00	20.816	23.30	0.84	0.02	20.16	0.47	0.01
21.68	0.00	21.715	24.22	1.03	0.02	21.05	0.45	0.01
22.67	0.00	22.709	25.09	1.04	0.02	21.91	0.23	0.01
23.63	0.00	23.671				22.80	0.16	0.00

MBAM2						MBAM3					
	C1			C2			C1			C2	
x [mm]	Lx/Tx	Lx/Tx Err.	x [mm]	Lx/Tx	Lx/Tx Err.	x [mm]	Lx/Tx	Lx/Tx Err.	x [mm]	Lx/Tx	Lx/Tx Err.
2.66	0.00	0.000	0.63	0.06	0.043	3.61	0.00	0.000	0.60	0.01	0.001
3.81	0.00	0.000	1.90	0.00	0.000	4.52	0.00	0.000	1.87	0.00	0.000
4.73	0.00	0.001	2.92	0.00	0.000	5.52	0.02	0.001	2.93	0.00	0.000
5.62	0.00	0.000	3.96	0.00	0.000	6.40	0.03	0.001	3.91	0.00	0.000
6.48	0.00	0.000	4.93	0.00	0.000	7.23	0.09	0.002	4.86	0.00	0.000
7.37	0.01	0.001	5.91	0.00	0.000	8.59	0.02	0.000	5.90	0.01	0.000
8.26	0.02	0.000	6.98	0.00	0.000	10.14	0.18	0.004	6.98	0.00	0.000
9.16	0.00	0.000	7.98	0.00	0.000	11.14	0.13	0.003	8.21	0.02	0.001
10.03	0.02	0.001	8.95	0.00	0.000	12.25	0.11	0.003	9.34	0.05	0.002
10.93	0.03	0.001	9.92	0.05	0.001	13.54	0.76	0.016			
11.85	0.02	0.000	10.91	0.04	0.001	14.75	0.89	0.020			
12.74	0.04	0.001	11.90	0.09	0.008	15.77	0.95	0.021			
13.63	0.05	0.001	12.94	0.07	0.002	16.68	1.04	0.025			
14.53	0.20	0.004	14.02	0.14	0.003	17.64	1.02	0.022			
15.65	0.45	0.010	15.10	0.43	0.009	18.53	0.95	0.021			
16.71	0.61	0.013	16.12	0.65	0.014	19.41	1.06	0.023			
17.62	0.79	0.018	17.13	0.79	0.017	20.42	0.86	0.019			
18.56	0.92	0.020	18.20	0.92	0.020	21.42	1.09	0.024			
19.44	0.96	0.024	19.18	0.97	0.021	22.38	1.03	0.022			
20.35	1.03	0.023	20.15	0.97	0.021	23.33	1.04	0.023			
21.28	1.02	0.023	21.16	0.83	0.018	24.29	1.03	0.027			
			22.25	1.02	0.022	25.21	0.92	0.021			
			23.33	1.09	0.025						
			24.31	1.18	0.026						

Table A4.5: Infrared stimulated luminescence at 50°C (IRSL50) experimental values of the calibration sites

MBTP7								
C1			C2			C3		
x [mm]	Lx/Tx	Lx/Tx Err.	x [mm]	Lx/Tx	Lx/Tx Err.	x [mm]	Lx/Tx	Lx/Tx Err.
0.33	0.00	0.000	0.36	0.05	0.001	0.40	0.00	0.000
1.34	0.00	0.000	1.46	0.00	0.000	1.59	0.00	0.000
2.49	0.00	0.000	2.64	0.01	0.000	2.75	0.00	0.000
3.65	0.01	0.000	3.77	0.01	0.000	3.88	0.00	0.000
4.73	0.01	0.000	4.84	0.02	0.000	5.01	0.01	0.000
5.84	0.02	0.001	5.91	0.03	0.001	6.06	0.02	0.000
6.91	0.11	0.002	6.96	0.06	0.001	7.11	0.03	0.001
7.93	0.17	0.004	7.97	0.07	0.002	8.15	0.12	0.003
8.96	0.38	0.008	8.99	0.16	0.003	9.19	0.36	0.008
10.06	0.51	0.011	9.99	0.42	0.009	10.29	0.69	0.015
11.16	0.66	0.014	11.04	0.62	0.013	11.38	0.66	0.014
12.09	0.94	0.020	12.10	0.72	0.015	12.42	0.84	0.018
13.11	0.99	0.021	13.12	0.87	0.019	13.44	0.87	0.018
14.22	1.02	0.022	14.20	1.06	0.023	14.45	0.92	0.023
15.35	1.05	0.022	15.28	1.00	0.021	15.63	0.67	0.014
16.50	0.98	0.021	16.28	1.00	0.021	16.81	1.03	0.022
17.54	1.03	0.022	17.26	1.01	0.021	17.89	1.18	0.025
18.61	1.09	0.023	18.32	1.03	0.022	18.97	1.02	0.022
19.61	1.12	0.024	19.64	0.88	0.019	20.01	0.91	0.019
20.60	1.05	0.023	20.88	1.04	0.022	21.03	0.95	0.020
21.63	0.93	0.020	21.89	1.10	0.023	22.07	0.98	0.021
22.65	0.93	0.020	22.93	1.02	0.022	23.11	0.96	0.020
23.80	0.87	0.019	23.95	0.97	0.021	24.20	0.97	0.021
			25.02	1.02	0.022			

MBTP8								
C1			C2			C3		
x [mm]	Lx/Tx	Lx/Tx Err.	x [mm]	Lx/Tx	Lx/Tx Err.	x [mm]	Lx/Tx	Lx/Tx Err.
2.00	0.00	0.000	2.00	0.00	0.000	2.33	0.00	0.000
2.95	0.00	0.000	2.95	0.00	0.000	3.34	0.01	0.000
3.92	0.00	0.000	3.92	0.00	0.000	4.41	0.02	0.000
4.93	0.00	0.000	4.93	0.00	0.000	5.44	0.08	0.002
5.93	0.00	0.000	5.93	0.00	0.000	6.49	0.04	0.001
6.90	0.01	0.000	6.90	0.01	0.000	7.56	0.05	0.001
7.87	0.09	0.002	7.87	0.09	0.002	8.61	0.06	0.001
8.87	0.32	0.007	8.87	0.32	0.007	9.63	0.07	0.002
9.85	0.64	0.013	9.85	0.64	0.013	10.62	0.09	0.002
10.81	0.81	0.017	10.81	0.81	0.017	11.60	0.08	0.002
11.77	0.80	0.017	11.77	0.80	0.017	12.56	0.57	0.012
12.74	0.99	0.021	12.74	0.99	0.021	13.49	0.61	0.013
13.72	0.93	0.020	13.72	0.93	0.020	14.48	1.01	0.021
14.67	0.84	0.018	14.67	0.84	0.018	15.53	1.44	0.031
15.86	0.89	0.019	15.86	0.89	0.019	16.76	1.16	0.025
17.06	1.11	0.024	17.06	1.11	0.024	17.94	0.89	0.019
18.01	0.83	0.018	18.01	0.83	0.018	18.92	0.92	0.019
18.98	1.06	0.023	18.98	1.06	0.023	19.95	0.81	0.017
19.93	1.12	0.02	19.93	1.12	0.024	20.99	0.88	0.019
20.88	1.12	0.024	20.88	1.12	0.024	23.03	0.99	0.021
21.83	0.97	0.020	21.83	0.97	0.020	24.05	1.00	0.021
22.78	1.06	0.022	22.78	1.06	0.022	25.08	1.05	0.022
23.73	1.09	0.023	23.73	1.09	0.023	26.11	0.85	0.018
24.66	1.00	0.021	24.66	1.00	0.021			

Table A4.6: Dosimetry calculations for the feldspar samples analyzed.

Sample ID	U [ppm]	Th [ppm]	K [ppm]
MBAM1	7.17 ± 0.16	25.0 ± 0.4	3.53 ± 0.05
MBAM2	7.34 ± 0.16	28.0 ± 0.5	3.85 ± 0.05
MBAM3	8.33 ± 0.18	20.0 ± 0.3	3.32 ± 0.04
MBTP1	5.69 ± 0.12	36.8 ± 0.6	2.56 ± 0.03
MBTP2	5.77 ± 0.13	20.0 ± 0.3	3.71 ± 0.05
MBTP5	7.37 ± 0.16	21.0 ± 0.4	3.68 ± 0.05
MBTP6	8.75 ± 0.19	26.0 ± 0.4	3.88 ± 0.05
MBTP9	2.76 ± 0.06	12.0 ± 0.2	5.14 ± 0.07
MBTP11	7.66 ± 0.17	19.0 ± 0.3	4.32 ± 0.07

Conversion factors has been chosen after Adamiec and Aitken (1998). Alpha-particle attenuation and Beta-particle attenuation factors have been chosen after Bell (1980) and Mejdahl (1979) respectively. Cosmic dose rates have been calculated using the method of Prescott and Hutton (1994), assuming an overburden density of 2.7±0.1 $g\ cm^{-3}$. Internal K concentration is assumed to be 12±0.5% for both samples. Environmental dose rates were calculated using DRAC online calculator (Durcan et al., 2015), assuming a grain size between 750 and 1000 μm and water content of 2%.

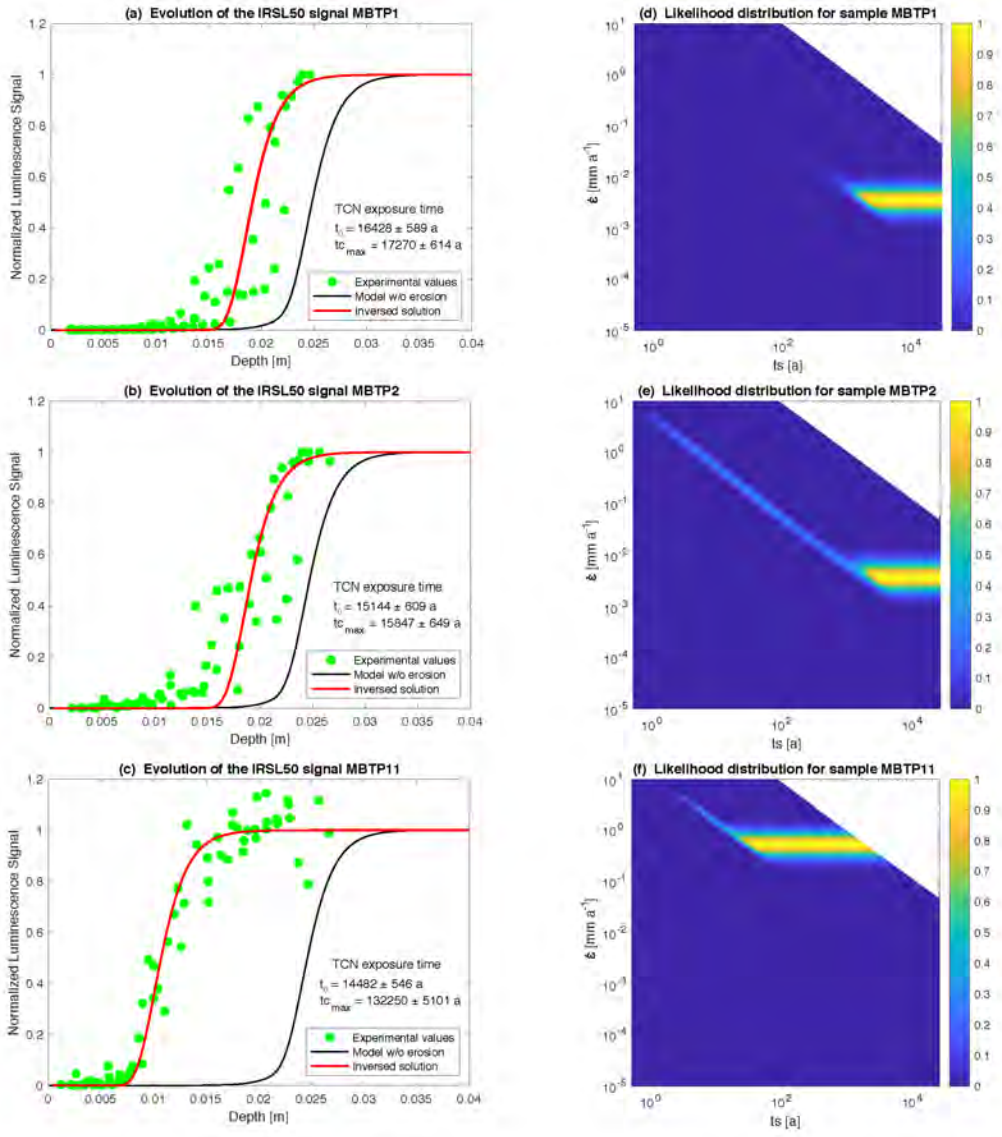

Figure A4.3: IRSL50 profiles and inversion results for samples MBTP1, MBTP2 and MBTP11. (a), (b) and (c) Green dots represent the measured IRSL50 profiles for samples MBTP1, MBTP2 and MBTP11 respectively. Black lines represent the reference profiles and taking the TCN exposure age with no erosion correction (t_0). Red lines represent inferred fits where the likelihood is greater 0.95. tc_{max} represents the maximum corrected TCN exposure age. (d), (e) and (f) represent the likelihood distributions inverted from respective insets (a), (b) and (c).

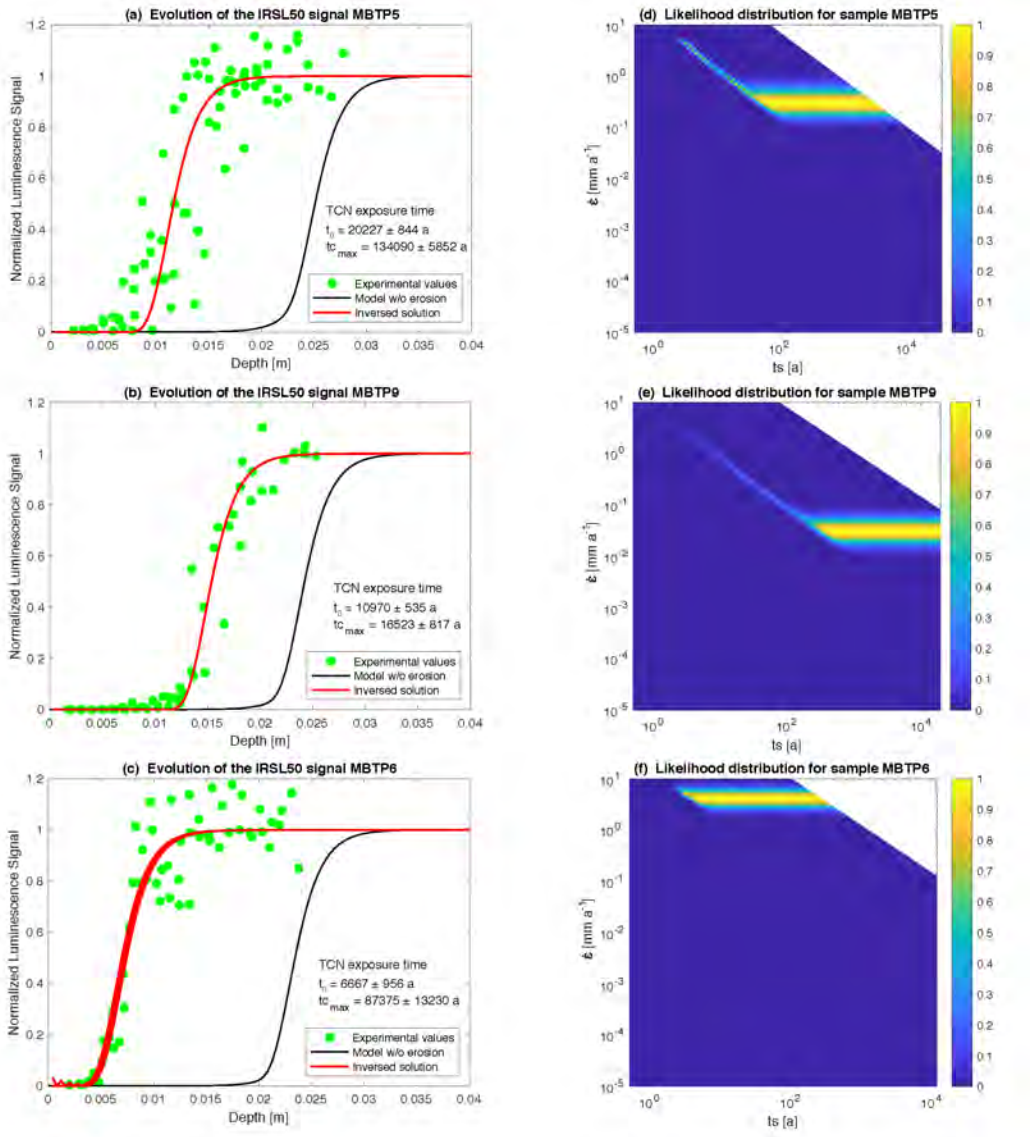

Figure A4.4: IRSL50 profiles and inversion results for samples MBTP5, MBTP9 and MBTP6. (a), (b) and (c) Green dots represent the measured IRSL50 profiles for samples MBTP1, MBTP2 and MBTP11 respectively. Black lines represent the reference profiles and taking the TCN exposure age with no erosion correction (t_0). Red lines represent inferred fits where the likelihood is greater 0.95. tc_{max} represents the maximum corrected TCN exposure age. (d), (e) and (f) represent the likelihood distributions inverted from respective insets (a), (b) and (c).

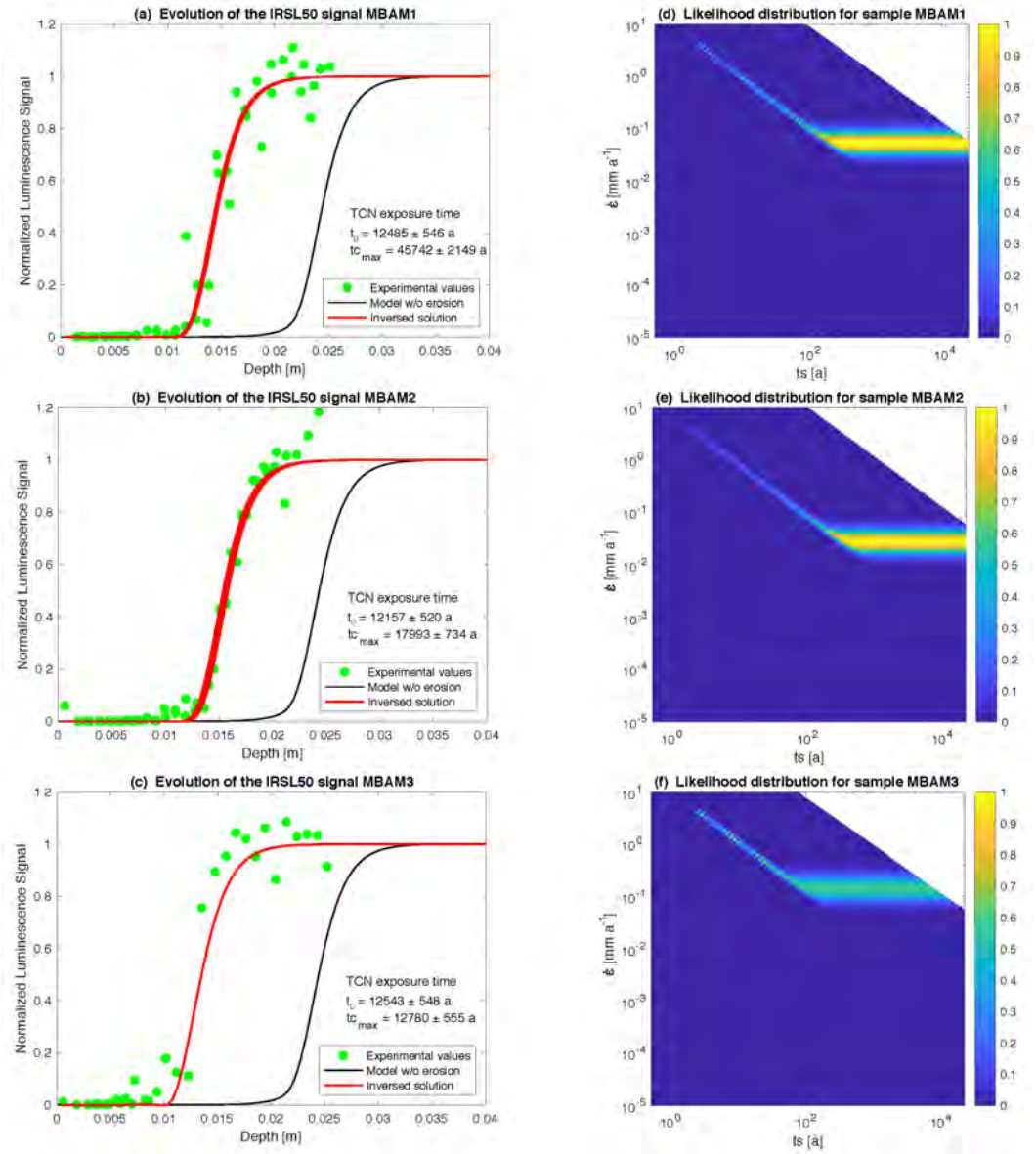

Figure A4.5: IRSL50 profiles and inversion results for samples MBAM1, MBAM2 and MBAM3. (a), (b) and (c) Green dots represent the measured IRSL50 profiles for samples MBTP1, MBTP2 and MBTP11 respectively. Black lines represent the reference profiles and taking the TCN exposure age with no erosion correction (t_0). Red lines represent inferred fits where the likelihood is greater 0.95. tc_{max} represents the maximum corrected TCN exposure age. (d), (e) and (f) represent the likelihood distributions inverted from respective insets (a), (b) and (c).

CHAPTER 8

OSL surface exposure dating protocols

The methodology for Optically Stimulated Luminescence (OSL) surface exposure dating sampling, preparation and analysis of bedrock surfaces was not clearly detailed nor properly developed when I started this PhD project. I have passed a significant amount of time testing, developing and improving each step, from the field to the lab, to allow this new dating method to perform at its full potential- both in terms of quality and reproducibility. In this chapter, I will detail each step, including field preparation, sampling strategy, field sampling as well as the coring of the samples in the lab, slicing of the cores and finally the luminescence analysis test (A6.1). The hope is that these detailed descriptions will benefit future studies using OSL surface exposure dating.

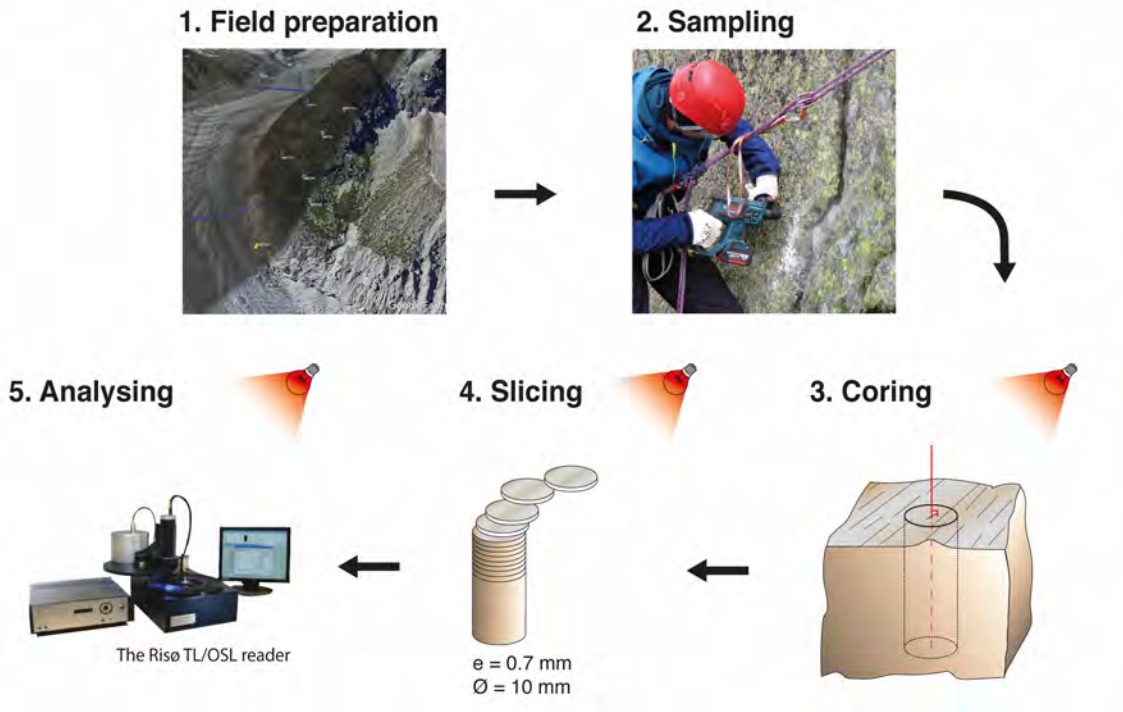

Figure 8.1: Schematic of all the steps needed to apply OSL surface exposure dating.

8.1 Field preparation

In terms of field and sampling preparation, one should clearly identify the geomorphological processes she/he wants to study and, by consequence, identify the natural structure best suited to study such processes. Two separated areas have to be considered: (1) the calibration sites and (2) the sites of unknown exposure age where the dating will be applied. Both sites need to be in the same geographic region, and from the same lithology. The calibration sites should reflect, as closely as possible, the topographic and geomorphic conditions of the bedrock surface where OSL surface exposure dating will be applied. These conditions include

the slope angle, orientation, presence of vegetation or topographic shielding, surface texture, mineral distribution and snow or lichen cover. Every bedrock surface with an independently known exposure age which meets the criteria mentioned above, and has experienced negligible erosion post-exposure, can be considered a valid calibration site. Such sites can be chosen from pre-existing bedrock surfaces present in mountainous environment, such as glacial polish with historically constrained ages, rock fall scars and road/track cuts. Alternatively, they can also be artificially created during a first phase of sampling and the fresh surfaces exposed during this sampling can be re-sampled at a later date. As mentioned above, the bedrock surface sampled has to be representative of the specific geomorphologic process of interest. For this study, the Trélaporte transect lies on a rock shoulder (green area in Fig. 8.2) and thus reflects the evolution of the main glacier, the Mer de Glace (blue area in Fig. 8.2). The potential influence of tributary glaciers is avoided (red dashed area in Fig. 8.2). All these preparation steps should be performed before the sampling campaign in order to make the sampling as efficient as possible. Once in the field, all preparation steps should be re-evaluated, since in-situ observations are complementary to information from maps, remote sensing and literature.

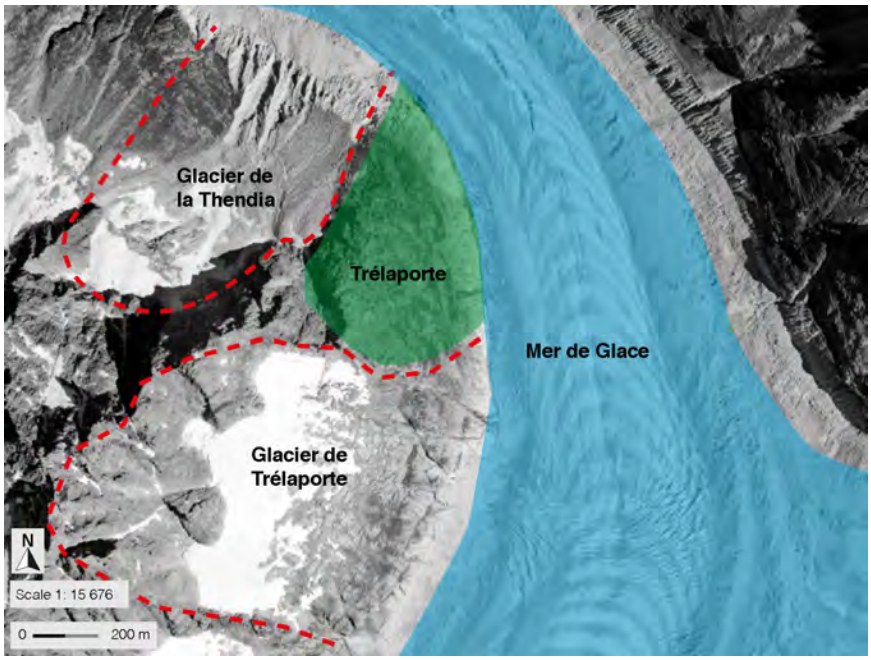

Figure 8.2: Schematic illustrating how best to choose the relevant sampling sites (green area) in order to study the ice-thickness fluctuations of the Mer de Glace (blue area) and avoid signals from the glacial tributaries (dashed red areas). The orthophotography was downloaded from geoportail.gouv.fr.

8.2 Sampling campaign

Surface conditions

To successfully date past ice thicknesses, the bedrock surfaces best suited for OSL surface exposure dating are those with well-preserved glacial erosion patterns (i.e., visible glacial striations, roches mountonnes). It is important to be sure that a sampled surface reflects a glaciological signal, showing that the surface was at some point covered by a glacier. Importance should be given to surfaces presenting striations parallel to the studied glacier flow, to minimize any potential influences of tributary glaciers (Fig. 8.2). Samples should be taken down a rough vertical transect adjacent to the glacier, to be able to capture the desired ice lowering signal. The same conditions must be selected to all surfaces over the same transect. Topographic shielding effects and vegetation cover (i.e., moss or lichen) should be kept to a minimum. Steep slopes are preferred (over 30° from the horizontal) to minimize the effect of snow cover shielding. The sampled surface should be at least 1.50 m from its relative ground level to reduce the possibility of cover from rock debris, vegetation or snow. Finally, luminescence signals are sensitive to rock water content, and so bedrock surfaces should be selected far from streams or any other traces suggesting a recurring presence of water flow.

In-situ measurements and observations

I recommend that the sampling protocol for Terrestrial Cosmogenic Nuclide (TCN) dating as proposed by Gosse and Phillips (2001) is followed, which includes:

1. Rationale for sample selection.
2. Description of object sampled.
3. Description of sample material.
4. Location of sample.
5. Orientation of sample.
6. Sample thickness.
7. Shielding geometry.
8. Subsurface profile samples.

I will not go into detail regarding this protocol here, and I refer the reader to Gosse and Phillips (2001) for a complete description of these in-situ observations and measurements.

Sampling equipment

The main difference between samples used for TCN compared to OSL surface exposure dating is the need to preserve the sample in its entirety to be able to perform coring in a direction perpendicular to the surface. While a sample for TCN dating can be fragmented for the purpose of being crushed and sieved once in the laboratory, OSL surface exposure dating requires an intact sample with enough material for a minimum of three cores. Furthermore, the coring location at the surface of a sample should be spaced approximately 2-3 *cm* from the edge of the sample, in order to avoid any side exposure contamination of the natural luminescence signal which may have occurred during sampling. To be able to satisfy all these conditions, the sample dimensions during sampling should therefore be at least 15x15 *cm* wide and 5 *cm* thick. The extraction of a sample with such dimensions in its entirety is challenging, and the ease of such sampling depends greatly on the lithology, the quality of the rock and the sampling equipment. In high mountain environments, the chosen equipment has to be adapted to the difficulties encountered with reaching the different bedrock surfaces. In conditions where the sites are easily accessible (e.g., the Gornergletscher with the Gornergrat train), heavy material and efficient equipment can be used. If the sites require abseiling or a long and steep approach, a more compact and easily manipulated equipment set is necessary. In the following sections, I will describe four sets of equipment which differ in efficiency and practicality. Note that during the sampling effort, part of the surface of interest can be damaged or can flake off. In order to be able to assess the amount of damage the surface has experienced, one should take a picture before sampling. It can also be beneficial to mark the surface using an indelible pen (as shown in Figs. 8.5c and 8.6b). There is a low risk of light contamination of the natural luminescence signal of the inner part of the sample just by exposing the fresh side for a few minutes. However, I recommend that the sample be packed into a black/opaque bag immediately after sampling to minimize this risk.

The starter pack

The starter pack is composed of chisels and a shorthanded sledgehammer. This set is really light and handy, but not the most efficient. It is adapted for metamorphic lithologies, with pre-existing fabrics which can be exploited in order to extract the sample. The most suitable rock surface will be one with existing free surfaces (Fig. 8.3).

The drilling pack

The second sampling equipment set is composed of chisels, a shorthanded sledgehammer and a battery powered rotary hammer (for example a GBH18V-26K24 Bosch model). The suitable site should present some free surfaces (red area in Fig. 8.3c). The sampling is made more

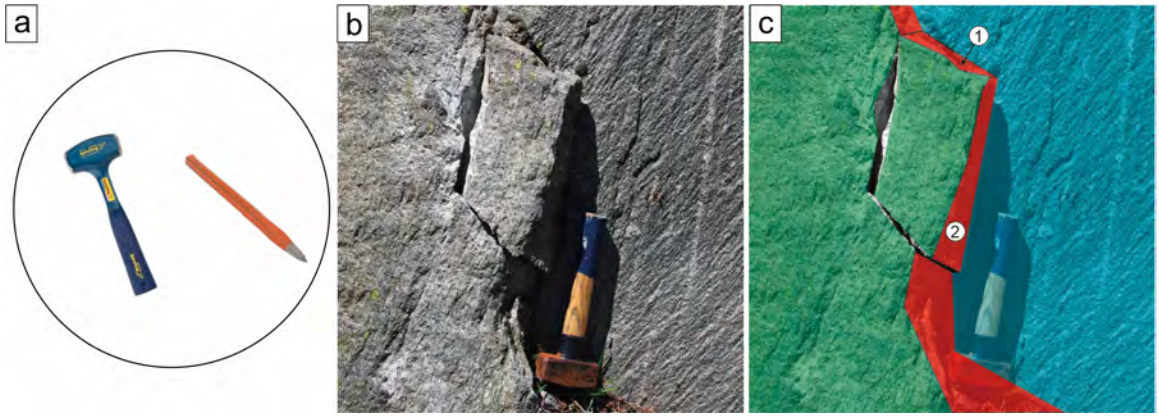

Figure 8.3: (a) Example of a chisel and shorthanded sledgehammer. (b) Picture of a surface sample along the Montenvers transect (sample MBMV7). (c) Schematic of the sample surface showing the surface of interest (in green), the free surfaces (1) horizontal and (2) vertical (in red) and the unwanted surface (in blue).

efficient by drilling a series of holes into the bedrock, organized in lines defining the dimension of the sample (white dots in Fig. 8.3c). Once these holes are made in a pattern thats close and deep enough, they can be punched with the chisel and sledgehammer to propagate the fracture along the hole lines. One should consider that the use of the rotary hammer should only be done for sites where sampling solely with a hammer and chisel is difficult, because the hammers battery capacity is limited. This approach is also costly in terms of drill heads, one should take the rock hardness into account and bring spare drill heads accordingly.

Figure 8.4: (a) Example of a battery powered rotary hammer (GBH18V-26K24 Bosch model). (b) Picture of a surface sample along the Moine transect. (c) Schematic of the sample surface showing the surface of interest (in green), the free surfaces (in red), the unwanted surface (in blue) and the drill holes (white dots), which should be later punched with a chisel and hammer to propagate the fracture and collect the sample.

The heavy pack

The third set of sampling equipment is composed of a fuel powered power cutter mounted with diamond blades (for example a Husqvarna power cutter K760 model, shown in Fig. 8.5a). This equipment considerably improves the ease of sampling a surface, without the need for free surfaces, and also enables the user to take more material. However, it is considerably heavier and less handy than the equipment set presented above (its total weight is about 12 kg, including a filled fuel tank and blade). Consequently, it is only suitable equipment for a location where the sampling surface is easy to reach, and where there is no need to perform abseiling or a long and steep approach. The saw makes it possible to take samples in really well-preserved polished bedrock surfaces, without the requirement of pre-existing fractures or free surfaces. Two vertical cuts along with three horizontal cuts are sufficient to isolate two blocks of bedrock. Once the cuts are performed, a flat head chisel is inserted into the cut and punched with a hammer to extract the sample block. One should consider the pre-existing fabric (such as foliation and schistosity) of the surface to avoid breaking the block apart during sampling, and thus not successfully collecting an intact whole sample. Experience has shown that punching the rock parallel to its surface avoids breaking the sample apart. The cutting induces a strong heating at the bedrock surface, which is not a problem for analysis, but can damage the equipment. If this is the case during sampling, one should take a break to allow the blade to cool down.

Figure 8.5: (a) Example of a fuel powered power cutter mounted with diamond blades (Husqvarna power cutter K760 model in the present case). (b) Sebastian Vivero sampling a polished bedrock surface on the side of the Gornergletscher for Joanne Elkadis PhD project. (c) Picture of the resulting cut in the bedrock, providing two blocks of sample (arrow showing the direction of the steepest descent in order to orientate the sample once in the lab).

The optimal pack

The last set of equipment presented in this section combines chisels, a shorthanded sledge-hammer, a battery powered rotary hammer and a battery powered angle grinder mounted with diamond blades (for example a Hilti AG 150-A36, shown Fig. 8.6a). This set is handy, light and suitable for locations where the sampling surfaces are difficult to reach, involving a long and steep approach or abseiling. The angle grinder blade does not allow a cut as deep into the bedrock surface as the power cutter. To overcome this limitation, the angle grinder can be used to start isolating the sample by remove a rock wedge (Fig. 8.6b and 1 in Fig. 8.6c), making it possible to drill and isolate the deepest part of the sample (Fig. 8.6b and 2 in Fig. 8.6c).

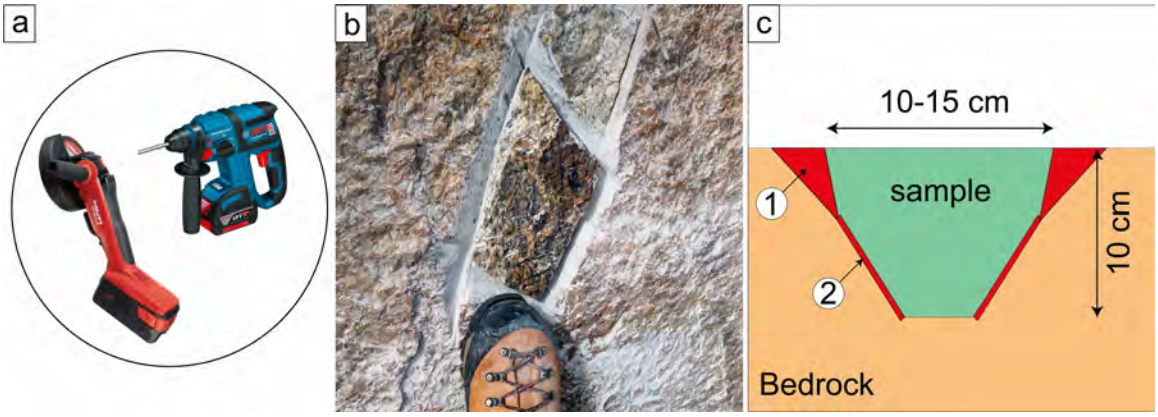

Figure 8.6: (a) Examples of a battery powered angle grinder (Hilti AG 150-A36 model) and battery powered rotary hammer (GBH18V-26K24 Bosch model). (b) Example of a surface sample while abseiling at the Aiguille du Midi for Dilan Rech's master project. (c) Schematic of a cross-section of a bedrock surface sampled with an angle grinder and a rotary hammer. First a rock wedge is removed using the angle grinder (1) and the base of the sample is isolated through drilling with rotary hammer (2).

General warning

In general, the use of all the equipment mentioned above needs training, practice, good balance and confidence. It also needs the proper set of personal protective equipment. The use of a helmet, adapted protective gloves and glasses, a dust mask and ear protection are strongly recommended. Working in steep and remote high mountainous environments requires skills in organizing the optimal timing, in using security equipment and in evaluating fast changing weather condition. One should be aware of the experience and fitness levels of team members and evaluate if the need of a high mountain guide is necessary. The sampling techniques mentioned above are considerably damaging to the bedrock surface and leave permanent scars in the landscape. One should be sure to have permission to sample such locations, requesting sampling permits from the corresponding authorities if necessary. It is also recommended to

sample far from touristic tracks or climbing routes to lower the visual impact of the sampling work.

8.3 Sample coring

Once the sample is collected in the field, it is brought to the laboratory to be cored. From this step onwards, all the sample preparation is done in subdued red-light conditions to avoid light contamination of the natural luminescence signal. The coring of the sample is the most uncertain preparation step as fully intact cores are required to proceed with the sample preparation. Unfortunately, depending on the lithology, a core can easily break while being made, rendering the use of that particular core impossible. In some cases, it can be quite laborious to produce 3 cores from a sample. Samples are collected from time consuming, costly, and physically demanding sampling campaigns, and should therefore be exploited to their maximum capacity in the lab. A lot of effort was invested during this PhD in making this step as efficient as possible. To achieve the most successful coring, the sample has to be stable. It is recommended to saw the base of the sample and create a flat surface parallel to the surface of interest (Fig. 8.7a). Following this, the coring is performed, in the Lausanne labs using a Husqvarna DM220 driller, in the presence of cold, running water (Fig. 8.8). During the coring, it is important that the sample is stabilized using either a clamp system or with the help of an assistant manually holding the sample. Cores have to be taken perpendicularly to the surface of interest (Fig. 8.7b), at 2-3 cm from the edge of the sample to avoid extracting a core with a potentially contaminated natural luminescence signal from side exposure during sampling. I recommend taking as many cores as possible.

The dimension of the cores is ideally ≤ 2 cm of diameter and ≥ 3 cm long. As mentioned previously, the cores break easily. Therefore, it is recommended to try different core diameters in order to find the appropriate diameter for the rock texture in question. If all the coring fails, in that every core has broken and there is limited sample material remaining, an alternative is to exploit the space remaining in between several attempted cores (illustrated by the red circle 2 in Fig. 8.7c). The sample can also be cut with a saw in cuboid. The principle aim from this sample preparation step is to have material that represents a continuous profile from the surface to the inner part of the sample, with a length of ≥ 3 cm. As such, the exact shape of this piece is a negligible point.

8.4 Rock slicing

Once extracted from the rock sample, the cores have to be sliced into approximately 0.7 mm thick discs. The Lausanne laboratories use a BUEHLER IsoMet low speed saw mounted with

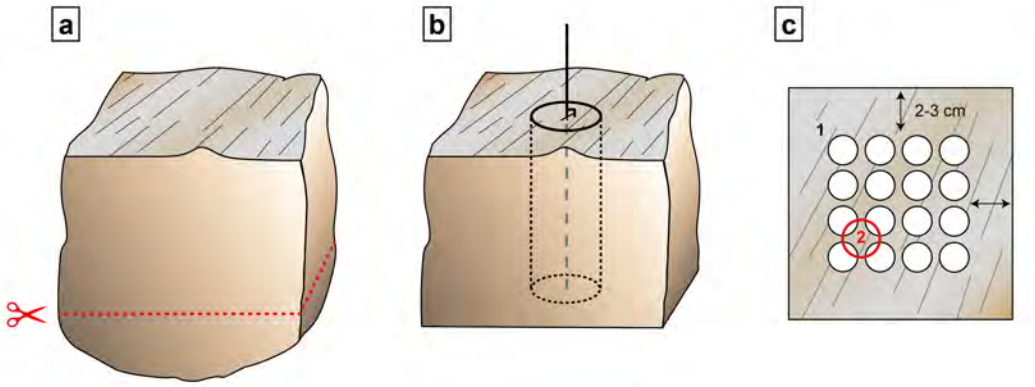

Figure 8.7: (a) Schematic of how the flat basal surface should be sawed parallel to the surface of interest. (b) Schematic of how a core should be made perpendicular to the surface. (c) Top view of a cored surface, highlighting the distance of the cores from the sample sides. 1 represents the conventional way to core, 2 shows an alternative method to exploit material if the previous coring attempts have failed.

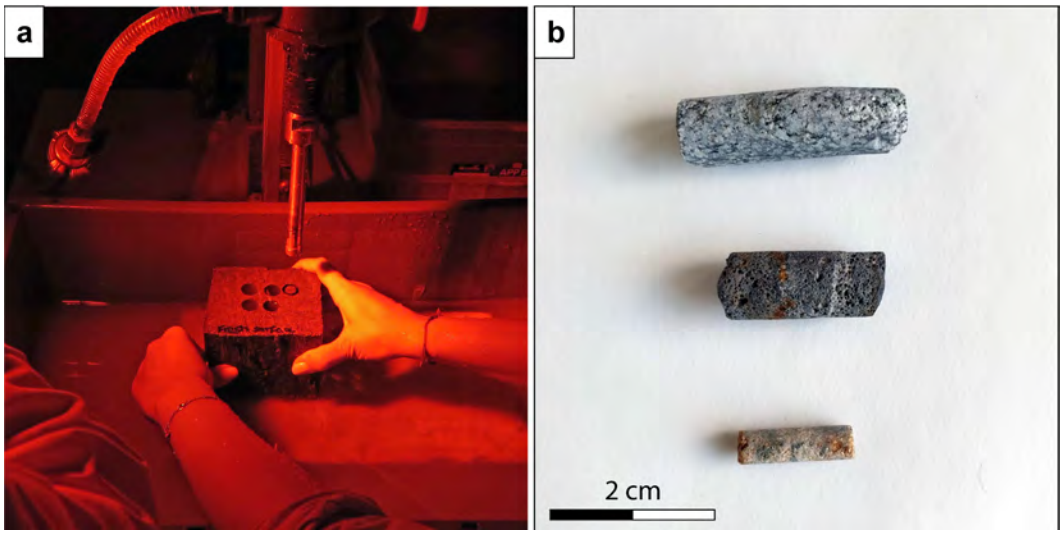

Figure 8.8: (a) Picture of coring performed by Joanne Elkadi and Dilan Rech. (b) Example of core sizes and lithologies.

a 0.3 *mm* thick wafering diamond blade. To make the slicing more efficient, and to preserve the luminescence signal, the blade rotates through a lubricant filled bucket. The first disc will usually have an irregular surface as a result of the natural surface present at the top of the core. This means that the depth of the first cut, and thus the thickness of the first disc, should be adapted to ensure that the second disk has a regular surface. The total number of slices required varies and is dependent on the depth of bleaching, enough discs should be made to attain the plateau of saturated traps at depth. In this stage of sample preparation, there is no problem if a disc fragments, it can still be used for analysis. If this happens, one should try to conserve all the available material. After being sliced, the rock disc or fragments are cleaned

with acetone, in order to remove the lubricant and any pen marks made during sampling. After slicing, each individual disc has its minimum and maximum thicknesses measured (e_{min} and e_{max}, respectively) using a TESA Digital Caliper, from which the mean thickness value of that particular disc is calculated. The first measured point of a profile is therefore located in $d_1 = 1/2\ e_1$ and the second point is in $d_2 = e_1 + 0.3 + 1/2\ e_2$ (0.3 mm representing the blade thickness) and so on.

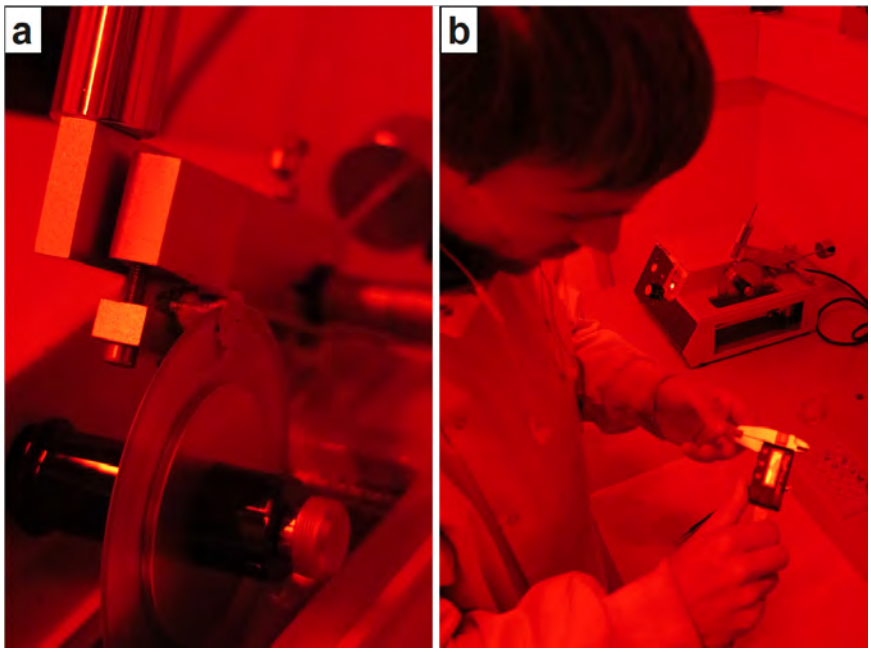

Figure 8.9: (a) Picture of a core being sliced using a 0.3 mm thick wafering diamond blade. (b) Dilan Rech measuring the thickness of a rock disc, with the BUEHLER IsoMet low speed saw seen in the back ground.

8.5 Analysis

Luminescence measurements are performed on Riso machines. After slicing, the rock slices can be directly loaded onto the classic Riso carousels (cup-carousel), if the slice still has the appropriate dimensions and didnt fragment during slicing (Fig. 8.10a). If this is not the case, the ideal way to load a fragment is through the use of an aluminum cup, which is subsequently placed on the carousel (Fig. 8.10b). In this way, the sample is both held on the carousel and heated optimally.

Tests should be performed in order to choose the best analysis settings. I recommend to execute a residual dose determination, a dose recovery and preheat-plateau tests. One should also choose the detection filter associated with the electronic energy level targeted. The heating ramp rate and pause duration after heating should also be carefully chosen to avoid

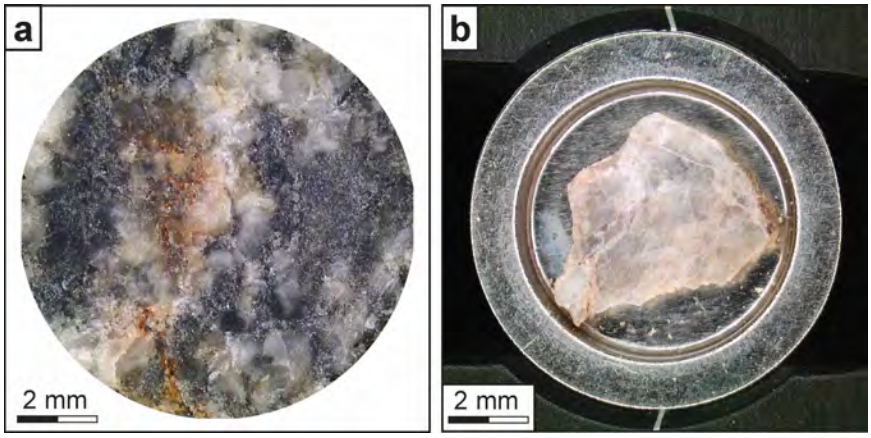

Figure 8.10: (a) Picture of rock disc. (b) Disc fragment mounted on an aluminum cup.

thermal lag and improve the quality of the measurement. I refer to the main part of the manuscript and the appendix for these different settings, which are already detailed and found existing literature.

CHAPTER 9

References

Agassiz L., 1837. Discours prononcé á l'ouverture des séances de la Soc. helv. sci. natur. à Neuchâtel, le 24 juillet 1837, par L. Agassiz, président: actes Soc. helv. sci. natur., réunie à Neuchâtel, 22. sess., Neuchâtel. 5-32.

Aitken, M.J., 1985. Thermoluminescence dating. Academic press.

Aitken, M.J., 1998. An Introduction to Optical Dating The Dating of Quaternary: Sediments by the Use of Photon-stimulated Luminescence. Oxford University press.

Anderson, R.S. 1998. Near-Surface Thermal Profiles in Alpine Bedrock: Implications for the Frost Weathering of Rock. Arct. Alp. Res. 30, 362.

Anderson, R.S., Anderson, S.P., 2010. Geomorphology: The Mechanics and Chemistry of Landscapes. United Kingdom at the University Press, Cambridge. ISBN: 9780521519786.

André, M.-F., 1996. Rock weathering rates in arctic and subarctic environments (Abisko Mts, Swedish Lappland). Zeitschrift fur Geomorphologie 40 (4), 499- 517.

André, M.-F.,2003. Do periglacial landscapes evolve under periglacial conditions? Geomorphology 52: 149-164.

Armesto-González, J., Riveiro-Rodrguez, B., González-Aguilera, D., Rivas-Brea, M.T., 2010. Terrestrial laser scanning intensity data applied to damage detection for historical buildings. Journal of Archaeological Science. 37 (12), 3037-3047.

Augustin, L., Barbante, C., Barnes, P. R. F., Barnola, J. M., Bigler, M., Castellano, E., Cattani, O., Chappellaz, J., Dahl-Jensen, D., Delmonte, B., Dreyfus, G., Durand, G., Falourd, S., Fischer, H., Fluckiger, J., Hansson, M. E., Huybrechts, P., Jugie, G., Johnsen, S. J., Jouzel, J., Kaufmann, P., Kipfstuhl, J., Lambert, F., Lipenkov, V. Y., Littot, G. C., Longinelli, A., Lorrain, R., Maggi, V., Masson-Delmotte, V., Miller, H., Mulvaney, R., Oerlemans, J., Oerter, H., Orombelli, G., Parrenin, F., Peel, D. A., Petit, J.-R., Raynaud, D., Ritz, C., Ruth, U., Schwander, J., Siegenthaler, U., Souchez, R., Stauffer, B., Steffensen, J. P., Stenni, B., Stocker, T. F., Tabacco, I. E., Udisti, R., van de Wal, R. S. W., van den Broeke, M., Weiss, J., Wilhelms, F., Winther, J.-G., Wolff, E. W., and Zucchelli, M., 2004. Eight glacial cycles from an Antarctic ice core, Nature, 429, 623-628.

Bailey, R.M., 2004. Paper I-simulation of dose absorption in quartz over geological timescales and its implications for the precision and accuracy of optical dating. Radiation Measurements 38, 299-310.

Baillie, M.G.L., Pilcher, J.R., 1973. A simple cross-dating program for tree-ring research. Tree-ring Bull. 33, 7-14.

Baillie, M.G.L., 1995. A Slice Through Time: dendrochronology and precision dating. London, Routledge, 176 p.

Balco, G., Stone, J.O., Lifton, N.A., Dunai, T.J., Lifton, A., Dunai, T.J., 2008. A complete and easily accessible means of calculating surface exposure ages or erosion rates from ^{10}Be and 26Al measurements. Quaternary Geochronology. 3, 174-195.

Balco, G., 2011. Contributions and unrealized potential contributions of cosmogenic nuclide exposure dating to glacier chronology, 1990-2010. Quaternary Science Reviews 30, 3-27.

Ballantyne C.K., 2002. Paraglacial geomorphology. Quaternary Science Reviews 21, 1935-2017.

Ballantyne, C. K. and Stone, J. O. 2015. Trimlines, blockfields and the vertical extent of the last ice sheet in southern Ireland, Boreas, 44, 277-287.

Beedle, M.J., Menounos, B., Luckman, B.H., Wheate, R., 2009. Annual push moraines as climate proxy. Geophys. Res. Lett. 36, 20.

Bennett, M., and N. F. Glasser. 2009. Glacial geology: ice sheets and landforms. Chichester, UK; Hoboken, NJ Wiley-Blackwell.

Berthel, N., Schworer, C., Tinner, W., 2012. Impact of Holocene climate changes on alpine and treeline vegetation at Sanetsch Pass, Bernese Alps, Switzerland. Rev. Palaeobot. Palynol. 174, 91-100.

Bierman, P.R., Nichols, K.K., 2004. Rock to sedimentslope to sea with ^{10}Berates of landscape change. Annual Review Earth Planetary Science. 32, 215-255.

Bini, A., Buoncristiani, J.-F., Couterrand, S., Ellwanger, D., Felber, M., Florineth, D., Graf, H. R., Keller, O., Kelly, M., Schluchter, C., and Schoeneich, P. 2009. Die Schweiz w'ahrend des letzteiszeitlichen Maximums (LGM), Bundesamt für Landestopografie swisstopo.

Biswas, R.H., Herman, F., King, G.E., Braun, J., 2018. Thermoluminescence of feldspar as a multi-thermochronometer to constrain the temporal variation of rock exhumation in the recent past. Earth and Planetary Science Letters. 495, 56-68.

Blarquez, O., Carcaillet, C., Bremond, L., Mourier, B., Radakovitch, O., 2010. Trees in the subalpine belt since 11 700 cal. BP: origin, expansion and alteration of the modern forest. Holocene 20, 139-146.

Blumthaler, M., Ambach, W., Ellinger, R., 1997. Increase in solar UV radiation with altitude. Journal of Photochemistry and Photobiology B: Biology 39, 130-134.

Boch, R., Sptl, C., 2011. Reconstructing palaeoprecipitation from an active cave flowstone. J. Quat. Sci. 26 (7), 675-687.

Bond G., Heinrich H., Broecker W.S., Labeyrie L., McManus J., Andrews J., Huon S., Jantschik R., Clasen S., Simet C., Tedesco K., Klas M., Bonani G. and Ivy S. 1992. Evidence for massive discharge of icebergs into the North Atlantic Ocean during the last glacial period. Nature, 360: 245-249.

Botter-Jensen, L., Thomsen, K.J., Jain, M., 2010. Review of optically stimulated luminescence (OSL) instrumental developments for retrospective dosimetry. Radiation Measurement. 45, 253-257.

Brandmeier, M., Kuhlemann, J., Krumrei, I., Kappler, A., Kubik, P.W., 2011. New challenges for tafoni research. A new approach to understand processes and weathering rates. Earth Surface Processes Landforms. 36, 839-852.

Broecker, W., Denton, G., 1990. What drives glacial cycles? Scientific American 262, 43-50.

Brown, N.D., Rhodes, E.J., Harrison, T.M., 2017. Using thermoluminescence signals from feldspars for low-temperature thermochronology. Quaternary Geochronology 42, 31-41.

Brozović, N., Burbank, D.W., and Meigs, A.J., 1997, Climatic limits on landscape development in the northwestern Himalaya: Science, v. 276, p. 571-574.

Burbank, D.W., Leland, J., Fielding, E., Anderson, R.S., Brozović, N., Reid, M.R., and Duncan, C., 1996, Bedrock incision, rock uplift and threshold hillslopes in the northwestern Himalayas: Nature.

Castiglioni, B. 1940. L'Italia nell'etá quaternaria, Carta delle Alpi nel Glaciale, (1 : 200 000 scale), in: Atlante fisico-economico d'Italia, edited by: Dainelli, G., Consociazione Turistica Italiana, Milano, Italy, Table 3.

Clark, P. U., Dyke, A. S., Shakun, J. D., Carlson, A. E., Clark, J., Wohlfarth, Mitrovica, J.X. B., Hostetler, S. W. and McCabe, A. M., 2009. The last glacial maximum. science, 325(5941), 710-714.

Claude, A., Ivy-Ochs, S., Kober, F., Antognini, M., Salcher, B., Kubik, P. W., 2014. The Chironico landslide (Valle Leventina, southern Swiss Alps): age and evolution: Swiss Journal of Geosciences, v. 107, no. 2-3, p. 273-291.

Champagnac, J-D., Molnar, P., Anderson, R. S., Sue, S. and Delacou, B., 2007. Quaternary erosion-induced isostatic rebound in the western Alps. Geology. 35, 195-197.

Choi, K.H., Seong, Y.B., Jung, P.M., Lee, S.Y., 2012. Using cosmogenic ^{10}Be dating to unravel the antiquity of a rocky shore platform on the West Coast of Korea. Journal of Coastal Research. 28 (3), 641-657.

Christl, M., Vockenhuber, C., Kubik, P.W., Wacker, L., Lachner, J., Alfimov, V., Synal, H.A., 2013. The ETH Zurich AMS facilities: performance parameters and reference materials. Nuclear Instruments and Methods in Physics Research Section B: Beam Interactions with Materials and Atoms. 294, 29-38.

Claude, A., S. Ivy-Ochs, F. Kober, M. Antognini, B. Salcher, and P. W. Kubik. 2014. The Chironico landslide (Valle Leventina, southern Swiss Alps); age and evolution. Swiss Journal of Geosciences. 107, 273-291.

Cohen, D., Gillet-Chaulet, F., Haeberli, W., Machguth, H., and Fischer, U. H. 2018. Numerical reconstructions of the flow and basal conditions of the Rhine glacier, European Central Alps, at the Last Glacial Maximum, The Cryosphere, 12, 2515-2544.

Colman, S.M., 1980. Rock-Weathering Rates as Functions of Time. Quaternary Research, 15, 250-264.

Cossart, E., Fort, M., Bourlés, D., Braucher, R., Perrier, R., and Siame, L. 2012. Deglaciation pattern during the Lateglacial/Holocene transition in the southern French Alps. Chronological data and geographical reconstruction from the Clarée Valley (upper Durance catchment, southeastern France), Palaeogeogr. Palaeocl., 315-316, 109-123.

Coutard, J.P., Francou, B., 1989. Rock temperature measurements in two alpine environments: implications for frost shattering. Arct. Alp. Res. 21, 399-416.

Coutterand, S., Buoncristiani, J.-F., 2006. Paléogéographie du dernier maximum glaciaire du Pléistocne récent de la région du massif du Mont Blanc, France. Quaternaire. Revue de l'Association franaise pour l'étude du Quaternaire 17, 35-43.

Coutterand, S. 2010. Etude géomorphologique des flux glaciaires dans les Alpes nord-occidentales au Pléistocne récent: du maximum de la dernire glaciation aux premires étapes de la déglaciation, PhD thesis, Université de Savoie.

Coutterand S. 2011. Les Alpes Occidentales au Dernier Maximum Glaciaire (LGM). Available at: www.glaciers-climat.com.

Dansgaard, W., Johnsen, S. J., Clausen, H. B., Dahl-Jensen, D., Gundestrup, N. S., Hammer, C. U., Hvidberg, C. S., Steffensen, J. P., Sveinbjornsdottir, A. E., Jouzel, J., and Bond, G.1993. Evidence for general instability of past climate from a 250-kyr ice-core record, Nature, 364, 218-220.

Deline, P., Gardent, M., Magnin, F., Ravanel, L., 2012. The morphodynamics of the Mont Blanc massif in a changing cryosphere: a comprehensive review. Geografiska Annaler: series A. Phys. Geogr. 94, 265-283.

Denton, G.H., Karlçen, W., 1973. Holocene climatic variations: their pattern and possible cause. Quat. Res. 3, 155-205.

Dielforder, A., Hetzel, R., 2014. The deglaciation history of the Simplon region (southern Swiss Alps) constrained by ^{10}Be exposure dating of ice-molded bedrock surfaces. Quat. Sci. Rev. 84, 26-38.

Dixon, J.C., Thorn, C.E. 2005. Chemical weathering and landscape development in midlatitude alpine environments. Geomorphology 67 (1-2), 127-145.

Dobmeier, C., 1998. Variscan P-T deformation paths from the southwestern Aiguilles Rouges massif (External massif, western Alps) and their implication for its tectonic evolution. Geologische Rundschau 87, 107-123.

Duffy, S., Bryan, P., Graeme, E., Beale, G., Pagi, H., and Kotoula, E., ,2013. Multi-light Imaging Techniques for heritage application: PTM Guidelines. English Heritage, UK.

Duller GAT. 2005. Luminescence Analyst. University of Wales: Aberystwyth.

Duller, G.A.T., 2008. Single-grain optical dating of Quaternary sediments: why aliquot size matters in luminescence dating. Boreas 37, 589-612.

Dunne, J., Elmore, D. and Muzikar, P., 1999. Scaling factors for the rates of production of cosmogenic nuclides for geometric shielding and attenuation at depth on sloped surfaces. Geomorphology. 27, 3-11.

Durcan, J.A., King, G.E., Duller, G.A.T., 2015. DRAC: Dose Rate and Age Calculator for trapped charge dating. Quaternary Geochronology. 28, 54-61.

Egholm, D., Nielsen, S., Pedersen, V.K., Lesemann, J.-E., 2009. Glacial effects limiting mountain height. Nature 460, 884-887.

Ehlers, J., Gibbard, P.L., 2007. The extent and chronology of Cenozoic Gobal Glaciation. Quaternary International 164-165, 6-20.

Emiliani, C. 1955. Pleistocene Temperatures, J. Geol., 63, 538-578.

EPICA community members. 2004. Eight glacial cycles from an Antarctic ice core. Nature, 429: 623-628.

Fabel, D., Ballantyne, C. K., and Xu, S. 2012. Trimlines, blockfields, mountain-top erratics and the vertical dimensions of the last British-Irish Ice Sheet in NW Scotland, Quaternary Sci. Rev., 55, 91-102.

Fischer, M., M. Huss, and M. Hoelzle, 2015. Surface elevation and mass changes of all Swiss glaciers 1980-2010, Cryosphere, 9, 525-540.

Florineth, D. 1998. Surface geometry of the Last Glacial Maximum (LGM) in the southeastern Swiss Alps (Graubünden) and its paleoclimatologicalsignificance, EandG Quaternary Sci. J., 48, 23-37.

Florineth, D., and Schluchter, C.,2000. Alpine evidence for atmospheric circulation patterns in Europe during the Last Glacial Maximum. Quaternary Research, 54(3), 295-308.

Fontana, A., Monegato, G., Zavagno, E., Devoto, S., Burla, I., Cucchi, F., 2014. Evolutionof an alpine fluvioglacial system at the LGM decay: the cormor megafan (NE Italy). Geomorphology 204, 136-153.

Freiesleben, T., Sohbati, R., Murray, A., Jain, M., Al Khasawneh, S., Hvidt, S., Jakobsen, B., 2015. Mathematical model quantifies multiple daylight exposure and burial events for rock surfaces using luminescence dating. Radiation Measurements 81, 16-22.

Fuchs, M., Owen, L.A., 2008. Luminescence dating of glacial and associated sediments: review, recommendations and future directions. Boreas 37, 636-659.

Gallach, X., Ravanel, L., Egli, M., Brandova, D., Schaepman, M., Christl, M., Gruber, S., Deline, P., Carcaillet, J. and Pallandre, F., 2018. Timing of rockfalls in the Mont Blanc massif (Western Alps): evidence from surface exposure dating with cosmogenic ^{10}Be. Landslides, 1-10.

Ganti, V., von Hagke, C., Scherler, D., Lamb, M.P., Fischer, W.W., Avouac, J.P. 2016. Time scale bias in erosion rates of glaciated landscapes. Science Advances. 2: e1600204.

Gardent, M., Rabatel, A., Dedieu, J.-P., Deline, P., 2014. Multitemporal glacier inventory of the French Alps from the late 1960s to the late 2000s. Global and Planetary Change 120, 24-37.

Gianotti F., Forno M.G., Ivy-Ochs S. and Kubik P., 2008. New chronological and stratigaphical data on the Ivrea amphitheatre (Piedmont, NW Italy). Quaternary International, 190: 123-135.

Gianotti F., Forno M.G., Ivy-Ochs S., Monegato G., Pini R. and Ravazzi C., 2015. Stratigraphy of the Ivrea Morainic Amphitheatre (NW Italy): an updated Synthesis. Alpine and Mediterranean Quaternary, 28: 29-58.

Giguet-Covex, C., Pansu, J., Arnaud, F., Rey, P.-J., Griggo, C., Gielly, L., Domaizon, I., Coissac, E., David, F., Choler, P., Poulenard, J., Taberlet, P., 2014. Long livestock farming history and human landscape shaping revealed by lake sediment DNA. Nat. Commun. 5, 3211.

Gliganic, L.A., Meyer, M.C., Sohbati, R., Jain, M., 2018. OSL Surface Exposure Dating of a Lithic Quarry in Tibet: Laboratory Validation and Application. Quat. Geochronol Special Issue related to the LED Cape Town.

Goehring, B.M., Schaefer, J.M., Schluechter, C., Lifton, N.A., Finkel, R.C., Jull, A.T., Akar, N., Alley, R.B., 2011. The Rhone Glacier was smaller than today for most of the Holocene. Geology 39, 679-682.

Goehring, B.M., Vacco, D.A., Alley, R.B., Schaefer, J.M., 2012. Holocene dynamics of the Rhone Glacier, Switzerland, deduced from ice flow models and cosmogenic nuclides. Earth and Planetary Science Letters 351, 27-35.

Goss, J.C., Phillips, F.M., 2000. Terrestrial in situ cosmogenic nuclides: theory and application. Quaternary Science Reviews. 20, 1475-1560.

Grab, S., 2007. Rock-surface temperatures of basalt in the Drakensberg alpine environment, Lesotho. Geogr. Ann. Ser. A Phys. Geogr. 89, 185-193.

Gruber, S., Hoelzle, M., Haeberli, W., 2004a. Rock-wall temperatures in the Alps: modelling their topographic distribution and regional differences. Permafr. Periglac. Process. 15:299-307.

Guralnik, B., Jain, M., Herman, F., Ankjrgaard, C., Murray, A.S., Valla, P.G., Preusser, F., King, G.E., Chen, R., Lowick, S.E., 2015. OSL-thermochronometry of feldspar from the KTB borehole, Germany. Earth and planetary science letters 423, 232-243.

Haas, J.N., Richoz, I., Tinner, W., Wick, L., 1998. Synchronous Holocene oscillations recorded on the Swiss Plateau and at timberline in the Alps. Holocene 8 (3), 301-309.

Habermann, J., Schilles, T., Kalchgruber, R., Wagner, G.A., 2000. Steps towards surface dating using luminescence. Radiation Measurements. 32, 847-851.

Haeberli, W., and Alean J., 1985. Temperature and accumulation of high altitude firn in the Alps, Ann. Glaciol., 6, 161-163.

Haeberli, W., and Funk, M., 1991. Borehole temperatures at the Colle Gnifetti core-drilling site (Monte Rosa, Swiss Alps), J. Glaciol., 37, 37- 46.

Hajdas, I., 2008. Radiocarbon dating and its applications in Quaternary studies. Eiszeitalter und Gegenwart Quaternary Science Journal 57, 24.

Hales, T.C., and Roering, J.J., 2007, Climatic controls on frost cracking and implications for the evolution of bedrock landscapes: Journal of Geophysical Research.

Hallet, B., Walder, J., Stubbs, C.W., 1991. Weathering by segregation ice growth in microcracks at sustained sub-zero temperatures: verification from an experimental study using acoustic emissions. Permafr. Periglac. Process. 2, 283-300.

Hall, K., Thorn, C., Sumner, P., 2012. On the persistence of “weathering”. Geomorphology. 149-150, 1-10.

Hantke, R. 2011. Eiszeitalter : Kalt-/Warmzeit-Zyklen und Eistransport im alpinen und voralpinen Raum, Ott, Bern.

H´auselmann, P., 2008. Surface corrosion of an alpine karren field: recentmeasurements at Innerbergli (Siebenhengste, Switzerland). International Journal of Speleology. 37, 107-111.

Hays, J. D., Imbrie, J., and Shackleton, N. J. 1976. Variations in the Earth’s Orbit: Pacemaker of the Ice Ages, Science, 194, 1121- 1132.

Heiri, O., Lotter, A.F., Hausmann, S., Kienast, F., 2003. A chironomid-based Holocene summer air temperature reconstruction from the Swiss Alps. Holocene 13, 477-484.

Heiri, O., Koinig, K. A., Spotl, C., Barrett, S., Brauer, A., Drescher- Schneider, R., Gaar, D., Ivy-Ochs, S., Kerschner, H., Luetscher, M., Moran, A., Nicolussi, K., Preusser, F., Schmidt, R., Schoeneich, P., Schworer, C., Sprafke, T., Terhorst, B., and Tinner, W. 2014. Palaeoclimate records 60-8 ka in the Austrian and Swiss Alps and their forelands, Quaternary Sci. Rev., 106, 186-205.

Herbert, T.D., Lawrence, K.T., Tzanova, A., Peterson, L.C., Caballero-Gill, R., Kelly, C.S., 2016. Late Miocene global cooling and the rise of modern ecosystems. Nature Geosci 9, 843-847.

Herman, F., Seward, D., Valla, P.G., Carter, A., Kohn, B., Willett, S.D., Ehlers, T.A., 2013. Worldwide acceleration of mountain erosion under a cooling climate. Nature 504, 423-426.

Herman, F., Beyssac, O., Brughelli, M., Lane, S. T., Leprince, S., Adatte, T., Lin, J. Y. Y., Avouac, J.-P., Cox, S. C., 2015. Erosion by an Alpine glacier. Science, Vol 350 Issue 6257

Herman, F., Champagnac, J.-D., 2016. Plio-Pleistocene increase in erosion rates in mountain belts in response to climate change. Terra Nova. 28, 2-10.

Hippe, K. 2017. Constraining processes of landscape change with combined in situ cosmogenic 14C-^{10}Be analysis, Quaternary Science Reviews. 173, 1-19.

Hoelzle, M., Haeberli, W., Dischl, M., Peschke, W., 2003. Secular glacier mass balances derived from cumulative glacier length changes. Glob. Planet. Change 36 (4), 77-89.

Hoke, G.D., Turcotte, D.L., The weathering of stones due to dissolution. Environmental Geology, 46:305-310

Hippe, K., Ivy-Ochs, S., Kober, F., Zasadni, J., Wieler, R., Wacker, L., Kubik, P.W., Schlüchter, C., 2014. Chronology of Lateglacial ice flow reorganization and deglaciation in the Gotthard Pass area, Central Swiss Alps, based on cosmogenic ^{10}Be and in situ 14C. Quaternary Geochronology 19, 14-26.

Holzhauser H., Magny M., Zumbühl H.J. 2005. Glacier and lake-level variations in west-central Europe over the last 3500 years. The Holocene 15, 6, 789-801.

Huntley, D.J., Godfrey-Smith, D.I., Thewalt, M.L., 1985. Optical dating of sediments. Nature 313, 105-107.

Ilyashuk, E.A., Koinig, K.A., Heiri, O., Ilyashuk, B.P., Psenner, R., 2011. Holocene temperature variations at a high-altitude site in the Eastern Alps: a chironomid record from Schwarzsee ob Solden, Austria. Quat. Sci. Rev. 30, 176-191.

Ivy-Ochs, S., 1996. The Dating of Rock Surfaces Using in Situ Produced ^{10}Be, 26Al and 36Cl, with Examples from Antarctica and the Swiss Alps (PhD thesis). ETH, Zurich.

Ivy-Ochs, S., Schaefer, J., Kubik, P., Synal, H.A., Schlüchter, C., 2004. Timing of deglaciation on the northern Alpine foreland (Switzerland). Eclogae Geol. Helvetiae 97, 47-55.

Ivy-Ochs, S., Kerschner, H., Reuther, A., Maisch, M., Sailer, R., Schaefer, J., Kubik, P.W., Synal, H.-A., Schluchter, C., 2006. The timing of glacier advances in the northern European Alps based on surface exposure dating with cosmogenic ^{10}Be, 26Al, 36Cl, and 21Ne. Geological Society of America Special Papers 415, 43-60.

Ivy-Ochs, S., Kerschner, H., Maisch, M., Christl, M., Kubik, P.W., Schluchter, C., 2009. Latest Pleistocene and Holocene glacier variations in the European Alps. Quaternary Science Reviews 28, 2137-2149.

Ivy-Ochs, S., Briner, J.P., 2014. Dating disappearing ice with cosmogenic nuclides. Elements 10, 351-356.

Ivy-Ochs, S., 2015. Glacier variations in the European Alps at the end of the last glaciation. Cuadernos de investigacin geográfica 41, 295-315.

Jenkins, G.T.H., Duller, G.A.T., Roberts, H.M., Chiverrell, R.C., Glasser, N.F., 2018. A new approach for luminescence dating glaciofluvial deposits - high precision optical dating of cobbles. Quaternary Science Reviews. 192, 263-273.

Joerin, U., Stocker, T.F., Schlüchter, C., 2006. Multicentury glacier fluctuations in the Swiss Alps. Holocene 16 (5), 697-704.

Jouzel, J., Masson-Delmotte, V., Cattani, O., Dreyfus, G., Falourd, S., Hoffmann, G., Minster, B., Nouet, J., Barnola, J. M., Chappellaz, J., Fischer, H., Gallet, J. C., Johnsen, S., Leuenberger, M., Loulergue, L., Luethi, D., Oerter, H., Parrenin, F., Raisbeck, G., Raynaud, D., Schilt, A., Schwander, J., Selmo, E., Souchez, R., Spahni, R., Stauffer, B., Steffensen, J. P., Stenni, B., Stocker, T. F., Tison, J. L., Werner, M., and Wolff, E. W. 2007. Orbital and Millennial Antarctic Climate Variability over the Past 800,000 Years, Science, 317, 793-796.

Kars, R.H., Reimann, T., Wallinga, J., 2014. Are feldspar SAR protocols appropriate for post-IR IRSL dating? Quaternary Geochronology. 22, 126-136.

Kellerer-Pirklbauer, A. 2017. Potential weathering by freeze-thaw action in alpine rocks in the European Alps during a nine year monitoring period. Geomorphology 296: 113-131.

Kelly, M. A., Buoncristiani, J.-F., and Schlüchter, C. 2004. A reconstruction of the last glacial maximum (LGM) ice surface geometry in the western Swiss Alps and contiguous Alpine regions in

Italy and France, Eclogae Geol. Helv., 97, 57-75.

King, G., Herman, F., Lambert, R., Valla, P., Guralnik, B., 2016. Multi-OSL-thermochronometry of feldspar. Quaternary Geochronology 33, 76-87.

King, G.E., Valla, P.G. and Lehmann, B., 2018. OSL Rock Surface and Rock Surface-Exposure Dating. Invited contribution to "Handbook of Luminescence Dating", Eds: M. Bateman and I. Bailiff.

Kirkbride, M.P., Bell, C.M., 2010. Edge-roundness of boulders of Torridonian Sandstone (northwest Scotland): applications for relative dating and implications for warm and cold climate weathering rates. Boreas 39, 187-198.

Klasen, N., Fiebig, M., Preusser, F., Reitner, J.M., Radtke, U., 2007. Luminescence dating of proglacial sediments from the Eastern Alps. Quat. Int. 164e165, 21-32.

Kleman, J. 1994. Preservation of landforms under ice sheets and ice caps, Geomorphology, 9, 19-32.

Kleman, J. and Borgstrom, I. 2006. Glacial land forms indicative of a partly frozen bed, J. Glaciol., 40, 255-264.

Kleman, J., Hattestrand, C., Stroeven, A. P., Jansson, K. N., De Angelis, H., and Borgstrom, I. 2006. Reconstruction of Palaeo- Ice Sheets - Inversion of their Glacial Geomorphological Record, in: Glacier Science and Environmental Change, edited by: Knight, P. G., Blackwell, Malden, MA.

Kleman, J., Jansson, K., De Angelis, H., Stroeven, A., Hattestrand, C., Alm, G., and Glasser, N. 2010. North American ice sheet build-up during the last glacial cycle, 115-21 kyr, Quaternary Sci. Rev., 29, 2036-2051.

Kohl, C.P., Nishiizumi, K., 1992. Chemical isolation of quartz for measurement of in-situ-produced cosmogenic nuclides. Geochimica Cosmochimica Acta. 56, 3583-3587.

Koppes, M. and Montgomery, D., 2009, The relative efficacy of fluvial and glacial erosion over modern to orogenic timescales, Nat. Geosci., 2, 644-647.

Kuhlemann, J., Rohling, E. J., Krumrei, I., Kubik, P., Ivy-Ochs, S., and Kucera, M., 2008. Regional synthesis of Mediterranean atmospheric circulation during the Last Glacial Maximum. Science, 321(5894), 1338-1340.

Laj, C., Kissel, C., Beer, J., 2004. High resolution global Paleointensity Stack since 75 kyr (GLOPIS-75) calibrated to Absolute values. Timescales Paleomagnetic Field. Geophysical Monograph Series.

145, 255-265.

Lal, D. and Peters, B. 1967. Cosmic ray produced radioactivity on the Earth. in Handbuch der Physick. Springer. Berlin. XLVI: 551-612.

Lal, D., 1991. Cosmic ray labeling of erosion surfaces: in situ nuclide production rates and erosion models. Earth and Planetary Science Letters 104, 424-439.

Lang, A., Honscheidt, S., 1999. Age and source of colluvial sediments at Vaihingen-Enz, Germany. Catena 38, 89-107.

Lasaga, A. C., J. M. Soler, J. Ganor, T. E. Burch, and K. L. Nagy, 1994, Chemical weathering rate laws and global geochemical cycles, Geochimica et Cosmochimica Acta 58: 2361-2386.

Laskaris, N., Liritzis, I., 2011. A new mathematical approximation of sunlight attenuation in rocks for surface luminescence dating. Journal of Luminescence 131, 1874-1884.

Le Roy, M., Nicolussi, K., Deline, P., Astrade, L., Edouard, J.-L., Miramont, C., Arnaud, F., 2015. Calendar-dated glacier variations in the western European Alps during the Neoglacial: the Mer de Glace record, Mont Blanc massif. Quaternary Science Reviews 108, 1-22.

Lean, J., 1987. Solar Ultraviolet Irradiance Variations: A review. Journal of Geophysical Research 92,839-968.

Lehmann, B., Valla, P. G., King, G. E., and Herman, F., 2018. Investigation of OSL surface exposure dating to reconstruct post-LIA glacier fluctuations in the French Alps (Mer de Glace, Mont Blanc massif). Quaternary geochronology, 44, 63-74.

Lehmann, B., Herman, F., Valla, P.G., King, G.R., Biswas, R.H., in review. Evaluating post-glacial bedrock erosion and surface exposure duration by coupling in-situ OSL and ^{10}Be dating. Earth Surf. Dynam.

Leloup, P.H., Arnaud, N., Sobel, E. R. and Lacassin, R., 2005. Alpine thermal and structural evolution of the highest external crystalline massif: The Mont Blanc. Tectonics 24, TC4002.

Lifton, N.A., Sato, T., Dunai, T.J., 2014. Scaling in situ cosmogenic nuclide production rates using analytical approximations to atmospheric cosmic-ray fluxes. Earth Planetary Science Letters. 386, 149-160.

Liritzis, I., 1994. A new dating method by thermoluminescence of carved megalithic stone building. Comptes rendus de l'Académie des sciences. Série 2. Sciences de la terre et des plantes 319, 603-610.

Liritzis, I., 2011. Surface dating by luminescence: an overview. Geochronometria 38, 292-302.

Lisiecki, L.E. and Raymo, M.E., 2005. A Pliocene-Pleistocene stack of 57 globally distributed benthic d 18O records. Paleoceanography, 20, PA1003.

Lisiecki, L.E. and Raymo, M.E., 2007. Plio-Pleistocene climate evolution: trends and transitions in glacial cycle dynamics. Quaternary Science Reviews. 26, 56-69.

Lister, G.S., 1988. A 15,000-year isotopic record from Lake Zürich of deglaciation and climatic change in Switzerland. Quat. Res. 29, 129-141.

Liu, T., Broecker, W.S., 2007. Holocene rock varnish microstratigraphy and its chronometric application in the drylands of western USA. Geomorphology. 84 (1-2), 1-21.

Łoziński, MW., 1909. uber die mechanische Verwitterung der Sandsteine im gemassibten Klima. Académie des sciences de cracovie, Bulletin internationale, classe de science, mathématiques et naturelles 1: 1-25. (English translation by Mrozek Teresa. 1992. On the mechanical weathering of sandstones in temperate climates. In Cold Climate Landforms, Evans DJA (ed.). Wiley: Chichester; 119-134.).

Luetscher, M., Boch, R., Sodemann, H., Spotl, C., Cheng, H., Edwards, R. L., Frisia, S. and Muller, W., 2015. North Atlantic storm track changes during the Last Glacial Maximum recorded by Alpine speleothems. Nature Communications, 6, 6344.

Luthi, M., and Funk, M., 2001. Modelling heat flow in a cold, high-altitude glacier: Interpretation of measurements from Colle Gnifetti, Swiss Alps, J. Glaciol., 47, 314- 324.

Maisch M., 1987. Zur Gletschergeschichte des alpinen Spatglazials: Analyse und Interpretation von Schneegrenzdaten. Geographica Helvetica 42, 63-71.

Maisch M., Wipf A., Denneler B., Battaglia J., Benz C., 1999. Die Gletscher der Schweizer Alpen. Gletscherhochstand 1850, Aktuelle Vergletscherung, Gletscherschwund- Szenarien. Vdf Hochschulverlag ETH Zürich, 373 p.

Matsuoka, N., 1990. The rate of bedrock weathering by frost action: field measurements and a predictive model. Earth Surf. Process. Landf. 15, 73-90.

Matsuoka, N., Murton, J., 2008. Frost weathering: recent advances and future directions. Permafr. Periglac. Process. 19:195-210.

Martin, L.C.P., Blard, P.-H., Balco, G., Lave J., Delunel, R., Lifton, N., Laurent V. 2017. The CREp program and the ICE-D production rate calibration database: A fully parameterizable and updated online tool to compute cosmicray exposure ages. Quaternary Geochronology. 38, 25-49.

Meyer, M.C., Gliganic, L.A., Jain, M., Sohbati, R., 2018. Lithological controls on light penetration into rock surfaces - implications for OSL and IRSL surface exposure dating. Radiation Measurements (LED proceedings).

Millet, L., Arnaud, F., Heiri, O., Magny, M., Verneaux, V., Desmet, M., 2009. Late-Holocene summer temperature reconstruction from chironomid assemblages of Lake Anterne, northern French Alps. Holocene 19 (2), 317-328.

Miller, K.G., Fairbanks, R.G. and Mountain, G.S., 1987. Tertiary oxygen isotope synthesis, sea level history, and continental margin erosion. Paleoceanography. 2, 1-19.

Mitchell, S.G., Montgomery, D.R., 2006. Influence of a glacial buzzsaw on the height and morphology of the Cascade Range in central Washington State, USA. Quat. Res. 65, 96-107.

Molnar, P. and England, P., 1990. Late Cenozoic uplift of mountain ranges and global climate change: Chicken or egg? Nature. 346, 29-34.

Monegato, G., Ravazzi, C., Donegana, M., Pini, R., Calderoni, G., and Wick, L. 2007. Evidence of a two-fold glacial advance during the last glacial maximum in the Tagliamento end moraine system (eastern Alps), Quaternary Res., 68, 284-302.

Montgomery, D.R., 2002. Valley formation by fluvial and glacial erosion. Geology 30, 1047-1050.

Moses, C., Robinson, D., Barlow, J. 2014. Methods for measuring rock surface weathering and erosion: A critical review. Earth-Science Reviews. 135, 141-161.

Murray, A.S., Roberts, R.G., 1998. Measurement of the equivalent dose in quartz using a regenerative-dose single- aliquot protocol. Radiation Measurements. 29, 503-515.

Murray, A.S., Wintle, A.G., 2000. Luminescence dating of quartz using an improved single-aliquot regenerative-dose protocol. Radiation measurements 32, 57-73.

Nicholson, D.T., 2008. Rock control on microweathering of bedrock surfaces in a periglacial environment. Geomorphology. 101, 655-665.

Nicolussi, K., Schlüchter, C., 2012. The 8.2 ka event e calendar dated glacier response in the Alps. Geology 40, 819-822.

Nicolussi, K., Kaufmann, M., Patzelt, G., van der Plicht, J., Thurner, A., 2005. Holocene tree-line variability in the Kauner Valley, Central Eastern Alps, indicated by dendrochronological analysis of living trees and subfossil logs. Veg. Hist. Archaeobot. 14, 221-234.

Nishiizumi, K., Imamura, M., Caffee, MW., Southon, JR., Finkel, RC., McAninch, J. 2007. Absolute calibration of ^{10}Be AMS standards. Nuclear Instruments and Methods in Physics Research Section B: Beam Interactions with Materials and Atoms. 258, 403-413.

Noetzli, J., Gruber, S., Kohl, T., Salzmann, N., Haeberli,W., 2007. Three-dimensional distribution and evolution of permafrost temperatures in idealized high-mountain topography. J. Geophys. Res. Earth Surf. 112 (F2): F02S13

Nussbaumer, S., Zumbuhl, H.J., Steiner, D., 2007. Fluctuations of the Mer de glace (Mont Blanc area, France) AD 1500-2050. An interdisciplinary approach using new historical data and neural network simulations. Zeitschrift fur Gletscherkunde und Glazialgeologie ZGG, 5-175.

Ou, X.J., Roberts, H.M., Duller, G.A.T., Gunn, M.D., Perkins, W.T., 2018. Attenuation of light in different rock types and implications for rock surface luminescence dating. Radiation Measurements. (in press).

Pavon-Carrasco, F.J., Osete, M.L., Torta, J.M., De Santis, A., 2014. A geomagnetic field model for the Holocene based on archaeomagnetic and lava flow data Earth and Planetary Science Letters. 388, 98-109.

Peizhen, Z., Molnar, P., Downs, W.R., 2001. Increased sedimentation rates and grain sizes 2-4 Myr ago due to the influence of climate change on erosion rates. Nature 410, 891-897.

Penck, A., Bruckner, E., 1901/1909. Die Alpen im Eiszeitalter. Tauchitz, Leipzig.

Penck, A., 1905. Glacial features in the surface of the Alps. The Journal of Geology 13, 1-19.

Penck, A. and Brückner, E. 1909. Die alpen im Eiszeitalter, Tauchnitz, Leipzig.

Polikreti, K., Michael, C., Maniatis, Y., 2002. Authenticating marble sculpture with thermoluminescence. Ancient TL 20, 11-18.

Polikreti, K., Michael, C., Maniatis, Y., 2003. Thermoluminescence characteristics of marble and dating of freshly excavated marble objects. Radiation Measurements 37, 87-94.

Portenga, E.W., Bierman, P.R., 2011. Understanding earth's eroding surface with ^{10}Be. GSA Today 21, 4-10.

Preusser, F. 2004. Towards a chronology of the Late Pleistocene in the northern Alpine Foreland, Boreas, 33, 195-210.

Preusser, F., Graf, H.R., Keller, O., Krayss, E., Schlüchter, C., 2011. Quaternary glaciation history of northern Switzerland. Quaternary Science Journal 60(2-3), 282-305.

Rabatel, A., Letréguilly, A., Dedieu, J., Eckert, N., 2013. Changes in glacier equilibrium-line altitude in the western Alps from 1984 to 2010: evaluation by remote sensing and modeling of the morpho-topographic and climate controls. Cryosphere 7, p. 1455-p. 1471.

Rabatel, A., Dedieu, J. P., Vincent, C. 2016. Spatio-temporal changes in glacier-wide mass balance quantified by optical remote sensing on 30 glaciers in the French Alps for the period 1983-2014. Journal of Glaciology, 62(236) 1153-1166.

Rades, E. F., Sohbati, R., Luthgens, C., Jain, M., Murray, A.S., 2018. First luminescence-depth profiles from boulders from moraine deposits: Insights into glaciation chronology and transport dynamics in Malta valley, Austria. Radiation Measurements.

Raup, B., Racoviteanu A., Khalsa S.J.S., Helm C., Armstrong R., Arnaud Y., 2007a. The GLIMS geospatial glacier database: a new tool for studying glacier change. Global and Planetary Change. 56 (1-2): 101-110.

Ravazzi, C., Badino, F., Marsetti, D., Patera, G., Reimer, P.J., 2012. Glacial to paraglacial history and forest recovery in the Oglio glacier system (Italian Alps) between 26 and 15 ka cal BP. Quat. Sci. Rev. 58, 146-161.

Raymo, M. E. and W. F. Ruddiman, 1992, Tectonic forcing of late Cenozoic climate, Nature. 359, 117-122.

Reber, R., Akcar, N., Ivy-Ochs, S., Tikhomirov, D., Burkhalter, R., Zahno, C., Lüthold A., Kubik, P.W., Vockenhuber, C., Schluchter, C., 2014. Timing of retreat of the Reuss glacier (Switzerland) at

the end of the last glacial maximum. Swiss J. Geosciences 1-15.

Regard, V., Dewez, T., Bourls, D.L., Anderson, R.S., Duperret, A., Costa, S., Leanni, L., Lasseur, E., Pedoja, K., Maillet, G.M., 2012. Late Holocene seacliff retreat recorded by ^{10}Be profiles across a coastal platform: theory and example fromthe English Channel. Quat. Geochronol. 11, 87-97.

Reitner, J., 2007. Glacial dynamics at the beginning of Termination I in the Eastern Alps and their stratigraphic implications. Quat. Int. 164-165, 64-84.

Rhodes, E.J., 2011. Optically stimulated luminescence dating of sediments over the past 200,000 years. Annual Review of Earth and Planetary Sciences 39, 461-488.

Richards, M.P., 1994. Luminescence dating of quartzite from the Diring Yuriakh site. M.A. Thesis, Simon Fraser University, unpublished.

Scherler, D., 2015, Climatic limits to headwall retreat in the Khumbu Himalaya, eastern Nepal, Geology; v. 42; no. 11; p. 1019-1022.

Schimmelpfennig, I., Schaefer, J.M., Akar, N., Koffman, T., Ivy-Ochs, S., Schwartz, R., Finkel, R.C., Zimmerman, S., Schluchter, C., 2014. A chronology of Holocene and Little Ice Age glacier culminations of the Steingletscher, Central Alps, Switzerland, based on high-sensitivity beryllium-10 moraine dating. Earth and Planetary Science Letters 393, 220-230.

Schindelwig I., Akçar N., Kubik P. and Schluchter C. 2012. Lateglacial and early Holocene dynamics of adjacent valley glaciers in the Western Swiss Alps. Journal of Quaternary Science, 27: 114-124.

Schluchter, C. 1988. A non-classical summary of the Quaternary stratigraphy in the northern alpine foreland of Switzerland, Bulletin de la Société Neuchâteloise de Géographie, 32, 143-157.

Schluchter, C., Rothlisberger, C., 1995. 100,000 jahre gletschergeschichte. In: Gletscher im standigen Wandel, pp. 47-63 vdf-Verlag: Zurich.

Schmidt, R., Roth, M., Tessadri, R., Weckstrom, K., 2008. Disentangling late- Holocene climate and land use impacts on an Austrian alpine lake using seasonal temperature anomalies, ice-cover, sedimentology, and pollen tracers. J. Paleolimnol. 40, 453-469.

Schumer, R., and Jerolmack, D. J., 2009. Real and apparent changes in sediment deposition rates through time. Journal of Geophysical Research, 114, F00A06.

Schweingruber, F.H., 2007. Wood structure and Environment. In: Springer Series in Wood Science. Springer, Heidelberg, 279 pp.

Seguinot, J., Ivy-Ochs, S., Jouvet, G., Huss, M., Funk, M. and Preusser, F. 2018. Modelling last glacial cycle ice dynamics in the Alps. The Cryosphere. 12, 3265-3285.

Shackleton, N. J. and Opdyke, N. D. 1973. Oxygen isotope and palaeomagnetic stratigraphy of Equatorial Pacific core V28-238: Oxygen isotope temperatures and ice volumes on a105 year and 106 year scale, Quaternary Res., 3, 39-55.

Siman-Tov, S., Stock, G. M., Brodsky, E. E., and White, J. C. 2017. The coating layer of glacial polish. The Geological Society of America. 11, 987-990.

Simkins, L.M., Simms, A.R., DeWitt, R., 2013. Relative sea-level history of Marguerite Bay, Antarctic Peninsula derived from optically stimulated luminescence-dated beach cobbles. Quaternary Science Reviews 77, 141-155.

Simms, A.R., DeWitt, R., Kouremenos, P., Drewry, A.M., 2011. A new approach to reconstructing sea levels in Antarctica using optically stimulated luminescence of cobble surfaces. Quaternary Geochronology 6, 50-60.

Singarayer, J.S., 2002. Linearly modulated optically stimulated luminescence of sedimentary quartz: Physical mechanisms and implications for dating. D.Phil. thesis, University of Oxford. 345 pp.

Six, D., Vincent, C., 2014. Sensitivity of mass balance and equilibrium-line altitude to climate change in the French Alps. J. Glaciol. 60 (223), 867-878.

Smiraglia, C., Azzoni, R. S., D'Agata, C., Matagno, D., Fugazza D., Diolaiutu, G. A., 2015. The evolution of the italian glaciers from the previous data base to the new italian inventory. Preliminary considerations and results. Geogr. Fis. Dinam. Quat. 38: 79-87.

Sohbati, R., Murray, A., Jain, M., Buylaert, J.-P., Thomsen, K., 2011. Investigating the resetting of OSL signals in rock surfaces. Geochronometria. 38, 249-258.

Sohbati, R., Jain, M., Murray, A., 2012a. Surface exposure dating of non-terrestrial bodies using optically stimulated luminescence: A new method. Icarus 221, 160-166.

Sohbati, R., Murray, A.S., Buylaert, J.-P., Almeida, N.A.C., Cunha, P.P., 2012b. Optically stimulated luminescence (OSL) dating of quartzite cobbles from the Tapada do Montinho archaeological site

(east-central Portugal). Boreas 41, 452-462.

Sohbati, R., Murray, A.S., Porat, N., Jain, M., Avner, U., 2015. Age of a prehistoric "Rodedian" cult site constrained by sediment and rock surface luminescence dating techniques. Quaternary Geochronology. 30, 90-99.

Sohbati, R., Liu, J., Jain, M., Murray, A., Egholm, D., Paris, R., Guralnik, B. 2018. Centennial-to millennial-scale hard rock erosion rates deduced from luminescence-depth profiles. Earth and Planetary Science Letters. 493, 218-230.

Stephenson, W.J., Finlayson, B.L., 2009. Measuring erosion with the microerosion metercontributions to understanding landform evolution. Earth-Science Reviews. 95, 53-62.

Stewart M., Grosjean M., Kuglitsch F.G., Nussbaumer S.U., von Gunten L., 2011b. Reconstructions of Late Holocene paleofloods and glacier length changes in the Upper Engadine, Switzerland (ca. 1450 BC - AD 420). Palaeogeography, Palaeoclimatology, Palaeoecology 311, 3-4, 215-123.

Stone, J.O., 2000. Air pressure and cosmogenic isotope production. Journal of Geophysical Research. 105759, 753-823.

Strandberg, G., Brandefelt, J., Kjellstrom, E., and Smith, B. 2001. High resolution regional simulation of last glacial maximum climate in Europe, Tellus A, 63, 107-125.

Sugden D.E., Glasser N. and Clapperton C.M.,1992. Evolution of large roches moutonnées. Geograska Annaler Series A. Physical Geography, 74: 253-264.

Suter, S., Laternser, M., Haeberli, W., Hoelzle, M., and Frauenfelder, R., 2001. Cold firn and ice of high-altitude glaciers in the Alps: Measurements and distribution modeling, J. Glaciol., 47, 85- 96.

Suter, S., 2002. Cold firn and ice in the Monte Rosa and Mont Blanc areas: Spatial occurrence, surface energy balance and climate evidence, Ph.D. thesis, Versuchsanst. fur Wasserbau, Hydrol. und Glaziol., ETH Zurich, Switzerland.

Tachiya, M. and Mozumder, A. 1974. Decay of trapped electronics by tunnelling to scavenger molecules in low-temperature glasses. Chemical Physics Letters. 28, 1.

Theocaris, P., Liritzis, I., Galloway, R., 1997. Dating of two Hellenic pyramids by a novel application of thermoluminescence. Journal of Archaeological Science 24, 399-405.

Tinner, W., Theurillat, J.P., 2003. Uppermost limit, extent, and fluctuations of the timberline and treeline ecocline in the Swiss Central Alps during the past 11 500 years. Arct. Antarct. Alp. Res. 35 (2), 158-169.

Turowski, J.M., Cook, K.L., 2017. Field techniques for measuring bedrock erosion and denudation. Earth Surface Processes Landforms. 42, 109-127.

Uppala, S.M., Kallberg, P.W., Simmons, A.J., Andrae, U., Bechtold, V.D.C., Fiorino, M., Gibson, J.K., Haseler, J., Hernandez, A., Kelly, G.A., Li, X., Onogi, K., Saarinen, S., Sokka, N., Allan, R.P., Andersson, E., Arpe, K., Balmaseda, M.A., Beljaars, A.C.M., Van De Berg, L., Bidlot, J., Bormann, N., Caires, S., Chevallier, F., Dethof, A., Dragosavac, M., Fisher, M., Fuentes, M., Hagemann, S., Holm, E., Hoskins, B.J., Isaksen, L., Janssen, P.A.E.M., Jenne, R., Mcnally, A.P., Mahfouf, J.-F., Morcrette, J.- J., Rayner, N.A., Saunders, R.W., Simon, P., Sterl, A., Trenberth, K.E., Untch, A., Vasiljevic, D., Viterbo, P., Woollen, J., 2005. The ERA-40 re-analysis. Quaterly Journal of the Royal Meteorological Society. 131, 2961-3012.

Vafiadou, A., Murray, A., Liritzis, I., 2007. Optically stimulated luminescence (OSL) dating investigations of rock and underlying soil from three case studies. Journal of Archaeological Science 34, 1659-1669.

Valla, P.G., Lowick, S.E., Herman, F., Champagnac, J.-D., Steer, P., Guralnik, B., 2016. Exploring IRSL50 fading variability in bedrock feldspars and implications for OSL thermochronometry. Quaternary Geochronology 36, 55-66.

van Husen, D. 1987. Die Ostalpen in den Eiszeiten, Geologische Bundesanstalt, Wien.

van Husen, D., 1997. LGM and late-glacial fluctuations in the Eastern Alps. Quat. Int. 38-39, 109-118.

Vescovi E., Ravazzi C., Arpenti E., Finsinger W., Pini R., Valsecchi V., Wick L., Ammann B. and Tinner W. 2007. Interactions between climate and vegetation during the Lateglacial period as recorded by lake and mire sediment archives in Northern Italy and Southern Switzerland. Quaternary Science Reviews, 26: 1650-1669.

Vincent, C., Le Meur E., Six, D., Possenti, P., Lefebvre E., Funk, M., 2007. Climate warming revealed by englacial temperatures at Col du Dme (4250 m, Mont Blanc area). Geophysical research letter, vol. 34, L16502.

Vincent, C., Harter, M., Gilbert, A., Berthier, E., Six, D., 2014. Future fluctuations of Mer de Glace, French Alps, assessed using a parameterized model calibrated with past thickness changes. Annals of Glaciology 55, 15-24.

Visocekas, R., 2002. Tunneling in afterglow, its coexistence and interweaving with thermally stimulated luminescence. Radiation Protection Dosimetry. 100, 45-54.

Višnjević, V., Herman, F., Podladchikov, Y., 2018.Reconstructing spatially variable mass balances from past ice extents by inverse modeling. Journal of Glaciology 64(248), 957-968.

Vollweiler, N., Scholz, D., Muhlinghaus, C., Mangini, A., Spotl, C., 2006. A precisely dated climate record for the last 9 kyr from three high alpine stalagmites, Spannagel Cave, Austria. Geophys. Res. Lett. 33 (L20703), 324.

von Blanckenburg, F., and Willenbring, J. K., 2014. Cosmogenic nuclides: Dates and rates of Earth-surface change. Elements, 10(5), 341-346.

Wallinga, J., Murray, A., Wintle, A., 2000. The single-aliquot regenerative-dose (SAR) protocol applied to coarse-grain feldspar. Radiation Measurements. 32, 529-533.

West, A. J., Thickness of the chemical weathering zone and implications for erosional and climatic drivers of weathering and for carbon cycle feedbacks. Geology, v. 40; no. 9; p. 811-814.

Winkler. 2004. Lichenometric dating of the 'Little Ice Age' maximum in Mt Cook National Park, Southern Alps, New Zealand. The Holocen 12,6, pp. 911-920.

Wintle, A.G., 1973. Anomalous fading of thermo-luminescence in mineral samples. Nature. 245, 143-144.

Wintle, A.G., Murray, A.S., 2006. A review of quartz optically stimulated luminescence characteristics and their relevance in single-aliquot regeneration dating protocols. Radiation Measurements 41, 369-391.

Wirsig, C., Zasadni, J., Ivy-Ochs, S., Christl, M., Kober, F., Schluchter, C., 2016a. A deglaciation model of the Oberhasli, Switzerland. Journal of Quaternary Science 31, 46-59.

Wirsig, C., Zasadni, J., Christl, M., Akçar, N., Ivy-Ochs, S., 2016b. Dating the onset of LGM ice surface lowering in the High Alps. Quaternary Science Reviews.143, 37-50.

Zachos, J.C., Pagani, M., Sloan, L., Thomas, E. and Billups, K., 2001. Trends, rhythms, and aberrations in global climate 65 Ma to present. Science. 292, 686-693.

Zachos, J.C., Shackleton, N.J., Revenaugh, J.S., Palike, H., Flower, B.P., 2001. Climate response to orbital forcing across the Oligocene-Miocene boundary. Science. 292, 274-278.

Zimmerman, S.G., Evenson, E.B., Gosse, J.C., Erskine, C.P., 1994. Extensive boulder erosion resulting from a range fire on the type-Pinedale moraines, Fremont Lake, Wyoming. Quat. Res. 42, 255-265.

Curriculum vitae

Education

- Ph.D., University of Lausanne, 2018 (defended on March 6st, 2019).
  - *Thesis title* Ice-extent variation and post-glacial erosion in the Mont Blanc massif
  - *Committee* Prof. Dr. Christian Kull, Prof. Dr. Fréricé Herman
    Prof. Dr. Georgina K. King, Prof. Dr. Andreas Lang
    Prof. Dr. Derek Fabel, Dr. Pierre Valla

- Master's degree in Earth and Environmental Sciences, University of Grenoble Alps, 2011.
- Bachelor in Geosciences, University of Grenoble Alps, 2009.
- Secondary school graduation, Lycée Champollion, Grenoble, 2006.

Professional Experiences

- Engineer in design and realization of field experiments in glaciology, meteorology and hydrology, November 2011- November 2013
  Scientific cooperation La Paz, Bolivia
  Glacioclim Observatory Andes, Institute for Research for Development (IRD), Institute Geophysic of Environment (IGE), University of Grenoble Alps
- Research assistant, September - October 2011
  Member of Geoch4D geochemistry team
  Institute of Earth Sciences (ISTERRE), University of Grenoble Alps

Fields of Research Interest

Interaction erosion and climate, Paleoenvironmental reconstruction, Geochronometer development, Glacier monitoring

Selected Scientific Publications

- Lehmann, B., Valla P.G., Herman, F. (2018). Investigation of OSL surface exposure dating to reconstruct post-LIA glacier fluctuations in the French Alps (Mer de Glace, Mont Blanc massif), Quaternary Geochronology. *Quaternary Geochronology*
- Lehmann B., Valla P.G., King G.E., Biswas R.H., Herman, F. (in review). Evaluating post-glacial bedrock erosion and surface exposure duration by coupling in-situ OSL and ^{10}Be dating. *Earth Surface Dynamics*
- Duverger A., Herman F., King G.E., Valla P.G., Lehmann B., Visnjevic V. and Cox S.C. (in review). Glacial erosion during a glacial cycle: insights from the Franz Josef Glacier/Ka Roimata o Hine Hukatere. *Journal of Geophysical Research: Earth Surface: Earth Surface*

Memberships and awards

- Ann Wintle Prize for Best oral for Applications, LED 2017 conference in Capetown (SA)
- Outstanding Student Poster and PICO (OSPP) Awards, EGU 2016 in Vienna (AUT)
- Student Poster Awards, UKLUM15 conference in Glasgow (UK)
- Member of the European Geoscience Union (EGU)

Teaching Experience

- BSc, Tectonic, Erosion Climate, Unil, 2014-2017.
- BSc, Numerical Modelling, Unil, 2017-2018.

Publication list

Publications in peer-reviewed scientific journals

- **Lehmann, B.**, Valla, P.G., King, G.E., Herman, F. (2018). Investigation of OSL surface exposure dating to reconstruct post-LIA glacier fluctuations in the French Alps (Mer de Glace, Mont Blanc massif). Quaternary Geochronology

- Duverger, A., Herman, F., King, G.E., Valla, P.G., **Lehmann, B.**, Visnjevic V. and Cox S.C. (in review). Glacial erosion during a glacial cycle: insights from the Franz Josef Glacier/Ka Roimata o Hine Hukatere.Journal of Geophysical Research: Earth Surface: Earth Surface

- **Lehmann, B.**, Herman, F., Valla, P.G., King, G.E., Biswas, R.H. (in review). Evaluating post-glacial bedrock erosion and surface exposure timing by coupling OSL and TCN dating. Earth surface dynamics

- Benoit, L., Gourdon, A., Vallat, R., Irarrazaval, I., Gravey, M., **Lehmann, B.**, Prasicek, G., Graff, D., Herman, F., Mariethoz, G. (in review). A high-frequency and high-resolution image time series of the Gornergletscher - Swiss Alps - derived from repeated UAV surveys.Earth System Science Data

- **Lehmann, B.**, Herman, F., Valla, P.G., King, G.E., Biswas, R.H., Ivy-Ochs, S., Kronig, O., Christl, M., (in prep.). Post-glacial erosion of polished bedrock surfaces and deglaciation timing: new insights from the Mont Blanc massif (Western Alps).

Book chapters

King, G.E., Valla, P.G. and **Lehmann, B.**. (Accepted) OSL Rock Surface and Rock Surface-Exposure Dating. Invited contribution to "Handbook of Luminescence Dating", Eds: M. Bateman and I. Bailiff

Scientific communication

Lehmann, B. (2108)Histoire et volution des glaciers de la vallé de Chamomix.Bulletin de la Socit vaudoise de science naturelle.

Conference participations

- **Lehmann, B.**, Valla, P. G., King, G. E., Ivy-Ochs, S., Kronig, O., Christl, M. and Herman, F. (2018) Talk. Constraining past ice-extent and post-glacial erosion by combining OSL and 10Be surface exposure dating.Europeen Geosciences Union, Vienne, Austria. Talk.
- **Lehmann, B.**, Valla, P. G., King, G. E., Ivy-Ochs, S., Kronig, O., Christl M. and Herman F. (2017) Talk. Constraining paleo-glacier extent and local erosion using OSL and 10Be surface exposure dating.Swiss Geosciences Meeting 2017. Davos, Switzerland.
- **Lehmann, B.**, Valla, P. G., King, G. E., Ivy-Ochs, S., Kronig, O., Christl, M. and Herman, F. (2017) Using OSL and 10Be surface exposure dating to constrain ice-extent histories and post-glacial erosion.15th International Conference on Luminescence and Electron Spin Resonance 11 15 September, Cape Town, South Africa.
- **Lehmann, B.**, Valla, P. G., King, G. E., Ivy-Ochs, S., Kronig, O., Christl, M. and Herman, F.(2017) Talk. Reconstruction of glacier fluctuations in the MontBlanc massif, western Alps: a multimethod approach.Europeen Geosciences Union, Vienne, Austria.
- **Lehmann, B.**, Valla, P. G., King, G. E. and Herman, F. (2017) Talk.Reconstruction of glacier fluctuations in the Mont-Blanc massif, western Alps: a multi-method approach.Swiss Geosciences Meeting. Geneva, Switzerland.
- **Lehmann, B.**, Valla, P. G., King, G. E. and Herman, F. (2016) Reconstruction of glacier fluctuations in the Western Alps since the LGM using OSL surface exposure dating.Europeen Geosciences Union, Vienne, Austria. Poster.
- **Lehmann, B.**, Valla, P. G., King, G. E. and Herman, F. (2016) Talk. OSL-surface exposure dating as a tool to constrain post-LGM glacier fluctuations in the Western Alps.Swiss Geosciences Meeting. Basel, Switzerland.

- **Lehmann, B.**, Valla, P. G., King, G. E. and Herman, F. (2015) Poster.Constraining post-LGM glacier fluctuations using OSL-surface exposure dating in the Western Alps.UK Luminescence and ESR Meeting, Glasgow, UK.
- Réveillet, M., Rabatel, A., **Lehmann, B.**,(2013) Poster. Bedrock mapping using Radar measurements on two tropical glaciers: Zongo and Charquini Sur (Cordillera Real, Bolivia)Alpine Glaciological Meeting at Grenoble, France.
- **Lehmann, B.**, Sobolev, A.V., Arndt, N.T., Chauvel, C., Poster. Mantle Source Composition of Magma from the North Atlantic Igneous ProvinceGoldschmidt conference at Prague, Czech Republic, 2011

CHAPTER 10

Publications

10.1 Large Investigation of OSL surface exposure dating to reconstruct post-LIA glacier fluctuation in the French Alps (Mer de Glace, Mont Blanc massif)

Benjamin Lehmann[1], Pierre G. Valla[1,2], Georgina E. King[1,2] and Frédéric Herman[1]

[1] Institute of Earth Surface Dynamics, University of Lausanne, Lausanne, 1012, Switzerland.
[2] Institute of Geological Sciences and Oeschger Centre for Climate Change Research, University of Bern, Bern, 3012, Switzerland.

Research paper

Quaternary Geochronology 44 (2018) 63-74

Author contributions. BL designed the study, collected the sample, prepared the samples, performed the analysis, ran the simulations, and wrote most of the manuscript. All authors contributed in interpreting the results and improving the text.

Quaternary Geochronology 44 (2018) 63–74

Contents lists available at ScienceDirect

Quaternary Geochronology

journal homepage: www.elsevier.com/locate/quageo

Research paper

Investigation of OSL surface exposure dating to reconstruct post-LIA glacier fluctuations in the French Alps (Mer de Glace, Mont Blanc massif)

Benjamin Lehmann[a,*], Pierre G. Valla[a,b], Georgina E. King[a,b], Frédéric Herman[a]

[a] Institute of Earth Surface Dynamics, University of Lausanne, Lausanne, 1012, Switzerland
[b] Institute of Geological Sciences and Oeschger Centre for Climate Change Research, University of Bern, Bern, 3012, Switzerland

ARTICLE INFO

Keywords:
Optically stimulated luminescence (OSL)
Surface exposure dating
Luminescence depth profile
Paleo-glacier reconstruction
Mont Blanc massif

ABSTRACT

Providing quantitative constraints on late Pleistocene glacier fluctuations remains an important challenge for understanding glacier response to past and future climate changes. In most mountainous settings, paleo-glacier reconstructions are limited because they often lack precise temporal constraints. Different geochronological methods have been developed and applied to date specific geomorphological or sedimentological markers for paleo-glacier dynamics. Recently, OSL (Optically Stimulated Luminescence) surface exposure dating has been introduced and provides us with an opportunity to improve paleo-glacier reconstructions. This method is based on the sensitivity of the OSL signal from rock minerals to light, resulting in bleaching of the OSL signal within the upper first millimeters of the exposed rock surface, a process that depends on the exposure age, the rock type and the local setting (e.g. topographic shielding, bedrock orientation etc.). Here, we investigate the potential of OSL surface exposure along a vertical cross-section of polished bedrock surfaces with known post-LIA (Little Ice Age) exposure ages (from 3 to 137 years) along the Mer de Glace glacier (Mont Blanc massif, France). The infrared stimulated luminescence (IRSL) signals from rock slices exhibit increasingly deep bleaching profiles with elevation and thus exposure age, which is consistent with progressive glacier thinning since the LIA. Our results show that OSL surface exposure dating can be applied to periglacial environments, and is a promising tool for high-resolution reconstruction of ice extent fluctuations, both in space and time.

1. Introduction

During the last ca. 5 Ma of Earth's history, global climate cooled and evolved towards oscillating climatic conditions that intensified towards the present (e.g. Zachos et al., 2001; Herbert et al., 2016). This climate shift left a strong imprint on mountain topography (e.g. Penck, 1905; Broecker and Denton, 1990; Molnar and England, 1990; Peizhen et al., 2001; Egholm et al., 2009; Herman et al., 2013). However, understanding paleo-climatic conditions in mountainous areas over the Plio-Pleistocene epochs remains difficult. Local records of successive glacial/interglacial cycles are scarce or poorly preserved over such long timescales (Ehlers and Gibbard, 2007). Polar ice-sheets and marine cores are useful for providing long-term global climatic records but are unable to describe regional continental climate. In contrast, glaciers and their fluctuations through time provide invaluable information on past mountain climatic conditions. Through mapping and dating moraine deposits and erratic boulders, it is possible to reconstruct the history of ice-extent (e.g. for the European Alps: Ivy-Ochs et al., 2006; Bini et al., 2009; Preusser et al., 2011; Schimmelpfennig et al., 2014; Ivy-Ochs, 2015; Wirsig et al., 2016).

Past glacier extents in the European Alps are well constrained since the Little Ice Age (LIA: 15th to 19th centuries). Using historical maps, survey reports and aerial photogrammetry, glacier fluctuations have been precisely reconstructed over the last two centuries (e.g. Vincent et al., 2014). To go further back in time into the Pleistocene, different geochronological methods can be used such as lichenometry (Winkler, 2004), varve chronologies (Stewart et al., 2011), dendrochronology (Baillie, 1995) and radiocarbon dating (Hajdas, 2008). However, organic matter can be scarce for glacial/periglacial deposits because of the extremely active geomorphic processes associated with glacial environments. In addition to these methods, surface exposure dating of polished bedrock or erratic boulders using terrestrial *in situ* cosmogenic nuclides has been developed over the last decades (Lal, 1991; Goss and Philips, 2000; Balco, 2011; Ivy-Ochs and Briner, 2014), and has been used in the European Alps (see Ivy-Ochs et al., 2006, 2009 for reviews). The combination of different cosmogenic nuclide pairs (e.g. ^{10}Be and ^{14}C: e.g. Goehring et al., 2012; Hippe et al., 2014) provides us with important information on Alpine glacier paleogeography since the Last Glacial Maximum (LGM; Ivy-Ochs et al., 2006; Wirsig et al., 2016).

* Corresponding author.
E-mail address: benjamin.lehmann@unil.ch (B. Lehmann).

https://doi.org/10.1016/j.quageo.2017.12.002
Received 7 July 2017; Received in revised form 23 November 2017; Accepted 3 December 2017
Available online 06 December 2017

However, the cosmogenic nuclide production rate and the integration of production over the first 1–2 m below a rock surface may limit the resolution of such methods for recent and/or complex exposure histories.

Here we investigate whether Optically Stimulated Luminescence (OSL) surface exposure dating can be used to reconstruct recent glacier fluctuation. Luminescence dating is based on the accumulation of trapped electrons through time in the crystalline lattice of certain minerals (e.g. quartz or feldspar). Some of these trapped electrons are sensitive to daylight exposure (Aitken, 1985; Huntley et al., 1985). Luminescence dating is commonly used to date sediment burial in a range of geomorphological environments (e.g. Duller, 2008; Rhodes, 2011; Fuchs and Owen, 2008) but can also be used to determine rates of bedrock cooling (Guralnik et al., 2015; King et al., 2016; Brown et al., 2017), and the exposure age of archaeological rock surfaces (Polikreti et al., 2003; Sohbati et al., 2011). This latter application is based on the principle that when a rock surface is exposed to light, the luminescence signal, which is initially homogenous within the rock sample (at a given level or in field steady-state; e.g. Valla et al., 2016), will progressively decrease at depth until being completely zeroed, a phenomenon called "bleaching" (Aitken, 1998). The assumption used in this study is that the longer a surface has been exposed to daylight, the deeper the signal bleaching will be (Polikreti et al., 2002). In granitic and gneissic rocks, bleaching through time has been shown to occur over the first few centimetres depth of the rock surface (Vafiadou et al., 2007; Sohbati et al., 2011; Freiesleben et al., 2015). In alpine environments, glacier advances during the late Pleistocene to Holocene have been associated with subglacial erosion of bedrock at the centimetre-scale (e.g. Goehring et al., 2011). This means that only the most recent exposure history of the bedrock will be recorded, as earlier exposure histories and OSL bleaching evidence will have been eroded by subsequent glacier advances. OSL surface exposure dating would thus in theory enable past glacier extents to be reconstructed with a high temporal resolution for both recent and complex exposure histories. Furthermore, this method is attractive because of the short time required for sample preparation (Sohbati et al., 2011), although one current disadvantage is the requirement for calibration of this chronometer on rock surfaces with independently-known exposure ages (Sohbati et al., 2012a).

In the following, we first introduce the study site, i.e. the Mer de Glace, and our sampling strategy. We have targeted several independently-dated glacially-eroded bedrock surfaces, which represent past elevations of the glacier surface since the LIA. We then review the basic principles of the method and present the luminescence signals for six different surfaces along an altitudinal cross-section above the present-day Mer de Glace. Our results show a strong correlation between sample elevation, exposure age and bleaching depth. Finally, we use this dataset to show that model calibration requires multiple samples of known age to take full advantage of OSL surface exposure dating in both glaciated and formerly glaciated environments.

2. Setting and sampling strategy

2.1. Geomorphological setting

The Mer de Glace glacier (Fig. 1) is about 11.5 km long and is located in the Mont Blanc massif. The modern glacier covers an area of 30.4 km^2 (excluding former tributary Talèfre Glacier) and spans an elevation range from 4205 m to 1531 m.a.s.l. (data from 2008; Gardent et al., 2014). The mean equilibrium line altitude (ELA), reconstructed using remote sensing methods, was about 2880 m.a.s.l. between 1961 and 1990 for five of the main north-facing Mont Blanc massif glaciers, including the Leschaux Glacier for the period 1984–2010 (Rabatel et al., 2013).

The Mer de Glace is an appropriate laboratory for validating the application of OSL surface exposure dating for paleo-glacier reconstruction. Numerous studies have provided detailed reconstructions of Mer de Glace fluctuations from the LGM towards the Holocene and present day (Coutterand and Buoncristiani, 2006; Nussbaumer et al., 2007; Vincent et al., 2014; Le Roy et al., 2015). The Montenvers site (Fig. 1) was chosen as an optimal study site as the evolution of glacier thickness since the LIA has been reconstructed by Vincent et al. (2014) using historical maps, aerial photogrammetry and satellite-derived digital elevation models (see Supplementary Material A1 for details). Furthermore, the rock type is generally homogenous along the valley flank (i.e. orthogneiss; Dobmeier, 1998), avoiding any lithological dependency of the OSL surface exposure dating approach although occasional granitic lenses are exposed in the lower part of the profile (see Section 2.2 for details).

Our sampling strategy was to collect glacially polished bedrock surfaces with the best-preserved erosion patterns (glacial striations, roches moutonnées; Fig. 2) to ensure that sample bleaching profiles reflect the period of time since post-LIA deglaciation. The samples were also selected to have low topographic shielding and vegetation cover (e.g. lichen). Steep slopes were selected (i.e. above 30°) to limit any potential snow cover effect. In particular, we focused on rock surfaces exhibiting striations parallel to the Mer de Glace flow line in order to avoid the potential influence of tributary glaciers.

2.2. Sample description

We collected six samples along the Montenvers profile during several field campaigns (2015–2016), ranging in elevation from 1841 to 1696 m.a.s.l. (Fig. 1 and Table 1). Samples MBMV1, MBMV7, MBMV8, MBMV10 and MBMV11 consist of coarse-grained orthogneiss, typical for the Aiguilles Rouges massif (Dobmeier, 1998). These rocks mainly comprise coarse K-feldspar crystals, quartz, biotite and muscovite. Only MBMV6 was collected from a granitic lens (Fig. 2b), which consists of bigger quartz and feldspar crystals than the orthogneiss (Fig. 3). Because differences in crystals properties may influence light penetration, i.e. due to both crystal size and distribution, sample MBMV6 is used to explore any potential lithological effect on the OSL surface exposure dating approach (see Tables 2 and 3).

2.3. Independent age calibration from glacier surface elevation reconstruction

We use the historical post-LIA reconstruction of the Mer de Glace ice-surface elevation (Vincent et al., 2014), which is available for two cross-sections: Montenvers and Echelets (Fig. 1). Samples MBMV1, MBMV7, MBMV10 and MBMV11 were collected from the same profile located 290 m upstream of the Montenvers cross-section and 690 m downstream of the Echelets cross-section (cross-section 1, Fig. 1 and Supplementary Fig. A1). Samples MBMV6 and MBMV8 were taken along a profile (cross-section 2, Fig. 1 and Supplementary Fig. A1) located 200 m upstream of cross-section 1. Because glacial thinning would progressively expose bedrock surfaces at lower elevations, we can use the relationship between exposure age and sample elevation to constrain the temporal evolution of glacial thickness (Fig. 1 and Supplementary Fig. A1).

Post-LIA glacier surface reconstructions of the Mer de Glace for cross-sections 1 and 2 have been interpolated from the Montenvers and Echelets cross-sections. Exposure ages from 2 to 137 years were obtained for the different samples, using either cross-section 1 (MBMV1, MBV7, MBMV10 and MBMV11) or cross-section 2 (MBMV6 and MBMV8) (see Supplementary Material A1). All exposure ages are relative to the first sampling campaign in summer 2015.

3. Methodology: OSL surface exposure dating

3.1. Theoretical approach

Minerals such as quartz and feldspar naturally contain defects or

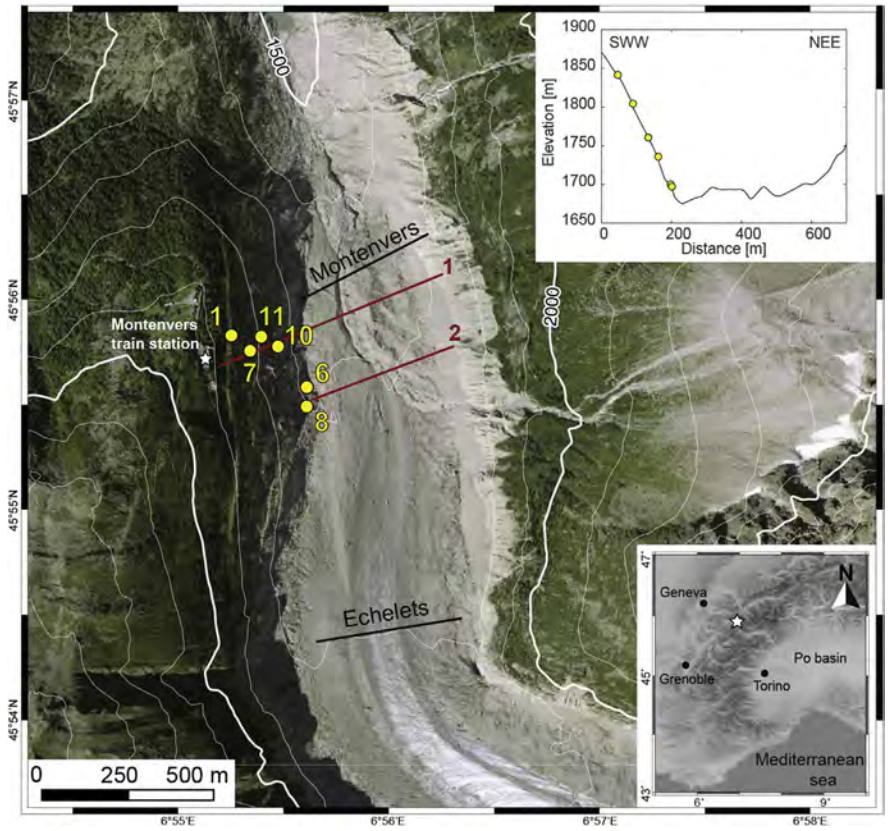

Fig. 1. Sampling map of the Montenvers site, Mer de Glace. The orthorectified aerial photograph of the Mer de Glace was acquired in 2016 (source: www.geoportail.gouv.fr). The black lines show the two cross-sections produced by Vincent et al. (2014) which we interpolated to reconstruct glacier surface elevations at two different locations (red lines 1 and 2, see Section 2.3 and Supplementary Fig. A1) where samples were collected (yellow dots with numbers). Upper right inset represents the collected samples projected along cross-section 1. Bottom right inset shows location of the study area within the western Alps.

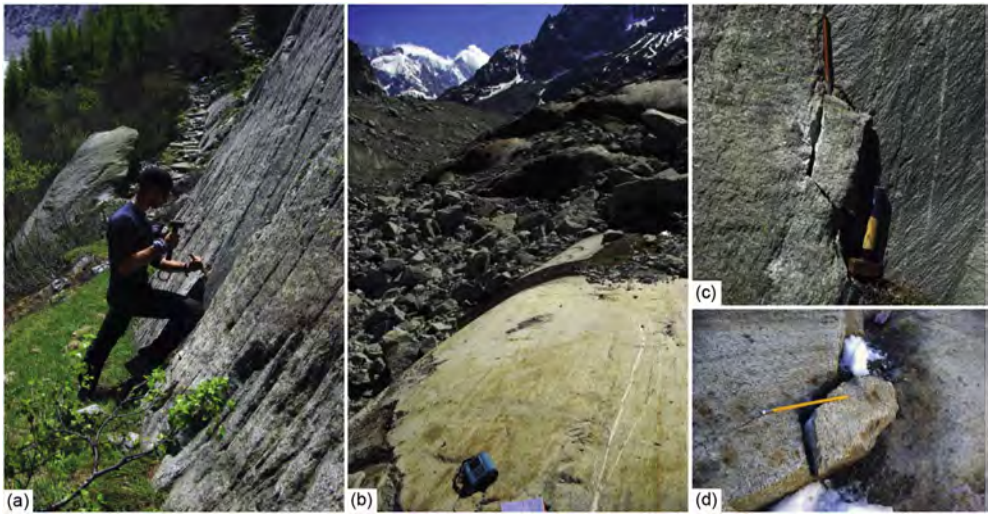

Fig. 2. Sampling sites and sample details at the Montenvers site. (a, b) Sampling sites for MBMV7 and MBMV6. (c, d) Outcrops and samples MBMV7 and MBMV6.

impurities in their crystal lattice. Energy released by ambient radiation (i.e. cosmic rays and the flux of high-energy solar particles and/or radioactive decay in the rock-matrix) excites electrons from their equilibrium state (valence band), and these can become trapped at higher energy levels within the crystal. Because of the finite number of traps, electron filling occurs until saturation is reached. By giving energy to the system in the form of light or heat (natural bleaching processes), electrons are released and return to their equilibrium state, producing photons. This phenomenon is called luminescence and the intensity of a given luminescence signal is thus proportional to the number of trapped electrons (Aitken, 1985, 1998). In a rock surface continuously exposed to daylight, the progressive bleaching of the luminescence signal is expected to propagate deeper into the surface with time (Habermann et al., 2000; Polikreti et al., 2002; Laskaris and Liritzis, 2011).

Rock surface dating was first used in archaeology, and was based on thermally-stimulated measurements, i.e. thermoluminescence (TL; Liritzis, 1994; Richards, 1994; Theocaris et al., 1997; Polikreti et al.,

Table 1
Sample characteristics from the Montenvers site. Estimated exposure ages were reconstructed using differential GPS and glacier surface-elevation reconstruction as shown in section 2.3. Shielding factors were calculated with the geometric shielding calculator (CRONUS-Earth project). Note that all estimated exposure ages are referenced from 2015 (date of the first field campaign).

Sample ID	Latitude	Longitude	Elevation	Lithology	Estimated Exposure Age	Topographic shielding factor	Surface orientation
	WGS 84		[m.a.s.l.]		[Year before 2015]		
MBMV1	N45°55′54.0″	E06°55′07.7″	1841	Gneiss	137	0.81	N8 55°E
MBMV6	N45°55′48.9″	E06°55′17.7″	1696	Granite	2	0.92	N0 30°E
MBMV7	N45°55′52.7″	E06°55′09.9″	1804	Gneiss	69	0.79	N374 60°E
MBMV8	N45°55′47.7″	E06°55′18.5″	1699	Gneiss	3	0.81	N13 54°E
MBMV10	N45°55′54.0″	E06°55′14.1″	1735	Gneiss	18	0.79	N0 60°E
MBMV11	N45°55′54.3″	E06°55′11.5″	1760	Gneiss	30	0.88	N355 75°E

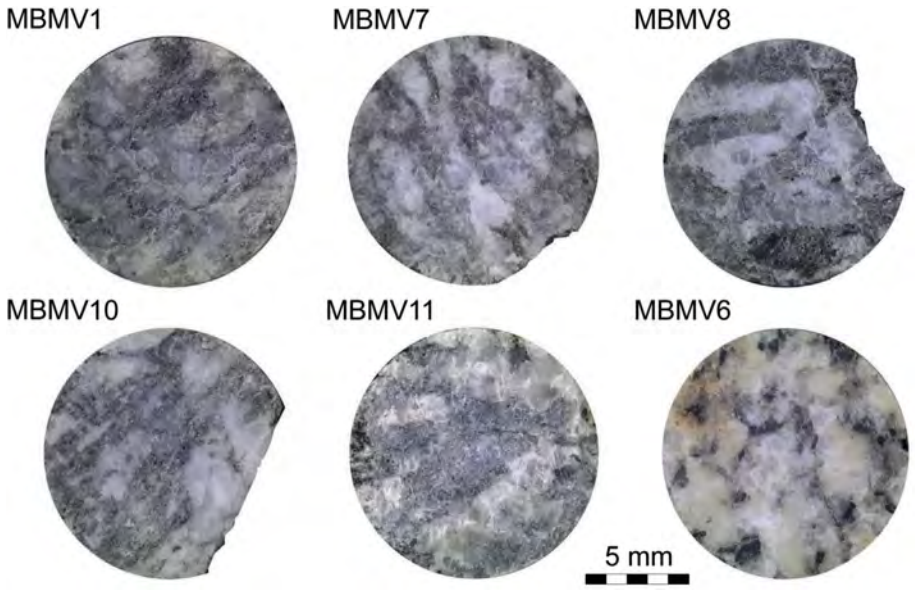

Fig. 3. Pictures of selected rock slices (see sections 2.2 and 4 for details), showing the difference in composition and texture between orthogneiss (MBMV1, MBMV7, MBMV8, MBMV10, and MBMV11) and granite (MBMV6).

2002, 2003). More recently, OSL dating (e.g. Habermann et al., 2000; Vafiadou et al., 2007) has been introduced to date surface exposure, which benefits from improved measurement reproducibility and more rapid signal bleaching following exposure to daylight than typically-used TL signals (e.g. the 325 °C TL peak in quartz). The potential of OSL for dating exposure events in geomorphological (Freiesleben et al., 2015; Sohbati et al., 2015) and archaeological (Liritzis, 2011) contexts has recently been investigated, and a range of applications including relative sea-level changes and coastal geomorphology (Simms et al., 2011; Simkins et al., 2013) have been published. However, OSL surface exposure dating has not yet been applied to glacially polished bedrock surfaces.

In mountainous environments, OSL dating can be used to evaluate the exposure age of a polished bedrock surface as described in Fig. 4. At the initial condition (t_1 in Fig. 4), the glacier has reached its maximum thickness. Ice and subglacial sediments cover the bedrock surface, and the luminescence signals of bedrock minerals are in field steady-state and uniform in the rock column. When the glacier retreats, freshly-eroded surfaces are exposed to daylight (point a at time t_2, Fig. 4). The initial luminescence signals start to bleach for these exposed surfaces, while the sample at lower elevation is still covered by the glacier and its luminescence signals remain uniform in the rock (point b at time t_2, Fig. 4). As the glacier continues to thin, the lower part of the bedrock flanks are uncovered (t_3, Fig. 4) and the luminescence signals start to bleach for the lower-elevation surfaces. Therefore, in a setting affected by progressive glacier retreat and thinning, there is a direct correlation between the elevation of the studied site and the exposure age, with the assumption that the longer a surface is exposed to daylight, the deeper into the rock the luminescence signal is bleached (Freiesleben et al., 2015; Sohbati et al., 2011).

3.2. Modelling approach

To assess rock surface exposure durations to daylight from a luminescence depth profile, we use the model proposed by Sohbati et al. (2011, 2012a,b) who provide an in-depth review of each parameter. When a rock surface is exposed to daylight, both detrapping (due to the release of energy by daylight) and trapping (due to absorption of energy from ambient radiation) occur simultaneously. The trapped-charge concentration during light exposure is given by the following differential equation:

$$\frac{\partial n(x,t)}{\partial t} = -E(x)\,n(x,t) + F(x)\,[N(x) - n(x,t)] \quad (1)$$

Where $n(x, t)$ is the trapped charge concentration [m^{-3}] at time t [s] and depth x [m], $N(x)$ is the concentration of sites [m^{-3}] available for trapping at depth x, $E(x)$ is the charge detrapping rate [s^{-1}], and $F(x)$ is the trap filling rate [s^{-1}] (Table 2). The charge detrapping rate, $E(x)$, is itself given by:

$$E(x) = \overline{\sigma\varphi}_0\, e^{-\mu x} \quad (2)$$

where $\varphi_0(\lambda, x)$ is the photon flux [$cm^{-2}\ s^{-1}$] (Table 2) describing the rate of incoming photons that can bleach the trap of interest. $\sigma(\lambda)$ is the photoionization cross section [cm^2] describing the probability of this

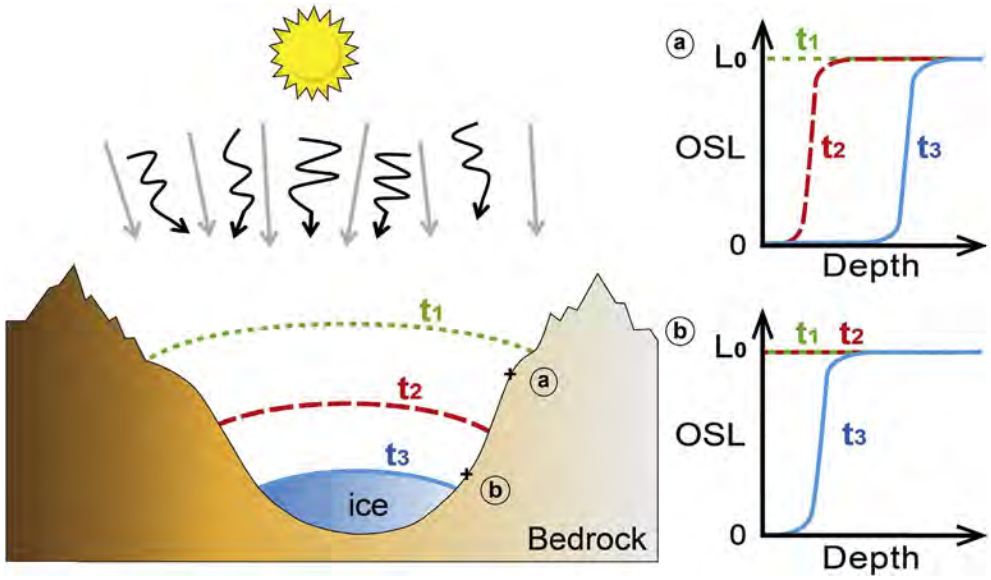

Fig. 4. Sketch linking glacier thinning and OSL signal evolution for two bedrock surfaces located at different elevations along the valley flank. Straight arrows (grey) represent cosmic rays and high-energy solar particle flux; this radiation, together with radioactive decay in the rock matrix build up the latent luminescence signal. Other arrows (black) represent low energy electromagnetic radiation from daylight; this radiation bleaches the latent luminescence signal. At the initial time t_1, the glacier is at its maximum extent and the OSL signals for both surfaces are in field steady-state and uniform within the rocks, L_0. At time t_2, the glacier has retreated and exposed the surface (a), the OSL signal begins to bleach whilst surface (b) remains covered with its luminescence signal unchanged. In the final step t_3, the glacier size has shrunk, surface (a) remains exposed and its OSL signal is bleached at greater depth while surface (b) has just been exposed to daylight and its OSL signal has been bleached just below the exposed surface.

specific trap being excited by light stimulation. It is averaged over the wavelengths present in the solar spectrum at the surface ($x = 0$). Here, we assume that the photon flux does not fluctuate through time, and we are only concerned with the product of the two parameters, which is given by $\overline{\sigma\varphi}_0$ [s^{-1}] (i.e. the effective decay rate of luminescence; Sohbati et al., 2011). Equation (2) also includes a decay term for light attenuation with depth. The light attenuation coefficient μ [m^{-1}] describes how deep into the rock a photon will penetrate and affect the luminescence signal. μ is assumed to be independent of wavelength in the spectral range of interest (Sohbati et al., 2011).

For surface exposure dating of terrestrial surfaces, the effect of trap filling during daylight exposure over short timescales (i.e. centuries) is often negligible (i.e. $F(x) \approx 0$) (see Supplementary Material A2). The trapped charge population at a given depth (x) can then be approximated by:

$$n(x) = n_0 e^{-E(x)t} \tag{3}$$

where n_0 is the initial charge population [m^{-3}] assumed to be constant with depth within the rock column prior to bleaching. Assuming that the luminescence signal (L) is proportional to n, Eq. (3) becomes:

Table 2
Summary of symbols.

Symbol	Unit	Definition
n	m^{-3}	Concentration of trapped charge
x	m	Depth
t	s	Time
N	m^{-3}	Concentration of sites available too trap charge
E	s^{-1}	Charge detrapping rate due to daylight radiation
F	s^{-1}	Charge trapping due to ionising radiation
σ	cm^2	Photoionisation cross-section
φ	$cm^{-2}\ s^{-1}$	Photon flux
$\overline{\sigma\varphi}_0$	s^{-1}	Charge detrapping rate
μ	m^{-1}	Attenuation coefficient
Lx	Counts	Regenerated luminescence signal
Tx	Counts	Test dose signal
L	Counts	Luminescence

$$L = \frac{Lx}{Tx} = L_0 e^{-\overline{\sigma\varphi}_0 t e^{-\mu x}} \tag{4}$$

where Lx/Tx is the normalized natural luminescence signal measured at depth x [m] after exposure age t [s]. L_0 is the normalized natural luminescence signal before bleaching (Fig. 4 and Table 2), which is sample dependent and can be constrained in the laboratory.

Equation (4) can predict the rock luminescence profiles for different exposure ages, however the mean photon flux φ_0, the photoionization cross-section σ, and the attenuation coefficient μ must first be quantified (cf. Table 2). φ_0 is mainly controlled by the latitude and the cloudiness; and it is broadly correlated with elevation (Blumthaler et al., 1997). The solar irradiance fluctuates over decadal timescales (Lean, 1987) making the independent determination of the photon flux impossible without knowing the time of exposure. The photoionization cross-section σ depends on both the mineral and the trap targeted (Bailey, 2004). For samples from the same region and from a similar lithology, $\overline{\sigma\varphi}_0$ is assumed to be uniform and μ is expected to be of the same order of magnitude between samples, but not necessarily equal.

The OSL-depth profile of exposed rock surfaces with independently-constrained exposure durations can be used to calibrate the $\overline{\sigma\varphi}_0$ and μ parameters by fitting the luminescence signal bleaching with depth (Singarayer, 2002; Sohbati et al., 2012a). These constrained parameters can then be used to determine the exposure histories of unknown-age surfaces from the same region.

Here, our objective is to demonstrate the validity of the proposed model (Eq. (4)) on polished bedrock surfaces and to calibrate the model parameters on surfaces with known exposure age. To do so, the unknown $\overline{\sigma\varphi}_0$ and μ parameters are inverted for each sample using a probability density function of the model parameters, given the observed OSL-depth profile data. This includes a least absolute deviation regression $\mathcal{L}_{sample}$ (Eq. (5)), in which we randomly prescribe a range of different $\overline{\sigma\varphi}_0$ and μ values. From the residual likelihood $\mathcal{L}_{sample}$ obtained, we select the maximum likelihood values of $\overline{\sigma\varphi}_0$ and μ. The modelled luminescence signals $\left(\frac{Lx}{Tx}\right)_m$ are calculated for each rock slice of a given sample using the known exposure age of each sampling site, giving:

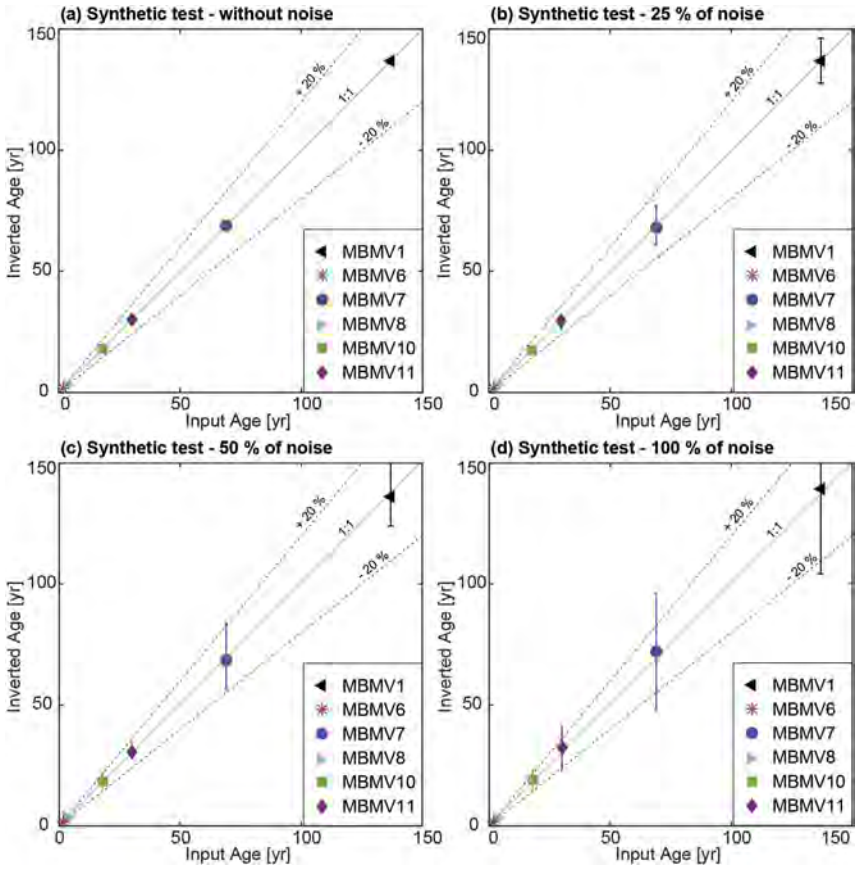

Fig. 5. Results (median value) of inverted exposure age from the synthetic test, (a) without noise on the luminescence signal, (b) with 25%, (c) 50%, and (d) 100% noise. Error bars represent ± 2σ on the inverted age.

$$\mathcal{L}_{sample} = \exp\left(-\frac{1}{2a}\sum_{i=1}^{n}\left|\left(\frac{Lx}{Tx}\right)_{obs}^{(i)} - \left(\frac{Lx}{Tx}\right)_{m}^{(i)}\right|\right) \quad (5)$$

where n is the number of rock slices per sample, $\left(\frac{Lx}{Tx}\right)_{m}^{(i)}$ is the luminescence signal calculated using Eq. (4), $\left(\frac{Lx}{Tx}\right)_{obs}^{(i)}$ is experimentally measured for each rock slice i and a is the uncertainty. Given that the scatter of the plateau signal (L_o) for every independent sample is larger than the analytical error, we use the standard deviation around the plateau value L_o to estimate a. Then, we compute the combined likelihood for a number of samples p using:

$$\mathcal{L}_{combined} = \prod_{j=1}^{p}\mathcal{L}_{sample(j)} \quad (6)$$

This approach provides the most likely common values of $\overline{\sigma\varphi}_0$ and μ. Once the parameters of the model are determined as shown above, it is possible to invert the exposure age for other rock surfaces using the constrained $\overline{\sigma\varphi}_0$ and μ values (cf. Eq. (5)).

In order to verify our modelling approach, we show a synthetic inversion. We produce a synthetic luminescence signal (Lx/Tx for depths in between 0 and 14 mm) using Eq. (4) and sample-specific $\overline{\sigma\varphi}_0$ and μ parameters (obtained from initially fitting every sample using their independent age control, see Section 5.2 for details) and assuming a constant μ value (i.e. homogenous lithology with rock depth). The first step of the synthetic test is to invert parameters $\overline{\sigma\varphi}_0$ and μ knowing the exposure age t for each individual sample as presented above. Then, using these $\overline{\sigma\varphi}_0$ and μ parameters, we subsequently invert for the exposure age t using Eq. (4). In order to study the effect of potential uncertainties from the experimental data on the exposure age determination, we reproduce this synthetic test with white noise on the luminescence signal, with four different amplitudes between 0 and 100% (Fig. 5). Our synthetic results show that our inversion approach can recover the exposure age with 0–50% noise. The synthetic test with 100% noise on the luminescence signal provided age outcomes with larger uncertainties (> 20%). The best results are obtained using the best-fit of $\overline{\sigma\varphi}_0$ and μ and the median value of the predicted exposure ages. The resulting uncertainties are correlated with the magnitude of the noise, however any potential variability in the luminescence signal does not appear to produce a significant bias on the inverted exposure age.

4. Sample preparation and analysis

The bedrock samples were cored to 30 mm depth using a Husqvarna DM220 drill, with 10-mm diameter. Cores were then sliced into 0.7-mm thick rock slices with a BUEHLER IsoMet low speed saw equipped with a 0.3-mm thick diamond blade. The samples were drilled and sliced under wet conditions (water and lubricant, respectively) to avoid any heating that could potentially reset the OSL signal. Sample preparation was done under subdued red light conditions. The thickness of each rock slice was measured to determine the precise depth of each luminescence measurement.

All luminescence measurements were performed using Risø TL-DA 20 TL/OSL luminescence readers (Bøtter-Jensen et al., 2010) equipped with ^{90}Sr beta sources at the University of Lausanne (Switzerland). The readers have dose rates of ~0.1 and ~0.2 Gy s^{-1} and measurement reproducibility of 1.14% and 1.26% respectively. We first perform a preheat at 250 °C before giving infrared (IR) stimulation (870 nm, FWHM 40 nm) at 50 °C. Luminescence signals are detected through a filter combination of a Schott BG-3 and Schott BG-39. A uniform test dose was used (27.2 Gy) to measure the subsequent luminescence

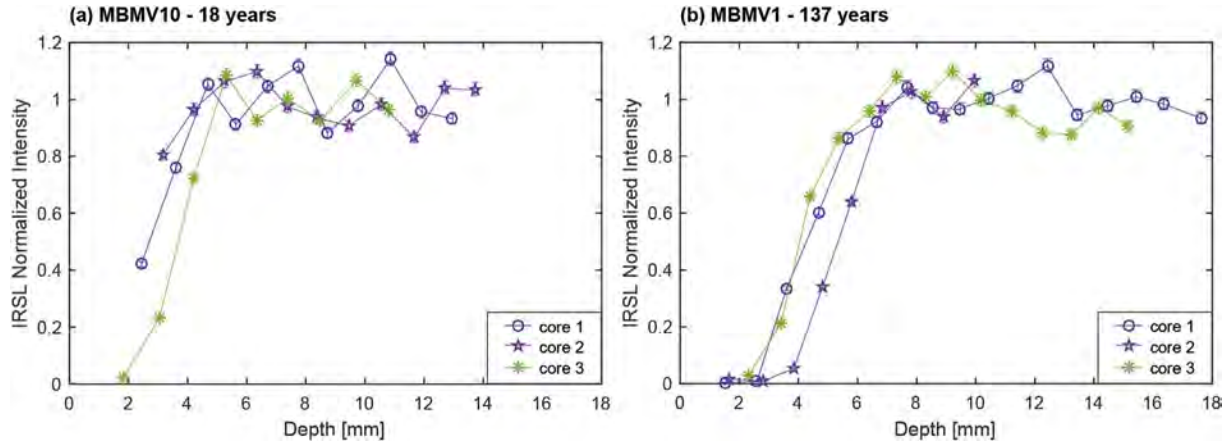

Fig. 6. Infrared stimulated luminescence (IRSL) signal with depth for samples (a) MBMV10 and (b) MBMV1. Each coloured data point represents an individual rock slice. IRSL signals were normalized by L_0, which was determined by taking the average of the luminescence measurements along the plateau. The plateau was defined when the luminescence signal is fluctuating by less than 20%.

Table 3
Best-fit values of $\overline{\sigma\varphi}_0$ and μ determined for every sample individually and for all samples excluding MBMV6. Combinations of three or four samples are presented in Table A3 (Supplementary Material).

Parameter	$\overline{\sigma\varphi}_0$ [s^{-1}]			μ [mm^{-1}]		
Samples	Best-fit	+1σ	-1σ	Best-fit	+1σ	-1σ
Individually						
MBMV1	$1.4{\cdot}10^{-8}$	$1.5{\cdot}10^{-8}$	$1.3{\cdot}10^{-8}$	1.07	1.08	1.05
MBMV6	$2.0{\cdot}10^{-6}$	$2.2{\cdot}10^{-6}$	$1.8{\cdot}10^{-6}$	0.92	0.95	0.92
MBMV7	$4.0{\cdot}10^{-6}$	$5.0{\cdot}10^{-6}$	$3.6{\cdot}10^{-6}$	2.52	2.56	2.46
MBMV8	$2.2{\cdot}10^{-7}$	$2.4{\cdot}10^{-7}$	$1.5{\cdot}10^{-7}$	1.89	1.98	1.70
MBMV10	$1.5{\cdot}10^{-7}$	$1.5{\cdot}10^{-7}$	$1.1{\cdot}10^{-7}$	1.82	1.87	1.75
MBMV11	$4.2{\cdot}10^{-8}$	$5.3{\cdot}10^{-8}$	$3.9{\cdot}10^{-8}$	1.21	1.22	1.13
All samples together excluding MBMV6	$1.0{\cdot}10^{-7}$	$1.1{\cdot}10^{-7}$	$9.5{\cdot}10^{-8}$	1.48	1.50	1.44

response (T_x) and to normalize the natural infrared stimulated luminescence (IRSL) signal (L_x) for every rock slice. Infrared stimulated luminescence was measured for 200 s and signals were integrated over the first 6 s whereas the background signal was integrated between 70 and 100 s. Measurements were analysed using Analyst v.3.22b (Duller, 2005). All thermal treatments and stimulations at temperatures greater than 200 °C (i.e. preheat step) were carried out in a nitrogen atmosphere. The experimental approach was validated using a dose recovery and preheat plateau test (see Supplementary Material A3; Murray and Wintle, 2000; Wintle and Murray, 2006).

5. Results

5.1. Experimental results

Fig. 6 shows the luminescence measurements for representative samples MBMV1 and MBMV10 (results of the other samples are presented in Fig. 8). Three replicates (i.e. individual cores) per sample were sliced in a way that a depth and an IRSL signal can be attributed to each rock slice (unique colour/symbol for each individual rock slice in Fig. 6). The results show similar behaviour between the different cores for a given sample (Fig. 6). The IRSL signal is bleached near the surface and reaches a plateau at depth. Furthermore, and more importantly, the transition from a bleached signal to the plateau varies with the exposure age. The three core measurements reproduce well for both samples illustrated in Fig. 6, with the mean standard deviation between the three cores ranging from 7 to 27% for all the studied samples. These results confirm experimentally that cores extracted from one individual sample record the same exposure history, supporting the proposed approach.

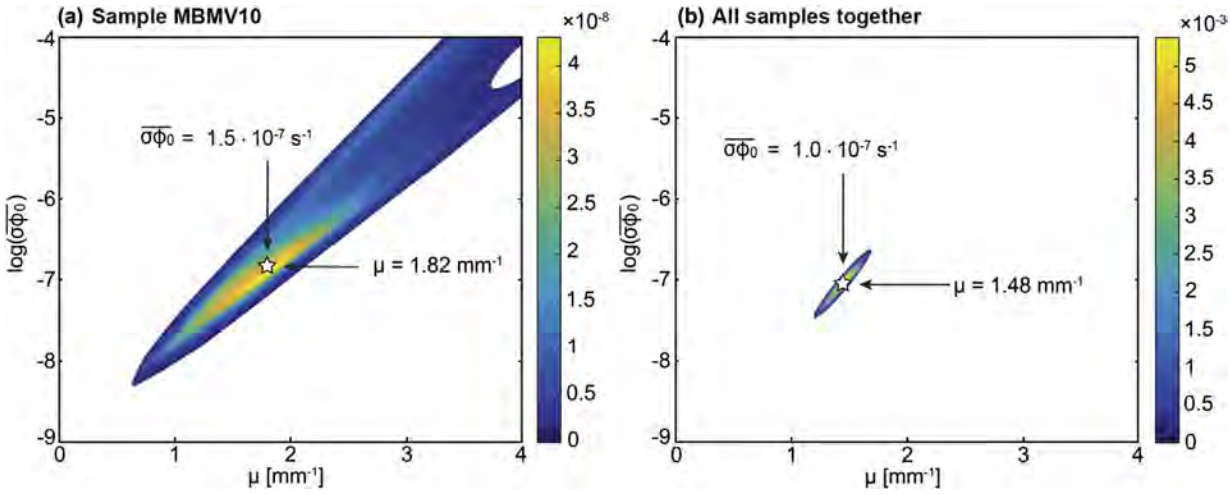

Fig. 7. Relationship between the $\overline{\sigma\varphi}_0$ and μ parameters (a) for sample MBMV10, and (b) for all of the gneiss samples (i.e. excluding MBMV6) enabling determination of the shared $\overline{\sigma\varphi}_0$ and μ parameters ($1.0{\cdot}10^{-7}$ s^{-1} and 1.48 mm^{-1} respectively). For both figures, the colour scale shows the likelihood between modelled and experimental data (Eq. (6), note the differences in scaling between the two panels), and the star shows the best-fit parameter values. Zero probability is not shown for clarity.

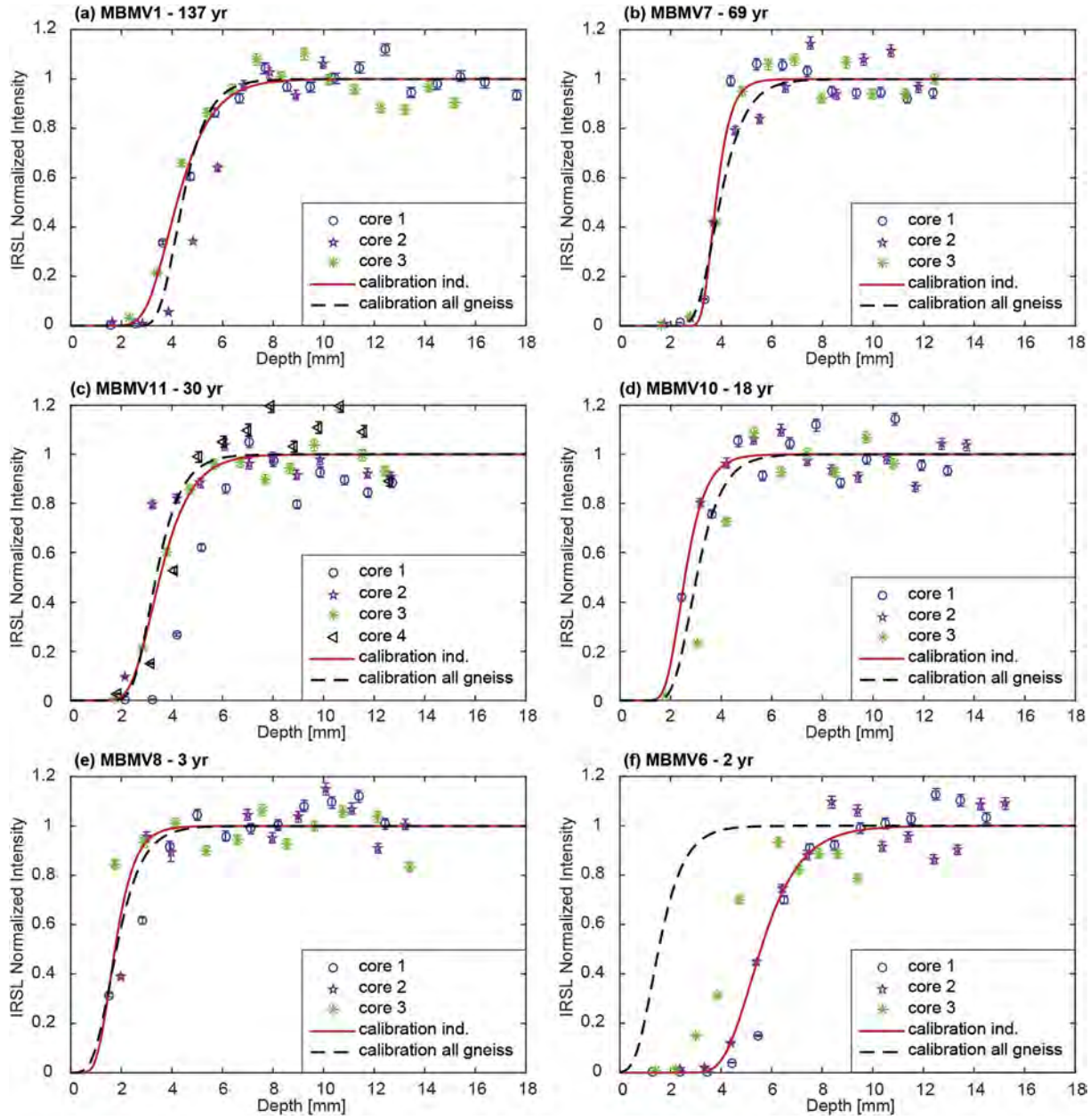

Fig. 8. Normalized infrared stimulated luminescence (IRSL) profiles with depth and best-fit models. Coloured data point represents individual rock slice (each symbol/colour represents one core). The red lines show the best-fit model for each sample taken individually. The dashed black lines represent the best-fit model from a common calibration of the parameters using all gneiss samples together ($\overline{\sigma\varphi}_0 = 1.0{\cdot}10^{-7}$ s^{-1} and $\mu = 1.48$ mm^{-1}, cf. Fig. 7b and Table 3). Raw IRSL data are presented in Table A3 (Supplementary Material).

5.2. Independent parameter determination

In this section, we determine the $\overline{\sigma\varphi}_0$ and μ parameters individually for each sample in order to study their potential variability from one rock surface to another (Table 3). As explained in Section 3.2, bedrock surfaces from the same location should share a common $\overline{\sigma\varphi}_0$ parameter (i.e. same order of magnitude; Blumthaler et al., 1997). Similarly, we expect that the μ parameter should be similar for samples from a uniform lithology. The determined parameters are then used in the inversion of the exposure ages for each sample individually (see Section 5.5). All inversion outcomes are summarized in Table 3. Samples MBMV1, MBMV8, MBMV10 and MBMV11 share similar effective decay rates ($\overline{\sigma\varphi}_0$) with the same order of magnitude (from $1.4{\cdot}10^{-8}$ to $2.2{\cdot}10^{-7}$ s^{-1}) and show attenuation coefficients (μ) between 1.07 and 1.89 mm^{-1}. Samples MBMV6 and MBMV7 behave differently with much higher effective decay rates ($\overline{\sigma\varphi}_0$ of $2.0{\cdot}10^{-6}$ and $4.2{\cdot}10^{-6}$ s^{-1}, respectively), and different attenuation coefficients (μ of 0.92 and 2.50 mm^{-1}, respectively).

5.3. Parameter determination from joint probability estimates

We evaluate now the parameter determination from joint probability estimates in order to illustrate the benefit of having several known-age calibration samples. Fig. 7a presents modelled results for sample MBMV10, which is representative of the other samples (except MBMV6 and MBMV7, see Section 5.2). The results show that log ($\overline{\sigma\varphi}_0$) and μ co-vary, which we attribute to measurement uncertainties and variability between the different cores. Fig. 7b shows the area of acceptable fits when all the gneissic samples are included (i.e. excluding granitic sample MBMV6).

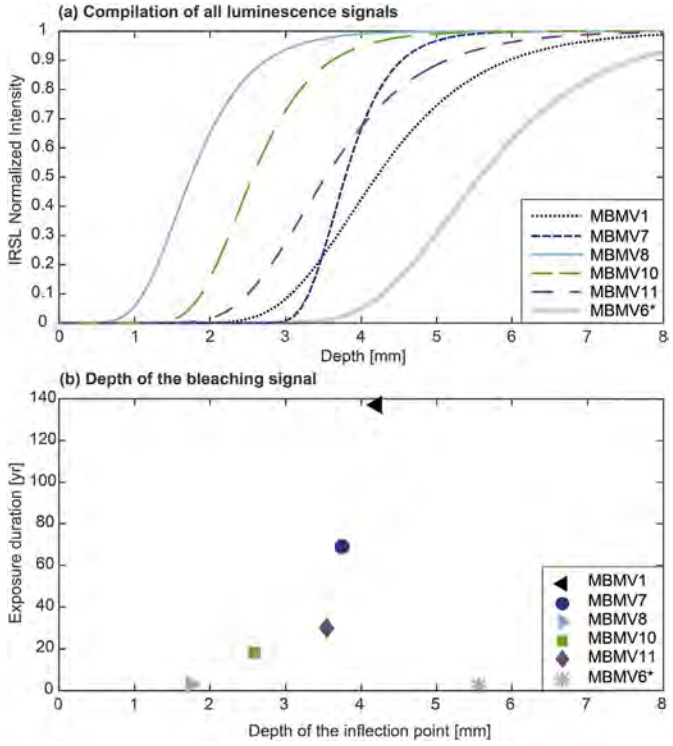

Fig. 9. (a) Compilation of the best-fit models for each individual sample (cf. red lines in Fig. 8). (b) Correlation between the IRSL bleaching depth (i.e. the inflection point of the models presented in (a)) and the exposure age of each individual sample. The * symbol indicates the granitic sample (MBMV6); all the other samples are gneiss.

We then contrasted individual estimates of $\overline{\sigma\varphi}_0$ and μ for each sample, using different combinations of samples to estimate these parameters. The results are summarized in Table 3 and A3. When inverting the model parameters with any combinations of three samples, all estimates of the effective decay rates are between $6.6{\cdot}10^{-8}$ and $1.4{\cdot}10^{-7}$ s^{-1}, and all estimates of the attenuation coefficients are between 1.33 and 1.57 mm^{-1}. Combinations of four samples provide $\overline{\sigma\varphi}_0$ values ranging from $7.2{\cdot}10^{-8}$ to $1.2{\cdot}10^{-7}$ s^{-1} and μ values between 1.38 and 1.53 mm^{-1}. According to Table 3 and Fig. 7b, a common likelihood exists for all the gneissic samples calibrated together, giving an effective decay rate of $1.0{\cdot}10^{-7}$ s^{-1} and an attenuation coefficient of 1.47 mm^{-1}.

Fig. 8 depicts the normalized IRSL signals measured for all samples and their individually-constrained best-fit models (red lines) as described previously and illustrated in Fig. 7a. The obtained outcomes show that the proposed model accurately describes the luminescence bleaching process through depth and time. The best-fit model calibrated with all of the gneissic samples together (black dashed lines, parameters in Table 3) fits close to the best-fit model determined for each sample individually (except MBMV6). These results confirm a key objective of the study, which is the possibility to calibrate the model parameters using different surfaces along an altitudinal cross-section, with the same lithology and different (independently-determined) exposure ages.

5.4. Evolution of the luminescence signal through time

Compiling the best-fit models determined for each sample individually, a positive correlation between the exposure age and the depth at which the natural IRSL signal is zeroed can be clearly observed for samples within the same lithology (Fig. 9a). If we consider the inflection point of each individual model ($Lx/Tx = 0.5$ on Fig. 9a) as a

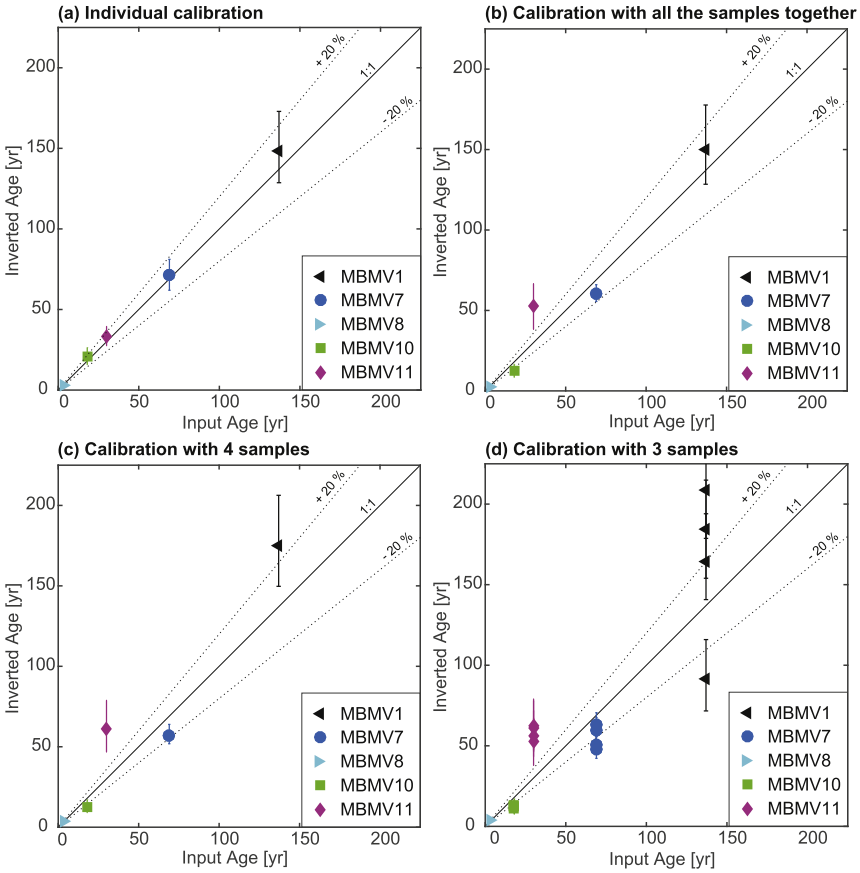

Fig. 10. Correlation between inverted (median values) and observed exposure ages resulting from different calibration combinations to constrain the model parameters. The error bars on the inverted exposure ages are ± 2σ as presented in Table 3 (all results presented in the Supplementary Table A4).

proxy for the bleaching depth, this value ranges between 1.7 and 4.2 mm for 3 and 137 years of daylight exposure, respectively (Fig. 9b). The granitic sample MBMV6 does not follow this correlation, its bleaching depth being at 7 mm after 2-yr exposure to daylight.

5.5. Inversion for exposure age

Once the model parameters have been determined by different sample combinations, it is possible to subsequently invert the exposure age as explained above. Fig. 10 compares the exposure ages inverted from the different sample combinations, with the independent age (all results are compiled in the Supplementary Table A4). Fig. 10a shows that our modelling approach is able to recover the observed exposure ages using parameters determined for each individual sample (< 10% difference). When the exposure ages are inverted using the parameters determined for all of the gneissic samples together (as shown in Fig. 7b), there are slight differences between the inverted exposure age and independent age control (Fig. 10b, Table A4). The inverted ages are almost all within 20% of the independent ages except for sample MBMV11, which is overestimated by 90%.

Taking different calibration combinations with four (Fig. 10c) or three (Fig. 10d) samples also results in different performance regarding age predictions. For all gneissic samples, except MBMV11, the inverted exposure ages at 2σ are still within 20% of the observed ages. Note that in our approach the inverted exposure ages with four and three sample calibration are only shown when the specific sample is not part of the calibration combination (grey shadow in the Supplementary Table A4). Although the match between the inverted and observed ages, as well as the trend between samples, is preserved independent of the calibration approach, our results show that the higher the number of calibration sites is, the better the inversion of exposure ages would be.

6. Discussion

Our results from the Mer de Glace glacier have allowed us to validate, over post-LIA timescales (i.e. over 2–137 years), the assumption that the longer a rock surface has been exposed to daylight, the deeper the luminescence signal has been bleached (Polikreti et al., 2002, 2003; Sohbati et al., 2011, 2012a,b). Using the mathematical model proposed by Sohbati et al. (2011), we accurately describe the time evolution of luminescence within a rock column. The different combinations of samples used to calibrate the model give parameter values ($\overline{\sigma\varphi}_0$ and μ) that are on the same order of magnitude for samples within a specific area and similar lithology, and which agree with literature values (Sohbati et al., 2011, 2012a,b).

We also observe that the evolution of luminescence signals with both time and depth within bedrock is mainly controlled by rock characteristics (lithology, texture, weathering and mineral composition). These rock properties will govern the light attenuation and penetration into rocks (parameter μ in Eq. (4)), and thus the net bleaching effect on the luminescence signal. At the regional scale, the lithology should preferably be uniform to enable model calibration on some known-age surfaces (through independent dating) before application to reconstruct the exposure history of other bedrock surfaces with unknown exposure age. We see that in a granitic rock, comprising coarse quartz and feldspar grains (translucent minerals), the luminescence-bleaching front will propagate much faster than in gneissic bedrock (Fig. 9).

Our inversion approach, to constrain rock surface exposure ages from OSL data, reveals that the number of calibration samples is critical for constraining the model parameters and thus obtaining accurate exposure ages. Fortunately, calibration rock surfaces in periglacial environments can often be found from historical or remote-sensing paleo-glacier reconstructions. Other types of bedrock surfaces can be used for independent constraint, e.g. anthropogenic structures such as road-cut outcrops (e.g. Sohbati et al., 2012a) or landslide scars. The combined investigation of OSL systems with other surface exposure dating methods such as terrestrial *in situ* cosmogenic nuclides will also enable us to quantitatively assess the method's accuracy over longer timescales such as the late Pleistocene.

Experimental luminescence data presented in Fig. 8 confirms that each individual sample's exposure history has been recorded in its luminescence depth profile. For the six bedrock surfaces studied here, each luminescence profile exhibits a fully-bleached signal at shallow depth (i.e. from 1 to 7 mm depending on both the exposure age and lithology, Fig. 9), followed by a sharp transition to a plateau of intensity deeper into the rock. These simple and homogeneous luminescence profiles can be compared with complex profiles previously observed and following multi-stage exposure histories obtained from buried cobbles (Freiesleben et al., 2015; Sohbati et al., 2015). This confirms that the glacially-polished surfaces we sampled along the Montenvers cross-sections have experienced a simple exposure history. Furthermore, field evidence for surface preservation with glacial features (striations, flutes) indicate that the bedrock surfaces have been eroded and polished by subglacial processes before deglaciation. Post-glacial weathering or mechanical erosion may lead to an underestimation of the true exposure age. Thereby, the inferred exposure history from these well-preserved rock surfaces can be used to reconstruct the paleo-glacier thickness and extent since the LIA.

Bleaching of the OSL signal has occurred at less than 1 cm depth below the exposed surface after more than 137 years of daylight exposure, highlighting the high temporal resolution of this novel method for paleo-glacier reconstruction. In mountainous locations such as the Mont Blanc massif, where the glacial history has been complex with several glacier fluctuations during the late Pleistocene to Holocene (recurrent retreat/advance cycles; e.g. Le Roy et al., 2015), the application of absolute dating methods such as terrestrial *in situ* cosmogenic nuclides are difficult due to potential inheritance from previous exposure events (e.g. Goehring et al., 2011). One of the main advantages of OSL surface exposure dating is that daylight bleaching of the OSL signal occurs within the first few millimeters below the exposed rock surface. Short glacier re-advances over the late Holocene (e.g. Le Roy et al., 2015) would have easily eroded the first centimetres of bedrock, consequently resetting the OSL system before the post-LIA glacier retreat. We have thus shown in this study that well-preserved polished bedrock surfaces can be used for the application of OSL surface exposure dating in order to constrain the timing of the last glacial retreat from the LIA to the present day, improving our temporal resolution for glacier reconstruction. Over such timescales, the contribution of the trap filling rate ($F(x)$ in Section 3.2) from radioactive decay in gneissic or granitic rock can be assumed to be negligible (see Supplementary Material A2). However, this contribution may have to be taken into account when extending paleo-glacier reconstruction using OSL surface exposure dating to longer timescales, e.g. since the Last Glacial Maximum or further back into the Quaternary. Over the same timescales, weathering and erosion of the surface are likely to play a significant role.

7. Conclusions

In this study, we have investigated the potential of OSL surface exposure dating for quantitatively reconstructing post-LIA glacier retreat. We worked along an altitudinal cross-section of the Mer de Glace glacier (Mont Blanc massif, France), and collected glacially-polished bedrock surfaces with known exposure ages (from 3 to 137 years) along the Montenvers profile from around 1841 m.a.s.l. elevation to the present-day glacier position (1696 m.a.s.l.). We have developed a statistical approach to calibrate the bleaching model parameters from known-age samples. Experimental IRSL depth-profile data for five different polished bedrock surfaces show an increase of the luminescence signal bleaching depth with exposure age. We conclude that OSL surface exposure dating can be applied to glacial and periglacial

environments, and is a promising tool for high-resolution reconstruction of recent ice-extent and thickness fluctuations, both in space and time. However, we find that several calibration samples must be used to calibrate the model parameters before inferring exposure ages on bedrock surfaces within a specific area, taking into account the potential variation in bedrock lithology. We also find that measurement uncertainties, intrinsic data noise or both can result in large uncertainties on inverted ages, especially when applying this method over 10^3–10^4 yr timescales.

Acknowledgements

We thank N. Brown and an anonymous reviewer for constructive and helpful comments. This work was supported by the Swiss National Science Foundation (SNFS) funded Swiss-AlpArray SINERGIA project (CRSII2_154434/1). PGV acknowledges support from SNFS grants PZ00P2_148191 and PP00P2_170559, and GEK from SNFS grant PZ00P2-167960. The authors would like to thank the French glacier observatory GLACIOCLIM (http://www-lgge.ujf-grenoble.fr/ServiceObs/index.htm) for providing their data. We are grateful to S. Coutterand, M. Delasoie, A. Licul, N. Stalder and V. Višnjević for fieldwork support; M. Faria and K. Häring for laboratory support.

Appendix A. Supplementary data

Supplementary data related to this article can be found at http://dx.doi.org/10.1016/j.quageo.2017.12.002.

References

Aitken, M.J., 1985. Thermoluminescence Dating. Academic press.
Aitken, M.J., 1998. An Introduction to Optical Dating the Dating of Quaternary: Sediments by the Use of Photon-stimulated Luminescence. Oxford University press.
Bailey, R.M., 2004. Paper I-simulation of dose absorption in quartz over geological timescales and its implications for the precision and accuracy of optical dating. Radiat. Meas. 38, 299–310.
Baillie, M.G.L., 1995. A Slice through Time: Dendrochronology and Precision Dating. Routledge, London, pp. 176.
Balco, G., 2011. Contributions and unrealized potential contributions of cosmogenic nuclide exposure dating to glacier chronology, 1990-2010. Quat. Sci. Rev. 30, 3–27.
Bini, A., Buoncristiani, J.F., Couterrand, S., Ellwanger, D., Felber, M., Florineth, D., Graf, H.R., Keller, O., Kelly, M., Schlüchter, C., Schoeneich, P., 2009. Switzerland during the Last Glacial Maximum 1: 500,000. Bundesamt für Landestopografie swisstopo.
Blumthaler, M., Ambach, W., Ellinger, R., 1997. Increase in solar UV radiation with altitude. J. Photochem. Photobiol. B Biol. 39, 130–134.
Bøtter-Jensen, L., Thomsen, K.J., Jain, M., 2010. Review of optically stimulated luminescence (OSL) instrumental developments for retrospective dosimetry. Radiat. Meas. 45, 253–257.
Broecker, W., Denton, G., 1990. What drives glacial cycles? Sci. Am. 262, 43–50.
Brown, N.D., Rhodes, E.J., Harrison, T.M., 2017. Using thermoluminescence signals from feldspars for low-temperature thermochronology. Quat. Geochronol. 42, 31–41.
Coutterand, S., Buoncristiani, J.-F., 2006. Paléogéographie du dernier maximum glaciaire du Pléistocène récent de la région du massif du Mont Blanc, France. Quat. Rev. l'Association française l'étude Quat. 17, 35–43.
Dobmeier, C., 1998. Variscan P–T deformation paths from the southwestern Aiguilles Rouges massif (External massif, western Alps) and their implication for its tectonic evolution. Geol. Rundsch. 87, 107–123.
Duller, G.A.T., 2005. Luminescence Analyst. University of Wales, Aberystwyth.
Duller, G.A.T., 2008. Single-grain optical dating of Quaternary sediments: why aliquot size matters in luminescence dating. Boreas 37, 589–612.
Egholm, D., Nielsen, S., Pedersen, V.K., Lesemann, J.-E., 2009. Glacial effects limiting mountain height. Nature 460, 884–887.
Ehlers, J., Gibbard, P.L., 2007. The extent and chronology of cenozoic gobal glaciation. Quat. Int. 164–165, 6–20.
Freiesleben, T., Sohbati, R., Murray, A., Jain, M., Al Khasawneh, S., Hvidt, S., Jakobsen, B., 2015. Mathematical model quantifies multiple daylight exposure and burial events for rock surfaces using luminescence dating. Radiat. Meas. 81, 16–22.
Fuchs, M., Owen, L.A., 2008. Luminescence dating of glacial and associated sediments: review, recommendations and future directions. Boreas 37, 636–659.
Gardent, M., Rabatel, A., Dedieu, J.-P., Deline, P., 2014. Multitemporal glacier inventory of the French Alps from the late 1960s to the late 2000s. Glob. Planet. Change 120, 24–37.
Goehring, B.M., Schaefer, J.M., Schluechter, C., Lifton, N.A., Finkel, R.C., Jull, A.T., Akçar, N., Alley, R.B., 2011. The Rhone Glacier was smaller than today for most of the Holocene. Geology 39, 679–682.
Goehring, B.M., Vacco, D.A., Alley, R.B., Schaefer, J.M., 2012. Holocene dynamics of the Rhone Glacier, Switzerland, deduced from ice flow models and cosmogenic nuclides. Earth Planet. Sci. Lett. 351, 27–35.
Goss, J.C., Phillips, F.M., 2000. Terrestrial in situ cosmogenic nuclides: theory and application. Quat. Sci. Rev. 20, 1475–1560.
Guralnik, B., Jain, M., Herman, F., Ankjærgaard, C., Murray, A.S., Valla, P.G., Preusser, F., King, G.E., Chen, R., Lowick, S.E., 2015. OSL-thermochronometry of feldspar from the KTB borehole, Germany. Earth Planet. Sci. Lett. 423, 232–243.
Habermann, J., Schilles, T., Kalchgruber, R., Wagner, G.A., 2000. Steps towards surface dating using luminescence. Radiat. Meas. 32, 847–851.
Hajdas, I., 2008. Radiocarbon dating and its applications in Quaternary studies. Eiszeitalter und Gegenwart Quat. Sci. J. 57, 24.
Herbert, T.D., Lawrence, K.T., Tzanova, A., Peterson, L.C., Caballero-Gill, R., Kelly, C.S., 2016. Late Miocene global cooling and the rise of modern ecosystems. Nat. Geosci. 9, 843–847.
Herman, F., Seward, D., Valla, P.G., Carter, A., Khon, B., Willett, S.D., Ehlers, T.A., 2013. Worldwide acceleration of mountain erosion under a cooling climate. Nature 504, 423–426.
Hippe, K., Ivy-Ochs, S., Kober, F., Zasadni, J., Wieler, R., Wacker, L., Kubik, P.W., Schlüchter, C., 2014. Chronology of Lateglacial ice flow reorganization and deglaciation in the Gotthard Pass area, Central Swiss Alps, based on cosmogenic ^{10}Be and in situ ^{14}C. Quat. Geochronol. 19, 14–26.
Huntley, D.J., Godfrey-Smith, D.I., Thewalt, M.L., 1985. Optical dating of sediments. Nature 313, 105–107.
Ivy-Ochs, S., 2015. Glacier variations in the European Alps at the end of the last glaciation. Cuad. Investig. geográfica 41, 295–315.
Ivy-Ochs, S., Kerschner, H., Reuther, A., Maisch, M., Sailer, R., Schaefer, J., Kubik, P.W., Synal, H.-A., Schlüchter, C., 2006. The timing of glacier advances in the northern European Alps based on surface exposure dating with cosmogenic 10Be, 26Al, 36Cl, and 21Ne. Geol. Soc. Am. Special Pap. 415, 43–60.
Ivy-Ochs, S., Kerschner, H., Maisch, M., Christl, M., Kubik, P.W., Schlüchter, C., 2009. Latest Pleistocene and Holocene glacier variations in the european Alps. Quat. Sci. Rev. 28, 2137–2149.
Ivy-Ochs, S., Briner, J.P., 2014. Dating disappearing ice with cosmogenic nuclides. Elements 10, 351–356.
King, G., Herman, F., Lambert, R., Valla, P., Guralnik, B., 2016. Multi-OSL-thermochronometry of feldspar. Quat. Geochronol. 33, 76–87.
Lal, D., 1991. Cosmic ray labeling of erosion surfaces: in situ nuclide production rates and erosion models. Earth Planet. Sci. Lett. 104, 424–439.
Laskaris, N., Liritzis, I., 2011. A new mathematical approximation of sunlight attenuation in rocks for surface luminescence dating. J. Luminescence 131, 1874–1884.
Le Roy, M., Nicolussi, K., Deline, P., Astrade, L., Edouard, J.-L., Miramont, C., Arnaud, F., 2015. Calendar-dated glacier variations in the western European Alps during the Neoglacial: the Mer de Glace record, Mont Blanc massif. Quat. Sci. Rev. 108, 1–22.
Lean, J., 1987. Solar ultraviolet irradiance variations: a review. J. Geophys. Res. 92, 839–968.
Liritzis, I., 1994. A new dating method by thermoluminescence of carved megalithic stone building. Comptes rendus de l'Académie des Sci. Série 2. Sci. de terre des planètes 319, 603–610.
Liritzis, I., 2011. Surface dating by luminescence: an overview. Geochronometria 38, 292–302.
Molnar, P., England, P., 1990. Late Cenozoic uplift of mountain ranges and global climate change: chicken or egg? Nature 346, 29–34.
Murray, A.S., Wintle, A.G., 2000. Luminescence dating of quartz using an improved single-aliquot regenerative-dose protocol. Radiat. Meas. 32, 57–73.
Nussbaumer, S., Zumbühl, H.J., Steiner, D., 2007. Fluctuations of the Mer de glace (Mont Blanc area, France) AD 1500-2050. An interdisciplinary approach using new historical data and neural network simulations. Z. für Gletscherkd. Glazialgeol. ZGG 5–175.
Peizhen, Z., Molnar, P., Downs, W.R., 2001. Increased sedimentation rates and grain sizes 2–4 Myr ago due to the influence of climate change on erosion rates. Nature 410, 891–897.
Penck, A., 1905. Glacial features in the surface of the Alps. J. Geol. 13, 1–19.
Preusser, F., Graf, H.R., Keller, O., Krayss, E., Schlüchter, C., 2011. Quaternary glaciation history of northern Switzerland. Quat. Sci. J. 60 (2–3), 282–305.
Polikreti, K., Michael, C., Maniatis, Y., 2002. Authenticating marble sculpture with thermoluminescence. Anc. TL 20, 11–18.
Polikreti, K., Michael, C., Maniatis, Y., 2003. Thermoluminescence characteristics of marble and dating of freshly excavated marble objects. Radiat. Meas. 37, 87–94.
Rabatel, A., Letréguilly, A., Dedieu, J., Eckert, N., 2013. Changes in glacier equilibrium-line altitude in the western Alps from 1984 to 2010: evaluation by remote sensing and modeling of the morpho-topographic and climate controls. Cryosphere 7, 1455–1471.
Rhodes, E.J., 2011. Optically stimulated luminescence dating of sediments over the past 200,000 years. Annu. Rev. Earth Planet. Sci. 39, 461–488.
Richards, M.P., 1994. Luminescence Dating of Quartzite from the Diring Yuriakh Site. M.A. Thesis. Simon Fraser University unpublished.
Schimmelpfennig, I., Schaefer, J.M., Akçar, N., Koffman, T., Ivy-Ochs, S., Schwartz, R., Finkel, R.C., Zimmerman, S., Schlüchter, C., 2014. A chronology of Holocene and Little Ice Age glacier culminations of the Steingletscher, Central Alps, Switzerland, based on high-sensitivity beryllium-10 moraine dating. Earth Planet. Sci. Lett. 393, 220–230.
Simms, A.R., DeWitt, R., Kouremenos, P., Drewry, A.M., 2011. A new approach to reconstructing sea levels in Antarctica using optically stimulated luminescence of cobble surfaces. Quat. Geochronol. 6, 50–60.
Simkins, L.M., Simms, A.R., DeWitt, R., 2013. Relative sea-level history of Marguerite Bay, Antarctic Peninsula derived from optically stimulated luminescence-dated beach cobbles. Quat. Sci. Rev. 77, 141–155.
Singarayer, J.S., 2002. Linearly Modulated Optically Stimulated Luminescence of Sedimentary Quartz: Physical Mechanisms and Implications for Dating. D.Phil. thesis. University of Oxford, pp. 345.
Sohbati, R., Murray, A., Jain, M., Buylaert, J.-P., Thomsen, K., 2011. Investigating the resetting of OSL signals in rock surfaces. Geochronometria 38, 249–258.
Sohbati, R., Jain, M., Murray, A., 2012a. Surface exposure dating of non-terrestrial bodies using optically stimulated luminescence: a new method. Icarus 221, 160–166.

Sohbati, R., Murray, A.S., Buylaert, J.-P., Almeida, N.A.C., Cunha, P.P., 2012b. Optically stimulated luminescence (OSL) dating of quartzite cobbles from the Tapada do Montinho archaeological site (east-central Portugal). Boreas 41, 452–462.
Sohbati, R., Murray, A., Porat, N., Jain, M., Avner, U., 2015. Age of a prehistoric "Rodedian" cult site constrained by sediment and rock surface luminescence dating techniques. Quat. Geochronol. 30, 90–99.
Stewart, M., Larocque-Tobler, I., Grosjean, M., 2011. Quantitative inter-annual and decadal summer temperature variability 570 BC–AD 120 (Iron Age Roman Period) reconstructed from the varved sediments of Lake Silvaplana, Switzerland. J. Quat. Sci. 26, 491–501.
Theocaris, P., Liritzis, I., Galloway, R., 1997. Dating of two Hellenic pyramids by a novel application of thermoluminescence. J. Archaeol. Sci. 24, 399–405.
Vafiadou, A., Murray, A., Liritzis, I., 2007. Optically stimulated luminescence (OSL) dating investigations of rock and underlying soil from three case studies. J. Archaeol. Sci. 34, 1659–1669.
Valla, P.G., Lowick, S.E., Herman, F., Champagnac, J.-D., Steer, P., Guralnik, B., 2016. Exploring $IRSL_{50}$ fading variability in bedrock feldspars and implications for OSL thermochronometry. Quat. Geochronol. 36, 55–66.
Vincent, C., Harter, M., Gilbert, A., Berthier, E., Six, D., 2014. Future fluctuations of Mer de Glace, French Alps, assessed using a parameterized model calibrated with past thickness changes. Ann. Glaciol. 55, 15–24.
Wirsig, C., Zasadni, J., Ivy-Ochs, S., Christl, M., Kober, F., Schlüchter, C., 2016. A de-glaciation model of the Oberhasli, Switzerland. J. Quat. Sci. 31, 46–59.
Winkler, S., 2004. Lichenometric dating of the 'Little Ice Age' maximum in Mt Cook National Park, Southern Alps, New Zeland. Holocene 16.6, 911–920.
Wintle, A.G., Murray, A.S., 2006. A review of quartz optically stimulated luminescence characteristics and their relevance in single-aliquot regeneration dating protocols. Radiat. Meas. 41, 369–391.
Zachos, J.C., Shackleton, N.J., Revenaugh, J.S., Pälike, H., Flower, B.P., 2001. Climate response to orbital forcing across the Oligocene-Miocene boundary. Science 292, 274–278.

10.2 Evaluating post-glacial bedrock erosion and surface exposure duration by coupling in-situ OSL and 10Be dating

Benjamin Lehmann[1],Frédéric Herman[1], Pierre G. Valla[2,3], Georgina E. King[1] and Rabiul Biswas [1]

[1] Institute of Earth Surface Dynamics, University of Lausanne, Lausanne, 1012, Switzerland. [2] Univ. Grenoble Alpes, Univ. Savoie Mont Blanc, CNRS, IRD, IFSTTAR, ISTerre, 38000 Grenoble, France. [3] Institute of Geological Sciences and Oeschger Centre for Climate Change Research, University of Bern, Bern, 3012, Switzerland.

Research paper

Earth Surface Dynamic

Author contributions. BL designed the study, collected the sample, prepared the samples, performed the analysis, ran the simulations, and wrote most of the manuscript. All authors contributed in interpreting the results and improving the text.

Earth Surf. Dynam., 7, 1–30, 2019
https://doi.org/10.5194/esurf-7-1-2019

Earth Surface Dynamics
Open Access
EGU

Evaluating post-glacial bedrock erosion and surface exposure duration by coupling in situ optically stimulated luminescence and ^{10}Be dating

Benjamin Lehmann[1], Frédéric Herman[1], Pierre G. Valla[2,3], Georgina E. King[1], and Rabiul H. Biswas[1]

[1]Institute of Earth Surface Dynamics, University of Lausanne, Lausanne, 1012, Switzerland
[2]University of Grenoble Alpes, University of Savoie Mont Blanc, CNRS, IRD,
IFSTTAR, ISTerre, 38000 Grenoble, France
[3]Institute of Geological Sciences and Oeschger Centre for Climate Change Research,
University of Bern, Bern, 3012, Switzerland

Correspondence: Benjamin Lehmann (lehmann.benj@gmail.com)

Received: 21 December 2018 – Discussion started: 29 January 2019
Revised: 14 May 2019 – Accepted: 21 May 2019 – Published:

Abstract. Assessing the impact of Quaternary glaciation at the Earth's surface implies an understanding of the long-term evolution of alpine landscapes. In particular, it requires simultaneous quantification of the impact of climate variability on past glacier fluctuations and on bedrock erosion. Here we present a new approach for evaluating post-glacial bedrock surface erosion in mountainous environments by combining terrestrial cosmogenic nuclide ^{10}Be (TCN) and optically stimulated luminescence (OSL) surface exposure dating. Using a numerical approach, we show how it is possible to simultaneously invert bedrock OSL signals and ^{10}Be concentrations into quantitative estimates of post-glacial exposure duration and bedrock surface erosion. By exploiting the fact that OSL and TCN data are integrated over different timescales, this approach can be used to estimate how bedrock erosion rates vary spatially and temporally since glacier retreat in an alpine environment.

1 Introduction

During the last few million years of the Earth's history, the global climate cooled and evolved towards cyclic glaciations in high-latitude and high-altitude regions (e.g. Miller et al., 1987; Zachos et al., 2001; Lisiecki and Raymo, 2005, 2007). It has been suggested that rates of erosion varied during these multiple cycles and that such variations could in turn feed back into climate (e.g. Molnar and England, 1990; Raymo and Ruddiman, 1992; Champagnac et al., 2007; Herman and Champagnac, 2016). Such erosion rate variations are most expressed in alpine environments, wherein the main erosion agents vary from ice to water and landslides during glacial and interglacial periods, respectively. However, quantifying how their respective contributions in sediment production have varied remains challenging because both ice-extent fluctuations and associated bedrock surface erosion must be reconstructed simultaneously.

Glacially polished bedrock offers the possibility to reconstruct past ice extents and quantify concomitant bedrock surface erosion. These landforms are smooth and glossy, resulting from glacial abrasion, quarrying and meltwater erosion during glacial periods (e.g. Bennett and Glasser, 2009; Siman-Tov, 2017). Following ice retreat, they are exposed to post-glacial erosion, which results in the transition from a well-preserved glacially polished surface (Fig. 1a and b) to a coarse-grained rough surface (Fig. 1c and d). Post-glacial bedrock surface erosion is due to the alteration of rock surfaces exposed to atmospheric conditions. Rock alteration can occur in different ways, involving physical (e.g. frost cracking), chemical and biological processes that weaken and modify the rock surface and ultimately result in its progressive erosion (e.g. Łoziński, 1909; Anderson and Anderson, 2010; Hall et al., 2012; Moses et al., 2014). Because we are concerned with the removal of bedrock surface material since exposure to the atmosphere following glacial retreat, rather

than the modification of its physical and chemical characteristics caused by weathering, we hereafter use the term "erosion". Our objective is to develop an approach that may be used to address the following questions: how fast is the transition from a polished bedrock to a coarse-grained surface (Fig. 1)? How much information about post-glacial exposure is preserved on weathered rock surfaces? What analytical tools or approaches can we use to quantify this morphological transition?

Analytical methods to quantify erosion of rock surfaces differ depending on the timescale of interest (see Moses et al., 2014, for a complete review). Over short timescales (from a few seconds to decades) erosion can be quantified through remote sensing (e.g. photogrammetric methods, terrestrial laser scanner; Armesto-Gonzàlez et al., 2010; Duffy et al., 2013) or measured relative to anthropogenic reference features (historic or experimental; e.g. Nicholson, 2008; Häuselmann, 2008; Stephenson and Finlayson, 2009). Over longer timescales (10^3–10^7 years), erosion can be measured relative to a natural reference feature (e.g. resistant mineral veins such as quartz or a surface of known age) or quantified using surface exposure dating with terrestrial cosmogenic nuclides (TCNs; Lal, 1991; Balco et al., 2008; Bierman and Nichols, 2004; Brandmeier et al. 2011; Liu and Broecker, 2007). TCN methods rely on the production of specific isotopes in terrestrial material by cosmic rays at or near the Earth's surface (Gosse and Philips, 2001), such as minerals located in the top few metres of soil or bedrock (Lal and Peters, 1967). In glacial and paraglacial environments, the formation of glacial landforms can be directly dated over timescales of 10^3 to 10^6 years with TCN surface exposure dating (Ivy-Ochs and Briner, 2014). However, TCN concentrations must also be corrected for surface erosion, which would otherwise lead to an underestimation of the exposure age (Gosse and Phillips, 2001). The combination of short-lived radionuclides such as ^{14}C with long-lived radionuclides (i.e. ^{10}Be, ^{26}Al, ^{36}Cl) can be used to resolve and quantify complex exposure histories with burial episodes, but this approach does not allow for the quantification of erosion during exposure (Hippe, 2017).

Consequently, complementary approaches are still needed to quantify bedrock erosion over multiple timescales, more specifically methods that can bridge short and long timescales. In this study, we couple TCN with optically stimulated luminescence (OSL) dating. Rock surface exposure dating using optically stimulated luminescence (named hereafter as OSL surface exposure dating) has recently shown promising potential (e.g. Sohbati et al., 2012a; 2018; King et al., 2019). Luminescence dating is based on the accumulation of trapped electrons through time in the crystalline lattice of specific minerals (e.g. quartz or feldspar), which are sensitive to daylight (Aitken, 1985; Huntley et al., 1985). In addition to its common application to dating sediment burial in a range of geomorphological environments (e.g. Duller, 2008; Rhodes, 2011; Fuchs and Owen, 2008), luminescence dating can also be used to determine the exposure of both naturally formed and anthropogenically formed rock surfaces (e.g. Polikreti et al., 2003; Sohbati et al., 2011; Gliganic et al., 2018; Lehmann et al., 2018). This latter application is based on the principle that when a rock surface is exposed to daylight, the luminescence signal, which is initially homogenous within the rock, will progressively decrease at depth until completely zeroed, a phenomenon called "bleaching" (Aitken, 1998). The assumption is that the longer a surface has been exposed to daylight, the deeper the OSL signal bleaching will be (Polikreti et al., 2002). In granitic and gneissic rocks, bleaching through time has been shown to occur over the first few millimetres to centimetres below the rock surface (Vafiadou et al., 2007; Sohbati et al., 2011; Freiesleben et al., 2015). Due to the attenuation of daylight, the bleaching rate decreases exponentially with depth. It becomes negligible at depth where the luminescence signal is effectively unbleached and remains in field saturation. For long timescales, trapping due to ionizing radiation will compete with detrapping due to daylight exposure at all depths (after $\sim 10^4$ years in Fig. A1), ultimately resulting in an equilibrium bleaching profile (after $\sim 10^6$ years in Fig. A1; Sohbati et al., 2012a).

For a bedrock OSL profile which is not in equilibrium, measuring and calibrating the depth-dependent luminescence signal beneath the exposed surface by generating multiple luminescence depth profiles enables the estimation of an apparent exposure age. OSL surface exposure dating is thus presented as a relatively new surface exposure dating method and has already been applied on both geological and archaeological rock surfaces (Polikreti, 2007; Sohbati et al., 2012a; Freiesleben et al., 2015; Lehmann et al., 2018; Meyer et al., 2018; Gliganic et al., 2018). Sohbati et al. (2012c) were able to quantify the exposure age of historic rock art from the Great Gallery rock art panel in Canyonlands National Park (southeastern Utah, USA). Some of the paintings were damaged by a rockfall event, and conventional luminescence was applied on a rockfall boulder and buried sediments (Chapot et al., 2012). This provided a minimum age for the event. Using a road cut of known age to constrain the bleaching rate for this specific site and lithology, Sohbati et al. (2012c) were able to quantify the exposure age of both the modern analogue ($\sim$ 130 years) and the rock art ($\sim$ 700 years). In a periglacial environment, Lehmann et al. (2018) showed that infrared stimulated luminescence at 50 °C (IRSL50) signals from crystalline bedrock slices exhibits increasingly deep bleaching profiles with elevation and thus exposure age, which is consistent with progressive glacier thinning since the Little Ice Age (LIA; 10^1–10^2 years). Note that several signals can be targeted in the same rock slice depending on the mineral (e.g. Sohbati et al., 2015; Jenkins et al., 2018). OSL is usually used to analysed the luminescence of quartz (Murray and Wintle, 2000) and IRSL for the potassium-rich feldspar signal (both at 50 and 225 °C; Buylart et al., 2009).

Recently, Sohbati et al. (2018) showed that surface erosion has to be taken into consideration when OSL surface exposure dating is applied to natural bedrock surfaces. Indeed,

removal of material would bring the bleaching front towards the surface, which may lead to a considerable underestimation of the OSL surface exposure age if not accounted for. When bedrock surface erosion is high ($> 10^{-2}$ mm a^{-1}), the competition between bleaching and surface removal will potentially prevent the use of OSL surface exposure dating as a chronometer for bedrock surface exposure (Sohbati et al., 2018). In practice, when erosion is maintained long enough, an equilibrium between trapping, bleaching (i.e. detrapping) and erosion is reached, and consequently the bleaching profile reaches steady state. Sohbati et al. (2018) explained that the sensitivity difference to erosion between TCN and OSL surface exposure dating can be exploited to calculate the erosion rate experienced by rock surfaces. Indeed, TCN dating is mainly sensitive to cosmic rays over the top $\sim$ 50–60 cm below the exposed bedrock surface (depending on rock density; Lal et al., 1991), while OSL surface exposure dating is sensitive to light penetration of only millimetres to centimetres (Sohbati et al., 2011, 2012a, b). Thus, using both OSL surface exposure dating and TCN methods, it is possible in theory to quantify surface erosion over different timescales (i.e. 10^2–10^4 years).

Here we couple TCN and OSL surface exposure dating to quantify post-glacial erosion in paraglacial environments. To achieve this, we developed a new model which depends on the exposure age, the surface erosion, the trapping and detrapping (bleaching) rates, and the athermal loss (see Eq. 1, Sect. 2.1). Using this model, we then investigate different synthetic scenarios in which erosion rates follow a series of step functions in time. After this synthetic experiment, the model is used to invert OSL surface exposure data from two glacially polished bedrock surfaces sampled along the Mer de Glace glacier (Mont Blanc massif, European Alps). We find that the relationships between the depth of luminescence bleaching, the exposure age and the surface erosion allow for discrimination between transient and steady-state regimes. Finally, we discuss our findings regarding post-glacial surface erosion in paraglacial environments and the benefits of OSL surface exposure dating combined with TCN surface exposure dating.

2 Methodology: combining TCN and OSL surface exposure dating

In the following, we focus on the theoretical aspects of both OSL and TCN surface exposure dating methods. We show how different time-dependent exposure and erosion histories are recorded by each technique. Finally, we combine OSL surface exposure and TCN dating to constrain erosion rate and exposure duration simultaneously. Note that all the symbols used below are defined in Table 1.

2.1 OSL surface exposure dating

2.1.1 The bleaching model

The intensity of a luminescence signal reflects the number of trapped electrons (Aitken, 1985). For a rock surface exposed to daylight, the luminescence signal intensity, i.e. the trapped electron concentration, is controlled by the competing processes of electron trapping in response to ambient radiation and electron detrapping due to daylight exposure combined with anomalous fading for feldspar IRSL (Habermann et al., 2000; Polikreti et al., 2003; Sohbati et al., 2011). Sohbati et al. (2011, 2012a, b) introduced a mathematical model that describes the process of luminescence bleaching with depth in a homogeneous lithology, enabling the quantification of rock surface exposure duration. Here we propose a new model describing the evolution of luminescence in rock surface as a function of different parameters characterizing the probability of charge trapping, the wavelength-specific photon flux (φ), the mineral- and wavelength-specific photoionization cross section (σ), and the lithology-specific light attenuation factor (μ) (Eq. 1). Thus, the measured luminescence signal $L(x,t,r')$ (dimensionless) at a given depth x (mm), time t (year) and recombination centre distance r' (dimensionless) can be described by the following differential equation:

$$\frac{\mathrm{d}L(x,t,r')}{\mathrm{d}t} = \frac{\dot{D}}{D_0}[1 - L(x,t,r')] - L(x,t,r')\overline{\sigma\varphi_0}e^{-\mu x} - L(x,t,r')\mathrm{s}e^{-\rho'^{-\frac{1}{3}}r'} + \dot{\varepsilon}(t)\frac{\mathrm{d}L(x,t,r')}{\mathrm{d}x}. \quad (1)$$

The first term on the right-hand side of Eq. (1) describes the electron-trapping rate in response to ambient radiation with $\dot{D}(x)$ the environmental dose rate (Gy a^{-1}) at depth x (m) and D_0 the characteristic dose (Gy). In the context of bedrock surface exposure dating, the dose rate can be approximated as a depth-independent constant in the case of homogeneous lithology, i.e. $\dot{D}(x) = \mathrm{const}$ (e.g. Sohbati et al., 2018).

The second term describes the electron detrapping or bleaching rate due to daylight exposure, where $\sigma(\lambda)$ is the luminescence photoionization cross section (mm^2) defining the probability of a specific trap being excited by light stimulation. $\varphi_0(\lambda, x)$ is the photon flux (mm^{-2} a^{-1}) as a function of wavelength at the rock surface ($x = 0$) and describes the rate of incoming photons that can bleach the trap of interest. Here we assume that the photon flux does not fluctuate through time (Sohbati et al., 2011). We are only concerned with $\overline{\sigma\varphi_0}$ (a^{-1}), which is the effective decay rate of luminescence at the rock surface following exposure to a particular light spectrum (Sohbati et al., 2011). The light attenuation coefficient μ (mm^{-1}) describes how deep into the rock a photon will penetrate and affect the luminescence signal. μ is assumed to be independent of wavelength in the spectral range of interest (Sohbati et al., 2011).

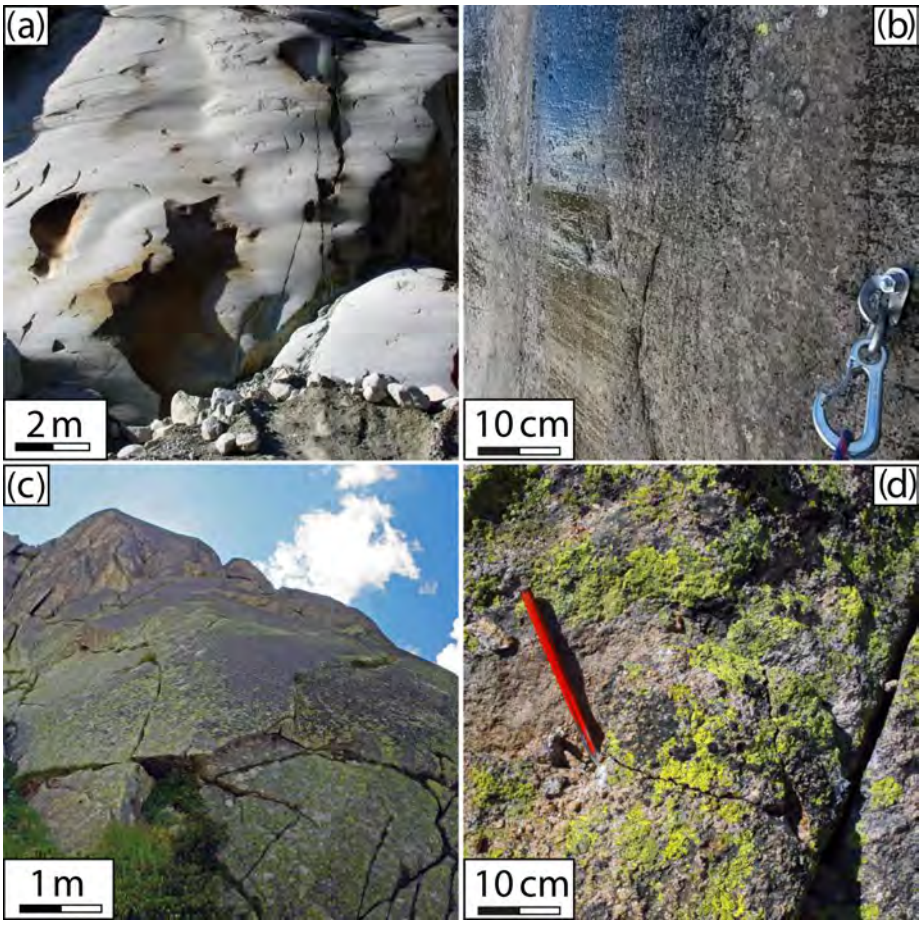

Figure 1. Granitic bedrock surfaces along the Mer de Glace glacier (Mont Blanc massif, European Alps). Surfaces **(a)** and **(b)** present well-preserved glacial morphologies exposed for only a few years (striations). Surfaces with longer aerial exposure (Late Glacial to Holocene timescales) show glacially abraded surfaces at the macro-scale **(c)**, but at the centimetre scale they reveal a coarse-grained rough surface **(d)**.

The third term on the right-hand side of Eq. (1) represents the athermal loss of the IRSL signal of feldspar thought to be due to quantum mechanical tunnelling of trapped electrons (Wintle, 1973; Visocekas et al., 1998) to the nearest available recombination centres (Huntley, 2006). s is the frequency factor equal to $3 \times 10^{15}\ \mathrm{s}^{-1}$, and ρ' is the dimensionless recombination centre density (Tachiya and Mozumder, 1974; Huntley, 2006).

The fourth term describes the advection of the luminescence signal in response to erosion $\dot{\varepsilon}(t) = \mathrm{d}x/\mathrm{d}t\ (\mathrm{mm\,a}^{-1})$ on the propagation of the luminescence bleaching front into the rock using an Eulerian system of reference. Equation (1) is solved using the finite-difference method including a second-order upwind scheme for the advection term. This approach is different to the one recently proposed by Sohbati et al. (2018), who used an analytical solution that is based on a confluent hypergeometric function and that requires steady erosion rates. We benchmarked our approach against that of Sohbati et al. (2018), and we obtain results which are similar to their results calculated using their analytical solution (Fig. A3).

Ou et al. (2018) experimentally derived μ for different rock types (greywacke, sandstone, granite and quartzite) using both direct measurements with a spectrometer and bleaching experiments. They showed that the attenuation coefficients are different according the energy of stimulation (e.g. IRSL measured at 50 °C and the post-IR IRSL signal measured at 225 °C). Meyer et al. (2018) and Gliganic et al. (2018) have shown that the distribution of opaque minerals between rock slices can significantly affect the reproducibility of luminescence–depth profiles. The conclude of the need for close petrographic analysis of luminescence–depth profile samples to ensure that the rock cores from calibration and application sites have a similar mineralogical composition and therefore share a similar μ parameter. In this study, we refer to Sohbati et al. (2011, 2012a) for a complete description of $\overline{\sigma\varphi_0}$ and μ parameters and their control on the penetration of the bleaching front into a rock surface.

Alternatively, $\overline{\sigma\varphi_0}$ and μ can be determined from a known-age rock surface with no erosion ($\dot{\varepsilon}(t) = 0$) with a uniform lithology (Sohbati et al., 2012a; Lehmann et al., 2018; Meyer et al., 2018) and a negligible contribution of athermal loss (as presented in Fig. A2). Under these conditions, Sohbati et al. (2012a) proposed the following analytical solution for Eq. (1), neglecting the athermal loss:

$$L(x,t) = \frac{\overline{\sigma\varphi_0} e^{-\mu x} e^{-t\left(\overline{\sigma\varphi_0} e^{-\mu x} + \frac{\dot{D}}{D_0}\right)} + \frac{\dot{D}}{D_0}}{\overline{\sigma\varphi_0} e^{-\mu x} + \frac{\dot{D}}{D_0}}. \quad (2)$$

For non-eroding surfaces, OSL surface exposure dating can theoretically be used for a broad range of timescales from 0.01 to 10^5 years (Fig. A1; and Sohbati et al., 2012a, b, 2018). Under these geomorphic conditions for natural rock surfaces (e.g. glacially polished bedrock), OSL surface exposure dating has been successfully applied by solving Eq. (2) over 10^1–10^2-year timescales (Lehmann et al., 2018; Gliganic et al., 2018). At longer timescales and/or for rock surfaces affected by erosion, the measured OSL signals reflect not only the exposure age.

2.1.2 Sensitivity analysis to model parameters

In this section, we investigate the respective contribution of the different terms in Eq. (1) for the interpretation of a measured OSL bleaching profile. We investigate the sensitivity of the model to athermal loss, trapping rate and erosion. We use $\overline{\sigma\varphi_0} = 129\,\mathrm{a}^{-1}$ and $\mu = 0.596\,\mathrm{mm}^{-1}$ that were determined from two calibration rock surfaces of similar granitic lithology from the Mont Blanc massif, with no erosion and known exposure age (Fig. A2). The values $\dot{D} = 8\,\mathrm{Gy\,ka}^{-1}$ (Table 2) and $D_0 = 500\,\mathrm{Gy}$ were selected as they are comparable to the average values for samples used in this study.

Athermal loss

In this section, we investigate the role of athermal loss when constant erosion rates are low (i.e. $10^{-5}\,\mathrm{mm\,a}^{-1}$) and high (i.e. $10^{1}\,\mathrm{mm\,a}^{-1}$). In Eq. (1), ρ' is varied between 10^{-10} and 10^{-5} (natural values vary between $10^{-6.5}$ and $10^{-5.1}$; Valla et al., 2016; King et al., 2018) and is integrated over dimensionless distances, r', ranging from 0 to 2.5 (Kars et al., 2008) in all cases. Four model runs were done to test whether the shape of the bleaching profile (i.e. luminescence signal vs. depth) changes with different athermal loss rates, rather than the absolute luminescence signal intensity level which reduces as ρ' increases. To remove this effect, the luminescence signals were normalized using the steady-state luminescence plateau as unity (NLS for normalized luminescence signal; Figs. 2 and A2a). Figure 2 shows that the shape of the IRSL profiles would be indistinguishable within uncertainties for the two endmember athermal fading rates. We thus find that athermal loss is negligible, and it is not included in the following calculations or considered further.

Trapping

Here we illustrate the importance of the trapping term and the effect of the different trapping parameters, i.e. the environmental dose rate ($\dot{D}$) and the characteristic dose of saturation (D_0), on OSL surface exposure dating. Assuming a non-eroding rock surface, the bleaching front will keep propagating with time if trapping is not accounted for (Fig. A1 of Sohbati et al., 2012). In contrast, a secular equilibrium (Sohbati et al., 2018) defined by the steady state between trapping and light-stimulated detrapping at depth can be reached when trapping is considered. In this case, the depth and the time at which the secular equilibrium occurs depend only on the $\dot{D}$, D_0, $\overline{\sigma\varphi_0}$ and μ parameters. Using the parameters mentioned in Sect. 2.1.2 and solving Eq. (1) without considering athermal loss, our simulations show that for typical granitic rocks (i.e. $\dot{D}$ between 2 and $8\,\mathrm{Gy\,ka}^{-1}$) the bleaching front stabilizes at around 20–25 mm of depth after an exposure duration of 10^5–10^6 years (Fig. 3).

In Fig. 4 we investigate the effects of $\dot{D}/D_0$ on setting the depth of the bleaching front. We use extreme values of D_0 of 100 and 2000 Gy and $\dot{D}$ of 2×10^{-3} and $10^{-2}\,\mathrm{Gy\,a}^{-1}$ (King et al., 2016; Jenkins et al., 2018; Biswas et al., 2018), resulting in $\dot{D}/D_0$ from 10^{-6} to $10^{-4}\,\mathrm{a}^{-1}$. Our simulations show that the higher the $\dot{D}/D_0$, the closer to the surface the steady-state bleaching profile, which is a consequence of the more rapid saturation of the sample luminescence signal. The steady-state bleaching depth varies between around 22 and 31 mm (measured at the inflection point) for our endmember simulations (Fig. 4). The influence of $\dot{D}/D_0$ on the bleaching profile is minor relative to the other parameters (μ, $\dot{\varepsilon}$); however, dose rate can vary by an order of magnitude between rock slices and may possibly explain part of the noise observed in reported experimental data (Meyer et al., 2018).

Erosion

The effect of surface erosion on the luminescence signal has recently been highlighted by Sohbati et al. (2018), who proposed an analytical solution to account for this process. In this section, we numerically solve Eq. (1), neglecting athermal loss, and test the effect of different erosion rates on luminescence profiles. Figure 5a shows the resulting synthetic luminescence profiles at steady state with erosion rates from 0 to $10^2\,\mathrm{mm\,a}^{-1}$. Under these synthetic conditions, the effect of surface erosion starts to be noticeable from around $10^{-4}\,\mathrm{mm\,a}^{-1}$; for an erosion rate of $10^2\,\mathrm{mm\,a}^{-1}$, the steady-state bleaching front is brought forward to 2 mm below the exposed surface. Indeed, surface erosion advects the luminescence signal closer to the surface (Fig. 5). As a result, rock luminescence profiles reflect a competition through time between erosion, trapping and detrapping. When the effects of the three processes are in disequilibrium, such as following initial bedrock surface exposure or the onset of surface erosion, a transient state occurs during which the lumines-

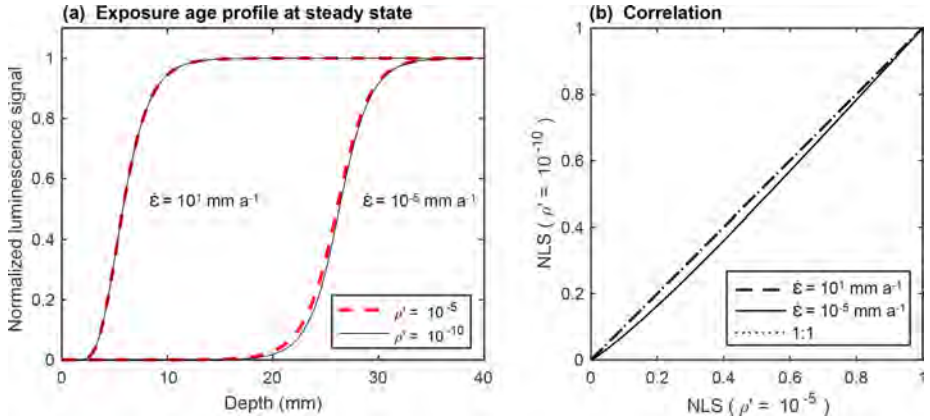

Figure 2. **(a)** Synthetic luminescence profiles predicted by Eq. (1) for two dimensionless recombination centre densities ρ' (10^{-10} and 10^{-5}) and two erosion rates $\dot{\varepsilon}$ (10^{-10} and 10^{-5} mm a^{-1}). **(b)** Comparison of the normalized luminescence signal (NLS) for the different values of ρ' and $\dot{\varepsilon}$. Values for the different parameters $\overline{\sigma\varphi_0}$, μ, $\dot{D}$ and D_0 are described in Sect. 2.1.2.

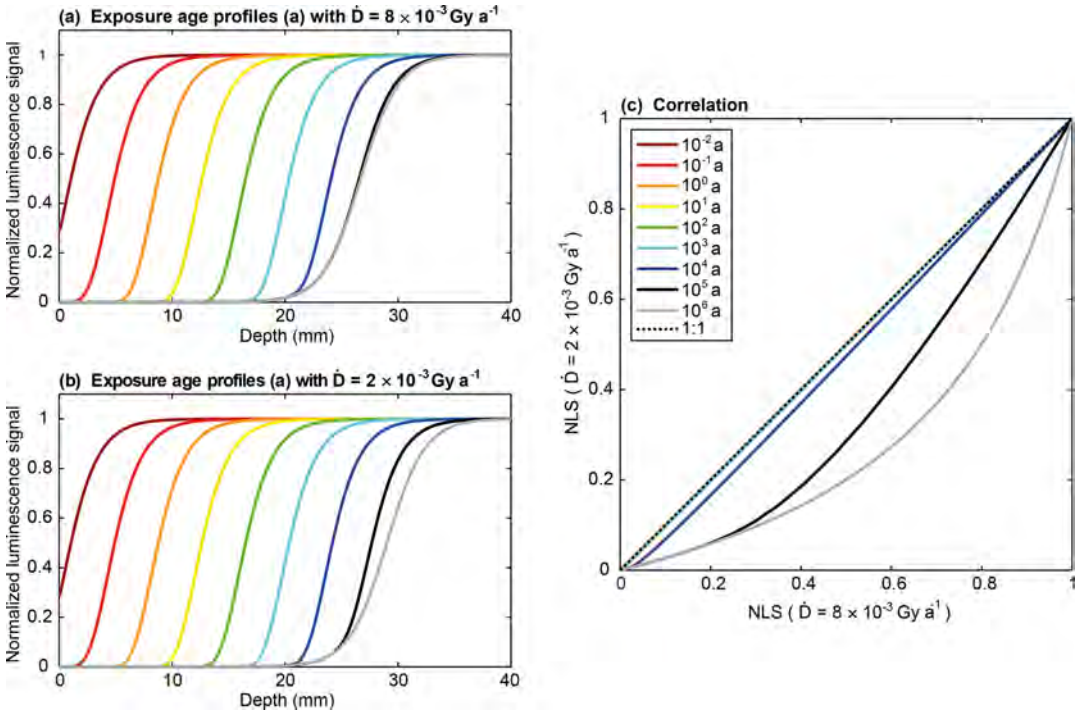

Figure 3. Synthetic luminescence profiles for bleaching models with exposure ages from 10^{-2} to 10^{-6} years and considering trapping rates of **(a)** 8×10^{-3} and **(b)** 2×10^{-3} Gy a^{-1}. Panel **(c)** shows the comparison of the normalized luminescence signal (NLS) for both models after the different exposure ages. As there is no difference between the modelled profiles for both scenarios between 10^{-2} and 10^{-3} years, the curves are overlying each other. The choice of parameters $\overline{\sigma\varphi_0}$, μ, $\dot{D}$ and D_0 is described in Sect. 2.1.2.

cence signal continues to evolve. After prolonged exposure and assuming constant erosion, the competing effects equilibrate, leading to a steady state at which the bleaching profile is no longer propagating into the rock. In Fig. 5b, we evaluate the evolution of the luminescence profiles from transient to steady state using a dimensionless parameter calculated from the product of the profile depth in which luminescence reaches 50 % of its saturation value ($x_{50\,\%}$), defined as the inflection point NLS($x_{50\,\%} = 0.5$) and the light attenuation coefficient μ (Sohbati et al., 2018). We see that the higher the erosion rate, the faster the system reaches steady state. Consequently, to characterize how a surface is affected by erosion through time, an independent temporal framework is needed to determine the duration of rock surface exposure. This can be achieved by combining OSL surface exposure with TCN dating, which is briefly introduced in the following section.

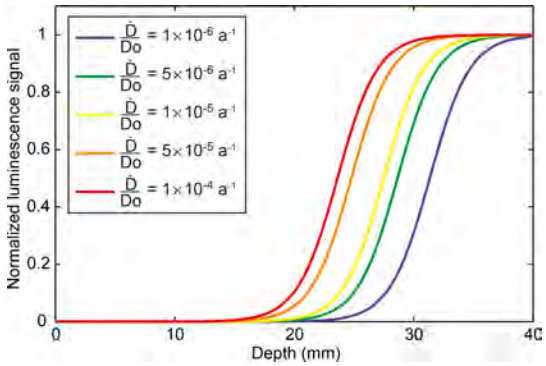

Figure 4. Synthetic luminescence profiles predicted by Eq. (1) for different values of the ratio $\dot{D}/D_0$ (10^{-6}, 5×10^{-6}, 10^{-5}, 5×10^{-5} and 10^{-4} a^{-1}) and assuming no erosion. The choice of parameters $\overline{\sigma\varphi_0}$, μ, $\dot{D}$ and D_0 is described in Sect. 2.1.2.

2.2 Terrestrial cosmogenic nuclide (TCN) dating

TCN dating is based on the observation that when cosmic rays reach Earth's surface, they produce cosmogenic isotopes in specific targets, such as the production of ^{10}Be in quartz (e.g. Gosse and Philips, 2001; Dunai, 2010). The in situ production of quartz ^{10}Be occurs predominantly within a few metres of Earth's surface and decreases exponentially with depth (Fig. A4a; Portenga and Bierman, 2011, and references therein). The evolution of cosmogenic nuclide C (atoms g^{-1}) in time t (year) and rock depth x (mm) is a function of the disintegration constant λ (a^{-1}), the production rate of a radionuclide P (atoms g^{-1} a^{-1}) and the erosion $\dot{\varepsilon}$ and can be described by the following equation (Gosse and Phillips, 2001):

$$\frac{dC(x,t)}{dt} = -C(x,t)\lambda + P(0,t)e^{-\nu x} + \dot{\varepsilon}(t)\frac{dC(x,t)}{dx}. \quad (3)$$

$P(0)$ is the production rate of the radionuclide at the target surface. The symbol ν defines the absorption coefficient (mm^{-1}) of the target: $\nu = \frac{\rho}{\Lambda}$. Λ is the mean attenuation length for nuclear particles interacting within the target ($g\,mm^{-2}$). If the radionuclide concentration at the surface represents the last exposure event, assuming there is no inheritance from a potential previous exposure and that the erosion rate is constant, Eq. (3) can be solved analytically (Lal, 1991), which gives

$$C(x,t) = \frac{P(0)}{\lambda + \nu\dot{\varepsilon}} e^{-\nu x}[1 - e^{-(\lambda+\nu\dot{\varepsilon})t}]. \quad (4)$$

When $t \gg 1/(\lambda + \nu\dot{\varepsilon})$ the radionuclide concentration reaches a steady state; i.e. a secular equilibrium is reached (Lal, 1991). Under these circumstances, a measured cosmogenic nuclide concentration can be interpreted in terms of a maximum steady-state erosion rate. Here we solve Eq. (3) numerically using the finite-difference method and use the analytical solution to estimate the maximum possible erosion rate.

The general behaviour of the quartz ^{10}Be concentration with erosion and exposure age is well documented in the literature (e.g. Lal, 1991), and we illustrate it in Fig. A4 for comparison with OSL surface exposure dating (Fig. 5). Note that for solving Eq. (3), the experimental measurement of ^{10}Be concentration C_{exp} must first be corrected by the depth normalization factor f_E and by the topographic shielding factor (SF) of the surface following the equation (Martin et al., 2017)

$$C_{corr} = \frac{C_{exp}}{f_E \times SF}, \quad (5)$$

with f_E computed by integrating average production over the sample thickness using a single exponential spallation attenuation equation (Balco et al., 2008):

$$f_E = \frac{\Lambda}{\rho \times E}\left[1 - \frac{-\rho \times E}{\Lambda}\right], \quad (6)$$

where ρ is the mean density of the targeted rock ($g\,mm^{-3}$) and E the sample thickness (mm). As we discussed previously, OSL surface exposure and TCN dating both depend on the timing of surface exposure and erosion. These two processes are recorded at different depths into the rock surface: centimetre scale for OSL surface exposure dating and metre scale for TCN; therefore, OSL surface exposure dating is potentially sensitive to surface erosion over shorter timescales than TCN dating. To combine the two methods, one needs to solve Eqs. (1) and (3) simultaneously, for which the two unknowns are the exposure age t and the erosion rate $\dot{\varepsilon}$.

3 Inversion approach for synthetic erosion rates

In this section, we generate a series of forward and inverse models. The forward model calculates a luminescence signal and a ^{10}Be concentration from synthetic erosion and exposure histories. The goal of the inverse model is to constrain the model parameters (i.e. erosion and exposure histories) using the data (i.e. IRSL signal and ^{10}Be concentration). To validate the inversion procedure, we use the forward model to create synthetic data, which we then recover using the inverse model. For these tests, we use the same OSL surface exposure dating parameters explored in the previous sections: $\overline{\sigma\varphi_0} = 129\,a^{-1}$ and $\mu = 0.596\,mm^{-1}$. The value $\dot{D} = 8 \times 10^{-3}$ Gy a^{-1} was selected as an average value obtained for samples used in this study ($\dot{D} = 7.4$ and 8.4×10^{-3} Gy a^{-1} in Table 2). $D_0 = 500$ Gy was selected as a representative value for IRSL50 signals from granite. The ^{10}Be exposure age is estimated using the measured quartz ^{10}Be concentration of sample MBTP1 collected on a polished granitic bedrock surface at 2545 m a.s.l. from the Tête de Trélaporte located on the left bank of the Mer de Glace glacier (Mont Blanc massif, European Alps). Note that the lithology of this sample is similar to that of the OSL surface exposure dating calibration site from which the model parameters are taken (Fig. A2; Lehmann et al., 2018). The sample was located

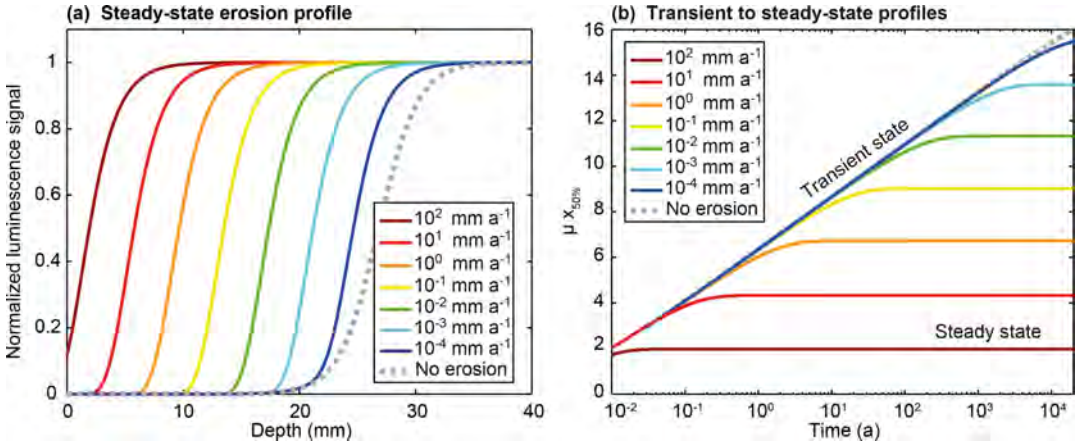

Figure 5. Sensitivity of luminescence–depth profiles with erosion. **(a)** Synthetic luminescence profiles at steady state with erosion rates from 0 to 10^2 mm a^{-1}. **(b)** Transient to steady-state profile for erosion rates from 0 to 10^2 mm a^{-1} as a function of time **(a)** and as the product of the attenuation factor μ (mm^{-1}) and the depth $x_{50\,\%}$ defined as NLS($x_{50\,\%} = 0.5$). The choice of parameters $\overline{\sigma\varphi_0}$, μ, $\dot{D}$ and D_0 is described in Sect. 2.1.2.

Table 1. Symbol table.

Symbol	Unit	Description
Both methods		
x	mm	Rock depth
t	a	Exposure age
$\dot{\varepsilon}$	mm a^{-1}	Erosion rate
t_S	a	Erosion onset time
OSL surface exposure dating		
n	mm^{-3}	Concentration of trapped charge
L	a^{-1}	Maximum possible number of trapped electrons
σ	mm^2	Luminescence photoionization cross section
φ_0	mm^{-2} a^{-1}	Photon flux
μ	mm^{-1}	Attenuation coefficient
λ	mm	Wave of light stimulation
$\dot{D}$	Gy a^{-1}	Environmental dose rate
D_0	Gy	Characteristic dose of saturation
s	s^{-1}	Frequency factor
ρ'		Dimensionless recombination centre density
r'		Dimensionless recombination centre distance
TCN dating		
t_0	a	TCN exposure age without erosion correction
t_C	a	TCN exposure age with erosion correction
C	atoms g^{-1}	Number of atoms of the radionuclide within the rock
P	atoms g^{-1} a^{-1}	Radionuclide production rate
ν	mm^{-1}	Absorption coefficient of the specific target
ρ	g mm^{-3}	Mean density of the targeted rock
Λ	g mm^{-2}	Absorption mean free path for nuclear interacting particles in the target
λ	a^{-1}	Disintegration constant
E	mm	Sample thickness
SF		Topographic shielding factor

on a surface presenting a shielding factor 0.963 and has a thickness of 8 cm (Table 2). Its non-corrected ^{10}Be concentration is equal to $47\,4750 \pm 17\,530$ atoms g_{qtz}^{-1} using the sea level high latitude (SLHL) rescaled local production rate of the Chironico landslide: 4.16 ± 0.10 atoms $g_{qtz}^{-1}\,a^{-1}$ (Claude et al., 2014). This is corrected for the sample longitude, latitude and elevation considering no erosion correction and the ERA40 atmospheric model (Uppala et al. 2005). We use a disintegration constant λ of $4.9 \times 10^{-7}\,a^{-1}$ and a mean attenuation length for nuclear interacting particles in the target Λ of $1.6 \times 10^{3}\,g\,mm^{-2}$ (Gosse and Phillips, 2001; Nishiizumi et al., 2007). The density of the Mont Blanc granite is measured at around $2.55 \times 10^{-3}\,g\,mm^{-3}$.

3.1 Forward modelling experiments

In the first scenario, a series of synthetic luminescence profiles were generated using Eq. (1) in a forward model, together with erosion rates of $\dot{\varepsilon} = 10^{-2}\,mm\,a^{-1}$ and $\dot{\varepsilon} = 1\,mm\,a^{-1}$. This range of values is based on the results of the numerical experiment reported in Sect. 2.1.2. For this scenario, erosion rates are assumed to be constant over the TCN exposure age $t_s = t_0$, with t_s being the onset time of erosion (dashed lines in Fig. 7a–d). A reference luminescence profile is also calculated, assuming no erosion, using t_0 and Eq. (2) (black dot in Fig. 6b and black lines in Figs. 6c and 7a–d). In the third scenario, another set of synthetic luminescence profiles was again generated using Eq. (1) in a forward model, but the erosion rate was allowed to vary with time (Fig. 6 and green dots in Fig. 7a–d). The assumption made here is that the evolution of erosion in time can follow a step function (Fig. 6a and b). Our objective is explore the effect of a non-constant erosion rate in time on both the luminescence signal and ^{10}Be concentration. This is the simplest possible time-varying erosion rate history. The erosion is initially equal to zero, i.e. between the corrected exposure age t_c and an onset time of erosion t_s, and increases to a fixed rate between t_s and today (Fig. 6a). Note that more sophisticated erosion rate histories could be tested with the same approach, which is beyond the scope of the current study. Figure 6 illustrates the schematic representation of four different erosion scenarios through time (Fig. 6a and b) and their resulting luminescence signal (Fig. 6c). Note that the corrected exposure age t_c is part of the calculation obtained by solving Eq. (3) using the nuclide concentration and an entire erosion rate history. We report the four model outputs calculated using t_s between 1 and 100 years and erosion rates $\dot{\varepsilon}$ between 10^{-2} and $1\,mm\,a^{-1}$ (green dots in Fig. 7a–d). Note that we added 10 % white noise to the predicted OSL surface exposure dating profiles (used for the inversion approach in Sect. 2).

By applying a constant erosion rate of $10^{-2}\,mm\,a^{-1}$ to a rock surface exposed since t_0 ($16\,428 \pm 707$ years), the luminescence signal is brought 7.8 mm closer to the surface (i.e. 17 mm deep from the surface) compared to the reference signal (luminescence signal exposed since t_0 and not affected by erosion; black line in Fig. 7a–d at 24.8 mm deep from the surface). For a constant erosion rate of $1\,mm\,a^{-1}$, the luminescence signal is brought 15.4 mm closer to the surface (i.e. 9.4 mm deep from the surface) compared to the reference signal (difference between black lines and dashed lines measured at NLS = 0.5 in Fig. 7a–d).

If an erosion rate of $10^{-2}\,mm\,a^{-1}$ is applied for a duration of 1 year before sampling and integrated over its specific corrected exposure age (since $t_c = 16\,428 \pm 707$ years), the luminescence signal is brought 0.4 mm closer to the surface compared to the reference signal (green dots in Fig. 7a) and 1.2 mm if the same erosion rate is applied for 100 years before sampling and integrated over its specific t_c ($16\,455 \pm 713$ years; green dots in Fig. 7b). In both scenarios, the predicted luminescence profiles do not overlap the luminescence profile predicted for a constant erosion rate, indicating that the system is in a transient state.

For an erosion rate of $1\,mm\,a^{-1}$ applied during 1 year before sampling and for an exposure time corrected with its specific erosion history t_c ($16\,455 \pm 713$ years), the luminescence profile (green dots in Fig. 7c) is brought 1.2 mm closer to the surface compared to the reference signal (black line in Fig. 7c). In this case, the luminescence profile is in a transient state with erosion because it is not overlapping the luminescence profile produced by applying the same erosion rate for an infinite time (dashed line in Fig. 7c). Interestingly, the same effect on the luminescence signal is produced by applying an erosion rate of $1\,mm\,a^{-1}$ during 1 year (green dots in Fig. 7c) and an erosion rate $10^{-2}\,mm\,a^{-1}$ during 100 years before sampling (green dots in Fig. 7b). For an erosion rate of $1\,mm\,a^{-1}$ applied during 100 years before sampling and for an exposure time corrected with its specific erosion history t_c ($16\,945 \pm 722$ years), the luminescence signal is brought 15.4 mm closer to the surface (green dots in Fig. 7d) compared to the reference signal (black lines in Fig. 7d). A similar result is obtained when the erosion rate is applied for an infinite time (dashed line in Fig. 7d): in this scenario, the steady state with erosion is reached.

3.2 Inverse modelling experiments

The synthetic data are now inverted to assess the extent to which it is possible to recover the values of $\dot{\varepsilon}$ and t_s. Ultimately, our objective is to establish and validate a numerical protocol that enables erosion rate histories to be estimated from paired OSL surface exposure and TCN dating measurements on bedrock surfaces. To find the most likely solutions, we test 10^4 pairs of both $\dot{\varepsilon}$ and t_s (combination of 100 values of both parameters) in log space. The range of possible erosion rates $\dot{\varepsilon}$ varies between 10^{-5} and $10^{1}\,mm\,a^{-1}$. These endmember values were selected from the erosion sensitivity test performed in Sect. 2.1.5. The erosion onset times t_s range between 5×10^{-1} years and 3×10^{4} years, with this range being arbitrarily decided with the upper boundary set to approximately twice the initial TCN age.

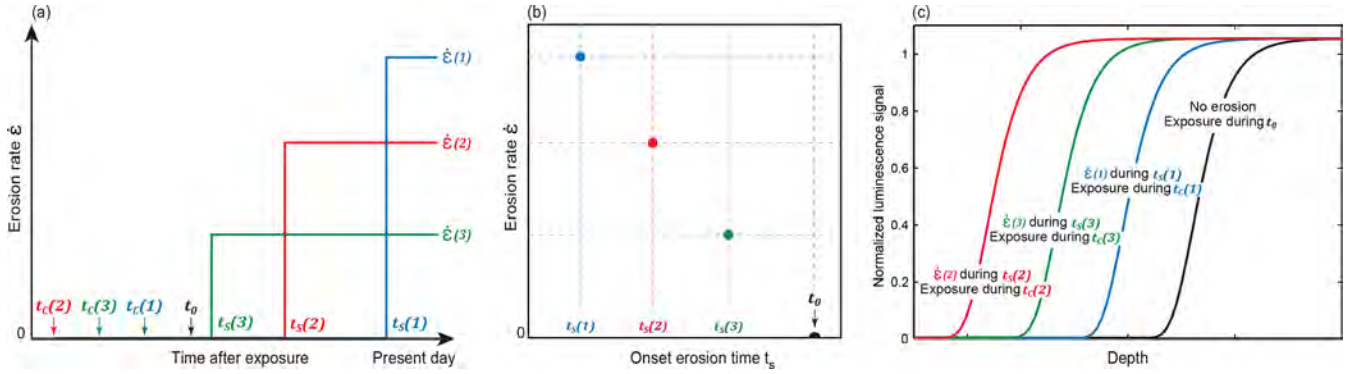

Figure 6. Schematic representation of four different erosion scenarios through time **(a, b)** and their resulting luminescence signal **(c)**. t_0 is the uncorrected ^{10}Be exposure age, t_s the onset times of erosion, t_c the corrected exposure ages and $\dot{\varepsilon}$ the erosion rate. Note that the luminescence plots in **(c)** are not model outputs but drawings, with the aim of conceptualizing how the experiments are designed.

As mentioned above, the measured ^{10}Be concentration has be to corrected for erosion. If the applied erosion rate is too high, the duration is too long or both, the ^{10}Be concentration must remain small (Fig. A4). On that basis, there is a range of solutions with high erosion rates and durations which is unable to predict the observed ^{10}Be concentration (Lal, 1991). We call this the "forbidden zone" and exclude it from the parameter search. Expressed differently, for each $\dot{\varepsilon}$ and t_s pair, Eq. (3) is first solved and a first estimate of the corrected exposure age t_c is calculated. However, Eq. (3) does not yield a solution for a range of values that produce too much erosion and thus a ^{10}Be concentration loss that is too high to fit the measured sample concentration. In the studied cases, the forbidden zone is defined by the values between the pairs $\dot{\varepsilon} = 10\,\mathrm{mm\,a^{-1}}$, $t_s \sim 110$ years and $\dot{\varepsilon} \sim 5 \times 10^{-1}\,\mathrm{mm\,a^{-1}}$, $t_s = 29\,210$ years.

For all the other pairs of $\dot{\varepsilon}$ and t_s, the corrected exposure age t_c is subsequently used to predict luminescence profiles ($\mathrm{NLS_{inverse}}$) that are compared to the synthetic luminescence profiles ($\mathrm{NLS_{forward}}$) presented in the previous section (green dots in Fig. 7a–d). The quality of these fits is evaluated using a misfit function, and the inversion results are converted into probability density functions using a likelihood function (Eq. 7). The least-squares deviation regression method minimizes the sum of the square differences between the forward $\mathrm{NLS_{forward}}$ and the inverted values $\mathrm{NLS_{inverse}}$, giving

$$\mathcal{L} = \exp\left(-\frac{1}{\sigma^2}\sum_{i=1}^{n}\left[\mathrm{NLS}^{(i)}_{\mathrm{forward}} - \mathrm{NLS}^{(i)}_{\mathrm{inverse}}\right]^2\right), \quad (7)$$

where n is the number of rock slices per sample and σ is the standard deviation of the normalized saturated luminescence signal intensities that form the plateau at depth ($0.053 \leqslant \sigma \leqslant 0.059$ for our samples).

The results of these inversions are shown in Fig. 7e–h with the parameter space for erosion rate and time as well as the resulting likelihood. The green circles depict the synthetic forward-modelled pair of $\dot{\varepsilon}$ and t_s ($\mathrm{NLS_{forward}}$), which should be recovered in the inversion (green dots in Fig. 7a–d), and the black circles show the $\dot{\varepsilon} - t_0$ pair used to produce the model assuming erosion is constant (dashed lines in Fig. 7a–d). We then select the pairs of $\dot{\varepsilon}$ and t_s leading to the maximum 5 % likelihood values that fit the synthetic data (the threshold of 5 % is arbitrarily chosen) and plot their corresponding luminescence profile values (red lines in Fig. 7a–d).

The first noticeable observation is that the erosion rate $\dot{\varepsilon} = 10^{-2}\,\mathrm{mm\,a^{-1}}$ could be applied over every time period below $\sim 3 \times 10^{-3}$ years. The numerical solutions for both constant and non-constant erosion rate are outside the forbidden zone (black and green circles, respectively, in Fig. 7e–f). As another example, an erosion rate equal to $\dot{\varepsilon} = 1\,\mathrm{mm\,a^{-1}}$ could also be applied for any time lower than 1200 years. Indeed, it is not possible to apply an erosion $\dot{\varepsilon} = 1\,\mathrm{mm\,a^{-1}}$ during t_0 as this pair of values would lie in the forbidden zone (Fig. 7g, h) since such a high erosion rate would imply a ^{10}Be concentration loss that is too high to fit the measured sample concentration.

For the first scenario, the synthetic luminescence profile produced by applying an erosion rate $\dot{\varepsilon} = 10^{-2}\,\mathrm{mm\,a^{-1}}$ during time period $t_s = 1$ year has a great number of possible pairs of $\dot{\varepsilon}$ and t_s that would reproduce this specific luminescence signal (normalized likelihood > 0.9; yellow area in Fig. 7e). The acceptable solutions range between pairs of values below $\dot{\varepsilon} \sim 2 \times 10^{-2}\,\mathrm{mm\,a^{-1}}$ with $t_s = 5 \times 10^{-1}$ years and $\dot{\varepsilon} = 10^{-5}\,\mathrm{mm\,a^{-1}}$ with $t_s = 10^3$ years. These low values do not produce enough erosion to significantly alter the TCN exposure age ($t_c \sim t_0$).

In the second scenario, the erosion rate is $\dot{\varepsilon} = 10^{-2}\,\mathrm{mm\,a^{-1}}$ during a time period $t_s = 100$ years, and the forward model pair values can be successfully recovered from the inversion with a more restrained range of numerical solutions (Fig. 7f). The transient state with erosion is well illustrated by trade-offs between erosion rate and time. To fit the forward luminescence profile, low erosion rates should be associated with long time periods following the trend from $\dot{\varepsilon} \sim$

$2\,\mathrm{mm\,a^{-1}}$ with $t_s = 5 \times 10^{-1}$ years to $\dot{\varepsilon} \sim 1.4 \times 10^{-4}\,\mathrm{mm\,a^{-1}}$ with $t_s = 1.2 \times 10^4$ years. When the erosion rate of $1.4 \times 10^{-4}\,\mathrm{mm\,a^{-1}}$ is applied longer than 1.2×10^4 years, a steady state with erosion is reached and this specific erosion rate could be applied for an infinite time. The highest correction of the TCN exposure age possible with these solutions is of the order of 0.1 % ($t_0 = 16\,428 \pm 707$ years and $t_c = 16\,455 \pm 713$ years), which is insignificant compared to the 3.6 % uncertainties on t_0.

The third scenario, in which the erosion rate is $\dot{\varepsilon} = 1\,\mathrm{mm\,a^{-1}}$ during time period $t_s = 1$ year, shares the exact same solution as the second case ($\dot{\varepsilon} = 10^{-2}\,\mathrm{mm\,a^{-1}}$ with $t_s = 100$ years). This confirms the observation made with the forward modelling whereby both scenarios predicted similar luminescence profile depths. This can be explained because both pairs of $\dot{\varepsilon} - t_s$ lie on the trend from $\dot{\varepsilon} \sim 2\,\mathrm{mm\,a^{-1}}$ with $t_s = 5 \times 10^{-1}$ years and $\dot{\varepsilon} \sim 1.4 \times 10^{-4}\,\mathrm{mm\,a^{-1}}$ with $t_s = 1.2 \times 10^4$ years.

In the fourth scenario, the erosion rate $\dot{\varepsilon} = 1\,\mathrm{mm\,a^{-1}}$ is applied during time $t_s = 100$ years, and the range of solutions is much more restrained than for the other scenarios. The synthetic luminescence profile is at steady state with erosion, wherein the erosion rate $\dot{\varepsilon} = 1\,\mathrm{mm\,a^{-1}}$ can be applied from 18 to 1200 years. For a longer time of erosion, the pairs of $\dot{\varepsilon} - t_s$ lie within the forbidden zone regarding the TCN concentration. In this case, the maximum correction of the TCN exposure age is around 3.1 % ($t_0 = 16\,428 \pm 707$ years and $t_{c_{max}} = 16\,945 \pm 722$ years), which is comparable to the initial uncertainty on t_0.

4 Application to natural samples

In this section, we apply the method presented above on two natural rock surfaces. Samples MBTP1 and MBTP6 were collected from glacially polished bedrock surfaces at 2545 and 2084 m a.s.l., respectively, from the Tête de Trélaporte located on the left bank of the Mer de Glace glacier (Mont Blanc massif, European Alps). Rock surfaces were collected for the application of both the TCN and OSL surface exposure dating methods (Fig. 9 and Tables 2 and 3.3). Both samples are from the same phenocrystalline granitic lithology of the Mont Blanc massif (Fig. 8).

4.1 Sample preparation, measurement and age calculation

The ^{10}Be sample preparation method is comprehensively described in the literature (e.g. Kohl and Nishiizumi, 1992; Ivy-Ochs, 1996). We used quartz separates from grain sizes between 250 µm and 1 mm. The addition of a commercial ^{9}Be carrier was followed by quartz dissolution in HF and Be purification using ion-exchange columns and selective precipitation. The ^{10}Be / ^{9}Be ratio was measured by accelerator mass spectrometry (AMS) on the 600 KV TANDY system at the Laboratory of Ion Beam Physics (LIP) at ETH Zürich (Switzerland) against the standard S2007N (Christl et al., 2013) that is calibrated against the 07KNSTD standard (Nishiizumi et al., 2007). We correct for a long-term average full chemistry procedural blank of ^{10}Be / ^{9}Be $(3.7 \pm 2.2) \times 10^{-15}$. Ages are calculated using the SLHL rescaled local production rate of the Chironico landslide, $4.16 \pm 0.10\,\mathrm{atoms\,g_{qtz}^{-1}\,a^{-1}}$ (Claude et al., 2014), corrected for the sample longitude, latitude and elevation considering no erosion correction, with the Lifton–Sato–Dunai (LSD) scaling scheme (Lifton et al., 2014), the ERA40 atmospheric model (Uppala et al., 2005) and the Lifton VDM 2016 geomagnetic database (for ages between 0 and 14 ka, Pavon-Carrasco et al., 2014, and for ages between 14 and 75 ka, GLOPIS-75, Laj et al., 2004) with a modified version of the CREp online calculator to process non-linear erosion rate correction by solving Eq. (3) (Martin et al., 2017). The reported errors propagate uncertainties from AMS standard reproducibility, counting statistics, the standard mean error of the samples, blank correction and the local production rate. These external errors are used to compare absolute ages to independent chronologies. All errors are reported at 1σ.

For luminescence analysis we followed the methodology of Lehmann et al. (2018). The bedrock samples were cored down to 30 mm of depth using a Husqvarna DM220 drill with a 10 mm diameter. Cores were then sliced into 0.7 mm thick rock slices with a Buehler IsoMet low-speed saw equipped with a 0.3 mm thick diamond blade. The samples were drilled and sliced under wet conditions (water and lubricant, respectively) to avoid any heating that could potentially reset the OSL signal. Sample preparation was done under subdued red-light conditions. The thickness of each rock slice was measured to determine the precise depth of each luminescence measurement. Luminescence measurements were performed using Risø TL-DA 20 TL–OSL readers (Bøtter-Jensen et al., 2010) equipped with ^{90}Sr beta sources at the University of Lausanne (Switzerland). We performed a preheat at 250 °C before giving infrared (IR) stimulation (870 nm, full width at half-maximum (FWHM) 40 nm) at 50 °C analysis are described in further detail in the Figs. A2 and A5). The calculation of $\dot{D}$ was achieved through the measurement of the concentrations of U, Th, K and Rb of the bulk rock sample and the use of the DRAC online calculator (Table 2 and details in Table A1; Durcan et al., 2015). The determination of D_0 was done by constructing a dose-response curve (DRC) of the IRSL signal measured at 50 °C using a single-aliquot regenerative dose (SAR) protocol (Murray and Wintle, 2000; Wallinga et al., 2000) and fitting the DRC with a single saturating exponential. The validity of the measurement protocol was confirmed using a dose-recovery experiment (Wallinga et al., 2000). Recovered doses were within 10 % of unity.

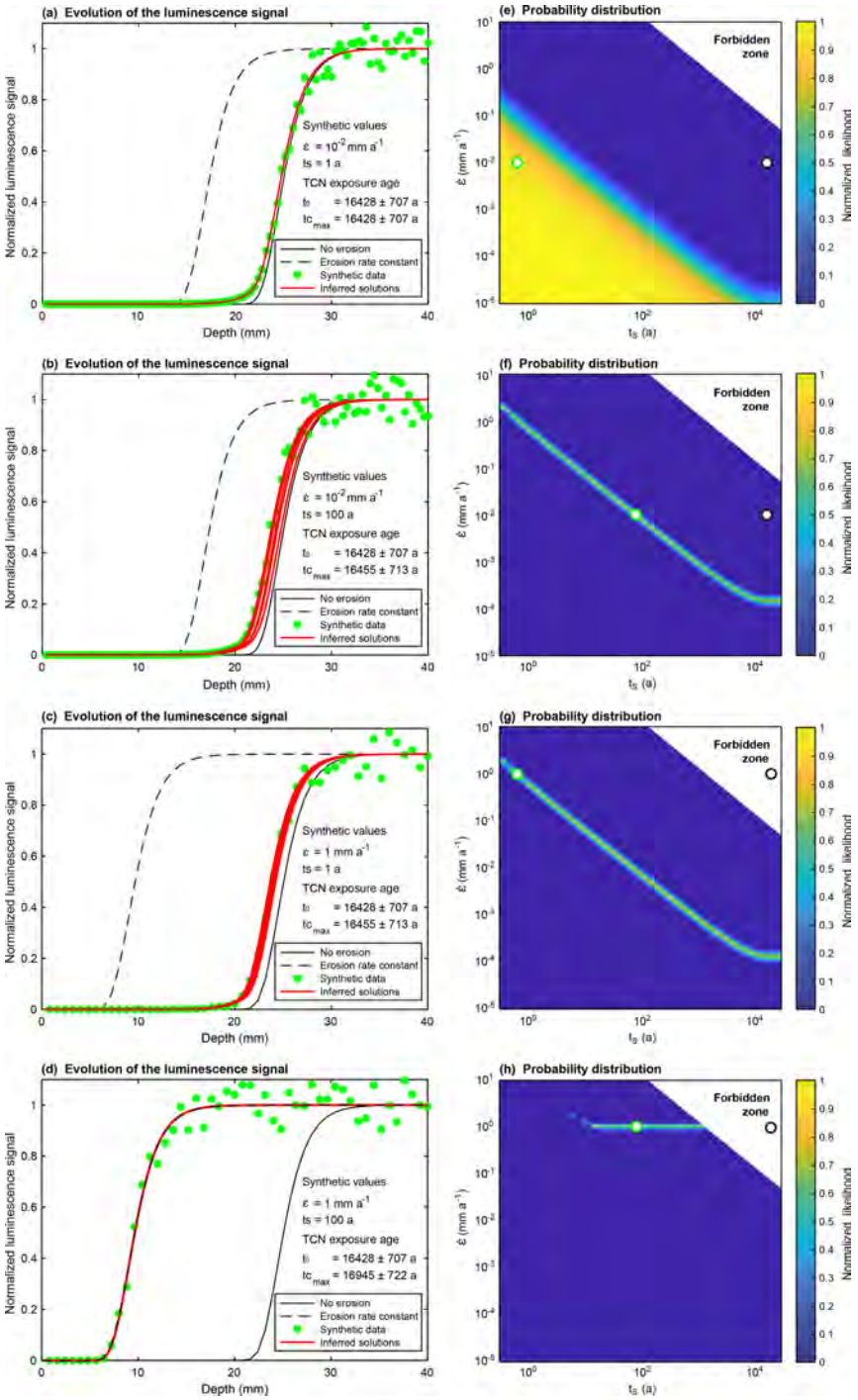

Figure 7. Results of forward and inverse modelling experiments. Green dots represent the simulated luminescence profiles for rock surfaces exposed to **(a)** an erosion rate of $\dot{\varepsilon} = 10^{-2}\,\mathrm{mm\,a^{-1}}$ during time $t_s = 1$ year, **(b)** an erosion rate of $\dot{\varepsilon} = 10^{-2}\,\mathrm{mm\,a^{-1}}$ during time $t_s = 100$ years, **(c)** an erosion rate of $\dot{\varepsilon} = 1\,\mathrm{mm\,a^{-1}}$ during time $t_s = 1$ year and **(d)** an erosion rate of $\dot{\varepsilon} = 1\,\mathrm{mm\,a^{-1}}$ during time $t_s = 100$ years. Black lines represent the reference luminescence profiles for a surface exposed since $t_0 = 16\,428 \pm 707$ years with no erosion. Dashed lines show the luminescence profiles produced by applying constant erosion rates of **(a, b)** $\dot{\varepsilon} = 10^{-2}\,\mathrm{mm\,a^{-1}}$ and **(c, d)** $\dot{\varepsilon} = 1\,\mathrm{mm\,a^{-1}}$ during t_0. Red lines represent the best-fitting profiles inverted for all numerical solutions with likelihood $> 5\,\%$. $t_{c_{max}}$ represents the maximum corrected TCN exposure age using the forward modelled values of $\dot{\varepsilon}$ and t_s. **(e–h)** The probability distributions inverted from the synthetic luminescence profiles, respectively, in **(a–d)**. Green open circles represent the pairs of values of $\dot{\varepsilon}$ and t_s used in the forward model to produce the profiles, and the black open circles represent the values $\dot{\varepsilon}$ and t_0 used to predict luminescence profiles with constant erosion (dashed line insets, **a–d**). All models were performed by solving Eq. (1) using the following parameters: $\overline{\sigma\varphi_0} = 129\,\mathrm{a^{-1}}$, $\mu = 0.596\,\mathrm{mm^{-1}}$, $\dot{D} = 8 \times 10^{-3}\,\mathrm{Gy\,a^{-1}}$ and $D_0 = 500\,\mathrm{Gy}$. TCN ages were calculated by solving Eq. (3) for the ^{10}Be concentration of sample MBTP1 presented in the following section.

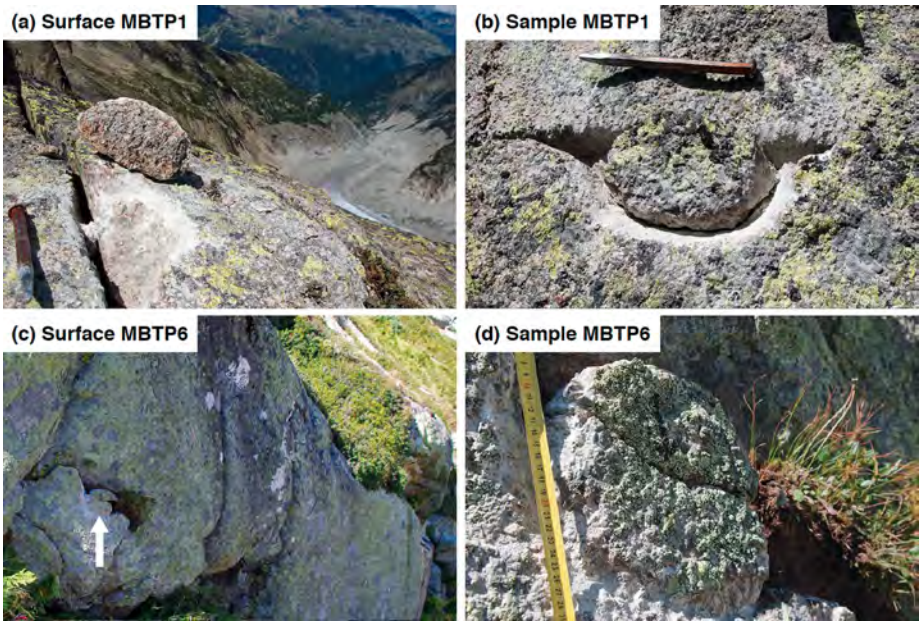

Figure 8. Locations and sample pictures of MBTP1 and MBTP6, both located on the Tête de Trélaporte along the Mer de Glace glacier (Mont Blanc massif, European Alps).

Table 2. Sample list and measurements.

Sample	Latitude	Longitude	Elevation	Thickness	Topographic	^{10}Be conc.[a]	$P(0)$ local[b]	$\dot{D}$ spec.[c]
ID	WGS 84		(m a.s.l.)	(cm)	shielding factor	(atoms g_{qtz}^{-1})	(atoms g_{qtz}^{-1})	(Gy a^{-1})
MBTP1	45.9083	6.9311	2545	8	0.963	$474\,750 \pm 17\,530$	30.20 ± 0.72	7.4×10^{-3}
MBTP6	45.9129	6.9326	2094	7	0.594	$84\,100 \pm 13\,060$	21.74 ± 0.52	8.4×10^{-3}

[a] Measured against standard 07KNSTD (Nishiizumi et al., 2007), corrected for full process blank of $(3.7 \pm 2.2) \times 10^{-15}$ ^{10}Be / ^{9}Be. [b] Local production rate using the sea level high latitude (SLHL) rescaled local production rate of the Chironico landslide, 4.16 ± 0.10 atoms g_{qtz}^{-1} a^{-1} (Claude et al., 2014), corrected for the sample longitude, latitude and elevation considering no erosion correction, with the LSD scaling scheme (Lifton et al., 2014), the ERA40 atmospheric model (Uppala et al., 2005) and the Lifton VDM 2016 geomagnetic database (for ages between 0 and 14 ka, Pavon-Carrasco et al., 2014, and for ages between 14 and 75 ka, GLOPIS-75, Laj et al., 2004). [c] Dose rates were calculated using the concentrations of U, Th and K of the bulk rock sample and the DRAC online calculator (details in Table A1; Durcan et al., 2015).

4.2 Experimental results

Sample MBTP1 provided a ^{10}Be concentration of $474\,750 \pm 17\,530$ atoms g_{qtz}^{-1}. The solution of Eq. (3) gives an apparent ^{10}Be age for sample MBTP1 of $t_0 = 16\,428 \pm 707$ years, assuming a sample thickness of 8 cm and a shielding factor of 0.963 (Tables 2 and 3). In the same way, the measured ^{10}Be concentration of $84\,100 \pm 13\,060$ atoms g_{qtz}^{-1} for sample MBTP6 gives a ^{10}Be age of $t_0 = 6667 \pm 965$ years, assuming a sample thickness of 7 cm and a shielding factor of 0.594 (Tables 2 and 3). Apparent ^{10}Be ages were calculated as described in Sect. 4.1, assuming no erosion.

Figure 9 shows the infrared stimulated luminescence at 50 °C (IRSL50, normalized signal) measurements for samples MBTP1 and MBTP6. Three replicates (i.e. individual cores) per sample were sliced in a way that a depth and an IRSL50 signal can be attributed to each rock slice (Tables A2 and A3). The IRSL50 signal is bleached near the surface and reaches a plateau at depth (even for sample MBTP1 for which the plateau is poorly defined). The scattering of the measurements between rock slices is probably due to the granitic nature of the samples. Indeed, the phenocryst lithology can cause heterogeneity in the resulting IRSL50 signals (Meyer et al., 2018) caused by differential bleaching and possibly variations in the environmental dose rate, mainly beta dose heterogeneity (Morthekai et al., 2006), and thus the rate of electron trapping.

As a reference profile, a model is computed by solving Eq. (2) using t_0 considering no erosion (black line in Fig. 9a) and lies at 25 mm below the rock surface. The bleaching front measured from the IRSL50 signal of sample MBTP1 (green dots in Fig. 9a) is located 4 mm closer to the surface compared to the reference profile (21 mm from the surface). The IRSL50 profile considering no erosion correction gives an

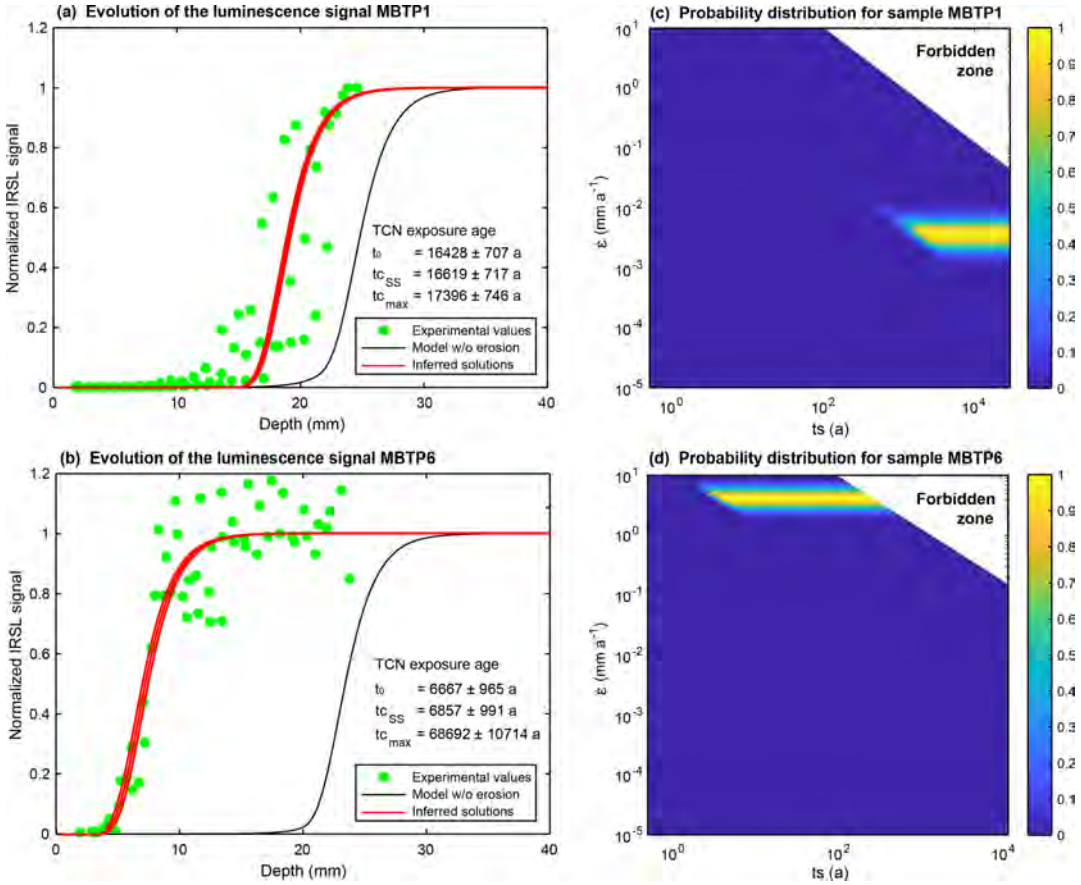

Figure 9. IRSL50 profiles and inversion results for samples MBTP1 and MBTP6. **(a, b)** Green dots represent the measured IRSL50 profiles for samples MBTP1 and MBTP6. Black lines represent the reference profiles calculated using Eq. (2) and taking the TCN exposure age with no erosion correction (t_0). Red lines represent inferred fits where the likelihood is greater than 0.95. $t_{c_{ss}}$ represents the corrected TCN exposure age calculated at steady state. $t_{c_{max}}$ represents the maximum corrected TCN exposure age. **(c, d)** The probability distributions inverted from the respective insets in **(a)** and **(b)**. All models were computed by solving Eq. (1) and using the following parameters: $\overline{\sigma\varphi_0} = 129\,\mathrm{a}^{-1}$, $\mu = 0.596\,\mathrm{mm}^{-1}$, $D_0 = 500\,\mathrm{Gy}$, $\dot{D} = 7.4\times10^{-3}\,\mathrm{Gy\,a}^{-1}$ and $\dot{D} = 8.4\times10^{-3}\,\mathrm{Gy\,a}^{-1}$ for samples MBTP1 and MBTP6. Dose rates were calculated using the concentrations of U, Th, K and Rb of the bulk rock sample and the DRAC online calculator (details in Table A1; Durcan et al., 2015).

apparent age about 2 orders of magnitude lower compared to t_0: about 642 ± 160 years (1σ; Table 3 and Fig. A5).

For sample MBTP6, the reference profile is 23.5 mm below the surface (black line in Fig. 9b). The measured IRSL50 profile (green dots in Fig. 9b) is approximately 16.5 mm closer to the surface in comparison to the reference profile (7 mm from the surface). The OSL surface exposure apparent age for sample MBTP6 is about 0.39 ± 0.02 years (1σ; Table 3 and Fig. A5).

4.3 Inversion results

In this section, we report the results from the inversion of $\dot{\varepsilon}$ and t_s for the IRSL50 profiles of samples MBTP1 and MBTP6 following the procedure presented in Sect. 2. For both samples, the corrected ^{10}Be ages are calculated using Eq. (3) with a range of erosion rates from 10^{-5} to $10^{1}\,\mathrm{mm\,a}^{-1}$ and t_s ranging from 5×10^{-1} years to $10^{\log(t_0)+0.25}$ years (this formula limits the search to ~ 30 ka because these surfaces are known to be post-LGM (Last Glacial Maximum); Coutterand and Buoncristiani, 2006).

The resulting forbidden zone for sample MBTP1 lies between the erosion rate–time pairs of $\dot{\varepsilon} = 10\,\mathrm{mm\,a}^{-1}$, $t_s \sim 110$ years and $\dot{\varepsilon} \sim 5\times10^{-1}\,\mathrm{mm\,a}^{-1}$, $t_s = 29\,210$ years (already discussed in Sect. 3.2). The inversion results indicate that sample MBTP1 reached a steady state with erosion characterized by an erosion rate of $\dot{\varepsilon} = (3.5 \pm 1.2)\times10^{-3}$ $(1\sigma)\,\mathrm{mm\,a}^{-1}$ applied during a minimum duration of 2300 years (Fig. 9c). In these conditions, the corrected TCN age is $t_{c_{ss}} = 16\,647 \pm 593$ years (1.1 % of correction). The maximum corrected TCN age $t_{c_{max}} = 17\,396 \pm 746$ years is obtained by using $\dot{\varepsilon} = (3.5\pm1.2)\times10^{-3}$ $(1\sigma)\,\mathrm{mm\,a}^{-1}$ and the maximum t_s possible (29 214 years); this comprises a correction of about 5.8 %.

For sample MBTP6, the forbidden zone lies between the erosion rate–time pairs of $\dot{\varepsilon} = 10\,\mathrm{mm\,a^{-1}}$, $t_s \sim 150$ years and $\dot{\varepsilon} \sim 1 \times 10^{-10}\,\mathrm{mm\,a^{-1}}$, $t_s = 11\,860$ years. The inversion results show that the IRSL50 profile of sample MBTP6 reaches steady state with erosion for an erosion rate $\dot{\varepsilon} = 4.3 \pm 0.56\,\mathrm{mm\,a^{-1}}$ (1σ) applied since at least 4 years. In these conditions, the corrected TCN age is $t_{c_{ss}} = 6857 \pm 991$ years (2.8 % of correction). This steady state cannot be maintained for longer than 344 years because further values correspond to the forbidden zone (Fig. 9d). The maximum corrected TCN age $t_{c_{max}} = 68\,692 \pm 10\,714$ years would represent a significant correction of 930 %.

At steady state, the surfaces MBTP1 and MBTP6 would have lost 8.05 mm and 17.2 mm, respectively. These values seem realistic regarding the natural surface textures observed on site: no smooth surface or striations are preserved on the roches moutonnées (Fig. 8). By taking the endmember hypothetical erosion values, the surfaces MBTP1 and MBTP6 would have lost a maximum of 102 and 1479 mm, respectively.

5 Discussion

The mismatch between OSL surface exposure and TCN ages presented in this study clearly shows how significant the impact of erosion for OSL surface exposure dating is. If the luminescence bleaching front is interpreted without considering erosion, the resulting exposure age will be strongly underestimated (Figs. 5, 7 and 9). For samples MBTP1 and MBTP6 the apparent OSL surface exposure ages are 642 ± 160 years and 0.32 ± 0.02 years, respectively, while apparent TCN exposure ages are $16\,428 \pm 707$ and 6667 ± 965 years, respectively. We demonstrated in Sect. 2.1 that OSL surface exposure dating is hardly applicable to natural rock surfaces that experience even a minimal erosion rate of about $10^{-4}\,\mathrm{mm\,a^{-1}}$. Our models and results show that the position of the bleaching front is highly sensitive to the erosion rate history. Recent studies (e.g. Freiesleben et al., 2015; Sohbati et al., 2012a, 2015; Rades el al., 2018) showed very convincingly that OSL rock surface dating can be used to identify multiple burial and exposure events in the history of a single clast. However, our results imply that erosion cannot be neglected. We show in this study that this high sensitivity to erosion can instead be used to estimate the erosion history of such rock surfaces.

To do so, we have numerically solved the equation describing the evolution of the luminescence signal of a rock surface exposed to light and erosion (Eqs. 1 and 3). The validation of the model was tested on synthetic data and applied to two different glacially polished bedrock surfaces. We assumed a simple erosion rate history following a step function. However, it is very likely that rock surfaces are subject to stochastic erosion processes (e.g. Ganti et al., 2016). These stochastic processes potentially cover temperature, moisture, snow cover or wind fluctuations along the year. The numerical approach adopted here would potentially enable us to consider any type of erosion history (inverse exponential, stochastic distribution, etc.). We considered the erosion rate to be non-constant in time but to follow a step function which changes from zero to a constant erosion rate at certain times in the exposure history. We observed that the resulting erosion histories can follow two states: a transient state or a steady state. Indeed, an experimental luminescence signal can be either at steady or transient state with erosion. To identify at which state the signal is, a model using Eq. (1) should try to fit the experimental luminescence signal considering a range of constant erosion rates applied over the TCN exposure age t_0 of the specific surface. If one specific erosion rate enables the model to fit the experimental luminescence signal, the system is at steady state with this specific erosion rate. If there is no unique solution, the system is at transient state with erosion. Note that some erosion rates cannot be applied for long durations. Indeed, the quantity of material removed and the concentration of cosmogenic nuclides in the rock surface would not match the measured nuclide concentrations. To avoid that, we have defined a forbidden zone which characterized the range of pairs $\dot{\varepsilon}$ and t_s for which Eq. (3) could not be solved.

When a luminescence profile is derived from multiple erosion rate $\dot{\varepsilon}$ and time t_s pairs, the system is experiencing a transient state with erosion. This situation is characterized by a trade-off between erosion rate and the time of erosion. During this state, the luminescence signal does not evolve with depth if an increase in the erosion time is compensated for by a decrease in the erosion rate. On the other hand, when a luminescence signal is derived from an erosion rate applied across a range of times t_s, the system can be considered at steady state regarding the luminescence profile. In this case, the erosion rate can be considered constant in time over the entire exposure age given by TCN dating, providing that this solution falls outside the forbidden zone. At steady state, the time during which the erosion rate is applied is always lower than or equal to the maximum corrected TCN age (i.e. $t_s \leq t_{c_{max}}$).

The luminescence profile from a given rock surface is able to give information about the erosion history of this surface at both transient and steady state with erosion. The coupling with TCN dating allows for the determination of a limit in time of the steady state with erosion, which cannot tend to infinity as discussed above (i.e. the forbidden zone). According to the inverse modelling of sample MBTP1, the total erosion experienced by the rock surface is about 8.05 mm when the system reached steady state with erosion ($\dot{\varepsilon} = 3.5 \times 10^{-3}\,\mathrm{mm\,a^{-1}}$ during $t_s = 2300$ years) and 17.2 mm for sample MBTP6 ($\dot{\varepsilon} = 4.3\,\mathrm{mm\,a^{-1}}$ during $t_s = 4$ years). This quantity of material removal is plausible given field observations, wherein the micro-structures of striations (coated layer and glacial polish) are not preserved but the macro-patterns of glacial erosion can still be observed (moulded

Table 3. TCN and OSL surface ages and inversion results for samples MBTP1 and MBTP6.

Sample ID	TCN apparent age $t_0^{(1)}$ (year)	TCN corr. age $t_{C_{ss}}^{(2)}$ (year)	TCN corr. age $t_{C_{max}}^{(2)}$ (year)	OSL surface exposure apparent age$^{(3)}$ (year)	t_S at SS* (year)	$\dot{\varepsilon}$ at SS* (mm a^{-1})	Total erosion at SS* (mm)
MBTP1	$16\,428 \pm 707$	$16\,619 \pm 717$	$17\,396 \pm 746$	642 ± 160	2300	$3.5 \pm 1.2 \times 10^{-3}$	8.05
MBTP6	6667 ± 965	6857 ± 991	$68\,692 \pm 10\,714$	0.39 ± 0.02	4	4.3 ± 0.56	17.2

Ages are calculated using the sea level high latitude (SLHL) rescaled local production rate of the Chironico landslide, 4.15 ± 0.10 atoms g^{-1} a^{-1}, rescaled for every longitude (Claude et al., 2014), latitude and elevation considering no erosion correction, with the LSD scaling scheme (Lifton et al., 2014), the ERA40 atmospheric model (Uppala et al., 2005) and the Lifton VDM 2016 geomagnetic database (for ages between 0 and 14 ka, Pavon-Carrasco et al., 2014, and for ages between 14 and 75 ka, GLOPIS-75, Laj et al., 2004) by solving Eq. (3). (2) TCN age corr. $t_{c_{max}}$ corresponds to the maximum corrected TCN exposure ages calculating from the best maximum 5 % solution. For (1) and (2) the errors represent the internal errors. (3) Ages were inverted (Fig. A5) using Eq. (2) and prescribing 10^6 solutions for a range of time from 0 to t_0 (TCN age calculated using the ^{10}Be concentration of each sample and solving Eq. (3) without erosion correction). All models were calculated using the following parameters: $\overline{\sigma\varphi_0} = 129$ a^{-1}, $\mu = 0.596$ mm^{-1}, $D_0 = 500$ Gy, $\dot{D} = 7.4 \times 10^{-3}$ Gy a^{-1} and $\dot{D} = 8.4 \times 10^{-3}$ Gy a^{-1} for sample MBTP1 and sample MBTP6. The uncertainties represent 1σ of the distribution presented in Fig. A5.
* SS means steady state.

forms, whalebacks, grooves). By taking the endmembers authorized by our model, we explore the limit of our method. The maximum total erosion is about 102 mm for MBTP1 (3.5×10^{-3} mm a^{-1} during 29 214 years) and about 1479 mm for MBTP6 (4.3 mm a^{-1} during 344 years). Such a high difference in erosion between two locations of the same vertical profile could be explained by the local topographic and environmental conditions, such as slope surface and snow cover, controlling the efficiency of frost cracking.

The quantification of the erosion rate distribution provides the opportunity to quantitatively correct TCN ages. These corrections can be minor but significant: for example, about 1.1 % for MBTP1 by taking the steady-state values and about 5.8 % using the endmember values. For sample MBTP6, the correction is about 2.8 % by taking the steady-state values. Using the endmember values, the maximum corrected TCN age for the highest sample is $t_{c_{max}}$(MBTP1) $= 17\,396 \pm 746$ years and the lowest sample is $t_{c_{max}}$(MBTP6) $= 68\,692 \pm 10\,714$ years (representing a maximum correction of about 930 %). The assumption that a surface at 2094 m a.s.l. (surface MBTP6) was exposed almost 50 kyr longer than a surface located 451 m higher (surface MBTP1 at 2545 m a.s.l.) on the same vertical profile in the context of glacial thinning is hardly acceptable. According to the known glaciological evolution of the western Alps during the LGM, exposure ages of > 25 ka are simply not possible. Surfaces at 2600 m a.s.l. located in accumulation zones of former glaciated areas were covered by ice at least until the LGM (e.g. Penck and Brückner, 1909; Bini et al., 2009; Coutterand, 2010; Seguinot et al., 2018), which implies that the age estimates must be treated with caution. However, our results imply that the uncertainty of the exposure age could be large. A correction of the exposure age of a few thousand years would have significant implications when investigating how post-LGM climate variability regionally impacted past ice extent.

We have presented the results using one luminescence signal only (IRSL50). Jenkins et al. (2018) and Sohbati et al. (2015) showed that multiple luminescence signals can be exploited. Since bleaching propagates at different rates within rocks (see Ou et al., 2018), using multiple signals (e.g. pIR225 and OSL125) should enable us to better assess whether the position of the bleaching front is steady or not and thus to further constrain the erosion history (both erosion rate and duration).

Our results confirm the results of Sohbati et al. (2018), who derived an analytical solution assuming steady erosion and using a confluent hypergeometric function. Here we solve the transient solution of Eq. (1) using the finite-difference method. An important difference to the earlier study of Sohbati et al. (2018) is that here the system is fully coupled between OSL and TCN surface exposure dating. OSL dating provides information about the evolution of the erosion rate in time, and TCN dating gives a realistic time frame for this evolution by setting a forbidden zone.

The most striking outcome of this new approach is the ability to quantify surface erosion rates over timescales from 10 to 10^4 years. The quantification of erosion rates using TCN concentration is limited (expressed in Sect. 2) with the minimum time given by $t \gg 1/(\lambda + \nu\dot{\varepsilon})$. By taking the two endmembers of erosion in this study, $\dot{\varepsilon} = 10^{-5}$ mm a^{-1} and $\dot{\varepsilon} = 10$ mm a^{-1}, the time limits are respectively 2×10^6 and 6×10^4 years, which means that one cannot use TCN to constrain the erosion history of post-LGM surfaces. Consequently, the coupling of OSL and TCN surface exposure dating makes the quantification of bare bedrock surface erosion possible at the timescale of a single interglacial event and might provide insight into the processes of topographic evolution in alpine environments.

6 Conclusions

In this study, we couple OSL and TCN surface exposure dating to constrain post-glacial bedrock erosion and surface exposure duration. We numerically solve the equation describing the evolution of luminescence signals in rock surfaces considering exposure age, bedrock surface erosion, and trapping and detrapping rates due to bleaching and athermal losses. We show that it is critical to account for bedrock surface erosion while interpreting luminescence bleaching pro-

files. Even at low erosion rates (10^{-4} mm a^{-1}) for periglacial environments, only a few years are needed to affect the luminescence profile of a rock surface.

We were able to discriminate between two regimes characterizing the relationships between the depth of the luminescence bleaching, the exposure age and the bedrock surface erosion. The transient state describes a rock surface with a luminescence profile in disequilibrium. In contrast, a rock surface in steady state is produced when the influence of bedrock surface erosion, exposure age and trapping rate compensate for one another. If the system is maintained under these conditions, the luminescence signal no longer evolves with time. Indeed, the determination of the time at which the steady state with erosion occurs is critical. For the two natural surfaces we analysed here, this time can range from 4 years (at an erosion rate of 4.3 mm a^{-1}) to 2300 years (at an erosion rate of 3.5×10^{-3} mm a^{-1}). The approach developed in this study thus represents a new asset to directly quantify an erosion correction for TCN dating. We see that this correction can range from 1.2 % to 930 % for natural surfaces, although one must keep in mind that the exposure age may be overestimated if not compared to independent observations.

Finally, this new approach enables the quantification of erosion rates over surfaces exposed for 10–10^4 years, filling a methodological gap between short timescales (from a few seconds to decades) and long timescales ($> 10^5$ years). The contribution of this approach will allow for the quantification of the contribution of bare bedrock surface in sediment production and the topographic evolution of alpine environments over glacial–interglacial cycles. Measurements at locations where bedrock surface erosion is very low (e.g. polar areas, high mountains) need to be investigated to check if OSL surface exposure is potentially applicable to timescales $> 10^2$ years without accounting for the effect of erosion rates. Another perspective is to investigate the control of temperature and climate on erosion rate evolution in time along an elevation transect. Using this approach, the contribution of post-glacial bedrock erosion can be quantified and the feedback between erosion and climate evaluated.

Code availability. The code used for the implementation of the algorithm, examples and benchmarks presented in this paper is available here: https://github.com/BenjaminLehmann/esurf2019.git (last access: 3 July 2019).

Appendix A

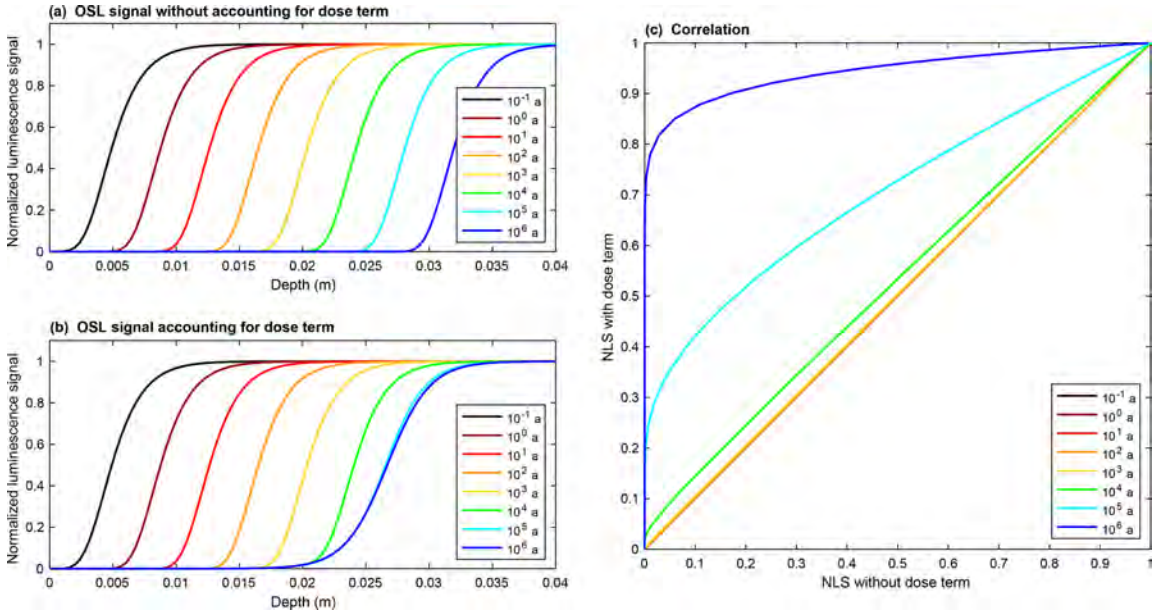

Figure A1. Modelled luminescence–depth profiles as predicted by Eq. (1) accounting for neither fading nor erosion, **(a)** without the trapping term and **(b)** with the trapping term, respectively. The selected parameter values are $\dot{D} = 8 \times 10^{-3}\,\mathrm{Gy\,a^{-1}}$, $D_0 = 500\,\mathrm{Gy}$, $\overline{\sigma\varphi_0} = 129\,\mathrm{a^{-1}}$ and $\mu = 0.596\,\mathrm{mm^{-1}}$. **(c)** Comparison between the normalized luminescence (NLS) signal for both scenarios shown in **(a)** and **(b)**.

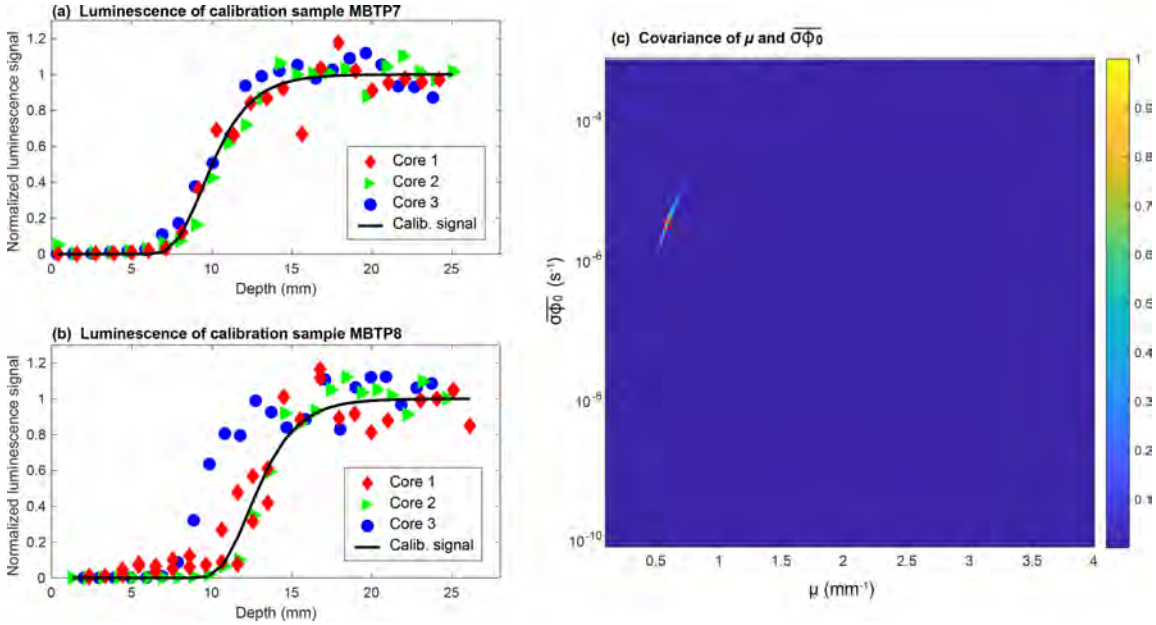

Figure A2. Calibration of the parameters μ and $\overline{\sigma\varphi_0}$ using two calibration samples, MBTP7 (1936 m a.s.l.) and MBPT8 (1995 m a.s.l.), with exposure ages of 2 ± 2 years and 11 ± 2 years, respectively. These samples were at the bottom of the Trélaporte vertical profiles in 2016. The surfaces are located between the present-day position of the glacier and the Little Ice Age maximal elevation. These ages were determined using the reconstruction from Vincent et al. (2014). The calibration is made through an inversion protocol by prediction 10^8 luminescence signals corresponding to the combinations of 10^4 values of $\overline{\sigma\varphi_0}$ in the logarithmic space and 10^4 values of μ. The inversed solutions are inferred using a least absolute deviation regression as described in Lehmann et al. (2018).

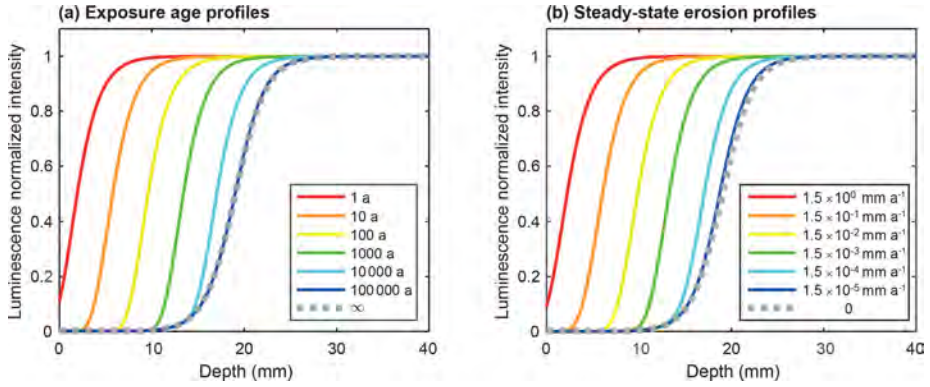

Figure A3. Modelled luminescence–depth profiles as predicted by Eq. (1) for a **(a)** non-eroding and **(b)** eroding rock surface, respectively. The selected parameter values are $\dot{D} = 6 \times 10^{-3}\,\mathrm{Gy\,a^{-1}}$, $D_0 = 250\,\mathrm{Gy}$, $\overline{\sigma\varphi_0} = 2200\,\mathrm{ka^{-1}}$ and $\mu = 0.6\,\mathrm{mm^{-1}}$, similar to Sohbati et al. (2018).

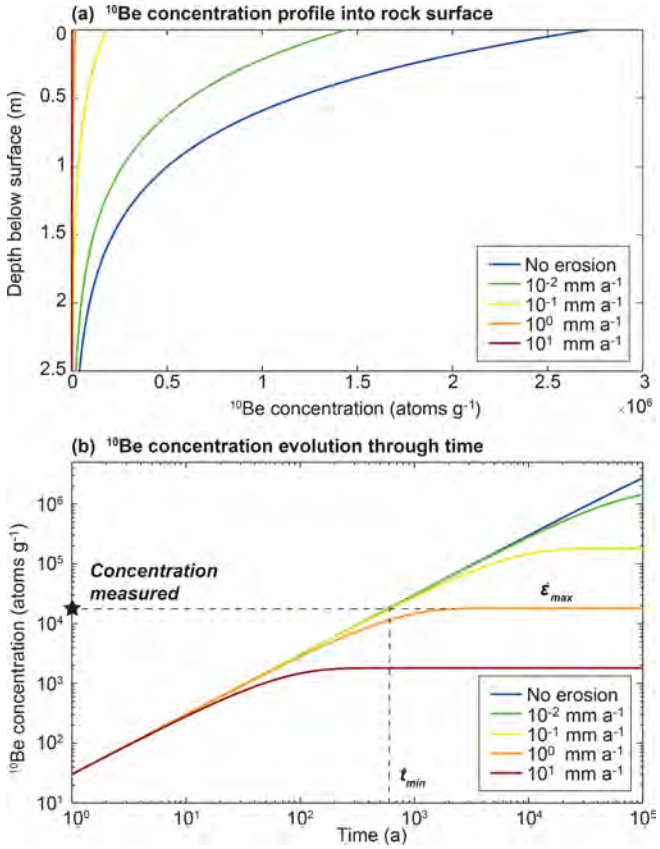

Figure A4. Evolution of the ^{10}Be production of a rock surface affected by different rates of erosion as a function of **(a)** the rock depth and **(b)** the exposure age calculated using a modified version of the CREp online calculator to process the non-linear erosion rate correction by solving Eq. (3) (Martin et al., 2017) as a modelling exercise and for comparison with OSL surface exposure curves in Fig. 5.

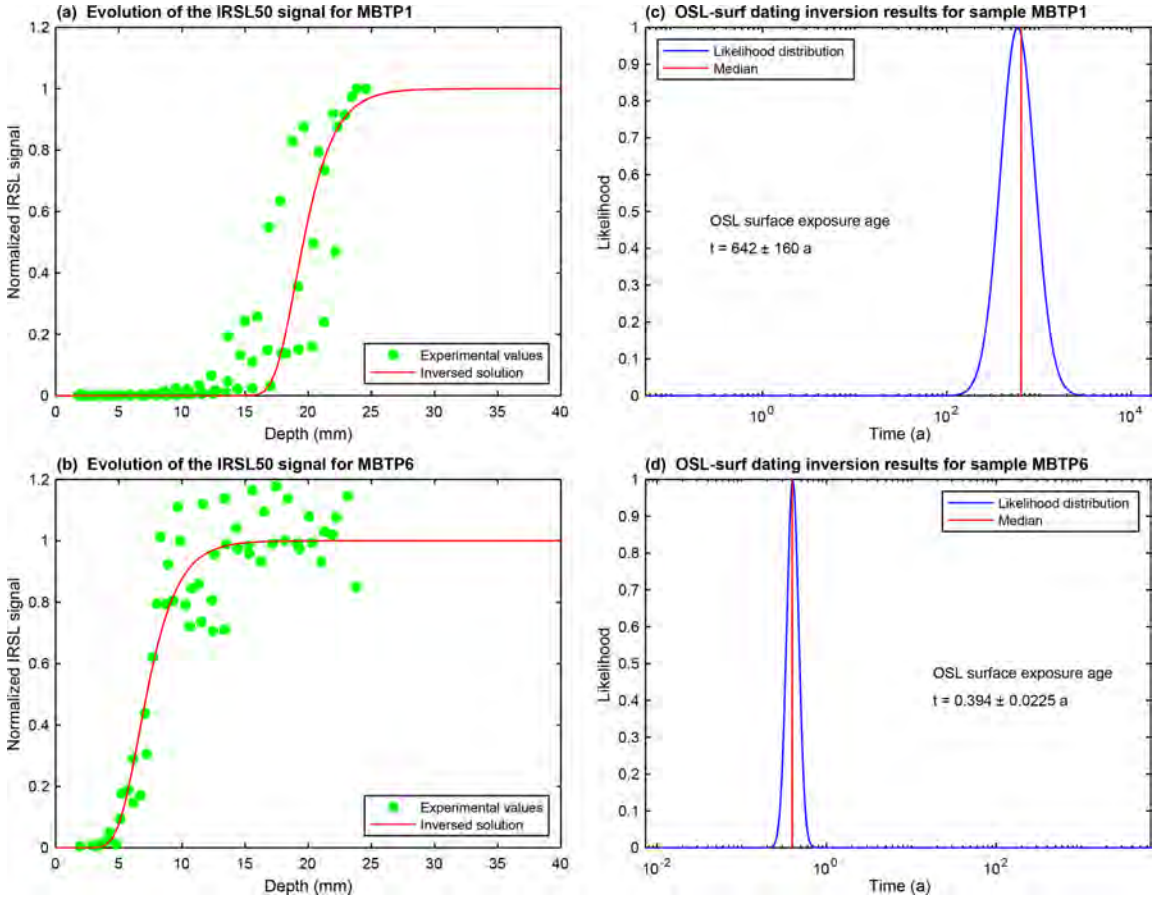

Figure A5. Determination of the apparent OSL surface exposure ages for samples MBTP1 and MBTP6. Experimental values in **(a)** and **(b)** correspond to the value measured for three cores per sample. The likelihood was determined using a probability density function following a least-squares deviation regression method minimizing the sum of the square differences between the experimental and the inverted values. Red lines in **(c)** and **(d)** represent the median value of the distribution. Apparent ages were inverted using Eq. (2) and prescribing 10^6 solutions for a range of time from 0 to t_0 (TCN age calculated using the nuclide concentration of each sample and solving Eq. (3) without erosion correction). All models were calculated using the following parameters: $\overline{\sigma\varphi_0} = 129\,\mathrm{a}^{-1}$, $\mu = 0.596\,\mathrm{mm}^{-1}$, $D_0 = 500\,\mathrm{Gy}$, $\dot{D} = 7.4 \times 10^{-3}\,\mathrm{Gy\,a}^{-1}$ and $\dot{D} = 8.4 \times 10^{-3}\,\mathrm{Gy\,a}^{-1}$ for sample MBTP1 and sample MBTP6 (see main text for details).

Table A1. Dosimetry calculations for the feldspar samples analysed. Conversion factors have been chosen after Adamiec and Aitken (1998). Alpha-particle attenuation and beta-particle attenuation factors have been chosen after Bell (1980) and Mejdahl (1979), respectively. Cosmic dose rates have been calculated using the method of Prescott and Hutton (1994), assuming an overburden density of $2.7 \pm 0.1\,\mathrm{g\,cm}^{-3}$. Internal K concentration is assumed to be 12 ± 0.5 % for both samples. Environmental dose rates were calculated using the DRAC online calculator (Durcan et al., 2015), assuming a grain size between 750 and 1000 µm and water content of 2 %.

Sample ID	U (ppm)	Th (ppm)	K (ppm)	Thickness (m)
MBTP1	5.69 ± 0.12	36.8 ± 0.6	2.56 ± 0.03	0.08 ± 0.02
MBTP6	8.75 ± 0.19	26.0 ± 0.4	3.88 ± 0.05	0.07 ± 0.02

Table A2. Infrared stimulated luminescence at 50 °C (IRSL50) experimental values for sample MBTP1.

MBTP1								
C1			C2			C3		
x (mm)	Lx/Tx	Lx/Tx Err.	x (mm)	Lx/Tx	Lx/Tx Err.	x (mm)	Lx/Tx	Lx/Tx Err.
1.81	0.00	0.000	2.24	0.00	0.000	1.97	0.00	0.005
2.80	0.00	0.000	3.16	0.00	0.001	2.91	0.00	0.001
3.76	0.00	0.001	4.14	0.00	0.001	3.96	0.00	0.000
4.70	0.00	0.001	5.09	0.00	0.001	4.99	0.00	0.001
5.72	0.00	0.001	6.07	0.00	0.001	5.95	0.00	0.001
6.80	0.00	0.001	7.10	0.00	0.000	6.85	0.00	0.002
7.77	0.00	0.002	8.04	0.00	0.001	7.72	0.01	0.003
8.68	0.00	0.002	8.89	0.00	0.001	8.62	0.01	0.007
9.52	0.00	0.001	9.77	0.00	0.002	9.54	0.03	0.013
10.49	0.01	0.003	10.72	0.01	0.002	10.42	0.02	0.004
11.53	0.01	0.002	11.70	0.01	0.003	11.36	0.04	0.022
12.49	0.01	0.002	12.64	0.02	0.008	12.32	0.07	0.011
13.47	0.01	0.006	13.63	0.05	0.010	13.65	0.19	0.109
14.41	0.02	0.018	14.63	0.13	0.175	15.00	0.24	0.073
15.56	0.02	0.014	15.60	0.11	0.032	15.95	0.26	0.100
17.02	0.03	0.005	16.76	0.15	0.072	16.88	0.55	0.193
18.25	0.14	0.176	17.93	0.14	0.127	17.79	0.63	0.109
19.24	0.15	0.149	19.19	0.36	0.091	18.73	0.83	0.171
20.30	0.16	0.108	20.38	0.50	0.101	19.65	0.87	0.150
21.23	0.24	0.179	21.29	0.74	0.125	20.82	0.79	0.165
22.16	0.47	0.348	22.30	0.88	0.118	21.98	0.92	0.136
			23.45	0.97	0.139	22.89	0.91	0.073
			24.59	1.00	0.082	23.86	1.00	0.082

Table A3. Infrared stimulated luminescence at 50 °C (IRSL50) experimental values for sample MBTP6.

MBTP6								
C1			C2			C3		
x (mm)	Lx/Tx	Lx/Tx Err.	x (mm)	Lx/Tx	Lx/Tx Err.	x (mm)	Lx/Tx	Lx/Tx Err.
1.96	0.00	0.000	1.96	0.01	0.000	3.32	0.01	0.000
3.00	0.01	0.000	2.90	0.01	0.000	4.30	0.05	0.001
4.05	0.02	0.001	3.84	0.02	0.000	5.25	0.18	0.004
5.11	0.09	0.002	4.80	0.01	0.000	6.17	0.15	0.003
6.13	0.29	0.007	5.76	0.19	0.004	7.09	0.44	0.010
7.19	0.30	0.008	6.72	0.17	0.004	8.00	0.79	0.017
8.29	1.01	0.022	7.71	0.62	0.013	8.93	0.92	0.020
9.29	0.81	0.017	8.69	0.79	0.017	9.85	1.00	0.021
10.27	0.79	0.019	9.68	1.11	0.024	10.76	0.85	0.018
11.34	0.86	0.019	10.61	0.72	0.016	11.67	1.12	0.024
12.39	0.81	0.020	11.53	0.73	0.018	12.58	0.96	0.021
13.40	1.14	0.025	12.46	0.71	0.016	13.50	0.99	0.021
14.29	1.04	0.023	13.40	0.71	0.017	14.41	0.97	0.021
15.26	0.98	0.023	14.49	1.23	0.026	15.33	0.96	0.021
17.48	1.28	0.028	15.56	1.16	0.025	16.25	0.93	0.021
			16.49	1.09	0.024	17.16	0.99	0.021
			17.45	1.18	0.025	18.14	1.00	0.021
			18.38	1.14	0.024	19.14	0.99	0.022
			19.32	0.97	0.021	20.07	1.08	0.023
			20.31	0.99	0.021	21.02	0.93	0.020

Author contributions. BL realized the fieldwork, the OSL and ^{10}Be preparation and analysis, and performed the modelling. FH and BL led the organization of the study, the development of the model, the interpretation of the results and the writing of the paper. PGV and GEK both contributed to the determination of the field strategy, the interpretation of both ^{10}Be and OSL results, and to the writing. RHB contributed to the interpretation of OSL results and to the writing.

Competing interests. The authors declare that they have no conflict of interest.

Acknowledgements. The authors thank Susan Ivy-Ochs, Marcus Christl, Olivia Kronig, Ewelina Opyrchal, Stefano Casale and the Laboratory of Ion Beam Physics (LIP) at ETH Zürich for making the TCN dating preparation and analysis possible. The authors thank Pierre-Henri Blard for sharing the code of the CREp calculator and Delphine Six and Christian Vincent for GLACIOCLIM Alps data availability. We thank Jean Braun for constructive input on the modelling. We thank Sylvain Coutterand for his expertise on the Quaternary and Mont Blanc massif and for his help during the sampling campaign. The authors would like to thank Nadja Stalder, Julia González Holguera, Gil Bustarret and Ugo Nanni for their support during field excursions; Micaela Faria and Kelian Haring are thanked for laboratory support.

Financial support. This research has been supported by the SNFS Swiss-AlpArray SINERGIA project (grant no. CRSII2_154434/1).

Georgina E. King and Pierre G. Valla acknowledge SNSF support (projects Pz00P2-167960 and PP00P2-170559, respectively).

Review statement. This paper was edited by Andreas Lang and reviewed by two anonymous referees.

References

Agassiz L.: Discours prononcé á l'ouverture des séances de la Soc. helv. sci. natur. à Neuchâtel, le 24 juillet 1837, par L. Agassiz, président: actes, Soc. helv. sci. natur., réunie à Neuchâtel, 22. sess., Neuchâtel, 5–32, 1837.

Aitken, M. J.: Thermoluminescence dating, Academic press, 1985.

Aitken, M. J.: An Introduction to Optical Dating The Dating of Quaternary: Sediments by the Use of Photon-stimulated Luminescence, Oxford University press, 1998.

Anderson, R. S.: Near-Surface Thermal Profiles in Alpine Bedrock: Implications for the Frost Weathering of Rock, Arct. Antarct. Alp. Res., 30, 362–372, 1998.

Anderson, R. S. and Anderson, S. P.: Geomorphology: The Mechanics and Chemistry of Landscapes, United Kingdom at the University Press, Cambridge, ISBN 9780521519786, 2010.

André, M.-F.: Rock weathering rates in arctic and subarctic environments (Abisko Mts, Swedish Lappland), Z. Geomorphol., 40, 499–517, 1996.

André, M.-F.: Do periglacial landscapes evolve under periglacial conditions?, Geomorphology, 52, 149–164, 2003.

Armesto-González, J., Riveiro-Rodríguez, B., González-Aguilera, D., and Rivas-Brea, M. T.: Terrestrial laser scanning intensity data applied to damage detection for historical buildings, J. Archaeol. Sci., 37, 3037–3047, 2010.

Augustin, L., Barbante, C., Barnes, P. R. F., Barnola, J. M., Bigler, M., Castellano, E., Cattani, O., Chappellaz, J., Dahl-Jensen, D., Delmonte, B., Dreyfus, G., Durand, G., Falourd, S., Fischer, H., Fluckiger, J., Hansson, M. E., Huybrechts, P., Jugie, G., Johnsen, S. J., Jouzel, J., Kaufmann, P., Kipfstuhl, J., Lambert, F., Lipenkov, V. Y., Littot, G. C., Longinelli, A., Lorrain, R., Maggi, V., Masson-Delmotte, V., Miller, H., Mulvaney, R., Oerlemans, J., Oerter, H., Orombelli, G., Parrenin, F., Peel, D. A., Petit, J.-R., Raynaud, D., Ritz, C., Ruth, U., Schwander, J., Siegenthaler, U., Souchez, R., Stauffer, B., Steffensen, J. P., Stenni, B., Stocker, T. F., Tabacco, I. E., Udisti, R., van de Wal, R. S. W., van den Broeke, M., Weiss, J., Wilhelms, F., Winther, J.-G., Wolff, E. W., and Zucchelli, M.: Eight glacial cycles from an Antarctic ice core, Nature, 429, 623–628, 2004.

Bailey, R. M.: Paper I-simulation of dose absorption in quartz over geological timescales and its implications for the precision and accuracy of optical dating, Radiat. Meas., 38, 299–310, 2004.

Baillie, M. G. L. and Pilcher, J. R.: A simple cross-dating program for tree-ring research, Tree-ring Bull. 33, 7–14, 1973.

Baillie, M. G. L.: A Slice Through Time: dendrochronology and precision dating, London, Routledge, 176 pp., 1995.

Balco, G., Stone, J. O., Lifton, N. A., and Dunai, T. J.: A complete and easily accessible means of calculating surface exposure ages or erosion rates from ^{10}Be and ^{26}Al measurements, Quat. Geochronol., 3, 174–195, 2008.

Balco, G.: Contributions and unrealized potential contributions of cosmogenic nuclide exposure dating to glacier chronology, 1990–2010, Quaternary Sci. Rev., 30, 3–27, 2011.

Ballantyne, C. K.: Paraglacial geomorphology, Quaternary Sci. Rev., 21, 1935–2017, 2002.

Ballantyne, C. K. and Stone, J. O.: Trimlines, blockfields and the vertical extent of the last ice sheet in southern Ireland, Boreas, 44, 277–287, 2015.

Beedle, M. J., Menounos, B., Luckman, B. H., and Wheate, R.: Annual push moraines as climate proxy, Geophys. Res. Lett. 36, L20501, https://doi.org/10.1029/2009GL039533, 2009.

Bennett, M. and Glasser, N. F.: Glacial geology: ice sheets and landforms, Chichester, UK, Hoboken, NJ Wiley-Blackwell, 2009.

Berthel, N., Schworer, C., and Tinner, W.: Impact of Holocene climate changes on alpine and treeline vegetation at Sanetsch Pass, Bernese Alps, Switzerland, Rev. Palaeobot. Palyno., 174, 91–100, 2012.

Bierman, P. R. and Nichols, K. K.: Rock to sediment—slope to sea with ^{10}Be—rates of landscape change, Annu. Rev. Earth Planet. Sci., 32, 215–255, 2004.

Bini, A., Buoncristiani, J.-F., Couterrand, S., Ellwanger, D., Felber, M., Florineth, D., Graf, H. R., Keller, O., Kelly, M., Schlüchter, C., and Schoeneich, P: Die Schweiz w´ahrend des letzteiszeitlichen Maximums (LGM), Bundesamt für Landestopografie swisstopo, 2009.

Biswas, R. H., Herman, F., King, G. E., and Braun, J.: Thermoluminescence of feldspar as a multi-thermochronometer to con-

strain the temporal variation of rock exhumation in the recent past, Earth Planet. Sc. Lett., 495, 56–68, 2018.

Blarquez, O., Carcaillet, C., Bremond, L., Mourier, B., and Radakovitch, O.: Trees in the subalpine belt since 11 700 cal. BP: origin, expansion and alteration of the modern forest, Holocene, 20, 139–146, 2010.

Blumthaler, M., Ambach, W., and Ellinger, R.: Increase in solar UV radiation with altitude, J. Photochem. Photobio. B, 39, 130–134, 1997.

Boch, R. and Spötl, C.: Reconstructing palaeoprecipitation from an active cave flowstone, J. Quaternary Sci., 26, 675–687, 2011.

Bond, G., Heinrich, H., Broecker, W. S., Labeyrie, L., McManus, J., Andrews, J., Huon, S., Jantschik, R., Clasen, S., Simet, C., Tedesco, K., Klas, M., Bonani G., and Ivy, S.: Evidence for massive discharge of icebergs into the North Atlantic Ocean during the last glacial period, Nature, 360, 245–249, 1992.

Botter-Jensen, L., Thomsen, K. J., and Jain, M.: Review of optically stimulated luminescence (OSL) instrumental developments for retrospective dosimetry, Radiat. Meas., 45, 253–257, 2010.

Brandmeier, M., Kuhlemann, J., Krumrei, I., Kappler, A., and Kubik, P. W.: New challenges for tafoni research, A new approach to understand processes and weathering rates, Earth Surf. Proc. Land., 36, 839–852, 2011.

Broecker, W. and Denton, G.: What drives glacial cycles?, Sci. Am., 262, 43–50, 1990.

Brown, N. D., Rhodes, E. J., and Harrison, T. M.: Using thermoluminescence signals from feldspars for low-temperature thermochronology, Quat. Geochronol., 42, 31–41, 2017.

Brozović, N., Burbank, D. W., and Meigs, A. J.: Climatic limits on landscape development in the northwestern Himalaya, Science, 276, 571–574, 1997.

Burbank, D. W., Leland, J., Fielding, E., Anderson, R. S., Brozović, N., Reid, M. R., and Duncan, C.: Bedrock incision, rock uplift and threshold hillslopes in the northwestern Himalayas, Nature, 379, 505–510, 1996.

Buylaert, J.-P., Murray, A. S., Thomsen, K. J., and Jain, M.: Testing the potential of an elevated temperature IRSL signal from K-feldspar, Radiat. Meas., 44, 560–565, 2009.

Castiglioni, B.: L'Italia nell'etá quaternaria, Carta delle Alpi nel Glaciale, (1 : 200 000 scale), in: Atlante fisico-economico d'Italia, edited by: Dainelli, G., Consociazione Turistica Italiana, Milano, Italy, Table 3.

Clark, P. U., Dyke, A. S., Shakun, J. D., Carlson, A. E., Clark, J., Wohlfarth, Mitrovica, J. X. B., Hostetler, S. W., and McCabe, A. M.: The last glacial maximum, Science, 325, 710–714, 2009.

Chapot, M. S., Sohbati, R., Murray, A. S., Pederson, J. L., and Rittenour, T. M.: Constraining the age of rock art by dating a rockfall event using sediment and rock-surface luminescence dating techniques, Quat. Geochronol., 13, 18–25, 2012.

Champagnac, J-D., Molnar, P., Anderson, R. S., Sue, S., and Delacou, B.: Quaternary erosion-induced isostatic rebound in the western Alps, Geology, 35, 195–197, 2007.

Choi, K. H., Seong, Y. B., Jung, P. M., and Lee, S. Y.: Using cosmogenic ^{10}Be dating to unravel the antiquity of a rocky shore platform on the West Coast of Korea, J. Coast. Res., 28, 641–657, 2012.

Christl, M., Vockenhuber, C., Kubik, P. W., Wacker, L., Lachner, J., Alfimov, V., and Synal, H. A.: The ETH Zurich AMS facilities: performance parameters and reference materials, Nucl. Instrum. Meth. B, 294, 29–38, 2013.

Claude, A., Ivy-Ochs, S., Kober, F., Antognini, M., Salcher, B., and Kubik, P. W.: The Chironico landslide (Valle Leventina, southern Swiss Alps); age and evolution, Swiss J. Geosci., 107, 273–291, 2014.

Cohen, D., Gillet-Chaulet, F., Haeberli, W., Machguth, H., and Fischer, U. H.: Numerical reconstructions of the flow and basal conditions of the Rhine glacier, European Central Alps, at the Last Glacial Maximum, The Cryosphere, 12, 2515–2544, https://doi.org/10.5194/tc-12-2515-2018, 2018.

Colman, S. M.: Rock-Weathering Rates as Functions of Time, Quaternary Res., 15, 250–264, 1980.

Cossart, E., Fort, M., Bourlés, D., Braucher, R., Perrier, R., and Siame, L.: Deglaciation pattern during the Lateglacial/Holocene transition in the southern French Alps, Chronological data and geographical reconstruction from the Clarée Valley (upper Durance catchment, southeastern France), Palaeogeogr. Palaeocl., 315–316, 109–123, 2012.

Coutard, J. P. and Francou, B.: Rock temperature measurements in two alpine environments: implications for frost shattering, Arct. Alp. Res., 21, 399–416, 1989.

Coutterand, S. and Buoncristiani, J.-F.: Paléogéographie du dernier maximum glaciaire du Pléistocène récent de la région du massif du Mont Blanc, France, Quaternaire, Revue de l'Association française pour l'étude du Quaternaire, 17, 35–43, 2006.

Coutterand, S.: Etude géomorphologique des flux glaciaires dans les Alpes nord-occidentales au Pléistocène récent: du maximum de la dernière glaciation aux premières étapes de la déglaciation, PhD thesis, Université de Savoie, 2010.

Dansgaard, W., Johnsen, S. J., Clausen, H. B., Dahl-Jensen, D., Gundestrup, N. S., Hammer, C. U., Hvidberg, C. S., Steffensen, J. P., Sveinbjornsdottir, A. E., Jouzel, J., and Bond, G.: Evidence for general instability of past climate from a 250-kyr ice-core record, Nature, 364, 218–220, 1993.

Deline, P., Gardent, M., Magnin, F., and Ravanel, L.: The morphodynamics of the Mont Blanc massif in a changing cryosphere: a comprehensive review, Geogr. Ann. A, 94, 265–283, 2012.

Denton, G. H. and Karlçen, W.: Holocene climatic variations: their pattern and possible cause, Quaternary Res., 3, 155–205, 1973.

Dielforder, A. and Hetzel, R.: The deglaciation history of the Simplon region (southern Swiss Alps) constrained by ^{10}Be exposure dating of ice-molded bedrock surfaces, Quaternary Sci. Rev., 84, 26–38, 2014.

Dixon, J. C. and Thorn, C. E.: Chemical weathering and landscape development in midlatitude alpine environments, Geomorphology, 67, 127–145, 2005.

Dobmeier, C.: Variscan P-T deformation paths from the southwestern Aiguilles Rouges massif (External massif, western Alps) and their implication for its tectonic evolution, Geol. Rundsch., 87, 107–123, 1998.

Duffy, S., Bryan, P., Graeme, E., Beale, G., Pagi, H., and Kotoula, E.: Multi-light Imaging Techniques for heritage application: PTM Guidelines, English Heritage, UK, 2013.

Duller, G. A. T.: Luminescence Analyst, University of Wales, Aberystwyth, 2005.

Duller, G. A. T.: Single-grain optical dating of Quaternary sediments: why aliquot size matters in luminescence dating, Boreas, 37, 589–612, 2008.

Dunne, J., Elmore, D., and Muzikar, P.: Scaling factors for the rates of production of cosmogenic nuclides for geometric shielding and attenuation at depth on sloped surfaces, Geomorphology, 27, 3–11, 1999.

Durcan, J. A., King, G. E., and Duller, G. A. T.: DRAC: Dose Rate and Age Calculator for trapped charge dating, Quat. Geochronol., 28, 54–61, 2015.

Egholm, D., Nielsen, S., Pedersen, V. K., and Lesemann, J.-E.: Glacial effects limiting mountain height, Nature, 460, 884–887, 2009.

Ehlers, J. and Gibbard, P. L.: The extent and chronology of Cenozoic Gobal Glaciation, Quatern. Int., 164–165, 6–20, 2007.

Emiliani, C: Pleistocene Temperatures, J. Geol., 63, 538–578, 1955.

EPICA community members: Eight glacial cycles from an Antarctic ice core, Nature, 429, 623–628, 2004.

Fabel, D., Ballantyne, C. K., and Xu, S.: Trimlines, blockfields, mountain-top erratics and the vertical dimensions of the last British-Irish Ice Sheet in NW Scotland, Quaternary Sci. Rev., 55, 91–102, 2012.

Fischer, M., Huss, M., and Hoelzle, M.: Surface elevation and mass changes of all Swiss glaciers 1980–2010, The Cryosphere, 9, 525–540, https://doi.org/10.5194/tc-9-525-2015, 2015.

Florineth, D.: Surface geometry of the Last Glacial Maximum (LGM) in the southeastern Swiss Alps (Graubünden) and its paleoclimatological significance, E&G Quaternary Sci. J., 48, 23–37, https://doi.org/10.3285/eg.48.1.03, 1998.

Florineth, D., and Schluchter, C.: Alpine evidence for atmospheric circulation patterns in Europe during the Last Glacial Maximum, Quaternary Res., 54, 295–308, 2000.

Fontana, A., Monegato, G., Zavagno, E., Devoto, S., Burla, I., and Cucchi, F.: Evolution of an alpine fluvioglacial system at the LGM decay: the cormor megafan (NE Italy), Geomorphology, 204, 136–153, 2014.

Freiesleben, T., Sohbati, R., Murray, A., Jain, M., Al Khasawneh, S., Hvidt, S., and Jakobsen, B.: Mathematical model quantifies multiple daylight exposure and burial events for rock surfaces using luminescence dating, Radiat. Meas., 81, 16–22, 2015.

Fuchs, M. and Owen, L. A.: Luminescence dating of glacial and associated sediments: review, recommendations and future directions, Boreas, 37, 636–659, 2008.

Gallach, X., Ravanel, L., Egli, M., Brandova, D., Schaepman, M., Christl, M., Gruber, S., Deline, P., Carcaillet, J., and Pallandre, F.: Timing of rockfalls in the Mont Blanc massif (Western Alps): evidence from surface exposure dating with cosmogenic ^{10}Be, Landslides, 15, 1–10, 2018.

Ganti, V., von Hagke, C., Scherler, D., Lamb, M. P., Fischer, W. W., and Avouac, J. P.: Time scale bias in erosion rates of glaciated landscapes, Sci. Adv., 2, e1600204, https://doi.org/10.1126/sciadv.1600204, 2016.

Gardent, M., Rabatel, A., Dedieu, J.-P., and Deline, P.: Multitemporal glacier inventory of the French Alps from the late 1960s to the late 2000s, Global Planet. Change, 120, 24–37, 2014.

Gianotti, F., Forno, M. G., Ivy-Ochs, S., and Kubik, P.: New chronological and stratigaphical data on the Ivrea amphitheatre (Piedmont, NW Italy), Quatern. Int., 190, 123–135, 2008.

Gianotti, F., Forno, M. G., Ivy-Ochs, S., Monegato, G., Pini, R., and Ravazzi, C.: Stratigraphy of the Ivrea Morainic Amphitheatre (NW Italy): an updated Synthesis, Alpine and Mediterranean Quaternary, 28, 29–58, 2015.

Giguet-Covex, C., Pansu, J., Arnaud, F., Rey, P.-J., Griggo, C., Gielly, L., Domaizon, I., Coissac, E., David, F., Choler, P., Poulenard, J., and Taberlet, P.: Long livestock farming history and human landscape shaping revealed by lake sediment DNA, Nat. Commun., 5, 3211, https://doi.org/10.1038/ncomms4211, 2014.

Gliganic, L. A., Meyer, M. C., Sohbati, R., and Jain, M.: OSL Surface Exposure Dating of a Lithic Quarry in Tibet: Laboratory Validation and Application, Quat. Geochronol Special Issue related to the LED Cape Town, 2018.

Goehring, B. M., Schaefer, J. M., Schluechter, C., Lifton, N. A., Finkel, R. C., Jull, A. T., Akçar, N., and Alley, R. B.: The Rhone Glacier was smaller than today for most of the Holocene, Geology, 39, 679–682, 2011.

Goehring, B. M., Vacco, D. A., Alley, R. B., and Schaefer, J. M.: Holocene dynamics of the Rhone Glacier, Switzerland, deduced from ice flow models and cosmogenic nuclides, Earth Planet. Sc. Lett., 351, 27–35, 2012.

Goss, J. C. and Phillips, F. M.: Terrestrial in situ cosmogenic nuclides: theory and application, Quaternary Sci. Rev., 20, 1475–1560, 2000.

Grab, S.: Rock-surface temperatures of basalt in the Drakensberg alpine environment, Lesotho. Geogr. Ann. Ser. A Phys. Geogr., 89, 185–193, 2007.

Gruber, S., Hoelzle, M., and Haeberli, W.: Rock-wall temperatures in the Alps: modelling their topographic distribution and regional differences, Permafrost Periglac., 15, 299–307, 2004a.

Guralnik, B., Jain, M., Herman, F., Ankjærgaard, C., Murray, A. S., Valla, P. G., Preusser, F., King, G. E., Chen, R., and Lowick, S. E.: OSL-thermochronometry of feldspar from the KTB borehole, Germany, Earth Planet. sSc. Lett., 423, 232–243, 2015.

Haas, J. N., Richoz, I., Tinner, W., and Wick, L.: Synchronous Holocene oscillations recorded on the Swiss Plateau and at timberline in the Alps, Holocene, 8, 301–309, 1998.

Habermann, J., Schilles, T., Kalchgruber, R., and Wagner, G. A.: Steps towards surface dating using luminescence, Radiat. Meas., 32, 847–851, 2000.

Haeberli, W., and Alean J.: Temperature and accumulation of high altitude firn in the Alps, Ann. Glaciol., 6, 161–163, 1985.

Haeberli, W. and Funk, M.: Borehole temperatures at the Colle Gnifetti core-drilling site (Monte Rosa, Swiss Alps), J. Glaciol., 37, 37–46, 1991.

Hajdas, I.: Radiocarbon dating and its applications in Quaternary studies, Quaternary. Sci. J., 57, 24, 2008.

Hales, T. C. and Roering, J. J.: Climatic controls on frost cracking and implications for the evolution of bedrock landscapes, J. Geophys. Res., 112, F02033, https://doi.org/10.1029/2006JF000616, 2007.

Hallet, B., Walder, J., and Stubbs, C. W.: Weathering by segregation ice growth in microcracks at sustained sub-zero temperatures: verification from an experimental study using acoustic emissions, Permafrost Periglac., 2, 283–300, 1991.

Hall, K., Thorn, C., and Sumner, P.: On the persistence of "weathering", Geomorphology, 149–150, 1–10, 2012.

Hantke, R.: Eiszeitalter: Kalt-/Warmzeit-Zyklen und Eistransport im alpinen und voralpinen Raum, Ott, Bern, 2011.

Häuselmann, P.: Surface corrosion of an alpine karren field: recent-measurements at Innerbergli (Siebenhengste, Switzerland), Int. J. Speleol., 37, 107–111, 2008.

Hays, J. D., Imbrie, J., and Shackleton, N. J.: Variations in the Earth's Orbit: Pacemaker of the Ice Ages, Science, 194, 1121–1132, 1976.

Heiri, O., Lotter, A. F., Hausmann, S., and Kienast, F.: A chironomid-based Holocene summer air temperature reconstruction from the Swiss Alps, Holocene, 13, 477–484, 2003.

Heiri, O., Koinig, K. A., Spotl, C., Barrett, S., Brauer, A., Drescher-Schneider, R., Gaar, D., Ivy-Ochs, S., Kerschner, H., Luetscher, M., Moran, A., Nicolussi, K., Preusser, F., Schmidt, R., Schoeneich, P., Schworer, C., Sprafke, T., Terhorst, B., and Tinner, W.: Palaeoclimate records 60-8 ka in the Austrian and Swiss Alps and their forelands, Quaternary Sci. Rev., 106, 186–205, 2014.

Herbert, T. D., Lawrence, K. T., Tzanova, A., Peterson, L. C., Caballero-Gill, R., and Kelly, C. S.: Late Miocene global cooling and the rise of modern ecosystems, Nat. Geosci., 9, 843–847, 2016.

Herman, F., Seward, D., Valla, P. G., Carter, A., Kohn, B., Willett, S. D., and Ehlers, T. A.: Worldwide acceleration of mountain erosion under a cooling climate, Nature, 504, 423–426, 2013.

Herman, F., Beyssac, O., Brughelli, M., Lane, S. T., Leprince, S., Adatte, T., Lin, J. Y. Y., Avouac, J.-P., and Cox, S. C.: Erosion by an Alpine glacier, Science, 350, 193–195, 2015.

Herman, F. and Champagnac, J.-D.: Plio-Pleistocene increase in erosion rates in mountain belts in response to climate change, Terra Nova, 28, 2–10, 2016.

Hippe, K.: Constraining processes of landscape change with combined in situ cosmogenic ^{14}C-^{10}Be analysis, Quaternary Sci. Rev., 173, 1–19, 2017.

Hippe, K., Ivy-Ochs, S., Kober, F., Zasadni, J., Wieler, R., Wacker, L., Kubik, P. W., and Schlüchter, C.: Chronology of Lateglacial ice flow reorganization and deglaciation in the Gotthard Pass area, Central Swiss Alps, based on cosmogenic ^{10}Be and in situ ^{14}C, Quat. Geochronol., 19, 14–26, 2014.

Hoelzle, M., Haeberli, W., Dischl, M., Peschke, W.: Secular glacier mass balances derived from cumulative glacier length changes, Global Planet. Change, 36, 77–89, 2003.

Hoke, G. D. and Turcotte, D. L.: The weathering of stones due to dissolution, Environ. Geol., 46, 305–310, 2002

Holzhauser, H., Magny, M., and Zumbühl, H. J.: Glacier and lake-level variations in west-central Europe over the last 3500 years, Holocene, 15, 789–801, 2005.

Huntley, D. J., Godfrey-Smith, D. I., and Thewalt, M. L.: Optical dating of sediments, Nature, 313, 105–107, 1985.

Ilyashuk, E. A., Koinig, K. A., Heiri, O., Ilyashuk, B. P., and Psenner, R.: Holocene temperature variations at a high-altitude site in the Eastern Alps: a chironomid record from Schwarzsee ob Solden, Austria, Quaternary Sci. Rev., 30, 176–191, 2011.

Ivy-Ochs, S.: The Dating of Rock Surfaces Using in Situ Produced ^{10}Be, ^{26}Al and ^{36}Cl, with Examples from Antarctica and the Swiss Alps (PhD thesis), ETH, Zurich, 1996.

Ivy-Ochs, S., Schaefer, J., Kubik, P., Synal, H. A., and Schlüchter, C.: Timing of deglaciation on the northern Alpine foreland (Switzerland), Eclogae Geol. Helv., 97, 47–55, 2004.

Ivy-Ochs, S., Kerschner, H., Reuther, A., Maisch, M., Sailer, R., Schaefer, J., Kubik, P. W., Synal, H.-A., and Schluchter, C.: The timing of glacier advances in the northern European Alps based on surface exposure dating with cosmogenic ^{10}Be, ^{26}Al, ^{36}Cl, and ^{21}Ne, Geol. S. Am. S., 415, 43–60, 2006.

Ivy-Ochs, S., Kerschner, H., Maisch, M., Christl, M., Kubik, P. W., and Schluchter, C.: Latest Pleistocene and Holocene glacier variations in the European Alps, Quaternary Sci. Rev., 28, 2137–2149, 2009.

Ivy-Ochs, S. and Briner, J. P.: Dating disappearing ice with cosmogenic nuclides, Elements, 10, 351–356, 2014.

Ivy-Ochs, S.: Glacier variations in the European Alps at the end of the last glaciation, Cuadernos de investigación geográfica, 41, 295–315, 2015.

Jenkins, G. T. H., Duller, G. A. T., Roberts, H. M., Chiverrell, R. C., and Glasser, N. F.: A new approach for luminescence dating glaciofluvial deposits – high precision optical dating of cobbles, Quaternary Sci. Rev., 192, 263–273, 2018.

Joerin, U., Stocker, T. F., and Schlüchter, C.: Multicentury glacier fluctuations in the Swiss Alps, Holocene, 16, 697–704, 2006.

Jouzel, J., Masson-Delmotte, V., Cattani, O., Dreyfus, G., Falourd, S., Hoffmann, G., Minster, B., Nouet, J., Barnola, J. M., Chappellaz, J., Fischer, H., Gallet, J. C., Johnsen, S., Leuenberger, M., Loulergue, L., Luethi, D., Oerter, H., Parrenin, F., Raisbeck, G., Raynaud, D., Schilt, A., Schwander, J., Selmo, E., Souchez, R., Spahni, R., Stauffer, B., Steffensen, J. P., Stenni, B., Stocker, T. F., Tison, J. L., Werner, M., and Wolff, E. W.: Orbital and Millennial Antarctic Climate Variability over the Past 800,000 Years, Science, 317, 793–796, 2007.

Kars, R. H., Reimann, T., and Wallinga, J.: Are feldspar SAR protocols appropriate for post-IR IRSL dating?, Quat. Geochronol., 22, 126–136, 2014.

Kellerer-Pirklbauer, A.: Potential weathering by freeze-thaw action in alpine rocks in the European Alps during a nine year monitoring period, Geomorphology, 296, 113–131, 2017.

Kelly, M. A., Buoncristiani, J.-F., and Schlüchter, C.: A reconstruction of the last glacial maximum (LGM) ice surface geometry in the western Swiss Alps and contiguous Alpine regions in Italy and France, Eclogae Geol. Helv., 97, 57–75, 2004.

King, G., Herman, F., Lambert, R., Valla, P., and Guralnik, B.: Multi-OSL-thermochronometry of feldspar, Quat. Geochronol., 33, 76–87, 2016.

King, G. E., Valla, P. G., and Lehmann, B.: OSL Rock Surface and Rock Surface-Exposure Dating, Invited contribution to "Handbook of Luminescence Dating", edited by: Bateman, M. and Bailiff, I., 2018.

Kirkbride, M. P. and Bell, C. M.: Edge-roundness of boulders of Torridonian Sandstone (northwest Scotland): applications for relative dating and implications for warm and cold climate weathering rates, Boreas, 39, 187–198, 2010.

Klasen, N., Fiebig, M., Preusser, F., Reitner, J. M., and Radtke, U.: Luminescence dating of proglacial sediments from the Eastern Alps, Quat. Int., 164, 21–32, 2007.

Kleman, J.: Preservation of landforms under ice sheets and ice caps, Geomorphology, 9, 19–32, 1994.

Kleman, J. and Borgstrom, I.: Glacial land forms indicative of a partly frozen bed, J. Glaciol., 40, 255–264, 2006.

Kleman, J., Hattestrand, C., Stroeven, A. P., Jansson, K. N., De Angelis, H., and Borgstrom, I.: Reconstruction of Palaeo- Ice Sheets – Inversion of their Glacial Geomorphological Record, in: Glacier Science and Environmental Change, edited by: Knight, P. G., Blackwell, Malden, MA, 2006.

Kleman, J., Jansson, K., De Angelis, H., Stroeven, A., Hattestrand, C., Alm, G., and Glasser, N.: North American ice sheet build-up

during the last glacial cycle, 115-21 kyr, Quaternary Sci. Rev., 29, 2036–2051, 2010.

Kohl, C. P. and Nishiizumi, K.: Chemical isolation of quartz for measurement of in-situ-produced cosmogenic nuclides, Geochim. Cosmochim. Ac., 56, 3583–3587, 1992.

Koppes, M. and Montgomery, D.: The relative efficacy of fluvial and glacial erosion over modern to orogenic timescales, Nat. Geosci., 2, 644–647, 2009.

Kuhlemann, J., Rohling, E. J., Krumrei, I., Kubik, P., Ivy-Ochs, S., and Kucera, M.: Regional synthesis of Mediterranean atmospheric circulation during the Last Glacial Maximum, Science, 321, 1338–1340, 2008.

Laj, C., Kissel, C., and Beer, J.: High resolution global Paleointensity Stack since 75 kyr (GLOPIS-75) calibrated to Absolute values, Timescales Paleomagnetic Field, Geoph. Monog. Series, 145, 255–265, 2004.

Lal, D. and Peters, B.: Cosmic ray produced radioactivity on the Earth, in Handbuch der Physick, Springer, Berlin, XLVI, 551–612, 1967.

Lal, D.: Cosmic ray labeling of erosion surfaces: in situ nuclide production rates and erosion models, Earth Planet. Sc. Lett., 104, 424–439, 1991.

Lang, A. and Honscheidt, S.: Age and source of colluvial sediments at Vaihingen-Enz, Germany, Catena, 38, 89–107, 1999.

Lasaga, A. C., Soler, J. M., Ganor, J., Burch, T. E., and Nagy, K. L.: Chemical weathering rate laws and global geochemical cycles, Geochim. Cosmochim. Ac., 58, 2361–2386, 1994.

Laskaris, N. and Liritzis, I.: A new mathematical approximation of sunlight attenuation in rocks for surface luminescence dating, J. Lumin., 131, 1874–1884, 2011.

Le Roy, M., Nicolussi, K., Deline, P., Astrade, L., Edouard, J.-L., Miramont, C., and Arnaud, F.: Calendar-dated glacier variations in the western European Alps during the Neoglacial: the Mer de Glace record, Mont Blanc massif, Quaternary Sci. Rev., 108, 1–22, 2015.

Lean, J.: Solar Ultraviolet Irradiance Variations: A review, J. Geophys. Res., 92, 839–968, 1987.

Lehmann, B., Valla, P. G., King, G. E., and Herman, F.: Investigation of OSL surface exposure dating to reconstruct post-LIA glacier fluctuations in the French Alps (Mer de Glace, Mont Blanc massif), Quat. Geochronol., 44, 63–74, 2018.

Leloup, P. H., Arnaud, N., Sobel, E. R., and Lacassin, R.: Alpine thermal and structural evolution of the highest external crystalline massif: The Mont Blanc, Tectonics, 24, TC4002, https://doi.org/10.1029/2004TC001676, 2005.

Lifton, N. A., Sato, T., and Dunai, T. J.: Scaling in situ cosmogenic nuclide production rates using analytical approximations to atmospheric cosmic-ray fluxes, Earth Planet. Sc. Lett., 386, 149–160, 2014.

Liritzis, I.: A new dating method by thermoluminescence of carved megalithic stone building, Comptes rendus de l'Académie des sciences, Série 2, Sciences de la terre et des planètes, 319, 603–610, 1994.

Liritzis, I.: Surface dating by luminescence: an overview, Geochronometria, 38, 292–302, 2011.

Lisiecki, L. E. and Raymo, M. E., A Pliocene-Pleistocene stack of 57 globally distributed benthic $d^{18}O$ records, Paleoceanography, 20, PA1003, https://doi.org/10.1029/2004PA001071, 2005.

Lisiecki, L. E. and Raymo, M. E.: Plio-Pleistocene climate evolution: trends and transitions in glacial cycle dynamics, Quaternary Sci. Rev., 26, 56–69, 2007.

Lister, G. S.: A 15,000-year isotopic record from Lake Zürich of deglaciation and climatic change in Switzerland, Quaternary Res., 29, 129–141, 1988.

Liu, T. and Broecker, W. S.: Holocene rock varnish microstratigraphy and its chronometric application in the drylands of western USA, Geomorphology, 84, 1–21, 2007.

Łoziński, M. W.: uber die mechanische Verwitterung der Sandsteine im gemassibten Klima. Académie des sciences de cracovie, Bulletin internationale, classe de science, mathématiques et naturelles 1: 1–25, 1909. (English translation by Mrozek Teresa: On the mechanical weathering of sandstones in temperate climates, In Cold Climate Landforms, Evans DJA , Wiley, Chichester, 119–134, 1992).

Luetscher, M., Boch, R., Sodemann, H., Spotl, C., Cheng, H., Edwards, R. L., Frisia, S., and Muller, W.: North Atlantic storm track changes during the Last Glacial Maximum recorded by Alpine speleothems, Nat. Commun., 6, 6344, https://doi.org/10.1038/ncomms7344, 2015.

Luthi, M. and Funk, M.: Modelling heat flow in a cold, high-altitude glacier: Interpretation of measurements from Colle Gnifetti, Swiss Alps, J. Glaciol., 47, 314–324, 2001.

Martin, L. C. P., Blard, P.-H., Balco, G., Lave J., Delunel, R., Lifton, N., and Laurent V.: The CREp program and the ICE-D production rate calibration database: A fully parameterizable and updated online tool to compute cosmicray exposure ages, Quat. Geochronol., 38, 25–49, 2017.

Matsuoka, N.: The rate of bedrock weathering by frost action: field measurements and a predictive model, Earth Surf. Process. Landf., 15, 73–90, 1990.

Matsuoka, N. and Murton, J.: Frost weathering: recent advances and future directions, Permafrost Periglac., 19, 195–210, 2008.

Meyer, M. C., Gliganic, L. A., Jain, M., and Sohbati, R.: Lithological controls on light penetration into rock surfaces – implications for OSL and IRSL surface exposure dating, LED proceedings, Radiat. Meas., 120, 298–304, 2018.

Millet, L., Arnaud, F., Heiri, O., Magny, M., Verneaux, V., and Desmet, M.: Late-Holocene summer temperature reconstruction from chironomid assemblages of Lake Anterne, northern French Alps, Holocene, 19, 317–328, 2009.

Miller, K. G., Fairbanks, R. G., and Mountain, G. S.: Tertiary oxygen isotope synthesis, sea level history, and continental margin erosion, Paleoceanography, 2, 1–19, 1987.

Mitchell, S. G. and Montgomery, D. R.: Influence of a glacial buzzsaw on the height and morphology of the Cascade Range in central Washington State, USA, Quaternary Res., 65, 96–107, 2006.

Molnar, P. and England, P.: Late Cenozoic uplift of mountain ranges and global climate change: Chicken or egg?, Nature, 346, 29–34, 1990.

Monegato, G., Ravazzi, C., Donegana, M., Pini, R., Calderoni, G., and Wick, L.: Evidence of a two-fold glacial advance during the last glacial maximum in the Tagliamento end moraine system (eastern Alps), Quaternary Res., 68, 284–302, 2007.

Montgomery, D. R.: Valley formation by fluvial and glacial erosion, Geology, 30, 1047–1050, 2002.

Moses, C., Robinson, D., and Barlow, J.: Methods for measuring rock surface weathering and erosion: A critical review, Earth-Sci. Rev., 135, 141–161, 2014.

Murray, A. S. and Roberts, R. G.: Measurement of the equivalent dose in quartz using a regenerative-dose single-aliquot protocol, Radiat. Meas., 29, 503–515, 1998.

Murray, A. S. and Wintle, A. G.: Luminescence dating of quartz using an improved single-aliquot regenerative-dose protocol, Radiat. Meas., 32, 57–73, 2000.

Nicholson, D. T.: Rock control on microweathering of bedrock surfaces in a periglacial environment, Geomorphology, 101, 655–665, 2008.

Nicolussi, K. and Schlüchter, C.: The 8.2 ka event e calendar dated glacier response in the Alps, Geology, 40, 819–822, 2012.

Nicolussi, K., Kaufmann, M., Patzelt, G., van der Plicht, J., and Thurner, A.: Holocene tree-line variability in the Kauner Valley, Central Eastern Alps, indicated by dendrochronological analysis of living trees and subfossil logs, Veg. Hist. Archaeobot., 14, 221–234, 2005.

Nishiizumi, K., Imamura, M., Caffee, M. W., Southon, J. R., Finkel, R. C., and McAninch, J.: Absolute calibration of ^{10}Be AMS standards, Nucl. Instrum. Meth. B, 258, 403–413, 2007.

Noetzli, J., Gruber, S., Kohl, T., Salzmann, N., and Haeberli,W.: Three-dimensional distribution and evolution of permafrost temperatures in idealized high-mountain topography, J. Geophys. Res.-Earth, 112, F02S13, https://doi.org/10.1029/2006JF000545, 2007.

Nussbaumer, S., Zumbuhl, H. J., and Steiner, D.: Fluctuations of the Mer de glace (Mont Blanc area, France) AD 1500-2050, An interdisciplinary approach using new historical data and neural network simulations, Zeitschrift fur Gletscherkunde und Glazialgeologie ZGG, 5–175, 2007.

Ou, X. J., Roberts, H. M., Duller, G. A. T., Gunn, M. D., and Perkins, W. T.: Attenuation of light in different rock types and implications for rock surface luminescence dating, Radiat. Meas., 120, 305–311, 2018.

Pavon-Carrasco, F. J., Osete, M. L., Torta, J. M., and De Santis, A.: A geomagnetic field model for the Holocene based on archaeomagnetic and lava flow data, Earth Planet. Sc. Lett., 388, 98–109, 2014.

Peizhen, Z., Molnar, P., and Downs, W. R.: Increased sedimentation rates and grain sizes 2-4 Myr ago due to the influence of climate change on erosion rates, Nature, 410, 891–897, 2001.

Penck, A. and Brückner, E.: Die Alpen im Eiszeitalter, Tauchitz, Leipzig, 1901/1909.

Penck, A.: Glacial features in the surface of the Alps, J. Geol., 13, 1–19, 1905.

Polikreti, K., Michael, C., and Maniatis, Y.: Authenticating marble sculpture with thermoluminescence, Ancient TL, 20, 11–18, 2002.

Polikreti, K., Michael, C., and Maniatis, Y.: Thermoluminescence characteristics of marble and dating of freshly excavated marble objects, Radiat. Meas., 37, 87–94, 2003.

Portenga, E. W. and Bierman, P. R.: Understanding earth's eroding surface with ^{10}Be, GSA Today 21, 4–10, 2011.

Preusser, F.: Towards a chronology of the Late Pleistocene in the northern Alpine Foreland, Boreas, 33, 195–210, 2004.

Preusser, F., Graf, H. R., Keller, O., Krayss, E., and Schlüchter, C.: Quaternary glaciation history of northern Switzerland, Quaternary Sci. J., 60, 282–305, 2011.

Rabatel, A., Letréguilly, A., Dedieu, J.-P., and Eckert, N.: Changes in glacier equilibrium-line altitude in the western Alps from 1984 to 2010: evaluation by remote sensing and modeling of the morpho-topographic and climate controls, The Cryosphere, 7, 1455–1471, https://doi.org/10.5194/tc-7-1455-2013, 2013.

Rabatel, A., Dedieu, J. P., and Vincent, C.: Spatio-temporal changes in glacier-wide mass balance quantified by optical remote sensing on 30 glaciers in the French Alps for the period 1983-2014, J. Glaciol., 62, 1153–1166, 2016.

Rades, E. F., Sohbati, R., Luthgens, C., Jain, M., and Murray, A. S.: First luminescence-depth profiles from boulders from moraine deposits: Insights into glaciation chronology and transport dynamics in Malta valley, Austria, Radiat. Meas., 120, 281–289, 2018.

Raup, B., Racoviteanu A., Khalsa S. J. S., Helm C., Armstrong R., and Arnaud Y.: The GLIMS geospatial glacier database: a new tool for studying glacier change, Global Planet. Change, 56, 101–110, 2007a.

Ravazzi, C., Badino, F., Marsetti, D., Patera, G., and Reimer, P. J.: Glacial to paraglacial history and forest recovery in the Oglio glacier system (Italian Alps) between 26 and 15 ka cal BP, Quaternary Sci. Rev., 58, 146–161, 2012.

Raymo, M. E. and Ruddiman, W. F.: Tectonic forcing of late Cenozoic climate, Nature, 359, 117–122, 1992.

Reber, R., Akcar, N., Ivy-Ochs, S., Tikhomirov, D., Burkhalter, R., Zahno, C., Lüthold A., Kubik, P. W., Vockenhuber, C., and Schluchter, C.: Timing of retreat of the Reuss glacier (Switzerland) at the end of the last glacial maximum, Swiss, J. Geosci., 1–15, 2014.

Regard, V., Dewez, T., Bourlès, D. L., Anderson, R. S., Duperret, A., Costa, S., Leanni, L., Lasseur, E., Pedoja, K., and Maillet, G. M.: Late Holocene seacliff retreat recorded by ^{10}Be profiles across a coastal platform: theory and example from the English Channel, Quat. Geochronol., 11, 87–97, 2012.

Reitner, J.: Glacial dynamics at the beginning of Termination I in the Eastern Alps and their stratigraphic implications, Quatern. Int. ,164–165, 64–84, 2007.

Rhodes, E. J.: Optically stimulated luminescence dating of sediments over the past 200,000 years, Annu. Rev. Earth Planet. Sci., 39, 461–488, 2011.

Richards, M.P .: Luminescence dating of quartzite from the Diring Yuriakh site, MA Thesis, Simon Fraser University, unpublished, 1994.

Scherler, D.: Climatic limits to headwall retreat in the Khumbu Himalaya, eastern Nepal, Geology, 42, 1019–1022, 2015.

Schimmelpfennig, I., Schaefer, J. M., Akçar, N., Koffman, T., Ivy-Ochs, S., Schwartz, R., Finkel, R. C., Zimmerman, S., and Schluchter, C.: A chronology of Holocene and Little Ice Age glacier culminations of the Steingletscher, Central Alps, Switzerland, based on high-sensitivity beryllium-10 moraine dating, Earth Planet. Sc. Lett., 393, 220–230, 2014.

Schindelwig, I., Akçar, N., Kubik, P., and Schluchter, C.: Lateglacial and early Holocene dynamics of adjacent valley glaciers in the Western Swiss Alps, J. Quaternary Sci., 27, 114–124, 2012.

Schluchter, C.: A non-classical summary of the Quaternary stratigraphy in the northern alpine foreland of Switzerland, Bulletin de la Société Neuchâteloise de Géographie, 32, 143–157, 1988.

Schluchter, C. and Rothlisberger, C.: 100,000 jahre gletschergeschichte, in: Gletscher im standigen Wandel, 47–63, 1995.

Schmidt, R., Roth, M., Tessadri, R., and Weckstrom, K.: Disentangling late- Holocene climate and land use impacts on an Austrian alpine lake using seasonal temperature anomalies, ice-cover, sedimentology, and pollen tracers, J. Paleolimnol., 40, 453–469, 2008.

Schumer, R. and Jerolmack, D. J.: Real and apparent changes in sediment deposition rates through time, J. Geophys. Res., 114, F00A06, https://doi.org/10.1029/2009JF001266, 2009.

Schweingruber, F. H.: Wood structure and Environment, in: Springer Series in Wood Science, Springer, Heidelberg, 279 pp., 2007.

Seguinot, J., Ivy-Ochs, S., Jouvet, G., Huss, M., Funk, M., and Preusser, F.: Modelling last glacial cycle ice dynamics in the Alps, The Cryosphere, 12, 3265–3285, https://doi.org/10.5194/tc-12-3265-2018, 2018.

Shackleton, N. J. and Opdyke, N. D.: Oxygen isotope and palaeomagnetic stratigraphy of Equatorial Pacific core V28-238: Oxygen isotope temperatures and ice volumes on a 105 year and 106 year scale, Quaternary Res., 3, 39–55, 1973.

Siman-Tov, S., Stock, G. M., Brodsky, E. E., and White, J. C.: The coating layer of glacial polish, Geol. Soc. Am., 11, 987–990, 2017.

Simkins, L. M., Simms, A. R., and DeWitt, R.: Relative sea-level history of Marguerite Bay, Antarctic Peninsula derived from optically stimulated luminescence-dated beach cobbles, Quaternary Sci. Rev., 77, 141–155, 2013.

Simms, A. R., DeWitt, R., Kouremenos, P., and Drewry, A. M.: A new approach to reconstructing sea levels in Antarctica using optically stimulated luminescence of cobble surfaces, Quat. Geochronol., 6, 50–60, 2011.

Singarayer, J. S.: Linearly modulated optically stimulated luminescence of sedimentary quartz: Physical mechanisms and implications for dating, D. Phil. thesis, University of Oxford, 345 pp., 2002.

Six, D. and Vincent, C.: Sensitivity of mass balance and equilibrium-line altitude to climate change in the French Alps, J. Glaciol., 60, 867–878, 2014.

Smiraglia, C., Azzoni, R. S., D'Agata, C., Matagno, D., Fugazza D., and Diolaiutu, G. A.: The evolution of the italian glaciers from the previous data base to the new italian inventory, Preliminary considerations and results, Geogr. Fis. Din. Quat., 38, 79–87, 2015.

Sohbati, R., Murray, A., Jain, M., Buylaert, J.-P., and Thomsen, K.: Investigating the resetting of OSL signals in rock surfaces, Geochronometria, 38, 249–258, 2011.

Sohbati, R., Jain, M., and Murray, A.: Surface exposure dating of non-terrestrial bodies using optically stimulated luminescence: A new method, Icarus, 221, 160–166, 2012a.

Sohbati, R., Murray, A. S., Buylaert, J.-P., Almeida, N. A. C., and Cunha, P. P.: Optically stimulated luminescence (OSL) dating of quartzite cobbles from the Tapada do Montinho archaeological site (east-central Portugal), Boreas, 41, 452–462, 2012b.

Sohbati, R., Murray, A. S., Porat, N., Jain, M., and Avner, U.: Age of a prehistoric "Rodedian" cult site constrained by sediment and rock surface luminescence dating techniques, Quat. Geochronol., 30, 90–99, 2015.

Sohbati, R., Liu, J., Jain, M., Murray, A., Egholm, D., Paris, R., and Guralnik, B.: Centennial-to millennial-scale hard rock erosion rates deduced from luminescence-depth profiles, Earth Planet. Sc. Lett., 493, 218–230, 2018.

Stephenson, W. J. and Finlayson, B. L.: Measuring erosion with the microerosion meter—contributions to understanding landform evolution, Earth-Sci. Rev., 95, 53–62, 2009.

Stewart, M., Grosjean, M., Kuglitsch, F. G., Nussbaumer, S. U.,and von Gunten, L.: Reconstructions of Late Holocene paleofloods and glacier length changes in the Upper Engadine, Switzerland (ca. 1450 BC – AD 420), Palaeogeogr. Palaeocl., 311, 215–123, 2011b.

Stone, J. O.: Air pressure and cosmogenic isotope production, J. Geophys. Res., 105759, 753–823, 2000.

Strandberg, G., Brandefelt, J., Kjellstrom, E., and Smith, B.: High resolution regional simulation of last glacial maximum climate in Europe, Tellus A, 63, 107–125, 2001.

Sugden, D. E., Glasser, N., and Clapperton, C. M.: Evolution of large roches moutonnées, Geograska Annaler Series A, Phys. Geogr., 74, 253–264, 1992.

Suter, S., Laternser, M., Haeberli, W., Hoelzle, M., and Frauenfelder, R.: Cold firn and ice of high-altitude glaciers in the Alps: Measurements and distribution modeling, J. Glaciol., 47, 85–96, 2001.

Suter, S.: Cold firn and ice in the Monte Rosa and Mont Blanc areas: Spatial occurrence, surface energy balance and climate evidence, PhD thesis, Versuchsanst. fur Wasserbau, Hydrol. und Glaziol., ETH Zurich, Switzerland, 2002.

Tachiya, M. and Mozumder, A.: Decay of trapped electronics by tunnelling to scavenger molecules in low-temperature glasses, Chem. Phys. Lett., 28, 87–89, 1974.

Theocaris, P., Liritzis, I., and Galloway, R.: Dating of two Hellenic pyramids by a novel application of thermoluminescence, J. Archaeol. Sci., 24, 399–405, 1997.

Tinner, W. and Theurillat, J. P.: Uppermost limit, extent, and fluctuations of the timberline and treeline ecocline in the Swiss Central Alps during the past 11 500 years, Arct. Antarct. Alp. Res., 35, 158–169, 2003.

Turowski, J. M. and Cook, K. L.: Field techniques for measuring bedrock erosion and denudation, Earth Surf. Proc. Land., 42, 109–127, 2017.

Uppala, S. M., Kallberg, P. W., Simmons, A. J., Andrae, U., Bechtold, V. D. C., Fiorino, M., Gibson, J. K., Haseler, J., Hernandez, A., Kelly, G. A., Li, X., Onogi, K., Saarinen, S., Sokka, N., Allan, R. P., Andersson, E., Arpe, K., Balmaseda, M. A., Beljaars, A. C. M., Van De Berg, L., Bidlot, J., Bormann, N., Caires, S., Chevallier, F., Dethof, A., Dragosavac, M., Fisher, M., Fuentes, M., Hagemann, S., Holm, E., Hoskins, B.J., Isaksen, L., Janssen, P. A. E. M., Jenne, R., Mcnally, A. P., Mahfouf, J.-F., Morcrette, J.-J., Rayner, N. A., Saunders, R. W., Simon, P., Sterl, A., Trenberth, K. E., Untch, A., Vasiljevic, D., Viterbo, P., and Woollen, J.: The ERA-40 re-analysis, Q. J. Royal Meteor. Soc., 131, 2961–3012, 2005.

Vafiadou, A., Murray, A., and Liritzis, I.: Optically stimulated luminescence (OSL) dating investigations of rock and underlying soil from three case studies, J. Archaeol. Sci., 34, 1659–1669, 2007.

Valla, P. G., Lowick, S. E., Herman, F., Champagnac, J.-D., Steer, P., and Guralnik, B.: Exploring IRSL50 fading variability in bedrock feldspars and implications for OSL thermochronometry, Quat. Geochronol., 36, 55–66, 2016.

van Husen, D.: Die Ostalpen in den Eiszeiten, Geologische Bundesanstalt, Wien, 1987.

van Husen, D.: LGM and late-glacial fluctuations in the Eastern Alps, Quatern. Int., 38–39, 109–118, 1997.

Vescovi E., Ravazzi C., Arpenti E., Finsinger W., Pini R., Valsecchi V., Wick L., Ammann B., and Tinner W.: Interactions between climate and vegetation during the Lateglacial period as recorded by lake and mire sediment archives in Northern Italy and Southern Switzerland, Quaternary Sci. Rev., 26, 1650–1669, 2007.

Vincent, C., Le Meur E., Six, D., Possenti, P., Lefebvre E., and Funk, M.: Climate warming revealed by englacial temperatures at Col du Dôme (4250 m, Mont Blanc area), Geophys. Res. Lett., 34, L16502, https://doi.org/10.1029/2007GL029933, 2007.

Vincent, C., Harter, M., Gilbert, A., Berthier, E., and Six, D.: Future fluctuations of Mer de Glace, French Alps, assessed using a parameterized model calibrated with past thickness changes, Ann. Glaciol., 55, 15–24, 2014.

Visocekas, R.: Tunneling in afterglow, its coexistence and interweaving with thermally stimulated luminescence, Radiat. Prot. Dosim., 100, 45–54, 2002.

Višnjević, V., Herman, F., and Podladchikov, Y.: Reconstructing spatially variable mass balances from past ice extents by inverse modeling, J. Glaciol., 64, 957–968, 2018.

Vollweiler, N., Scholz, D., Muhlinghaus, C., Mangini, A., and Spotl, C.: A precisely dated climate record for the last 9 kyr from three high alpine stalagmites, Spannagel Cave, Austria, Geophys. Res. Lett., 33, L20703, https://doi.org/10.1029/2006GL027662, 2006.

von Blanckenburg, F. and Willenbring, J. K., Cosmogenic nuclides: Dates and rates of Earth-surface change, Elements, 10, 341–346, 2014.

Wallinga, J., Murray, A., and Wintle, A.: The single-aliquot regenerative-dose (SAR) protocol applied to coarse-grain feldspar, Radiat. Meas., 32, 529–533, 2000.

West, A. J.: Thickness of the chemical weathering zone and implications for erosional and climatic drivers of weathering and for carbon cycle feedbacks, Geology, 40, 811–814, 2012.

Winkler, S.: Lichenometric dating of the "Little Ice Age" maximum in Mt Cook National Park, Southern Alps, New Zealand, Holocene, 12, 911–920, 2004.

Wintle, A. G.: Anomalous fading of thermo-luminescence in mineral samples, Nature, 245, 143–144, 1973.

Wintle, A. G. and Murray, A. S.: A review of quartz optically stimulated luminescence characteristics and their relevance in single-aliquot regeneration dating protocols, Radiat. Meas., 41, 369–391, 2006.

Wirsig, C., Zasadni, J., Ivy-Ochs, S., Christl, M., Kober, F., and Schluchter, C.: A deglaciation model of the Oberhasli, Switzerland, J. Quaternary Sci., 31, 46–59, 2016a.

Wirsig, C., Zasadni, J., Christl, M., Akçar, N., and Ivy-Ochs, S.: Dating the onset of LGM ice surface lowering in the High Alps, Quaternary Sci. Rev., 143, 37–50, 2016b.

Zachos, J. C., Pagani, M., Sloan, L., Thomas, E., and Billups, K.: Trends, rhythms, and aberrations in global climate 65 Ma to present, Science, 292, 686–693, 2001.

Zimmerman, S. G., Evenson, E. B., Gosse, J. C., and Erskine, C. P.: Extensive boulder erosion resulting from a range fire on the type-Pinedale moraines, Fremont Lake, Wyoming, Quaternary Res., 42, 255–265, 1994.

10.3 A high-frequency and high-resolution image time series of the Gornergletscher - Swiss Alps - derived from repeated UAV surveys

Lionel Benoit[1], Aurelie Gourdon[1,2], Raphaal Vallat[1], Inigo Irarrazaval[1], Mathieu Gravey[1], Benjamin Lehmann[1], Gunther Prasicek[1,3], Dominik Graff[4], Frederic Herman[1], Gregoire Mariethoz[1].

[1] Institute of Earth Surface Dynamics, University of Lausanne, Lausanne, 1012, Switzerland. [2] Ecole Normale Supérieure de Lyon, Département des Sciences de la Terre, Lyon, France. [3] Department of Geography and Geology, University of Salzburg, Salzburg, Austria. [4] Laboratory of Hydraulics, Hydrology and Glaciology (VAW), ETH Zurich, Zurich, Switzerland.

Research paper

Earth System Science Data Discussion, https://doi.org/10.5194/essd-2018-145

Author contributions. BL help designing the sampling strategy and to realized the field campaign and participate to improve the manuscript.

Earth Syst. Sci. Data, 11, 579–588, 2019
https://doi.org/10.5194/essd-11-579-2019

Open Access Earth System Science Data

A high-resolution image time series of the Gorner Glacier – Swiss Alps – derived from repeated unmanned aerial vehicle surveys

Lionel Benoit[1], Aurelie Gourdon[1,2], Raphaël Vallat[1], Inigo Irarrazaval[1], Mathieu Gravey[1], Benjamin Lehmann[1], Günther Prasicek[1,3], Dominik Gräff[4], Frederic Herman[1], and Gregoire Mariethoz[1]

[1]Institute of Earth Surface Dynamics (IDYST), University of Lausanne, Lausanne, Switzerland
[2]Ecole Normale Supérieure de Lyon, Département des Sciences de la Terre, Lyon, France
[3]Department of Geography and Geology, University of Salzburg, Salzburg, Austria
[4]Laboratory of Hydraulics, Hydrology and Glaciology (VAW), ETH Zürich, Zürich, Switzerland

Correspondence: Lionel Benoit (lionel.benoit@unil.ch)

Received: 27 November 2018 – Discussion started: 10 December 2018
Revised: 6 April 2019 – Accepted: 17 April 2019 – Published: 30 April 2019

Abstract. Modern drone technology provides an efficient means to monitor the response of alpine glaciers to climate warming. Here we present a new topographic dataset based on images collected during 10 UAV surveys of the Gorner Glacier glacial system (Switzerland) carried out approximately every 2 weeks throughout the summer of 2017. The final products, available at https://doi.org/10.5281/zenodo.2630456 (Benoit et al., 2018), consist of a series of 10 cm resolution orthoimages, digital elevation models of the glacier surface, and maps of ice surface displacement. Used on its own, this dataset allows mapping of the glacier and monitoring surface velocities over the summer at a very high spatial resolution. Coupled with a classification or feature detection algorithm, it enables the extraction of structures such as surface drainage networks, debris, or snow cover. The approach we present can be used in the future to gain insights into ice flow dynamics.

1 Introduction

Glacier ice flows by deformation and sliding in response to gravitational forces. As a glacier moves, internal pressure gradients and stresses create visible surface features such as glacial ogives and crevasses (Cuffey and Paterson, 2010). Furthermore, the surface of glaciers is also shaped by local weather conditions, which are responsible for the snow accumulation and ablation. Related processes generate distinct morphologies such as supraglacial streams, ponds, and lakes.

Glacier surface features evolve continuously, and these changes provide insights into the structure, internal dynamics, and mass balance of the glacier. Important efforts have been made to monitor glacier surfaces, from early stakes measurements at the end of the 19th century (Chen and Funk, 1990) to present-day in situ topographic surveys (Ramirez et al., 2001; Aizen et al., 2006; Dunse et al., 2012; Benoit et al., 2015) and remotely sensed data acquired from diverse platforms: ground-based devices (Gabbud et al., 2015; Piermattei at al., 2015), aircraft (Baltsavias et al., 2001; Mertes et al., 2017), or satellites (Herman et al., 2011; Kääb et al., 2012; Dehecq et al., 2015; Berthier et al., 2014). Recently, the development of unmanned aerial vehicles (UAVs) has enabled glaciologists to carry out their own aerial surveys autonomously, rapidly, and at reasonable costs (Whitehead et al., 2013; Immerzeel et al., 2014; Bhardwaj et al., 2016; Jouvet et al., 2017; Rossini et al., 2018). This technology is particularly attractive to map alpine glaciers whose limited size allows a satisfying coverage at a centimeter to decimeter spatial resolution.

Here we provide a homogenized and high-resolution remote-sensing dataset covering about 10 km^2 of the ablation zone of the Gorner Glacier glacial system (Valais, Switzerland, Fig. 1). The raw images have been acquired by UAV

flights carried out approximately every 2 weeks during the summer of 2017 (from 29 May to 30 October). The dataset comprises 10 consecutive digital elevation models (DEMs) and associated orthomosaics of the area of interest at a 10 cm resolution. It is therefore one of the most exhaustive surveys of the short-term surface evolution of a temperate glacier currently available. Geometrical coherence of the dataset is ensured through the application of comprehensive photogrammetric processing (i.e., images are ortho-rectified and properly scaled). In addition, the orthomosaics are stackable thanks to a co-registration procedure. The dataset can therefore be seen as a high-resolution time lapse of the Gorner Glacier ablation zone, combining spectral (orthomosaics) and geometrical (DEMs) information on the glacier surface. In addition to orthomosaics and DEMs that are snapshots of the area of interest, we also provide a product that we call matching maps (MMs) to achieve temporal monitoring of the glacier. In practice, a MM associates with each pixel of an orthomosaic (respectively a DEM) the corresponding pixel in the next orthomosaic recorded 2 weeks later. MMs can then be used to track the flow of ice over time, and in turn to quantify ice surface displacements.

Potential uses of this dataset are numerous. Single orthomosaics and DEMs can be used to map the surface of the glacier and to extract features of interest such as the surface drainage network (Yang and Smith, 2012; Rippin et al., 2015), debris, or snow cover (Racoviteanu and Williams, 2012). Alternatively, the complete time series of orthomosaics and DEMs can be used for detection and quantification of changes at the surface of the glacier (Barrand et al., 2009; Berthier et al., 2016; Fugazza et al., 2018). Finally, the time lapse coupled with the MMs is an interesting tool to monitor ice surface velocity and deformation (Ryan et al., 2015; Kraaijenbrink et al., 2016), and in turn ice flow dynamics at the glacier surface (Brun et al., 2018). The MMs provide a quantification of the ice velocity at every location on the surface of the glacier, which can be used to calibrate or to validate ice flow models, especially for the Gorner Glacier, which was extensively used as a modeling benchmark (see for instance Werder and Funk, 2009; Riesen et al., 2010; Sugiyama et al., 2010; Werder et al., 2013).

2 Data acquisition

2.1 Study site

The Gorner Glacier is located in the Valais Alps in southern Switzerland (Fig. 1a). It is part of a glacier system involving five tributaries and ranges from 2200 to 4634 m a.s.l. (Fig. 1b). The ablation area, which is the main focus of this study, is a 4 km long and relatively flat ice tongue (slope around 6 %, i.e., 3.4°) that is deeply incised by meltwater channels and partially debris covered (Fig. 1c). This ablation area is preceded by a steeper part (southwest of the Monte Rosa Hut, Fig. 1c) characterized by the presence of numerous crevasses. The entire Gorner Glacier system (i.e., the terminal tongue and its five tributaries) covers an area of almost 50 km^2 and its central flow line is 12 km long, making it one of the largest European glaciers (Sugiyama et al., 2010).

The Gorner Glacier system has been widely studied since the 1970s due to its significant size, its accessibility, and because a glacier-dammed lake threatened the downstream Matter valley with glacier outburst floods (Sugiyama et al., 2010; Werder et al., 2009, 2013). The long history of glaciological studies in this area has shown that the mass balance of the Gorner Glacier system was stable from the 1930s to the early 1980s, and significantly dropped since then (Huss et al., 2012). This can be associated with the rise of its equilibrium line altitude (ELA) due to an increase in the local average yearly temperature. The ELA is at around 3300 m today according to studies carried out at the neighboring Findel Glacier (Sold et al., 2016).

In this context, the current dataset aims at complementing existing studies about the Gorner Glacier system by documenting the behavior of its ablation zone during an entire summer, at a time when this glacial system is thought to be out of equilibrium with a clear trend toward glacial retreat. In particular, this dataset focuses on the monitoring of the glacier surface at high spatial and temporal resolution.

2.2 UAV surveys

The primary data are RGB images acquired by repeated UAV surveys over an area of 10 km^2. A fully autonomous fixed-wing UAV of type eBee from SenseFly, equipped with a 20-megapixel SenseFly S.O.D.A camera, has been used for image acquisition (Vallet et al., 2011). The camera was static within the UAV body (no gimbal) and therefore all pictures are quasi-nadir (i.e., images are taken with an angle $\pm 10°$ from the vertical line). For flight planning and UAV piloting, the eMotion3 software was used.

Raw images were acquired with a ground resolution ranging from 7.3 to 8.8 cm for the glaciated parts of the area of interest. For the requirements of photogrammetric processing, flight plans have been designed to allow for an overlap between images ranging from 70 % to 85 % in the flight direction and from 60 % to 70 % in the cross-flight direction. These specifications have led to flight altitudes ranging from 300 to 600 m above ground. The flight time was limited to about 30 min in field conditions. Thus, the coverage of the full area of interest required four to eight separate flights per session, i.e., each day of acquisition (Table 1). Overall, 10 sessions were conducted in 2017, from 29 May to 30 October. The main features of these flights are summarized in Table 1.

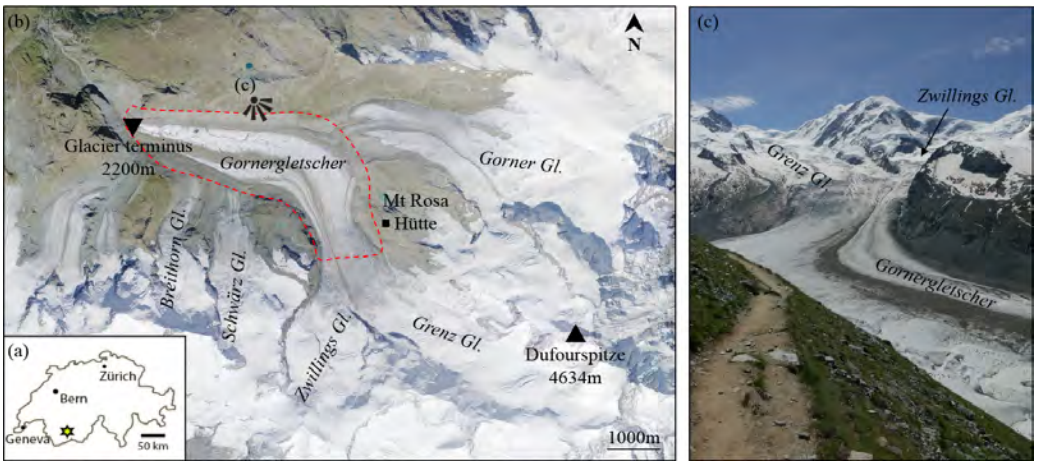

Figure 1. The Gorner Glacier system. **(a)** Situation map. **(b)** Overview of the Gorner Glacier system; dashed red line: area of interest. **(c)** Picture of the glacier tongue.

Table 1. UAV flights carried out for raw glacier image acquisition.

Date	Acquisition time (CET)	No. of flights	No. of pictures
2017/05/29	14:00–16:00	4	749
2017/06/09	12:30–15:30	8	935
2017/06/21	11:30–13:30	7	930
2017/06/27	11:30–14:00	5	1059
2017/07/13	12:30–14:00	4	830
2017/07/26	13:00–16:00	6	1125
2017/08/15	12:30–16:00	7	1121
2017/10/04	12:00–15:30	7	1107
2017/10/18	13:00–15:00	4	846
2017/10/30	13:00–15:30	6	1084

3 Data processing

3.1 Generation of co-registered orthomosaics and DEMs

Pictures have been processed separately for each acquisition date with the photogrammetric software pix4DMapper version 3.1 (Vallet et al., 2011, Fig. 2) using default parameters for nadir flights (see the processing reports for details about these parameters). The output resolution has been set to 10 cm per pixel in order to prescribe a constant resolution across all final products. During the photogrammetric processing, the raw pictures are first oriented by bundle adjustment, and then a DEM and an ortho-rectified image (orthomosaic) are generated for each day of interest. Since the only geolocation information included into the bundle adjustment procedure is the trajectory of the UAV derived from code-only GPS data, the initial geo-referencing of the orthomosaics and DEMs is limited to a few meters.

To improve the coherence of the co-referencing of the different sessions, all products are co-registered to the reference of the 9 June acquisition (Fig. 2). To this end, the coordinates of several stable points of the landscape (16 to 70 among a set of 74; see Table 2 and Fig. 4) are extracted from the bundle adjustment of 9 June, and used as manual tie points for the bundle adjustments of the other dates. These stable points are mostly salient features of the bedrock or erratic boulders on the deglaciated banks of the glacier. The co-registration leads to orthomosaics and DEMs that are stackable. Therefore, in the final products, the bedrock remains stable between consecutive dates, while the glaciated parts move and deform. Consequently, if a time lapse is created from the co-registered products, the glacier appears to flow while the surrounding landscape remains static. Figure 2 summarizes the acquisition and processing chain used to derive the final products of the dataset.

After co-registration, all final products (orthomosaics and DEMs) are in the reference frame of the bundle adjustment of 9 June 2017 (hereafter referred to as master bundle adjustment). This local reference frame is a realization of the WGS84 reference system (with Universal Transverse Mercator (UTM zone 32) projection) using code-only GPS data as input for referencing. The absence of ground control points (GCPs) and the use of consumer-grade GPS observations in the bundle adjustment procedure can result in meter-level geolocation errors and internal deformations of the master bundle adjustment (James and Robson, 2014; Gindraux et al., 2017). While the internal deformations of the local reference frame lead to relative measurement errors of small amplitude (on the order of 1/1000; see Sect. 4.1 for details), the geolocation errors related to the absence of GCPs can impair comparisons with other datasets covering the same geographic area. To improve absolute georeferencing and to link our dataset with the Swiss national reference system, Table 2 provides the parameters of the affine transformation be-

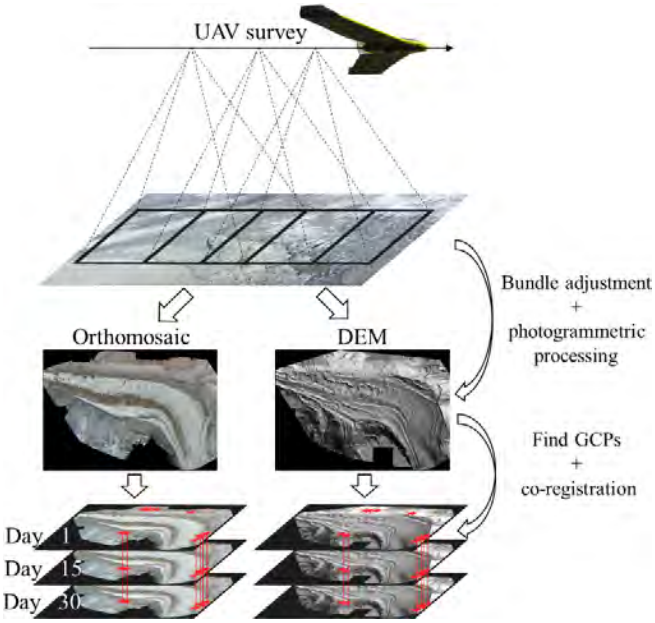

Figure 2. Acquisition and processing chain used to derive the co-registered orthomosaics and DEMs.

Table 2. Parameters of the affine transformation between the Swiss reference system (CH1903 – LV03) and the local reference frame defined by the master bundle adjustment of 9 June 2017. Note that no shear nor reflection is considered. Locations of the manual tie points used to estimate the transformation parameters are shown in Fig. 4.

Translation eastward (m)	Translation northward (m)	Rotation (°)	Scale
321 800.8	−5 009 609.3	1.1357	1.0004

tween the local reference frame of this dataset and the Swiss CH1903 – LV 03 reference system. This transformation has been estimated from 81 manual tie points identified in (1) the orthomosaic derived from the master bundle adjustment and (2) a 50 cm resolution orthomosaic of 2009 processed and georeferenced by the Swiss mapping agency swisstopo.

3.2 Surface displacement tracking: generation of MMs

Consecutive co-registered orthomosaics enable us to quantify horizontal displacements at the surface of the glacier. In the present dataset, this information about ice surface displacements is provided by the MMs (Fig. 3). In practice, a MM is an image that pairs the positions of similar ice patches at times t and $t + \mathrm{d}t$ ($\mathrm{d}t$ being the time span between consecutive acquisitions) (Fig. 2). The footprint of the MM is the overlap of the footprints of the orthomosaics at times t and $t + \mathrm{d}t$. MMs inherit the spatial resolution of the original orthomosaics (i.e., 10 cm) and can therefore be used to directly relate any pixel of a given orthomosaic to its counterpart in the following orthomosaic (and therefore easily navigate within the whole dataset).

The MMs are obtained by image matching of pairs of orthomosaics. The orthomosaic at time t is taken as a reference, and for each pixel of the reference, a 51×51 pixel (5.1 m × 5.1 m) patch is extracted and searched for in the orthomosaic corresponding to the next session (time $t + \mathrm{d}t$). To speed up the processing and avoid wrong matches with very distant patches, the homologous patch at time $t + \mathrm{d}t$ is searched for in a neighborhood with a 200-pixel (20 m) radius centered on the position of the original patch at time t whose size has been established based on prior knowledge about the approximate surface velocity of the Gorner Glacier. The criterion used to evaluate the similarity between both patches is the mean absolute error (MAE) between pixels computed on grayscale images (Liu and Zaccarin, 1993; Chuang et al., 2015). The MAE has been selected as the similarity score because it is fast to compute, especially on large images using convolutions. Its disadvantage is the sensitivity to illumination differences between consecutive orthoimages. However, in practice, no adverse effects have been observed, mostly because the images were acquired roughly at the same time of the day (between 11:30 and 16:00), and because the orthoimages used to generate the MMs are always separated by less than 1 month, which mitigates the illumination differences. The patch of the image $t + \mathrm{d}t$ leading to the lowest MAE with the original patch at time t is then considered the counterpart of the original patch. Finally, the displacements (in pixels) between the two patches along the east–west and the north–south directions are recorded into the MM. This operation is repeated for all possible patches in the reference orthomosaic. The MMs have been calculated using an open-source utility called MatchingMapMaker developed as part of this project, and made available along with the dataset (see Sect. 5.2 for code availability). The MatchingMapMaker tool has been designed to account for the specificities of UAV-based orthoimages, and in particular their very high resolution. To ensure the reliability of this utility, MMs have been benchmarked against horizontal displacement maps calculated using well-established image correlation algorithms, namely IMCORR (Scherler et al., 2008) and CIAS (Heid and Kääb, 2012). The results of this benchmark (see Sect. 5.2) show a very good agreement between horizontal displacement maps derived from MatchingMapMaker, IMCORR, and CIAS.

The raw MMs can be noisy due to the presence of outliers in the pattern matching procedure (speckled areas in the raw displacement maps in Fig. 3). These outliers originate from the dissimilarity between subsequent orthomosaics, due to, for example, changing shadows or changes at the glacier surface (snowfall, snow, or ice melting, etc.). To mitigate the impact of these outliers, we first locate them, then we mask the impacted areas (pink areas in Fig. 3), and finally we interpolate the remaining reliable displacements to fill the gaps generated by the mask. To limit the processing time, a sim-

plistic outlier detection method based on signal processing has been preferred over more sophisticated approaches based on glacier physics (Maksymiuk et al., 2016). Unreliable areas in the raw MMs are assumed to be aggregates of pixels with spatially incoherent displacement values embedded in a matrix of displacements that vary smoothly in space (i.e., the reliable displacements). The borders of unreliable areas are detected as locations with strong spatial displacement gradients, with a detection threshold set to 15 cm of horizontal deformation per day. A mask of reliability is then created by setting the areas with a strong gradient to 0 and the remainder of the mask image to 1. The outlier areas (i.e., small aggregates of unreliable values) are then filtered out by applying the opening operator of mathematical morphology to this mask with a structuring element of the size 50×50 pixels. This operation leads to switch the value of the mask from 1 to 0 for all aggregates of pixels smaller than 50×50 pixels. Hence, we obtain a mask with 1 at locations with reliable displacements and 0 where the measured displacements are considered outliers. Finally, the values of the MM at masked locations are interpolated from the non-masked measurements using a bilinear interpolation. The selected procedure is iterative. At each iteration, it attributes to the masked values the mean of the reliable values in a 500-pixel neighborhood in the east–west and north–south directions. The values that remain masked after 10 iterations are considered to be too far from the informed areas to be filled and are set to -99 to denote no data. Figure 3 summarizes how MMs are derived from pairs of consecutive co-registered orthomosaics and filtered to remove outliers.

Because MMs pair the positions of similar ice patches between consecutive orthomosaics, they can be used to derive maps of the horizontal displacements occurring at the surface of the glacier. To this end, displacements from the masked MMs are converted to meters per day and resampled at a 5 m resolution to remove the dependence between neighboring locations that is introduced during the image matching procedure. Horizontal displacement maps at 5 m resolution are provided in addition to the full-resolution MMs in order to facilitate the use of the present dataset in the context of ice flow studies.

4 Quality assessment

4.1 Bundle adjustment and co-registration

A first validation of this dataset can be performed by checking the relative orientation of the cameras during the bundle adjustment, as well as the co-registration of orthomosaics and DEMs. Processing reports detailing the quality of the bundle adjustment for each session are available along with the dataset (see Sect. 5.1).

Table 2 displays three indices summarizing the quality of both bundle adjustment steps. First, the mean reprojection error (in pixels) quantifies the mismatch in the raw images between the observed and the modeled position of tie points used during the relative orientation step. The sub-pixel level of errors (Table 2, column 2) ensures that the orientations of the camera are reliable. Next, the co-registration step is assessed by the mean root-mean-square error (RMSE) of manual tie point coordinates. This statistic measures the stability of manual tie point coordinates between different bundle adjustments. Under ideal conditions, the value of the mean RMSE on manual tie points should be close to the ground pixel resolution of the raw images (i.e., 7.3 to 8.8 cm) because an operator is able to identify points of interest with a pixel level precision. The slightly higher values obtained in the present case (9 to 21 cm, Table 2, column 3) can be due to the difficulty of precisely identifying manual tie points under changing environmental conditions (e.g., sunlight exposition or snow cover). The errors in manual tie point identification degrade the mean RMSE, but they are expected to have a mild impact on the co-registration itself because they are not correlated and tend to compensate for each other. Note that late in the season (i.e., for the last acquisition on 30 October) it became difficult to identify manual tie points due to strong shadows, hence the small number of manual tie points at that time.

Another important validation consists of assessing possible internal deformations within the local reference frame of the dataset. Figure 4a displays the residuals of the co-registration of the master bundle adjustment on a georeferenced orthoimage, which are a proxy for the internal deformations of the master bundle adjustment. The results show that the internal deformations have a meter-level amplitude (mean deformation $= 1.07$ m; max deformation $= 2.83$ m) and are smoothly spread over the area of interest due to the bundle adjustment procedure, which tends to distribute errors over space. It follows that, considering the extent of the study area (a few square kilometers), the relative error induced by the internal deformations of the local reference frame is on the order of $1/1000$. Thanks to the co-registration procedure, the internal deformations of all orthomosaics and DEMs are similar to the ones of the local reference frame defined by the master adjustment. When measuring changes at the surface of the glacier from the present dataset, the error related to internal deformations is therefore on the order of 1 ‰ of the measured distances. This results in relatively small absolute errors because the changes at the ice surface of the Gorner Glacier are of moderate amplitude (e.g., ice ablation reaches a few centimeters per day, and ice flows at less than $1\,\mathrm{m\,d^{-1}}$ in the ablation zone). For instance, in the case of horizontal velocity measurements, the order of magnitude of glacier displacement between two acquisition dates is $30\,\mathrm{cm\,d^{-1}} \times 14\,\mathrm{d} = 4.2$ m. It follows that the error in velocity due to internal deformations is $4.2\,\mathrm{m} \times 1/1000/14\,\mathrm{d} = 0.3\,\mathrm{mm\,d^{-1}}$, which is very small in comparison with the amplitude of the ice surface velocity itself.

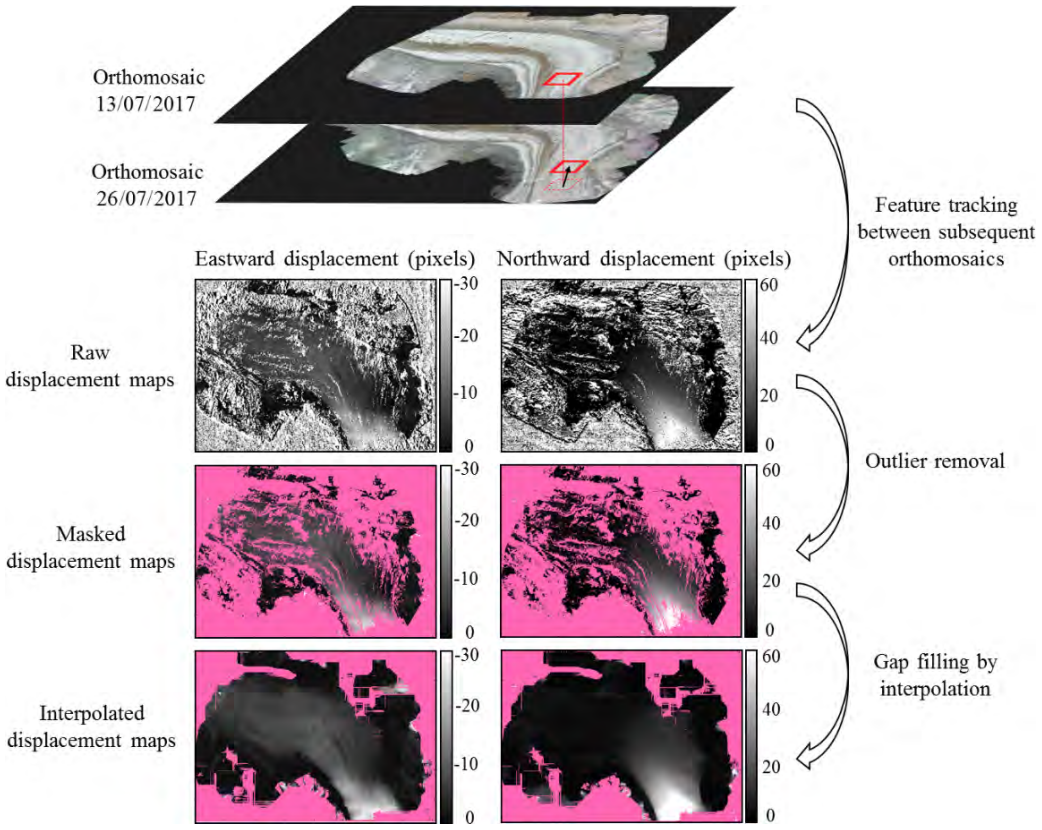

Figure 3. Processing chain used to compute a MM between two subsequent orthomosaics. The procedure is illustrated for the 13 July 2017–26 July 2017 period. In displacement maps, masked areas are displayed in pink.

Table 3. Quality assessment of the bundle adjustment procedure.

Date	Relative orientation: mean reprojection error (pix)	Co-registration: mean RMSE (m)	Co-registration: no. of manual tie points
2017/05/29	0.138	0.210	66
2017/06/09	0.136	Reference	Reference
2017/06/21	0.123	0.189	66
2017/06/27	0.146	0.193	68
2017/07/13	0.120	0.107	63
2017/07/26	0.117	0.206	70
2017/08/15	0.118	0.175	69
2017/10/04	0.125	0.122	38
2017/10/18	0.127	0.146	43
2017/10/30	0.125	0.092	16

4.2 Orthomosaics and DEMs

In addition to the bundle adjustment, we also validate the final products of the photogrammetric processing (Fig. 4a), i.e., the co-registered orthomosaics and DEMs. To this end, individual orthomosaics and DEMs have first been visually checked to track the presence of artifacts. A careful examination of all products shows that the glaciated parts (Fig. 4b) as well as the neighboring ice-free areas (Fig. 4c) are well reconstructed in both orthomosaics and DEMs. On the edges of the area of interest artifacts can be present due to the low number of overlapping images in these areas (see the processing reports to identify them). This leads to unreliable photogrammetric reconstructions and in particular shear lines (Fig. 4d). Despite these relatively minor artifacts restricted to the edges of the surveyed area, all glaciated parts and nearby unglaciated margins are satisfyingly reconstructed in both orthomosaics and DEMs.

4.3 MMs

In addition to the visual inspection of individual photogrammetric products, we also assess the quality of the co-registration procedure by quantifying in the MMs the stability of several areas that are most likely static, as well as the observed spatial patterns of glacier surface velocity. We select several validation locations on and off the glacier (Fig. 5) and compute their horizontal velocity by dividing the displacements recorded in the MMs by the time elapsed between the acquisitions. Note that in Fig. 5 the velocity is averaged over $10 \times 10\,m^2$ areas, corresponding to 10 000 single measurement points, centered on the validation points.

Figure 5b displays the observed horizontal velocities in the domain for summer 2017. In the case of perfect photogrammetric processing, co-registration, and feature tracking, the apparent velocity of the ice-free areas (in green in Fig. 5) should be zero. While it is not exactly the case due to inherent processing errors and measurement noise, the mean velocity is very low ($1.2\,cm\,d^{-1}$ on average over the five ice-free validation locations), which reflects an appropriate processing. The observed patterns of glacier surface velocity are also in accordance with typical patterns of ice flow, such as velocities decreasing from the center of the glacier towards the edges (compare the velocity in TH3 and TH5) and higher velocities at steep parts of Grenz Glacier than on the flat tongue of Gorner Glacier (compare TH2 and CM5 to CM1). Finally, the velocities derived from UAV correspond to independent data collected by differential GNSS measurements a few hundred meters upstream of the area of interest (points GO01, GO02, and GO03 in Fig. 5). The higher velocity measured at the locations monitored by GNSS (points GO01–G003) compared to the downstream locations monitored by UAV (points TH1–TH3) is coherent with the increase in glacier velocity at the steeper upstream part of Grenz Glacier (approx. 13.5 % at GO02 compared to 7.5 % at TH2). Finally, the trend of deceleration over the course of the summer recorded by GNSS is in good agreement with the UAV-based velocities throughout the glacier.

5 Data and code availability

5.1 Structure and availability of the dataset

All the data presented in this dataset are available in the following repository (Rep): https://zenodo.org/record/2630456, with the following DOI: https://doi.org/10.5281/zenodo.2630456 (Benoit et al., 2018).

The results of the photogrammetric processing, i.e., the orthomosaics and the DEMs, are available in the compressed folder Rep\Photogrammetric_Products.zip. Within this folder, the products are grouped in sub-folders by acquisition date using the following standard: 2017_mm_dd with "mm" the month and "dd" the day of acquisition. Finally, these sub-folders contain the following files:

- 2017_mm_dd_orthomosaic.tiff: contains the orthomosaic.
- 2017_mm_dd_dem.tiff: contains the DEM.
- 2017_mm_dd_report.pdf: contains the processing report (generated by Pix4D Mapper) that summarizes the quality of the photogrammetric processing for the date of interest.

The MMs are stored in the compressed folder Rep\Matching_Maps.zip. Within this folder, full-resolution MMs are stored in the \Full_resolution_Matching_Maps sub-folder. In this folder, individual maps are grouped in sub-folders named according to the acquisition date of the pair of subsequent orthomosaics used to generate the MM: 2017_mm_dd_2017_nn_ee with "mm" (resp. "dd") and "nn" (resp. "ee") the acquisition months (resp. days). These sub-folders contain the following files:

- 2017_mm_dd_2017_nn_ee_disp_Eastward: contains the MM of eastward displacements.
- 2017_mm_dd_2017_nn_ee_disp_Northward: contains the MM of northward displacements.
- 2017_mm_dd_2017_nn_ee__disp_mask: contains the mask of reliable displacements after filtering: 1 if the location corresponds to a reliable displacement, 0 otherwise.

In addition to the full-resolution MMs, displacement maps at 5 m resolution are stored in the \Final_Displacement_Maps sub-folder. Note that in contrast to the MMs, the displacement maps are in meters per day. Displacement maps follow the same file nomenclature as MMs, except the _Res5m suffix that allows us to distinguish displacement maps from MMs.

5.2 Code availability

The photogrammetric processing has been carried out using the proprietary software Pix4D Mapper, commercially available at https://pix4d.com/ (last access: 16 November 2018).

The MM have been computed using MATLAB routines written by Mathieu Gravey. The related utilities are freely available on the following repository: https://github.com/GAIA-UNIL/MatchingMapMaker (Gravey, 2018). The sub-repository Benchmarking_tests contains the results of benchmarking tests aiming at comparing the displacement maps computed by the MatchingMapMaker utility (i.e., MMs) with displacement maps computed by well-established glacier surface tracking algorithms, namely IMCORR (https://nsidc.org/data/velmap/imcorr.html, last access: 29 April 2019) and CIAS (https://www.mn.uio.no/geo/

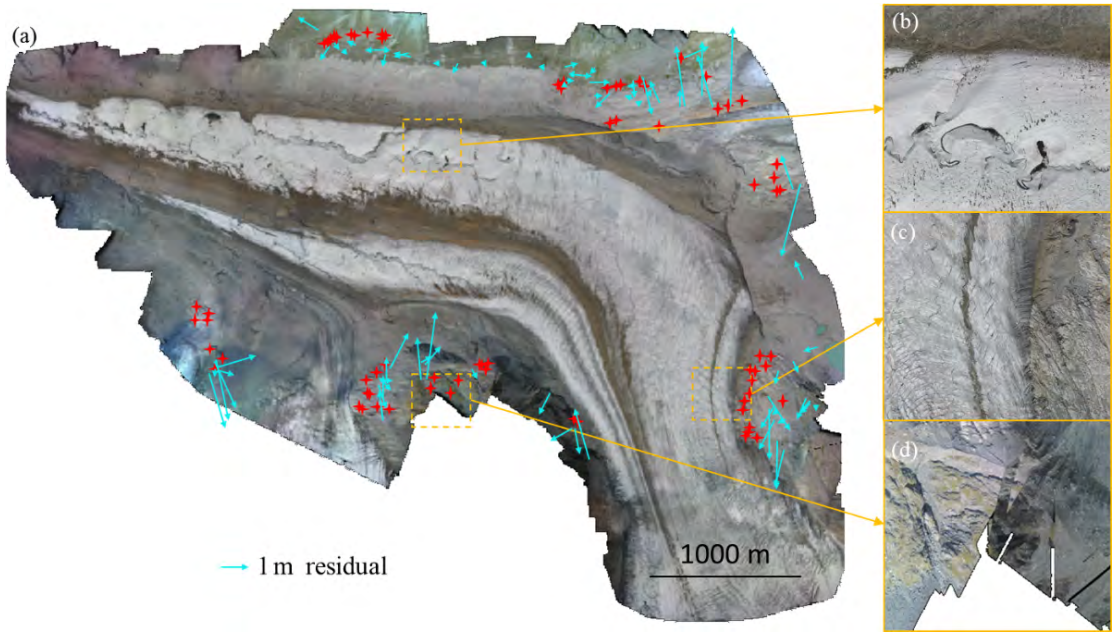

Figure 4. Quality assessment of the orthomosaics. **(a)** Overview of one orthomosaic (15 August 2017). Red stars: manual tie points used for co-registration. Blue arrows: residuals after co-registration of the master bundle adjustment on a 50 cm resolution orthoimage acquired in 2009. The affine transformation described in Table 2 has been used for co-registration. **(b–c)** Examples of areas where the photogrammetric processing worked properly. **(d)** Example of area on the boundary of the domain where the photogrammetric processing produced artifacts (mostly shear lines).

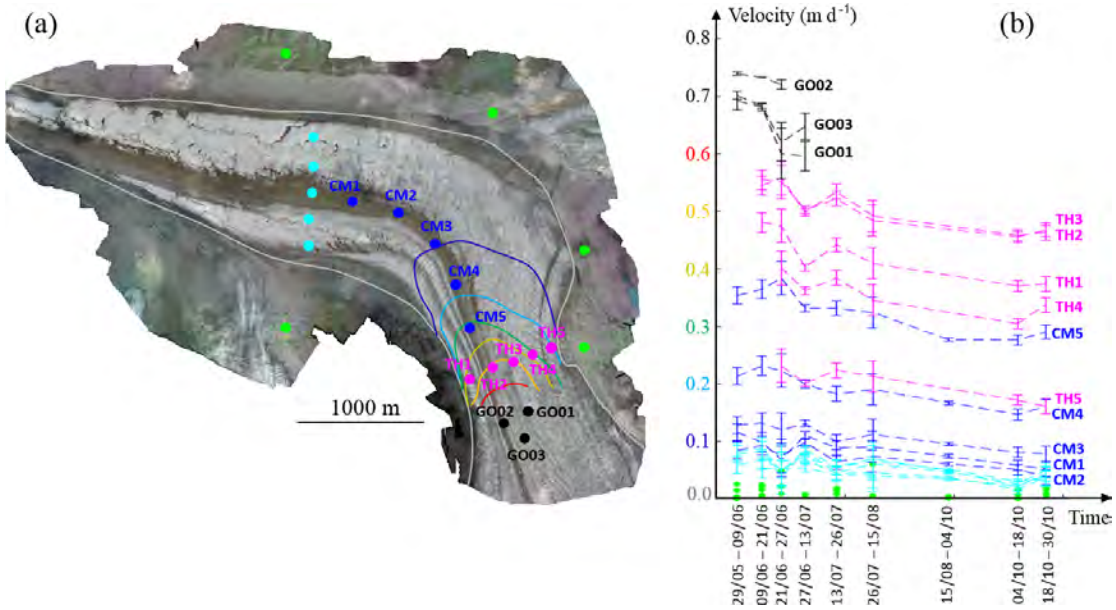

Figure 5. Quality assessment of the MMs. **(a)** Locations of the validation points. The contour lines represent the horizontal surface velocity derived from the MM related to the period 13–26 July. **(b)** Observed horizontal surface velocities at validation locations. Error bars show 1σ errors. The errors reported for UAV-based velocities are empirical errors and are equal to the quadratic mean of velocities recorded at ice-free locations (green dots in **b**). The errors reported for GNSS-based velocities (i.e., at locations GO01, GO02, and GO03) are theoretical errors accounting for the uncertainty induced by the tilt of the support of GNSS receivers over time due to glacier movement.

english/research/projects/icemass/cias/, last access: 29 April 2019). The sub-repository Similarity_score_tests contains the results of tests assessing the sensitivity of the MatchingMapMaker output to the similarity score used to define patch matches.

6 Conclusions

The present dataset compiles 10 UAV surveys of the Gorner Glacier carried out during summer 2017. Photogrammetric processing leads to a set of 10 cm resolution orthomosaics, DEMs, and glacier displacement maps for each acquisition date. This dataset can be used for change detection and quantification at the glacier surface, and in particular to investigate glacier surface dynamics at high temporal and spatial resolution.

Author contributions. AG, FH, and GM designed the experiment. AG, RV, II, BL, GP, and LB carried out the acquisitions. AG, RV, and LB performed the photogrammetric processing. MG, LB, and AG computed the matching maps. DG recorded differential GNSS data used for validation. LB wrote the paper with inputs from all authors.

Competing interests. The authors declare that they have no conflict of interest.

Acknowledgements. The authors are grateful to Philippe Limpach from ETH Zürich who processed the GNSS data.

Review statement. This paper was edited by Reinhard Drews and reviewed by Bas Altena and one anonymous referee.

References

Aizen, V. B., Kuzmichenok, V. A., Surazakov, A. B., and Aizen, E. M.: Glacier changes in the central and northern Tien Shan during the last 140 years based on surface and remote-sensing data, Ann. Glaciol., 43, 202–213, 2006.

Baltsavias, E. P., Favey, E., Bauder, A., Bösch, H., and Pateraki, M.: Digital surface modelling by airborne laser scanning and digital photogrammetry for glacier monitoring, Photogramm. Rec., 17, 243–273, 2001.

Barrand, N. E., Murray, T., James, T. D., Barr, S. L., and Mills, J. P.: Optimizing photogrammetric DEMs for glacier volume change assessment using laser-scanning derived ground-control points, J. Glaciol., 55, 106–116, 2009.

Benoit, L., Dehecq, A., Pham, H., Vernier, F., Trouvé, E., Moreau, L., Martin, O., Thom, C., Pierrot-Deseilligny, M., and Briole, P.: Multi-method monitoring of Glacier d'Argentière dynamics, Ann. Glaciol., 56, 118–128, 2015.

Benoit, L., Gourdon, A., Vallat, R., Irarrazaval, I., Gravey, M., Lehmann, B., Prasicek, G., Gräff, D., Herman, F., and Mariethoz, G.: A high-frequency and high-resolution image time series of the Gornergletscher – Swiss Alps – derived from repeated UAV surveys, https://doi.org/10.5281/zenodo.2630456, 2018.

Berthier, E., Vincent, C., Magnússon, E., Gunnlaugsson, Á. Þ., Pitte, P., Le Meur, E., Masiokas, M., Ruiz, L., Pálsson, F., Belart, J. M. C., and Wagnon, P.: Glacier topography and elevation changes derived from Pléiades sub-meter stereo images, The Cryosphere, 8, 2275–2291, https://doi.org/10.5194/tc-8-2275-2014, 2014.

Berthier, E., Cabot, V., Vincent, C., and Six, D.: Decadal Region-Wide and Glacier-Wide Mass Balances Derived from Multi-Temporal ASTER Satellite Digital Elevation Models. Validation over the Mont-Blanc Area, Front. Earth Sci., 4, 63, https://doi.org/10.3389/feart.2016.00063, 2016.

Bhardwaj, A., Sam, L., Akanksha, Martín-Torres, F. J., and Kumar, R.: UAVs as remote sensing platform in glaciology: Present applications and future prospects, Remote Sens. Environ., 175, 196–204, 2016.

Brun, F., Wagnon, P., Berthier, E., Shea, J. M., Immerzeel, W. W., Kraaijenbrink, P. D. A., Vincent, C., Reverchon, C., Shrestha, D., and Arnaud, Y.: Ice cliff contribution to the tongue-wide ablation of Changri Nup Glacier, Nepal, central Himalaya, The Cryosphere, 12, 3439–3457, https://doi.org/10.5194/tc-12-3439-2018, 2018.

Chen, J. and Funk, M.: Mass balance of Rhonegletscher during 1882/83–1986/87, J. Glaciol., 36, 199–209, 1990.

Chuang, M.-C., Hwang, J.-N., Williams, K., and Towler, R.: Tracking Live Fish from Low-Contrast and Low-Frame-Rate Stereo Videos, IEEE T. Circ. Syst. Vid., 25, 167–179, 2015.

Cuffey, K. M. and Paterson, W. S. B.: The physics of glaciers, Elsevier Science, 2010.

Dehecq, A., Gourmelen, N., and Trouvé, E.: Deriving large-scale glacier velocities from a complete satellite archive: Application to the Pamir–Karakoram–Himalaya, Remote Sens. Environ., 162, 55–66, 2015.

Dunse, T., Schuler, T. V., Hagen, J. O., and Reijmer, C. H.: Seasonal speed-up of two outlet glaciers of Austfonna, Svalbard, inferred from continuous GPS measurements, The Cryosphere, 6, 453–466, https://doi.org/10.5194/tc-6-453-2012, 2012.

Fugazza, D., Scaioni, M., Corti, M., D'Agata, C., Azzoni, R. S., Cernuschi, M., Smiraglia, C., and Diolaiuti, G. A.: Combination of UAV and terrestrial photogrammetry to assess rapid glacier evolution and map glacier hazards, Nat. Hazards Earth Syst. Sci., 18, 1055–1071, https://doi.org/10.5194/nhess-18-1055-2018, 2018.

Gabbud, C., Micheletti, N., and Lane, S. N.: Lidar measurement of surface melt for a temperate Alpine glacier at the seasonal and hourly scales, J. Glaciol., 61, 963–974, 2015.

Gindraux, S., Boesch, R., and Farinotti, D.: Accuracy assessment of digital surface models from Unmanned Aerial Vehicles' imagery on glaciers, Remote Sensing, 9, 186, https://doi.org/10.3390/rs9020186, 2017.

Gravey, M.: MatchingMapMaker utilities, available at: https://github.com/GAIA-UNIL/MatchingMapMaker (last access: 29 April 2019), 2018.

Heid, T. and Kääb, A.: Evaluation of existing image matching methods for deriving glacier surface displacements globally from op-

tical satellite imagery, Remote Sens. Environ., 118, 339–355, 2012.

Herman, F., Anderson, B., and Leprince, S.: Mountain glacier velocity variation during a retreat/advance cycle quantified using sub-pixel analysis of ASTER images, J. Glaciol., 57, 197–207, 2011.

Huss, M., Hock, R., Bauder, A., and Funk, M.: Conventional versus reference-surface mass balance, J. Glaciol., 58, 278–286, 2012.

Immerzeel, W. W., Kraaijenbrink, P. D. A., Shea, J. M., Shrestha, A. B., Pellicciotti, F., Bierkens, M. F. P., and de Jong, S. M.: High-resolution monitoring of Himalayan glacier dynamics using unmanned aerial vehicles, Remote Sens. Environ., 150, 93–103, 2014.

James, M. R. and Robson, S.: Mitigating systematic error in topographic models derived from UAV and ground-based image networks, Earth Surf. Proc. Land., 39, 1413–1420, 2014.

Jouvet, G., Weidmann, Y., Seguinot, J., Funk, M., Abe, T., Sakakibara, D., Seddik, H., and Sugiyama, S.: Initiation of a major calving event on the Bowdoin Glacier captured by UAV photogrammetry, The Cryosphere, 11, 911–921, https://doi.org/10.5194/tc-11-911-2017, 2017.

Kääb, A., Berthier, E., Nuth, C., Gardelle, J., and Arnaud, Y.: Contrasting patterns of early twenty-first-century glacier mass change in the Himalayas, Nature, 488, 495–498, 2012.

Kraaijenbrink, P., Meijer, S. W., Shea, J. M., Pellicciotti, F., De Jong, S. M., and Immerzeel, W. W.: Seasonal surface velocities of a Himalayan glacier derived by automated correlation of unmanned aerial vehicle imagery, Ann. Glaciol., 57, 103–113, 2016.

Liu, B. and Zaccarin, A.: New Fast Algorithms for the Estimation of Block Motion Vectors, IEEE T. Circ. Syst. Vid., 3, 148–157, 1993.

Maksymiuk, O., Mayer, C., and Stilla, U.: Velocity estimation of glaciers with physically-based spatial regularization – Experiments using satellite SAR intensity images, Remote Sens. Environ., 172, 190–204, 2016.

Mertes, J. R., Gulley, J. D., Benn, D. I., Thompson, S. S., and Nicholson, L. I.: Using structure-from-motion to create glacier DEMs and orthoimagery from historical terrestrial and oblique aerial imagery, Earth Surf. Proc. Land., 42, 2350–2364, 2017.

Piermattei, L., Carturan, L., and Guarnieri, A.: Use of terrestrial photogrammetry based on structure-from-motion for mass balance estimation of a small glacier in the Italian alps, Earth Surf. Proc. Land., 40, 1791–1802, 2015.

Racoviteanu, A. and Williams, M. W.: Decision tree and texture analysis for mapping debris-covered glaciers in the Kangchenjunga area, Eastern Himalaya, Remote Sensing, 4, 3078–3109, 2012.

Ramirez, E., Francou, B., Ribstein, P., Descloitres, M., Guérin, R., Mendoza, J., Gallaire, R., Pouyaud, B., and Jordan, E.: Small glaciers disappearing in the tropical Andes: a case-study in Bolivia: Glaciar Chacaltaya (16° S), J. Glaciol., 47, 187–194, 2001.

Riesen, P., Sugiyama, S., and Funk, M.: The influence of the presence and drainage of an ice-marginal lake on the flow of Gornergletscher, Switzerland, J. Glaciol., 56, 278–286, 2010.

Rippin, D. M., Pomfret, A., and King, N.: High resolution mapping of supra-glacial drainage pathways reveals link between micro-channel drainage density, surface roughness and surface reflectance, Earth Surf. Proc. Land., 40, 1279–1290, 2015.

Rossini, M., Di Mauro, B., Garzonio, R., Baccolo, G., Cavallini, G., Mattavelli, M., De Amicis, M., and Colombo, R.: Rapid melting dynamics of an alpine glacier with repeated UAV photogrammetry, Geomorphology, 304, 159–172, 2018.

Ryan, J. C., Hubbard, A. L., Box, J. E., Todd, J., Christoffersen, P., Carr, J. R., Holt, T. O., and Snooke, N.: UAV photogrammetry and structure from motion to assess calving dynamics at Store Glacier, a large outlet draining the Greenland ice sheet, The Cryosphere, 9, 1–11, https://doi.org/10.5194/tc-9-1-2015, 2015.

Scherler, D., Leprince, S., and Strecker, M. R.: Glacier-surface velocities in alpine terrain from optical satellite imagery – Accuracy improvement and quality assessment, Remote Sens. Environ., 112, 3806–3819, 2008.

Sold, L., Huss, M., Machguth, H., Joerg, P. C., Leysinger Vieli, G., Linsbauer, A., Salzmann, N., Zemp, M., and Hoelzle, M.: Mass balance re-analysis of Findelengletscher, Switzerland; benefits of extensive snow accumulation measurements, Front. Earth Sci., 4, 18, https://doi.org/10.3389/feart.2016.00018, 2016.

Sugiyama, S., Bauder, A., Riesen, P., and Funk, M.: Surface ice motion deviating toward the margins during speed-up events at Gornergletscher, Switzerland, J. Geophys. Res.-Earth, 115, F03010, https://doi.org/10.1029/2009JF001509, 2010.

Vallet, J., Panissod, F., Strecha, C., and Tracol, M.: Photogrammetric performance of an ultra light weight swinglet "UAV", International Archives of the Photogrammetry, Remote Sensing and Spatial Information Sciences, XXXVIII-1, 253–258, 2011.

Werder, M. A. and Funk, M.: Dye tracing a jökulhlaup: II. Testing a jökulhlaup model against flow speeds inferred from measurements, J. Glaciol., 55, 899–908, 2009.

Werder, M. A., Loye, A., and Funk, M.: Dye tracing a jökulhlaup: I. subglacial water transit speed and water-storage mechanism, J. Glaciol., 55, 889–898, 2009.

Werder, M. A., Hewitt, I. J., Schoof, C. G., and Flowers, G. E.: Modeling channelized and distributed subglacial drainage in two dimensions, J. Geophys. Res.-Earth, 118, 2140–2158, 2013.

Whitehead, K., Moorman, B. J., and Hugenholtz, C. H.: Brief Communication: Low-cost, on-demand aerial photogrammetry for glaciological measurement, The Cryosphere, 7, 1879–1884, https://doi.org/10.5194/tc-7-1879-2013, 2013.

Yang, K. and Smith, L. C.: Supraglacial Streams on the Greenland Ice Sheet Delineated From Combined Spectral – Shape Information in High-Resolution Satellite Imagery, IEEE Geosci. Remote S., 10, 801–805, 2012.

10.4 Rock surface burial and exposure dating

Georgina E. King[1], Pierre G. Valla[1], Benjamin Lehmann[2]

[1] Institute of Geological Sciences and Oeschger Centre for Climate Change Research, University of Bern, Bern, 3012, Switzerland. [2] Institute of Earth Surface Dynamics, University of Lausanne, Lausanne, 1012, Switzerland.

Book Chapter

invated contribution to "Handbook of Luminescence Dating, Eds, M. Bateman and I. Bailiff" (Accepted)

Author contributions. BL was part of the redaction of the manuscript.

11 ROCK SURFACE BURIAL AND EXPOSURE DATING

GEORGINA E. KING[1], PIERRE G. VALLA[1] AND BENJAMIN LEHMANN[2]

[1]Institute of Earth Sciences (ISTerre), Université Grenoble-Alpes CNRS, France
[2]Institute of Earth Surface Dynamics, University of Lausanne, Switzerland

ABSTRACT: In addition to the versatile ways in which luminescence dating can be applied to sediments, it can also be used for dating rock surfaces. This can either be done using a similar approach to sediment burial dating, i.e. constraining the last exposure to daylight for grains extracted from a buried rock surface, or it can be used to date the exposure history of a surface to daylight. In this chapter we discuss the practicalities of rock surface and rock surface-exposure dating using luminescence techniques as well as the latest model(s) for describing signal bleaching of rock surfaces, a range of different applications, and the challenges that need to be overcome before these methods can become as routine as luminescence dating of sediments.

KEYWORDS: rock surface, bleaching model, heterogeneous dosimetry

11.1 INTRODUCTION

Within the Earth and Archaeological Sciences there are many examples of rock surfaces with unknown absolute ages. In archaeology there are numerous buildings, pavements and artefacts of unknown age, the dating of which would contribute to our understanding of human–environment interactions and the emergence of societies and culture. Dating glacially polished bedrock, moraine boulders and glacial erratics gives insight into ice-dynamics, whereas measuring the age of rock-fall boulder debris can indicate rates of mass wastage and the frequency of hazardous events. Furthermore, in some environments, unconsolidated sedimentary deposits are absent or not representative of the depositional setting and/or processes of deposition. The ability to directly date the surfaces of larger clasts (pebbles/cobbles) or polished bedrock increases the applicability of luminescence dating, allowing new research questions to be addressed.

11.1.1 Key principles

In a rock surface continuously exposed to daylight, bleaching of the luminescence signal is expected not only to occur for minerals at the rock surface, but also to progressively propagate deeper into the surface with time (e.g. Habermann *et al.* 2000; Polikreti *et al.* 2002; Vafiadou *et al.* 2007). When this rock surface is buried, for example following

a rock fall (Chapot *et al.* 2012) or within a channel (Sohbati *et al.* 2012a), or when it simply becomes positioned facedown within a relict geomorphological feature protected from daylight (Simms *et al.* 2011; Sohbati *et al.* 2011), a luminescence signal can begin to accumulate. Dating of this rock surface can yield a burial age in the same way as for luminescence dating of sediments, with the only contrast being that the rock surface must be prepared either as rock slices of ~1 mm thickness (e.g. Sohbati *et al.* 2011), or following crushing and preparation of a specific mineral and grain-size fraction (e.g. Simms *et al.* 2011). In contrast, in rock surface–exposure dating, the luminescence bleaching profile is measured with depth through/into the rock sample, and a model which describes the rate of bleaching with time is used to determine the duration of daylight exposure and thus the surface-exposure age (Sohbati *et al.* 2011; Lehmann *et al.* 2018).

11.1.2 Method development

The potential of luminescence dating of rock surfaces was initially recognised for archaeological applications (e.g. Liritzis 1994; Richards 1994). Whilst the dating of burnt lithics such as flint, which can become buried after thermal resetting in a fire, has been widely investigated (e.g. Aitken 1985; Gösku *et al.* 1974), efforts to use optically reset signals from rock surfaces are relatively recent and were initially predominantly linked to the investigation of archaeological monuments (e.g. megalithic structures). Richards (1994) used optically stimulated luminescence (OSL) to date quartzite pebble hand axes, whereas the potential of dating calcitic (limestone, marble) megalithic structures using thermoluminescence (TL) was recognised by Liritzis (1994; Liritzis *et al.* 1996; Polikreti *et al.* 2003). This method works on the principle that a rock surface can be bleached optically, like sediment, and then accumulates a luminescence signal again after subsequent burial. Burial could be by sediment, or alternatively by another rock such as within a building.

An important consideration, applicable in any luminescence dating study, is that the luminescence signal is effectively zeroed before/during the event investigated. Where a megalithic structure is under investigation, sufficient daylight exposure must have occurred prior to burial; similarly, where a transport event that led to the deposition of a glacial/fluvial cobble is to be measured, daylight exposure must have been sufficient to bleach the luminescence signal of the cobble surface. Thermoluminescence dating can be limited by relatively high uncertainties related to multiple-aliquot measurement protocols and bleaching rates which are less rapid than for optically stimulated luminescence signals (Tribolo *et al.* 2003). Habermann *et al.* (2000), Greilich *et al.* (2005) and Greilich and Wagner (2006) confirmed that bedrock infrared stimulated luminesence (IRSL) and OSL signals can be fully reset by daylight and so are appropriate for dating of rock surfaces. These observations have paved the way for later applications (see Section 11.7 for details), such as to lithic artefacts (Morgenstein *et al.* 2003), soil floors and overlaying pebbles (Vafiadou *et al.* 2007), cobble surfaces (e.g. Simms *et al.* 2011; Sohbati *et al.* 2011; Jenkins *et al.* 2018; Rades *et al.* 2018) and rock-fall deposits (Chapot *et al.* 2012).

Richards (1994) first showed that the optically stimulated signal of quartz changes with depth through quartzite pebble hand-axes (Fig. 11.1A). Using a 'micro-stratigraphic' approach, whereby multiple layers 250 μm thick were removed from the pebbles in a series of 30-minute hydrofluoric acid (HF) etches, Richards (1994) was able to determine that the rate of light transmittance was reduced to 1–8% after 0.25–0.6mm depth. Polikreti *et al.*

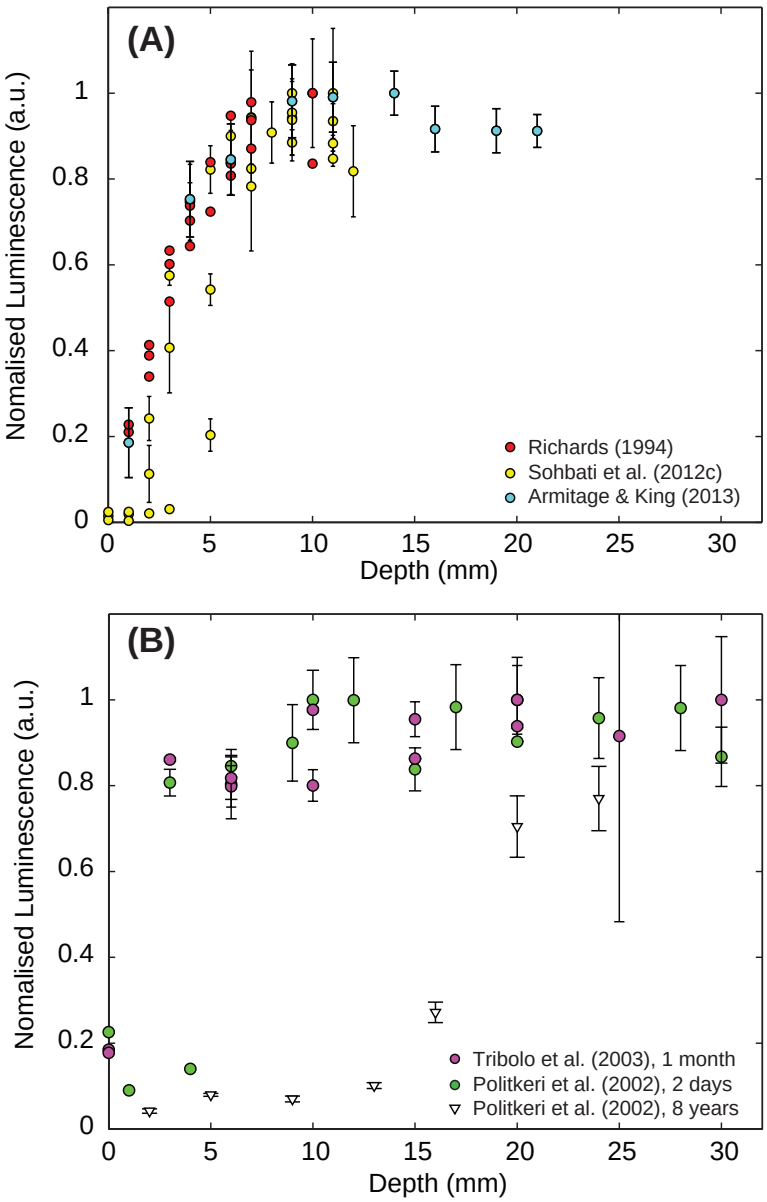

Figure 11.1 A) Quartz OSL signal change with depth for grains extracted from quartzite (Richards 1994, data reported in Roberts 1997) and sandstone (Armitage and King, 2013; Sohbati *et al.* 2012c). Note that the samples have been exposed for different durations and are from different geological and/or archaeological settings. **B**) TL signal reduction with depth for rock slices of marble (Polikreti *et al.* 2002) and quartzite (Tribolo *et al.* 2003) exposed to daylight for different durations.

(2002, 2003) investigated how TL signals changed with depth following daylight exposure through exposing blocks of marble to daylight for different durations of up to 70 days. They observed that the luminescence signal can be reset to increasing depths, following increasing bleaching durations (Fig. 11.1B). Polikreti *et al.* (2002, 2003) suggested that these bleaching profiles could be used for the authentication of marble sculptures, with rock surfaces of sufficient antiquity experiencing deeper maximum bleaching depths (Fig. 11.1B). Following these earlier studies, Sohbati *et al.* (2011) proposed that OSL signals from quartz and feldspar could be used for rock surface-exposure dating. In the remainder of this chapter, the models of luminescence signal bleaching through bedrock are presented, as well as the various methodological considerations necessary for bedrock surface and surface-exposure dating. A number of detailed case studies are given as well as an outlook for this developing technique.

11.2 MODEL OF LUMINESCENCE SIGNAL BLEACHING

A rock surface that has not been exposed to daylight has a luminescence signal reflecting an equilibrium between electron trapping, due to ambient radiation (cosmic rays, high-energy solar particle flux and radioactive decay in the rock matrix) and electron detrapping due to anomalous fading and/or thermal signal losses. This condition is often termed field saturation or field steady-state and is the starting point (i.e. the initial condition) prior to any signal loss through exposure to daylight. If this rock surface is then continuously exposed to daylight, luminescence signal bleaching is expected to propagate deeper into the surface with time (Polikreti *et al.* 2002; Sohbati *et al.* 2011). This can be seen schematically for an example from a glacial setting in Figure 11.2. Polikreti *et al.* (2002) were the first to develop a model for luminescence signal bleaching with depth following daylight exposure. More recently, Sohbati *et al.* (2011) have presented a model for the depletion of optically stimulated luminescence signals with depth. Although this model has been recently challenged (Laskaris and Liritzis, 2011), here we focus on the model of Sohbati *et al.* (2011) as it remains the most widely used approach in recent applications.

The intensity of a luminescence signal can be considered to reflect the number of trapped electrons, n. For a rock surface exposed to daylight, the trapped electron concentration (and thus the luminescence signal intensity) is governed by competing processes of electron detrapping due to daylight exposure, and of electron trapping in response to ambient

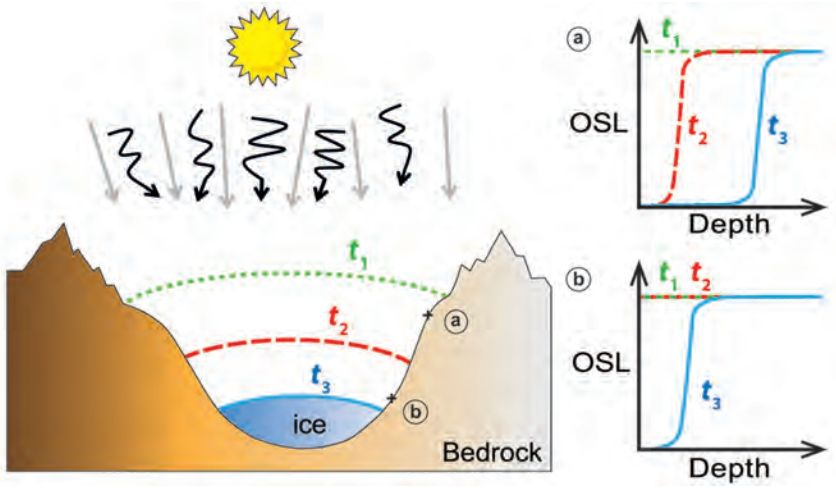

Figure 11.2 Sketch of bedrock luminescence signal evolution following exposure to daylight caused by glacial retreat, modified from Lehmann *et al.* (2018). Prior to bedrock surface exposure when the glacier is at its maximum extent (time t_1), the luminescence signals of both surfaces (a) and (b) are in field-saturation. Following progressive glacial retreat (time t_2), surface (a) becomes exposed and the luminescence signal begins to bleach at depth. In contrast, surface (b) remains covered and its luminescence signal remains unchanged. Following further glacial retreat (time t_3), surface (a) remains exposed and its luminescence signal is more deeply bleached whereas surface (b) is only now exposed to daylight, with its luminescence signal bleached to a shallow depth. Straight arrows (grey) represent cosmic rays and the flux of high-energy solar particles, which together with radioactive decay in the rock-matrix build the latent luminescence signal. Black arrows represent low energy electromagnetic radiation from the sun, which following bedrock exposure bleach the latent luminescence signal.

radiation. Thus the concentration of trapped electrons $n(x,t)$ at a given depth x(mm) and time t(s) can be described by the following differential equation (Sohbati *et al.* 2012b):

$$\frac{\partial n(x,t)}{\partial t} = -E(x)n(x,t) + F(x)[N(x) - n(x,t)] \quad (1)$$

where $N(x)$ is the maximum possible number of trapped electrons at depth x, and $E(x)$ (s^{-1}) and $F(x)$(s^{-1}) are the rates of charge detrapping and trapping respectively. The rate of charge detrapping is given by:

$$E(x) = \overline{\sigma\varphi_0}\ e^{-\mu x} \quad (2)$$

where $\sigma(\lambda)$ is the luminescence photoionisation cross-section (cm^2) and φ_0 is the photon flux ($cm^{-2}\ s^{-1}$) as a function of wavelength at the surface of the rock ($x = 0$). The product of these two terms, $\overline{\sigma\varphi_0}$ is thus the effective decay rate (s^{-1}) of luminescence at the rock surface, following exposure to a particular spectrum of light. The final parameter of equation (2), μ, is the light attenuation coefficient of the rock (mm^{-1}).

In addition to electron detrapping, equation (1) contains term F(x) to describe electron trapping, which whilst of lesser importance for young terrestrial surfaces (i.e. <10 ka) may be significant for extra-terrestrial applications where radiation dose rates, particularly from cosmic rays, are greater (Sohbati *et al.* 2012b). The rate of charge trapping due to ionising radiation is given by:

$$F(x) = \frac{\dot{D}(x)}{D_0} \quad (3)$$

where $\dot{D}$ is the environmental dose rate (Gy s^{-1}) and D_0 is the characteristic dose of saturation (Gy) for the luminescence signal being investigated.

It is assumed that the number of trapped electrons at a given depth $n(x)$ is proportional to the measured luminescence signal $L(x)$, and thus assuming $F(x) \approx 0$, the luminescence can be described following Sohbati *et al.* (2012c) as:

$$L(x) = L_0\ e^{-\overline{\sigma\varphi}_0 te^{-\mu x}} \quad (4)$$

where L_0 is the field-saturation luminescence signal (i.e. equilibrium level for a trapped electron population of N), assumed to have been constant at all depths prior to bleaching (i.e. at $t = 0$). For the case where $F(x) > 0$, this equation becomes (Sohbati *et al.* 2012b):

$$L(x) = \frac{\frac{\overline{\sigma\varphi_0}\ e^{-\mu x}}{e^{-t(\overline{\sigma\varphi_0}\ e^{-\mu x} + \frac{\dot{D}}{D_0})}} + \frac{\dot{D}}{D_0}}{\overline{\sigma\varphi_0}\ e^{-\mu x} + \frac{\dot{D}}{D_0})} \quad (5)$$

Or where a surface has been completely bleached, i.e. $L_0(x) = 0$, for example following a meteorite impact (Sohbati *et al.* 2012b):

$$L(x) = \frac{\frac{\dot{D}(x)}{D_0}\left\{1 - e^{-t[\overline{\sigma\varphi_0}\ e^{-\mu x} + \frac{\dot{D}(x)}{D_0}]}\right\}}{\overline{\sigma\varphi_0}\ e^{-\mu x} + \frac{\dot{D}(x)}{D_0}} \quad (6)$$

Applications of luminescence surface-exposure dating are likely to be more common in terrestrial settings for rock-surface exposures of <10 ka; therefore, we will consider equation (4) whilst discussing the model. However, for older rock surfaces, an equilibrium between electron detrapping by daylight exposure and electron retrapping due to environmental radiation may occur (Sohbati *et al.* 2012c). Equation (4) contains three unknown parameters: $\overline{\sigma\varphi_0}$, the luminescence signal decay rate at the rock surface; μ the rock attenuation coefficient; and *t*, the exposure time. A range of values have been reported for $\overline{\sigma\varphi_0}$ and μ for different minerals and rock samples; however, here for illustration we use the values from Sohbati *et al.* (2012c) for quartz minerals to explore the luminescence signal behaviour described in equation (4).

Equation (4) describes how bleaching of a luminescence signal propagates with time and depth into a rock surface. Figure 11.3A shows how luminescence signals may bleach to different depths for $\overline{\sigma\varphi_0}$ of 6.8×10^{-9} s^{-1} and μ of 1.01 mm^{-1} for different time periods. As the exposure duration increases, the depth to which the luminescence signals are reset within the sample increases. In order to calculate an exposure age, both $\overline{\sigma\varphi_0}$ and μ must be constrained, which remains the largest barrier to the routine application of luminescence surface-exposure dating (Sohbati *et al.* 2011, 2015). Before considering the ways through which this challenge can be addressed, we first consider the variables that control these two parameters.

11.2.1 Controls on luminescence signal bleaching rate

The luminescence signal bleaching rate $\overline{\sigma\varphi_0}$ is controlled by the photon flux at the sample location (i.e. $\varphi(\lambda,0)$) which is affected by variability in the daylight spectrum. The effect of varying $\overline{\sigma\varphi_0}$ on the measured luminescence bleaching profile is shown in Figure 11.3B. Spooner (1994) investigated the optical bleaching of feldspar minerals in response to different wavelengths of light. Using these data, Sohbati *et al.* (2011) attempted to determine $\overline{\sigma\varphi_0}$ from first principles, by calculating the annual wavelength dependent flux of incident photons at the Earth's surface for the latitude and longitude of the Danish cobble that they were investigating. Unfortunately, the value of $\overline{\sigma\varphi_0}$ they determined of ~1.2×10^{-4} s^{-1} equated to an exposure time of ~30 minutes, considerably shorter than anticipated. They attributed this difference to the fact that the bleaching of feldspar is known not to be exponential for small residual signals (Kars *et al.* 2014), and thus their calculated value likely underestimated the time required for luminescence signal bleaching to occur.

The attenuation coefficient of a sample (μ) is dependent upon its lithology. The effect of varying μ on the measured luminescence bleaching profile is shown in Figure 11.3C. Rock-types with many dark minerals (i.e. melanocratic lithologies such as basalts, mica-rich metasediments etc.) will have higher μ values than those comprising many translucent minerals (i.e. leucocratic lithologies such as sandstone or quartz-rich lithologies). Average grain size and density of grain packing are also expected to affect the light attenuation rate. However, in their successful validations of OSL surface-exposure dating, Sohbati *et al.* (2012c) and more recently, Lehmann *et al.* (2018) have shown that it is possible to assume that the attenuation factor (μ) is similar for samples of the same lithology.

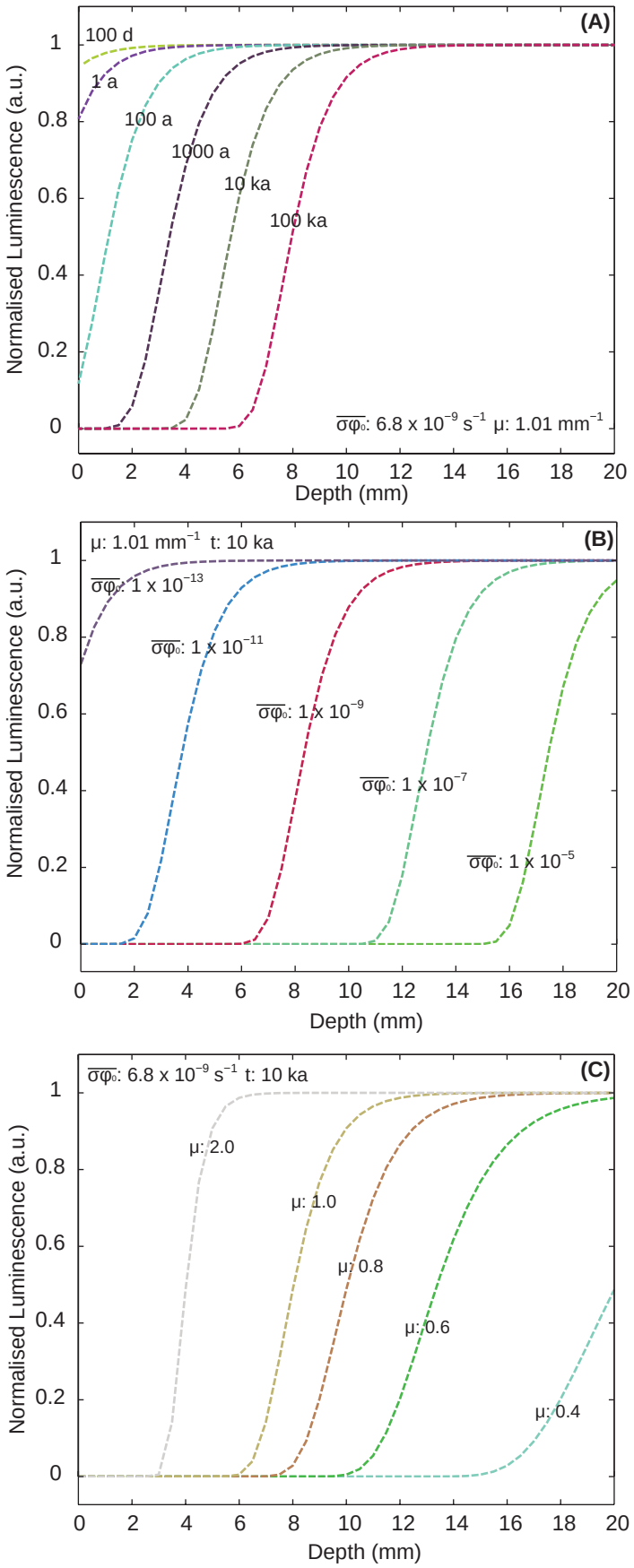

Figure 11.3 Modelled luminescence bleaching profiles using equation (4) and parameters for quartz OSL following Sohbati *et al.* (2012c). A) Changing luminescence signal bleaching depth with increasing exposure time from 100 days to 100 ka for fixed μ and $\overline{\sigma\varphi_0}$ parameters. B) Assuming an exposure time of 10 ka and keeping μ = 1.01 mm^{-1} (after Sohbati *et al.* 2012c), changing $\overline{\sigma\varphi_0}$ causes the depth of luminescence signal bleaching to shift, with smaller values indicative of lower bleaching rates resulting in a shallower bleaching profile. C) Assuming an exposure time 10 ka and keeping $\overline{\sigma\varphi_0}$ as 6.89 × 10^{-9} s^{-1} (after Sohbati *et al.* 2012c) changing μ values result in different depths and gradients of signal bleaching, with larger values indicating higher levels of attenuation and shallowing signal bleaching.

11.3 ROCK SURFACE-EXPOSURE DATING

Whilst only a limited number of studies have been published to date, a large degree of variability in μ and $\overline{\sigma\varphi_0}$ has been recorded (e.g. Sohbati *et al.* 2012c; Lehmann *et al.* 2018). Site-specific calibration may be the only possibility for constraining $\overline{\sigma\varphi_0}$, whilst it is possible to determine μ in the laboratory, although recent studies have shown this to be challenging (see Gliganic *et al.* in press; Meyer *et al.* in press). Constraining these parameters is the major limitation affecting the widespread uptake of luminescence surface-exposure dating. Site-specific calibration samples can comprise bedrock exposed for a known duration, e.g. in a road-cut (Sohbati *et al.* 2012c) or quarry (Polikreti *et al.* 2002), or surfaces of known-age constrained through historical records (Lehmann *et al.* 2018). Alternatively, Polikreti *et al.* (2002) determined the TL signal bleaching parameters of marble through exposing bedrock samples to natural daylight for known durations of between 2 and 70 days in an experiment (Fig. 11.1B). A known exposure-age allows *t* to be fixed in equation (4), $\overline{\sigma\varphi_0}$ and μ can then be derived through fitting the data and solving the equation for only these two unknown parameters. However, it should also be noted that for a rock with large heterogeneous crystals, μ may vary spatially across the rock surface and with depth (Meyer *et al.* 2018). Alternatively, μ can be estimated using numerical modelling. Sohbati *et al.*

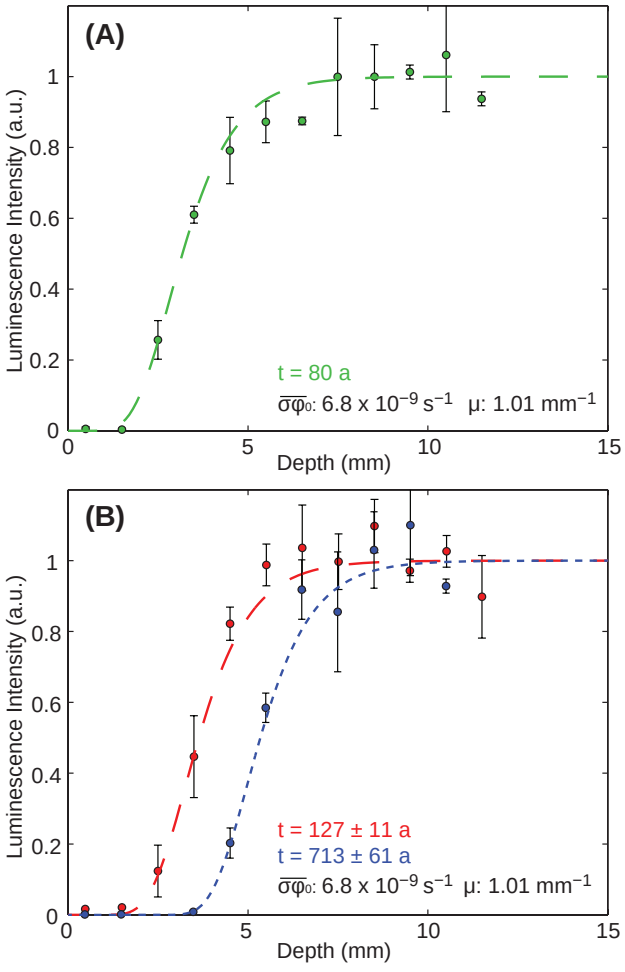

Figure 11.4 A) Quartz OSL signal increase with depth for a sandstone sample of known age (HS-OSL-29) taken from Sohbati *et al.* (2012c). Fitting these data with equation (4) and known exposure time, *t*, allows parameters μ and $\overline{\sigma\varphi_0}$ to be estimated.
B) Using these parameters, it is possible to fit the quartz OSL data of two samples of the same lithology and from the same location to derive unknown exposure time, *t*. The raw data of sample HS-OSL-25 ($t = 713 \pm 61$ yr) have been adjusted to remove a burial dose (Chapot *et al.* 2012; Sohbati *et al.* 2012c).

(2015) treated μ as a shared parameter when fitting luminescence bleaching profiles of the same core, but for signals which have different bleaching rates. Once these parameters are constrained, equation (4) can be solved again with t as the only unknown parameter, through fitting the luminescence data for the sample of unknown age; this is illustrated in Figure 11.4 for a specific case study detailed below.

Sohbati *et al.* (2012c) used luminescence surface-exposure dating to determine the age of Barrier Canyon Style rock art from Canyonlands National Park, Utah, USA. Through fitting the measured luminescence signals of a known-age sample of the Navajo Sandstone and determining $\overline{\sigma\varphi_0}$ and μ (Fig. 11.4A), Sohbati *et al.* (2012c) were able to input these values into equation (4), and to fit the luminescence data of samples of unknown age to determine the exposure time (Fig. 11.4B). Subsequent work by Lehmann *et al.* (2018) also employed a similar approach. Working on glacially polished bedrock, Lehmann *et al.* (2018) took a transect of known-exposure-age samples from near to the Mer de Glace (Mont Blanc massif, France). They found that a minimum of 4 different calibration samples were required in order to accurately constrain the parameters for a further sample of the same lithology. Further details of these two case studies are given in Section 11.4.

11.3.1 Identifying complex daylight exposure histories and incomplete bleaching

In common with luminescence sediment dating, rock surface dating is reliant on the assumption that a rock surface has been fully bleached prior to burial. This can be evaluated in a number of different ways including using laboratory experiments and through the measurement of modern analogue samples (e.g. Simms *et al.* 2011), as well as through contrasting luminescence ages of overlaying sediments and rock surfaces (e.g. Chapot *et al.* 2012; Sohbati *et al.* 2012c). The consistency between ages of different rock surfaces sampled from the same depositional setting can also be evaluated (e.g. Simms *et al.* 2011). A complementary approach is to model the luminescence bleaching profile of a rock sample, and to extrapolate back to the initial level of signal resetting (Freiesleben *et al.* 2015; Sohbati *et al.* 2015).

The variation of luminescence signals with depth through a cobble or a clast may record evidence of multiple bleaching events (Freiesleben *et al.* 2015; Sohbati *et al.* 2012a). This is because following initial signal resetting, if the clast or surface is buried again, a new luminescence signal will accumulate, which can then be reset by a second period of daylight exposure (provided that this is shorter than the previous bleaching event to preserve information about the older episode). Such multiple exposure histories result in a 'stepped' succession of luminescence level plateaus (Fig. 11.5). Using quartz OSL, Sohbati *et al.* (2012a) determined two bleaching events for a cobble from the Tapada do Montinho archaeological site (east-central Portugal). Measurements using a single-aliquot regenerative dose protocol revealed that the maximum D_E of 67 Gy at >5 mm depth into the cobble, was not in saturation. This indicated that the cobble had previously been bleached sufficiently to reset the luminescence signal at this depth and a more recent bleaching event affecting only the first 2 mm of the cobble could also be detected. Freiesleben *et al.* (2015) modified the model of Sohbati *et al.* (2012b; equation (1) of this chapter) to fit clast and rock surface luminescence profiles generated by multiple daylight exposure and burial events. Their new model works on the premise that the final luminescence signal intensity (L_1) of one event, which can be

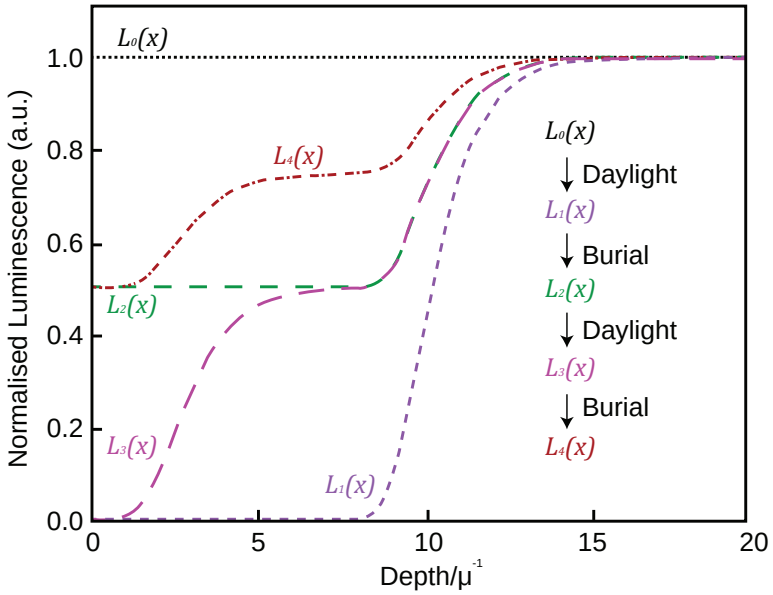

Figure 11.5 Evolution of luminescence signals following multiple burial and exposure cycles, modified after Freiesleben *et al.* (2015). It is assumed that the environmental dose rate is constant with depth, and that no trap filling has occurred during the exposure periods. The depicted burial/exposure history comprises (1) burial of the sample for sufficient duration that all of the electron traps are saturated (L_0), (2) the sample is exposed to daylight for a duration sufficient for complete signal resetting to occur to a depth of 8 mm (L_1), (3) the sample is buried allowing electron trapping and signal accumulation to occur (L_2), (4) the sample is exposed again for a short duration, resulting in complete signal bleaching to a depth of 2 mm (L_3), the sample is buried once more for the same duration as in stage (3) allowing signal accumulation (L_4). The profiles of all the previous exposure/burial periods are recorded in profile (L_4).

thought of as its final condition ($n_{f,1}$), becomes the initial condition of the following burial or exposure event ($n_{i,2}$); thus the event series in Figure 11.4 can be described as:

$$n_{i,1} \xrightarrow{\text{Exposure } (t_{e1})} n_{f,1} = n_{i,2} \xrightarrow{\text{Burial } (t_{b1})} n_{f,2} = n_{i,3} \xrightarrow{\text{Exposure } (t_{e2})} n_{f,3} = n_{i,4} \xrightarrow{\text{Burial } (t_{b2})} n_{f,4} \quad (7)$$

and following Sohbati *et al.* (2015) as:

$$\mathrm{L}(x) = \left(\left(\left(\mathrm{e}^{-t_{e1}\overline{\sigma\varphi_0}\,\mathrm{e}^{-\mu x}} - 1\right)\mathrm{e}^{-\frac{\dot{\mathrm{D}}(x)}{D_0}t_{b1}} + 1\right)\mathrm{e}^{-t_{e2}\overline{\sigma\varphi_0}\,\mathrm{e}^{-\mu x}} - 1\right)\mathrm{e}^{-\frac{\dot{\mathrm{D}}(x)}{D_0}t_{b2}} + 1 \quad (8)$$

where $t_{e1(2)}$ and $t_{b1(2)}$ are the exposure period and burial period 1 (2), respectively.

Freiesleben *et al.* (2015) successfully used this model to fit the $IRSL_{50}$ and post-IR $IRSL_{290}$ signals of feldspars in rock slices from a granite cobble excavated from an archaeological site near Aarhus (Denmark). Sohbati *et al.* (2015) were also able to use this approach to model whether the $IRSL_{50}$ and post-IR $IRSL_{225}$ signals of their cobble samples from the Negev desert, Israel had been fully reset. Thus, the ability to measure luminescence depth

profiles through bedrock surfaces may offer an advantage over conventional sediment luminescence dating approaches for determining whether samples have been fully reset. However, sediment dating also provides insights into deposit bleaching histories (see Chapter 1) through, for example, the degree of overdispersion (OD) of equivalent dose values (cf. Duller 2008), or the ratio of IRSL and post-IR IRSL signals (Buylaert *et al.* 2013).

11.3.2 Environmental dose rate determination

A major challenge for rock surface and surface-exposure dating is to quantitatively constrain the environmental dose rate, which determines the rate of luminescence signal accumulation. In many sedimentary applications of luminescence dating, it is possible to make an infinite matrix assumption (Aitken 1985; Durcan *et al.* 2015; Chapter 1). This is because the chemical composition of surrounding sediments is the same as the sample under investigation; in the case of cobble or rock surface(-exposure) dating this is almost never the case (although see Simms *et al.* 2011). Instead the principle of superposition must be applied, which uses the geometry of the cobble/rock surface and the surrounding material to scale the relative dose contributions. For example, Sohbati *et al.* (2012a) followed the equations of Appendix H of Aitken (1985) in order to scale infinite matrix beta and gamma dose rates for a range of geometries to obtain the dose rate of their investigated cobbles (Fig. 11.6). If we assume that a buried rock surface has a given thickness h, and infinite lateral extent, the beta-dose contribution to the environmental dose rate can be approximated following Freiesleben *et al.* (2015) as:

$$\dot{\mathrm{D}}(x)_{\beta}^{\mathrm{Cobble}} = \dot{D}_{\mathrm{Rock},\beta}^{\mathrm{inf}}\left[1 - 0.5\left(\mathrm{e}^{-bx} + \mathrm{e}^{-b(h-x)}\right)\right] + \dot{D}_{\mathrm{Sed},\beta}^{\mathrm{inf}}\, 0.5\left(\mathrm{e}^{-bx} + \mathrm{e}^{-b(h-x)}\right) \quad (9)$$

where b is the beta dose grain-size attenuation factor (e.g. Guérin *et al.* 2012) and $D_{\mathrm{Rock},\beta}^{\mathrm{inf}}$ and $D_{\mathrm{Sed},\beta}^{\mathrm{inf}}$ are the water content corrected infinite matrix beta-dose rates for the rock and sediment respectively (see Durcan *et al.* 2015 for a detailed description of environmental dose-rate calculations). The same approach can be used for the gamma, alpha and cosmic dose-rate contributions and the final dose rate with depth is given from the sum:

$$\dot{\mathrm{D}}(x)^{\mathrm{Cobble}} = \dot{\mathrm{D}}(x)_{\alpha}^{\mathrm{Cobble}} + \dot{\mathrm{D}}(x)_{\beta}^{\mathrm{Cobble}} + \dot{\mathrm{D}}(x)_{\gamma}^{\mathrm{Cobble}} + \dot{\mathrm{D}}_{\mathrm{Cosmic}}^{\mathrm{Cobble}} \quad (10)$$

where the cosmic dose rate is assumed not to vary significantly over the mm-scale depths typically investigated in rock surface dating. Changes in U, Th and K content and grain size may result in significant changes in the environmental dose rate with depth and must be corrected for.

Grain-size variability between minerals that contribute to measured luminescence signals is a major source of uncertainty in luminescence dating applications using rock samples (Simkins *et al.* 2016; Sohbati *et al.* 2013). Increasing grain sizes result in greater external radiation dose attenuation and thus for grains without a significant internal dose rate (see below), a reduced overall dose. In order to estimate the environmental dose rate effectively, the grain size of the minerals that contribute to the measured luminescence signal

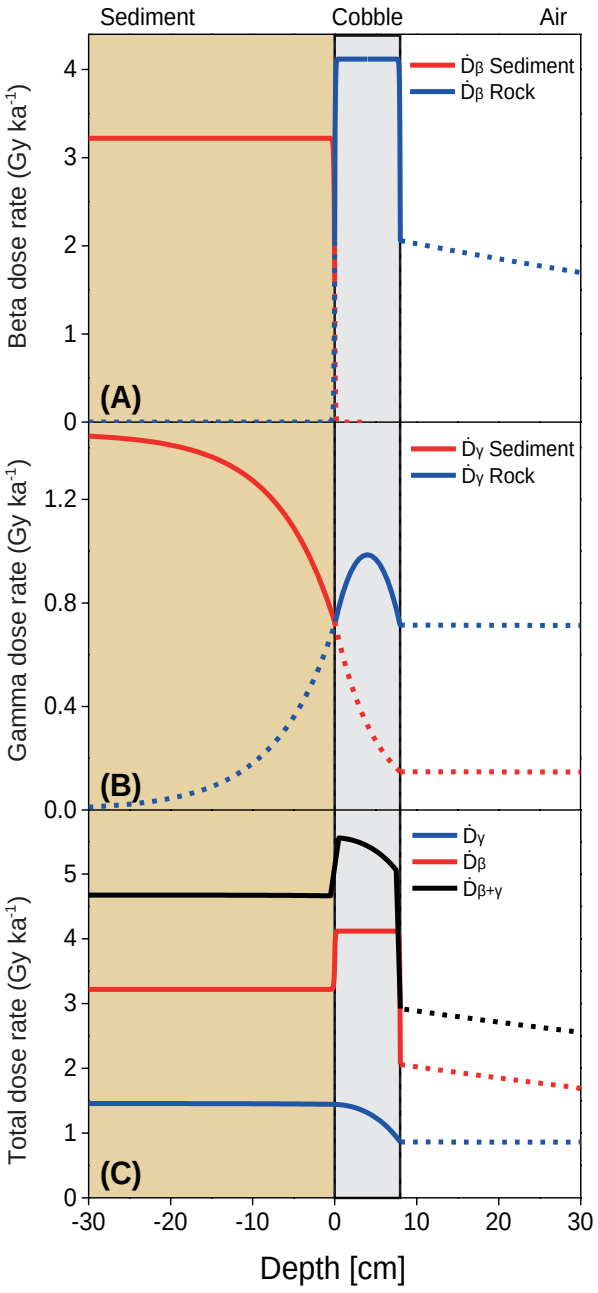

Figure 11.6 Schematic showing how the environmental dose rate ($\dot{D}$) changes between sediment, a cobble and air, modified from Sohbati *et al.* (2015). A) Beta, B) gamma and C) total (i.e. beta + gamma) environmental dose rates. The dose rate in each of the three mediums is shown as a solid line, whereas the dose rate due to the adjacent medium is shown as a dashed line.

must be known. Simms *et al.* (2011) took care to crush their quartzite rock slices gently, so that the constituent grains were not broken, and thus the obtained 90–250 μm fraction could be used to calculate the dose rate. An alternative approach was used by King *et al.* (2016a) when determining the dose rate of grains extracted from bedrock samples for investigation using OSL-thermochronometry. Instead, they used software that could determine the grain-size distribution from high-resolution thin-section images (Buscombe 2013), and calculated their environmental dose rates using maximum and minimum grain-size values.

Feldspar minerals are commonly used in rock surface(-exposure) dating, because of their greater luminescence sensitivity relative to quartz grains extracted from bedrock,

and also because of the difficulty of isolating quartz grains that are not contaminated by other minerals (e.g. Guralnik *et al.* 2015). However, the internal dose rate of feldspars varies considerably, dependent upon their chemical composition (e.g. Smedley and Pearce 2016; Smedley *et al.* 2012). For example, the internal K-content ranged from 0.1 to 15% measured using electron probe micro-analysis for feldspars with density <2.58 g cm^{-3} extracted from the same rock sample (NB126; King *et al.* 2016b). Furthermore, for grains with a significant internal dose contribution, such as K-feldspars, increasing grain size results in an increasing dose rate, which may significantly affect age calculations from rock surfaces (Greilich and Wagner 2006; Sohbati *et al.* 2011). Sohbati *et al.* (2013) suggested that because Na-feldspar grains have much lower internal K contents and thus avoid this inter-grain variability, they could comprise a more suitable target mineral for rock surface dating. However, Sohbati *et al.* (2013) found that the IRSL emission detected in the blue part of the emission spectrum may derive from K-feldspar inclusions within Na-feldspar extracts, and thus instead suggested that the yellow emission could be targeted to isolate the Na-feldspar luminescence signal.

11.3.3 Sample preparation and measurement protocols

Sample preparation and luminescence measurement protocols for rock surface dating are still under development with procedures less established compared to sediment dating. Rock surface sample preparation is also dependent on the lithology studied: whereas sandstones can be gently abraded/rubbed (e.g. Sohbati *et al.* 2012c; Liritzis *et al.* 2013; Liritzis and Vafiadou 2015), granitic/metamorphic lithologies require sample coring and are generally sliced to produce 1-mm thick rock slices (e.g. Vafiadou *et al.* 2007; Simms *et al.* 2011; Sohbati *et al.* 2011; 2012a). Following rock slicing for granitic or metamorphic lithologies, subsequent sample preparation then differs between studies. Rock slices can either be crushed to extract specific target minerals following classical chemical/physical procedures (i.e. quartz or K-feldspar, Simms *et al.* 2011; 2012; Sohbati *et al.* 2011; 2012a) or whole rock slices can be measured directly without any further treatment (e.g. Freiesleben *et al.* 2015; Sohbati *et al.* 2015; Lehmann *et al.* 2018). Sohbati *et al.* (2011) showed better IRSL D_E reproducibility between intact rock slices compared to K-feldspar extracts from bedrock, which could not be related to crushing or to partial bleaching. Conversely, Sobhati *et al.* (2012a) found good agreement between equivalent doses and luminescence characteristics of rock slices and quartz grains extracted from the same quartzite lithology. These different outcomes may be explained by feldspar microdosimetry (e.g. Smedley and Pearce 2016). This is because whereas the luminescence signal from a rock slice may be averaged across many grains, such differences may become visible during measurement of a purified separate. However, comparison between these two experimental approaches requires further investigation and rock-slice crushing could result in the loss of information regarding the original grain-size distribution (Section 11.5).

Rock surface dating measurement protocols have been developed based on existing procedures established for sediment dating and vary depending on sample preparation and the scientific question that is to be addressed. TL MAAD (multi-aliquot additive dose) protocols have been applied to both marble (Polikreti *et al.* 2003) and sandstone (Liritzis and Vafiadou 2015) lithologies. OSL SAR (single-aliquot regenerative) measurement protocols have been applied to quartz mineral extracts from crystalline pebbles (Simms *et al.* 2011;

2012; Sohbati *et al.* 2012a; Simkins *et al.* 2013), and to quartzite pebbles using solid rock slices (Vafiadou *et al.* 2007; Sohbati *et al.* 2012a). However, bedrock quartz often shows poor luminescence sensitivity and measurement reliability (e.g. Guralnik *et al.* 2015), and thus equivalent dose scatter (e.g. Simms *et al.* 2011). Recent investigations by Simkins *et al.* (2016) suggest that this scatter in D_E values may originate from heterogeneity in the environmental dose rate due to changing water content and/or grain-size effects, as well as post-crystallisation transport histories (Sawakuchi *et al.* 2011). IRSL SAR measurement protocols have also been successfully applied to date rock slices, by using either one IR stimulation at 50°C (Sohbati *et al.* 2011; Lehmann *et al.* 2018) or different post-IR IRSL protocols at 225°C (Sohbati *et al.* 2015) or 290°C (Freiesleben *et al.* 2015; Liu *et al.* 2016). Such post-IR IRSL protocols can provide two datasets of information for rock surface (-exposure) dating, as the different temperature IR signals have been shown to have different bleaching rates (e.g. Sohbati *et al.* 2015). Furthermore, IRSL stimulation of rock slices may allow the investigation of specific feldspars using either blue (K-feldspar) or yellow (Na-feldspar) emissions (Sohbati *et al.* 2013). However, IRSL protocols on rock slices may be associated with high residual doses (Vafiadu *et al.* 2007), and post-IR IRSL protocols may be problematic due to high levels of recuperation after IR stimulation, which appear to be dependent on the temperature of the first IR stimulation (Liu *et al.* 2016).

11.4 APPLICATIONS

11.4.1. Archaeological case studies

Rock surface dating has been widely used to study archaeological artefacts, especially megalithic structures, with first attempts applying TL dating. Liritzis (1994) investigated the optical bleaching properties of TL in limestone experimentally (275°C TL peak), and used these properties to date megalithic structures in Peloponnese (Greece), yielding ages of around 3 ka, which are in agreement with independent archaeological ages. Theocaris *et al.* (1997) were also able to successfully use this approach to date two Hellenic pyramids, with the resultant ages showing them to be prehistoric. Polikreti *et al.* (2002; 2003) investigated marble objects for authentication purposes, and experimentally determined TL bleaching properties and bleaching depth following daylight exposure (Fig. 11.7A). They proposed using the 290°C TL peak because of favourable luminescence characteristics for dating marble artefacts, which were commonly used for construction throughout antiquity. Using the MAAD protocol, they provided a burial age for a temple artefact (Macedonia, Greece) of 2.6±0.4 ka, in relatively close agreement with the archaeological age. Building on these results, more recent archaeological studies have applied OSL dating.

Vafiadu *et al.* (2007) investigated SAR OSL protocols on whole rock slices from granitic, ultramafic and quartz metamorphic rocks sampled from archaeological sites (Greece, Denmark and Sweden). Their results showed good OSL signal bleaching properties and successful tests regarding the application of the SAR protocol on whole rock slices, with obtained burial ages in agreement with independent archaeological estimates. The SAR OSL protocol has also been applied in combination with the SAAD (single-aliquot additive dose) OSL protocol, to provide new dates for megalithic structures from Egypt and Saudi Arabia (Liritzis *et al.* 2013). Using quartz grains extracted from sandstones and granitic rocks, Lirtizis *et al.* (2013) provided burial ages between 3–4 ka for these structures and suggested that

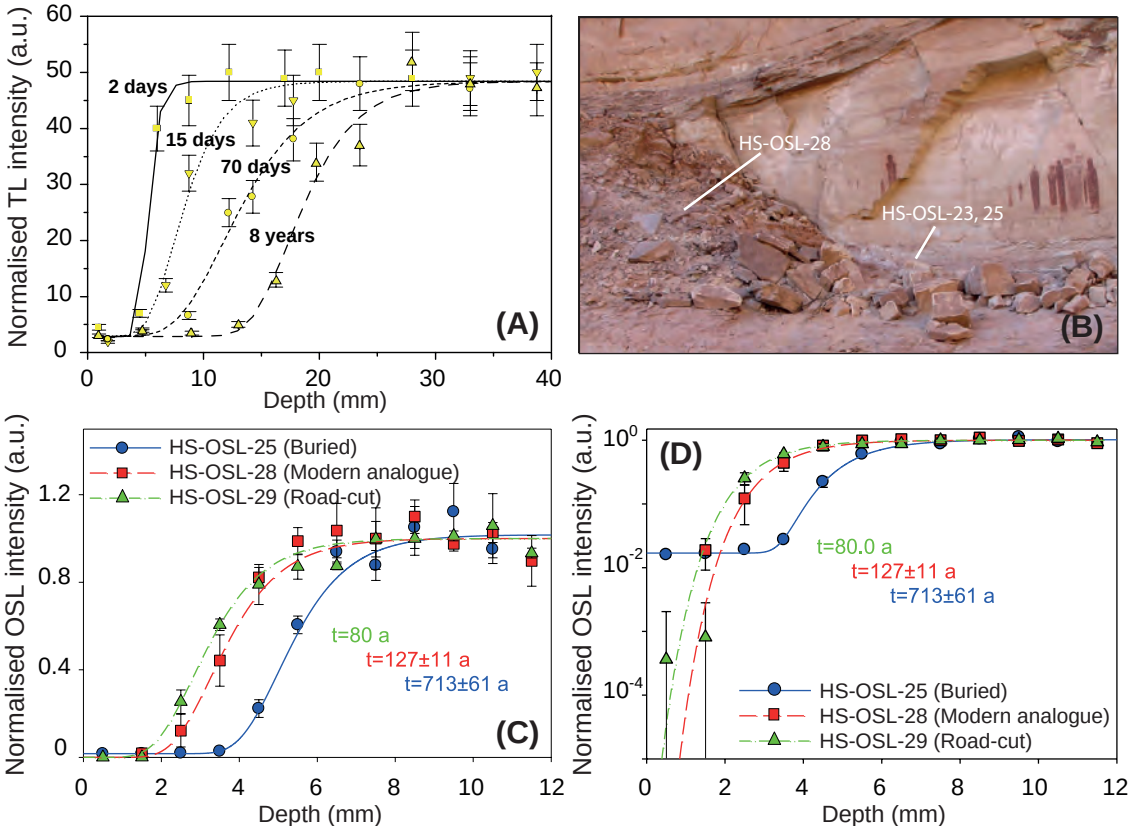

Figure 11.7 A) Experimental quantification of TL signal bleaching within a marble surface for various exposure times (Pentelic marble); modified from Polikreti *et al.* (2003). B) Picture of the Great Gallery rock art panel (southeastern Utah, USA) showing rock art, the rockfall and sample locations of the buried rock art (HS-OSL-25, ~40-cm thick), the underlying sediments (HS-OSL-23) and the modern analogue sample (HS-OSL-28); modified from Chapot *et al.* (2012). C) and D) OSL data from different samples (average of at least three aliquots for each depth, error bars represent one standard error) and fitted bleaching model to constrain the bleaching parameters (road cut) and quantify the exposure time (modern analogue and buried sample). See locations in (B) and note the logarithmic scale in (D) from which the OSL signal build up in sample HS-OSL-25 can be assessed and related to post-rockfall burial; modified from Sohbati *et al.* (2012c).

cross-checking following combined OSL protocols is recommended for applying rock surface dating in archaeological investigations. This approach has recently been used by Liritzis and Vafiadou (2015), who obtained ages between 3 and 8 ka for several archaeological sites located in Egypt. They extracted grains from various lithologies (granite, limestone, sandstone, dacite etc.) and used different OSL (SAR and SAAD) and TL (MAAD) protocols. Their strategy allowed them to compare the bleaching properties of different lithologies and stimulation types (e.g. the OSL signal is bleached more rapidly in sandstone than in granite, whereas the opposite trend can be observed for the TL signal). They also confirmed the potential of dating old archaeological monuments composed of carved granites, sandstones or limestones, using a combined TL and OSL approach, although the latter may present several advantages (except for limestone) regarding dating accuracy and measurement efficiency.

Another original application of rock surface dating, coupled with surface-exposure dating, is the investigation of historical rock art from the Great Gallery rock art panel in the Canyonlands National Park (southeastern Utah, USA; Fig. 11.7B). The age of the paintings has been highly debated, with hypotheses spanning the entire Holocene epoch (Pederson *et al.* 2014). Some of the paintings were damaged by a rockfall, burying them under sediment (HS-OSL-25 and -23 on Fig. 11.7B respectively). This configuration allowed investigation of both (1) the exposure time of the painted rock surface, and (2) the burial time of the rock and sediments using rock surface OSL dating (Chapot *et al.* 2012; Sohbati *et al.* 2012c). Rock samples (sandstones) were gently abraded to extract quartz grains from different depths below the painted surface (HS-OSL-25, Fig. 11.7B) and below the exposed surface of a modern analogue rock fall (HS-OSL-28, Fig. 11.7B). The OSL signals were then measured and showed bleaching within the first 2–5 mm below the exposed surface (Fig. 7C). Using a road cut of known age (HS-OSL-25, Fig. 11.7C) to constrain the bleaching rate for this specific site and lithology, Sohbati *et al.* (2012c) were able to quantify the exposure time of both the modern analogue (~130 years) and the rock art (~700 years, Fig. 11.7C). By further investigating the dose within the first ~2 mm below the surface, they were also able to quantify a finite OSL signal that had accumulated during burial subsequent to the rockfall (Fig. 11.7D, note the logarithmic-scale of the *y*-axis) which was not observed for the road cut nor the modern analogue (Fig. 11.7D). A burial age of ~900 yr was obtained for this sample, in agreement with the OSL age of the underlying sediment (Chapot *et al.* 2012). This original approach provided a precise time range (i.e. between 900 and 1600 years) for the origin of the Great Gallery rock art panel, coinciding with the development of the local Fremont culture (Pederson *et al.* 2014).

The application of OSL rock surface dating to buried cobbles/pebbles, in association with classical OSL dating of surrounding sediments, has also been successfully investigated in various archaeological contexts. Sohbati *et al.* (2012a) analyzed quartzite cobbles deposited by alluvial processes within an archaeological pavement (Tapada do Montinho, Portugal). Based on OSL rock surface dating they identified different potential resetting events (i.e. daylight exposure of the cobbles) of as old as 40–45 ka and between 20 and 14 ka. Sohbati *et al.* (2012a) thus proposed a complex evolutionary history for this pavement, with surficial erosion due to anthropogenic activity. They further investigated this complex history with potential multiple exposure/burial events for the pavement cobbles, their results (1) explained the younger than expected OSL ages obtained for the overlying sediments, and (2) provided a chronology for the evolution of this archaeological site.

Freiesleben *et al.* (2015) and Sohbati *et al.* (2015) have developed and successfully applied a mathematical model to quantify multiple exposure/burial events from the OSL rock surface dating of a single cobble (see Section 11.4). Freiesleben *et al.* (2015) investigated IRSL signals ($IRSL_{50}$ and $pIR\text{-}IRSL_{290}$) from a cross-section of a granitic cobble excavated from an archaeological site (Aarhus, Denmark). The measured IRSL profiles through the cobble (~70 mm in total) allowed them to identify a first exposure event of ~0.5 ka (cobble usage) before burial during 1.3–1.7 ka and recent excavation. Moreover, they also showed that different cobble surfaces (i.e. bottom *vs.* top surfaces) might yield complementary information about the cobble's full exposure/burial history (Freiesleben *et al.* 2015).

Sohbati *et al.* (2015) investigated a prehistoric cult site in the Negev desert (Israel) using a pavement cobble (Fig. 11.8B) and underlying sediments for OSL dating. They

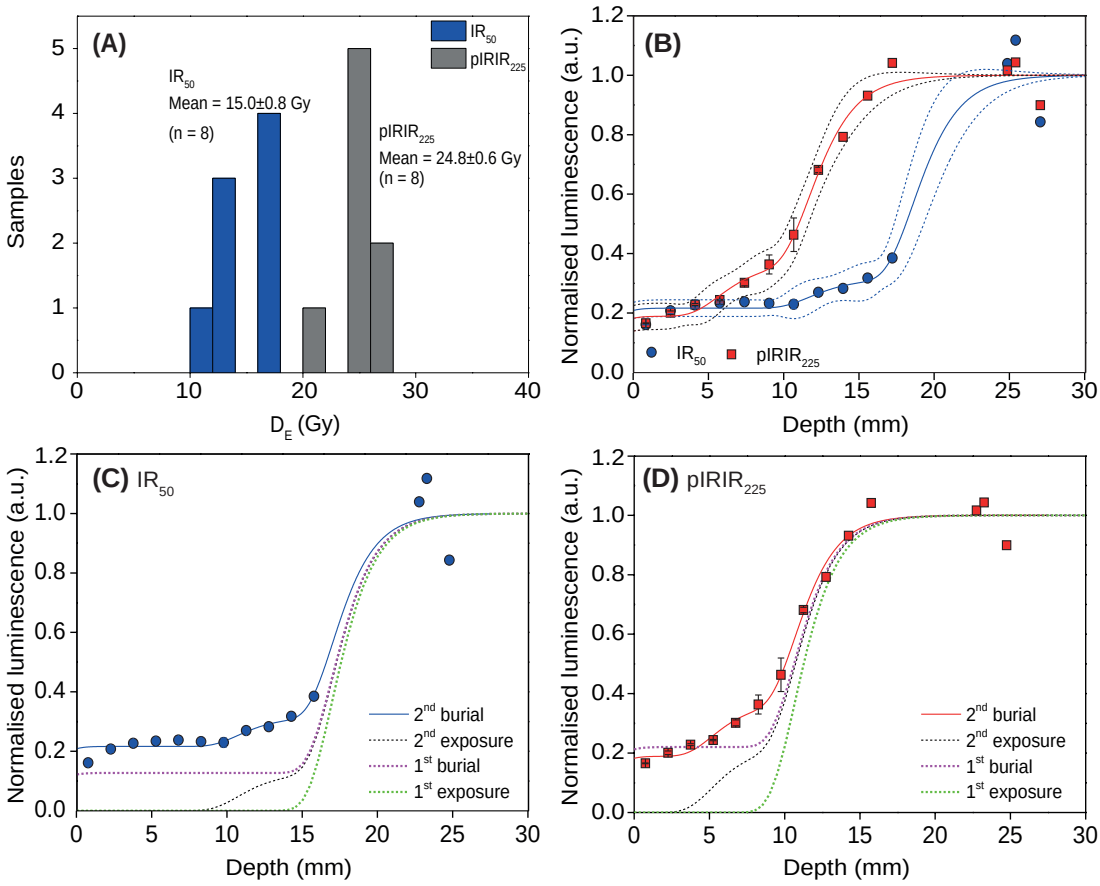

Figure 11.8 OSL rock surface dating (exposure and burial) of desert pavement. A) Equivalent doses using two IRSL signals from surface rock slices extracted from the buried cobble in the pavement. B) Measured IRSL signals with depth into the buried surface of the cobble, showing different bleaching characteristics between the two IRSL signals. The envelopes represent the model fits shown in C and D. C) and D) Model fits comprising multiple exposure/burial events which are able to reproduce the measured IRSL signals with depth; modified from Sohbati *et al.* (2015).

used two complementary IRSL signals (Fig. 11.8) to first derive equivalent doses from surface rock slices (Fig. 11.8A) and thus to determine the latest burial event at ~4 ka, consistent with OSL ages from underlying sediments. However, these well-constrained burial ages differed by 3–4 ka from the expected construction age of this archaeological site, indicating a potentially complex exposure history of the studied pavement. Using the full IRSL profiles from the cobble (Fig. 11.8B), Sohbati *et al.* (2015) showed that it had experienced at least two exposure events (with the earlier event having a longer duration than the more recent one) separated by an intermediate burial event which is of similar duration to the latest burial event (4–5 ka). This complex history is in agreement with the expected construction age of the site (~7–8 ka) and indicates later human intervention with the pavement (~4 ka ago). This highlights the potential of OSL rock surface dating and luminescence-depth profiles to provide tight temporal constraints on the bleaching history of rock surfaces that may not be available from conventional OSL dating on the underlying unconsolidated sediments.

11.4.2 Palaeoenvironmental applications

One novel and promising application of OSL rock surface dating has been proposed by Simms *et al.* (2011) for relative sea-level reconstructions from raised beaches in Antarctica (Fig. 11.9). They proposed the application of OSL dating on quartz mineral extracts from beach cobbles. Simms *et al.* (2011) focused on small granitic cobbles (maximum 1 dm^3, Fig. 11.9A) to ensure that the cobbles had been rotated in the intertidal zone before beach fossilisation and thus that the OSL signal has been fully bleached before beach abandonment. Simms *et al.* (2011) obtained OSL ages for beach fossilisation over the last ~2 ka that were in good agreement with independent ^{14}C dating (Fig. 11.9B), confirming the potential of the method for investigating beach dynamics, especially in high-latitude environments where organic matter is scarce and thus ^{14}C dating may not be applicable.

Based on these promising results, Simms *et al.* (2012) quantified the timing of the most recent Neoglacial ice advance during the Little Ice Age (~300–500 yr ago) and subsequent glacio-isostatic adjustment of raised beaches in Antarctica (South Shetland Islands), revealing an increase in surface uplift rates (from ~2 to 12 mm yr^{-1}) following the ice retreat. Simkins *et al.* (2013) also investigated raised beaches in Antarctica (Marguerite Bay, western Antarctic Peninsula), showing that raised beaches more than 21 m above sea level. might be of pre-LGM age and have been reworked during late-Pleistocene glacial advances. As a result, they proposed that the relative sea-level fall in the area has been only half that previously quantified for the Holocene period. Moreover, their study indicates potential complexities for luminescence dating of modern and recently raised beaches due to post-depositional reworking of cobbles by storm waves. The impact of storm events requires further investigation for studies focused on Holocene sea-level reconstruction which use fossil beach ridges as well as the modern beach surface to quantitatively evaluate the bleaching variability in cobbles and their associated burial ages.

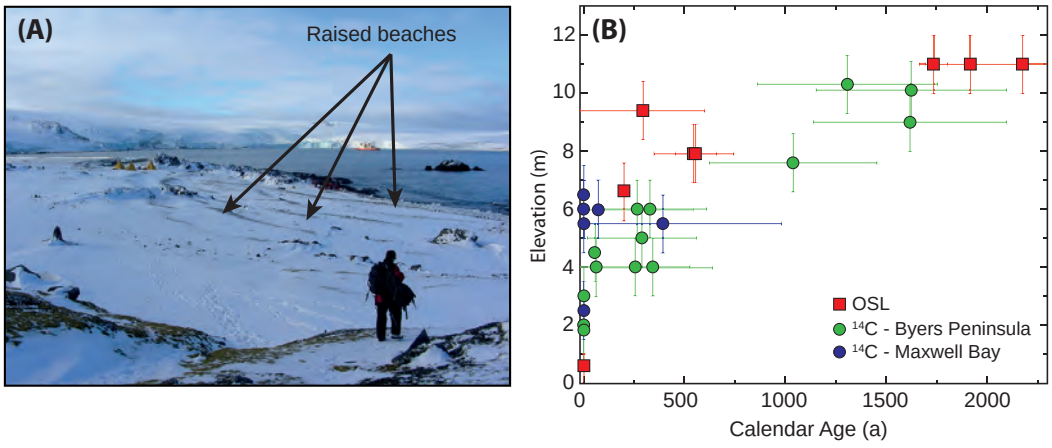

Figure 11.9 A) Picture of raised beaches (South Shetland Islands, Antarctica). B) Relative sea-level reconstruction from raised marine features in the South Shetland Islands, showing good agreement between OSL rock surface dating and independent ^{14}C dating. Modified from Simms *et al.* (2011).

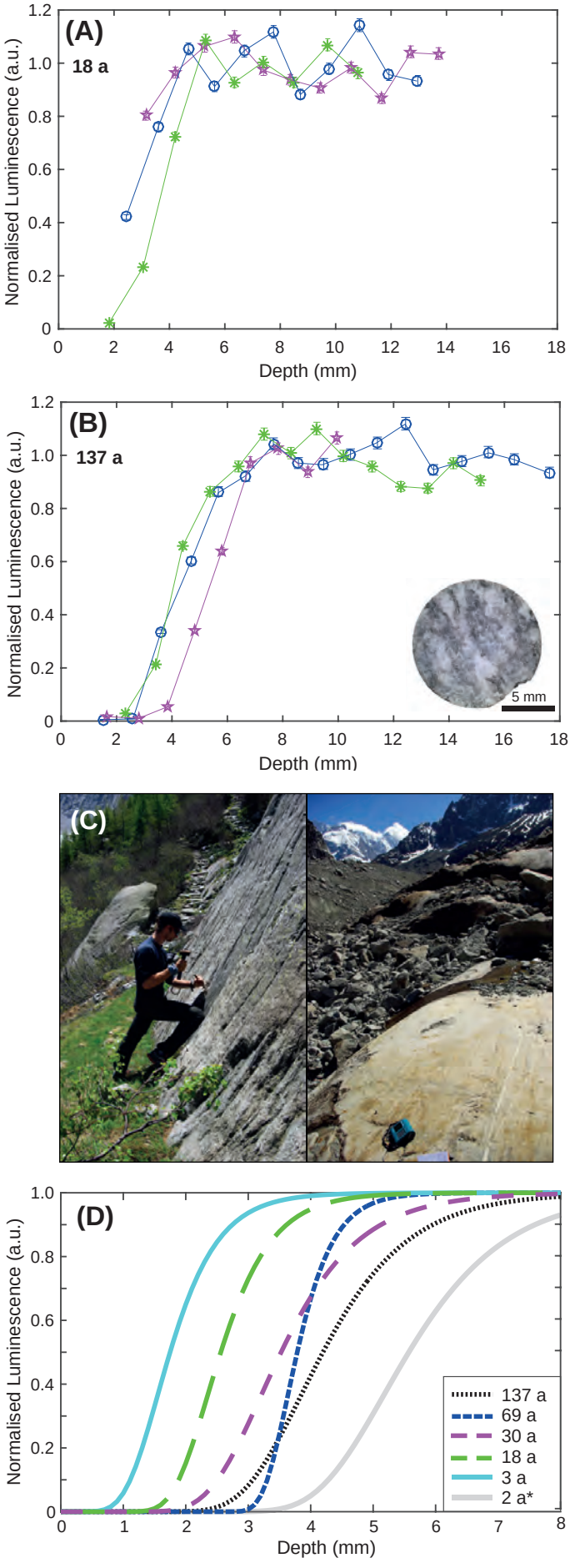

Figure 11.10 Palaeo-glacier reconstruction of the Mer de Glace (Mont-Blanc massif, France) since the Little Ice Age (LIA). A) and B) IRSL signal (measured at 50°C) with depth for two samples with exposure durations of 18 yr (A) and 137 yr (B). Exposure times are reconstructed from historical archives (Vincent *et al.* 2014). Each coloured data point represents an individual rock slice (example shown as inset in B), with three cores for each sample. C) Pictures of sampling sites for LIA (left) and modern (right) glacially polished bedrock surfaces. D) Best-fitting models for IRSL data for all samples studied (raw data are shown for two samples in panels A–B; the reader is referred to Lehmann *et al.* 2018 for the complete dataset), showing a propagating bleaching front within the first 1–4 mm with increasing exposure time (3–137 yr). Note that the granitic sample (*) with 2-yr exposure shows a completely different bleaching profile, highlighting the influence of lithology for OSL rock surface-exposure dating. Modified from Lehmann *et al.* (2018).

Finally, OSL rock surface dating has also been recently investigated in glacial and proglacial environments, with interesting potential for dating palaeo-glacier fluctuations and associated sediment deposits. These applications are especially promising as conventional OSL sediment dating can be challenging in such environments (Fuchs and Owen 2008; Chapter 6). Lehmann *et al.* (2018) worked on glacially polished bedrock surfaces from the Mer de Glace (Mont-Blanc massif, France; Fig. 11.10) to investigate whether post-Little Ice Age (LIA) glacier retreat can be constrained from OSL rock surface-exposure dating. They collected glacially polished bedrock surfaces with morphological evidence for glacier erosion (i.e. glacial striations; Fig. 11.10C) and measured the IRSL signal at 50°C on individual rock slices (see example in Fig. 11.10B). Their results showed bleaching of the IRSL signal at different depths, dependent on the exposure time (Fig. 11.10A–B). Using the bleaching model proposed by Sohbati *et al.* (2012c), they were able to reproduce the observed IRSL data and bleaching depths for exposed glacial bedrock surfaces from 3 to 137 years (Fig. 11.10D). Their results also confirmed the strong dependence of IRSL signal bleaching on rock lithology, with significant differences in the bleaching profiles between gneiss and granite rock surfaces with similar exposure times (Fig. 11.10D). This study highlights the potential of using OSL rock surface-exposure dating to reconstruct recent (i.e. post-LIA) glacier fluctuations, especially because the technique is sensitive over the first 1 cm of the bedrock (Fig. 11.10), which would be eroded even during a short (decades long) glacial re-advance. Further investigation is needed to evaluate the possibility of extending this approach over longer timescales (i.e. Late Pleistocene to Holocene) for which surface weathering and thus erosion might be problematic (c.f. Sohbati *et al.* 2018).

OSL rock surface-exposure dating applied to glacially polished bedrock can also be combined with another application of OSL rock surface dating focused on glacial/proglacial deposits, opening new directions for palaeoglacier reconstructions. Rades *et al.* (2018) sampled morainic boulders in the Malta valley (Austrian Alps) and measured $IRSL_{50}$ profiles, revealing that the IRSL signals had been fully bleached before deposition and thus demonstrating the potential of cobble surface dating for constraining the timing of moraine deposition. Jenkins *et al.* (2018) followed the same approach by collecting fluvioglacial cobbles within a late-glacial sandur (Isle of Man and Scotland). They measured both $IRSL_{50}$ and post-IR $IRSL_{225}$ signal depth profiles, showing that some of the collected pebbles have experienced bleaching of the IRSL signal into the cobble subsurfaces to ~4–10 mm, allowing the dose acquired post-burial to be quantified and thus to evaluate the depositional age of those cobbles. These two preliminary studies have revealed the potential of OSL rock surface dating in glacial and periglacial environments, where conventional sediment dating can be difficult due to challenges of partial bleaching within unconsolidated sediments (Chapter 6). However, further investigations are required regarding dose rate determination in such settings, where sediment grain size as well as water content is highly variable (see Section 11.5).

11.5 CONCLUSIONS AND OUTLOOK

Luminescence rock surface and rock surface-exposure dating are techniques that are in their early stages of development. They offer the potential to constrain surface processes and archaeological events that were previously challenging to date, and it is anticipated that both methods will be widely developed and applied over the coming years. Sample

preparation protocols must become more firmly established including identifying the causes of variability between luminescence measurements from rock slices and grains extracted from bedrock. Once this has been achieved the more significant challenges can be addressed. For luminescence rock surface dating, this comprises developing strategies for robust environmental dose rate determination, where complex geometries, varied clast sizes, varied water contents and microdosimetry influence the precision of determined ages. For luminescence rock surface-exposure dating, a means of robustly determining the light attenuation and luminescence signal bleaching rates for samples of different lithologies and locations is essential for this method to be widely adopted. Furthermore, the effect (if any) of erosion on the determination of luminescence surface-exposure ages must also be quantified. Nonetheless, both rock surface and rock surface-exposure dating are incredibly promising, and represent exciting new frontiers in luminescence dating research.

REFERENCES

Aitken, M.J. 1985. *Thermoluminescence Dating*. Academic Press.

Armitage, S.J. and King, G.E. 2013. Optically stimulated luminescence dating of hearths from the Fazzan Basin, Libya: A tool for determining the timing and pattern of Holocene occupation of the Sahara. *Quaternary Geochronology* 15, 88–97.

Buscombe, D. 2013. Transferable wavelet method for grain-size distribution from images of sediment surfaces and thin sections, and other natural granular patterns. *Sedimentology* 60, 1709–1732.

Buylaert, J.P. Murray, A.S. Gebhardt, C. Sohbati, R. Ohlendorf, C. Thiel, C. and Zolitschka, B. 2013. Luminescence dating of the PASADO 5022-1D core using IRSL signals from feldspar. *Quaternary Science Reviews* 71, 70–80.

Chapot, M.S. Sohbati, R. Murray, A.S. Pederson, J.L. Rittenour, T.M. 2012. Constraining the age of rock art by dating a rockfall event using sediment and rock-surface luminescence dating techniques. *Quaternary Geochronology* 13, 18–25.

Duller, G.A. 2008. Single-grain optical dating of Quaternary sediments: Why aliquot size matters in luminescence dating. *Boreas* 37, 589–612.

Durcan, J.A. King, G.E. and Duller, G.A. 2015. DRAC: Dose rate and age calculator for trapped charge dating. *Quaternary Geochronology* 28, 54–61.

Freiesleben, T. Sohbati, R. Murray, A. Jain, M. Al Khasawneh, S. Hvidt, S. and Jakobsen, B. 2015. Mathematical model quantifies multiple daylight exposure and burial events for rock surfaces using luminescence dating. *Radiation Measurements* 81, 16–22.

Fuchs, M. Owen, L.A. 2008. Luminescence dating of glacial and associated sediments: review, recommendations and future directions. *Boreas* 37, 636–659.

Gliganic, L.A., Meyer M.C., Sohbati, R., Jain, M., Barrett, S. (in press). OSL surface exposure dating of a lithic quarry in Tibet: Laboratory validation and application. *Quaternary Geochronology*.

Gösku, H.Y. Fremlin, J.H. Irwin, H.T. and Fryxell, R. 1974. Age determination of burned flint by a thermoluminescent method. *Science* 183, 651–654.

Greilich, S. Wagner, G. A. 2006. Development of a spatially resolved dating technique using HR-OSL. *Radiation Measurements* 41, 738–743.

Greilich, S. Glasmacher, U.A. Wagner, G.A. 2005. Optical dating of granitic stone surfaces. *Archaeometry* 47, 645–665.

Guérin, G. Mercier, N. Nathan, R. Adamiec, G. and Lefrais, Y. 2012. On the use of the infinite matrix assumption and associated concepts: A critical review. *Radiation Measurements* 47, 778–785.

Guralnik, B. Ankjærgaard, C. Jain, M. Murray, A.S. Müller, A. Wälle, M. Lowick, S.E. Preusser, F. Rhodes, E.J. Wu, T.S. and Mathew, G. 2015. OSL-thermochronometry using bedrock quartz: A note of caution. *Quaternary geochronology* 25, 37–48.

Habermann, J. Schilles, T. Kalchgruber, R. Wagner, G.A. 2000. Steps towards surface dating using luminescence. *Radiation Measurements* 32, 847–851.

Jenkins, G. T. H., Duller, G. A. T., Roberts, H. M., Chiverrell, R. C. and Glasser, N. F. 2018. A new

approach for luminescence dating glaciofluvial deposits: High precision optical dating of cobbles. *Quaternary Science Reviews* 192, 263–273.
Kars, R.H. Reimann, T. Ankjærgaard, C. and Wallinga, J. 2014. Bleaching of the post-IR IRSL signal: New insights for feldspar luminescence dating. *Boreas* 43, 780–791.
King, G.E. Herman, F. Lambert, R. Valla, P.G. and Guralnik, B. 2016a. Multi-OSL-thermochronometry of feldspar. *Quaternary Geochronology* 33, 76–87.
King, G.E. Herman, F. and Guralnik, B. 2016b. Northward migration of the eastern Himalayan syntaxis revealed by OSL thermochronometry. *Science* 353, 800–804.
Laskaris, N. Liritzis, I. 2011. A new mathematical approximation of sunlight attenuation in rocks for surface luminescence dating. *Journal of Luminescence* 131, 1874–1884.
Lehmann, B. Valla, P.G. King, G.E. Herman, F. 2018. Reconstruction of glacier vertical fluctuation in the Western Alps using OSL surface exposure dating. *Quaternary Geochronology* 44, 63–74.
Liritzis, I. 1994. A new dating method by thermoluminescence of carved megalithic stone building. *Comptes rendus de l'Académie des sciences. Série 2. Sciences de la terre et des planets* 319, 603–610.
Liritzis, I. Vafiadou, A. 2015. Surface luminescence dating of some Egyptian monuments. *Journal of Cultural Heritage* 16, 134–150.
Liritzis, I. Guibert, P. Foti, F. and Schvoerer, M. 1996. Solar bleaching of thermoluminescence of calcites. *Nuclear Instruments and Methods in Physics Research Section B: Beam Interactions with Materials and Atoms* 117, 260–268.
Liritzis, I. Vafiadou, A. Zacharias, N. Polymeris, G.S. and Bednarik, R.G. 2013. Advances in surface luminescence dating: New data from selected monuments. *Mediterranean Archaeology and Archaeometry* 13, 105–115.
Liu, J. Murray, A. Sohbati, R. and Jain, M. 2016. The effect of test dose and first IR stimulation temperature on post-IR IRSL measurements of rock slices. *Geochronometria 43*, 179–187.
Meyer, M.C., Gliganic, L.A., Jain, M., Sohbati, R., Schmidmair, D. (in press). Lithological controls on light penetration into rock surfaces: Implications for OSL and IRSL surface exposure dating. *Radiation Measurements*.
Morgenstein, M. E. Luo, S. Ku, T. L. and Feathers, J. 2003. Uranium-series and luminescence dating of volcanic lithic artefacts. *Archaeometry* 45, 503–518.
Pederson, J.L. Chapot, M.S. Simms, S.R. Sohbati, R. Rittenour, T.M. Murray, A.S. Cox, G. 2014. Age of Barrier Canyon-style rock art constrained by cross-cutting relations and luminescence dating techniques. *Proceedings of the National Academy of Sciences*, 111(36), 12986–12991.
Polikreti, K. Michael, C.T. and Maniatis, Y. 2002. Authenticating marble sculpture with thermoluminescence. *Ancient TL* 20, 11–18.
Polikreti, K. Michael, C.T. and Maniatis, Y. 2003. Thermoluminescence characteristics of marble and dating of freshly excavated marble objects. *Radiation Measurements* 37, 87–94.
Rades, E.F., Sohbati, T., Lüthgens, C., Jain. M. and Murray, A.S. 2018. First luminescence-depth profiles from boulders from moraine deposits: Insights into glaciation chronology and transport dynamics in Malta valley, Austria. *Radiation Measurements*.
Richards, M.P. 1994. Luminescence dating of quartzite from the Diring Yuriakh site. M.A. thesis, Simon Fraser University, unpublished.
Roberts, R.G. 1997. Luminescence dating in archaeology. *Radiation Measurements* 27, 819–892.
Sawakuchi, A.O. Blair, M.W. DeWitt, R. Faleiros, F.M. Hyppolito, T. Guedes, C.C.F. 2011. Thermal history versus sedimentary history: OSL sensitivity of quartz grains extracted from rocks and sediment. *Quaternary Geochronology* 6, 261–272.
Simkins, L.M. Simms, A.R. DeWitt, R. 2013. Relative sea-level history of Marguerite Bay, Antarctic Peninsula derived from optically stimulated luminescence-dated beach cobbles. *Quaternary Science Reviews* 77, 141–155.
Simkins, L.M. DeWitt, R. Simms, A.R. Briggs, S. and Shapiro, R.S. 2016. Investigation of optically stimulated luminescence behavior of quartz from crystalline rock surfaces: A look forward. *Quaternary Geochronology* 36, 161–173.
Simms, A.R. DeWitt, R. Kouremenos, P. and Drewry, A.M. 2011. A new approach to reconstructing sea levels in Antarctica using optically stimulated luminescence of cobble surfaces. *Quaternary Geochronology* 6, 50–60.
Simms, A.R. Ivins, E.R. DeWitt, R. Kouremenos, P. Simkins, L.M. 2012. Timing of the most recent Neoglacial advance and retreat in the South Shetland Islands, Antarctic Peninsula: Insights from raised beaches and Holocene uplift rates. *Quaternary Science Reviews* 47, 41–55.

Smedley, R.K. Duller, G.A.T. Pearce, N.J.G. and Roberts, H.M. 2012. Determining the K-content of single-grains of feldspar for luminescence dating. *Radiation Measurements* 47, 790–796.
Smedley, R.K. and Pearce, N.J.G. 2016. Internal U, Th and Rb concentrations of alkali-feldspar grains: Implications for luminescence dating. *Quaternary Geochronology* 35, 16–25.
Sohbati, R. Murray, A. Jain, M. Buylaert, J.P. and Thomsen, K. 2011. Investigating the resetting of OSL signals in rock surfaces. *Geochronometria 38*, 249–258.
Sohbati, R. Murray, A.S. Buylaert, J.P. Almeida, N.A. and Cunha, P.P. (2012a). Optically stimulated luminescence (OSL) dating of quartzite cobbles from the Tapada do Montinho archaeological site (east-central Portugal). *Boreas* 41, 452–462.
Sohbati, R. Jain, M. Murray, A.S. (2012b). Surface exposure dating of non-terrestrial bodies using optically stimulated luminescence: A new method. *Icarus* 221, 160–166.
Sohbati, R. Murray, A.S. Chapot, M.S. Jain, M. Pederson, J. 2012c. Optically stimulated luminescence (OSL) as a chronometer for surface exposure dating. *Journal of Geophysical Research: Solid Earth* 117(B9).
Sohbati, R. Murray, A.S. Jain, M. Thomsen, K. Hong, S-C. Yi, K. Choi, J-H. 2013. Na-rich feldspar as a luminescence dosimeter in infrared stimulated luminescence (IRSL) dating. *Radiation Measurements* 51–52, 67–82.
Sohbati, R. Murray, A.S. Porat, N. Jain, M. Avner, U. 2015. Age of a prehistoric 'Rodedian' cult site constrained by sediment and rock surface dating techniques. *Quaternary Geochronology* 30, 90–99.
Sohbati, R., Liu, J., Jain, M., Murray, A., Egholm, D., Paris, R., Guralnik, B. 2018. Centennial- to millennial-scale hard rock erosion rates deduced from luminescence-depth profiles. *Earth and Planetary Science Letters* 493, 218–230.
Spooner, N.A. 1994. The anomalous fading of infrared-stimulated luminescence from feldspars. *Radiation Measurements*, 23, 625–632.
Theocaris, P.S. Liritzis, I. Galloway, R.B. 1997. Dating of two Hellenic pyramids by a novel application of thermoluminescence. *Journal of Archaeological Science*, 24, 399–405.
Tribolo, C. Mercier, N. Valladas, H. 2003. Attempt at using the single-aliquot regenerative-dose procedure for the determination of equivalent doses of Upper Palaeolithic burnt stones. *Quaternary Science Reviews* 22, 1251–1256.
Vafiadou, A. Murray, A.S. Liritzis, I. 2007. Optically stimulated luminescence (OSL) dating investigations of rock and underlying soil from three case studies. *Journal of Archaeological Science* 34, 1659–1669.
Vincent, C. Harter, A. Gilbert, A. Berthier, E. Six, D. 2014. Future fluctuations of Mer de Glace, French Alps, assessed using a parameterized model calibrated with past thickness changes. *Annals of Glaciology* 55, 15–24.

10.5 Rétrospective : Histoire et évolution des glaciers de la vallée de Chamonix

Benjamin Lehmann[1]

[1] Institute of Earth Surface Dynamics, University of Lausanne, Lausanne, 1012, Switzerland.

Communication paper

Bulletinde la Société de des Sciences Naturelles Vaudoise

Author contributions. BL write the manuscript.

Tableau 14. Résultats des captures des musaraignes effectuées en juin 2017 dans les bois du Jorat lors des journées de la biodiversité.

Lieu-dit	Taxon	Sexe	Poids (g)	État
Ruisseaux de Latigny (Bérallaz)	*Noemys fodiens*	Femelle	24	Post-allaitante
		Mâle	14	Jeune
		Mâle	13	Jeune
		Mâle	15	Jeune
		Mâle	14	Jeune
		Femelle	15	Jeune
		Femelle	16	Jeune
		Femelle	15	Jeune
	Sorex minutus	Femelle	5.5	Post-allaitante
Ruisseau de Bénenté	-			
Ruisseau le Talent, lieu-dit les trois fontaines	*Neomys fodiens*	Mâle	20	Adulte
	Sorex coronatus/araneus	Mâle	10	Jeune

Bibliographie

Cantoni D., 1995. *Neomys fodiens*. *In* Hausser, J. (Ed.). Mammifères de la Suisse. Mémoires de l'Académie Suisse des Sciences Naturelles, Volume 103. Birkhaüser Verlag, Basel. 501 p.

Churchfield S., 1985. The feeding ecology of the European Water shrew. *Mammal Review* 15: 13-21.

Dupasquier A. & Cantoni D., 1992. Shifts in benthic macroinvertebrate community and food habits of the water shrew, Neomys *fodiens* (Soricidae, Insectivora). *Acta Oecologica* 13: 81-99.

Genoud M., 1995. *Crocidura russula*. *In* Hausser, J. (Ed.). Mammifères de la Suisse. Mémoires de l'Académie Suisse des Sciences Naturelles, Volume 103. Birkhaüser Verlag, Basel. 501 p.

Greenwood A., Churchfield S., Hickey C., 2002. Geographical distribution and habitat occurrence of the Water Shrew (*Neomys fodiens*) in the Weald of South-East England. *Mammal Review* 32: 40-50.

Hausser J., 1995. *Sorex coronatus*. *In* Hausser, J. (Ed.). Mammifères de la Suisse. Mémoires de l'Académie Suisse des Sciences Naturelles, Volume 103. Birkhaüser Verlag, Basel. 501 p.

Lugon-Moulin N., 2003. Les musaraignes, biologie, écologie, répartition en Suisse. Éditions Porte-Plumes, Vissoie (Suisse). 308 p.

Scott D. M., Southgate F., Overall A. J., Waite S. & Tolhurst B. A., 2012. The Eurasian water shrew: an unsuitable candidate species for a vertebrate bio-indicator of aquatic pollution. *Journal of Zoology* 286: 30-37.

Tiberti R. & Mori E., 2016. Considerations on the vulnerability of the Eurasian water shrew *Neomys fodiens* to the presence of introduced brown trout *Salmo trutta*. *Biologia* 71: 721-725.

Vogel P., 1976. Energy consumption of European and African shrews. *Acta Theriol*. 21: 195-206.

Vogel P., 1980. Metabolic levels and biological strategies in shrews. *In*: Schmidt-Nielsen K., Bolis L. & Taylor C. R. (eds.) Comparative physiology: Primitive mammals. Cambridge University Press. Cambridge (UK) 338 pp.

Rétrospective

Par

Benjamin LEHMANN

Histoire et évolution des glaciers de la vallée de Chamonix

Bulletin d'observation glaciaire il y a 150 ans

« Il y a 10 ans, lorsque je plantai mes premiers jalons pour étudier le mouvement du glacier des Bois, il était à 200 mètres de la pierre qui porte la date de 1826, il avait donc pendant les 29 ans fait une retraite moyenne de 7 mètres environ par an. » C'est ainsi que le naturaliste chamoniard, Venance Payot décrivit il y a 150 ans le retrait du Glacier du Bois, la Mer de Glace comme on l'appelle maintenant (Payot 1868). La pierre dont il fait la référence fut placée en 1826 pour matérialiser le plus grand développement du glacier durant le siècle. Ce fut le dernier sursaut glaciaire d'une époque plus froide en Europe entre 1350 et 1850: le Petit Âge Glaciaire. Cette période propice au développement des glaciers fut la plus grande poussée glaciaire depuis la fin de la dernière glaciation, il y a 11 000 ans. Les glaciers alpins entamèrent par la suite un inexorable recul.

L'origine de la glaciologie

L'intérêt scientifique pour ces géants alpins fut d'abord stimulé par la crainte plus que par la curiosité. En mai 1595, la rupture d'une poche de glace du glacier du Giétroz situé dans le Val de Bagnes, à la hauteur de l'actuel barrage de Mauvoisin, détruisit plus de 500 bâtiments et tua 140 personnes. Une autre catastrophe historique survint après un éboulement au prin-

Figure 1. Le lac de Mauvoisin et glacier du Giétroz en 1818 (gietroz1818.ch)

Figure 2. Bloc erratique « La Pierre à Cambot » à Lausanne, canton de Vaud en Suisse. Photo L. Péron (wikimedia.org)

temps 1818, les blocs de glace bloquèrent les eaux de la Dranse et créèrent un barrage naturel. Un lac de 60 mètres de profondeur pour 3,5 km de longueur se forma en amont. Le 16 juin 1818, il se déversa brutalement ses 20 millions de mètres cube dans la vallée de la Dranse de Bagnes (figure 1). L'inondation et les blocs de glace atteignirent Martigny en 90 minutes et provoquèrent la mort de 44 personnes ainsi que de nombreux dégâts dans la région. La préoccupation engendrée par ces catastrophes glaciaires répétées mena à la réalisation de premières études scientifiques sur les glaciers. Il fallait les comprendre pour mieux s'en protéger.

La découverte de blocs de roches de provenances éloignées et donc qualifiés d'erratiques stimula aussi l'étude des glaciers. La taille des blocs, leur nature contradictoire avec leur environnement et leurs positions inexplicables par des processus géomorphologiques connus avaient intrigués les géologues. L'existence de ces blocs fut d'abord interprétée comme une preuve biblique du déluge. Louis Agassiz fut le premier à défendre la « théorie glaciaire » (Agassiz 1837). Il défendit durant le fameux « discours de Neuchâtel » et devant l'Académie helvétique des Sciences naturelles que les énormes accumulations de blocs erratiques avaient été formés par une ancienne extension glaciaire (figure 2). Dès lors l'intérêt scientifique pour les glaciers alpins ne fut que croissant.

Les glaciers alpins en chiffres

En 2017, les glaciers d'Europe centrale et d'Europe de l'Ouest représentaient une surface de 2000 km^2 (WGMS report, 2017). La plus grande partie de ces glaces est située dans les Alpes et le Grosser Aletschgletscher en Oberland bernois suisse est le plus grand. Les Alpes représentent le château d'eau de l'Europe et sont la source des bassins versants de la Mer Méditerranée, la Mer du Nord, le Nord de l'Océan Atlantique ainsi que la Mer Noire.

Dans le massif du Mont-Blanc, les glaciers couvrent une superficie de 145 km^2, dont 105 km^2 en France. Il abrite plus de 101 glaciers dont 15 glaciers de plus de 5 km^2 et parmi eux la Mer de Glace (34 km^2 et 11 km de longueur). Le volume d'eau solide des glaciers représente approximativement 12 km^3 (figure 3).

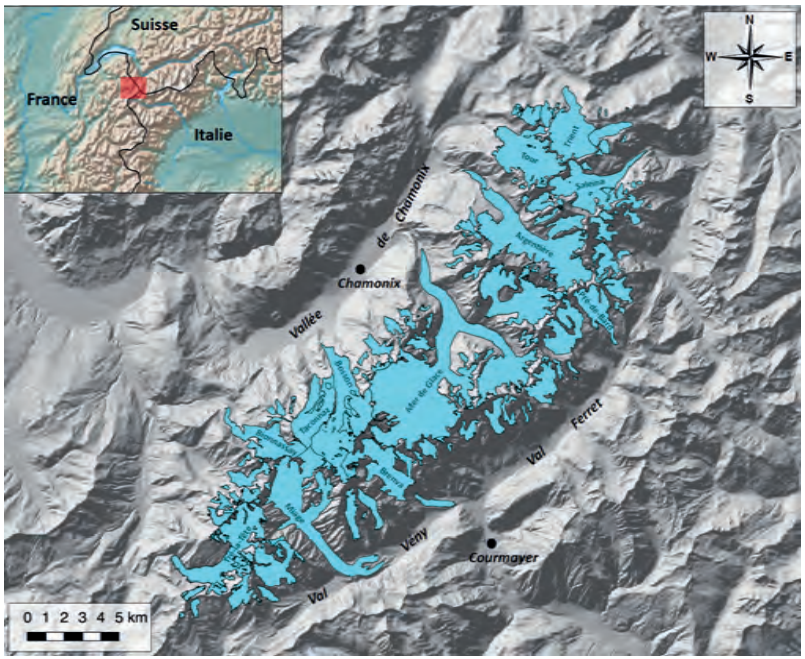

Figure 3. Etendue des glaciers du massif du Mont-Blanc. L'étendue des glaces a été téléchargée à partir de la base de données GLIMS (Global Land Ice Measurements from Space, Raup et al., 2007). Les étendues de glace de Suisse ont été produites à partir d'images de 2011 par Smiraglia *et al.* (2015). Les étendues de glace d'Italie ont été produites à partir d'images de 2009 par Fischer *et al.* (2015). Les étendues de glace de France ont été produites à partir d'images de 2004 par Rabatel *et al.* (2016).

Cela est bien peu par rapport aux glaciers de l'Antarctique (26 millions de km^3), du Groenland (4 millions de km^3), ou de l'ensemble des glaciers alpins (115 km^3). Si l'Antarctique venait à fondre en totalité, le niveau des mers remonterait de 60 mètres et de 7 mètres pour la fonte du Groenland. La contribution de la fonte des glaciers du Mont-Blanc serait, elle, inférieure à 1 centimètre.

L'histoire de l'étude des glaciers dans le Mont-Blanc

Dans le massif du Mont-Blanc, un événement décisif se produisit en 1741. Deux anglais, William Windham et Richard Pocke entreprirent un voyage à Chamonix, voyage motivé par la visite des « glacières » (le mot « glacier » étant encore inconnu). Guidés par les cristalliers, ancêtres des guides de Chamonix, ils atteignirent en quelques heures le site du Montenvers et découvrirent la « grande vallée de glace ». Windham en fit une description qui resta dans les mémoires « Il faut vous imaginer votre lac [le Léman] agité d'une grosse brise et gelé tout d'un coup. Encore ne sais-je si cela ferait précisément le même effet ». De cette comparaison est née l'expression « Mer de Glace », qui sera reprise pratiquement dans les mêmes termes d'un voyageur à l'autre. Cet événement marqua le début du tourisme alpin.

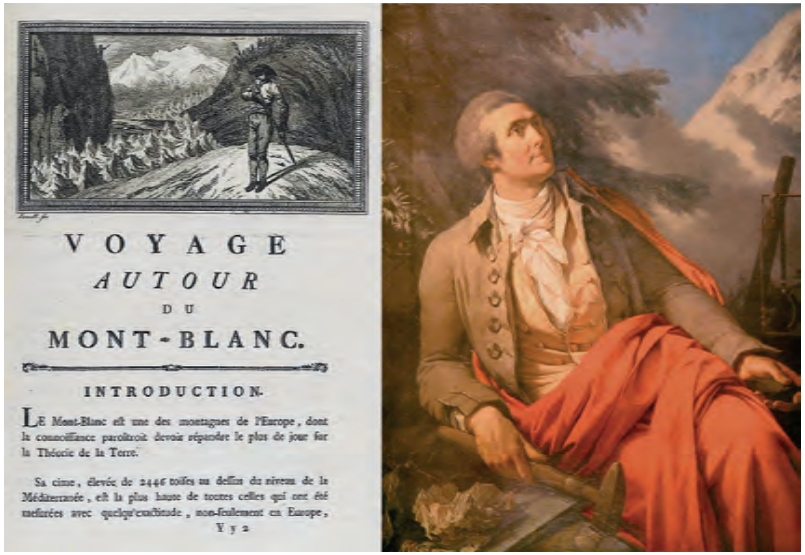

Figure 4. À gauche la première de couverture de d'œuvre de H.-B. de Saussure. À droite, son portait peint par Saint-Ours en 1796 (glaciers-climat.com).

Un autre personnage historique marqua l'exploration des glaciers du Mont-Blanc fut Horace-Bénédict de Saussure (1740-1799). Il peut être considéré comme le premier et, en quelque sorte, le plus grand savant de la montagne. De Saussure avait une réelle passion pour les montagnes, mais ses excursions étaient avant tout justifiées par la poursuite de la science. En parcourant de nombreuses régions des Alpes, de Saussure influença et stimula l'exploration et l'étude des milieux alpins. Son ouvrage « Voyages dans les Alpes » (de Saussure, 1779-1796), dont le premier volume parut en 1779, est devenu rapidement un classique (figure 4). Il fournit une quantité inégalée d'informations et d'observations sur la topographie, la géologie, les glaciers et la météorologie des Alpes.

En 1842, le physicien James David Forbes s'est établi sur la Mer de Glace et débuta une longue série de mesures du mouvement et de la température de la glace. C'est véritablement à la fin du XIX^{e} siècle que commencèrent les mesures systématiques. En France, de 1891 à 1899, Joseph Vallot mesura la vitesse de la glace sur la langue terminale de la Mer de Glace avec une ligne de pierres peintes. Cette méthode de relevés fut ensuite adoptée par les Eaux et Forêts de 1907 à 1960, fournissant une base de données unique sur un demi-siècle pour les changements de forme et d'écoulement des glaciers.

En raison de la facilité d'accès aux glaciers depuis la vallée de Chamonix, le massif du Mont-Blanc a vu se succéder des glaciologues de toutes nationalités. Les Liboutry, Reynaud, pour ne citer qu'eux, étudièrent les phénomènes glaciaires les plus variés. Depuis les années 1960, l'Institut des Géosciences de l'Environnement (IGE) de Grenoble a pris la suite.

Qu'est-ce qu'un glacier ?

Un glacier est un système pérenne à l'échelle humaine, stock d'eau solide (neige, névé, glace). Il se renouvelle continuellement, par le jeu combiné de l'accumulation (chutes de neige, neige apportée par le vent ou par les avalanches) en amont et de l'ablation à l'aval (fonte). Il s'écoule en permanence sous l'effet de son poids, des parties hautes, où l'accumulation l'emporte, vers les parties basses, où l'ablation domine (figure 5). L'altitude à laquelle l'accumulation égale l'ablation, où le bilan de masse entre le gain et la perte est nul, correspond à la ligne d'équilibre.

Dans la zone d'accumulation, l'apport de neige se transforme en glace. Les gels et dégels successifs compactent et arrondissent rapidement les cristaux de neige initiaux tandis que la porosité diminue. L'eau de fonte superficielle percole vers les couches inférieures et contribue au changement d'état de la neige, à sa métamorphose. La densité évolue de 0,04 à 0,40 pour la neige de saison, entre 0,5 et 0,7 pour une neige de névé et enfin de 0,84 à 0,90 pour la glace. En profondeur de la Mer de Glace, la glace a un âge supérieur à 100 ans. Suivant les conditions de pressions, de températures et les contraintes, les cristaux de glaces, tout petits au départ, vont croître d'environ un à deux dixièmes de millimètres par an, atteignant ainsi au cours du temps des tailles de plusieurs centimètres.

En dessous de la ligne d'équilibre, la glace apparaît à nu : la fonte annuelle devient plus importante que l'accumulation. Dans les Alpes, la position de cette ligne d'équilibre va dépendre de l'exposition et du vent mais est principalement contrôlée par la quantité de précipitation hivernale et par les températures estivales (Oerleman 2005).

Le rapport entre la surface de la zone d'accumulation d'un glacier et sa surface totale détermine l'état de santé du glacier. Il est couramment admis que si les deux tiers de la surface du glacier se situent en zone d'accumulation, le glacier est en équilibre climatique. Les mesures effectuées ces quinze dernières années dans les Alpes montrent que, en moyenne, seulement 30

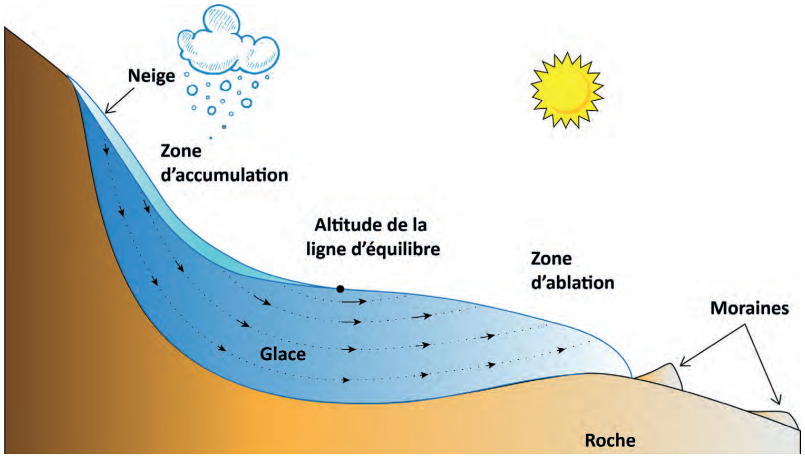

Figure 5. Coupe schématique d'un glacier. Les flèches représentent les vecteurs de vitesse d'écoulement. La glace est formée dans la zone d'accumulation à partir de la compaction de couches de neige. La glace disparaît dans la zone d'ablation. L'altitude de la ligne d'équilibre représente l'altitude où l'accumulation équivaut à l'ablation.

à 40 % de la surface totale des glaciers alpins est située en zone d'accumulation, démontrant la tendance inéluctable à la baisse de volume des glaciers.

Le bilan de masse d'un glacier tient compte, d'une part, de la quantité de glace accumulée, exprimée en hauteur d'eau et provenant des chutes de neige, et d'autre part de la quantité de glace perdue, elle aussi exprimée en hauteur d'eau, et principalement due à la fonte estivale. À une altitude de 2 890 m au-dessus du niveau marin et sur la période de 1995 à 2011 (Réveillet *et al.* 2017), la plupart des précipitations ont lieu sous forme solide sur le glacier d'Argentière. À partir de juin, la fusion estivale commence. Il reste en moyenne 3 à 4 m au col du Midi à 3 500 m représentant une accumulation équivalente à 2 m d'eau.

Il doit être mesuré tous les ans afin de connaître l'état de santé du glacier. La méthode classique consiste à mesurer l'émergence de balises implantées dans la glace en zone d'ablation. Ces balises permettent de connaitre la quantité de glace perdue mais aussi de mesurer le déplacement annuel du glacier. En zone d'accumulation, les mesures sont faites par pesée d'une carotte de neige subsistant à la fin de l'été. Toutes ces mesures sont converties en équivalence de hauteur d'eau. Au gain de la zone d'accumulation est soustrait la perte de la zone d'ablation. Si le bilan est positif, la ligne d'équilibre s'abaisse et, par conséquent, la masse du glacier augmente, ce qui se traduira après un laps de temps variable par une avancée du front du glacier. Si le bilan est négatif, le front du glacier recule, là aussi avec un certain décalage temporel. Le suivi annuel des bilans de masse constitue donc un indicateur fiable des modifications climatiques. C'est le cas depuis plus d'un demi-siècle pour la Mer de Glace et le glacier d'Argentière car la reconstitution historique de leurs variations a été possible.

L'étude du bilan de masse et plus généralement des glaciers a vécu une révolution technologique durant cette dernière décennie avec l'apparition de modèles numériques de terrain de haute précision. Ces modèles représentent numériquement la géographie d'une zone spécifique où à chaque pixel est attribué une latitude, une longitude et une altitude. La comparaison de modèles numériques de terrain de différentes époques permet d'étudier l'évolution de volumes au cours du temps. Le développement technologique de la dernière décennie a révolutionné les techniques de télédétection. Cette pratique d'acquisition à distance de données environnementales peut être effectuée depuis l'espace grâce aux satellites, depuis le ciel grâce à des avions ou des drones, ou depuis le sol en utilisant des caméras ou des lasers.

Le Petit Âge Glaciaire

Le Petit Âge Glaciaire (en anglais Little Ice Age) s'étendant de 1350 à 1850 après J.-C, et est caractérisé par la plus importante récurrence glaciaire des temps postglaciaires, avec quatre maxima : vers 1350, 1600, 1820 et 1850.

Cette période climatique froide a touché l'ensemble du globe et se caractérise par des avancées successives des glaciers, auxquelles correspondent plusieurs minima de températures moyennes très nets (1 à 1,5 °C de moins qu'aujourd'hui). Elle succède à l'optimum climatique médiéval. Elle est contemporaine d'une série d'hivers froids et d'étés frais. Ce refroidissement général est probablement la conséquence d'une période de faible activité solaire. Les études récentes de l'Institut des Géosciences de l'Environnement de Grenoble (IGE) et de l'Ecole Polytechnique Fédérale de Zurich (ETHZ) nous éclairent sur les causes de ces avancées glaciaires. Elles suggèrent qu'elles seraient plutôt dues à une augmentation notable des précipitations qu'à une baisse des températures. Ainsi, les crues glaciaires seraient la conséquence d'une

hausse de plus de 25 % des chutes de neige, tout particulièrement durant la première partie du Petit Âge Glaciaire. Cette situation a généré des bilans de masse positifs et, en conséquence un important développement des langues glaciaires.

Dans les Alpes, les traces du Petit Âge Glaciaire sont généralement bien soulignées par les immenses moraines latérales bâties ou simplement rechargées à cette époque, ainsi que par quelques moraines frontales situées à l'aval.

Dans le cas de La Mer de Glace, ou plutôt le Glacier des Bois comme il était nommé à l'époque, l'avancée maximale du front glaciaire est matérialisée par la pierre gravée 1926 mentionnée par Venance Payot en introduction. Un lent recul va ensuite débuter. Mais à partir de 1840, le Glacier des Bois progresse de nouveau et atteint une nouvelle position extrême en 1852. C'est à partir de 1870 qu'intervient le grand recul du Glacier des Bois. Après une courte crue en 1890 la langue glaciaire perd plus de 800 mètres en une quinzaine d'années (Mougin 1912). La glace se retire dans la gorge de l'Arveyron et disparaît aux yeux des Chamoniards après 1900 (figures 6 et 7).

L'évolution des glaciers du Mont-Blanc depuis le Petit Âge Glaciaire

L'histoire des glaciers alpins est faite de cycles, pouvant aller de quelques dizaines d'années à de longues périodes, comme le Petit Âge Glaciaire. Amorcé bien avant l'avènement de l'ère industrielle, le recul des glaciers a ensuite été constant, même si des ralentissements ou inversions ponctuelles de tendance au retrait ont été observés au XX^{e} siècle. À l'échelle des Alpes,

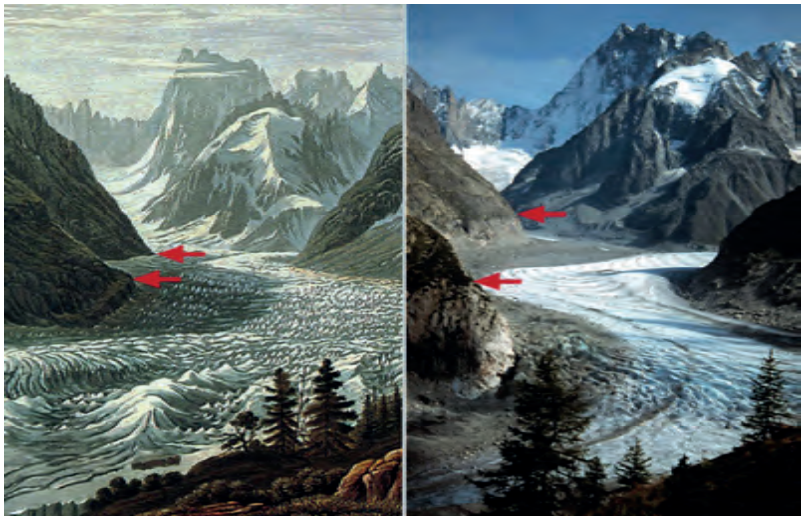

Figure 6. La Mer de Glace vue depuis le Montenvers, massif du Mont-Blanc, alpes françaises. À gauche, une peinture de Birman juste après le maxima du Petit Âge Glaciaire. La photographie de droite fut prise à la même position en 2000. Les flèches indiquent les mêmes positions sur la marge du glacier, et indiquent le niveau d'abaissement de la surface des glaciers. Peinture de la collection Gugelmann, Bibliothèque nationale suisse, Berne. Photo de M. J. Hambrey, 2000 (swisseduc.ch).

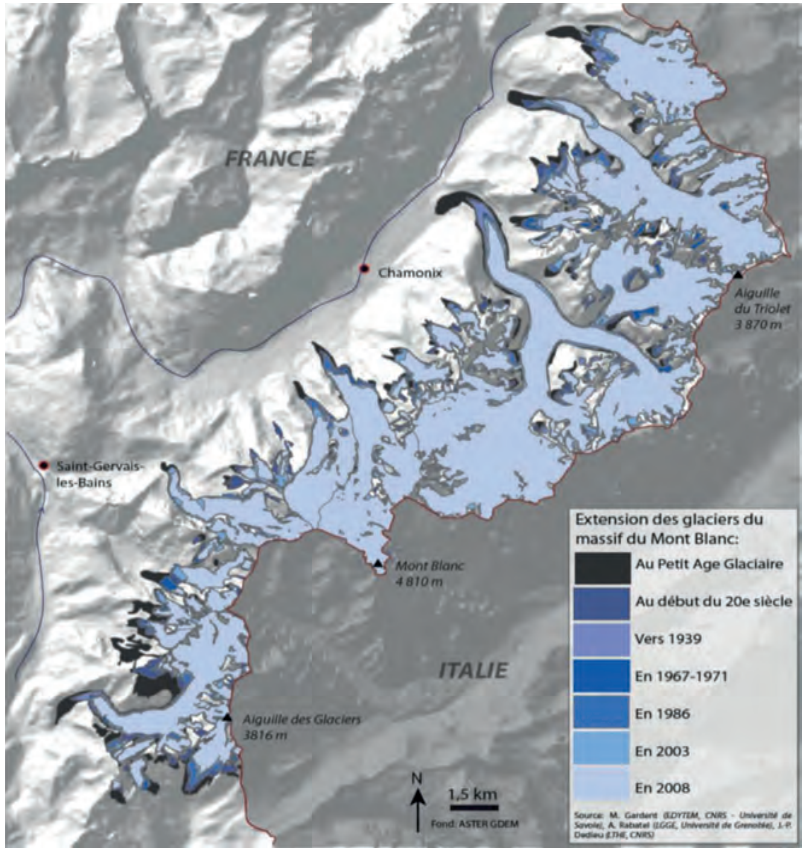

Figure 7. Carte diachronique d'extension des glaciers du massif du Mont-Blanc (Garden *et al.* 2014).

les glaciers alpins ont perdu 35 % de leur superficie totale entre 1850 et 1970 et près de 50 % en 2000 (Zemp *et al.* 2006).

L'analyse des mesures annuelles et des bilans de masse des glaciers du Mont-Blanc depuis le début du XX^{e} siècle montre quatre périodes d'alternance de crues et de décrues glaciaires. Entre le début du XX^{e} siècle et 1941, les glaciers alpins français ont perdu régulièrement de leur surface malgré une crue marquée entre 1915 et 1925. Entre 1941 et 1953, les glaciers ont subi des déficits importants à cause de précipitations hivernales réduites et d'importantes ablations estivales. Durant cette décennie, le glacier du Bosson perd 700 m de longueur (figures 7 et 8). Entre 1954 et 1981, les bilans de masse généralement positifs sont responsables d'une importante crue glaciaire (+ 300 m pour le front de la Mer de Glace, + 450 m pour le glacier d'Argentière et + 540 m pour les Bossons). Depuis 1982, les bilans de masse sont en déficit

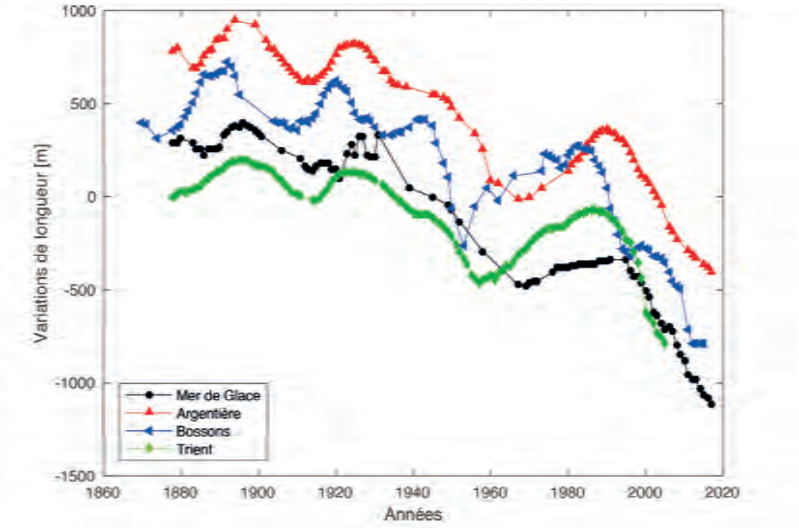

Figure 8. Évolution du front des glaciers de la Mer de Glace, d'Argentière, des Bossons et du Trient dans le massif du Mont Blanc (données Glacioclim).

(hormis deux années, 1995 et 2001), à cause d'un niveau élevé d'ablation estivale contrôlé par une augmentation des températures durant l'été (de 1,9 mètres à 2,8 mètres à 2 800 m d'altitude).

Ces bilans de masse négatifs sont le reflet d'une élévation de la limite des neiges permanentes, c'est-à-dire de la ligne d'équilibre glaciaire, d'environ 150 m dans les Alpes occidentales, mais variant fortement suivant les régions et les glaciers. À cette élévation en altitude correspond une augmentation de la température moyenne annuelle d'environ 2 °C depuis un siècle à Chamonix (1 °C à l'échelle de la planète).

À la Mer de Glace, le retrait du glacier s'est traduit par une perte d'épaisseur de 190 m en 150 ans au niveau de la gare du Montenvers (figure 8). Malgré tout, cette décrue a été interrompue par quelques avancées au XX^{e} siècle, dont la dernière entre 1970 et 1993. Depuis 1993, le recul du glacier n'a fait que s'accélérer (-700 m et une perte d'épaisseur de près de 70 m au niveau de la Grotte de Glace). Un premier lac est apparu au front en 1998 à l'intérieur des moraines déposées par le glacier en 1993, puis le glacier se retirant encore, un deuxième lac s'est formé en 2001 ; le contact de l'eau avec la glace a accéléré encore le recul du glacier. Au glacier des Bossons, le retrait considérable de la langue glaciaire est encore plus démonstratif, car bien visible aux regards des touristes et habitants de la vallée ; il atteint plus d'un kilomètre depuis 1885.

Une étude récente publiée par des chercheurs français de l'Université de Grenoble montre que, depuis 40 ans, la surface des glaciers des Alpes françaises a diminué d'environ 26 % (Vincent *et al.* 2005).

Les prédictions

Afin d'étudier l'évolution des glaciers dans le futur, les scientifiques utilisent des simulations numériques à l'aide d'outils mathématiques sophistiqués. Ces modèles numériques permettent alors de reconstruire l'évolution du climat dans le passé et de simuler celle du futur. Ces modèles sont basés sur les connaissances théoriques acquises sur la mécanique des fluides géophysiques, les lois de conservation de l'énergie et de l'eau. Des processus tels que les transferts radiatifs à la surface du glacier et la convection de la glace sont mis en équations. Ces modèles sont évalués sur leur capacité à reproduire le climat du passé et en particulier celui du XX^{e} siècle pour lequel on dispose de nombreuses séries météorologiques.

Depuis 1988, Le Groupe d'experts intergouvernemental sur l'évolution du climat (GIEC) est mandaté par l'ONU pour évaluer les informations scientifiques et les impacts socio-économiques potentiels liés au changement climatique. Leurs prédictions sur l'évolution du climat ne sont pas optimistes sur l'avenir des glaciers.

Ils interprètent le dérèglement de climat global comme une conséquence de l'activité anthropique depuis l'ère industrielle à travers une intense production de gaz à effet de serre. Afin de produire des simulations du climat dans le futur et d'évaluer les impacts sur les autres composantes de notre environnement (banquises, glaciers, végétation, niveau des mers etc.), la communauté scientifique s'appuie sur des scénarios d'émission de gaz à effet de serre au cours du XXI^{e} siècle dénommées *Represantative Concentration Pathway* (RCP) (figure 9). Le scenario RCP2.6, le plus optimiste, correspond à un forçage radiatif de 2,6 W/m^2 (pour information 1 W est la puissance développée par une ampoule lumineuse). À l'inverse, le scénario RCP8.5, le plus pessimiste, correspond à un forçage de 8,5 W/m^2. Le premier modèle prend en compte une société qui à réduit de façon drastique ses émissions, tandis que le second projette une société qui continue de croitre et à émettre sans se soucier des conséquences. Selon les compilations du GIEC, la température moyenne de l'air à la surface du globe devrait augmenter de 0,3 à 1,7 °C suivant le scénario optimiste (RCP2.6) et de 2,6 à 4,8 °C suivant le scénario pessimiste (RCP8.5). Ces chiffres représentent les températures moyennes des deux dernières décennies du XXI^{e} siècle (2081-2100) par rapport à celles de la période de référence 1986-2005.

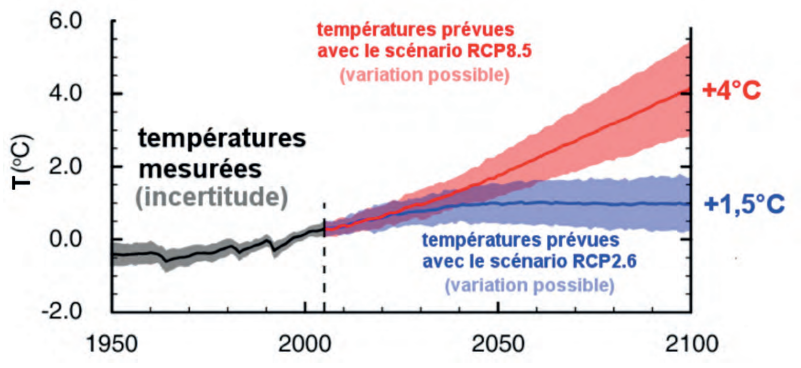

Figure 9. Températures historiques pour la période 1950-2005 et températures simulées jusqu'à 2100 par rapport à la période de référence 1986-2005. Plusieurs sorties de modèles ont été utilisées pour confectionner ces courbes. À droite, valeurs médianes des divers scenarios RCP pour la période 2081-2100 avec leur intervalle de confiance (GIEC, 2014).

Comme discuté ci-dessus, les glaciers alpins ont fortement diminué au cours du XX^{e} et début du XXI^{e} siècle. Les glaciers devraient donc continuer à décliner dans les années à venir. Zemp *et al.* (2006) ont estimé qu'une augmentation des températures estivales de 3 °C d'ici la fin du XXI^{e} siècle devrait entraîner une diminution de 80 % de la surface glaciaire des Alpes, et qu'une augmentation de 6 °C entraînerait la disparition totale de leurs glaciers. En ce qui concerne la Mer de Glace, le front glaciaire devrait reculer de 1 000 m à 1 200 m d'ici 2040, selon différents scénarios (+ 0 °C à + 4 °C de réchauffement sur un siècle). L'étude montre qu'à l'échelle de quelques décennies, les scénarios climatiques ne prédominent pas sur le retrait du glacier (figure 10). Paradoxalement, c'est son comportement passé qui conditionne les prochaines décennies. En effet, le glacier est en déséquilibre important avec le climat depuis trente ans, ce qui implique que sa surface doit se réadapter aux nouvelles conditions climatiques par une diminution appropriée. Par conséquent, ce déséquilibre implique que le glacier rétrécisse, même si les conditions climatiques restent stables à l'avenir. À l'échelle des trente prochaines années, le front reculera plus vite si le réchauffement s'accentue, mais à peine plus vite que si les conditions restent stables.

Conclusion

L'histoire des glaciers de la vallée de Chamonix est directement liée à l'évolution de la présence humaine dans les Alpes. De par leur proximité, ils furent d'abord craints, puis fantasmés par les artistes, et enfin étudiés sous tous les angles. Leurs observations firent naitre une science en constante progression, la glaciologie. Au cours des derniers 150 ans, les glaciers alpins ont perdu près de 50 % de leur surface. La Mer de Glace a perdu 190 m d'épaisseur au niveau du Montenvers et a vu sa langue glaciaire se retirer de plus de 1300 m dans la vallée. Les prédictions futures ne sont guère optimistes. La poursuite des mesures ainsi que le développement de nouvelles techniques d'observation sur les glaciers alpins est donc primordiale pour évaluer et s'adapter aux futurs changements.

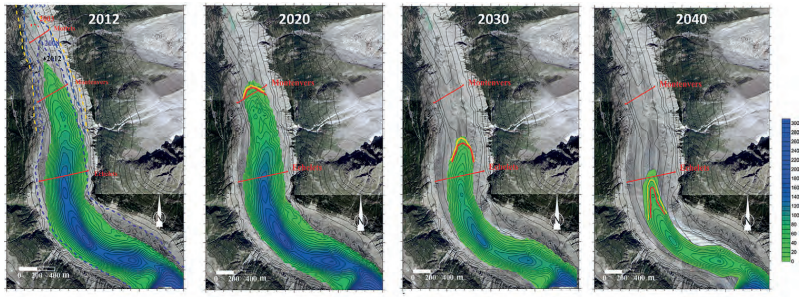

Figure 10. Évolution de la langue de la Mer de Glace depuis 1958 et simulations en 2020, 2030 et 2040, suivant les différents scénarios. L'échelle des couleurs représente les changements négatifs d'épaisseur de glace en mètre (Vincent *et al.* 2014).

Remerciements

Je remercie Delphine Six de l'Institut de Géosciences de l'Environnement (IGE, Université Grenoble Alpes) et le service d'Observation GLACIOCLIM (glacioclim.osug.fr) pour avoir mis à ma disposition leurs précieuses données. Je recommande aussi de consulter le site internet du Dr Sylvain Coutterand (glaciers-climat.com), ce site étant une mine d'informations sur les glaciers alpins du passé, du présent et du futur. Merci à Olivier Glaizot pour m'avoir donné l'opportunité d'écrire cette rétrospective. Finalement, merci à Cécile et Michel Lehmann pour leurs révisions ainsi que pour leurs conseils avisés dans la rédaction.

Bibliographie

Agassiz L., 1837. Discours prononcé à l'ouverture des séances de la Soc. helv. sci. natur. à Neuchâtel, le 24 juillet 1837, par L. Agassiz, président. Actes de la Société Helvétique des sciences naturelles, réunie à Neuchâtel, 22. sess., Neuchâtel. 5-32.

Fischer M., Huss M. & Hoelzle M., 2015. Surface elevation and mass changes of all Swiss glaciers 1980-2010, *Cryosphere*, 9: 525-540.

Gardent M., Deline P. & Schoeneich P., 2014. Inventaire et retrait des glaciers dans les alpes françaises depuis la fin du Petit Âge Glaciaire. Thèse de doctorat. HAL archives-ouvertes.fr. 455 p.

Mougin P., 1912. Études glaciologiques. Savoie - Pyrénées. Tome III. Imprimerie Nationale, Paris. 166 p.

Oerleman J., 2005. Extracting a climate signal from 169 glacier records. *Science* 308: 675-677.

Payot V., 1868. Oscillations des 4 grands glaciers de la vallée de Chamounix pendant le XIX^{e} siècle. *Bulletin de la Société Vaudoise des Sciences Naturelles* 9: 319-325.

Raup B., Racoviteanu A., Khalsa S.J.S., Helm C., Armstrong R. & Arnaud Y., 2007. The GLIMS geospatial glacier database: a new tool for studying glacier change. *Global and Planetary Change*. 56 (1-2): 101-110.

Rabatel A., Dedieu J.-P. & Vincent C., 2016. Spatio-temporal changes in glacier-wide mass balance quantified by optical remote sensing on 30 glaciers in the French Alps for the period 1983-2014. *Journal of Glaciology* 62 (236): 1153-1166.

Réveillet M., Vincent C., Six D. & Rabatel A., 2017. Which empirical model is best suited to simulate glacier mass balances? *Journal of Glaciology* 63 (237): 39-54.

Smiraglia C., Azzoni R. S., D'agata C., Matagno D., Fugazza D. & Diolaiutu G.A., 2015. The evolution of the italian glaciers from the previous data base to the new italian inventory. Preliminary considerations and results. *Geografia Fisica e Dinamica Quaternaria* 38: 79-87.

Vincent C., Le Meur E., Six D. & Funk M., 2005. Solving the paradox of the end of the Little Ice Age in the Alps, *Geophysical Research Letters* 32: L09706.

Vincent C., Harter M., Gilbert A., Berthier E. & Six D., 2014. Future fluctuations of Mer de Glace, French Alps, assessed using a parameterized model calibrated with past thickness changes. *Annals of Glaciology* 55: 15-24.

Zemp M.W., Haeberli M. & Paul F., 2006. Alpine glaciers to disappear within decades? *Geophysical Research Letters* 33: L13504.

Beaud, P & Beaud, E. 2018. *Les oiseaux nicheurs de la commune de Haut-Intyamon en Gruyère: Albeuve - Lessoc - Monthovon - Neirivue.* Cercle ornithologique de Fribourg (Fribourg, Suisse). 222 p.

En 2018, les médias ont attiré l'attention et ému la population en divulguant les résultats alarmants d'une étude scientifique : les populations d'oiseaux des campagnes françaises se sont réduites d'un tiers en quinze ans ! Ces résultats n'ont cependant pas surpris les scientifiques ou les ornithologues amateurs, ni les milieux de protection de la nature qui étudient l'évolution des populations et essaient de sensibiliser le grand public à la disparition des milieux et des espèces. Mais l'ampleur du phénomène a cette fois touché monsieur et madame tout le monde. En effet, les oiseaux, contrairement à d'autres groupes d'animaux aux mœurs discrets comme par exemple les chauves-souris, s'observent ou s'entendent facilement. Ils font partie intégrante de notre vie quotidienne. Ils ont la particularité d'attirer une foule de passionnés qui les observent et les recensent dans tous les pays du monde. La mise en commun des données récoltées par des ornithologues professionnels et amateurs des cercles ornithologiques régionaux regroupant des passionnés de tout âge, ont permis de réaliser en France cette étude à long terme aux conclusions alarmantes.

Le cercle ornithologique de Fribourg publie cette année un livre intitulé « Les oiseaux nicheurs de la commune de Haut-Intyamon en Gruyère » qui synthétise les observations ornithologiques récoltées depuis plus de vingt ans par deux ornithologues passionnés, Pierre et Eliane Beaud, avec la collaboration du biologiste Jérôme Gremaud. Ce travail bénévole est précieux car il nous renseigne, à l'échelle d'un petit territoire bien délimité regroupant les villages d'Albeuve, de Lessoc, de Montbovon et de Neirivue, sur les espèces d'oiseaux présentes et sur l'évolution de leurs effectifs.